# Flow Induced Electrification of Liquid Insulated Systems

by

Andrew Patrick Washabaugh

B.S.E., The University of Michigan, 1987
S.M., Massachusetts Institute of Technology, 1989
E.E., Massachusetts Institute of Technology, 1991

Submitted to the
Department of Electrical Engineering and Computer Science
in partial fulfillment of the requirements
for the degree of

Doctor of Science

at the

Massachusetts Institute of Technology

December 1994

© Massachusetts Institute of Technology, 1994
All rights reserved

Signature of Author _____
Department of Electrical Engineering and Computer Science
December 16, 1994

Certified by _____
Markus Zahn
Thesis Supervisor

Accepted by _____
Frederic R. Morgenthaler
Chairman, Departmental Committee on Graduate Students

MASSACHUSETTS INSTITUTE
OF TECHNOLOGY
APR 13 1995
ARCHIVES

To my parents,
Geraldine M. Washabaugh and
the late E. Peter Washabaugh, Jr.

**Flow Induced Electrification of Liquid Insulated Systems**

by

Andrew Patrick Washabaugh

Submitted to the Department of Electrical Engineering and Computer Science on December 16, 1994 in partial fulfillment of the requirements for the degree of Doctor of Science.

## Abstract

The transport or motion of semi-insulating liquids has led to flow induced static electrification and catastrophic failures in several industries. While techniques for reducing the hazard have been developed, the roles of seemingly important parameters are poorly understood. The objective of this thesis was to measure and understand the fundamental parameters of the flow electrification process that, together with the laws of electroquasistatics and physicochemical hydrodynamics, can be used to predict the performance of complex flow systems, with particular attention to transformer applications.

A rotating cylindrical electrode apparatus, which provided cylindrical Couette flow, was used to simulate flow electrification in an electric power transformer. The apparatus had Shell Diala A transformer oil filling the annulus between coaxial cylindrical stainless steel electrodes that were either bare metal, or covered by a thin copper sheet and/or EHV-Weidmann HiVal pressboard insulation. Extensive experiments characterized the time transient and steady state behavior of the electrification through measurements of the volume charge density, the terminal voltage, and the terminal current as the system was driven out of equilibrium by changes in the flow rate (inner cylinder rotation rates of 100-1400 rpm, Reynolds numbers of $5\times10^3$–$5\times10^5$), temperature (15–70°C), insulation moisture content (0.5–20 ppm in the oil), applied voltage (0–2 kV DC), and concentration of the non-ionizable anti-static additive 1,2,3 benzotriazole (BTA, 0–60 ppm).

Generally, the electrification increased with flow rate and temperature but the BTA appeared to cause competing effects: it decreased the volume charge density on the liquid side of the interface (by a factor of 4), which reduces the electrification, but also decreased the oil conductivity (by a factor of 10), which enhances the electrification. A critical oil BTA concentration of 5–8 ppm minimized the electrification. The volume charge density was sensitive to the current flowing through the interface and surface charge accumulation. With pressboard covering the cylinders, the electrification effects of the temperature and moisture were decoupled during the transient following step reductions in the temperature. The oil moisture content did not significantly affect the oil conductivity, but the volume charge density varied inversely with the moisture content during an initial equilibration period just after the oil had been added to the system. The greatest electrification was observed during this equilibration period.

Measurement techniques for monitoring the dielectric properties of the insulation were developed. Impedance measurements of an air-gap variable capacitor, immersed in the oil, at single (0.1 Hz) and multiple (5 mHz - 10 kHz) frequencies were used to determine the oil conductivity as a function of time as system variables, such as temperature, moisture and BTA concentration, were changed. At high oil conductivities

(above 5 pS/m), interfacial double layer effects were observed. The effective dielectric properties of the pressboard insulation in the rotating cylindrical electrode apparatus were obtained from time transient decay measurements of the short-circuit current or open-circuit voltage after disconnecting a DC voltage source from across the cylinders or stopping the rotation of the inner cylinder.

A physical model for the electrification, which used established representations for the interfacial charge transfer boundary condition, was developed. According to the model, the critical flow parameter is the thickness of the diffusion sublayer relative to the Debye length; the greatest electrification tends to occur when the sublayer thickness is small compared to the Debye length. Volume charge densities on the liquid side of the interfaces ($\rho^w$'s) of 1-20 mC/m$^3$ were estimated from the open-circuit data, with the stainless steel $\rho^w$ typically larger than that of the copper but smaller than that of the pressboard. Arrhenius temperature dependencies of 0.16 eV for pressboard and 0.25 eV for stainless steel were obtained. From the short-circuit data, the interfacial charge transfer reaction velocities, estimated to be of order $10^{-5}$ m/s, were not large enough to make the terminal current transport limited. This contradicts the often used assumption in the literature that the reaction velocities can be considered "infinite".

While this model was able to describe a wide range of experimental observations, it was not able to explain all of the data and an improved boundary condition for the interfacial charge transfer, based on interfacial chemical reactions, was developed. This boundary condition extended the established relations by including the effects of interfacial surface charge. A general methodology was developed for combining the volume and terminal measurements to estimate the parameters describing the interfacial charge transfer kinetics.

A system model was developed for electrification in a flow loop and investigated the volume charge accumulation due to recirculatory flow between a charge source and several charge relaxation regions. Enhanced charge densities were predicted when the source was a paper filter and the residence time in the relaxation regions was small compared to the liquid dielectric relaxation time. Small scale flow loop experiments verified the enhanced charge densities.

Thesis Supervisor: Markus Zahn
Title: Professor of Electrical Engineering

## Acknowledgments

The work described in this thesis was performed in the Laboratory for Electromagnetic and Electronic Systems and sponsored by the Electric Power Research Institute under the management of Mr. Stan Lindgren. The National Science Foundation also provided initial financial support through a Graduate Fellowship.

I am grateful to several faculty members for their contributions to this thesis. I want to thank Prof. Markus Zahn for his enthusiasm, support, and supervision. His comments and suggestions were instrumental in focusing this thesis. I also want to thank Prof. Alan Grodzinsky and Prof. Ain Sonin for participating on my thesis committee and providing useful discussions and suggestions throughout the thesis. Lastly, I wish to acknowledge the late Prof. James Melcher. His initial encouragement motivated me to participate in this area of research and he originally conceived the idea of recirculatory flow enhanced charge densities (Chapter 7).

The assistance of several research staff members is greatly appreciated. Mr. Paul Warren maintained the computers in the lab, provided general information about resources at MIT, and contributed practical experience to various experiments. Mr. Wayne Ryan maintained the flow loop facility, fabricated several components in the Couette facility, and was the "extra pair of hands" occasionally needed on the experiments. Mr. Rocco Albano also machined several components of the Couette facility. Mr. David Otten developed some of the data acquisition hardware and software used in this thesis. Dr. Eliot Frank wrote the plotting program Plop, used throughout the thesis.

I am also grateful for the help from various students in the lab, including Minerva Garcia, Dr. Neil Goldfine, Janet Lou, Dan Sobek and Yanko Sheiretov. Dr. Philip von Guggenberg deserves special recognition. His frequent questions and comments led to detailed discussions and provided useful insight into many aspects of this research project. One of these discussions led to the model developed in Appendix B.

Lastly, numerous family members, friends, and my "foster" lab group (the Continuum Electromechanics group) contributed greatly to keeping this thesis in perspective. I am especially grateful to Mike, Lisa, Kyle and Jenna for the (rejuvenating!) summer vacations in Maine.

# Contents

# List of Figures

# List of Tables

# Chapter 1

# Introduction

In several industries concerned with the transport or motion of semi-insulating liquids, catastrophic failures have been attributed to flow induced static electrification. In particular, in the electric power industry, static electrification appears to have caused more than two dozen failures of very large forced-oil-cooled transformers since 1983. With the cost of the unexpected power outage and transformer replacement being in the millions of dollars, prevention techniques are essential, but the conditions leading to transformer failure are not well understood. This thesis is an attempt at developing a fundamental understanding of problems caused by flow electrification, with a particular emphasis on transformers. This first chapter describes the objective of the thesis, the approach taken for accomplishing the thesis objective, and an outline for the remainder of the thesis.

## 1.1 Thesis Objective

The objective of this thesis was to measure and understand the fundamental parameters of the flow electrification process that, together with the laws of electroquasistatics and physicochemical hydrodynamics, could be used to predict the performance of complex systems, such as transformers.

Flowing insulating liquids, used for both heat transfer and electrical insulation, have led to failures of very high voltage forced-oil-cooled transformers. The flowing liquid causes the transport and accumulation of charge that can create electric fields which exceed the breakdown strength of the materials in the transformer. While techniques for reducing the electrification, such as lowering the flow rate, have been incorporated into the design and operation of the transformers, the processes that ultimate lead to failure and the roles of seemingly important parameters are poorly understood.

The key contributions of this thesis are the development of a well-monitored experimental facility for studying the charge and mass transfer dynamics involved in flow electrification and the methodology associated with correlating extensive electrification measurements to both physical and mathematical models. These contributions lead to a better understanding of the electrification processes inside a transformer so that hazardous conditions can be prevented. In addition, the techniques developed in this thesis are not limited to transformer materials and can be applied to the study of interfacial

kinetics in other electrolytic systems.

## 1.2 Research Approach

The thesis investigation essentially consisted of three phases: (1) an empirical investigation to determine how various critical parameters affect the electrification processes, (2) the development of experimental techniques and physical and mathematical models for studying the interfacial charge transfer kinetics in semi-insulating nonaqueous electrolytic systems, and (3) an investigation of recirculatory flow enhanced volume charge accumulation as a mechanism leading to system failure.

The first phase was concerned with developing a well-instrumented rotating cylindrical electrode experiment, the Couette facility (CF), in which transformer oil filled the annulus between coaxial cylindrical stainless steel electrodes that were either bare metal or covered by copper and/or pressboard (pb) insulation. This facility provides a compact, convenient and controllable system for studying flow electrification. Improvements of this facility over past experiments are:

1. All of the sensors for monitoring the critical parameters were located in the same well-mixed flow region so that transport effects between different sensor locations were eliminated. Such careful monitoring of parameters that cause competing effects on the electrification processes helps to explain apparently contradictory past work.

2. While most past experimental investigations determined the electrification behavior from a single type of measurement, such as the leakage current, the electrification process in the CF was monitored in several different ways: (1) through volume measurements of the net charge density in the well-mixed core region of the flow and terminal measurements of the (2) open-circuit voltage or (3) short-circuit current between the electrodes. Each method provides different information about the interfacial kinetics and allows the self-consistency between the measurements to be explored.

3. Simultaneous and continuous measurements of the electrification data and the critical material properties were performed. In the past, measurements of the oil moisture content and conductivity were only performed off-line when samples were withdrawn from the system.

Using the CF, extensive measurements were performed to determine the steady state and time transient behavior of the electrification data (volume charge density, terminal voltage, and terminal current) as the system was driven out of equilibrium by changes in the flow rate, temperature, insulation moisture content, applied voltage, and concentration of the additive 1,2,3 benzotriazole (BTA). A summary of significant results follows:

1. BTA acts as both an electrification and oil conductivity suppressant. While the decreasing conductivity increases the electrification, the long term effect of the BTA is a reduction in the electrification. The balance between these competing effects helps to explain the contradictory results in the literature.

2. Surface charge accumulation can influence the electrification charge transfer processes. Past work focussed on the effects of AC and DC energization but did not show that the surface charge accumulation from the electrification itself could influence the charge being generated by the electrification.

3. The mass transfer *dynamics* of moisture between the oil and pressboard insulation was measured as the system was driven out of equilibrium by changes in the temperature. These measurements could not be performed until sensors were developed that could continuously measure the oil moisture content during the transients, especially at low moisture levels, that appear to have led to transformer failures.

4. The effects of temperature and moisture on the electrification processes under *transient* conditions were separated. The oil moisture content only appears to affect the volume charge density during an initial equilibration period as the system becomes "conditioned." This helps explain past results where some measurements show a dependence on moisture content while others show little or no effect.

5. The greatest electrification was usually observed at high flow rates, high temperatures, and during the initial equilibration (or "conditioning") period after the system had been filled with oil. This equilibration period appears to correlate with transformer failures occurring during the start-up transients.

In the second phase, theoretical models were developed and compared to the experimental data to obtain information about the interfacial kinetics critical to the electrification processes. Physical and mathematical arguments were used to describe data covering a wide range of operating conditions, including both steady state and transient conditions. Significant results are:

1. A wide range of experimental measurements were fit to a model incorporating previously postulated boundary conditions for the interfacial current density. The general form of these boundary conditions, in which the interfacial charge transfer reaction rates are finite, was shown to be necessary through measurements of the volume charge density and the terminal variables as the terminal constraints were varied.

2. An improved boundary condition was developed to describe the accumulated surface charge effects on the interfacial current density. This boundary condition reduces to the previously postulated condition as a limiting case; the derivation provides a stronger physical basis for the interfacial dynamics.

3. A methodology was developed for using combinations of volume and electrical terminal measurements to estimate the parameters describing the interfacial charge transfer kinetics.

4. BTA was shown to reduce the volume charge density on the liquid side of pressboard/oil and stainless steel/oil interfaces.

In the third phase, a recirculatory flow loop experiment was developed and modeled to simulate some aspects of the electrification in a transformer. A "system" approach was used to model the flow electrification and flow recirculation was studied as a mechanism leading to enhanced volume charge densities and system failure. Significant results are:

1. A "system" approach for superimposing the electrification contributions of separate components into a "system" response, as in a transformer, was verified. In this approach, the volume charge density at the output of each section was used as the input to the next section.

2. The recirculatory nature of the flow led to enhanced volume charge densities under some conditions. Prior to the development of sensors that could unambiguously measure the volume charge density, this type of charge density enhancement could not be measured since earlier measurements required complete charge relaxation somewhere in the loop.

3. In actual transformers, the residence times in the sections of the transformer are long enough compared to the oil dielectric relaxation time that recirculatory flow enhanced volume charge densities are probably not significant.

A brief overview of the thesis is shown in the schematic of Fig. 1.1. To put the research involved in this thesis in context, the phenomenon of flow electrification is separated into the stages of charge generation, charge transport, charge accumulation and charge leakage. Taken together, these stages can lead to system failure if the charge leakage rate is too low. While the electrification stages typically overlap spatially and the individual stages are difficult to isolate, well-designed experiments can explore aspects of each stage while minimizing the contributions from the other stages. In this thesis, the charge generation stage is conveniently controlled and explored using the Couette facility and the (volume) charge accumulation stage is best explored in the Flow Loop facility.

The Couette facility was used to determine conditions which lead to the enhancement or reduction of the generated charge. Part of the experimental work involved developing instrumentation and techniques for monitoring apparently significant factors in field failures, such as the oil moisture content and the dielectric properties of the insulation. Once this instrumentation was in place, the electrification effects of a wide range of parameters were explored. These results were then used in electrification models to estimate some of the effective interfacial parameters and applied to transformers.

The Flow Loop facility was used to determine the electrification contributions from various components in a loop and the effects of *charge* recirculation. Theoretical models were developed for the individual components of the loop and then combined into a "system" model. The flow recirculation is observed to enhance the volume charge density when the charge is not allowed to relax completely at some location in the loop. Comparing the data with the model allows effective electrification parameters to be estimated and then applied to transformers.

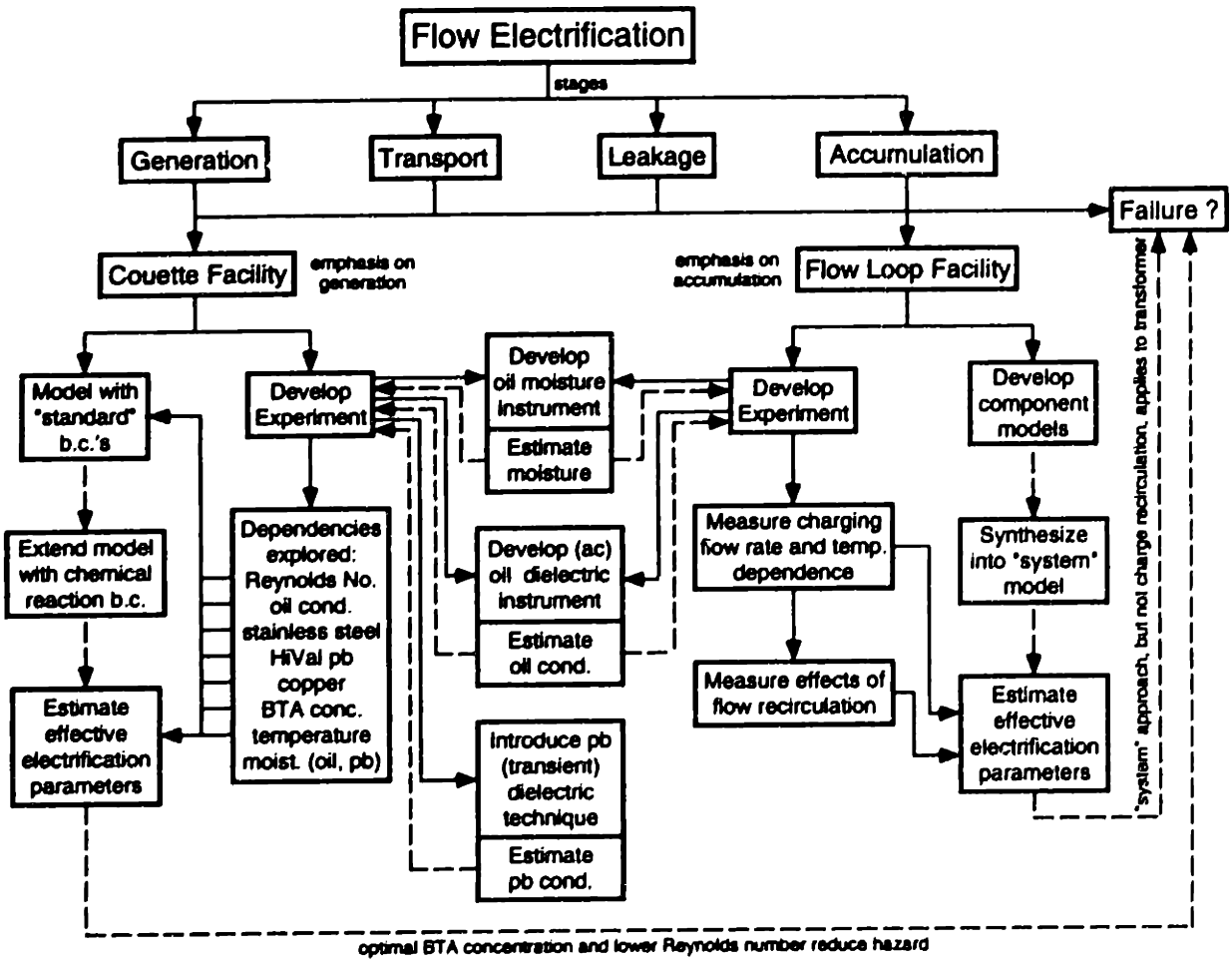


Figure 1.1: A schematic outline for the research described in this thesis. The solid lines indicate direct input and outputs between the various modules while the dashed lines indicate that calculated quantities or model results were being passed between the modules.

## 1.3 Thesis Outline

Chapter 2 provides a brief background of the basic electrification processes and a literature review of the experiences that several industries have had with electrification hazards. Because this thesis focuses on electric power transformers, considerable attention is given to the evidence for electrification in transformers and the research that has been performed in the electric power industry.

Chapter 3 describes the Couette experimental facility for studying flow electrification. The main motivation behind these experiments was to have a well-defined and controlled system for simulating the conditions that appear to have led to field failures of transformers. Extensive measurements of the electrification volume charge density, ter-

minal current, and terminal voltage are shown for a wide range of operating conditions. Conditions leading to possibly hazardous conditions are explored. The terminal current data is shown to be in good agreement with accepted relations from classical aqueous electrochemical experiments.

An essential factor in making the Couette facility well-instrumented was having the ability to continuously measure the oil moisture content at low moisture levels and to monitor the dielectric properties of the oil and the pressboard. The oil moisture measurement is addressed in Chapter 3. Chapter 4 provides a detailed description of the experimental techniques for determining the dielectric properties of semi-insulating materials.

In Chapter 5 a general theoretical model is developed for the electrification between rotating cylindrical electrodes using *previously postulated* boundary conditions for the interfacial charge transfer processes. Comparisons between the data and the model usually show good agreement under open-circuit conditions when the volume charge density on the liquid side of the solid/liquid interface is a constant, independent of flow rate, but poor agreement under short-circuit and energization conditions when the dynamics associated with interfacial reactions are significant. In Chapter 6 an improved boundary condition, which has a more physical basis than the postulated conditions, is derived and then incorporated into the electrification model. This model is then used to describe a wider range of data than the previous models.

Chapter 7 presents the Flow Loop facility and model. Similar to general transformer electrification models, the model superimposes the contributions from several components to obtain a "system" response. Enhanced volume charge densities by the flow recirculation are then experimentally verified and effective electrification parameters are estimated.

Chapter 8 highlights the major conclusions and provides a series of recommendations for future work. A series of appendices are then added to complement some of the ideas in the thesis and to document some of the experimental procedures. Several of the Appendices serve as support to other measurement methods of interest to the Electric Power Research Institute: Appendix A documented the BTA measurement protocols, Appendix B describes a model for the original version of the "Nilsson Plate," which is a leakage current probe for monitoring electrification in a transformer, and Appendix C describes a general calibration technique that was applied to the moisture sensors. Appendix D contains a model for charge relaxation in a pipe under laminar and turbulent flow conditions. Appendix E lists the primary computer programs used in this thesis.

# Chapter 2

# Background

Whenever two dissimilar materials are in relative motion, triboelectric charge can be created. If these materials are also insulating or parts of the system are electrically isolated, the charge can accumulate to create large electric fields and possibly hazardous situations. Indeed, several industries have had catastrophic failures attributed to liquid flow induced electrification. This chapter provides an overview of the fundamental concepts and physical mechanisms involved in flow electrification. A literature review of the manifestations of electrification in various industries is also presented.

## 2.1 Basic Electrification Processes

The process of flow electrification can be separated into four stages: generation, transport, accumulation, and leakage [1]. In the generation stage, charged species can be created by chemical reactions in the bulk region of the fluid and at the interface between the fluid and the solid. In most systems, there is typically a preferential adsorption of one of the charged species at the interface with the opposite polarity species diffusely distributed throughout the fluid. When the fluid is stationary, this equilibrium separation of the charge carriers is called the electrical double layer. When the fluid is in motion, some of the distributed charge from the double layer is entrained in the fluid flow and transported downstream where it can accumulate on insulating surfaces, on conducting but electrically isolated surfaces, or in the fluid volume. The charge accumulates until the charge leakage rate balances the charge accumulation rate or a spark discharge occurs.

The stages of electrification are identical to those found in a Van de Graaff generator in which an insulating belt transports charge from a corona source to a conducting dome. The charge can accumulate on the dome until the accumulation rate balances the leakage rate to ground or a discharge occurs. However, unlike the Van de Graaff generator, the stages of flow electrification are not necessarily spatially distinct and most factors, such as the temperature, are involved in more than one stage [2]. This coupling of the stages makes it difficult to isolate the individual stages that are occurring in many structures, such as pipes, ducts, pumps, and filters. Nevertheless, most structures can be categorized according to their net contribution to the fluid volume charge density as the fluid flows through them, as either a charge generator if the charge density increases or

a charge relaxer if the charge density decreases. While this categorization is useful when trying to understand the role of each component in a flow network, it doesn't necessarily lead to a better understanding of the dynamics occurring inside each structure. Indeed, the categorization of some structures may be influenced by other factors such as the temperature or the contamination level from impurities.

In order to get a better understanding of the various processes involved in flow electrification and possibly predict the effects of various factors, numerous models have been developed. These models describe the interactions between the chemical, electrical and fluid mechanical processes that are occurring. For example, the generation and recombination of the various charged and neutral species in the liquid volume and at the interface between the liquid and the solid are described by chemical reactions. Since some of the species from these chemical reactions carry a net charge, the laws of electroquasistatics are necessary to describe the concomitant electric fields. The laws of fluid mechanics then describe the resulting transport of the individual species by the fluid flow.

Several fields, such as physicochemical hydrodynamics and colloid chemistry have focused on the interdisciplinary nature of processes similar to flow electrification. Usually these fields are concerned with aqueous solutions where the electrical double layer has a significant effect on the interfacial dynamics and also on measurements of the bulk properties. Because of the importance of the double layer, the general term *electrokinetic phenomena* has been coined to describe the interaction of an electric field with the mobile charge in the double layer [3]. Electrokinetic phenomena have been classified according to the interfacial material that is moving (the liquid or the solid) and whether the motion is driven by an electric field or an electric field is created by the motion. The case in which an electric field is created by a liquid flowing past a stationary surface has been termed the streaming potential or streaming current. From this description, it is clear that flow electrification is a subset of what can be considered electrokinetic phenomena. However, the liquids of interest in electrification hazards tend to be nonaqueous rather than aqueous so the research results from these other fields are not always directly applicable.

## 2.2 Electrification in industry

Several industries have had to address the problems and hazards posed by flow electrification. This section describes the relevant experiences of the petroleum industry, the electric power industry, and the automotive industry, all of which involve the flow or transport of semi-insulating liquids.

### 2.2.1 Petroleum industry

One of the first industries to identify flow electrification as a serious hazard was the petroleum industry. Numerous explosions during fuel handling operations, occasionally resulting in fatalities, could not be attributed to any mechanism other than flow electrification [4,5]. In this industry, some of the various hydrocarbons liquids refined from crude oil are insulating when in a pure state. The transport of these insulating liquids between storage tanks and/or vehicles allowed for significant charge to accumulate in the

liquid volume, at the surface between the liquid and vapor spaces, and even on the container itself if the container was not grounded. With the vapor above the liquid typically combustible, if a spark of sufficient energy discharges through the vapor an explosion results.

Several factors were found to compromise the safety of any particular fuel transfer or mixing operation. These included the fluid flow rate, the fluid conductivity, and the moisture content of the fluid [4]. More specifically, as the flow rate increased, the net charge being entrained and transported by the fluid also increased. The dependence on the fluid conductivity was found to have two competing effects. As the conductivity increased, the number of charged species available for transport by the flowing fluid also increased, but the time for the charge to relax decreased, reducing the distance over which the charge could be transported before being neutralized. The net result was that significant charge accumulation only occurred over an intermediate regime of fluid conductivity where there was enough charge to be separated by the fluid flow and the relaxation time was large enough for charge to be transported over an appreciable distance. Finally, while water was not found to be a problem in low concentrations, the presence of the water led to hazardous conditions when its volume fraction with respect to the hydrocarbon liquid was on the order of a few percent. Subsequent investigations found that water in trace amounts could significantly increase the charge being generated without raising the fluid conductivity appreciably [6].

To eliminate the hazard, ionizable additives were developed to greatly increase the liquid conductivity even when added in trace amounts (mass fractions on the order of parts per million) [4,7]. Because of the quantities of liquid involved in the industry, only additives that significantly increased the conductivity when present in trace amounts were considered feasible.

Several other techniques were also explored to eliminate the hazard, but these had limited applicability. For example, the "Static Charge Reducer" was a passive technique for reducing the charge density in the fluid, essentially consisting of a section of pipe that had grounded needle electrodes sticking into fluid [8]. By placing the reducer downstream of a charging element, such as a filter, the high fields associated with a charged fluid around the electrodes caused the opposite polarity charge to be injected into the fluid, thereby reducing the net charge density. While this worked satisfactorily under some conditions, it was susceptible to contamination and there was no guarantee that it would reduce the charge density in the fluid under all operating conditions.

An active technique for reducing the charge density was also developed [9]. This technique consisted of measuring the streaming current from a short pipe section, to infer the net charge density in the liquid, and injecting opposite polarity charge from an upstream set of electrodes. Using the streaming current, the appropriate voltages could be applied to the electrodes to cancel the charge already present in the fluid. One of the difficulties with this instrument was that the measured streaming current results from charge relaxation in the pipe section. As the fluid becomes more insulating, less charge relaxation occurs so that the charge cannot be determined very easily and the necessary voltage to be applied to the electrodes is unclear. While better instruments for measuring the charge density have been developed [10,11], these active techniques will probably not become widely used because they only apply to a local operation while the

additives reduce the electrification hazard over a much larger portion of the distribution network.

### 2.2.2 Electric power industry

As the population increases and the demand for electricity increases, electric utility companies have been forced to design and construct compact electric power apparatus that operate at higher power levels. This has led to the use of new dielectric materials, changes in the chemical composition of insulating liquids used to transfer heat and withstand high electric stress, an increase in flow speeds for greater cooling, and, unfortunately, electrification problems [12].

Numerous failures of very high voltage forced-oil-cooled transformers have been attributed to flow electrification [13–15], causing disruptions in the distribution of electric power and an appreciable financial burden on the utilities [16,17]. In these transformers, insulating oils are used for both electrical insulation and heat transfer, with the oil recirculated from the windings of the transformer to heat exchangers so that the transformer can be operated at higher power levels. With paper cellulose pressboard providing an insulating support structure for the windings and the oil itself being insulating, it is possible for significant charge accumulation to occur. Significantly, factory measurements show **electrostatic discharges in unenergized transformers** [18], which indicates that at least some of the discharge activity is not associated with the applied voltage.

A schematic representation of the oil flow paths in a transformer is given in Fig. 2.1. The oil flow is typically driven by pumps into a baffle and a plenum region beneath the windings. Flow stops and channels then direct the oil flow across the layered sections of the copper windings and pressboard insulation. The oil is then collected in a header region and transported through a heat exchanger. To help put the large size of these transformers in perspective, these high voltage transformers usually contain on the order of 10,000 gallons of oil and have numerous (five to eight) pumps that are typically rated at about 800 gpm. A more detailed schematic of the exit flow region at the top of the windings, which has essentially the same geometry as the entrance region at the bottom of the windings, is given in Fig. 2.2. Although the geometry of the pressboard insulation in a transformer is complex, the figure attempts to illustrate the three-dimensional nature of the oil flow paths. Layers of pressboard insulation are used to guide the oil flow across the faces of the windings. Along the sides, the pressboard insulation ends at a "45°" line, going from the core to the (rounded) corner of the pressboard washers. The outermost pressboard layers are blocked to prevent oil from flowing through the layers and also staggered (in width) to guide the oil through openings in the insulation. The oil then follows a tortuous path across the ends of the insulation washers until it is next to the pancake windings of the transformer. The flow is then prevented from going upward by flow blocks (and the core) and must go around the core, along the windings and the pressboard washers. Numerous pressboard spacer blocks provide mechanical support and create tortuous flow paths along the face of the washers and local regions of well-mixed secondary flows that may also enhance the electrification.

A representative sketch of a pressboard washer is given in Fig 2.3. The most prominent discharges in failed and test transformers appear as subsurface channels ("wormholes")

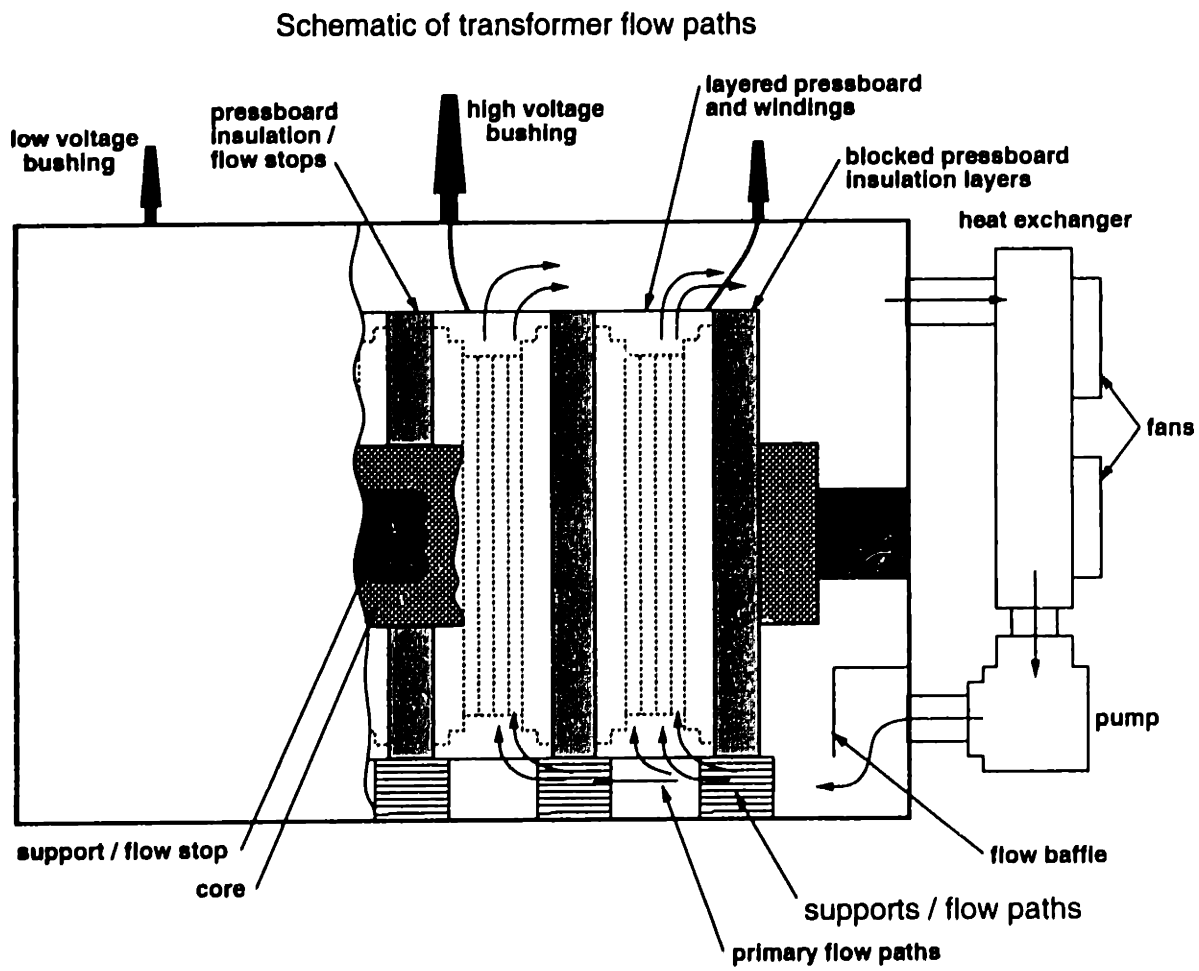


Figure 2.1: Representative flow paths in a transformer.

and surface tracking along the surface of the pressboard [13,20]. This activity appears to be concentrated at the "45° line", at the entrance flow region, where the pressboard insulation along the sides of the washer ends. Most of this activity has been along washers **that are blocked**, so that the oil doesn't go along the face of the washers. Although this may be due to flow leakage paths for the oil along these washers, it is likely that the local turbulence in the plenum region leads to enhanced electrification. Furthermore, earlier transformer designs, which appear to have electrification problems, had washers extending a significant distance into the plenum region [19], which enhances the turbulence.

Electrification in field transformers appears to be most significant when a cold transformer is being brought on-line and when the transformer (oil and pressboard insulation) is considered "dry" [14,18,21]. Laboratory experiments simulate some of this behavior and show that the electrification charge density increases as the temperature increases [22–26], just as a transformer heats up when it is energized. The dependence of the charge density on the moisture content of the insulation is not as clear though. While numerous bench-top experiments have shown that the charge density decreases with in-

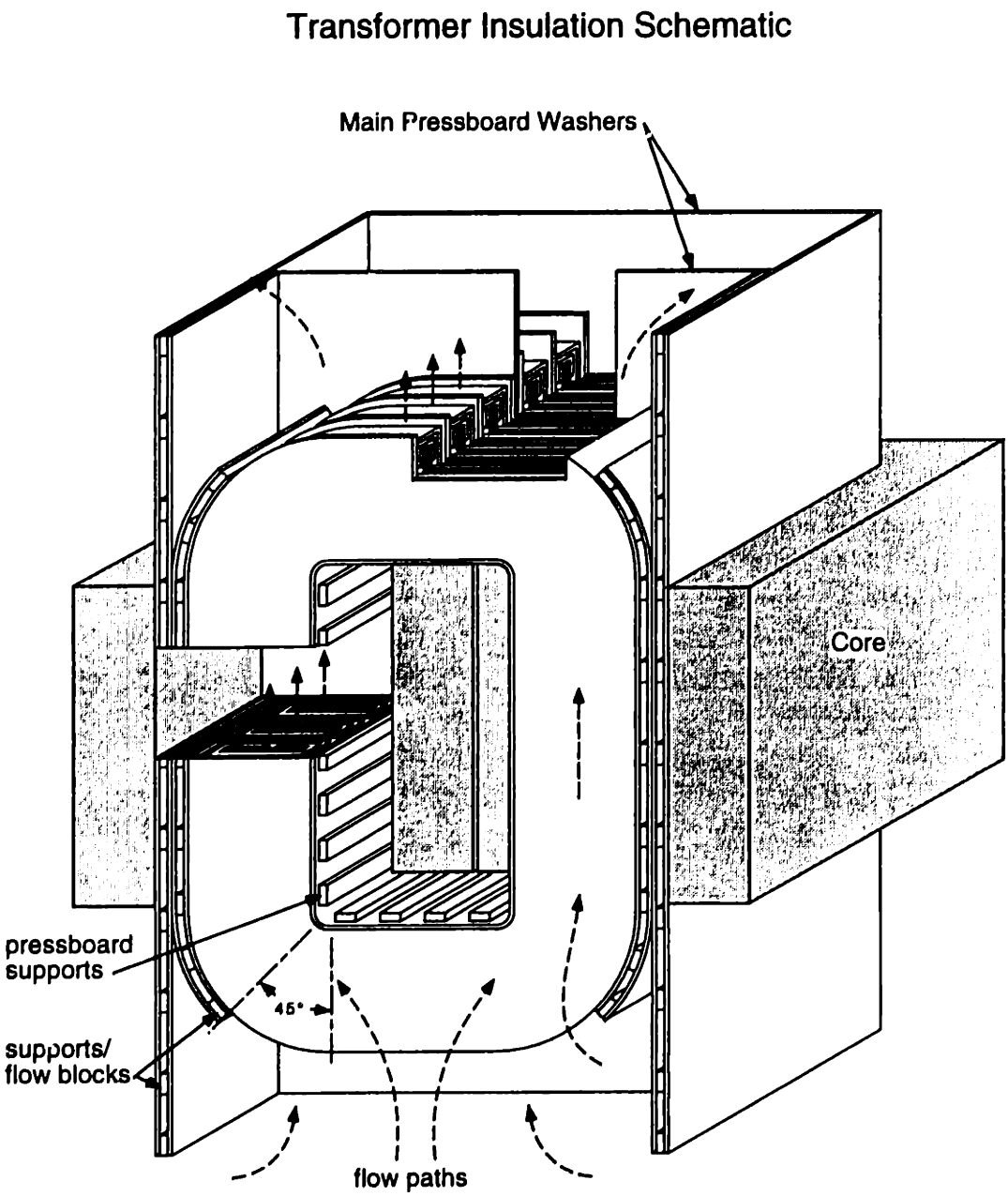


Figure 2.2: Detailed schematic of the windings and insulation of a single phase of a shell type transformer, after [19].

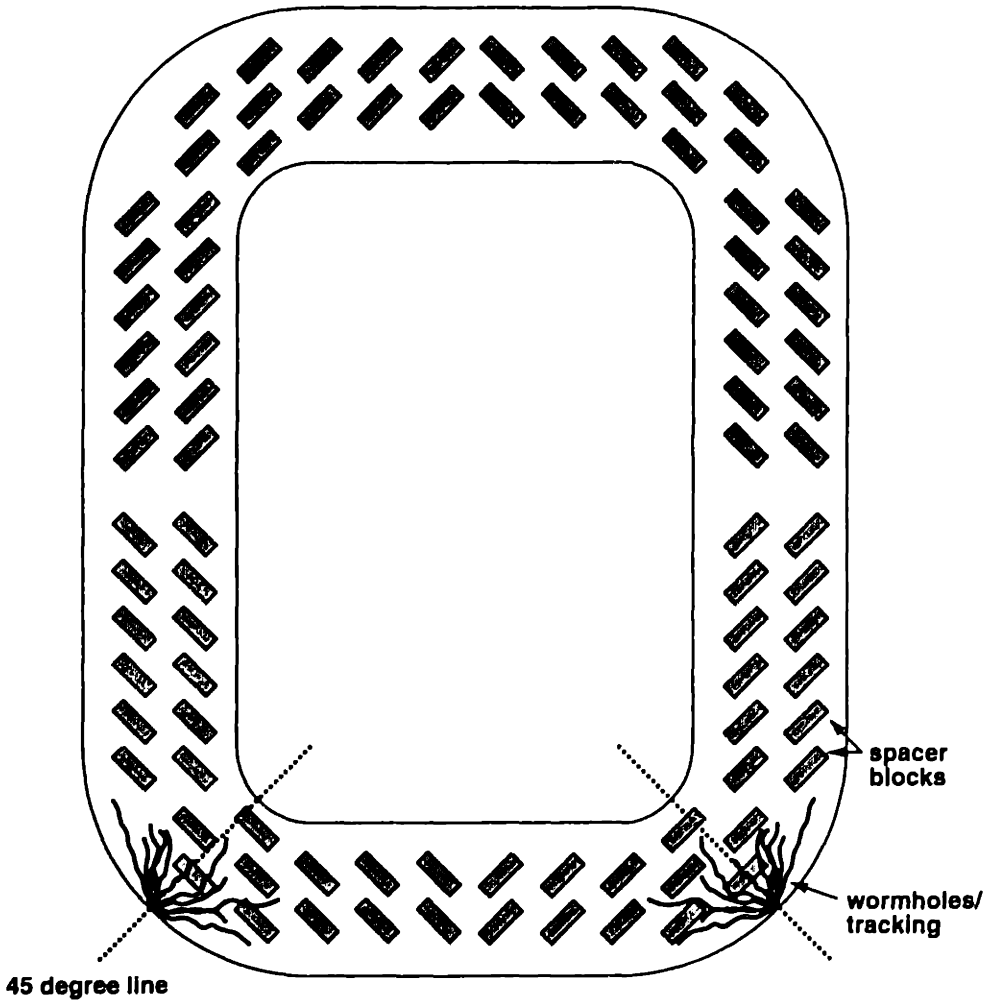


Figure 2.3: A schematic view of a pressboard washer, showing the spacer blocks and the regions of significant discharge activity.

creasing moisture content [2,22,23,26,27] and a peak in the charge density sometimes occurs, where the charge density increases with the moisture content at low moisture levels [28], others measurements have shown that the charge density is essentially constant with insulation moisture content [29,30].

While there is still some uncertainty whether "dryer" conditions lead to increased charge generation and larger charge densities, it is well known that moisture plays a role in the accumulation and leakage processes. For example, the dielectric loss of the pressboard increases significantly with increasing moisture contents and temperatures [17]. In fact, the reduction in the dielectric loss has been used advantageously in the manufacture and operation of transformers; by vacuum drying the transformers, less electric power is dissipated in the insulation and the transformer has a higher operating efficiency. Even though "dryer" insulation leads to reduced electrical leakage and higher operating efficiencies, it also leads to increased charge accumulation, exacerbating the

electrification problem. As to the oil insulation, there are indications that increased oil moisture content increases the oil conductivity [29,30], but other measurements showed the conductivity being essentially independent of the moisture content as the moisture was varied from 12 to 57 ppm at room temperature [31].

The moisture dependent losses of the pressboard in contact with the oil may also play a significant role in the accumulation of charge during the startup transient of a transformer. During this transient, when the insulation is being heated, moisture is transferred from the pressboard to the oil, creating a relatively dry zone at the pressboard/oil interface [17,32]. This dry zone can be highly insulating and allows for significant charge accumulation to occur. Evidence of surface discharges along pressboard surfaces in the entrance region to the transformer windings has been found [13] and discharges from the oil volume to the pressboard surfaces have been observed in the header region as the oil exits the windings [30].

Another important factor for electrification in transformers is the energization of the windings. Laboratory experiments have shown that energization causes an increase in the electrification charge density [2,24,25] and the leakage current [33–36]. When the AC energization is superimposed with the DC field created by the flow electrification, it is possible for the total field to exceed the breakdown strength of the insulation.

As in the petroleum industry, one possible solution to the electrification problem is to place additives into the oil. In this case, raising the conductivity of the oil to increase leakage is not an option because the oil needs to remain electrically insulating in order to maintain the integrity of the apparatus, which in this case means the high breakdown strength of the insulation and the low electric power dissipation. Ideally, the additive should eliminate the electrification hazard without raising the conductivity and without having any other deleterious effects. One such additive, 1,2,3 benzotriazole (BTA), has been promoted by several Japanese utilities because it appears to reduce electrification, as evidenced by a reduction in the streaming current measured from the windings to ground, without affecting the conductivity [30]. Many utilities have been reluctant to use BTA, though, because its role in reducing the electrification is not well understood. In actual transformers, the BTA concentration in the oil has been found to decrease with time [30,37], indicating that the BTA is being absorbed by the solid insulation, adsorbed onto the various material surfaces, or decomposing. The streaming current from the windings also decreases with time, possibly because of BTA being adsorbed onto the solid insulation, but it is not clear if the streaming current would have decreased without the addition of the BTA.

Laboratory measurements which studied the effects of BTA on the electrification charge density also produced mixed results. In some of the original experiments used as proof that BTA reduces the electrification charge density, the charge density decreases monotonically with increasing additive concentration (from a positive level toward zero), while other experiments taken over the same range in concentration show the charge density decreasing from a positive level, passing through zero, and becoming negative, with a magnitude that increases with BTA concentration [30]. Early laboratory measurements showed that the BTA had little [38,39] or no [23,27] effect on the electrification process, but subsequent measurements have shown that the BTA causes the charge density to become smaller or more negative [40] and long term effects of the BTA can cause

a reversal in the temperature dependence of the charge density, so that it decreases as the temperature increases [41]. In addition, data with several types of paraffinic oil has shown that the BTA causes the charge density to become more positive, independent of the polarity of the charge density without any BTA, and reduces the oil resistivity [42]. This suggests that the concentration of BTA that is necessary for reducing the charge density to zero depends upon the initial charge density in the oil and care must also be taken to maintain the electrical integrity of the insulation.

Another additive, alkyl benzene, has also been suggested as an electrification suppressant [30,42]. It has not been studied as extensively as BTA, but it appears to reduce the charge density when present in relatively large quantities such that the mass fractions of the alkyl benzene and oil are comparable. In contrast, the BTA is only used with a mass fraction of order 10-100 ppm.

In lieu of an additive that consistently reduces the electrification charge density, the main technique for reducing the hazard is to lower the flow velocity of the oil through the transformer [13,30]. The flow velocity can be lowered by automatically controlling the pumps so that the pumps are only operational when the transformer needs the cooling capability and by redesigning the flow pattern so that lower flow rates result in the same heat transfer. Additionally, attempts are being made to determine "low-charging" oils, but there is no understanding of what makes an oil "low-charging" and there is no guarantee that the oil will remain "low-charging" under all of the operating conditions of a transformer.

### 2.2.3 Automotive industry

Recently, flow electrification has become a concern in the automobile industry [43,44]. With the increased usage of polymeric materials that can be easily manufactured and installed in automobiles, automobile manufacturers are finding it economically advantageous to replace many of the metal components in the fuel transfer system, such as the fuel lines, fuel pumps and filter housings, with polymeric components [45,46]. These polymeric materials tend to be sufficiently insulating that charge can accumulate and the potential can rise high enough for spark discharges to occur. Even though gasoline is doped with additives to raise its conductivity, the leakage of charge through the liquid is insufficient for preventing the accumulation of charge. This problem was not as significant when metal components were used throughout the fuel system because all of the components were grounded and significant voltages could not arise to create spark discharges. On the other hand, if, for example, polymeric fuel lines are connected to a metal filter and the filter is not grounded externally, the electric potential of the filter and the potential distribution along the insulating pipes can rise.

Although a recent minor recall was prompted by electrification while the cars were being fueled [44], problems resulting from electrification in these fuel transfer systems generally only occur under extreme conditions such as very low temperatures. When discharges do occur, their energy tends to be insufficient to cause an explosion. But repeated discharges at the same location degrade the materials and eventually lead to "pinhole" failures and fuel leakages. Depending upon the location of the leak, a hazardous condition can still result.

One promising technique for eliminating this hazard is to raise the conductivity of the polymeric components so that significant charge cannot accumulate. Even though additives are currently used in these polymers for creating the desired mechanical properties such as toughness, stress resistance, chemical inertness, and resistance to swelling [45,46], additives for raising the electrical conductivity have not been very successful; the additives tend to be unstable and leach out of the polymers. While raising the conductivity of the gasoline is an option, it is not practical due to the tentative nature of the hazard and the inherent costs of doping the fuel with more additives. Of course, it may also be more economical to return to the use of grounded metal fuel system components.

# Chapter 3

# Electrification Measurements in a Couette Facility

In order to study the flow electrification, a well-instrumented rotating cylindrical electrode experimental facility was developed. This facility provides a compact, convenient and controllable system for monitoring the effects of a wide variety of parameters on the electrification processes. This chapter describes the primary experimental facility for the electrification measurements, the experimental approach, the application of newly developed sensors, and representative results.

## 3.1 Introduction

Fundamental to any description of flow electrification is the charge transfer process that occurs at the interface between the liquid and the solid phases. In essence, it is the preferential adsorption (or difference in interfacial reaction rates) of one of the charged species that leads to the generation of the electrical double layer and it is the diffuse charge in the electrical double layer that is transported by the fluid to accumulate or leak away at a downstream location. As a result, in order to develop a comprehensive understanding of flow electrification, it is important to characterize the solid/liquid interface. For example, one technique for studying interfacial charge transfer processes, developed in the field of electrochemistry, is to measure the current that flows between a stationary electrode and a rotating disk electrode [47] or a rotating cylindrical electrode [48,49]. This terminal current can be related to parameters that describe the chemical reaction, such as rate constants, if the reacting species and the fluid flow profile are known.

Experiments with rotating electrodes are advantageous over stationary electrode or pipe flow experiments because they allow the kinetic processes at the electrodes to be studied under steady state and fully developed flow conditions. The rotating electrode imposes a fluid flow profile that dominates the convection caused by the motion of the individual charged species in an electric field. For rotating disks, the fluid flow is stable up to high Reynolds numbers and laminar flow conditions are generally studied. In contrast, for rotating cylinders, the flow becomes unstable at low Reynolds numbers and turbulent flow conditions are usually studied. In electrochemistry, aqueous electrolytic

solutions having well-defined ionic species are usually treated. With the electrode material also known, the oxidation-reduction reaction that occurs at the interface can then be formulated. This chemical reaction describing the interfacial mass and charge transfer, coupled with the equations that describe the transport of the reacting species to the interface, can then be related to the terminal current [48].

The rotating electrode technique for studying interfacial kinetics in electrolytic solutions has also been used to study the charge separation process of flow electrification in non-aqueous semi-insulating liquids [2,25,50–56]. While many of the fundamental concepts apply to both aqueous and non-aqueous systems, there are two significant differences. First, aqueous liquids tend to be much more conducting than the semi-insulating hydrocarbon liquids being considered here. This increased conductivity in aqueous liquids leads to increased charge relaxation so that the net charge density in the bulk of the fluid flow is near zero and interfacial properties must be inferred from terminal current measurements. For the semi-insulating liquids used in electric power apparatus, the net charge density in the bulk region of the fluid flow, the terminal current, and the terminal voltage can be measured and related to the interfacial properties [2,10,11]. Second, while the identity of the ionic species are usually known apriori in aqueous solutions, the ionized species of interest in flow electrification problems with insulating liquids are usually formed by trace impurities. The unknown composition of these trace impurities leads to inherent difficulties in creating reproducible measurements; one way to account for this complication is to use experimental materials that are the same as those typically used in electric power apparatus.

This chapter describes an experimental investigation of flow electrification in a rotating cylindrical electrode system in which the effects of various parameters, such as temperature, moisture concentration, oil conductivity, terminal constraints, energization and additive concentration, on flow electrification are explored. Section 3.2 presents preliminary measurements with newly developed sensors and methodologies. Based on these initial measurements, the experimental facility was then improved as discussed in Section 3.3, with Section 3.4 providing a comprehensive summary of the experimental results. As mentioned earlier, these measurements are similar to those performed in aqueous electrochemical systems; a comparison between them is made in Section 3.5. Section 3.6 provides a concluding discussion.

## 3.2 Preliminary Measurements

In order to get the base-line response of the system, several initial measurements were performed with newly developed sensors incorporated into an existing facility. This section describes the original experimental facility and presents some preliminary results.

### 3.2.1 Experimental apparatus

To simulate the flow electrification processes in a transformer and to study the effects that the oil and pressboard properties, such as moisture content, conductivity, and tem-

perature, have on these processes, a Couette experimental facility (CF) was developed[1]. The CF had transformer oil filling the annulus between coaxial cylindrical electrodes that were bare metal (stainless steel in this work) or covered with sleeves of other materials, such as copper and/or pressboard insulation. The inner cylinder could rotate at speeds giving controlled turbulent flow so that electric charge was transported from the electrical double layers at the solid/liquid interfaces to the volume of the fluid and the mass transfer of moisture between the oil and the pressboard was enhanced. By measuring the charge density in the liquid, the voltage across the cylinders and the current flowing between the cylinders, the electrification processes under various operating conditions could be studied. Similarly, by measuring the moisture in the oil as the operating conditions are changed, the mass transfer dynamics between the oil and the pressboard could be studied.

### Couette facility

The original CF, as shown in Fig. 3.1, consisted of a Couette charger (CC), which contained the rotating cylindrical electrodes, two units for monitoring the oil properties, and a reservoir for the oil [2,25]. A small recirculatory flow rate was imposed so that the oil from the CC passed by the sensors in the units, with the fluid flow going from unit 2, to the CC, to unit 3, to the reservoir, and then returning again to unit 2. The CC and the reservoir were equipped with heating tape and a cooling coil such that the temperature was controlled from 15°C to 100°C. The units were only equipped with heating tape, so their temperatures could only be maintained at levels above ambient. The system contained 3.0 gal (11.4 l) of transformer oil, with the CC containing 2.0 gal (7.5 l) and each unit 0.5 gal (1.9 l). A nominal flow rate of approximately 1 ml/sec for recirculation of the oil throughout the system gave a residence time for one pass through the system of 3.2 hours and a residence time for oil in the CC of 2.1 hours.

In this facility, the inner cylinder had a radius of 7.62 cm, the outer cylinder had a radius of 10.16 cm, and the cylinders had a height of 0.4 m. For these particular experiments, both cylinders were covered by 0.040 inch (1 mm) thick EHV-Weidmann HiVal™ pressboard insulation. The gap between the cylinders was filled with Shell Diala A transformer oil. To create a measurable volume charge density inside the oil, the inner cylinder was rotated at angular rotation rates up to 2000 rpm. For transformer oil, rotation rates greater than about 60 rpm leads to turbulent flow in the oil-filled gap between the cylinders [25]. In turn, the mixing due to the turbulent flow led to a region of essentially uniform charge density (for the semi-insulating hydrocarbon liquids of interest here), which could then be measured.

The pressboard and oil were vacuum processed to the dry conditions found in actual transformers by pulling a vacuum on the system and raising the temperature. The drying time was based on previous experience in drying the pressboard. Typically, the CC and units were kept at a pressure of 0.1 to 0.25 Torr and a temperature of 90°C for a few days while the reservoir was kept at 0.1 Torr and 70°C for a few hours. After the drying

[1]The facility was named after M. Couette (1890), who studied the shear flows between concentric rotating cylinders and parallel plates, which is now generally known as "Couette flow" [57].

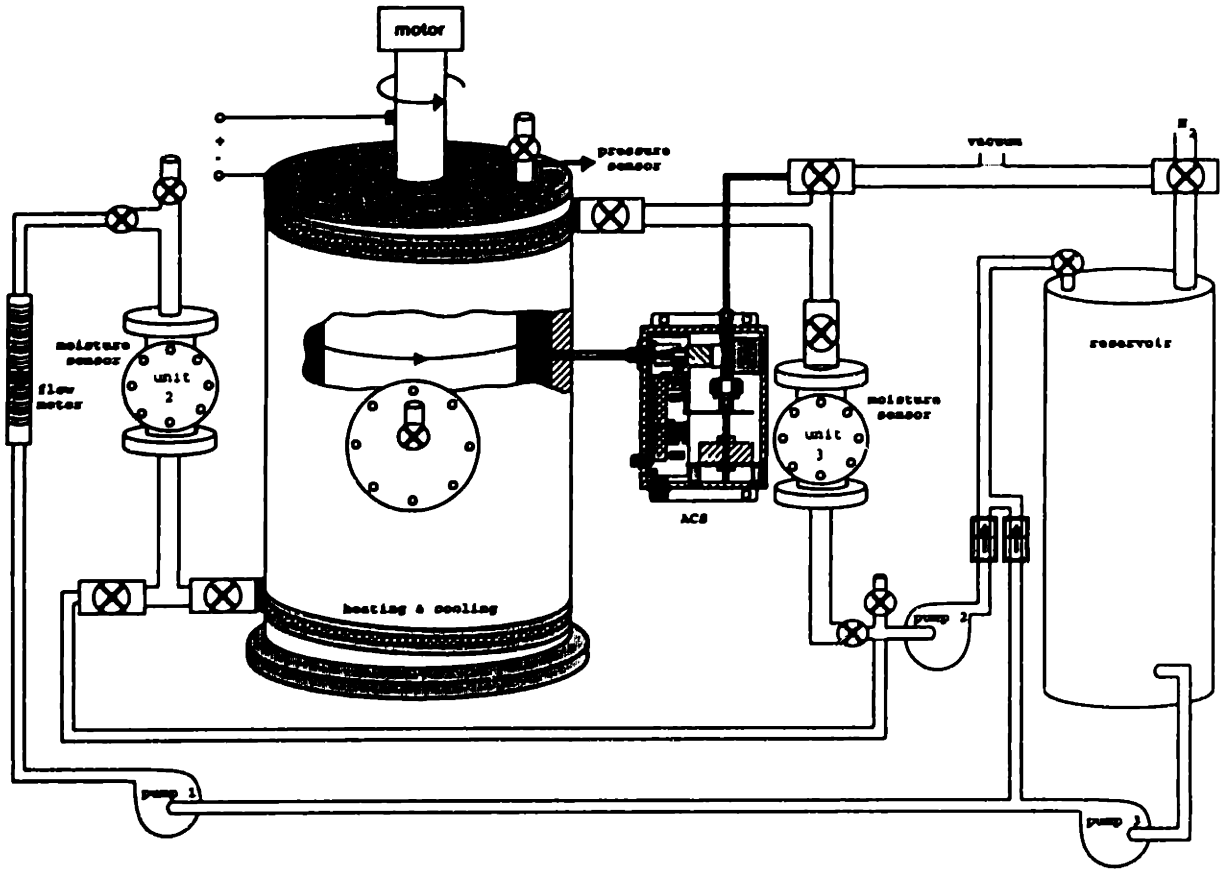


Figure 3.1: The original Couette facility. An Absolute Charge Sensor (ACS) was used to measure the charge density in the oil region between the coaxial cylinders of the Couette charger (CC). Moisture sensors were installed in unit 2 and either in the CC or unit 3. A flex sensor was mounted in unit 2 for oil conductivity measurements. From [25].

process was completed, the pressboard was oil impregnated by backfilling the units and the CC with the oil from the reservoir. Sacrificial samples of pressboard were placed in the units and used to measure the moisture content of the pressboard after the impregnation process using the water vaporizer accessory part of a Mitsubishi CA-05 Moisture Meter (MM).

The charge density in the oil between the cylinders was measured using an Absolute Charge Sensor (ACS), which brings a sample of fluid from the turbulent core of the CC into a Faraday cage [11]. The ACS sampling probe was mounted so that its end was flush with the edge of the outer cylinder (metal or pressboard) that was in contact with the oil (to within 1 mm). In this position, the sampling probe should have had a minimal effect on the electrification process being studied. The terminal voltage and current were measured using a Keithley 614 electrometer.

In addition to the ACS and the electrometer, sensors for monitoring the oil conduc-

tivity, oil moisture content, and temperature were incorporated into the CF. A data acquisition program (**cf6.bas** in Appendix E) was used to take the measurements and periodically set the rotation rate of the inner cylinder. Typically, an entire set of measurements took about 3 minutes with most of the time spent on the charge density and conductivity measurements. Since some of the sensors were newly developed, their application into the facility required special considerations, as discussed below.

### Conductivity measurements

The conductivity of the oil was measured with an interdigital electrode structure (flex sensor) mounted in unit 2 [17]. Initially, the sensor was only used for periodic measurements but, in later experiments, the conductivity measurement was incorporated into the data acquisition program so that the conductivity could be monitored continuously. This conductivity sensor has one set of electrodes driven at a 1 V peak, 5 mHz to 10 kHz AC voltage, while the other set of electrodes, the sensing electrodes, measure a signal that is attenuated and phase delayed with respect to the driven signal. The measured signals depend upon the permittivity and conductivity of the oil and were used in a parameter estimation routine to calculate the oil conductivity [58].

### Oil moisture measurements

The oil moisture level was measured using two techniques. The first technique was to occasionally withdraw samples of oil from both units and to measure the moisture content with the MM, which performs a Karl-Fisher titration. This technique is accurate for moisture contents above 1–2 ppm. Since one of the goals of this research was to understand the electrification process at low temperatures where the moisture levels can be below 1 ppm, another method for measuring the moisture was required.

The second technique was to continuously monitor the moisture level in the oil using newly developed polyimide-based capacitive humidity sensors [17,59] that were originally produced by Hy-Cal engineering for relative humidity measurements in air but are also being developed by J.W. Harley, Inc for use with transformer oil. For these preliminary experiments, a Hy-Cal CT-880-BN-H (0/100%)-X instrument was used. The instrument essentially consists of a moisture sensor that is connected to a housing for circuit electronics through a probe. The electronics measures the slight change in capacitance (a few pF) as moisture is absorbed or desorbed into the sensor. The output signal from the electronics, which varies from 4 to 20 mA, was sent through a 250 Ω load resistor to give a signal range of 1 to 5 V.

In the measurements discussed here, one Hy-Cal instrument was mounted so that the sensor was placed in the inlet unit to the CC, unit 2. A second sensor was mounted so that the moisture sensor was first placed in the outlet unit from the CC, unit 3, and later in the oil-filled gap between the rotating cylinders. (To be placed inside this gap, the probe that connects the sensor to the instrument electronics was passed through the top flange of the CC.) The second sensor was moved into the CC so that the moisture measurements would more accurately reflect the moisture dynamics inside the CC, which was found to be particularly important during imposed temperature transients. The moisture sensor

placed in the oil-filled gap was in a well-mixed region of turbulent flow. As a result, this sensor could quickly reach moisture equilibrium with the oil and respond rapidly to any time transients in the system. In contrast, the units were not well-mixed by the slow recirculatory fluid flow and the moisture sensor in unit 2 took a long time to reach equilibrium with the oil around it. This time delay for equilibrium to be reached after a step change in temperature was measured to be on the order of an hour. Thus, the moisture sensor in unit 2 only responded accurately to transients varying on time scales longer than an hour.

The output voltage from these instruments is linearly related to the relative saturation of moisture in the oil, with an empirical calibration used to find the slope and offset of the line. Once the relative saturation was known, the absolute moisture content was determined from the product of the relative saturation and the solubility of moisture in the oil. For example, the solubility of moisture in Shell Diala A transformer oil can be expressed as

$$x^s = x_o e^{-E_a/T} \tag{3.1}$$

where $x^s$ is the mass fraction of moisture in the oil at saturation, $x_o$ and $E_a$ are constants for the oil, and $T$ is the temperature in $K$. For Shell Diala A oil, $x_o = 15.6 \times 10^6$ ppm and $E_a = 3680$ K [17,59]. When used properly, these moisture instruments have an estimated accuracy of 1% of the saturation moisture content in the oil.

Although the calibration relating the instrument voltage to the relative saturation of oil was a straightforward process, the calibration was found to change under some conditions. The calibration involved measuring the oil moisture content with the MM and the corresponding output voltage from the Hy-Cal instrument for numerous oil temperatures and moisture contents. After converting the absolute moisture contents into relative saturation values (by dividing by the solubility), a least squares fit was used to determine the calibration slope and offset. A technique for setting the calibration parameters was also developed, as discussed in Appendix C.

Usually, the moisture instrument calibration was performed in a reaction vessel outside of the CF and then the instruments were installed in the CF when the moisture measurements were to be performed. However, by comparing the MM moisture contents with those predicted by the Hy-Cal instruments, it was found that the calibration shifted when the instruments were mounted in the facility and when the temperature of the instrument electronics was changed. In an attempt to compensate for these calibration shifts, in situ calibrations were performed in which the instruments were mounted in the facility and then calibrated against moisture samples taken throughout the duration of the experiments. When the moisture sensors were placed in the units, the output voltages were calibrated against moisture samples taken from the unit in which the sensor was placed. When the sensor was placed inside the CC, the output voltage was calibrated against the moisture levels from samples taken from unit 3, on the outlet of the CC.

Subsequent investigations of the Hy-Cal instrument correlated the calibration shift with the mounting process to a change in the effective capacitance in the cable connecting the sensor to the electronics. The change in capacitance was caused by a compression of the probe housing by a Swagelok™ fitting, which in turn compressed MgO powder between the probe housing and the cable, and finally compressed the cable itself. Also,

the calibration shifts with the instrument electronics temperature could be compensated by measuring the electronics temperature and calibrating for the temperature changes. Based on this better understanding of the operation of the moisture instruments, later experiments used calibrations from the reaction vessel outside of the CF, which tended to be more accurate than those done in situ because a wider range of moisture levels could be obtained.

### Temperature measurements

While measurements of the temperature were straightforward, care had to be taken to ensure that the measured temperatures were meaningful. The initial experiments discussed here followed the work of previous researchers [25,60] with the CC oil temperature measured with a thermocouple probe that was passed through the wall and pressboard on the outer cylinder of the CC so that the probe tip penetrated about 1 mm into the oil. Later experiments with a thermocouple probe inserted into the center of the oil-filled gap of the CC showed that the oil temperature could be different than the temperature measured at the outer wall by more than 10°C. Accurate measurements of the temperature are important because the temperature is used to relate the oil relative saturation to the absolute oil moisture content and in the equilibrium curves describing the partitioning of moisture between the pressboard and the oil [61].

Thermal gradients in the CC were significant when attempting to maintain the system at temperatures below ambient with high rotation rates as the heat caused by the viscous shear of the rotating inner cylinder became appreciable, or during imposed temperature transients. Because the oil was well-mixed, these gradients occurred across thin boundary layers at the oil/pressboard interface. At the elevated temperatures, where the oil temperature was greater than that caused by the viscous shear alone, the steady state thermal gradients in the CC were small. For example, when the outer wall temperature was at 71°C, the oil temperature was measured to be 69°C. Extrapolation of this thermal gradient to the inner cylinder gives an estimated temperature of 67°C, which is not significantly different than the outer cylinder temperature. In contrast, when the nominal CC temperature was set to 15°C (at the outer wall), the oil temperature was measured to be closer to 20°C at a rotation rate of 1000 rpm. The inner wall is then estimated to be at 25°C. To minimize the effects of the temperature gradients, the oil temperature was measured through the top flange of the CC and the experiments were performed at rotation rates and temperatures which cause the heat generated by the viscous shear to be negligible. For example, the inner cylinder rotation rate was generally kept below 800 rpm at 15°C.

## 3.2.2 Representative results

Two sets of representative results are presented here. The first set presents the transient electrification charge density and moisture content as the temperature is changed. The second set has the temperature and moisture decoupled so that the effects of the moisture alone can be investigated.

### Transient measurements during step changes in temperature

The data shown in Fig. 3.2 was an attempt at simulating the start-up temperature transient in a transformer. In this experiment, the rotation rate was 1000 rpm and the pressboard had a moisture content of 0.7%, based on the weight of the pressboard before impregnation. The oil conductivity was measured at the end of the experiment to be 7.5 pS/m at 70°C.

Over the first 300 hours, the CC temperature was maintained at 15°C, the charge density decreased slowly from 30 $\mu C/m^3$ to 15 $\mu C/m^3$, and the oil moisture level in unit 2, at the CC inlet, decreased from 5.4 ppm to 1.1 ppm. From the equilibrium curves relating the oil and pressboard moisture contents, the oil moisture level should have been 0.7 ppm, which is in reasonable agreement with the measured steady state value [61]. The time constant for the initial decrease in the moisture level is probably related to the residence time for the wet oil in the units and the reservoir to be replaced by dry oil from the CC. The difference between the residence time of about 1.7 hours and the decay time in Fig. 3.2 being on the order of 20 hours, is probably due to the units not being well-mixed.

There was also a long time transient, on the time scale of 100 hours, that may be attributed to the oil and pressboard in the CC approaching their equilibrium moisture levels. Since the oil in the CC was well-mixed by the turbulent flow, the limiting time constant was the diffusion time for moisture in the pressboard. With the oil moisture level higher than its equilibrium value, there was a mass transfer of water from the oil into the pressboard, creating a "wet zone" at the oil/pressboard interfaces that is the inverse of the previously predicted "dry zone" [17,32]. Alternatively, since there were stagnant flow regions in the units, this long time transient may also be the result of moisture redistribution in the units, where moisture from the initially "wet" oil slowly diffused out of the stagnant regions.

At hour 310, the temperature was increased to 70°C. Both the charge density and the moisture level followed the temperature transient. The rapid increase in the moisture response was surprising because the moisture sensors were located in the units and the moisture level was expected to increase up to its steady state value with a time constant similar to that observed during the drying phase of the experiment. While it is possible that the moisture measurement during the transient was flawed by the sensor not being in a well-mixed region and the measured oil temperature not being the actual sensor temperature, the moisture level tracked with the MM after the temperature stabilized, which lends some confidence to the measurement. One explanation for the rapid increase in moisture during the transient is that the relatively "wet" oil from the stagnant flow regions was mixed into the remainder of the oil in the unit because of increased thermal convection as the temperature was raised above ambient.

At this elevated temperature, the charge density went from a peak value of 211 $\mu C/m^3$ immediately after the transient to an apparent steady state level of 54 $\mu C/m^3$. The moisture level went from a peak value of 6.7 ppm to about 4.6 ppm. These measurements show that the effects of the temperature and moisture on the charge density were coupled in this experiment. While it may appear that the moisture and charge density were related in this test, the results are not definitive because the moisture was measured in

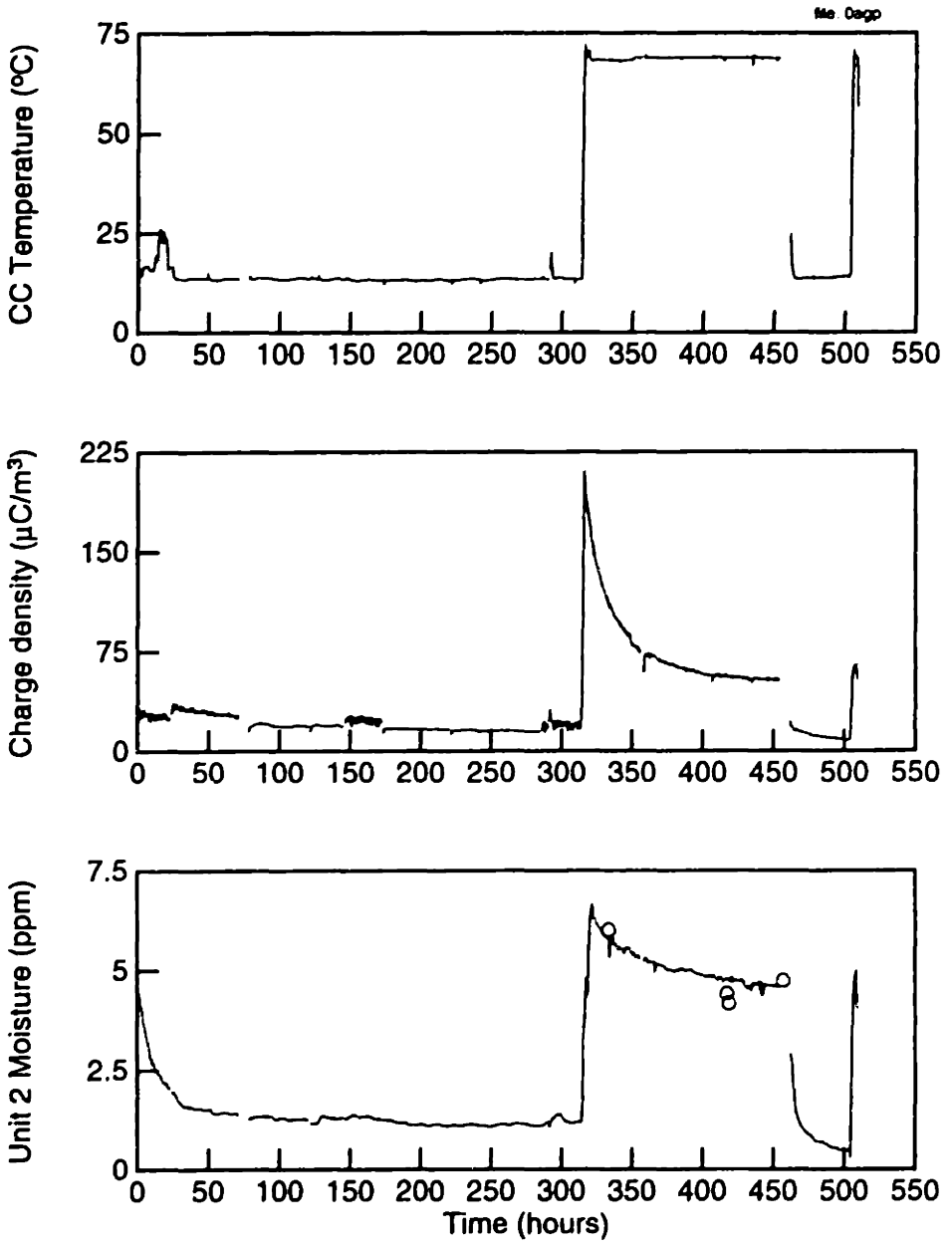


Figure 3.2: Imposed temperature transient data for HiVal pressboard covering both cylinders, Shell Diala A transformer oil and a rotation rate of 1000 rpm. The conductivity was only measured at the end of the experiment and was 7.5 pS/m at 70°C. The circles are oil moisture levels obtained with the MM. The gaps in the data occurred when the data acquisition program was restarted.

a unit and the charge density was measured in the CC. Moisture measurements in the outlet unit, unit 3, (not shown in Fig. 3.2) showed an initial drop in the moisture level after the temperature transient which steadied to a constant level while the moisture measured in unit 2 continued to decrease. Thus, it is possible that the moisture content in the CC remained constant in the CC, even as the moisture content in unit 2 decreased. Indeed, the decreasing moisture content may be due to the residence time for oil to be convected into unit 2 or, since the moisture level in unit 2 was measured after the oil passes through the reservoir, the vapor space above the oil in the reservoir may have been drying the oil.

As a check of the reproducibility of the measurements, the system temperature was lowered to 15°C at hour 455. As in the beginning of the experiment, once the temperature reached a steady state, the charge density and moisture continued decreasing, with the charge density going down to 8 $\mu C/m^3$ and the moisture level going down to 0.5 ppm. Both of these values are lower than what they had been before the elevation in temperature, indicating that the charge density and the moisture level depend upon the past history of the system. Then, another step increase in temperature to 70°C showed that the charge density and moisture once again tracked with temperature, going to 65 $\mu C/m^3$ and 5.0 ppm, respectively. Again, these values are lower than what had been observed in the first temperature transient, but they appear to be the same as the values that they had just before the previous step down in temperature.

### Transient conditions at a constant temperature, I

The previous experiment showed that the charge density changed greatly during the temperature transient, but the effects of the temperature and oil moisture content on the charge density could not be separated because the moisture content also depends upon the temperature. This next experiment was an attempt to decouple the effects of the temperature and the moisture on the charge density by keeping the temperature constant and monitoring the charge density as the pressboard dried the moist oil.

In this experiment, attempts were made to dry the system as much as possible. New HiVal pressboard was installed on the cylinders and sacrificial pressboard samples were placed in unit 2. After oil impregnating the pressboard with oil dried in the reservoir, the moisture content was found to be near 0.2%, based on the weight of the pressboard before oil impregnation. A series of tests were then performed to check the sensors and to qualitatively verify the previously observed effect of temperature transients on the charge density. For reference, with the inner cylinder stationary the system temperatures were then set to 15°C and one gallon of fresh oil (moisture content of about 20 ppm) was then added to the reservoir and recirculated through the system. After waiting eight hours to ensure that the system had reached thermal equilibrium, the data shown in Fig. 3.3 was obtained.

The data of Fig. 3.3 shows that the charge density transient was related to a mass transfer process, possibly only that of moisture, between the oil and the pressboard because the temperatures in the system remained constant. This conclusion holds, even though there were steady state temperature gradients in the system. The temperature gradients in the CC itself due to viscous heating were negligible because temperatures

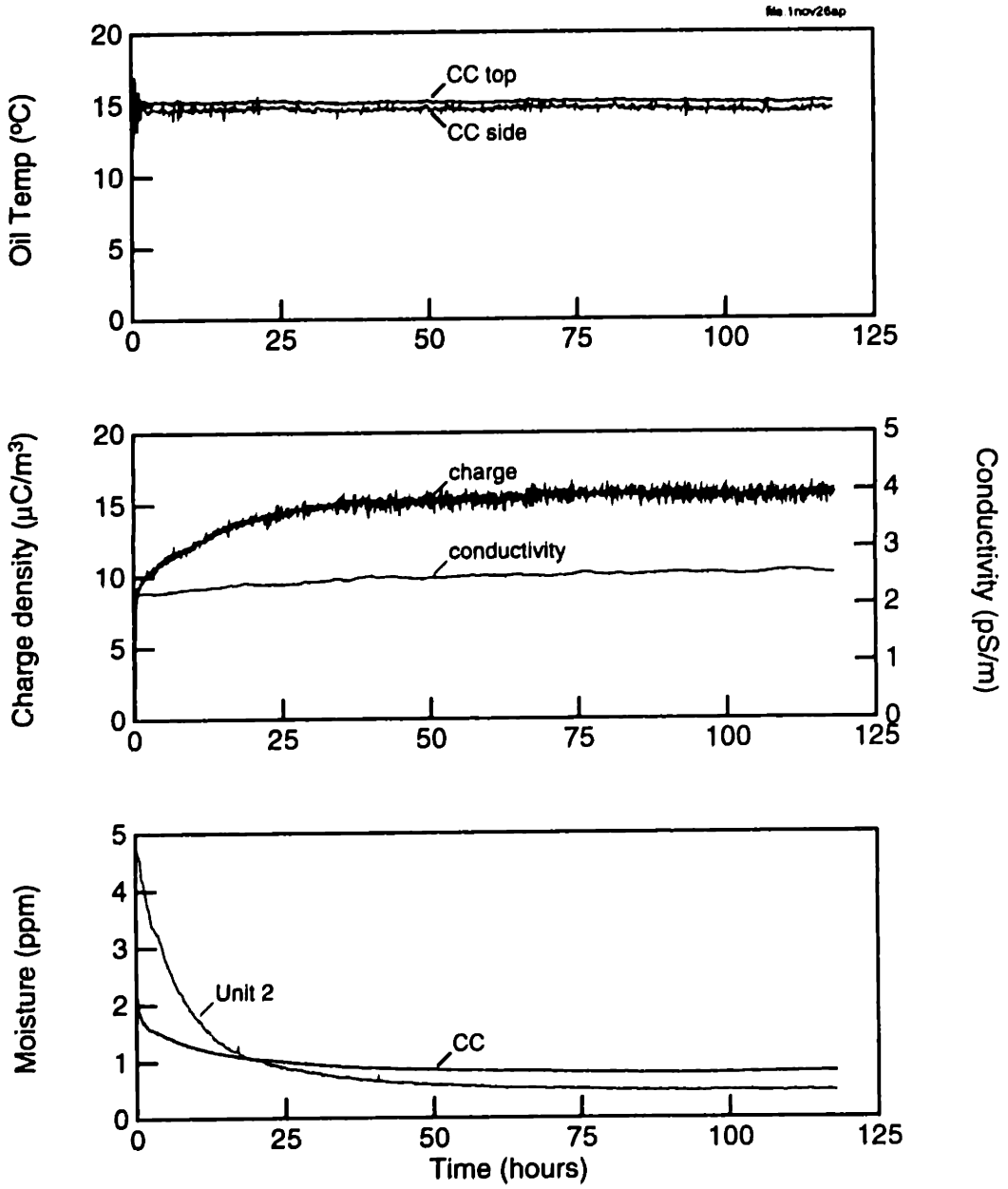


Figure 3.3: Initial 15°C equilibration for HiVal pressboard (0.2% moisture content) covering both cylinders, Shell Diala A transformer oil, and a rotation rate of 400 rpm. The temperature of the oil in the gap between the cylinders (CC Top) and that of the wall (CC Side) were constant at 15°C. The temperature of unit 2 was nearly constant at 29°C. The charge density and CC moisture levels had transient time constants of about 25 hours. The oil moisture levels were measured with the MM just before the start of the run to be 9.9 ppm in unit 2 and 1.7 ppm in unit 3.

measured in the CC top and side were the same. But the temperature of unit 2 was at 29°C and a recirculatory flow of 1.4 ml/sec transported the warm oil into the cooled CC. Since the temperatures did not change with time, the observed transient in charge density results from the mass transfer transient, indicated by the moisture measurement.

During this experiment, moisture was transferred from the oil to the pressboard. The high initial moisture content resulted from the system being operated at elevated temperatures during prior measurements and from fresh oil being added to the reservoir, which typically had a moisture content greater than 10 ppm. As expected, the moisture transients in the CC and unit 2 were different because the moisture in the unit depended upon the residence time for the oil in the unit and the dryness of the oil entering while the oil moisture in the CC depended on the dryness of oil entering and the diffusion time for moisture in the pressboard. Even if the moisture in the CC remained constant, the moisture in the unit could have a transient with a time constant dominated by the oil recirculation time. If the equilibration process between the moisture levels in the oil and the pressboard was very slow compared to the residence time for oil to flow through the system (which was on the order of a few hours), both moisture levels should have decreased with similar transients, which appears to have happened here.

Prior to the start of this experiment, the flex sensor response in air indicated that the sensor was slightly contaminated. To reduce the error caused by the contamination, the sensor was operated at a frequency of 0.1 Hz, where the contamination had a minimal effect on the response in air. Fig. 3.3 shows that the oil conductivity slightly increased over the duration of the experiment, as the oil moisture content decreased. This indicates that water was not the primary dissociating species responsible for the oil conduction at these moisture levels; otherwise the conductivity and moisture should have varied in the same direction. Undoubtably, other species were involved in the mass transfer and moisture was only one of them.

In the steady state, the moisture level should have been constant throughout the system. The measured levels of about 0.8 ppm (1.8% rS) in the CC and 0.5 ppm (1.1% rS) in unit 2 are reasonably close and within the accuracy of the instrument. These measured values are also very close to the level of 0.2 ppm (0.45% rS) based on the equilibrium curves relating the oil moisture content to the pressboard moisture content [61]. The measured values are higher than the equilibrium level probably because the oil was equilibrating with a thin interfacial zone and not the bulk of the pressboard.

### Transient conditions at a constant temperature, II

While the previous experiment showed that the moisture dynamics could be decoupled from the temperature, the flow recirculation through the system and steady state temperature gradients between different system components complicated the interpretation of the data. In the next series of experiments, the charge density and moisture dynamics were measured at a constant temperature with the recirculatory flow eliminated by valving off the CC from the rest of the system. While this meant that the conductivity of the oil could not be measured (because the flex sensor was in unit 2, not the CC), it allowed for the charge density dependence on moisture to be explored without the complicating effects of the flow recirculation. These tests used the same materials as those

of the previous experiment, with fresh oil (about 20 ppm moisture content) added to the reservoir.

In each of these experiments, the inner cylinder was kept stationary as the temperature was set. Then, the relatively wet oil from the reservoir was circulated through the system, which raised the average moisture content of the oil in the CC. After closing the valves to the CC, preventing any flow recirculation, the inner cylinder was rotated and the electrification data was taken. In each case, the oil temperature was measured in the gap between the CC cylinders. In Figs. 3.4 and 3.5, the temperature was below ambient and the charge density was constant while the oil moisture content decreased as the pressboard dried the relatively wet oil. In Figs. 3.6 and 3.7, the temperature was higher than ambient and the charge density, terminal current, and oil moisture content appeared to have similar transients. This data indicates that the charge density does not depend strictly upon the oil moisture content, at least at low temperatures.

Also shown in Figs. 3.6 and 3.7 are the transient effects associated with shutting off the rotation of the inner cylinder. Although the charge density went to zero quickly, the terminal current reversed polarity and then decayed slowly. The charge density decayed with the oil relaxation time, which is short on this time scale. On the other hand, the electrification current caused surface charge to accumulate at the oil/pressboard interfaces and electric fields to develop inside the pressboard. As will be discussed in Chapter 4, the decay of surface charge at the oil/pressboard interfaces has a time constant that depends upon the dielectric properties and the geometry of each of the layers. With the pressboard relaxation time long compared to the time scale of these measurements, the terminal current also had a relatively long time constant. The terminal current reversed polarity as the system went from being charged (by the action of the fluid flow) to being discharged, where the fields inside the system decayed. This is analogous to monitoring the terminal current as a Maxwell-Wagner capacitor is first charged by a current source and then discharged through a short-circuit.

### 3.2.3 Discussion

These preliminary experiments showed that the moisture dynamics, charge density and terminal current are strongly influenced by the temperature. While the interpretation of some of the data is complicated by the instrumentation and the system, several important observations can be made. First, the mass transfer of moisture between the pressboard insulation and the transformer oil essentially followed that expected from the equilibrium curves, with the time transients at high temperatures rapid compared to the experimental sampling time but slow at low temperatures. Second, the charge density and oil moisture content did not consistently track with one another during time transients. This may have resulted from the charge density being more sensitive to some other impurity being transferred between the oil and pressboard or perhaps the moisture only affects the electrification through its effect on the pressboard conductivity. Finally, cycling the temperature caused the charge density and oil moisture content to return to close, but not exactly, to their original levels. This may be an indication that an irreversible process, possibly associated with the mass transfer of impurities, was taking place.

One of the other possible complications associated with these measurements comes

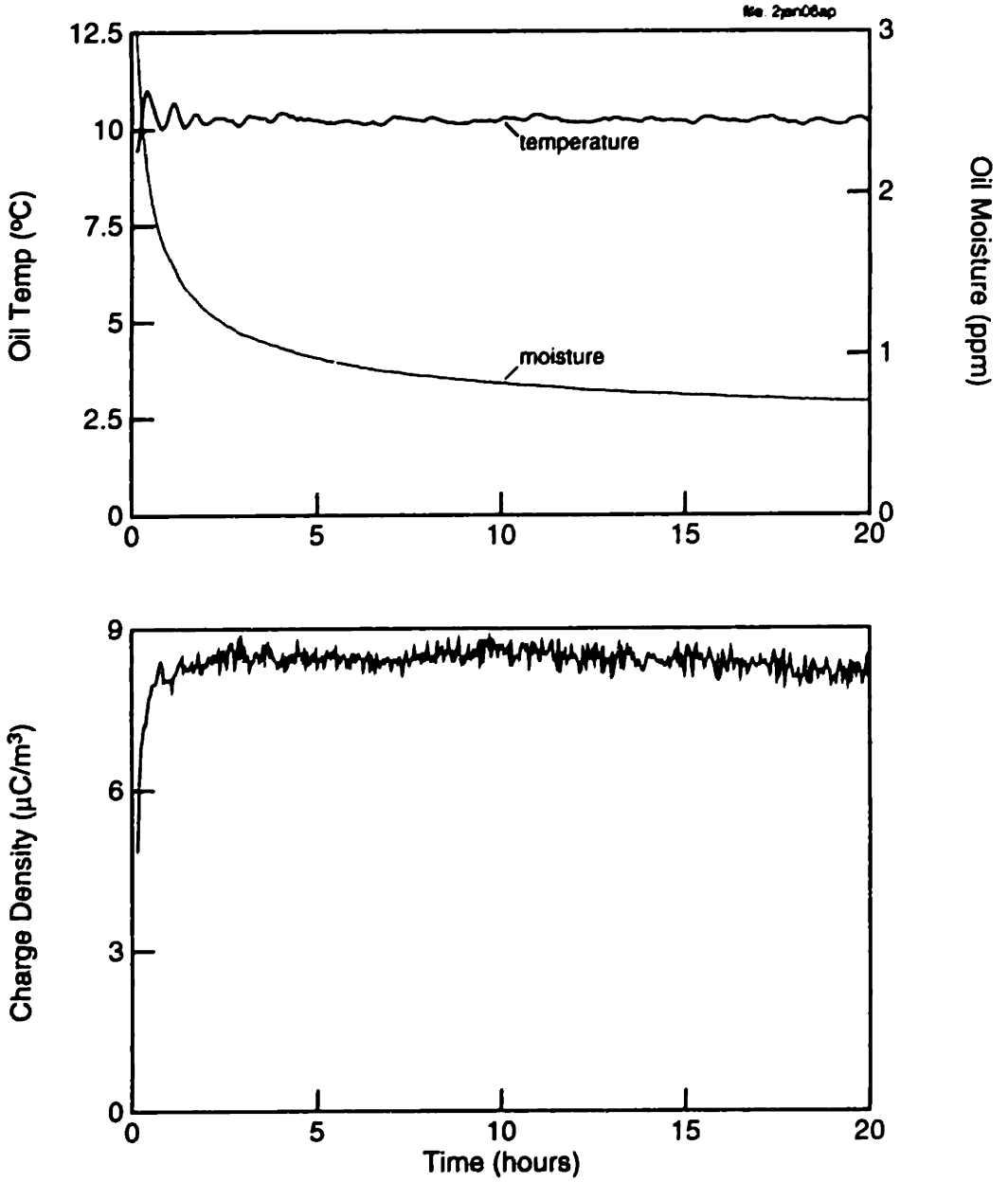


Figure 3.4: Preliminary moisture transient data for HiVal pressboard covering both cylinders, Shell Diala A transformer oil, and a rotation rate of 400 rpm at 10°C. While the oil temperature measured in the CC gap and the charge density were essentially constant, the oil moisture content decreased as the pressboard dried the oil. The CC was valved off from the units so there wasn't any flow recirculation.

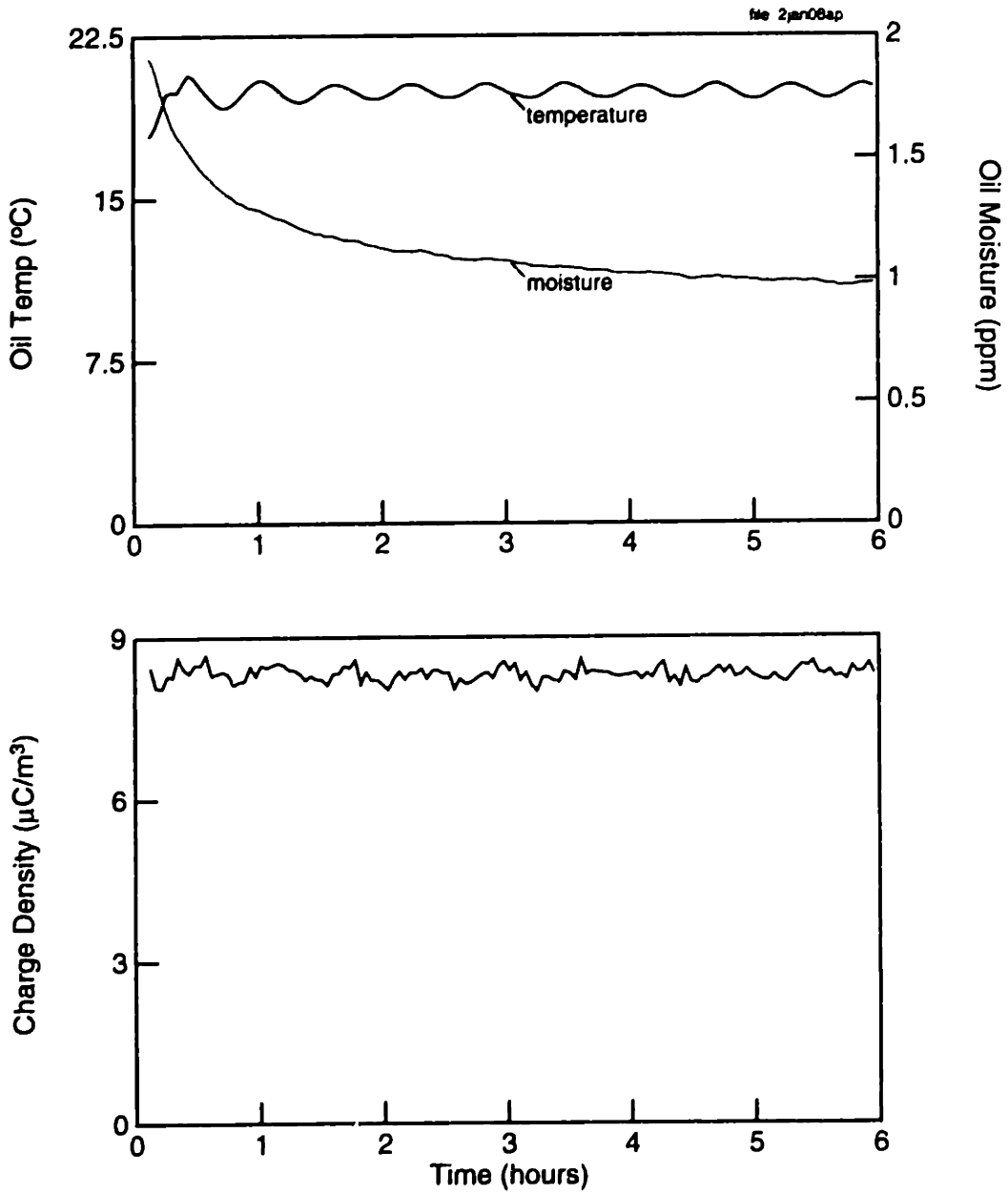


Figure 3.5: Preliminary moisture transient data for HiVal pressboard covering both cylinders, Shell Diala A transformer oil, and a rotation rate of 400 rpm at 20°C. Although the CC was valved off from the system during this measurement, relatively wet oil from the reservoir was circulated into the CC (with the inner cylinder stationary) prior to this measurement. The temperature and charge density remained constant as the moisture decreased.

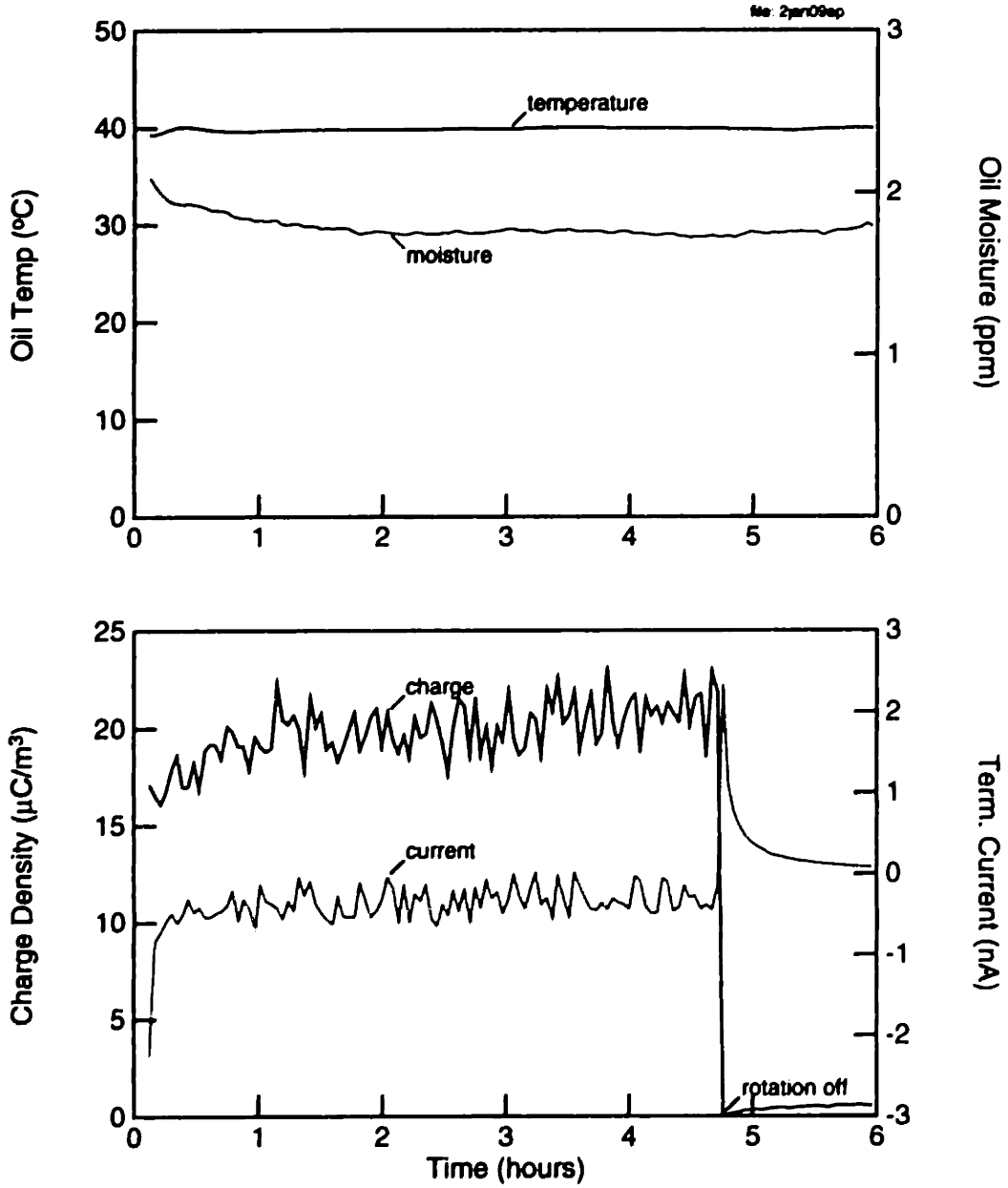


Figure 3.6: Preliminary moisture transient data for HiVal pressboard covering both cylinders, Shell Diala A transformer oil, and a rotation rate of 400 rpm at 40°C. Prior to this measurement, the temperature was set with the inner cylinder stationary and "wet" oil from the reservoir was valved though the CC. The CC was valved off from the rest of the system so there wasn't any recirculatory flow. The charge density and moisture varied slightly over the duration of the measurement. After shutting off the rotation, the charge density went to zero quickly but the terminal current reversed polarity and decayed slowly.

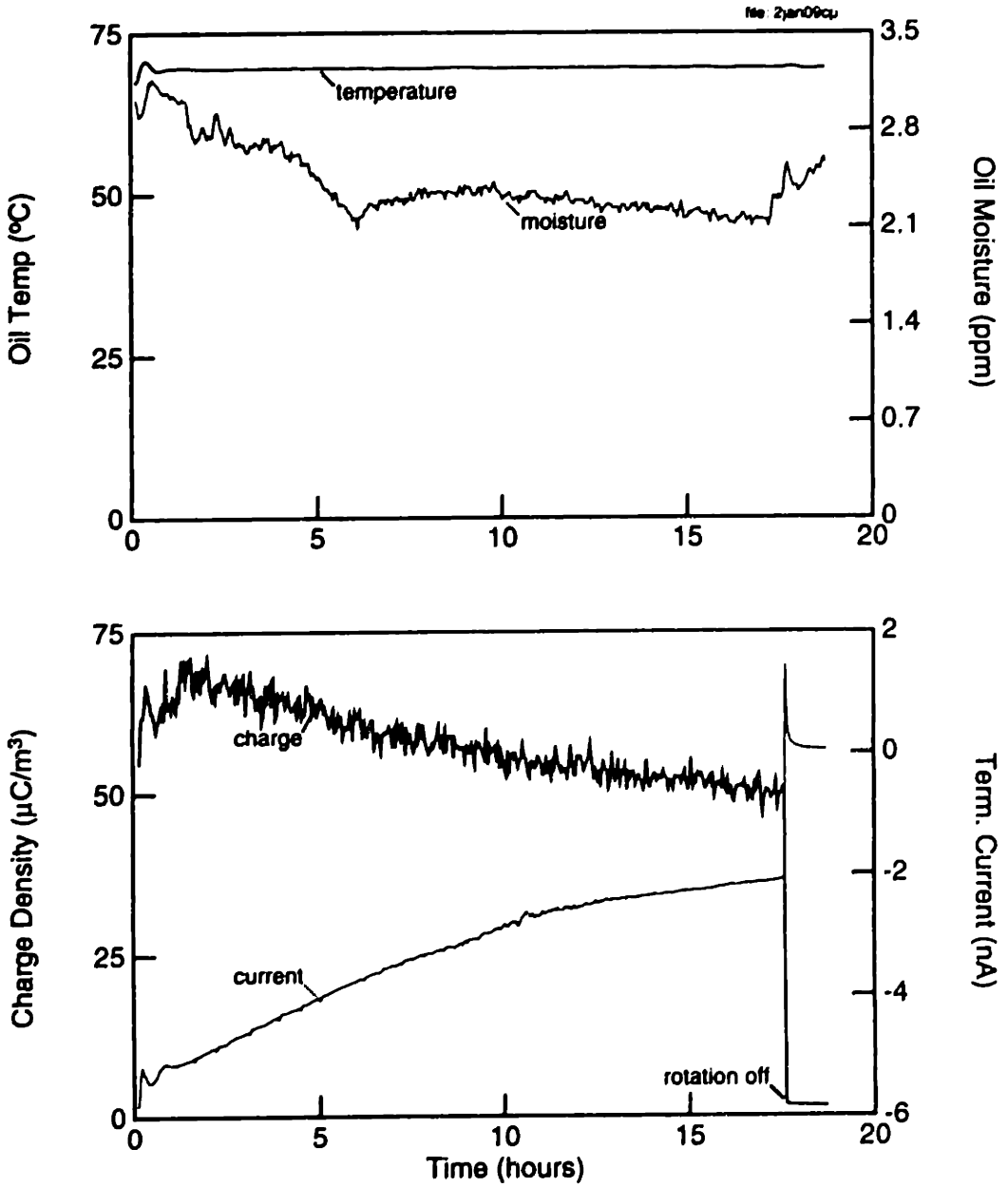


Figure 3.7: Preliminary moisture transient data for HiVal pressboard covering both cylinders, Shell Diala A transformer oil, and a rotation rate of 400 rpm at 70°C. Prior to this measurement, the temperature was set and the inner cylinder was stationary. The CC was valved off from the rest of the system preventing flow recirculation. The charge density, terminal current, and oil moisture content all decreased with a long time constant. After shutting off the rotation, the moisture content apparently increased because the CC was no longer well-mixed and the moisture sensor temperature was probably not the same as the measured value.

from the oil temperature being maintained by the heating and cooling of the inner cylinder. In these measurements, a layer of pressboard insulation, which is an electrical and thermal insulator, covered the outer cylinder and hindered the heat transfer. This temperature difference makes it quite likely that the pressboard insulation on the inner and outer cylinders experienced different dynamics, especially during the temperature transients.

## 3.3 Experimental Apparatus

In the final, improved version of the experimental apparatus, the sensors for determining the oil properties were moved into the CC. This eliminated any complications associated with having the oil transported to the poorly-mixed units, where the sensors had initially been located, and allowed the units and recirculatory flow to be removed. The improved facility, shown in Fig. 3.8, still contains the CC as the charging source and the reservoir for storing the oil, but the critical sensors are installed in the CC.

For these experiments, the outer stainless steel cylinder was always kept bare and was used as a reference electrode. This helped make the temperature through the CC more uniform and avoided complications in interpreting moisture measurements since the mass transfer dynamics only occurred at the inner pressboard cylinder. Experiments were performed with the bare stainless steel inner cylinder, with a sheet of 0.010 inch (0.254 mm) copper epoxied to the inner cylinder, and with 0.040 inch (1 mm) thick EHV-Weidmann HiVal$^{TM}$ pressboard insulation epoxied to either the inner cylinder or the copper sheet. The gap between the cylinders was filled with Shell Diala A transformer oil.

As in the original facility, the charge density in the oil between the cylinders was measured using an Absolute Charge Sensor (ACS). The temperature was measured with a thermocouple probe passed through the top flange of the CC so that the oil temperature in the well-mixed flow region could be measured. The temperature of the outer cylinder (CC side) was also measured and rotation rates were limited to keep the side and oil temperatures approximately equal, to within a few °C. Before each experiment, with and without the pressboard, the system was vacuum processed prior to transferring oil from the reservoir to the CC. The moisture was measured with a Harley Moisture Sensor, model CT-880-BN-H (0/100%)-X, with the sensor itself placed in the gap between the cylinders.

The terminal voltage and current were measured using a Keithley 617 electrometer. In some cases, DC voltages were applied across the cylinders. These voltages were initially set manually with a Hewlett Packard 6218C power supply, but later measurements had the capability of controlling the voltage built into the data acquisition software. When set automatically, the voltage was generated by a Wavetek Arbitrary Waveform Generator, model 75, and amplified by either a Trek 20/20 High-Voltage Amplifier or a Heathkit High Voltage Operational Amplifier, model EUW-19A.

In this improved facility, a ganged parallel plate capacitor was mounted in the oil space above the inner cylinder and used as a conductivity sensor. Similar to the flex sensor, one set of plates was driven at a 1 V peak sinusoid and the other set of plates

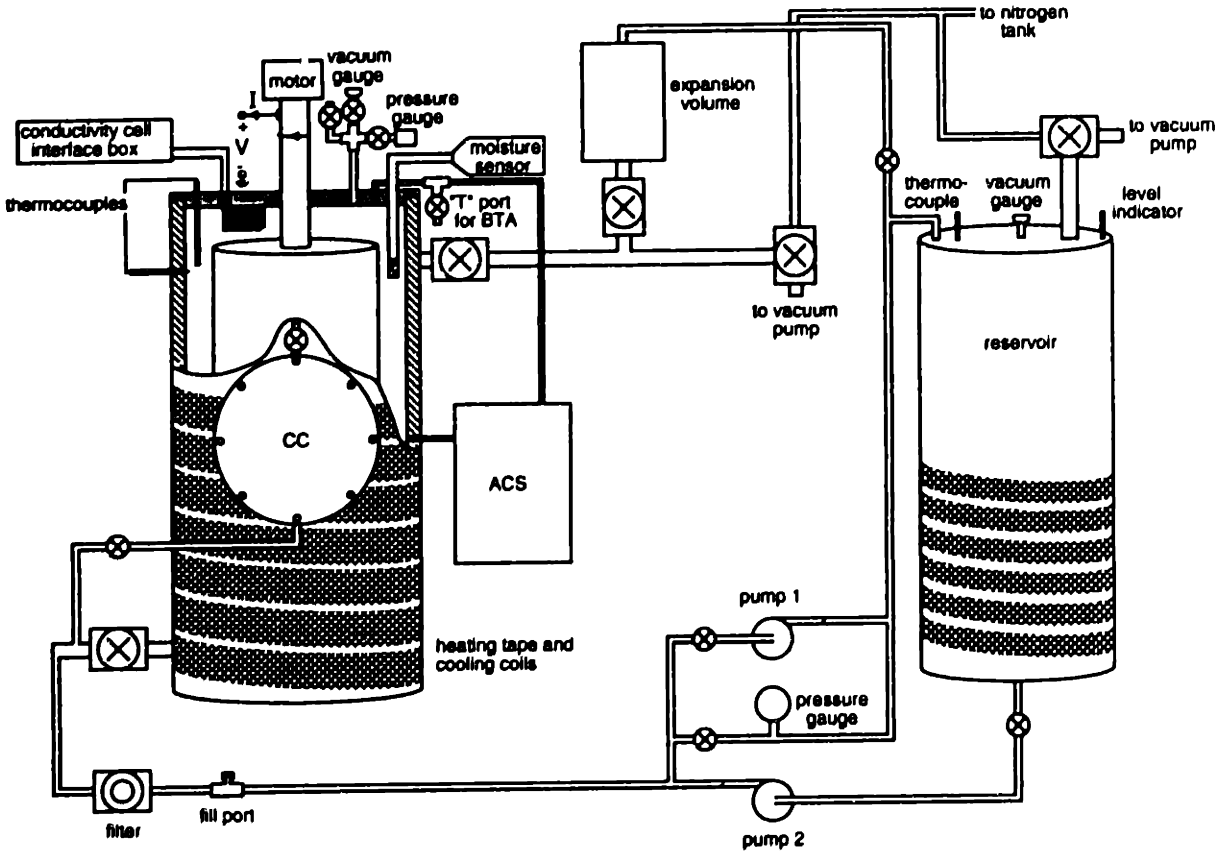


Figure 3.8: The improved Couette facility had all of the measurements made in the Couette charger (CC). Rotation of the inner cylinder created controlled turbulent flow. An Absolute Charge Sensor (ACS) was used to measure the charge density in the oil region between the coaxial cylinders of the CC. A moisture sensor was placed in the oil gap between the cylinders. A conductivity sensor was mounted above the inner cylinder. The expansion volume and the reservoir were used to allow the oil to expand and contract as the temperature of the CC varied.

were used as sensing electrodes. A grounded stainless steel mesh surrounded the plates to act as a shield and to reduce the flow rate of the oil between the plates, thereby reducing electrification along the plates themselves. The mesh size was on the order of 1 mm so oil was also able to circulate through the sensor. The details relating the measured gain and phase of the sensing voltage as compared to the driven signal are given in more detail in Chapter 4. The conductivity was typically measured at 0.1 Hz.

In several experiments, the additive 1,2,3 benzotriazole (BTA) was added to the CC to determine its effects on the electrification processes. The procedure for adding the BTA to the oil was to first have the CC operating at an elevated temperature (such as 70°C), then a concentrated solution of BTA in oil (such as 300 ppm weight BTA/weight oil), which was prepared in a beaker at elevated temperatures outside the CF, was added to the CC through a "T" connection where the ACS discharge line returned to the CC, as shown in Fig. 3.8. Since the CC contained approximately 7.5 l of oil, or 6.75 kg using

a mass density of 0.9 gm/ml, only about 125 ml of the concentrated solution had to be added to raise the average BTA concentration 5 ppm. To monitor the BTA content of the oil, samples of oil were withdrawn from the CC and the BTA concentration measured by ultraviolet spectrophotometry, as described in Appendix A. Although the same port of the CC was used for both adding and withdrawing the BTA filled oil, the discharge from the ACS circulated the oil from the "T" into the CC and the sampling line was always flushed with oil from the CC before a sample was withdrawn.

## 3.4 Representative Results

This section provides some sample results from the improved version of the CF. The initial focus of these results was to develop a base-line response for the system with bare metal cylinders and with HiVal pressboard covering the inner cylinder. Then the effects of adding copper, which is present in large quantities in transformers, and the additive BTA were explored. To develop this base-line, the controllable parameters (inner cylinder rotation rate, temperature, and applied DC voltage) were varied as the measurable quantities (charge density, terminal current or voltage, oil moisture content, oil conductivity, and pressboard conductivity) were monitored. When possible, both steady state and transient conditions were explored.

The approach used for these experiments was self-critical, with the measurements occasionally being repeated up to 20 or 30 times for a given set of conditions. To check reproducibility, measurements were taken for both increasing and decreasing rotation rates and temperatures. To further check the reproducibility, the oil and/or the pressboard in the system were periodically replaced. Although aspects of the data were quite reproducible, such as an increase in the charge density with rotation rate, some of the details of transient measurements were not reproducible. Whenever possible, representative measurements from numerous experiments are provided. The general order of the experiments was to perform a series of measurements with bare metal cylinders, with pressboard on the inner cylinder, and then again with bare metal cylinders. Copper was then attached to the inner cylinder and measurements were performed with the metal cylinders, with pressboard covering the copper on the inner cylinder, and again with the metal cylinders. The final set of experiments were performed with pressboard covering the copper on the inner cylinder and BTA periodically added to the oil in the CF.

In this presentation, the basic data from the experiments are plotted. While it is natural to express the measured quantities in terms of nondimensional parameters, such as the hydrodynamic Reynolds number, most of the interdependencies of the various quantities are not known so it is more convenient at this time to express the data in dimensional form. An exception is the comparison to classical electrochemistry subsection, where normalizations motivated by the electrification models and the electrochemistry literature are presented. In Chapters 5 and 6 the electrification models are developed and some of the data is then presented in a nondimensional form.

### 3.4.1 Rotation rate dependence

The obvious variable parameter that is critical to flow electrification is the fluid flow rate. To explore the effects of this parameter in the CF, where the flow rate was controlled by the rotation rate of the inner cylinder, the inner cylinder was rotated at speeds which cause turbulent motion in the fluid. Physically, as the rotation rate increased, the flow rate also increased but the diffusion sublayer thickness, which is the thickness of the interfacial region where the effective diffusivity from the turbulence is dominated by molecular diffusion, decreased. The net result was that the core charge density tended to increase with rotation rate as the sublayer thickness decreased and more charge was transported (by convection) out of the interfacial electrical double layers into the core region of the flow.

Sample sets of steady state electrification data are shown in Fig. 3.9 for identical bare stainless steel cylinders and in Fig. 3.10 for pressboard insulation covering a copper layer on the inner cylinder. For the bare cylinders, the charge density had the same polarity as the terminal current and voltage at high rotation rates, but the opposite polarities at low rotation rates. (As shown in Fig. 3.8 and in more detail in Fig. 5.2, the electrometer measured the terminal voltage and current in the external circuit from the inner cylinder to the grounded outer cylinder.) In contrast, when pressboard insulation covered the inner cylinder, the charge density had a polarity opposite that of the terminal current and voltage for all rotation rates. Also significant about this data is that the measured quantities tended to increase in magnitude as the rotation rate increased and didn't reach a limiting or saturation value. This indicates that the interfacial charge transfer process was probably rate limited by the transport of ionic species to the interface, not the interfacial reaction rate.

Also shown in Figs. 3.9 and 3.10 is the rate of change of the core charge density for small DC applied voltages ($D_V \rho_o$). Although this parameter is inherently noisy because it reflects measurements of a *perturbation* in the charge density as the voltage is varied, the sign of the derivative is significant and leads to some insight into the interfacial charge transfer boundary condition. More will be said about this in the electrification models of Chapters 5 and 6.

The polarity reversal of the terminal quantities as the rotation rate increased is shown more clearly in Fig. 3.11. As in Fig. 3.9, this experiment was done with bare metal cylinders. At each temperature, the short-circuit current or the open-circuit voltage was monitored as the rotation rate was varied. The current was measured during both the startup and shutdown transients for the rotation of the inner cylinder. In one case (35°C and 800 rpm) two transients at the same rotation rate are given. For the voltage measurements, the voltage was set to zero while the inner cylinder rotation was started, then the terminals were open-circuited and the voltage was measured during the transient in which the inner cylinder stopped rotating. In two cases (15°C 400 rpm and 70°C 1000 rpm) the electrometer was zeroed during the open-circuit measurement and the transient associated with the voltage rising to its steady state level was repeated. The rapid increase in current as the rotation was started was probably due to the redistribution of charge in the oil by the turbulent mixing. Similarly, during the shutdown transient, some of the response can be attributed to the relaxation of the charge in the bulk of the oil, but it

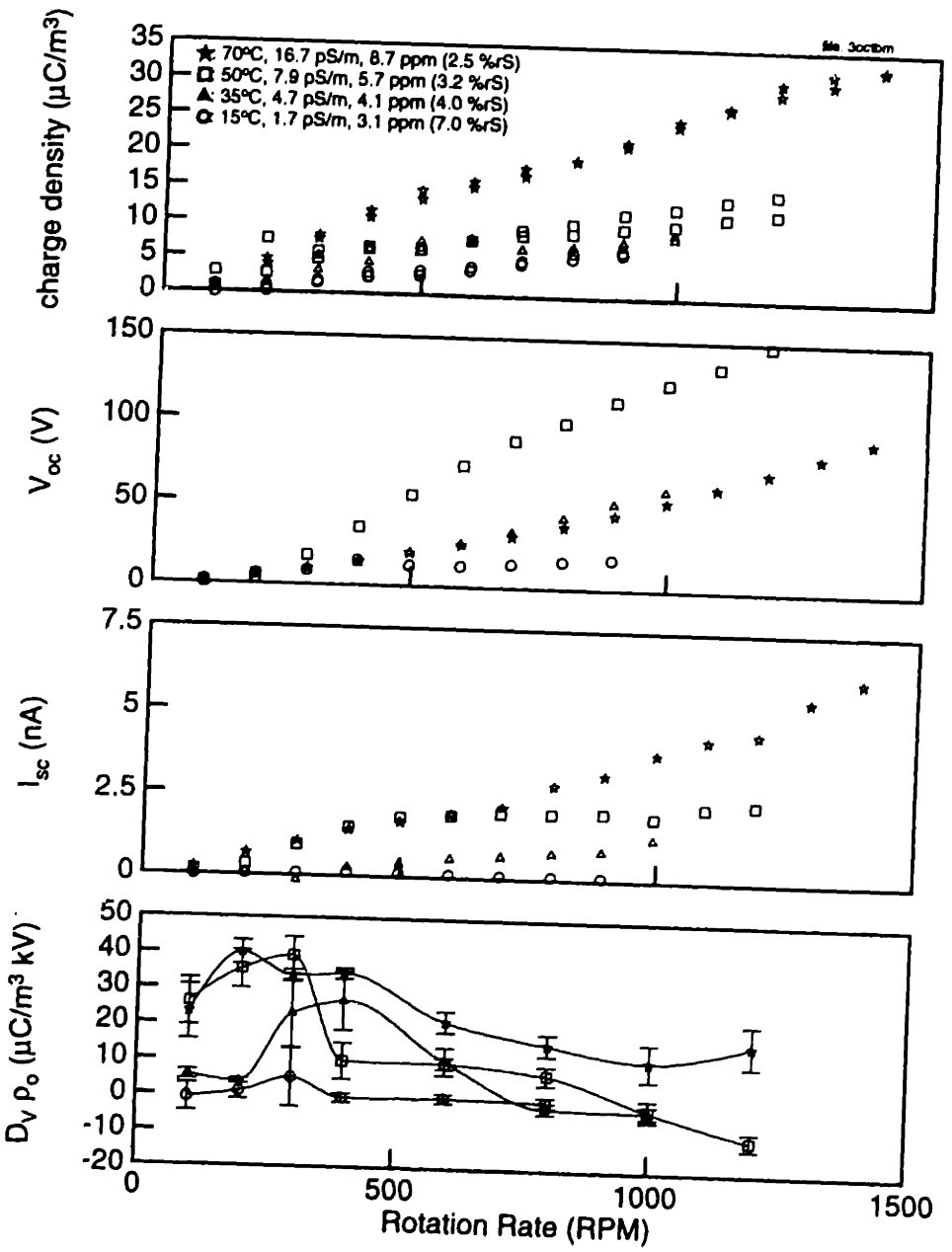


Figure 3.9: A set of electrification measurements for bare stainless steel cylinders and Shell Diala A transformer oil. The charge density, open-circuit voltage and short-circuit current usually had the same polarity and increased with rotation rate. At each temperature and rotation rate, the open-circuit and short-circuit charge densities are plotted and appear to be essentially the same. The maximum voltage for each rotation rate appeared at an intermediate temperature (50°C). The charge density variation with applied voltage was usually positive and decreased at the higher rotation rates.

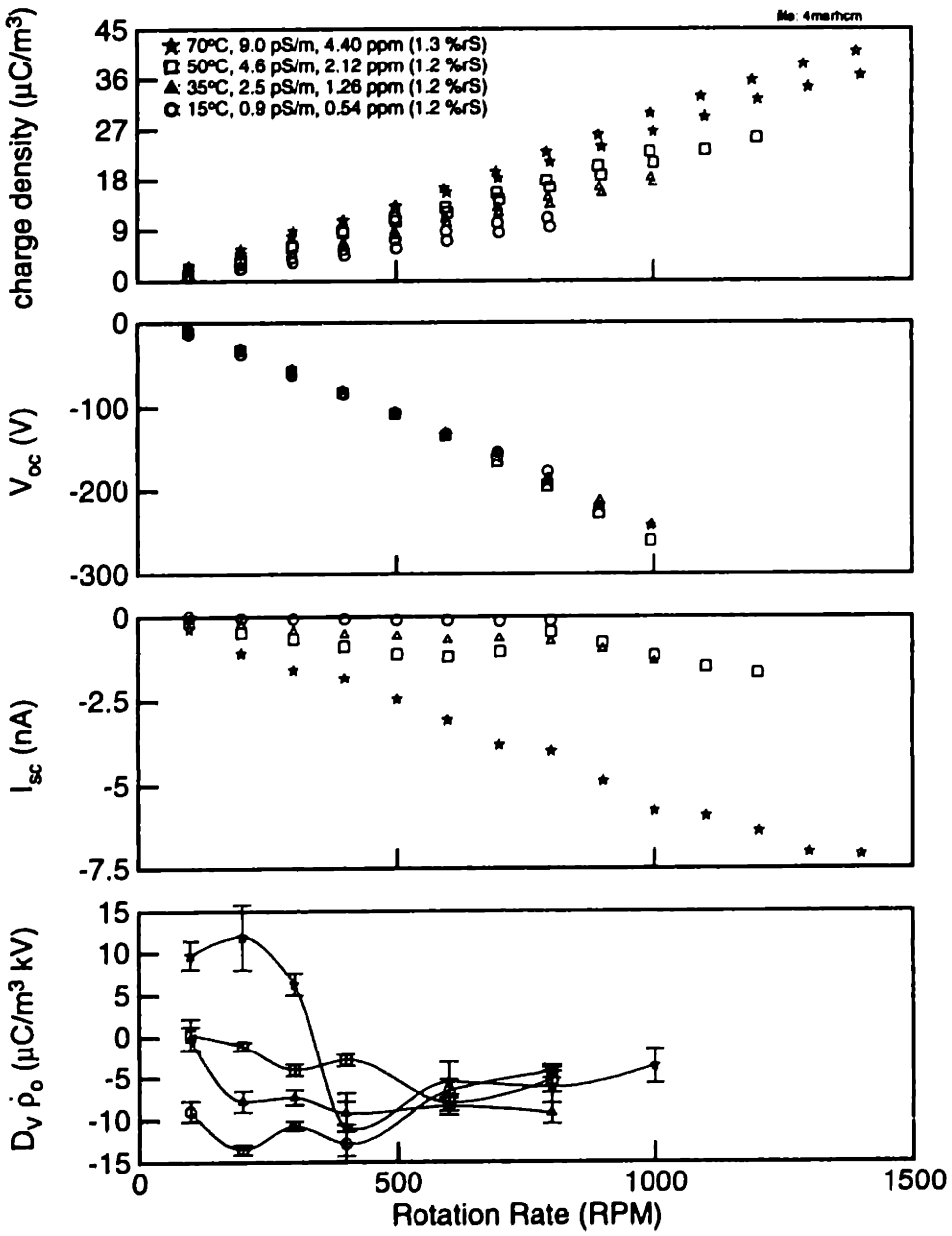


Figure 3.10: A set of electrification measurements for HiVal pressboard insulation covering a copper sleeve on the inner cylinder, a bare stainless steel outer cylinder and Shell Diala A transformer. The charge density (open and short-circuit) had a polarity opposite that of the terminal voltage and current at each temperature.

also took a few seconds (usually 10 to 30, depending upon the temperature and the oil viscosity) for the inner cylinder to stop rotating and the oil to come to rest.

In the measurements in Fig. 3.11, the terminal current and voltage were usually negative and became more negative as the rotation rate increased. Exceptions to this occurred at the lower rotation rates and the higher temperatures where the current and voltage were actually slightly positive. Although the charge density was not monitored because the sampling time for the ACS was long compared to the duration of the transients, the steady state charge density and short-circuit current were measured immediately prior to the transient measurements. These measurements, given in Fig. 3.12, show that the charge density always remained positive, *even when the current reversed polarity.* As will be discussed in the electrification modeling chapters, the charge density involves the sum of the electrification contributions from each interface while the terminal voltage and current involve the difference. The polarity reversals with rotation rate allow the suitability of various boundary conditions for the interfacial charge transfer to be explored.

The transient associated with step changes in the rotational speed also provides some insight into the electrification processes. While the development time for the fluid mechanics to reach a steady state is on the order of a few seconds, the time necessary for the electrical variables to reach a steady state depends upon the terminal connections. With the terminals open-circuited, no current flows through the external circuit and the charge density and voltage reach a steady state with the dielectric relaxation time of the oil (approximately 1-20 seconds) as the time constant. Since the sampling time between the experimental measurements was typically longer than the oil relaxation time, the charge density and voltage changed with the rotation rate, as shown in Fig. 3.13 for pressboard insulation covering the inner cylinder. Note that this development time was *independent* of the pressboard dielectric properties because there was no net current flow. When leakage currents flowed through the pressboard, for example through a relatively low impedance path between the grounded conductivity cell shield and the top of the inner cylinder, a field developed inside the pressboard with the relaxation time of the pressboard as the time constant. To minimize the effect of the pressboard field gradually increasing, the conductivity cell was disconnected and the experiments had a relatively short duration during open-circuit measurements.

A sample set of measurements showing the build-up of a significant field inside the pressboard is given in Fig. 3.14. In this measurement, the CC terminals were open-circuited, but the conductivity cell shield was grounded, which provided a path for leakage current through the pressboard. The charge density quickly attained a steady state value after the rotation was started, and then decayed quickly (on this time scale), once the rotation was shut off, because the oil dielectric relaxation time was roughly 10 seconds. With the start of rotation, the terminal voltage, which is due to the field across the pressboard and the field across the oil, went to a large negative value quickly as the charge was redistributed in the oil volume. As the field inside the pressboard increased due to the leakage current, the net voltage measured at the terminals became smaller. After shutting off the rotation, the field in the oil decayed quickly with the oil relaxation time, but the field through the pressboard decayed slowly. Using a peak positive voltage of 100 V across the 1 mm thick pressboard, the corresponding pressboard field is estimated to be $10^5$ V/m. This data shows that significant fields can develop in the pressboard for

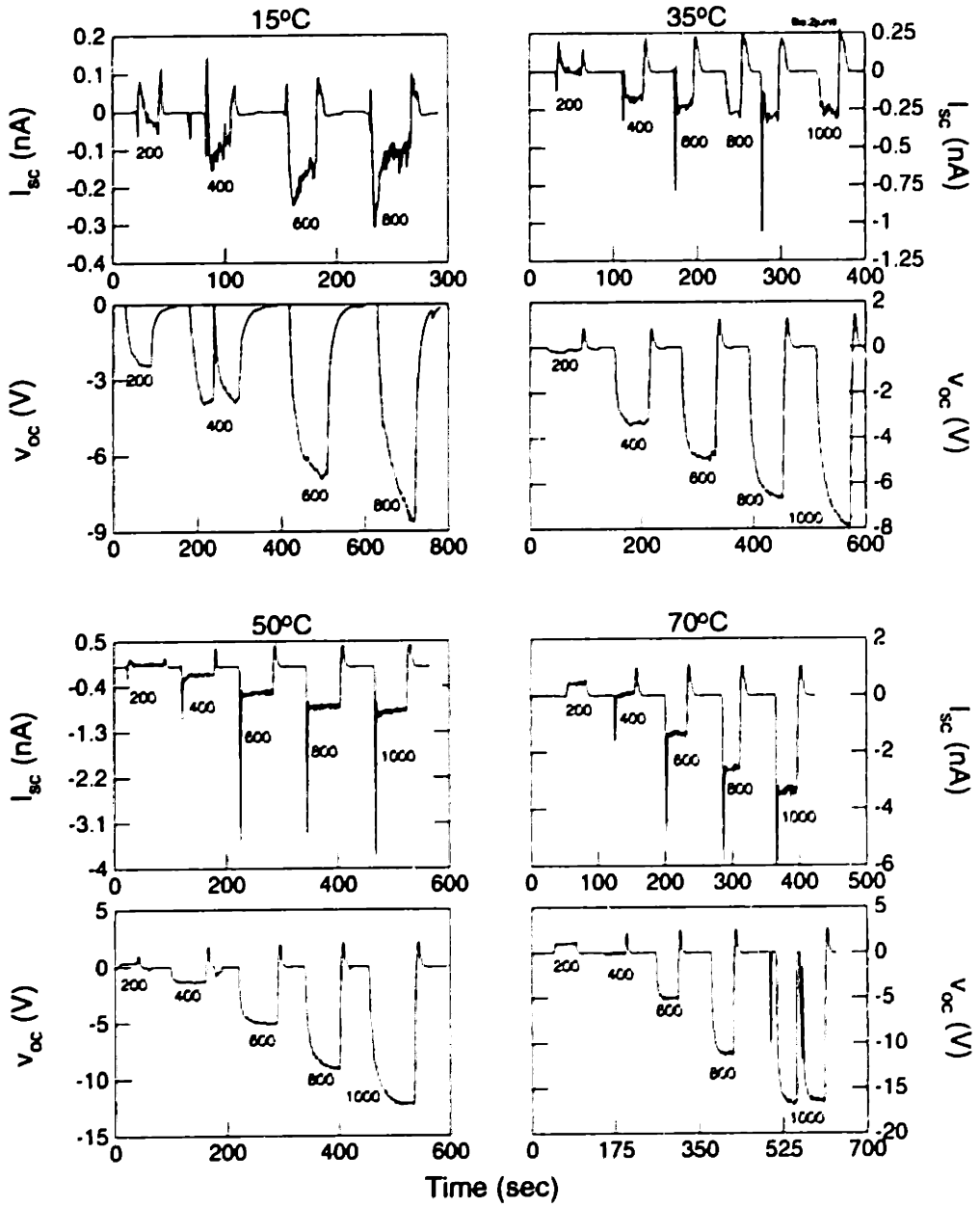


Figure 3.11: A set of time transient terminal measurements with bare stainless steel cylinders and Shell Diala A transformer oil for various inner cylinder rotational speeds between 200 and 1000 rpm. The short-circuit current and open-circuit voltage are shown for four temperatures. The current and voltage were set to zero as the rotation rate (in rpm) was set. At the lower temperatures, the voltage and current approached a negative steady state value, but at the higher temperatures, they had a positive polarity at low rotation rates but negative at high rotation rates.

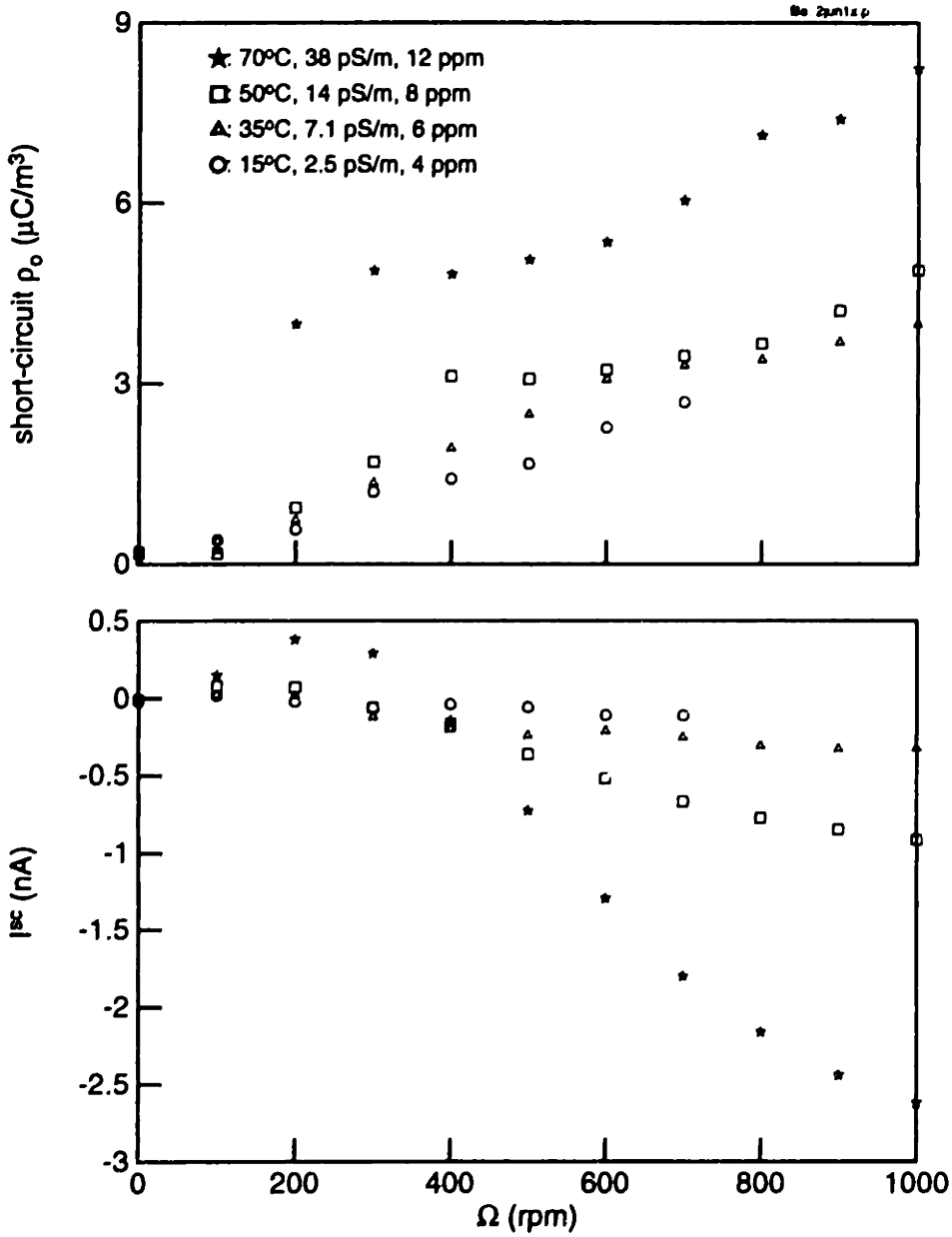


Figure 3.12: Steady state short-circuit charge density and current measurements corresponding to the transient measurements of Fig. 3.11. The temperature, oil conductivity and moisture content are indicated. The charge density was positive, even though the current reversed polarity.

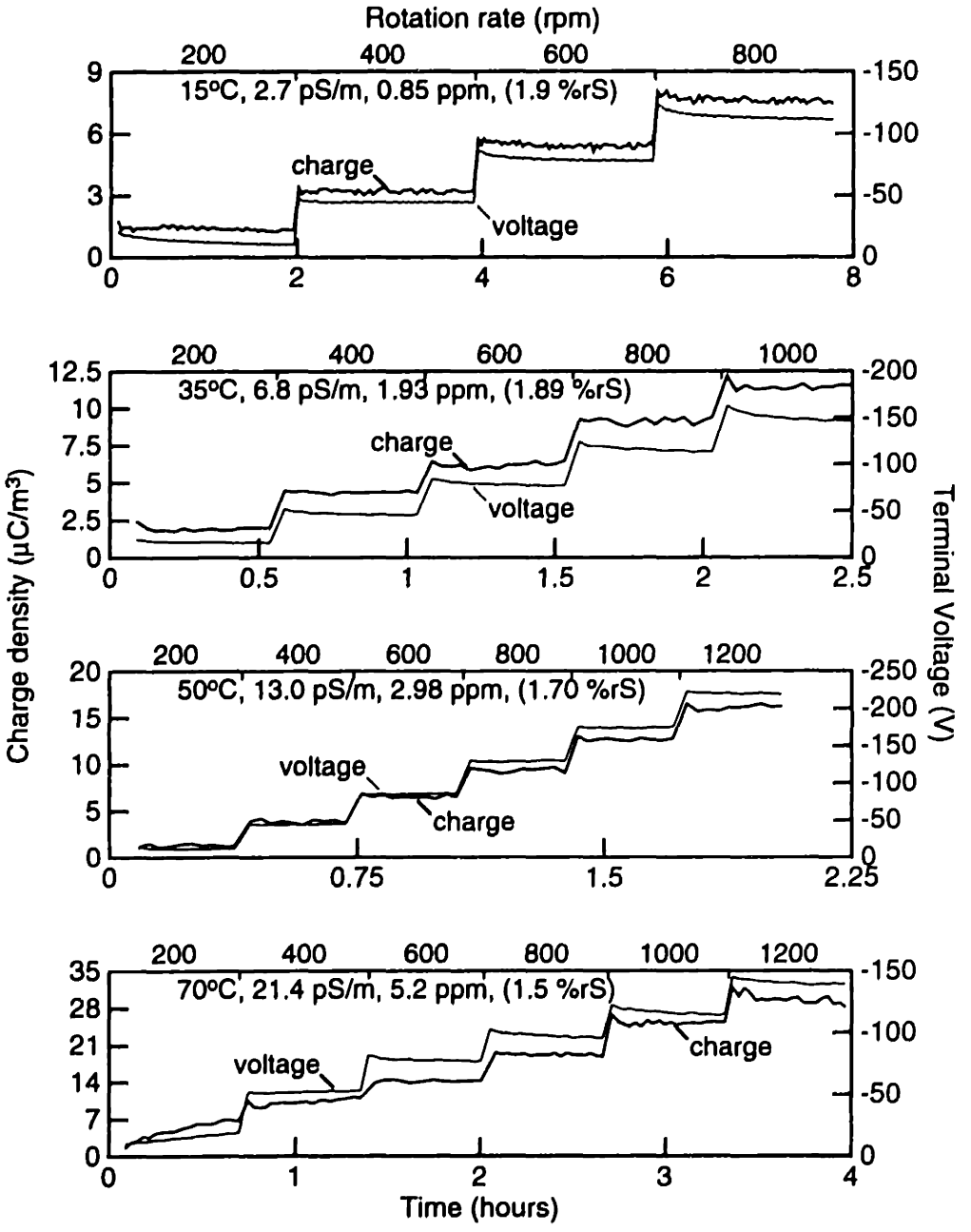


Figure 3.13: Transient open-circuit voltage and charge density measurements for HiVal pressboard insulation covering the inner cylinder, a bare stainless steel outer cylinder and Shell Diala A transformer. The open-circuit voltage and charge density follow step changes in the rotation rate.

modest volume charge densities.

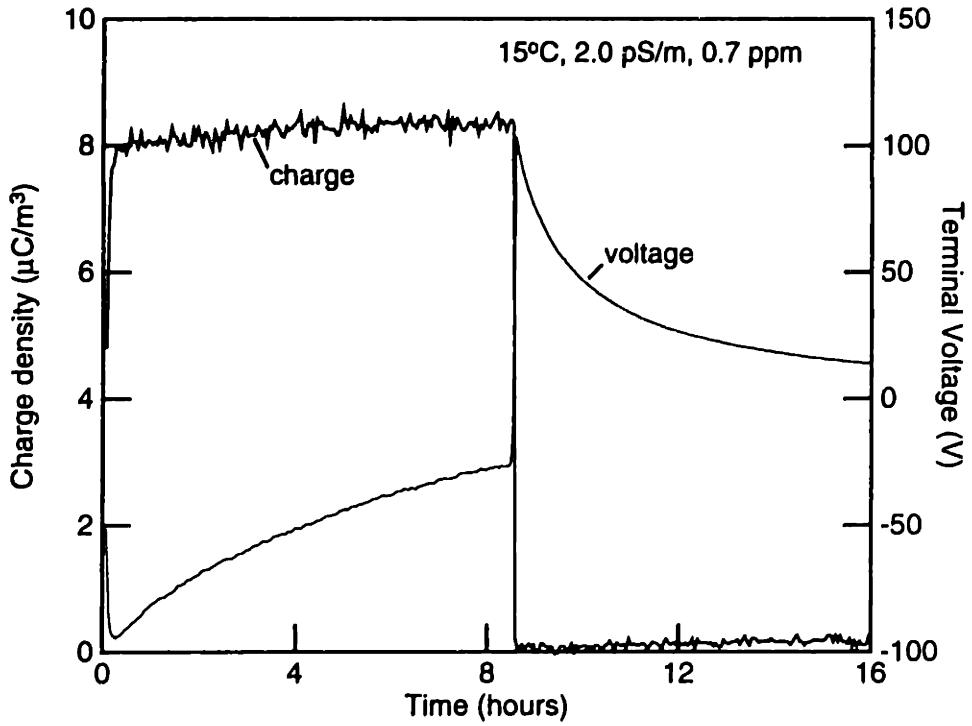


Figure 3.14: Transient open-circuit voltage and charge density measurements for pressboard insulation covering the inner cylinder as the rotation was started and then stopped. A rotation rate of 800 rpm was started at time 0 and turned off at hour 8.5. A grounded shield provided a path for leakage current through the pressboard. The slow decay of the voltage was due to the relaxation of a field in the pressboard.

In contrast with the open-circuit measurements, when the terminals are short-circuited the time constant for reaching steady state depends intimately upon the pressboard dielectric properties. While the charge density still attained a steady state quickly as the rotation rate was changed, as shown in Fig. 3.15, the terminal current changed abruptly and then slowly approached its steady state level. This long time constant probably resulted from surface charge accumulating at the interface between the pressboard and the oil. The charge density remained essentially constant over this period, indicating that the redistribution of charge and the volume charge densities on the liquid side of the interfaces were independent of the current flowing through the system. Even though surface charge was accumulating at the oil/pressboard interface, it only led to an electric field inside the pressboard, not in the oil. The decrease in the steady state current at

70°C and the higher rotation rates is not fully understood. Some of the model predictions in Chapter 6 show that the current can reach a peak magnitude as the rotation rate is increased, depending upon the interfacial parameters, but the decreasing current at the higher rotation rates may have been an experimental artifact resulting from the brush making poor electrical contact with the inner cylinder.

### 3.4.2 Temperature dependence

The system temperature is one of the other parameters which can be readily controlled. Unfortunately, many of the material properties (viscosity, conductivity, relative moisture content between the oil and the pressboard, ion mobility and diffusivity, and the interfacial zeta potentials creating the electrical double layers) are temperature dependent and changes in the temperature can lead to competing effects. For example, the viscosity of the oil decreases as the temperature increases, which causes the diffusion sublayer thickness to decrease and more charge to be carried out of the electrical double layers into the bulk of the fluid. On the other hand, the conductivity increases with temperature, which results in an increase in charge relaxation and a decrease in the volume charge density. Long time transient, "conditioning" behavior, driven by elevated temperatures has also been observed, but this will be discussed in Section 3.4.6.

Sample sets of steady state electrification data showing the variations with temperature are given in Figs. 3.9 and 3.10. In both sets of data, the charge density and short-circuit current increased with temperature at each rotational speed, to within the accuracy of the measurement. In contrast, the open-circuit voltage was largest at an intermediate temperature (near 50°C) for the bare metal cylinders but essentially independent of the temperature when pressboard covered the inner cylinder. Although these pressboard measurements had a copper sleeve over the inner cylinder, measurements without the copper sleeve present gave similar results.

During temperature transients, the short-circuit current, charge density, moisture, and conductivity usually increased in magnitude with the temperature, as shown in Fig. 3.16 for a step-increase in temperature and in Fig. 3.17 for some temperature cycling. The charge density and current also showed long time scale transients after the temperature stabilized. While the accumulation of surface charge at the pressboard/oil interface was too short, at the elevated temperatures, to describe this transient, it is possible that the properties of the pressboard itself were changing. The data in Fig. 3.16 shows the response of the first temperature increase in the system after oil impregnating the pressboard. In Chapter 4, the effective conductivity of the pressboard *decreased* after initial low temperature electrification measurements. The slow decrease in the terminal current at 70°C is consistent with a slowly decreasing pressboard conductivity. After a few days at the elevated temperature, the data of Fig. 3.17 was taken. Since the current did not appear to change appreciably with time at 70°C the pressboard conductivity apparently reached a steady state.

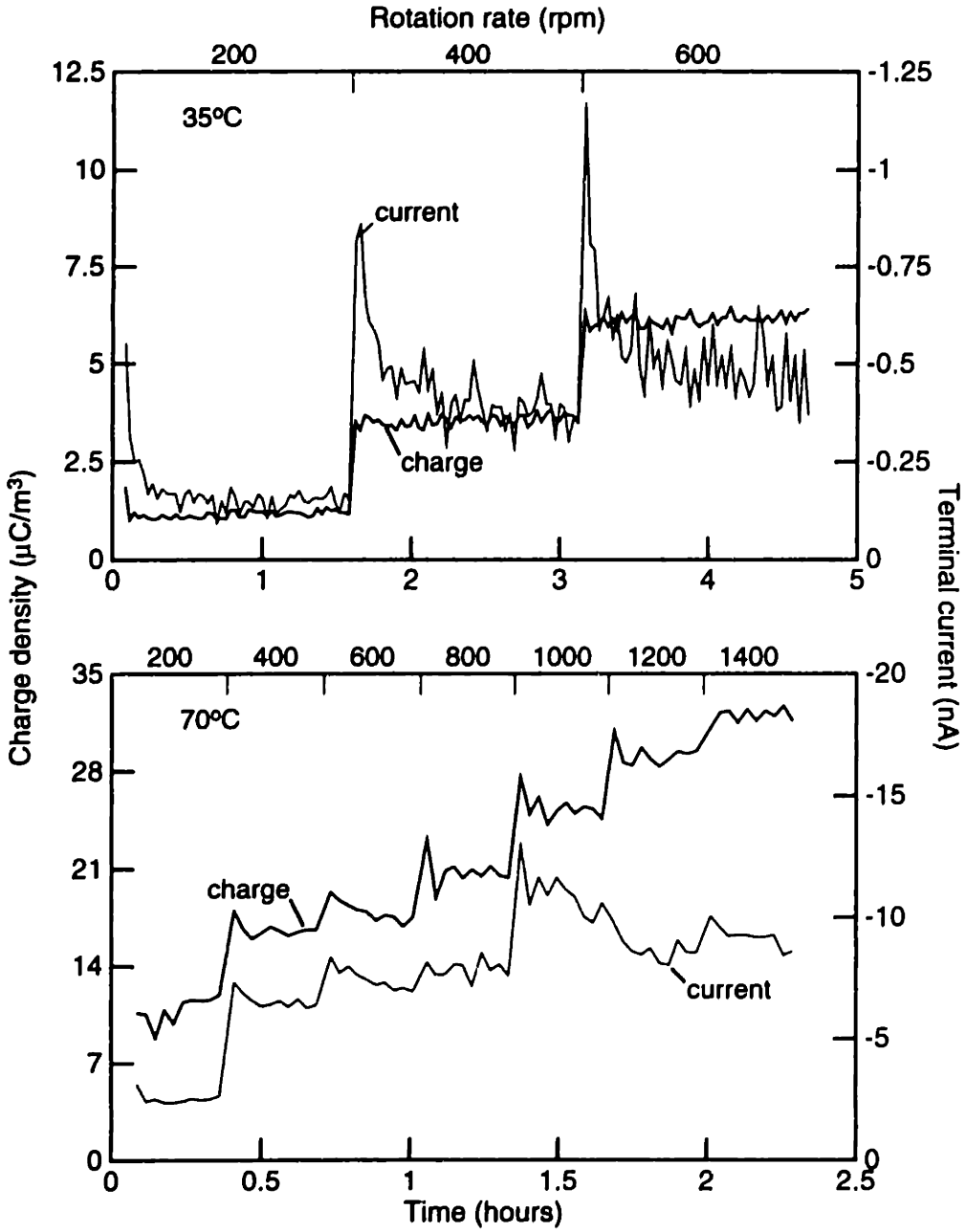


Figure 3.15: Transient short-circuit current and charge density measurements using the same materials as Fig. 3.13, with HiVal pressboard insulation covering the inner cylinder, a bare stainless steel outer cylinder and Shell Diala A transformer. While both the charge density and the current change with the rotation rate, the current slowly approached its steady state level as surface charge accumulated at the interface between the pressboard and the oil.

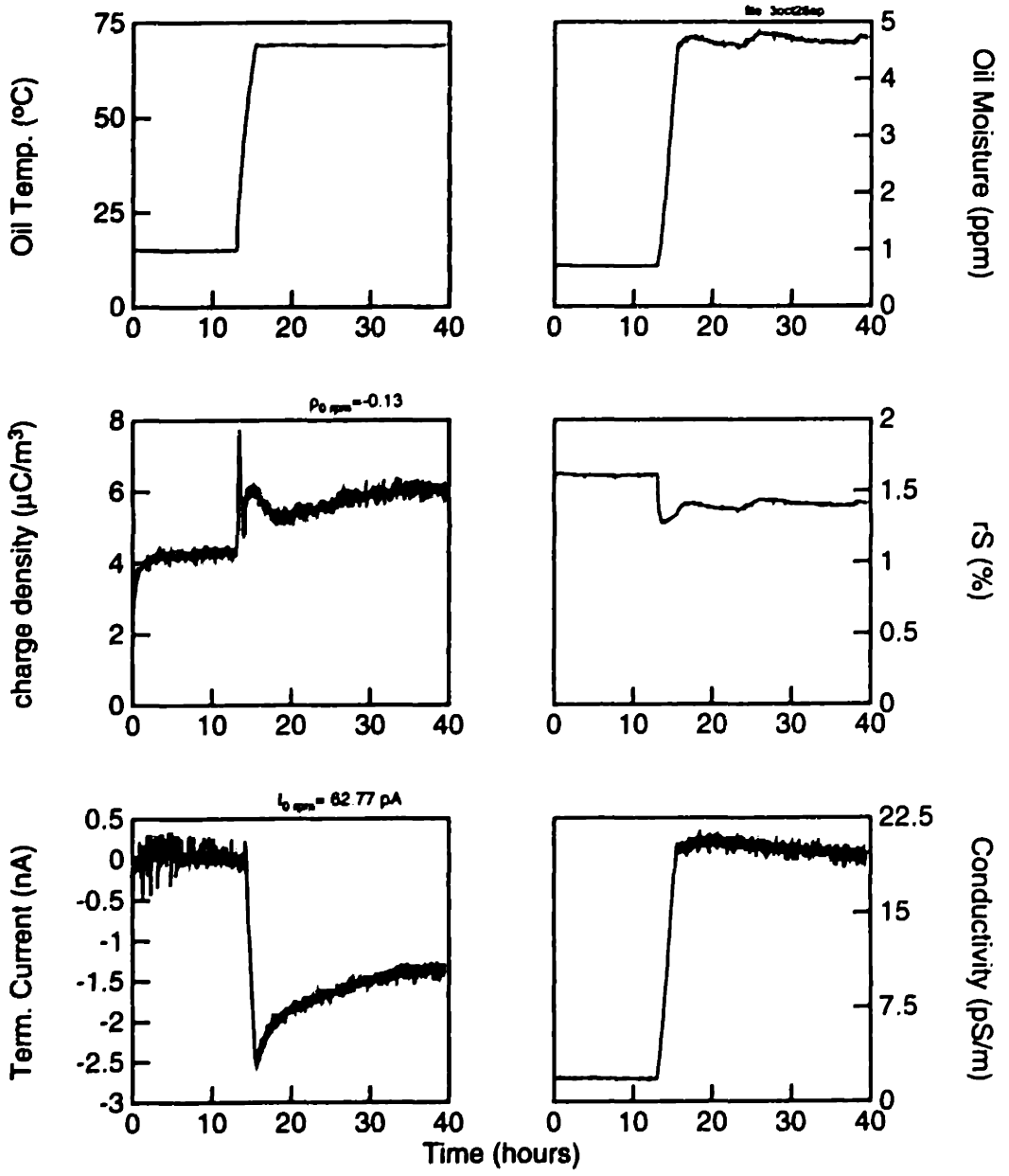


Figure 3.16: Temperature driven transient measurements for HiVal pressboard insulation covering the inner cylinder, a bare stainless steel outer cylinder, Shell Diala A transformer and a rotation rate of 400 rpm. The oil moisture content and conductivity followed the temperature. This indicated a relatively rapid mass transfer of moisture from the pressboard into the oil at elevated temperatures. The current and charge density became larger as the temperature increased.

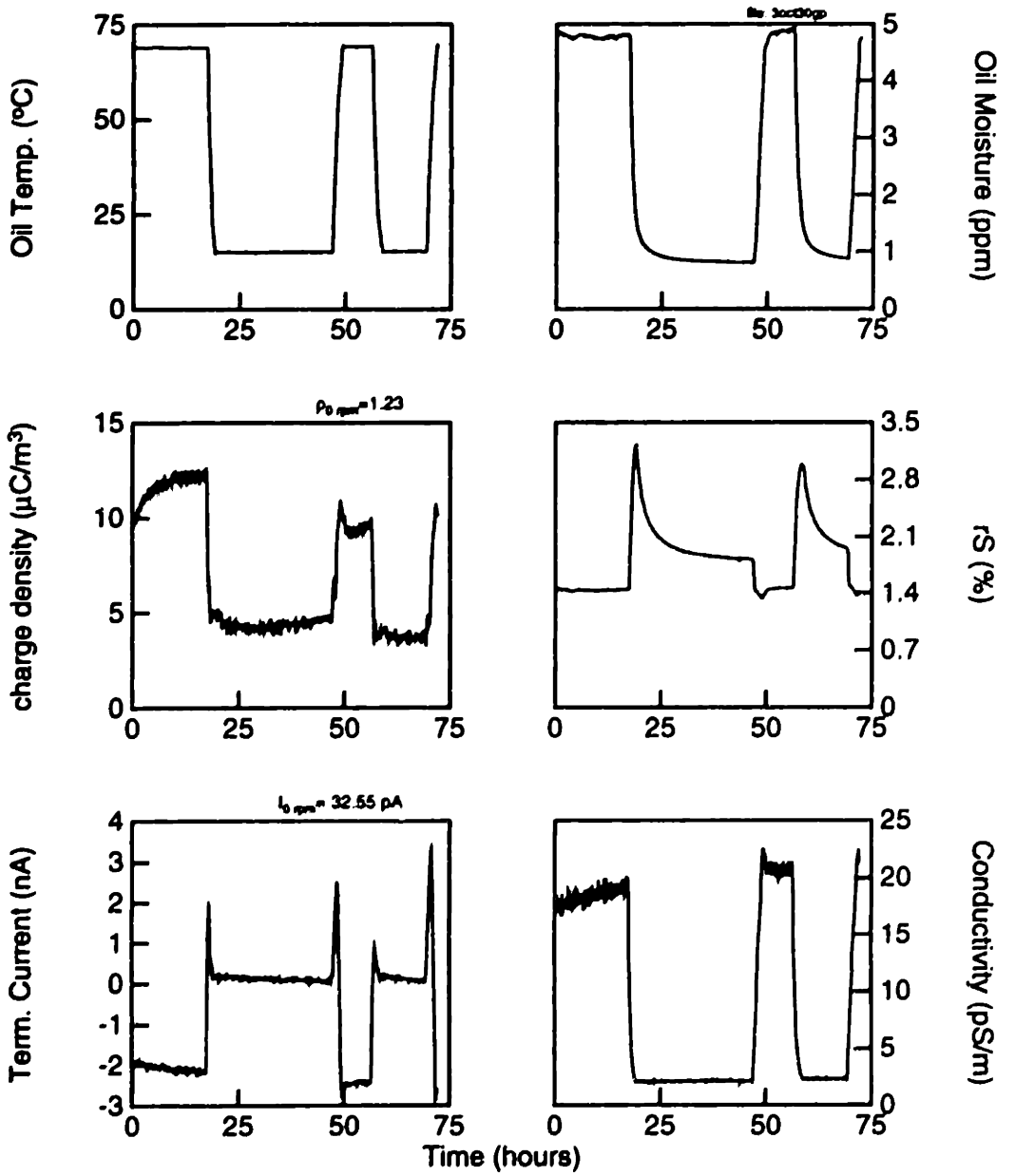


Figure 3.17: Temperature driven transients for HiVal pressboard insulation covering the inner cylinder, a bare stainless steel outer cylinder, Shell Diala A transformer and a rotation rate of 400 rpm. This data is a continuation of that given in Fig. 3.16. The charge density decreased slightly with time as the oil became more conducting. The oil moisture content reached a steady state level quickly at 70°C but slowly at 15°C. Since the charge density quickly reached steady state at the low temperatures, the charge density appeared to be independent of the oil moisture content in this "dry" regime. The current usually followed the temperature, except during the transient in which the temperature was changed.

### 3.4.3 Moisture dependence

One ubiquitous impurity that is known to be present in both the solid and liquid insulation is water. Standard procedures for reducing the moisture content of the insulation include heating the system and vacuum processing, but some water is always present. In the steady state, the moisture equilibration curves show that the concentration of water in the hydrophilic pressboard is much greater than that of the hydrophobic oils. Unless the volume of oil is extremely large compared to the volume of pressboard, most of the water is contained in the pressboard. In the CC, when the inner cylinder is covered with pressboard, the pressboard volume is about 200 $cm^3$ while the oil volume is about 7500 $cm^3$. Using mass densities of 1.0 $g/cm^3$ for the pressboard and 0.9 $g/cm^3$ for the oil, it is estimated that a 3 ppm (moisture weight / oil weight) change in oil moisture content only leads to an average change in the paper moisture content of 0.01%.

A sample set of data showing the effect of moisture on the electrification charge density and conductivity under relatively "dry" conditions is shown in Fig. 3.18. This data showed a decrease in oil moisture content, approaching equilibrium, after the pressboard was oil impregnated at elevated temperatures and the temperature was lowered with the inner cylinder fixed. During the moisture transient, the charge density and oil conductivity were relatively constant, indicating that both were independent of the oil moisture content. In contrast, after additional vacuum processing the charge density and oil moisture content (and probably the pressboard moisture content) were reduced, but the conductivity increased slightly, probably due to oxidation at the elevated temperatures. While some of the decrease in charge density may have been caused by the lower moisture content changing the interfacial properties, part of it was probably caused by the conductivity increase, as will be discussed in the next subsection.

Moisture transients were induced by changing the temperature of the system, as the equilibrium pressboard and oil moisture contents changed. In Fig. 3.19, moisture was transferred from the pressboard into the oil as the temperature was raised from 15°C to 70°C. The moisture content followed the temperature and approached a steady state level of about 7 ppm after the first temperature increase, but after additional vacuum processing, the oil moisture content no longer followed the temperature closely and slowly increased with time. This slow increase in moisture was probably not due to a leak to atmosphere since the 70°C oil conductivity slowly decreased, indicating a lack of oxygen for oxidation of the oil, and the absolute rate of increase of the moisture did not remain constant even though the relative humidity of the air was essentially constant. It was probably not due to the redistribution of moisture in the pressboard, either, because the initial experiment (case a) showed the moisture reaching a steady state quickly and a moisture dynamics model for the CC suggests that the mass transfer in the CC is rapid at elevated temperatures [17]. Rather, this data suggests that vacuum processing affects the manner in which water is held in the pressboard, such as decreasing the diffusivity of water in the pressboard, possibly through degradation of the cellulose fibers. This decreased diffusivity is consistent with the observations of Foss, in which the moisture concentration $C$ (in percent) affected the diffusivity $D$ according to

$$D = D_o e^{0.5C} \tag{3.2}$$

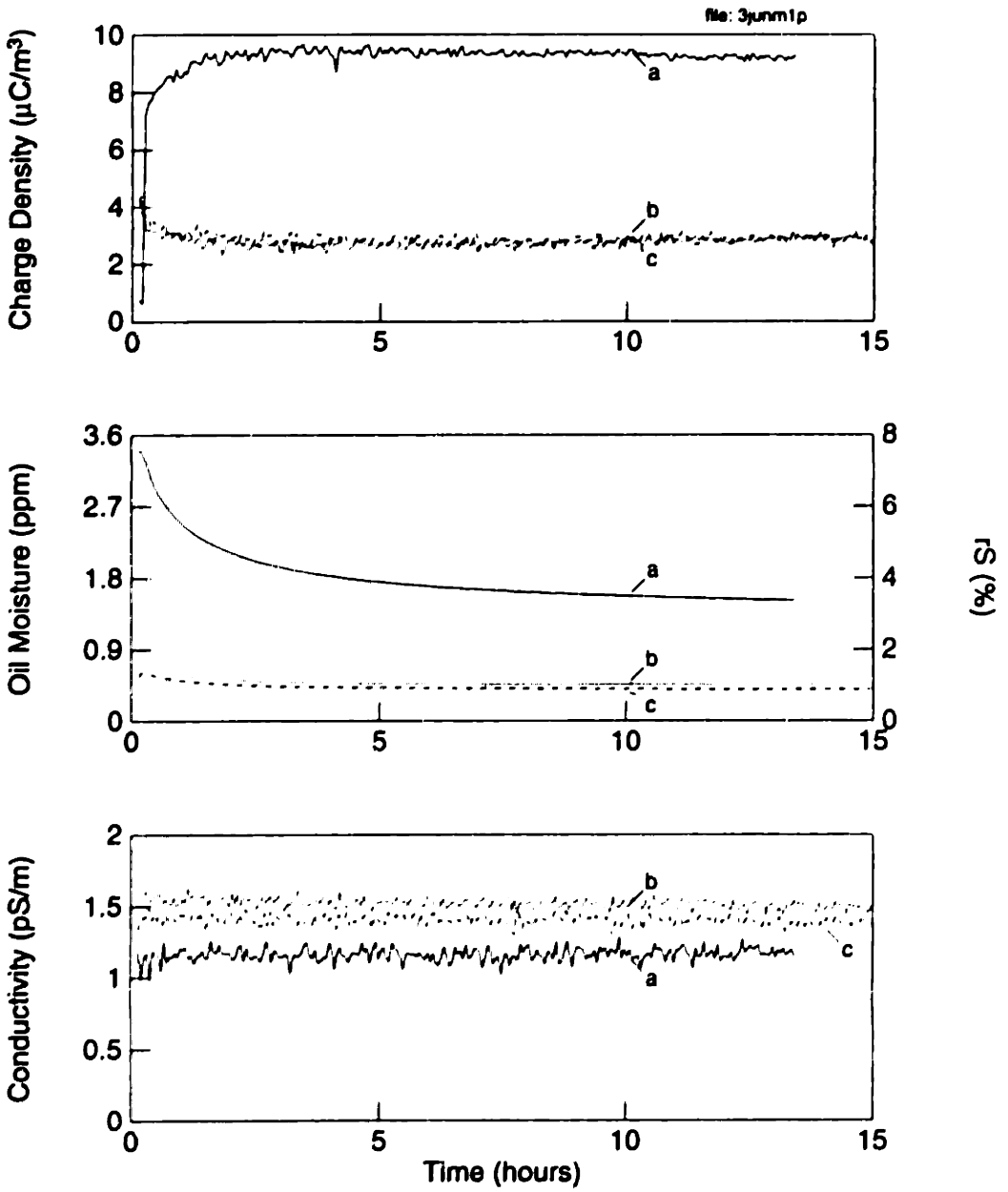


Figure 3.18: Moisture driven transients for HiVal pressboard insulation covering the inner cylinder, a bare stainless steel outer cylinder and Shell Diala A transformer at a rotation rate of 400 rpm and 15°C. Each set of data was taken after vacuum processing the system, oil impregnating the pressboard, and lowering the temperature without rotation. Case (a) used fresh oil and pressboard. Cases (b) and (c) used the same materials as (a) with additional vacuum processing. The charge density and conductivity were essentially independent of the oil moisture content during the transient, but extra vacuum processing caused a decrease in the charge density.

with $D_o$ a temperature dependent coefficient [62]. Using the measured oil moisture content and the Norris curves relating the equilibrium concentrations of moisture in the oil and the paper, the pressboard moisture concentrations can be inferred [61]. For this experiment, the pressboard moisture content appeared to decrease from 0.74% in case (a) to 0.14% in case (c). The diffusivity in case (c) is then estimated to be 0.74 times the diffusivity of case (a). While the decreased diffusivity doesn't appear to completely describe the long time transient moisture behavior, it is consistent with the measurement.

This data also showed that the charge density was independent of the absolute oil moisture content. While the largest charge densities were initially obtained with the wettest oil, comparable charge densities were also obtained at lower moisture contents after the initial vacuum processing. Although the oil conductivity also changed slightly, the rate of increase in the charge density corresponded too closely to the rate of increase in the moisture to be ignored. Measurements of the pressboard dielectric relaxation time, as discussed in Chapter 4, at 70°C gave 108 sec for case (a), 89 sec for case (b) and 191 sec for case (c), which suggests that the conduction through the bulk of the pressboard did not change appreciably throughout these measurements. These observations implicate the "conditioning" or past history of the system, not simply the oil moisture content, as having a critical role in determining the charge density.

### 3.4.4 Oil conductivity dependence

Since the conductivity of the oil was not controlled by means of dissolving additives into the oil, the oil conductivity had a tendency to change with time. In some cases, the conductivity decreased, possibly indicating an adsorption of the trace impurities to the walls of the CC or even an absorption of the impurities into the pressboard insulation. There were also many situations in which the conductivity increased with time. While it is possible that the pressboard insulation was releasing impurities into the oil in these cases, the conductivity increase was usually most pronounced at elevated temperatures, which suggests that the oil was probably being oxidized. The oxygen required for this oxidation process was probably provided by slight leaks across the seals or possibly by trapped air bubbles.

The time variation of the oil conductivity was used to explore the charge density dependence on the conductivity when the other parameters such as the temperature and moisture content remained reasonably constant. One set of data that satisfied these criteria is shown in Fig. 3.20. The oil moisture content initially decreased as the pressboard dried the oil because immediately prior to the measurement the system had been at 80°C and a high oil moisture content. The moisture content then remained essentially constant, only increasing slightly, over the duration of this test. In contrast, the oil conductivity increased almost linearly with time. Except for an initial increase in charge density, possibly due to the accumulation of surface charge at the oil/pressboard interface, the charge density decreased almost linearly with time. The decreasing charge density with increasing conductivity is consistent with a "constant wall charge density ($\rho^w$)" model in which the charge density goes as $\rho_o \approx \rho^w \tau_{oil}/\tau_d$, with $\tau_d$ the diffusion time across the interfacial diffusion sublayers [2,25]. This suggests that one way to factor the conductivity dependence out of the charge density data is to multiply by the conductivity.

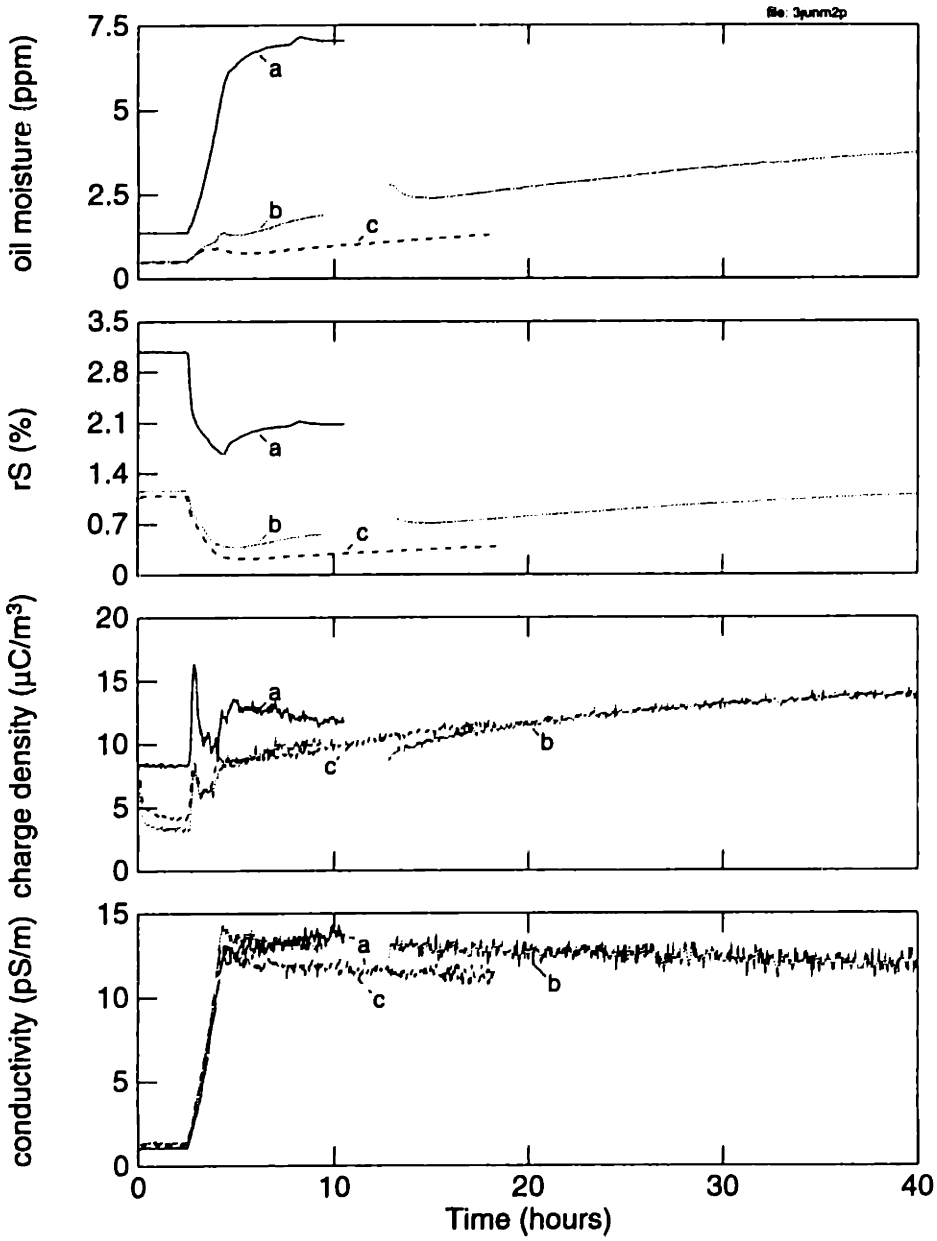


Figure 3.19: Temperature driven moisture transients for HiVal pressboard insulation covering the inner cylinder, a bare stainless steel outer cylinder and Shell Diala A transformer at a rotation rate of 400 rpm. This transient data was taken after the initial moisture equilibration periods shown in Fig. 3.18. The temperature was raised from 15°C to 70°C at hour 2.5. The conductivity followed the temperature and then decreased slowly. With increased vacuum processing the oil moisture content decreased but it took longer to reach steady state levels at 70°C. The charge density increased with the temperature and appeared to be independent of the absolute oil moisture content.

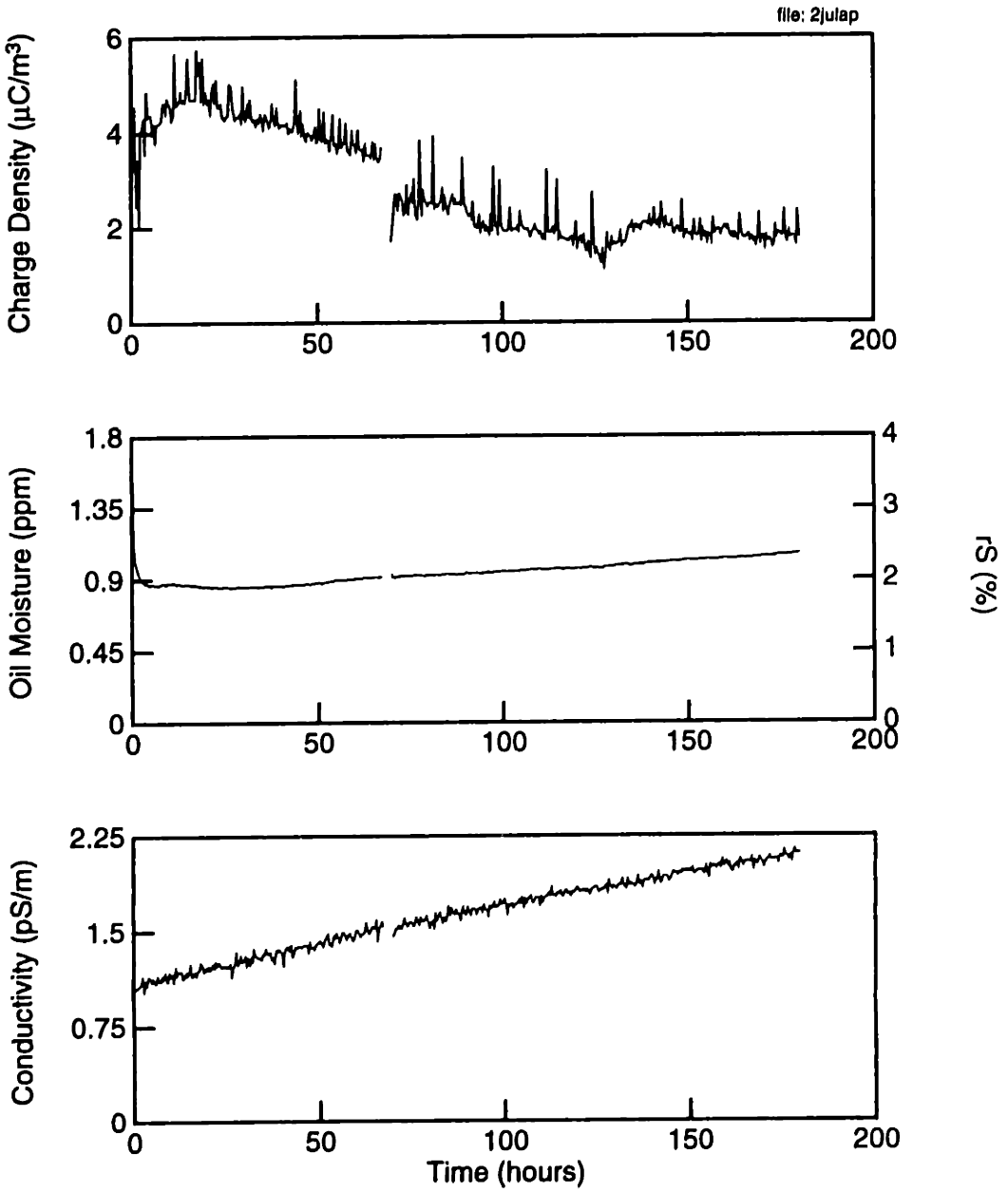


Figure 3.20: Oil conductivity effects on the charge density with HiVal pressboard insulation covering the inner cylinder, a bare stainless steel outer cylinder and Shell Diala A transformer oil. The temperature was 15°C and the rotation rate was 400 rpm. The gap in the data at time 65 hours occurred when the data acquisition program was restarted.

### 3.4.5 Applied DC voltage dependence

Many researchers have shown that the electrification charge density can be increased by high voltage AC energization [25,63]. The applied field enhances the migration of charge across the diffusion sublayers which, on average, leads to an increase in the net charge density in the well-mixed core region of the flow. If the field is large enough, which is typically the case in electric power apparatus, charge can also be injected into the fluid. While this has practical application in electric power apparatus, it only provides limited information about the electrification processes since new parameters, such as an "injection" charge density [25], are also introduced to explain the phenomenon. In contrast, application of DC voltages causes net (DC) charge to develop on the interfaces in the system, similar to the separation and accumulation of charge inherent in the flow electrification processes. In this section, some transient measurements with high DC voltages applied across the cylinders are presented, but the bulk of the measurements utilize relatively small DC voltages under steady state conditions. These are the measurements to be discussed in the models.

Representative measurements of the charge density variation with small DC applied voltages are shown in Fig. 3.21 for bare metal (stainless steel) electrodes and in Fig. 3.22 for pressboard insulation covering the inner cylinder electrode. The charge density increased linearly with the applied voltage in both cases, with the slope of the line decreasing as the rotation rate increased. The resolution of the measurements is illustrated by the scatter in the data at each voltage. Even though the charge densities were quite small and near the resolution of the instrument, the linear variation in charge density was quite distinct.

This linear dependence on the applied voltage does not appear to be an experimental artifact of the ACS. The ACS determines the volume charge density by drawing a sample of fluid into a Faraday cage which is grounded through a current measuring electrometer. By dividing the measured current by the fluid volume flow rate into the ACS, which is set by the expansion rate of a mechanical bellows, the charge density of the sampled fluid is found. The effects of flow electrification at the probe tip are reduced by subtracting an offset current, measured with stationary bellows, from the current used to obtain the charge density. Since this offset current was found to be constant and independent of the applied voltage, any leakage currents through the ACS due to the applied field were negligible.

Related measurements showed that the charge density had a slight dependence on the terminal constraints, under some conditions. As shown in Fig. 3.23, toggling the electrometer between voltage (open-circuit) and current (short-circuit) mode could lead to perturbations in the volume charge density. At the low rotation rates, when the terminal voltage and current were small, the charge density was unaffected by the terminal impedance. At the higher rotation rates, when the terminal current became appreciable the short-circuit charge density was found to be smaller than the open-circuit charge density. Again, although somewhat noisy, the trend was clear. These results are consistent with the applied voltage measurements showing the largest change in the charge density (with applied voltage) at the lowest rotation rates. When the applied voltage is large compared to the open-circuit voltage, as at low rotation rates, the perturbation in the charge den-

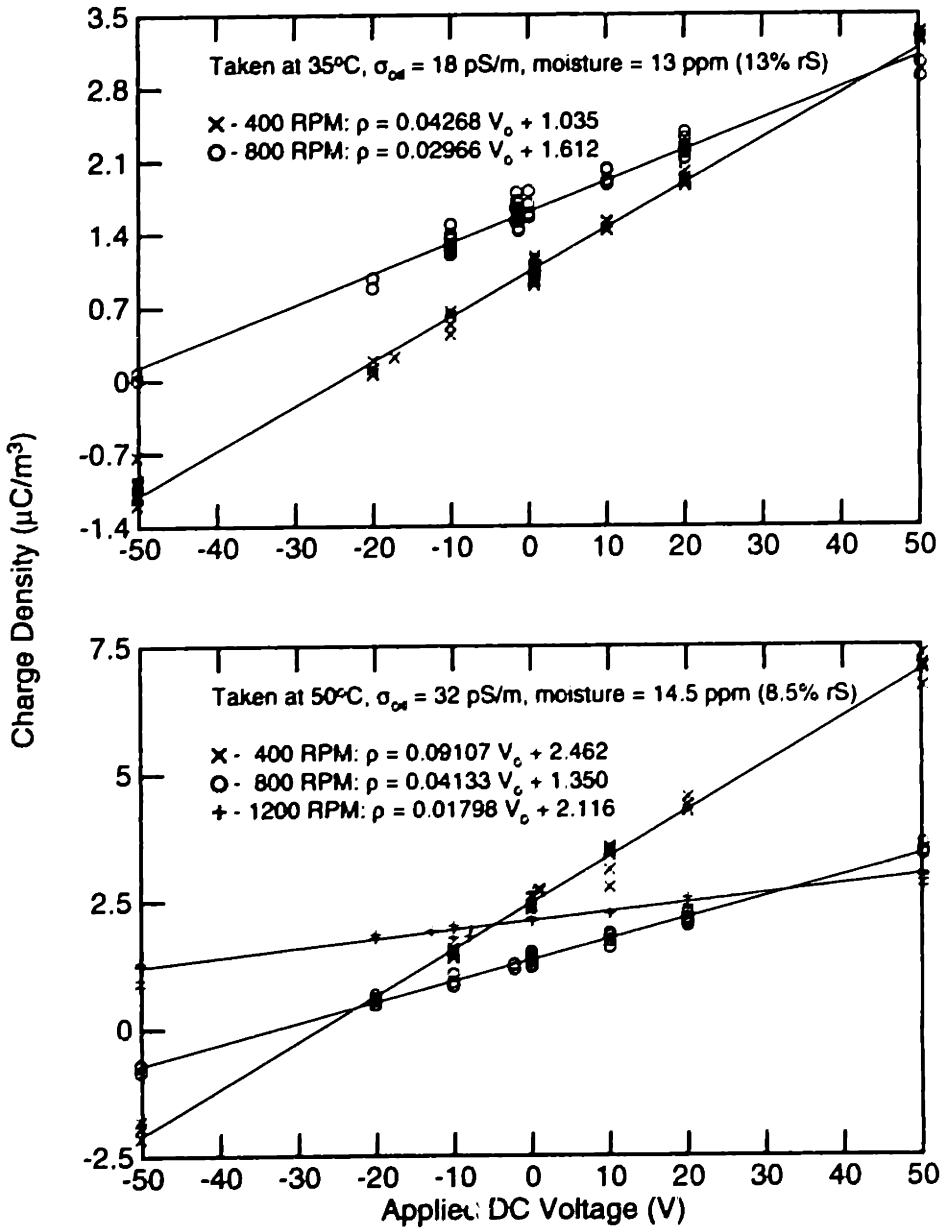


Figure 3.21: Charge density measurements using bare stainless steel cylinders and Shell Diala A transformer oil. The DC voltage was applied between the inner and outer cylinders. The inner cylinder rotation rate and oil properties are indicated.

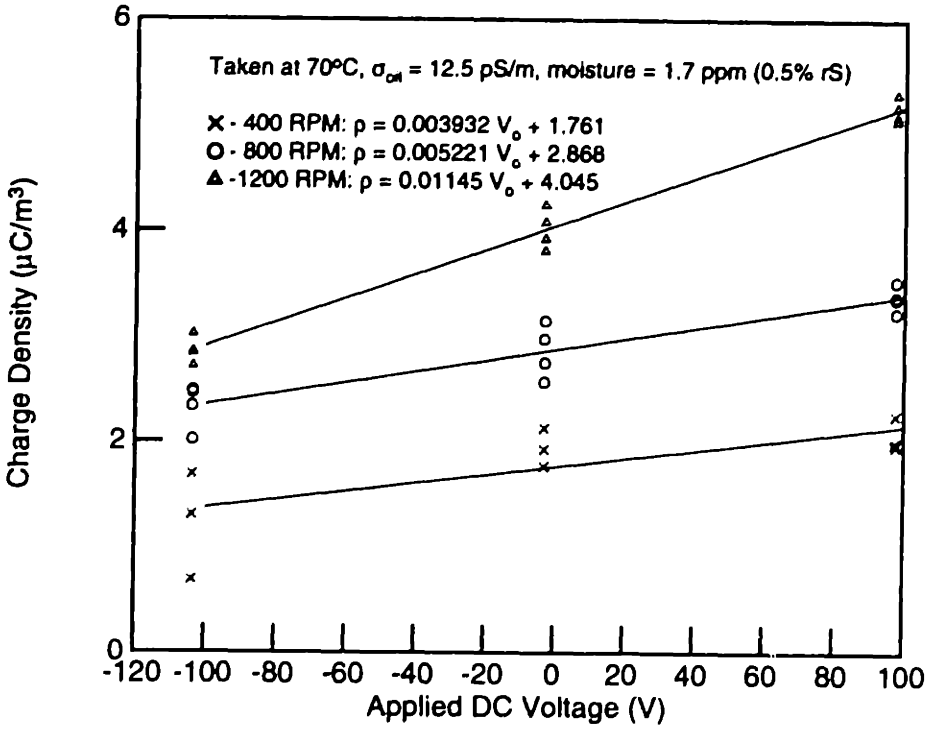


Figure 3.22: Charge density variation with applied DC voltage for HiVal pressboard covering the inner cylinder, a bare stainless steel outer cylinder and Shell Diala A transformer oil. The DC voltage was applied between the inner and outer cylinders.

sity is greater than that observed by changing the load impedance, but when the applied voltage is small compared to the open-circuit voltage, as at high rotation rates, the charge density perturbation is also smaller. In general, accurate measurements of the *change* in the charge density with the terminal impedance were only obtained in this type of experiment; comparing sets of data, with the rotation rate varied, between open-circuit and short-circuit conditions, usually showed similar trends, but small relative changes in the system temperature and oil conductivity obfuscated the results.

In general, measurements of the open-circuit voltage and the short-circuit current only give two of the points along the "I-V" characteristic of the CC. More points along the characteristic can be obtained by varying the applied DC voltage. In this case, the voltage source $V_o$ was connected to a 9.8 GΩ (current measuring) load resistor and the terminal voltage of the CC was monitored as the rotation rate was varied. The terminal

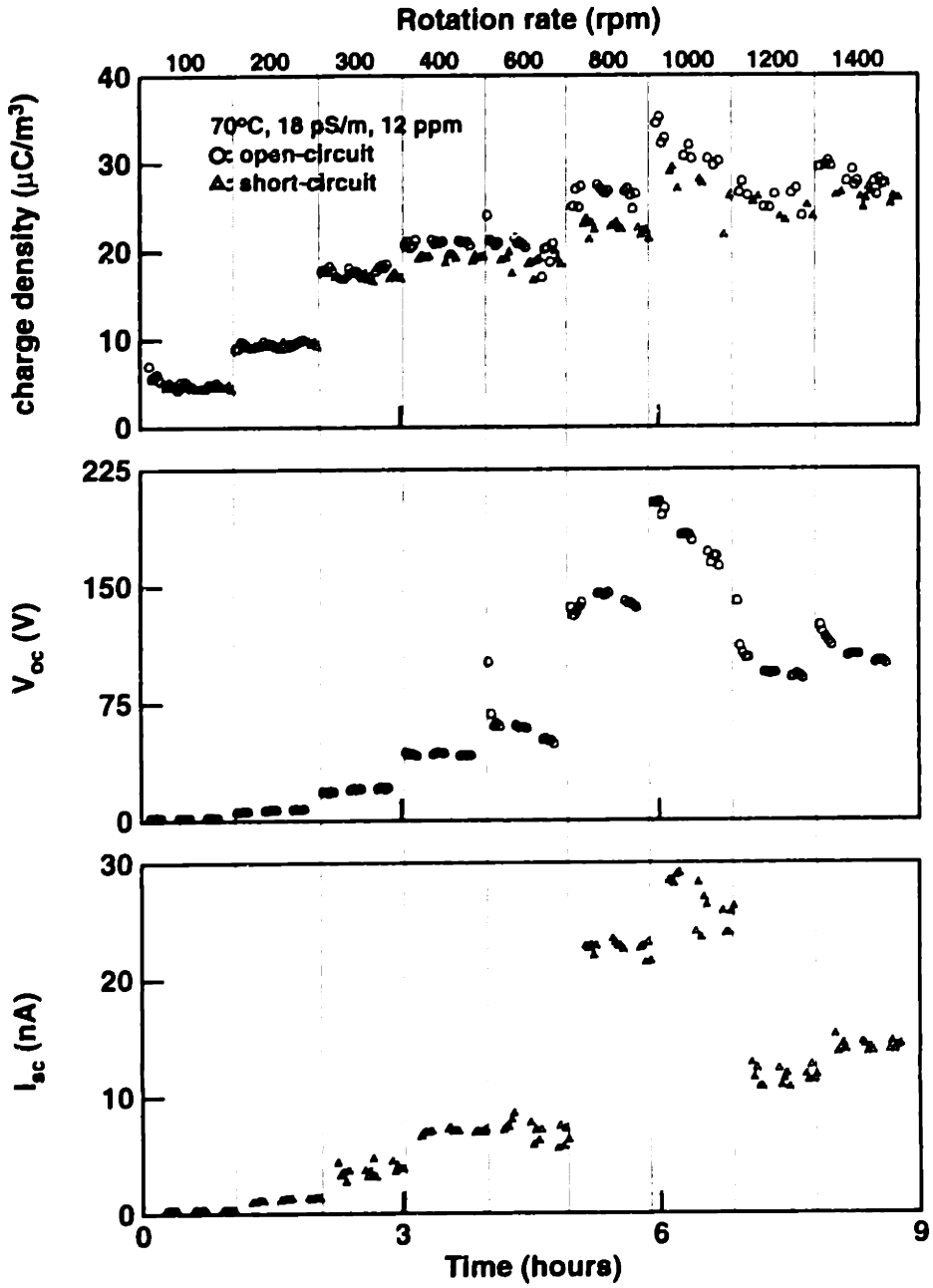


Figure 3.23: Charge density variation with terminal constraints for a copper sleeve covering the inner cylinder, a bare stainless steel outer cylinder and Shell Diala A transformer oil. The charge density with open-circuit terminals tends to be larger than when the terminals are short-circuited for this set of data.

current going into the CC[2] was calculated as the difference in the potentials across the load resistor divided by the load resistance. A representative plot of the terminal current and voltage for bare stainless steel cylinders is given in Fig. 3.24. When the applied voltage was constant and the rotation rate was varied, the terminal current and voltage were linearly related by the load resistance. When the rotation rate was constant and the applied voltage was varied, the terminal current and voltage were essentially linearly related, for small applied voltages, with the slope depending upon the rotation rate. Also notice that when the terminal voltage was equal to the the open-circuit voltage, at each rotation rate, the terminal current became zero. This "I-V" characteristic is similar to the current / interfacial overpotential curve described in the electrochemistry literature [64], except that it contains the contributions from reactions at *two* interfaces.

Transient measurements in which the charge density was measured after starting rotation and changing the terminal voltage provide insight into the charge transfer mechanism. The time transients in the core charge density were only measurable at the lower temperatures because the development times were longer than the sampling time of the charge sensor. Representative transient measurements, shown in Figures 3.25 and 3.26 for a temperature of 15°C show that the charge density decreased immediately after applying a positive voltage and then decayed back to near its steady state level while the voltage was applied. The charge density increased when negative voltages were applied. The applied voltage did not appear to appreciably affect the steady state charge density, in contrast to the results of Fig. 3.22, probably because the relative conductivity of the pressboard to the oil is much lower at lower temperatures [65].

One qualitative description of these transients comes from considering the stationary case so that the oil and pressboard can be described as simple dielectrics which have a single permittivity and conductivity. Electrically, the system can then be modeled as a Maxwell capacitor in cylindrical coordinates [66: pp.184-188]. If the system starts from an uncharged state in which the interface between the oil and the pressboard is free of charge, then the application of a DC voltage between the electrodes will cause a current to flow through the system and a surface charge $\sigma_f$ to develop on the interface according to

$$\sigma_f = \frac{\epsilon_2\sigma_1 - \epsilon_1\sigma_2}{\sigma_1 \ln(R_2/a) + \sigma_2 \ln(a/R_1)} \frac{V_o}{a} \left(1 - e^{-t/\tau_c}\right) \tag{3.3}$$

with $R_1$ the inner cylinder radius, $a$ the radius of the pressboard sleeve ($a - R_1$ the pressboard thickness), $R_2$ the outer cylinder radius, $V_o$ the applied voltage, $\epsilon_1$ the pressboard permittivity, $\sigma_1$ the pressboard conductivity, $\epsilon_2$ the oil permittivity, $\sigma_2$ the oil conductivity, and $\tau_c$ the charging time constant given by

$$\tau_c = \frac{\epsilon_1 \ln(R_2/a) + \epsilon_2 \ln(a/R_1)}{\sigma_1 \ln(R_2/a) + \sigma_2 \ln(a/R_1)} \tag{3.4}$$

(The geometry is described in detail in Section 5.4.) When the voltage source is disconnected, the decay of this surface charge depends upon the terminal connections. If the terminals are short-circuited by a current measuring electrometer, the current is the

[2]Note that this is the opposite polarity convention from the other measurements described here.

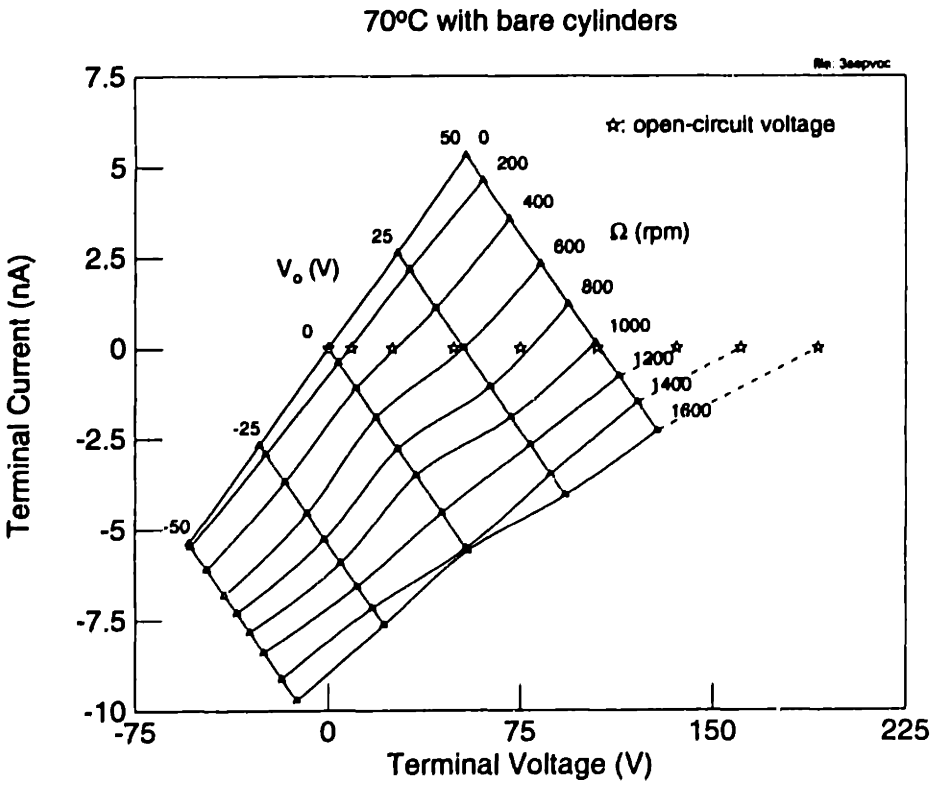


Figure 3.24: Measured "I-V" characteristic for the CC, with bare stainless steel cylinders and Shell Diala A transformer oil filling the gap between the cylinders. The voltage $V_o$ was applied to the CC through a 9.8 GΩ resistor. The current going into the CC was obtained from the measured difference in voltage across the load resistor at each rotation rate. The triangles indicate measured values while the stars indicate the measured open-circuit voltage at each rotation rate.

same through both the oil and the pressboard regions and the decay time is the same as the charging time constant $\tau_c$. On the other hand, if the terminals are open-circuited then the fields in each region decay independently so that there isn't any current flow through the terminals. The open-circuit voltage decay can be expressed as

$$v_{oc}(t) = v_1(0^-)e^{-t/\tau_1} + v_2(0^-)e^{-t/\tau_2} \tag{3.5}$$

where $v_1(0^-)$ is the initial voltage across the pressboard region, $v_2(0^-)$ is the initial voltage across the oil region, $\tau_1 \equiv \epsilon_1/\sigma_1$ is the pressboard dielectric relaxation time and $\tau_2 \equiv \epsilon_2/\sigma_2$ is the oil relaxation time. The first term reflects the decay of the field stored in the pressboard while the second term comes from the decay of the field across the oil. If a steady state had been achieved during the charging period ($t \gg \tau_c$), then the

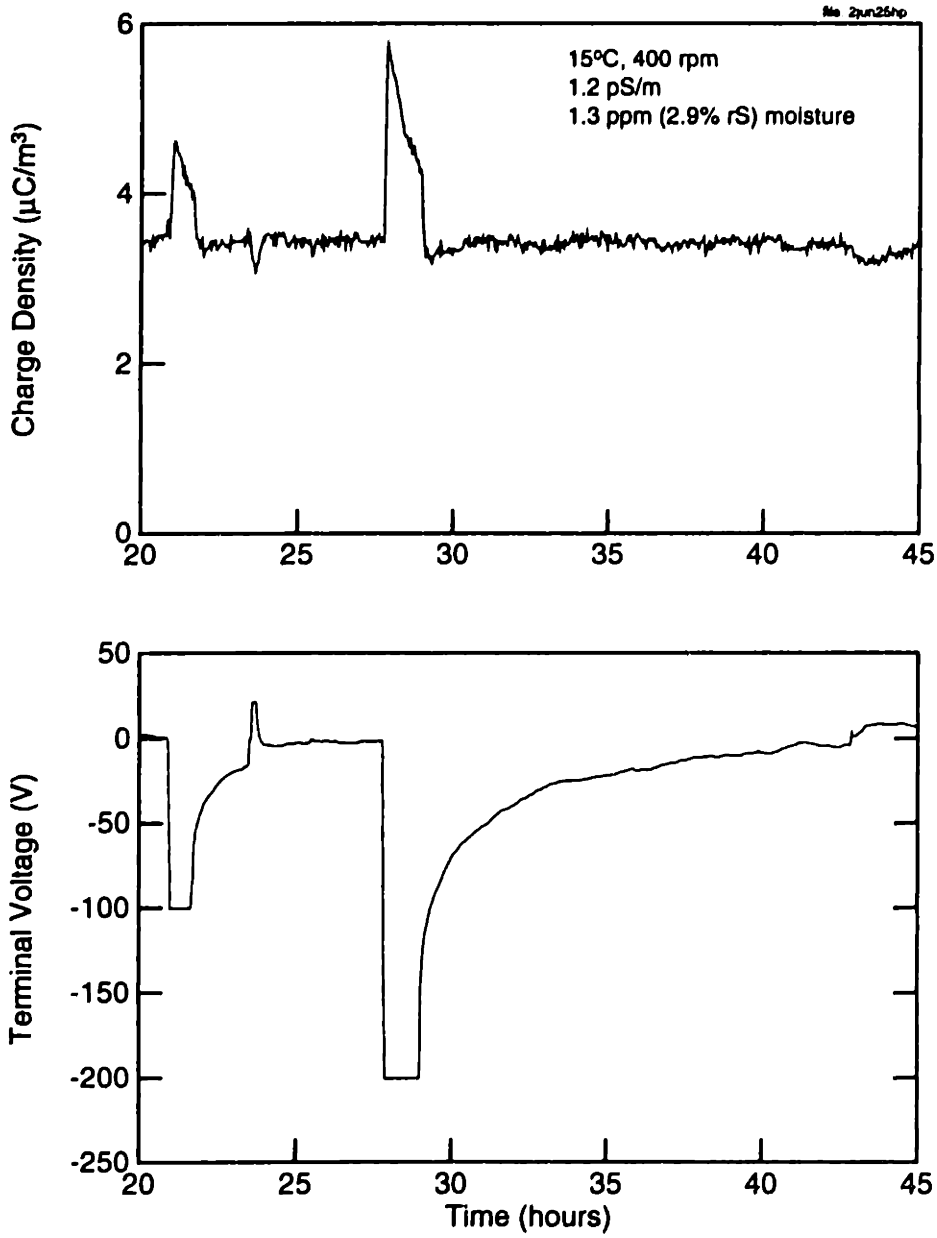


Figure 3.25: Transient voltage effect on the core charge density with HiVal pressboard covering the inner cylinder and a bare stainless steel outer cylinder. The temperature was lowered (from 70°C) at time zero and the inner cylinder rotation was started at hour 10.6. DC voltages of -100 V, 22.5 V, and -200 V were then applied to the cylinders. The open-circuit terminal voltage was measured when the voltage source was disconnected. The average pressboard moisture content was measured to be between 0.4 and 0.5%.

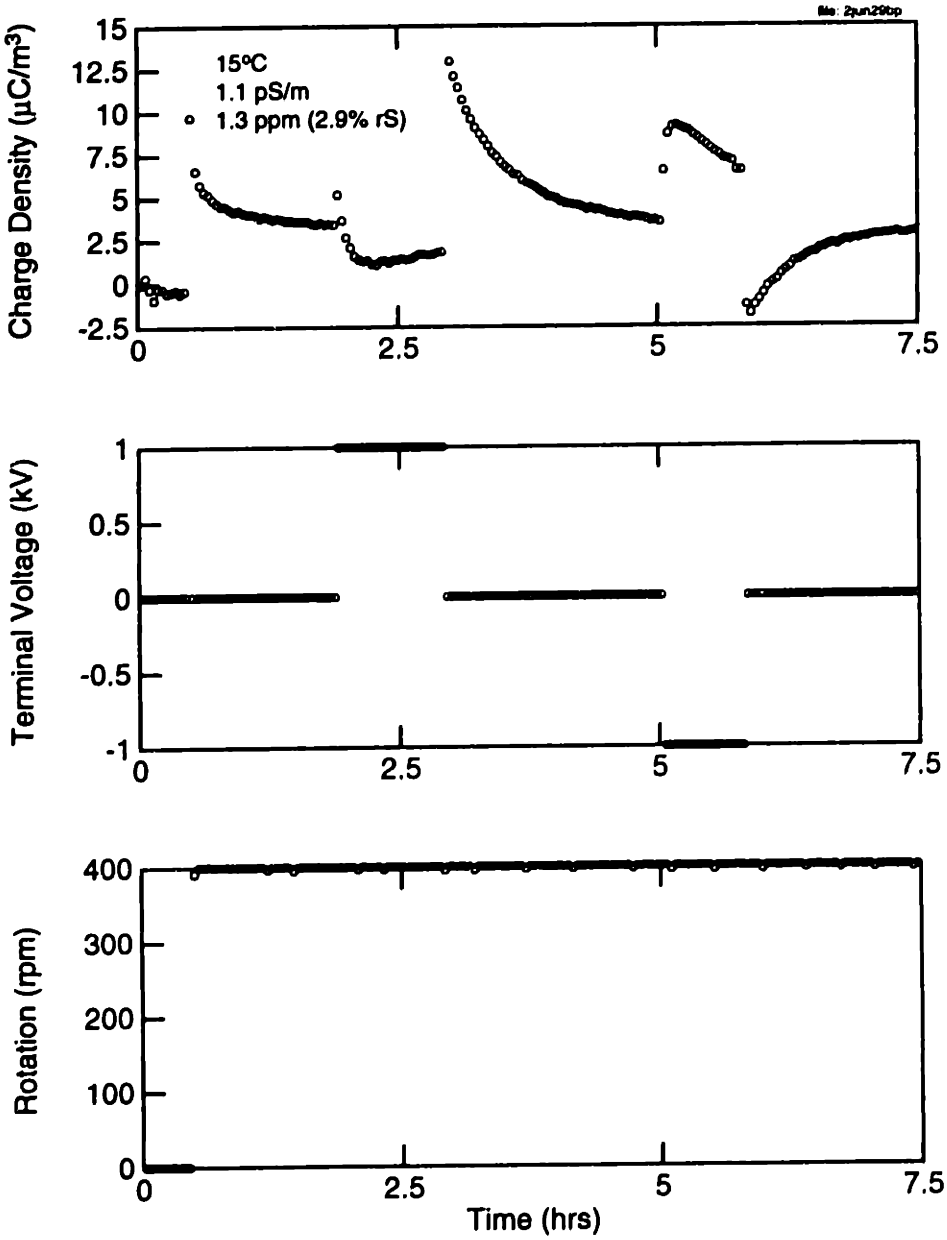


Figure 3.26: Voltage (±1 kV) and rotation transient effects on the core charge density with HiVal pressboard covering the inner cylinder and a bare stainless steel outer cylinder. This experiment used the same materials as those of Fig. 3.25.

discharging transient becomes

$$v_{oc}(t) = V_o \left[ \frac{\sigma_2 \ln(a/R_1) e^{-t/\tau_1} + \sigma_1 \ln(R_2/a) e^{-t/\tau_2}}{\sigma_1 \ln(R_2/a) + \sigma_2 \ln(a/R_1)} \right] \tag{3.6}$$

If the pressboard is much more insulating than the oil (so that the geometrical factors can be neglected), then the electrical energy is essentially stored in the field inside the pressboard and the free surface charge at the oil/pressboard interface is imaged to the inner cylinder. As the pressboard conductivity becomes comparable to the oil conductivity, more of the electric field passes through the oil and more of the free surface charge is imaged to the outer cylinder.

To qualitatively explain the experimentally observed transients in Figs. 3.25 and 3.26, first assume that the effects of the applied voltage on the inner cylinder dominate those at the outer cylinder. To justify this assumption, note that the electric field is larger at the inner cylinder than the outer cylinder by the ratio of $R_2/a \approx 4/3$, the amount of charge taken from the inner cylinder sublayer is larger by the same ratio because the diffusion sublayer on the outer cylinder is larger by that ratio and less charge would be stripped away from the interface (as described in more detail in Section 5.6), and the inner cylinder surface area is smaller by the ratio $a/R_2$. The net contribution to the charge density should be greater from the inner cylinder by the ratio $R_2/a$ so only the charge dynamics near the inner cylinder interface will be discussed. Also, to be consistent with the measured volume charge densities, assume that without rotation and without an applied voltage the chemically adsorbed surface charge on the inner cylinder is negative so that a positive volume charge density develops in the electrical double layer on the liquid side of the interface.

As the rotation of the inner cylinder is started, some of the positive volume charge is transported by the fluid into the core region. When a positive voltage is applied, the volume charge near the interface is decreased as negative volume charge accumulates to shield the applied field from the bulk of the fluid. This leads to a decrease in the core charge density as well. As some of this negative charge gets adsorbed onto the interface to form a surface charge, the volume charge densities return to near their steady state levels. After removing the voltage source and keeping the terminals open-circuited (as in Fig. 3.25), the accumulated surface charge leads to a terminal voltage that decays with the relaxation time of the pressboard. The charge density rapidly returns to its original level because the oil relaxation time is small compared to the charge density measurement time. In contrast, after removing the voltage source and keeping the terminals short-circuited (as in Fig. 3.26), the accumulated (negative) surface charge is imaged by a positive volume charge on the liquid side of the interface and the core charge density then increases. As the surface charge decays, the core charge density also decays. The charging and discharging transients have similar time constants, consistent with the accumulation and decay of interfacial free surface charge discussed for ohmic dielectrics between stationary cylinders. The opposite polarity effect occurs when a negative voltage is applied.

A representative plot of the time transients in the charge density as the terminal voltage was varied for two rotation rates is given in Fig. 3.27. By increasing the rotation rate, the diffusion sublayer thicknesses were decreased. Since the measured time con-

stants associated with the transient decays in the charge densities were roughly the same at both rotation rates, the charge dynamics were probably reaction limited. In contrast, the charge density increased with rotation rate when there wasn't a DC excitation, suggesting that the charge dynamics were at least partially transport limited. From these observations it would appear that the transport rate and the reaction rate for charge transfer at the interface are comparable for these semi-insulating materials.

### 3.4.6 "Conditioning" transients

While most of the measurements discussed thus far have focussed on experiments that had a relatively short duration, long time transient variations were also observed in the experiments. In general terms, electrification (charge density, terminal current and voltage) measurements showed long time variations that were not correlated to measurements of the moisture content or conductivity. Since the electrification data is sensitive to the interfacial properties, it is concluded that the interfacial dynamics (adsorption and desorption of ions) are significant over these long transients.

One example of a "conditioning" transient occurred with bare stainless steel cylinders as shown in Fig. 3.28. In this case, electrification measurements were performed at 15, 35, 50, and then 70°C. Initially, the charge density and terminal voltage had opposite polarities, but after reaching 70°C they had the same polarity. Subsequent measurements (in the second set) showed that the charge density and voltage still had the same polarity, even at the lower temperatures. The terminal current was relatively noisy, but usually followed the voltage. These measurements indicate that the system was "conditioned" by some process. The terminal voltage showed the "conditioning" process more markedly than the core charge density because, as will be discussed in Chapter 6, the terminal voltage and current are more sensitive than the core charge density to *differences* in the interfacial properties. One possible mechanism for the "conditioning" is that the different current densities at the cylinder interfaces led to the formation of oxide layers of different thicknesses. Indeed, related measurements of the leakage current as oil flows through a sintered filter have also shown passivation effects in which the current tends to decrease with time once the filter has come into contact with the fluid [67,68].

Another example of a "conditioning" transient, from the preliminary experiments, was shown in Fig. 3.2 in which the charge density changed with a long time constant. A similar set of data was obtained in the improved Couette Facility, as shown in Fig. 3.29. This improved measurement had more diagnostics and did not have the complication associated with the convective transport times through the various sections of the experimental apparatus. During the initial equilibration period, the charge density appeared to vary inversely with the oil moisture content, but the charge density did not appear to follow the oil moisture content after that period; the moisture only appeared to be important during the initial phase. As in previous measurements, the low temperature charge density decreased as the conductivity increased. At the higher temperatures, the charge density did not consistently track with the conductivity. Thus, although the charge density occasionally tracked with the oil moisture and conductivity, the long time transient change in the charge density was probably not caused by either of these.

The temperature cycling did not always lead to simple "conditioning" transients

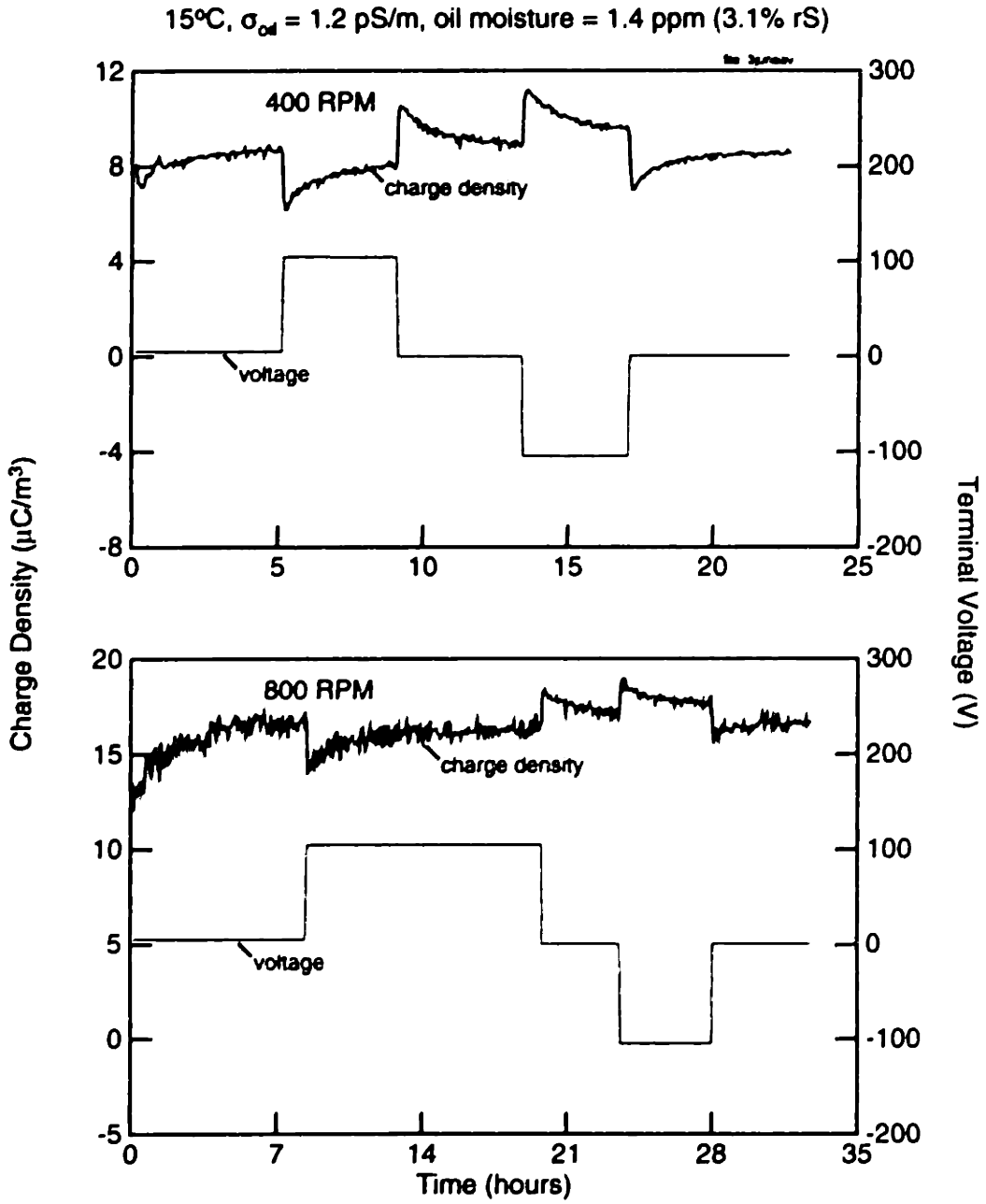


Figure 3.27: Voltage transient effects on the core charge density with HiVal pressboard insulation covering the inner cylinder and a bare stainless steel outer cylinder.

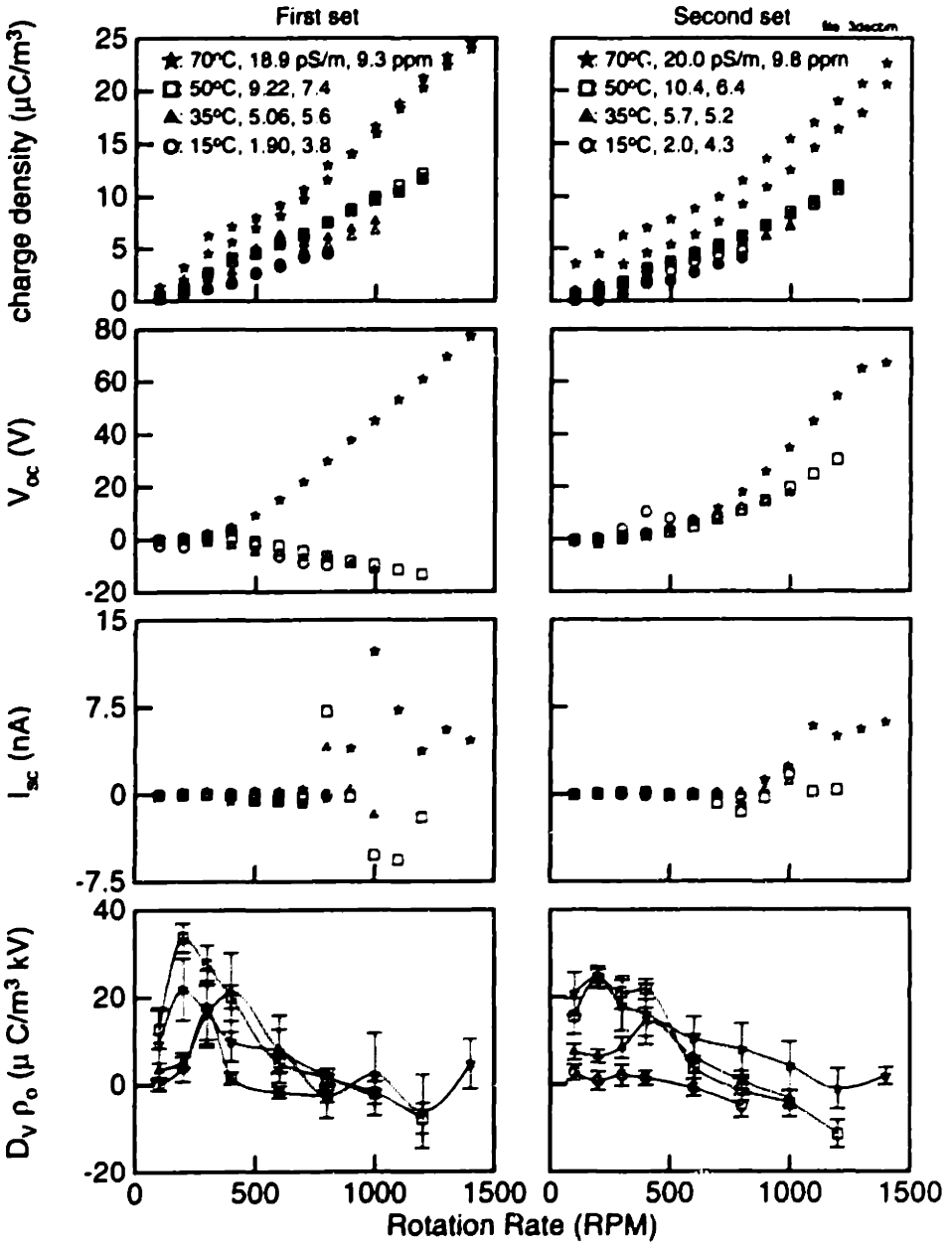


Figure 3.28: Two sets of measurements for bare stainless steel inner and outer cylinders and Shell Diala A transformer oil which show the system being "conditioned." In both sets, the temperature was raised from 15°C to 70°C, with the second set taken after the first set. The oil conductivity and moisture content are indicated. Both open-circuit (open symbols) and short-circuit (filled symbols) charge densities are plotted. Initially, the voltage had a polarity opposite the charge density, but after reaching 70°C they had the same polarity. Subsequent measurements showed the charge density and voltage having the same polarity.

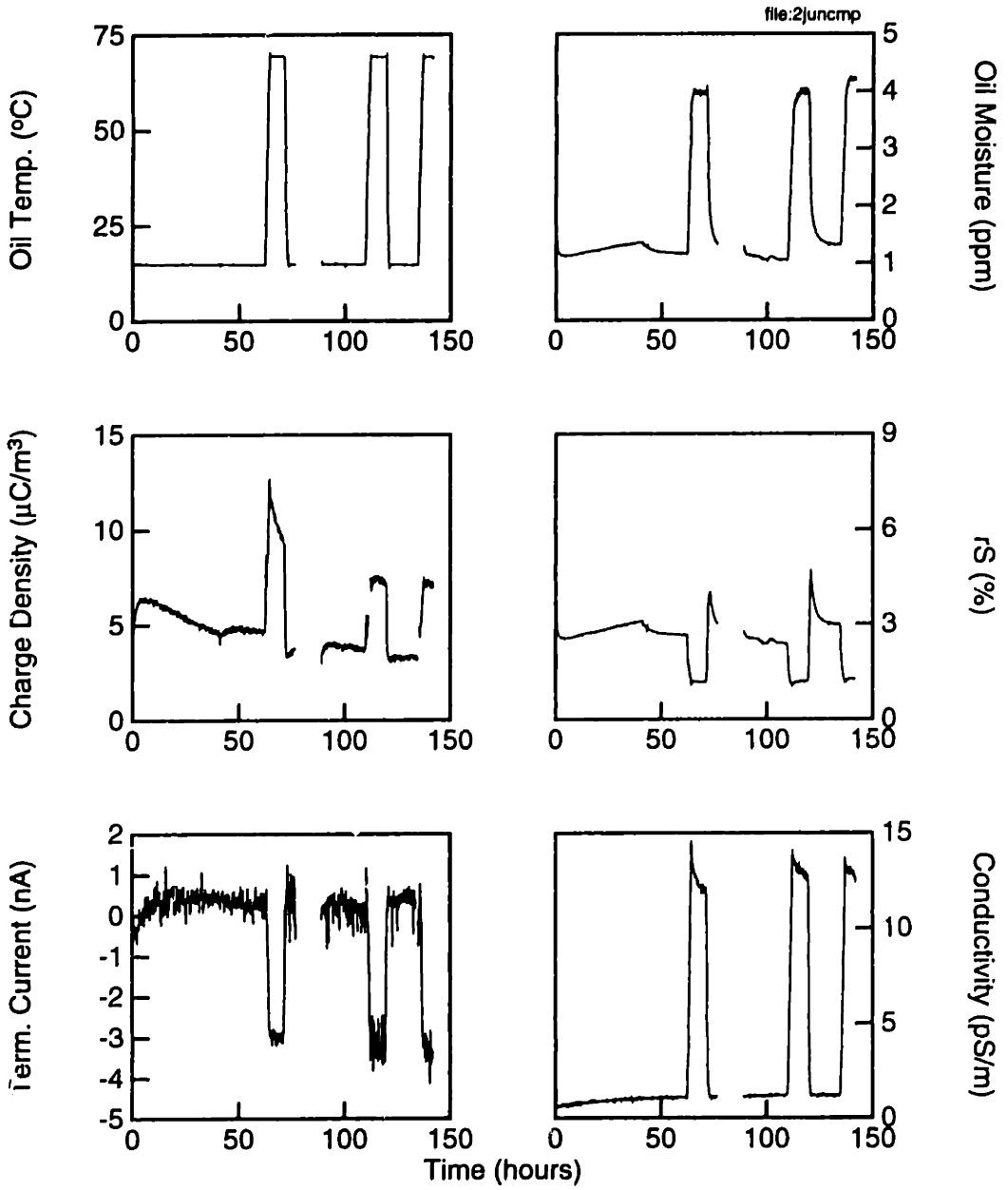


Figure 3.29: "Conditioning" transient during temperature cycling for HiVal pressboard covering the inner cylinder, a bare stainless steel outer cylinder, Shell Diala A transformer oil and a rotation rate of 400 rpm. There wasn't any rotation between hours 77–89. Initially the charge density appeared to vary inversely with the oil moisture content. After raising the temperature, the charge density followed the conductivity while the moisture remained constant. Repeated temperature cycling did not result in the sharp peak in charge density associated with the initial temperature transient increase.

though. Another set of data, given in Fig. 3.30, was performed over a longer scale than that of Fig. 3.29 but used materials (pressboard and oil) from the same batch as that experiment. Again, the largest charge densities occurred during the initial transients when the rotation was started and the temperature was increased. In this case, the charge density never reached steady state (at 70°C) and even reversed polarity. After the brief initial decrease in moisture content as the pressboard dried the oil, the moisture content slowly increased, possibly due to leaks in the system. The increasing conductivity, particularly at higher temperatures, is consistent with the oil being exposed to air and being oxidized. While changes in the oil conductivity affect the magnitude of the charge density and current, as illustrated in Section 3.4.4, the different impurities that change the conductivity may also affect the surface charge densities. Additional measurements on this system indicated that the polarity reversal in the charge density may be caused by the processing of the pressboard. Replacing the oil with fresh (unused) oil, drying the pressboard in the CC (at elevated temperatures and under vacuum) and stepping the system temperature from 15 to 70°C led to a similar initial transient in which the moisture content and conductivity increased with time, the charge density decreased with time, eventually reversing polarity, and the current remained essentially constant.

Although relatively rare, the oil volume charge density was occasionally negative. Usually this resulted from long time transient changes in the system, but on one occasion, the charge density was negative immediately after the rotation was started. As shown in Fig. 3.31, during the initial 15°C equilibration period, the moisture in the oil migrated into the pressboard and the oil conductivity remained essentially constant. On the other hand, the charge density was negative and the terminal current was positive and relatively large. During this period, sharp discontinuities in the charge density and current were present, which appear to be consistent with discharges in the system. Subsequent measurements, given in Fig. 3.32, showed the charge density and current repeatedly reversing polarity. Some of these polarity reversals were driven by changes in the temperature but others occurred at a constant temperature. Since the moisture content and conductivity were increasing slowly with time, the system was probably slightly exposed to the atmosphere.

One possible mechanism leading to the discharges is that surface charge was accumulating at the oil/pressboard interface as the fluid flow redistributed the charge in the system. Once enough surface charge accumulated, the associated electric field exceeded the local breakdown field which, in turn, caused all of the accumulated charge to discharge. The discharge appeared to be global, rather than local, because the terminal current, which gives the net current flowing across the *entire* inner and outer cylinder interfaces, was discontinuous. The total charge involved in the discharge can be estimated from the discontinuity in the charge density and the volume of the annular gap. Using a volume of 6500 $cm^3$ and a charge density change of 4 $\mu C/m^3$, 26 nC of charge were discharged. With a rotational speed of 400 rpm corresponding to an average oil velocity of 190 cm/sec (based on a radius of 9 cm), this quantity of charge is consistent with published magnitudes for electrostatic discharges created by flowing oils [30].

These results were somewhat surprising because discharges were not seen in previous or subsequent measurements. Although the oil moisture content was very low in this measurement, indicating that the pressboard insulation was also very dry, other experiments that achieved similar moisture contents did not exhibit these discharges.

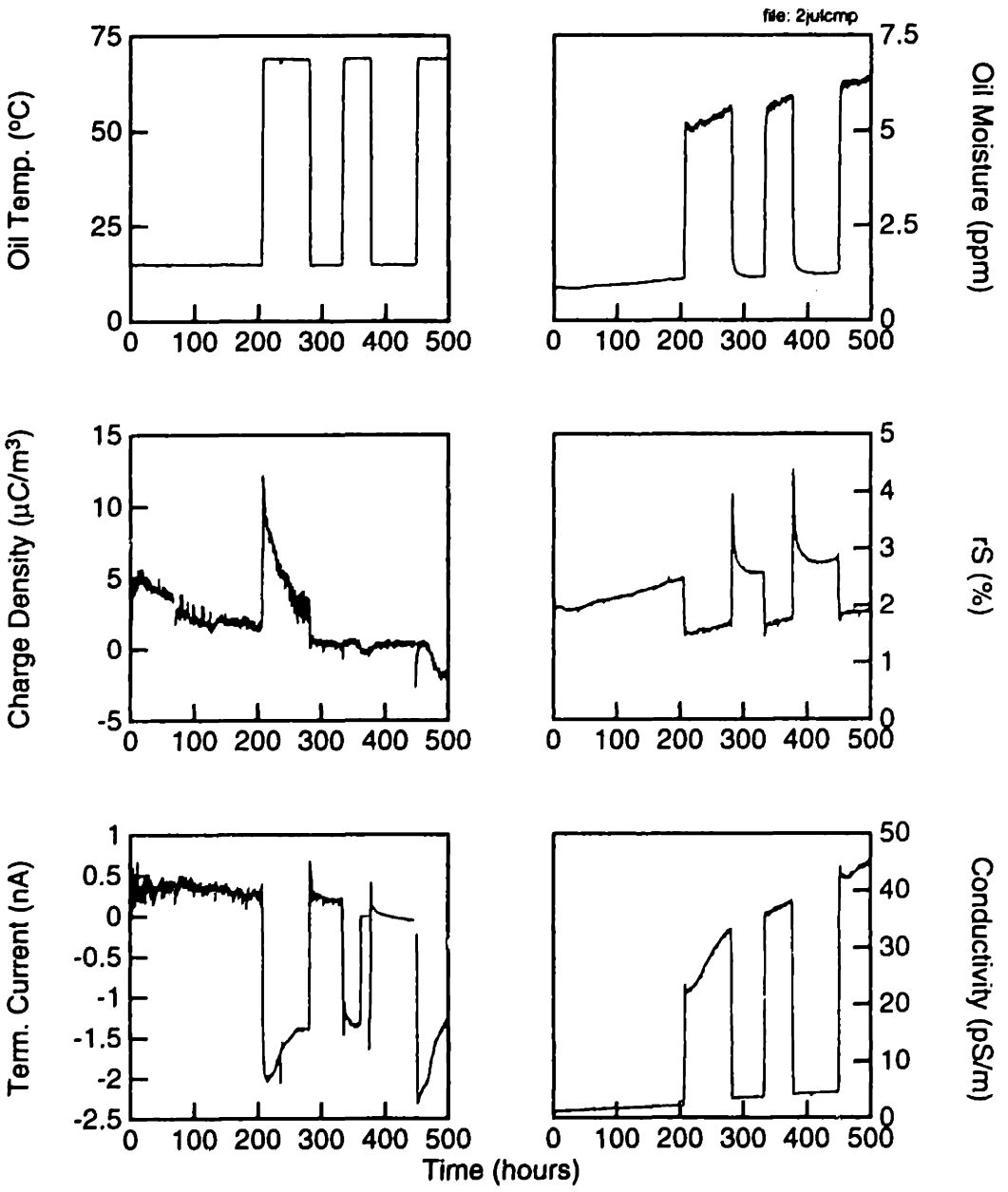


Figure 3.30: "Conditioning" transient during temperature cycling for HiVal pressboard covering the inner cylinder, a bare stainless steel outer cylinder, Shell Diala A transformer oil and a rotation rate of 400 rpm. The moisture content slowly increased, possibly due to leaks in the system. The increasing conductivity, particularly at higher temperatures, is consistent with the oil being slightly exposed to air and being oxidized. Cycling the temperature showed the migration of moisture between the oil and the pressboard. The charge densities were largest during the initial "conditioning" phase.

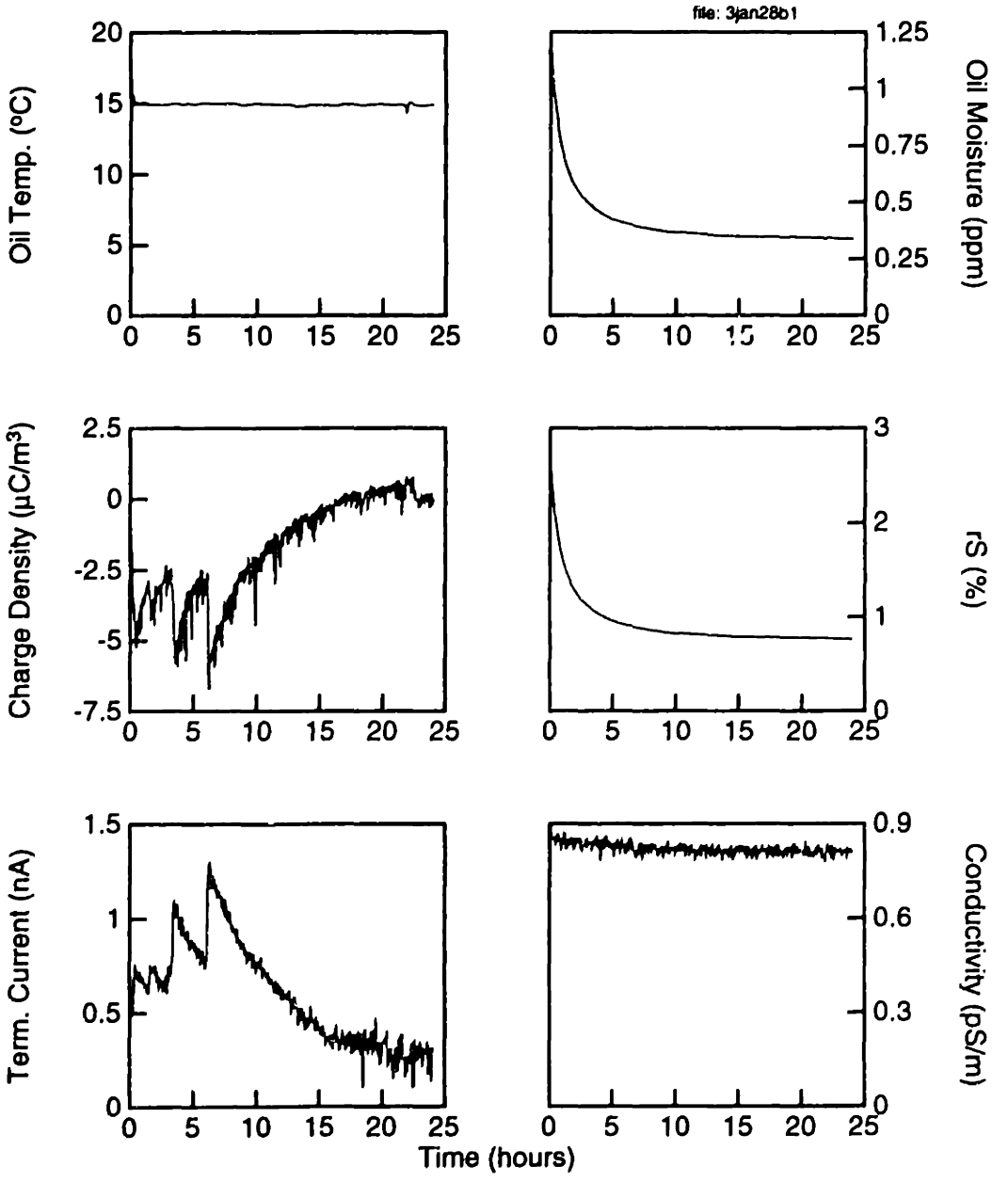


Figure 3.31: Initial 15°C equilibration period for HiVal pressboard covering the inner cylinder, a bare stainless steel outer cylinder, Shell Diala A transformer oil and a rotation rate of 400 rpm. The oil moisture content slowly decreased as the pressboard dried the oil. The sharp discontinuities in the charge density and terminal current appear to be consistent with discharges in the system.

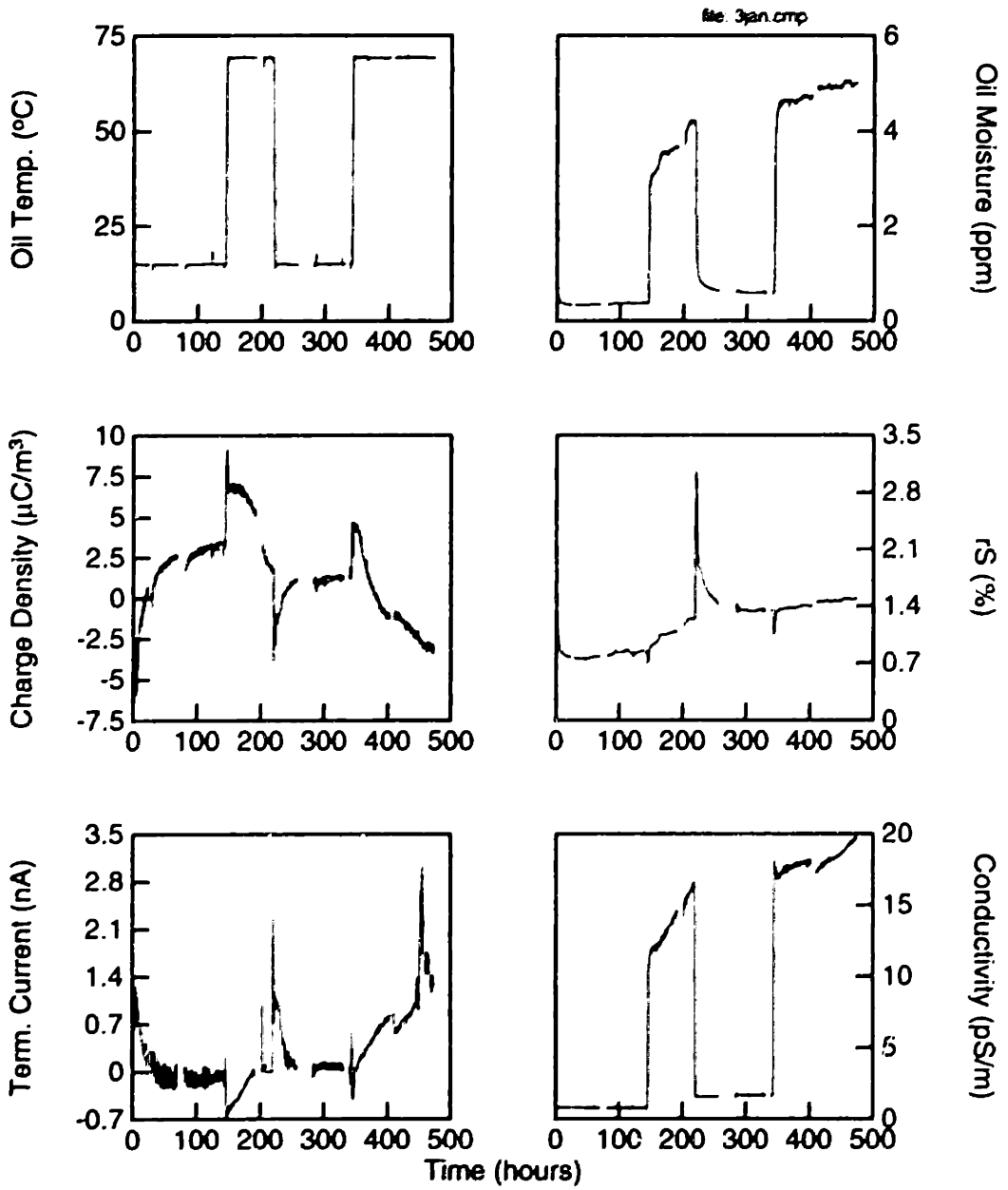


Figure 3.32: Transients during temperature cycling for HiVal pressboard covering the inner cylinder, a bare stainless steel outer cylinder, Shell Diala A transformer oil and a rotation rate of 400 rpm. This data is a continuation of that shown in Fig. 3.31. The charge density and the terminal current typically changed polarity together. Repeated temperature cycling appeared to drive some of the polarity reversals. The moisture content and conductivity increased slowly, probably indicating a slight leak to atmosphere.

Furthermore, the change in the volume charge density as a result of the discharge was relatively small; other measurements showed larger volume charge densities at the same temperature, but no discharges. After disassembling the system and looking at the pressboard, the only surface blemish that was found was near the top of the inner cylinder. The blemish was slightly darker than the surrounding area and could have been due to the discharges. Apparently, once the local area of the discharge had been damaged, the discharges stopped.

In summary, these experiments highlight some of the difficulties associated with the electrification measurements. While numerous sets of experiments showed the same general trends (such as increased currents, voltages, and charge densities as the rotation rate or temperature were raised), there were also a number of experiments that exhibited longer time transient, "conditioning" behavior. Even though these experiments showed some of the nonreproducibility associated with the measurements, possibly due to leaks in the system or other uncontrolled parameters, they also showed long time scale dynamics. In a real transformer, both the initial conditioning phase, immediately after processing, and long time transient phases will be present. These measurements seem to indicate that the initial phase, immediately after processing led to the greatest electrification behavior.

### 3.4.7 Effects of copper

Since copper is present in large quantities in a transformer and deactivated by BTA[3], a thin sheet of copper was attached to the inner cylinder. Although the copper in a transformer is typically covered by paper or pressboard insulation, initial measurements were performed with bare copper on the inner cylinder. A representative set of steady state electrification measurements, with the outer cylinder kept as bare stainless steel, is shown in Fig. 3.33. Before obtaining these results, the system went through the same type of "conditioning" transient observed with bare stainless steel cylinders in which the charge density and the terminal variables had opposite polarities at low temperatures, but after increasing the temperature up to 70°C and then returning again to the lower temperatures the charge density and terminal variables had the same polarity. These results are similar to those shown in Fig. 3.9 for bare stainless steel cylinders. In general, copper and stainless steel appeared to have similar electrification characteristics.

For comparison to earlier data without the copper, moisture and temperature transient measurements were also performed with HiVal pressboard insulation covering the copper sheet. For example, Fig. 3.34, which can be compared to Fig. 3.18, shows the initial 15°C equilibration after the pressboard was oil impregnated and the temperature was lowered. The charge density increased slightly with time, but did not track with the decreasing moisture content. The oil conductivity was essentially constant. In this set of data, the terminal current was also measured cleanly and found to have a small magnitude.

Fig. 3.35, like Fig. 3.16, shows the result of a step increase in temperature from 15 to

[3]BTA reacts with copper ions and oxygen to create a copper/BTA complex and, in oil, forms a passivating film on copper surfaces [69].

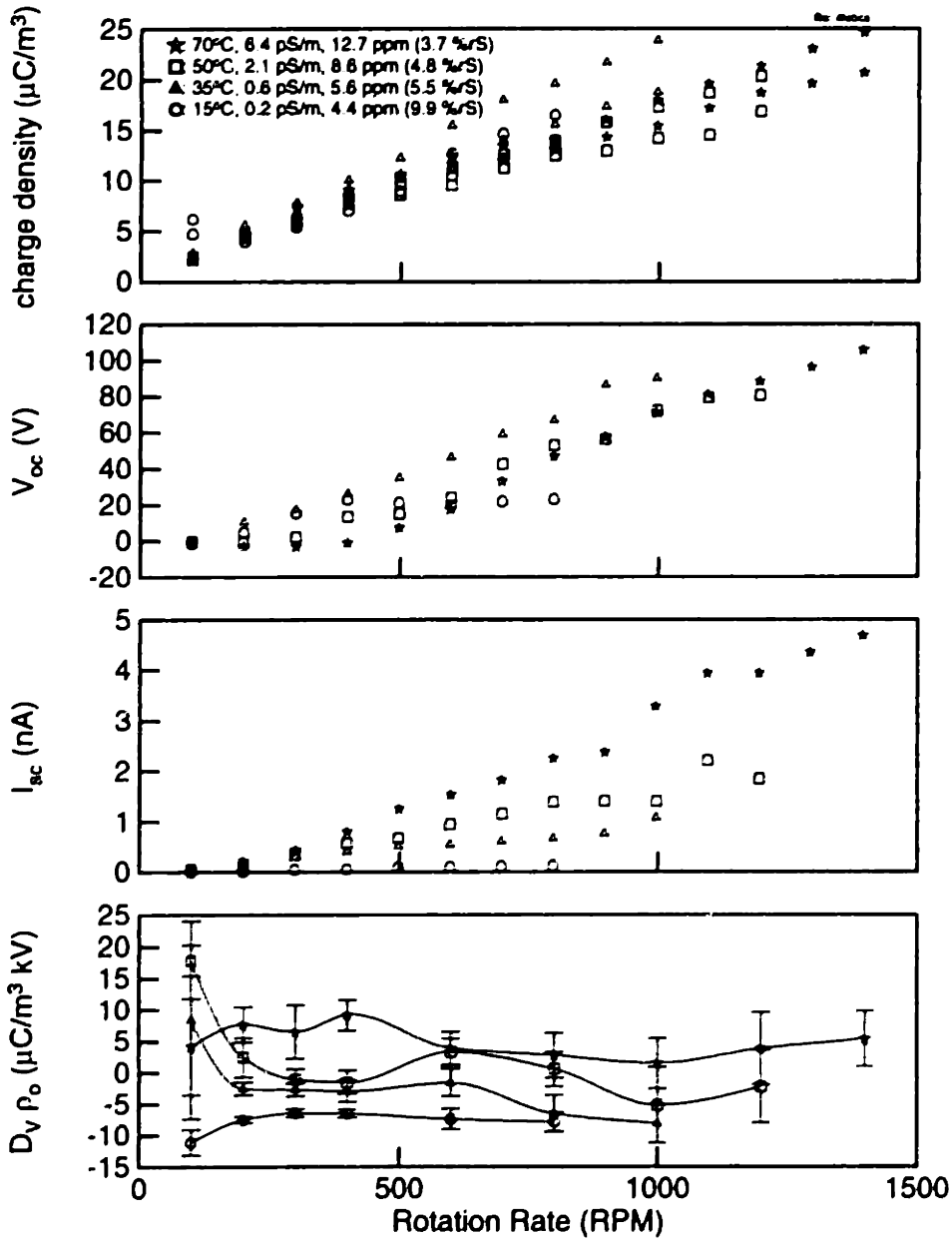


Figure 3.33: A set of electrification measurements for a copper sleeve on the inner cylinder, a bare stainless steel outer cylinder and Shell Diala A transformer oil. The charge density (open and short-circuit), voltage, and current usually had the same polarity and increased with rotation rate. The charge density and voltage had maxima at 35°C for each rotation rate. The charge density variation with applied voltage tended to be negative at low temperatures but positive at high temperatures.

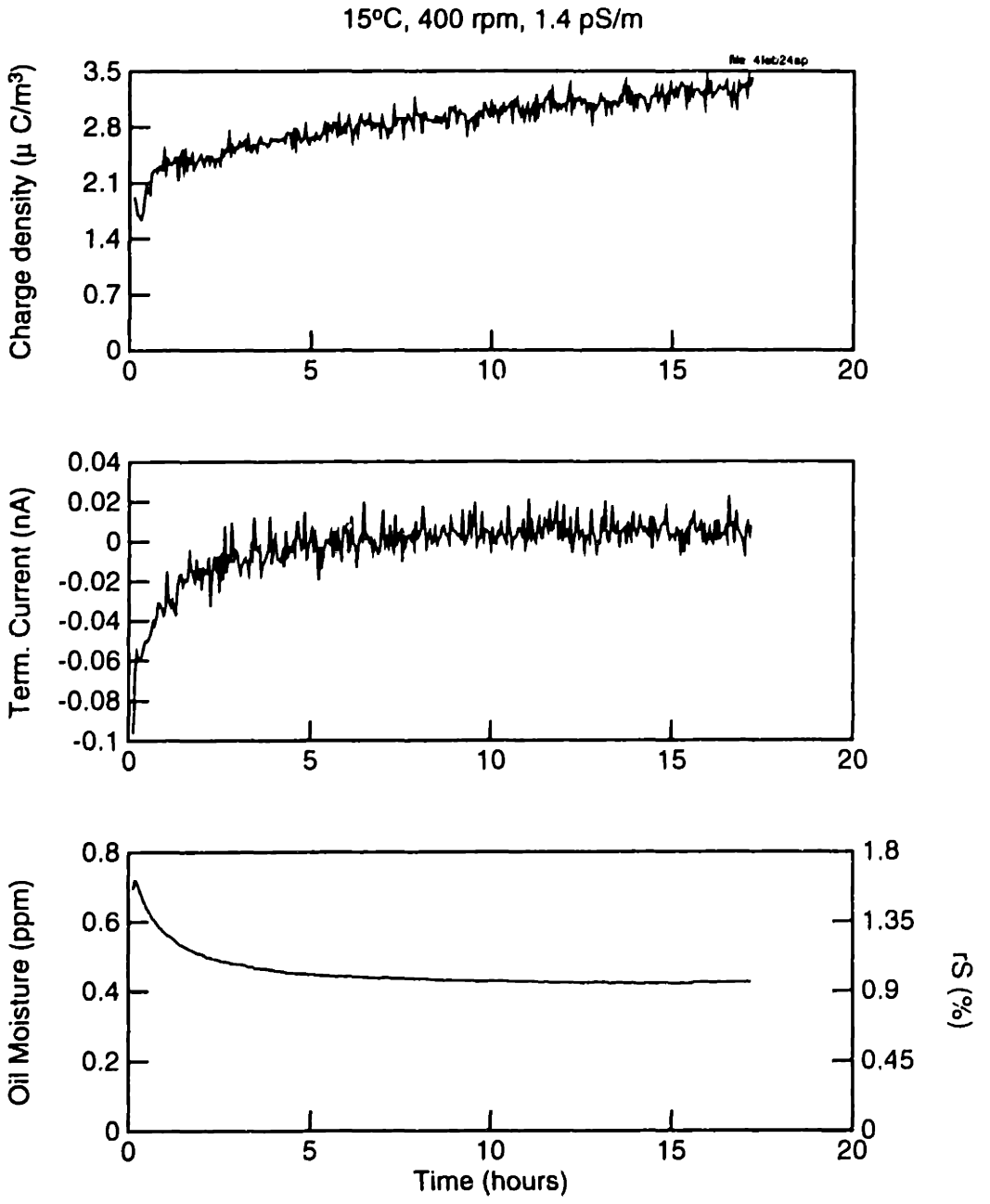


Figure 3.34: Initial equilibration for HiVal pressboard covering the copper sleeve on the inner cylinder, a bare stainless steel outer cylinder and Shell Diala A transformer oil. The current decreased in magnitude as moisture migrated into the pressboard from the oil. Similar to the measurements without the copper sleeve, the charge density appeared to be independent of the oil moisture content.

70°C. The moisture content tracked with the temperature and remained essentially constant once the temperature stabilized. The conductivity increased during the transient, then decreased slowly, even though the temperature was constant, possibly because of ionic absorption by the pressboard. The terminal current also decreased in magnitude, possibly as part of a "conditioning" phase in which the pressboard became more insulating with time. The charge density initially increased with the decreasing conductivity then remained essentially constant. Since a higher oil conductivity usually leads to a lower charge density, this suggests that another competing process canceled the effects of the oil conductivity on the charge density.

As a final example, Fig. 3.36 shows the results of the temperature being cycled between 15 and 70°C. As in Fig. 3.17, this data clearly shows the moisture dynamics, with water transferred from the oil into the pressboard at low temperatures and from the pressboard into the oil at high temperatures. The long time constant for the moisture at 15°C, which is most visible in the relative saturation curve, showed that the mass transfer was a slow process at low temperatures. In contrast, at elevated temperatures the moisture essentially followed the temperature, indicating rapid mass transfer. The moisture levels were essentially the same before and after the temperature decrease, indicating that the system was reasonably well sealed. Similar to the moisture, the conductivity and charge density followed the temperature closely. The terminal current had a strong temperature dependence, but also showed a tendency to decrease in magnitude at 70°C.

### 3.4.8 Effects of BTA

The effects of the additive BTA were measured during the transient period in which the BTA was added to the oil in the CF and also during relatively short duration measurements in which the charge density, voltage, and current were measured as the rotation rate and temperature were varied. In addition to the electrification data, the oil moisture content and conductivity were monitored and the pressboard properties were inferred from periodic transient measurements of the open-circuit voltage and short-circuit current decays, just after disconnecting a DC voltage source or abruptly stopping the rotation of the inner cylinder. In the experiment discussed here, concentrated solutions of the BTA were periodically added to the oil, with the same oil and pressboard used throughout the experiment.

#### BTA measurements in oil

Before considering the effects of the BTA on electrification, first consider the mass transfer dynamics of the BTA in the oil. After adding the BTA to the oil in the CF, the BTA concentration slowly decreased, as shown in Fig. 3.37 for several different initial BTA concentrations. This decrease in BTA concentration is similar to that observed in actual transformers [37]. Some of the concentration decrease can be attributed to the BTA absorption into the paper. Like any constituent present in trace amounts, the relative concentrations of the BTA in the oil and pressboard are determined by partition coefficients at each temperature. Although the details of the experiment were not

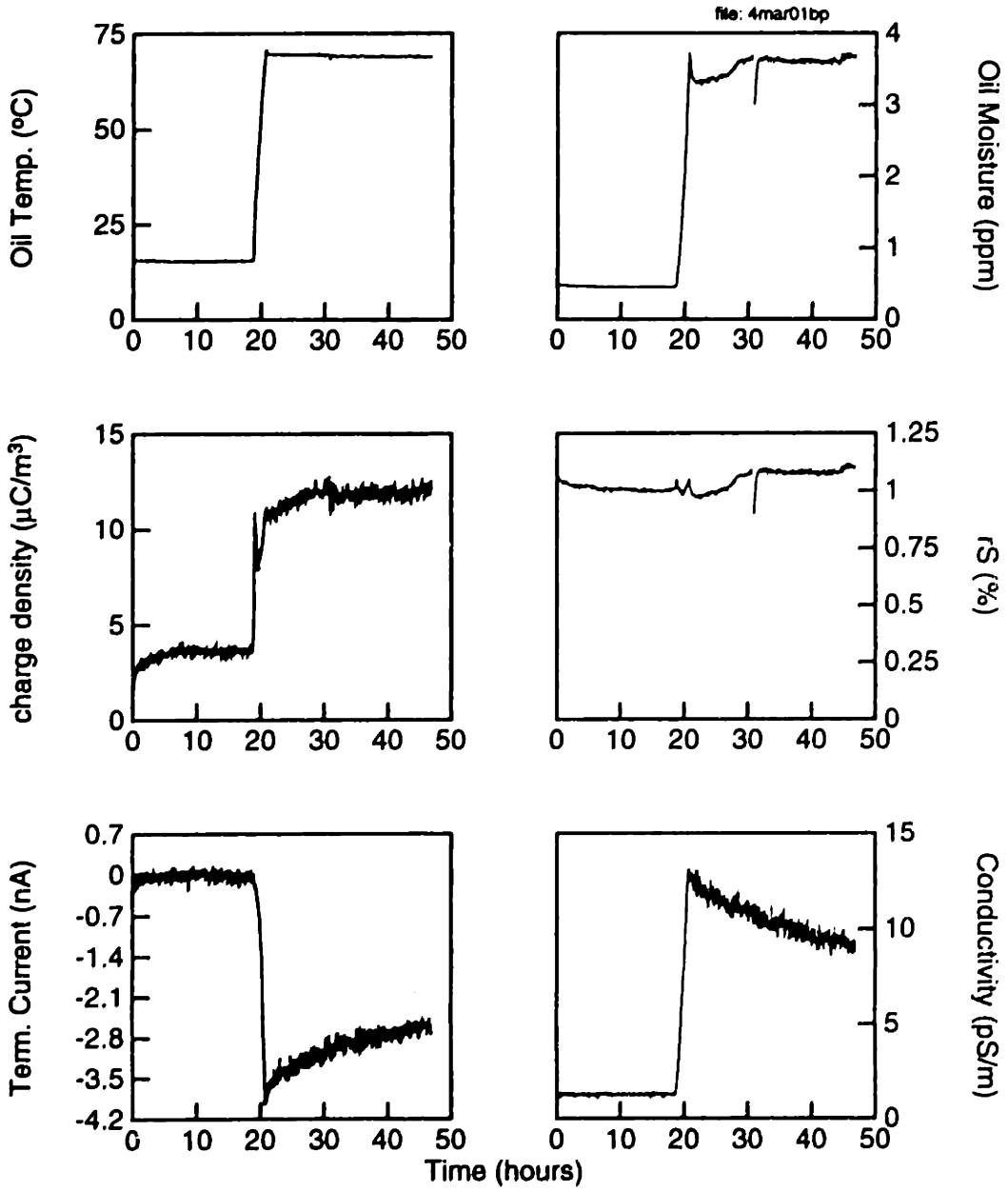


Figure 3.35: Initial temperature transient for HiVal pressboard covering the copper sleeve on the inner cylinder, a bare stainless steel outer cylinder, Shell Diala A transformer oil and a rotation rate of 400 rpm. These results are similar to those shown in Fig. 3.16, which were taken without the copper sleeve.

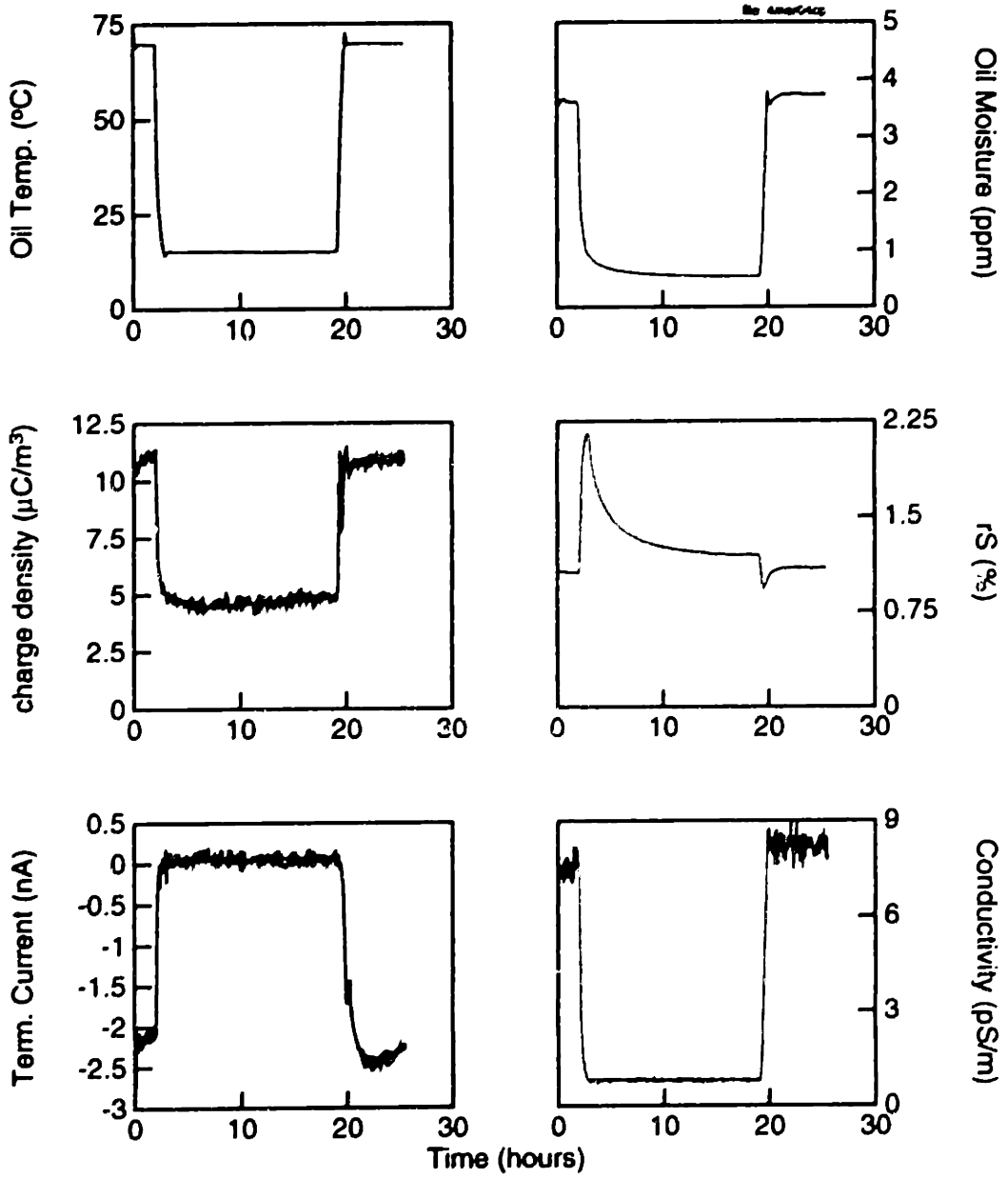


Figure 3.36: Temperature cycling for HiVal pressboard covering the copper sleeve on the inner cylinder, a bare stainless steel outer cylinder, Shell Diala A transformer oil and a rotation rate of 400 rpm. The charge density, terminal current, conductivity, and oil moisture content followed the temperature. The relative saturation shows that the oil took a long time to reach moisture equilibrium at 15°C.

provided[4], the "equilibrium" adsorption content of BTA in paper insulation has been given as 4.2 ppm of BTA ($\mu$g BTA / g pressboard) at 15°C and 21 ppm of BTA at 70°C [37]. Since the BTA content of the oil was not reported, this would appear to be the solubility of BTA in the paper, but the measurements given in the next subsection contradict this conclusion. For reference, the oil volume in the CC was about 7500 $cm^3$ and the pressboard covering the inner cylinder only had a volume of about 200 $cm^3$ so only a small fraction of the BTA was expected to be transferred from the oil into the pressboard.

### BTA measurements in pressboard

Direct measurements of the BTA in the pressboard, described in Appendix A, showed that significant amounts of BTA were present in the pressboard. When the pressboard was diced, peeled, and mixed thoroughly with the extract solutions, the pressboard BTA concentration was estimated to be 130 ppm ($\mu$g BTA / g pressboard). The concentration was reasonably uniform over the height of the cylinder, being roughly 123 ppm at the top of the inner cylinder and 139 ppm BTA at the bottom. Additional measurements were performed to determine if the BTA was in the bulk of the pressboard or at the surface. In this case the pressboard samples were diced, but not peeled, and were mixed less thoroughly with the extract solutions to yield BTA concentrations of 67 ppm at the top of the inner cylinder, 62 ppm in the middle, and 59 ppm at the bottom. In the first set of measurements, the peeling of the pressboard increased the surface area exposed to the extract solution which, with the extra mixing, apparently allowed more of the BTA to be extracted from the pressboard. These results indicate that most of the BTA came from the bulk of the pressboard and not the surface. Otherwise, the second set of measurements would have had BTA concentrations comparable to those of the first measurement. Based on these measurements, the solubility of the BTA in the pressboard is much higher than that given by the previously mentioned "equilibrium" levels.

### Electrification measurements

Consider next the transient when the concentrated solution of BTA was added to the oil in the CF, as shown in Figs. 3.38 and 3.39. These measurements show that the BTA had both short term and long term effects. In the short term, immediately after adding the BTA, the charge density decreased and the current became positive and large. After this initial transient period, the charge density tended to be slightly enhanced and the current tended to become more negative. In the long term, the charge density and current were initially reduced when the BTA concentration was increased to about 10 ppm, but the magnitudes of the charge density and current were increased when the BTA concentration was increased further.

[4]Similar results have also been obtained by adding BTA to a beaker containing known masses of oil and paper insulation. By measuring the decrease in the oil BTA concentration and assuming that the concentration decrease was due to BTA migrating into the paper, the BTA concentration in the paper was calculated [70].

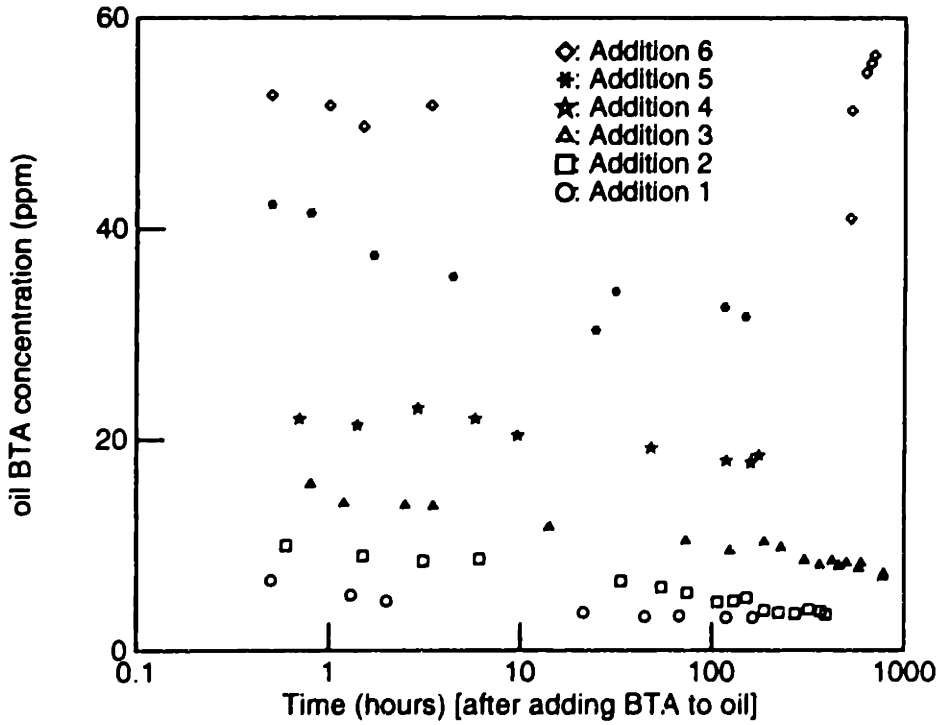


Figure 3.37: A series of measurements of the oil BTA concentration in the CC, which contained Shell Diala A transformer oil, a copper sheet over the inner cylinder, and HiVal pressboard over the copper sheet. Each symbol denotes a different initial BTA concentration. Throughout these transients, electrification measurements at numerous rotation rates and temperatures (15°C to 70°C) were performed. The decrease in BTA concentration appeared to be independent of the temperature and flow conditions.

After the BTA concentrated oil was added, the oil was mixed for about 30 minutes before samples were withdrawn for BTA concentration measurements. The initial decay of the BTA was probably caused by the BTA being absorbed into the pressboard, but it could also have been an experimental artifact because the BTA had not yet been uniformly mixed into the oil of the CF or because the same "T" port was used for both adding the BTA filled oil and withdrawing oil samples. The much slower decay of the BTA probably resulted from further absorption into the pressboard, adsorption onto the interfaces, or degradation of the BTA molecule itself, which is known to be light sensitive. These experiments were done with a minimal exposure to light so the degradation should have been small.

In these measurements, the oil moisture content remained essentially constant and

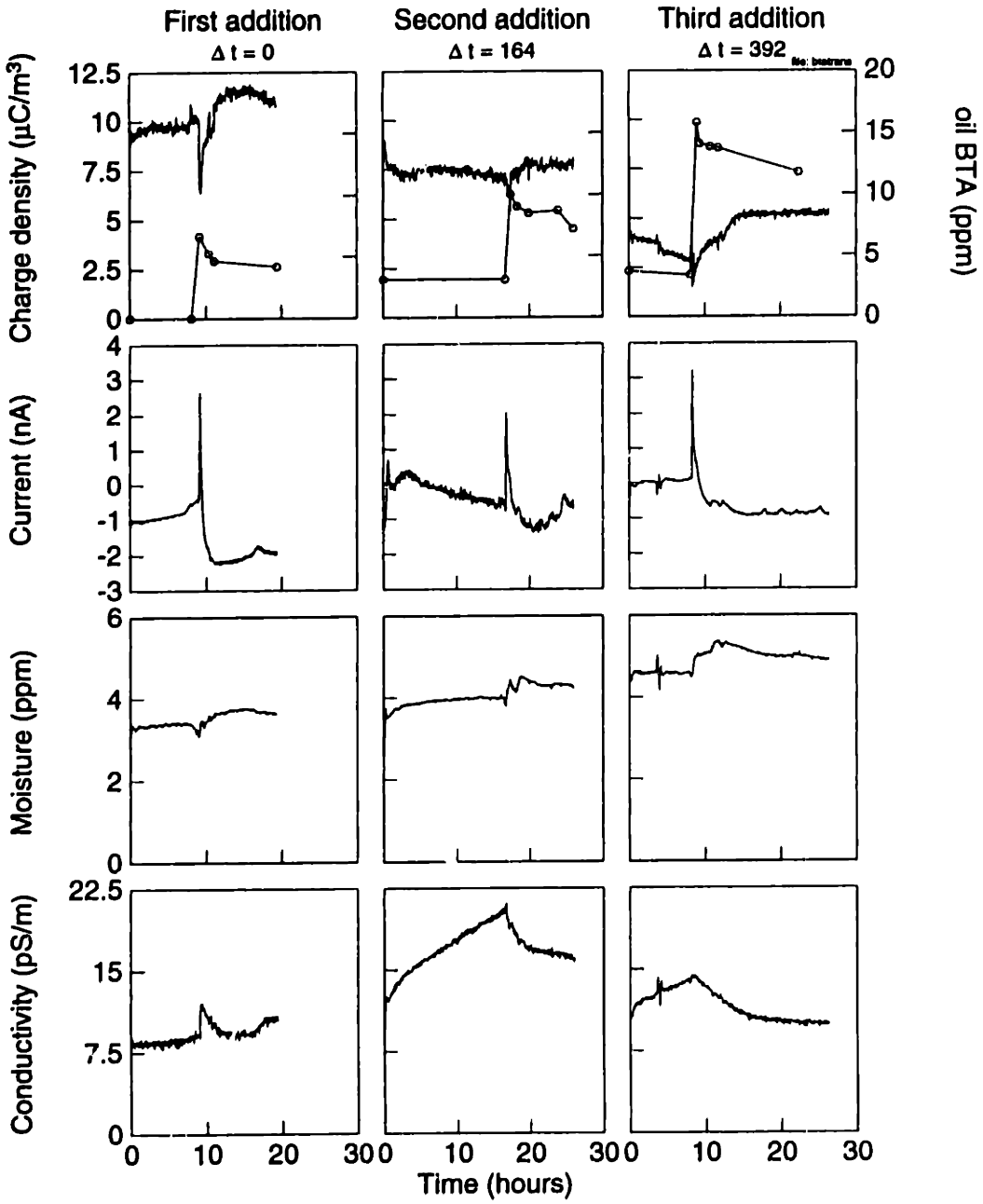


Figure 3.38: The first series of time transient measurements associated with the addition of BTA to oil in the CF. The system was at 70°C with HiVal pressboard covering the copper sleeve on the inner cylinder, a bare stainless steel outer cylinder, Shell Diala A transformer oil and a rotation rate of 400 rpm. Concentrated solutions of BTA in oil, also at 70°C, were added as indicated. The oil was periodically sampled and the BTA concentration measured using ultraviolet spectrophotometry. The time $\Delta t$ in hours between additions of the BTA is indicated.

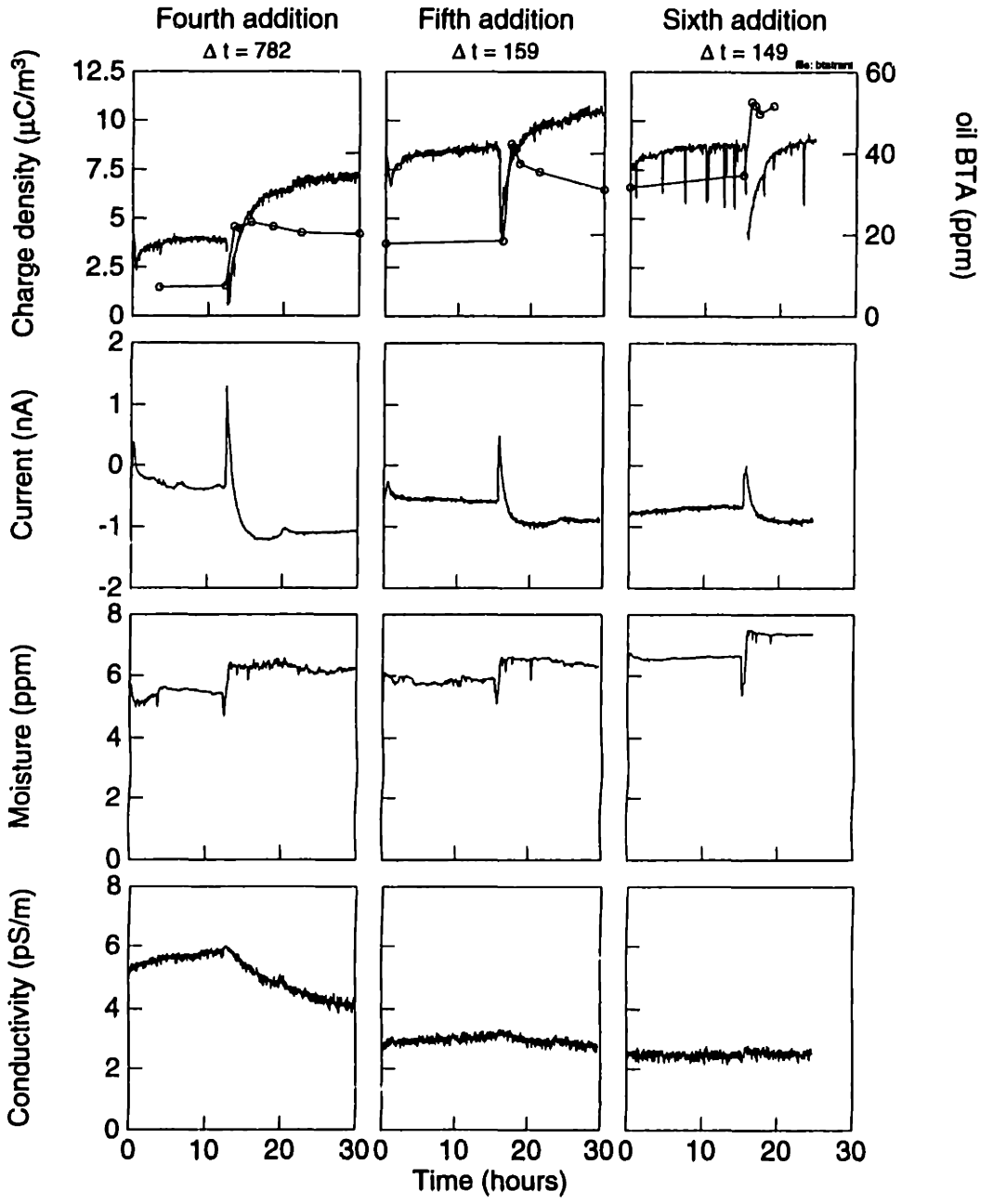


Figure 3.39: The second series of time transient measurements associated with the addition of BTA to oil in the CF. This data is a continuation of that given in Fig. 3.38.

only increased when the relatively "wet" BTA concentrated oil (which had been exposed to a relatively high humidity atmosphere and contained about 15 ppm of water) was added to the system. The fact that the moisture content remained nearly constant indicates that the system was reasonably well sealed.

On the other hand, the BTA appeared to have a strong effect on the oil conductivity. This was a surprising result because BTA has been found to contribute little to the oil conductivity [30,69] or to increase it [42]. (But those measurements showing an increased conductivity were performed with paraffinic oils, rather than the naphthenic oils typically used in domestic transformers and in the measurements reported here.) One possible mechanism by which the BTA can reduce the conductivity of the oil is that the BTA molecules cluster around the ionic species, similar to the hydration of ions in water, thereby increasing the effective size and reducing the mobility of the ions. If the mobility is reduced enough, the clustering of the BTA around the ions could effectively reduce the number density of ions contributing to the conduction process. During the first addition, the conductivity increased probably as a result of the BTA concentrated oil having a high conductivity; in subsequent additions, the kettle containing the BTA concentrated oil, which was open to atmosphere, was raised to 70°C for much shorter periods of time so that oil oxidation would be minimized. The significant increases in conductivity before the second and third additions of BTA may have been caused by the BTA concentrated oil not being degassed so that the oil could be oxidized more readily. The pressboard conductivity appeared to be unaffected by the BTA, but once the oil became very insulating, the pressboard appeared to become more insulating as well.

To help explain the role that the BTA played in reducing, and then enhancing, the electrification charge density, data was also obtained at various rotation rates and temperatures for experiments having a short duration compared to the decay in oil BTA concentration. The results are shown in Figs. 3.40, 3.41, and 3.42. During each measurement, the BTA concentration was essentially constant at the indicated levels.

At each BTA concentration, the charge density usually increased with both rotational speed and temperature, consistent with previous measurements. Similarly, the open-circuit voltage and short-circuit current tended to become larger in magnitude as the rotational speed and the temperature increased. Exceptions to this behavior occurred when the BTA concentration was near 5-10 ppm; the voltage then decreased as the rotation rate increased, in some cases, and the current occasionally reversed polarity. Measurements of the rate of change of the charge density with respect to the applied DC voltage show that both positive and negative values were obtained, but the scatter in the data prevents more detailed observations from being made.

The primary goal of this particular experiment was to determine the effect of the BTA on the electrification processes. These measurements showed that the addition of small concentrations of BTA, less than about 10 ppm, did not significantly affect the electrification data (charge density, voltage, and current). Once the oil contained more than about 10 ppm of BTA, the magnitudes of the charge density, voltage and current were reduced. The electrification data remained at these reduced magnitudes even as the oil BTA concentration decayed. As more BTA was added, the charge density, voltage and current increased with BTA concentration. The last two series of plots in Fig. 3.42, where the BTA concentration was essentially unchanged for 515 hours, show that once the BTA

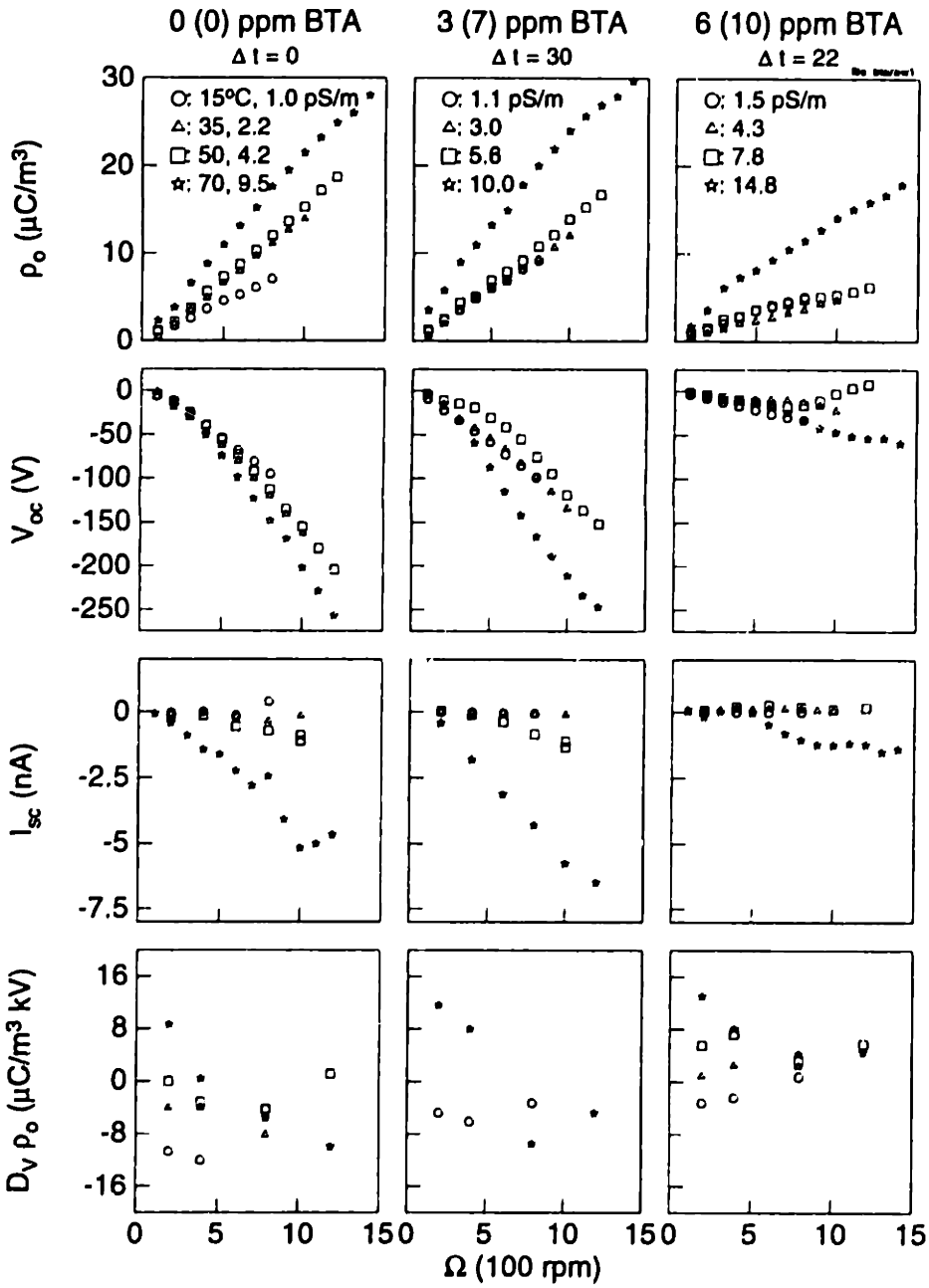


Figure 3.40: The first of a series of plots showing the steady state electrification data as the rotation rate of the inner cylinder, the temperature, and the BTA concentration are varied. The system had HiVal pressboard covering the copper sleeve on the inner cylinder, a bare stainless steel outer cylinder, and Shell Diala A transformer oil. The oil BTA concentration during the reported measurements is given, with the number in parentheses denoting the initial measured concentration. The time $\Delta t$ in hours between the current addition of BTA and the start of the set of electrification measurements is indicated.

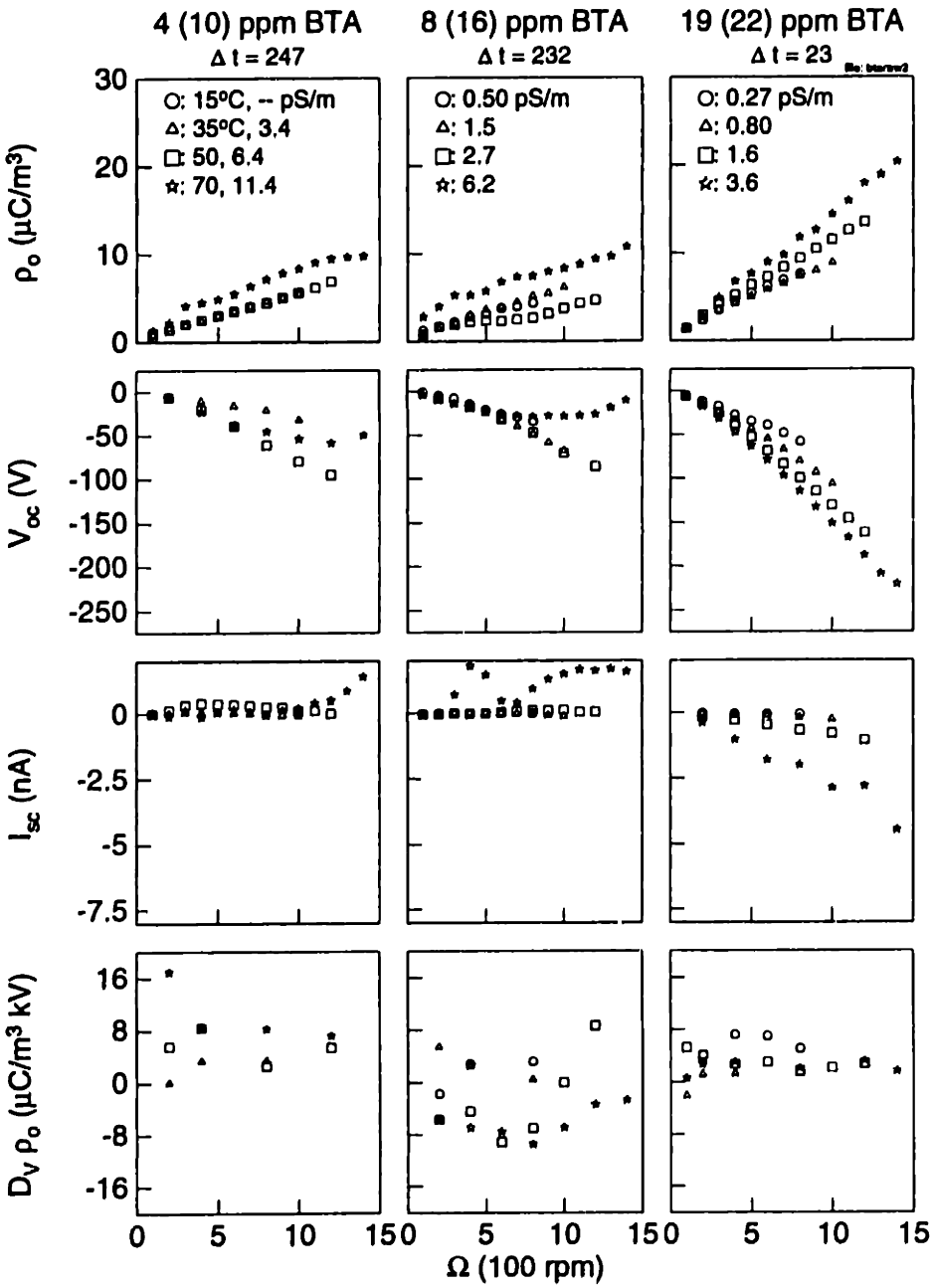


Figure 3.41: The second of a series of plots showing the steady state electrification data as the rotation rate of the inner cylinder, the temperature, and the BTA concentration are varied. This data is a continuation of that shown in Fig. 3.40.

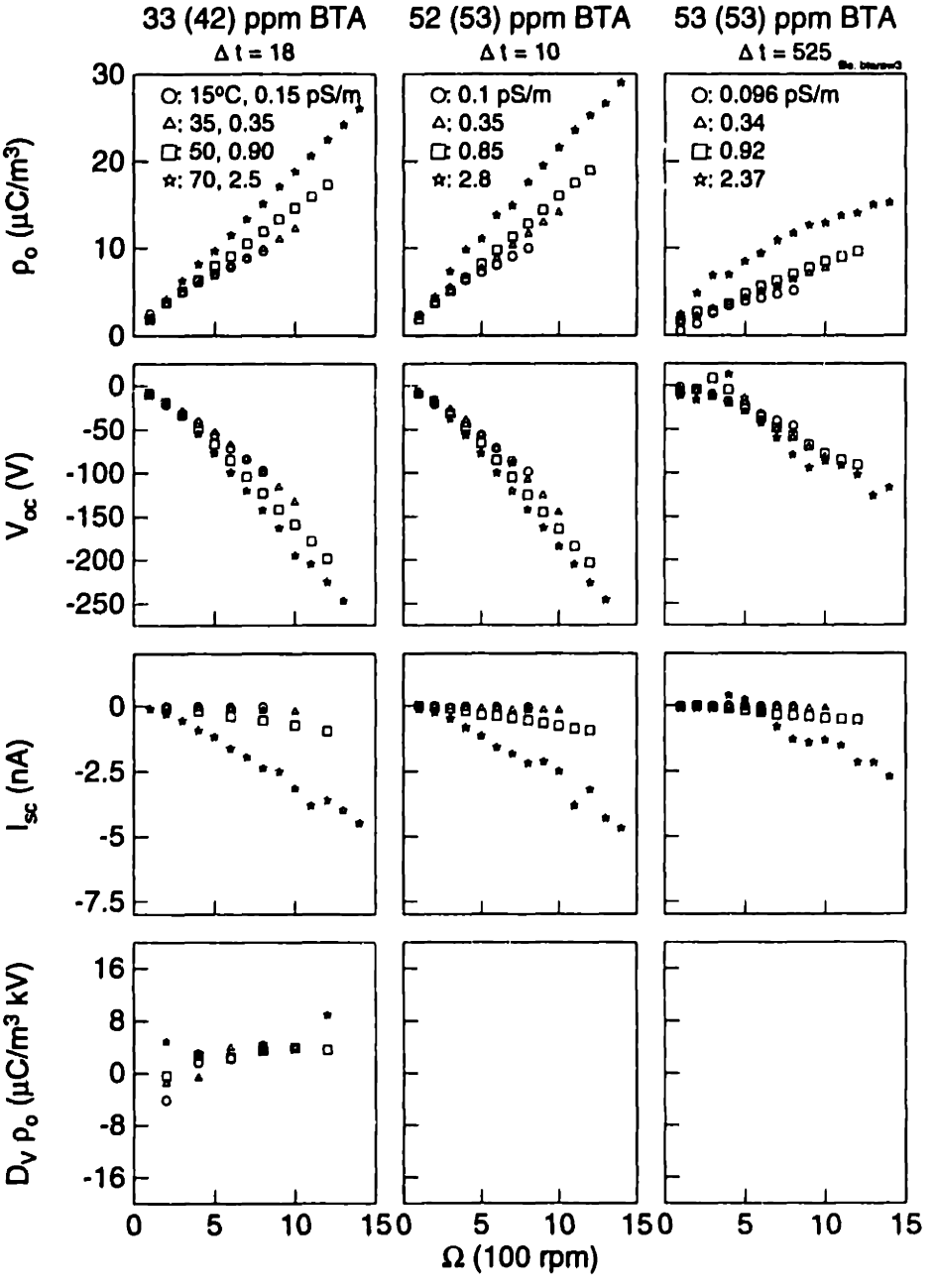


Figure 3.42: The last in a series of plots showing the steady state electrification data as the rotation rate of the inner cylinder, the temperature, and the BTA concentration are varied. This data is a continuation of that shown in Figs. 3.40 and 3.41.

had been present in the system a long time, the electrification data again became smaller in magnitude.

Physically, it appears that the BTA had two separate, but competing, effects on the electrification. As an illustration, consider for the moment that the volume charge density on the liquid side of the solid/liquid interfaces can be represented by a wall charge density $\rho^w$. This wall charge density is assumed to be a constant at a given temperature that is independent of rotational speed but dependent upon the BTA that has been added to the system. The first effect of the BTA was to reduce $\rho^w$, which reduces the charge in the interfacial electrical double layers and the magnitudes of the core charge density, voltage and current. The second effect of the BTA was to reduce the oil conductivity, which tends to cause an increase in the charge density. An exception to these effects is the data showing a decrease in the charge density as the oil conductivity increased; this increase in conductivity does not appear to be associated with the BTA and was probably the result of oil oxidation. In essence, the measurements are a superposition of the effects of the BTA reducing the wall charge density and the variations in the oil conductivity.

This physical model can also be used to qualitatively describe the time transient data as the BTA is added into the CF. On the short time scale, as the BTA is added to the oil, some of the BTA is immediately *absorbed* into the pressboard or, at least, onto the surface so that it can diffuse into the pressboard. The BTA disrupts the diffuse charge distribution in the double layer, possibly by shielding the adsorbed interfacial surface charge. In the limit that all of the surface charge is shielded, then the wall charge density at the pressboard interface would become zero. The net effect is that the core charge density would also be reduced since charge would only be getting stripped away from the outer cylinder interface. Furthermore, the terminal current would become positive, assuming positive charge is diffusely distributed in the outer cylinder double layer, as positive charge is entrained in the fluid flow and transported away from the outer cylinder interface. As the BTA diffuses into the bulk of the pressboard, less is present to shield the surface charge at the pressboard interface and the charge density and current return to their original levels. On the long time scale, as the BTA gets *adsorbed* onto the interface, the diffuse charge in the double layer is again reduced. Although somewhat speculative, this physical picture appears to be consistent with the essential features of the data.

## 3.5 Comparison to Classical Electrochemistry

As discussed in the introduction, rotating cylindrical electrodes have been used to study mass transfer rates in aqueous electrolytic solutions. These studies typically use ionic salts which undergo a known chemical reaction with the electrode materials. Since the solutions typically have a conductivity on the order of 1 S/m, a net-charge does not develop in the bulk of the liquid and the terminal (short-circuit) current is used to infer the chemical reaction rates at the inner cylinder. In general the current is affected by the transport of the ions to the interface and the interfacial chemical reaction. To reduce the effects of the transport so that only the reaction is being studied, supporting electrolytes are added which raise the conductivity of the liquid but don't react at the interface. This reduces the electric field in the bulk of the solution so that the transport is essentially

given by diffusion of the reacting species to the surface. By raising the rotational speed of the inner cylinder, the transport can be made fast compared to the reaction rates and the current is rate limited by the interfacial reactions. This is experimentally observed as a limiting current as the rotation rate is increased.

Extensive measurements have found that the nondimensional mass transfer rate, the Sherwood number $Sh$, is related to the drag coefficient $C_f$, Reynolds number $R$ and Schmidt number $Sc$ via

$$Sh \equiv \frac{2aJ_L}{zqc_oD_m} = \frac{C_f}{2}RSc^{0.356} \tag{3.7}$$

where $J_L$ is the limiting current density at the inner cylinder, $z$ is the valence of the reacting ion, $q$ is the charge of a single electron, and $c_o$ is the bulk concentration of the reacting species [71]. The drag coefficient can be expressed as (see Section 5.6 for more details)

$$\frac{1}{\sqrt{C_f}} \approx -0.6 - 4.07\log_{10}\left(\frac{2}{R\sqrt{C_f}} + 0.215\frac{e}{a}\right) \quad ; \quad 8\times 10^2 < R < 8\times 10^5 \tag{3.8}$$

with $e/a$ the surface roughness height divided by the inner cylinder radius. Since the ionic species and concentrations in the Couette facility measurements are not known, the terminal current is converted into a Sherwood number using

$$Sh = \frac{Ib}{\pi H\sigma_2 D_m} = \frac{Iqz}{\pi H\sigma_2 kT} \tag{3.9}$$

with $H$ the cylinder height, $\sigma_2$ the oil conductivity, $b$ the ionic mobility, $D_m$ the molecular diffusivity of the ions, Boltzmann's constant $k = 1.38\times 10^{-23}$ J/K$= 8.6167\times 10^{-5}$ eV/K, and $T$ the temperature in Kelvin. The last equality uses Einstein's relation

$$\frac{D_m}{b} = \frac{kT}{qz} \tag{3.10}$$

to relate the mobility and diffusivity. In this work the Schmidt number and Reynolds number are given by

$$Sc \equiv \frac{\nu}{D_m} \quad ; \quad R \equiv \frac{2\Omega a^2}{\nu} \tag{3.11}$$

with $\Omega$ the cylinder angular velocity (rad/sec) and $\nu$ the kinematic viscosity of the fluid, given by

$$\nu = \nu_o e^{W_\nu/kT} \tag{3.12}$$

where $\nu_o = 3.956\times 10^{-10}$ m$^2$/s and $W_\nu = 0.2725$ eV [23]. Since the ionic species are not known, the ionic diffusivity must be estimated and a valence of $z = 1$ was assumed. Empirically, the ion mobility (SI units of m$^2$/volt-sec) in hydrocarbon liquids has been related to the viscosity (SI units of kg/m-sec) by Walden's rule as [72]

$$b\eta \approx 2\times 10^{-11} \tag{3.13}$$

with $\eta = \rho_m \nu$ the dynamic viscosity of the liquid and $\rho_m \approx 886$ kg/m$^3$ the oil mass density [73]. Thus, the temperature sets the viscosity of the oil and the ionic diffusivity can be estimated from the calculated mobility and the Einstein relation.

Representative plots comparing the nondimensional current from the Couette facility to accepted correlations based on aqueous electrochemical measurements are given in Figures 3.43 and 3.44. In general, the Couette facility values are in very good agreement with the accepted values. This is somewhat surprising because the ionic species are not known and estimates for the ionic diffusivity had to be used, the accepted correlations were found for lower Schmidt number fluids ($10 < Sc < 10^4$) as opposed to the $10^4 < Sc < 10^6$ range for transformer oil, and the current densities for the semi-insulating oils are much lower than those found in aqueous experiments (recall that the Sherwood number has the terminal current divided by the liquid conductivity). In light of these differences, the deviations of the experimental data from the accepted limiting current Sherwood numbers are not significant.

This data suggests that the transport of the ions to the interface and the reaction rates must be treated on equal footing. For low Reynolds numbers, the Couette facility Sherwood numbers are much lower than the reaction limited values. In contrast, at high Reynolds numbers the data approach a line that is roughly parallel to the reaction limited current. This indicates that the experiments span the transition from the transport limited regime to the reaction limited regime.

## 3.6 Discussion

This chapter presented a relatively extensive set of experimental measurements. Some of the data is used on a purely empirical basis to determine how specific parameters affect the electrification processes. But, more importantly, when the data is compared to the electrification models in Chapters 5 and 6, some of the fundamental mechanisms for the interfacial charge transfer can be explored. The following summarizes the important observations from the experiments.

Measurements of the core charge density between rotating cylindrical electrodes tended to show an increase with the rotation rate of the inner cylinder and with temperature. These measurements are similar to leakage current measurements in pipe flow experiments which show the leakage current becoming larger as the fluid velocity and the temperature increase. In addition, measurements of the terminal voltage and current between the cylinders usually track with the charge density, but occasionally they showed peaks at intermediate rotation rates and temperatures. Similarly, in transformers, measurements of the leakage current from the windings have shown peak magnitudes at intermediate temperatures.

Measurements of the charge density and terminal current at low oil moisture contents showed that the oil moisture content does not have a significant effect on the electrification processes. In contrast, the conduction through pressboard is strongly moisture dependent and decreasing the pressboard moisture content leads to less conduction and smaller terminal currents. An exception to the oil moisture dependence of the charge density was during the initial equilibration period, immediately after processing of the pressboard, in

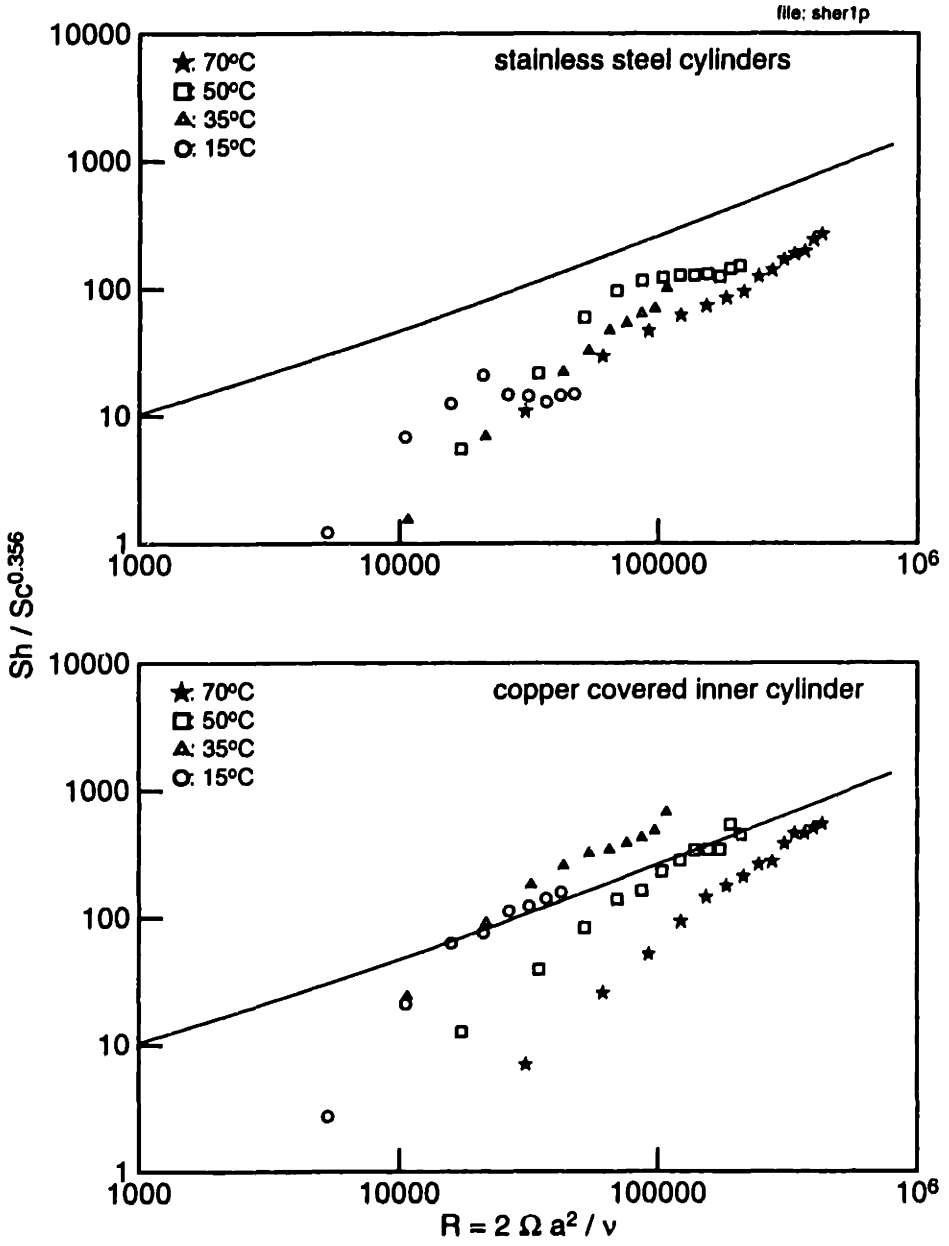


Figure 3.43: A comparison to classical electrochemical measurements for metal cylinders using the data of Figures 3.9 and 3.33. The Sherwood number $Sh$ gives the normalized current, the Schmidt number $Sc$ is the ratio of the viscosity to the molecular diffusivity, and the Reynolds number $R$ gives the normalized rotation rate. The solid line represents the accepted current for reaction limited conditions (Eqs. 3.7 and 3.8) with $e/a = 0$. The current appeared to be transport limited at the lower Reynolds numbers and rate limited at the higher Reynolds numbers.

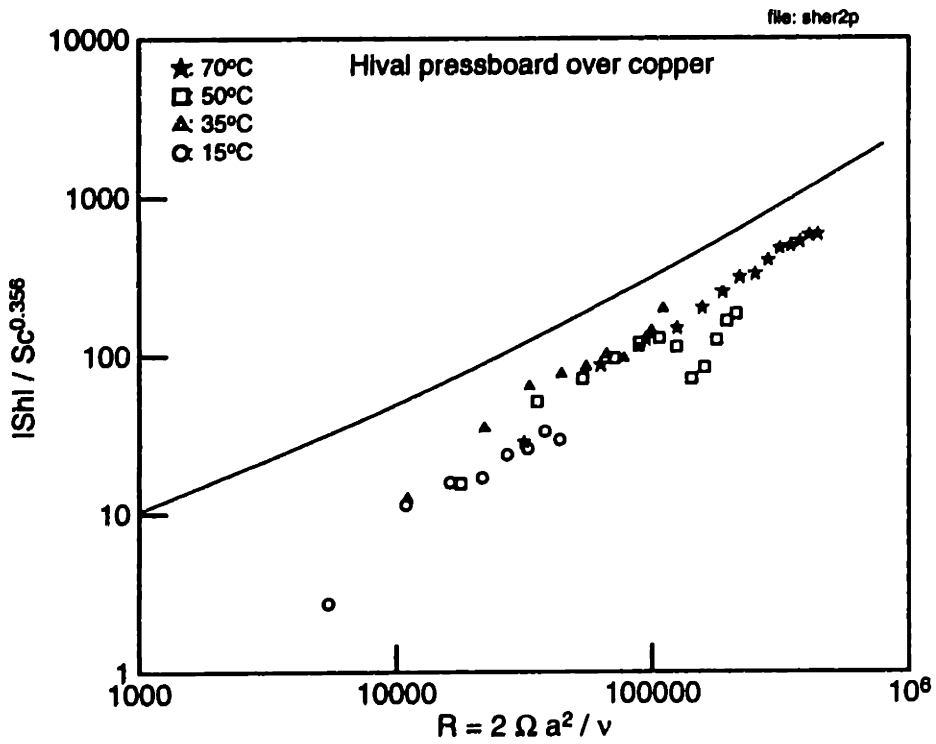


Figure 3.44: A comparison to electrochemical measurements for rough cylinders and HiVal pressboard covering the inner cylinder. The Sherwood number $Sh$ gives the normalized current, the Schmidt number $Sc$ is the ratio of the viscosity to the molecular diffusivity, and the Reynolds number $R$ gives the normalized rotation rate. The solid line represents the accepted current for reaction limited conditions (Eqs. 3.7 and 3.8), assuming a pressboard surface roughness of 100 $\mu$m [26] so that $e/a = 0.0013$. The current appeared to be transport limited at the lower Reynolds numbers and rate limited at the higher Reynolds numbers.

which the oil was brought into contact with the pressboard. During this period, before the system was raised in temperature, the charge density appeared to vary inversely with the oil moisture content. This result seems to be consistent with ministatic tester measurements which show that the leakage current resulting from oil flowing through a paper filter increases as the oil moisture content decreases [23]. Furthermore, the charge density not appearing to change with the moisture content after the initial "conditioning" phase suggests that the ministatic tester measurements do not represent equilibrium measurements. Indeed, similar measurements with hydrocarbon liquids flowing through a filter required a "conditioning" phase in which the filter was immersed in the liquid being studied for a few hours or days before consistent and reproducible measurements were obtained [74]. Long time transients were also observed in experiments using an earlier version of the CF [2]. These "conditioning" transients, which had been associated with the oil and paper insulation coming to moisture equilibrium, were eliminated by heat treating and processing the paper. The processing was similar to the vacuum drying and oil impregnation of the pressboard performed in the experiments presented here. The difference in results may be due to the oil impregnation process happening more rapidly in the relatively thin paper (in the earlier measurements in the CF) versus the thick pressboard used in these measurements.

Numerous measurements also showed that DC applied voltages, surface charge accumulation and terminal constraints can affect the electrification charge density. In particular, while it is well known that energization itself, AC for power transformers, can enhance the charge density, measurements performed here showed that if the pressboard/oil interface accumulates charge from an external source *and the source is then removed*, the electrification charge density can then be increased or decreased, depending upon the polarity of the accumulated surface charge. The terminal constraints (open or short-circuit) are also important in determining whether the electric field associated with the surface charge is through the pressboard or the oil; if the field is through the oil, the charge in the electrical double layer and the electrification charge density can be affected.

Copper was also added to the system to simulate the presence of copper in an actual transformer and the additive BTA tends to deactivate copper. Comparisons between the electrification data obtained with and without copper covering the stainless steel inner cylinder showed that the copper gave results similar to those with the stainless steel electrodes.

The effects of the additive 1,2,3 benzotriazole (BTA) were also studied. The BTA content of the oil in the Couette facility decayed with time, similar to that observed in actual transformers, but on a different time scale. This confirms that the CF is a convenient facility for simulating at least the mass transfer dynamics in a full-scale transformer. The decrease in oil BTA content may be the result of the BTA being absorbed into the bulk of the pressboard, adsorbed onto the surfaces in the system, or even decomposition of the BTA molecule itself, which is known to be light sensitive. Direct measurements showed that significant amounts of BTA could be stored in the pressboard, but measurements of several standard solutions stored in amber high density polyethylene bottles, in the absence of any light and pressboard, also showed concentration decreases. It is likely that all three factors contribute to the decrease in BTA concentration.

In regards to electrification, nominal BTA concentrations near 10 ppm appear to

have caused a reduction in the magnitudes of the electrification data. But the BTA also appeared to decrease the oil conductivity, which tends to increase the magnitudes of the electrification data. These competing effects limit the effectiveness of the BTA, but over long periods of time the BTA appeared to cause a continual net decrease in the electrification charge density, possibly as a result of slow electrochemical adsorption of the BTA onto the interfaces. As will be discussed in Chapter 6, the BTA apparently caused a reduction in the charge density on the liquid side of the interface. This would cause a decrease in the magnitude of the electrification data, but the decreasing oil conductivity leads to larger charge densities as the Debye length increases and more charge is stripped out of the electrical double layer at a given flow rate.

Some of the experiments were also compared to established correlations from aqueous electrochemical measurements. The data was in surprisingly good agreement with the established results, even though the liquid conductivities (and the resulting current densities) are roughly 12 orders of magnitude smaller and the charge carrying species are not known. This comparison also indicates that the electrification measurements are in a regime in which the charge transfer is transport limited at the lower Reynolds number flows and rate limited at the higher Reynolds numbers.

# Chapter 4

# Dielectric Property Measurements

Since flow electrification is a complicated process that depends upon a wide variety of parameters, it is critical to determine and monitor those parameters which can be accurately measured. Some of the fundamental parameters that influence the field distributions and the time constants with which charge redistributes itself are the dielectric properties of the materials. This chapter presents techniques for determining the dielectric properties of the liquid and solid insulation.

## 4.1 Introduction

The basic method for obtaining the dielectric properties of a material is to apply a single frequency sinusoidal voltage to a test cell containing the material and measure the effective impedance. Relating these measurements to models then yields the effective dielectric properties at the excitation frequency. Section 4.2 discusses the use of single frequency and multiple frequency measurements for determining the effective dielectric properties of a semi-insulating liquid. For the solid insulation, although sensors for making in-situ measurements of the dielectric spectrum are in the process of being developed [17], none are readily available. In this work, in order to get an estimate of the pressboard properties in the electrification experiments, time domain transient measurements of the terminal voltage and current were performed. As discussed in Section 4.3, after disconnecting a DC voltage source from across the cylinders, the short-circuit current or open-circuit voltage decay can be used to determine the effective dielectric properties of the pressboard. Section 4.4 provides concluding statements.

## 4.2 Liquid Properties

To determine the liquid's dielectric properties, an air-gap variable capacitor was immersed in the liquid and the impedance measured over a range of frequencies. These impedances were then used to determine element values in an equivalent electrical circuit, where each element was a lumped parameter representation of the liquid dielectric properties. This approach is similar to that recently proposed for use in electrochemical impedance spectroscopy [75] and provides results similar to those obtained from other

liquid dielectrometry techniques [76].

### 4.2.1 Test cell impedance measurement

The impedance of the test cell was determined by connecting the cell to the circuit shown in Fig. 4.1 and measuring the voltage gain across the circuit ($v_o/v_s$). The voltage source generated a sinusoidal signal having a peak amplitude of 1 V at a frequency that could be varied from 5 mHz to 10 kHz. The output voltage was fed into a high impedance operational amplifier, which acted as a voltage follower. By comparing the measured voltage to the source signal, the decrease in voltage magnitude and the change in the phase across the network was determined. These gain and the phase measurements were performed by a computer controlled data acquisition unit which was originally designed[1] for use with interdigitated dielectric sensors [17]. While the controller can generate the source signal and measure the output voltage, an interface box containing the known electrical load and the high impedance operational amplifier was required for connection to the interdigitated sensors. By modifying the interface box to allow BNC cable connections for the source and output signals[2], other dielectric sensors, such as the air-gap capacitor, could also be used [77]. To shield the test lead connections and minimize the effect of cable capacitance, the BNC cable connecting the output side of the test cell to the interface box had the inner conductor at the measured voltage $v_o$ and the outer conductor connected to the output of the voltage follower operational amplifier to serve as a guard.

To relate the impedance of the test cell to the measurements of the gain and the phase, begin by assuming the circuit is in sinusoidal steady state so that the circuit variables can be expressed in terms of complex amplitudes. For example, the voltages can be written as $v(t) = \mathrm{Re}\{\hat{V}e^{j\omega t}\}$, with $\hat{V}$ the complex voltage amplitude, $j = \sqrt{-1}$, and $\omega$ the angular frequency. This allows the complex gain $G$ to be expressed as

$$G = |G|e^{j\phi} = \frac{\hat{V}_o}{\hat{V}_s} = \frac{Y_1}{Y_1 + Y_2} = \frac{Z_2}{Z_1 + Z_2} \tag{4.1}$$

where $|G|$ is the magnitude of the gain, $\phi$ is the phase, $\hat{V}_s$ is the complex amplitude of the source voltage, $\hat{V}_o$ is the complex amplitude of the output voltage, and $Y_i$ is the admittance and $Z_i$ is the impedance for the test cell when $i = 1$ and for the load when $i = 2$. Solving for the unknown test impedance $Z_1$ gives

$$Z_1 = Z_2\left(\frac{1}{G} - 1\right) \tag{4.2}$$

[1]The controller was designed by David Otten in the Laboratory for Electromagnetic and Electronic Systems at the Massachusetts Institute of Technology to control and make measurements with an Absolute Charge Sensor [11], to perform gain-phase measurements with application to interdigital dielectrometry, and to serve as a multichannel A/D data acquisition unit.

[2]Often the roles of the test and load impedances are interchanged and the voltage across the unknown test impedance is measured directly. In this case, the voltage across the *known* impedance was measured, as is done with the interdigitated dielectric sensors, to minimize the number of modifications to be made to the interface box.

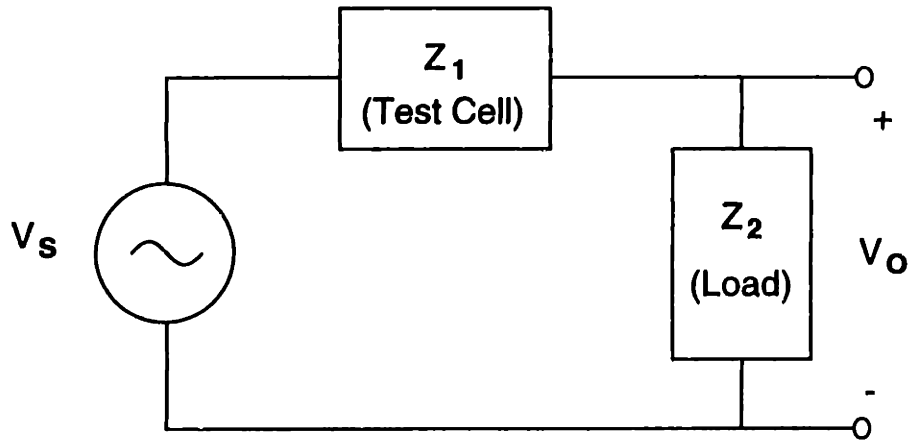


Figure 4.1: An electrical circuit diagram for the liquid dielectric measurements. By measuring the voltage $v_o(t)$ across a known load impedance $Z_2$ and comparing it to the sinusoidal source voltage $v_s(t)$ the test cell impedance $Z_1$ can be determined.

Thus, with the load impedance known, the impedance of the test cell can be determined from measurements of the complex gain.

In the measurements discussed here, the load is composed of a resistor $R_2$ in parallel with a capacitor $C_2$ so that the load impedance is

$$Z_2 = \frac{R_2}{1 + j\omega R_2 C_2} \tag{4.3}$$

Using this load impedance the test cell impedance can be expressed as

$$Z_{1r}^m = \frac{R_2}{1 + (\omega R_2 C_2)^2} \left[ \left( \frac{1}{|G|} \cos\phi - 1 \right) - \frac{\omega R_2 C_2}{|G|} \sin\phi \right] \tag{4.4}$$

$$Z_{1i}^m = -\frac{R_2}{1 + (\omega R_2 C_2)^2} \left[ \frac{1}{|G|} \sin\phi + \omega R_2 C_2 \left( \frac{1}{|G|} \cos\phi - 1 \right) \right] \tag{4.5}$$

where $Z_{1r}$ is the real part of the test cell impedance, $Z_{1i}$ is the imaginary part of the test cell impedance, and the superscript $m$ indicates a measured quantity. The load resistance and capacitance can be selected to provide optimum measurement sensitivity for the desired test cell and range in liquid properties (permittivity and conductivity) of interest. For the measurements presented here, the transition frequency $1/R_2C_2$, where the dominant load impedance switches between the capacitance and the resistance, was chosen to be below the frequencies range of the measurements. The actual load had the nominal input impedance of the operational amplifier as the load resistance ($R_2$ = 1000 G$\Omega$) and a load capacitor ($C_2$ = 750 pF). More precise values for the load impedance can be obtained by calibrating against a known test resistance and capacitance, such as

$R_1$ = 48.9 GΩ as determined by a Keithley 614 electrometer and $C_1$ = 120.0 pF as determined by a HP 4192A LF Impedance Analyzer.

### 4.2.2 Lumped parameter *RC* model

From the measured impedance, the bulk conductivity and permittivity of the liquid can be found by relating a model for the electrical impedance of the liquid filled capacitor to the terminal measurements. The simplest model is to assume that the test cell impedance can be represented by lumped elements, such as a resistor $R_1$ in parallel with a capacitor $C_1$, as shown in Fig. 4.2. The admittance of the test cell can then be written in terms of the measured gain and phase as

$$\frac{1}{R_1} + j\omega C_1 = \frac{1}{Z_2}\left(\frac{G}{1-G}\right) \tag{4.6}$$

Equating the real and imaginary parts then gives

$$\frac{R_1}{R_2} = \frac{|G|^2 - 2|G|\cos\phi + 1}{|G|\left(\cos\phi - |G| - \omega R_2 C_2 \sin\phi\right)} \tag{4.7}$$

$$\frac{C_1}{C_2} = \frac{|G|\left(\cos\phi - |G|\frac{\sin\phi}{\omega R_2 C_2}\right)}{|G|^2 - 2|G|\cos\phi + 1} \tag{4.8}$$

These expressions relate the effective test cell resistance and capacitance at each frequency, $f = \omega/2\pi$, to the measured gain and phase, for a known load resistance and capacitance.

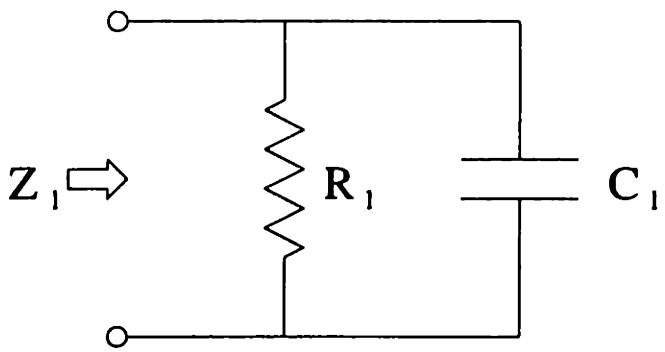


Figure 4.2: A simple lumped parameter model for the impedance of the fluid between the plates of the test cell, consisting of a resistor connected in parallel with a capacitor.

Once the values for these lumped elements have been determined, the dielectric prop-

erties of the liquid can be found. Assuming that the test cell consists of two parallel plates of cross-sectional area $A$, separated by a distance $d$, and neglecting fringing fields, the lumped parameters are related to the dielectric properties by

$$R_l = \frac{d}{\sigma A} \quad ; \quad C_l = \frac{\epsilon A}{d} \tag{4.9}$$

with $\sigma$ the liquid conductivity and $\epsilon$ the liquid permittivity. To determine the dielectric properties absolutely, the geometric factor $A/d$ must be found. This can be accomplished by measuring the capacitance of the structure in air so that

$$C_{air} = \frac{\epsilon_o A}{d} \tag{4.10}$$

with $\epsilon_o = 8.854 \times 10^{-12}$ F/m the permittivity of free space. The bulk properties of the liquid can then be obtained from

$$\epsilon_r = \frac{\epsilon}{\epsilon_o} = \frac{C_l}{C_{air}} \quad ; \quad \sigma = \frac{\epsilon_o}{R_l C_{air}} \tag{4.11}$$

where $\epsilon_r$ is the relative permittivity of the liquid.

For the capacitors used in the experiments, the air capacitance was typically measured to be 50 pF. Using micrometers to measure the capacitor dimensions, the capacitors were found to have a plate spacing of $d = 0.152$ cm and an effective plate area[3] of $A = 71.8$ cm$^2$. This gives an air capacitance of 41.8 pF, which is significantly less than the measured capacitance. The likely cause of this difference is the fringing of the electric field around the edges of the electrodes. The extra capacitance $C_e$ due to the fringing fields between parallel plate electrodes in air can be written as [78: p. 1-58]

$$C_e = \frac{\epsilon_o w}{2\pi}\left[1 + \ln\left(\frac{2\pi\ell}{d}\right)\right] \tag{4.12}$$

where $w$ is the electrode width and $2\ell$ is the electrode depth. Using the micrometer measurements, the total capacitance associated with the fringing fields is then estimated to be 11.2 pF. The total capacitance in air, including the fringing capacitance is then expected to be 53.0 pF. The actual measured air capacitance is less than this because the capacitors are composed of many interleaved plates which only have the fringing fields at the ends of the electrodes and not the fringing fields that would be present on the back sides of a single pair of parallel plate electrodes. In the experiments, the measured air capacitance is used in the calibration so that the appropriate amount of the fringing field capacitance is being used.

Representative measurements of the relative permittivity and conductivity of Shell Diala A transformer oil are given in Fig. 4.3 for two different temperatures. The program

[3] A typical capacitor consists of $N$ interleaved plates so that each plate then serves as both an upper and lower electrode. The effective area is then $(2N - 1)$ times the geometric area on the side of a single plate. In this case, $N$ is 13.

**prc.c** in Appendix E was used to process the data. At high frequencies such that $\omega\epsilon/\sigma \gg 1$, the sensor responds to the oil permittivity and is insensitive to the conductivity. As the frequency is lowered, the sensor becomes more sensitive to the oil conductivity and the estimates of the permittivity and conductivity eventually become independent of the frequency. If the frequency is too small though, the effective permittivity increases and the conductivity decreases with respect to the mid-frequency values. These low frequency variations in the estimation of the permittivity and conductivity (which is most evident in the 70°C plot) are probably caused by electrical double layers at the electrode interfaces, which are not accounted for in this simple model for the test cell.

One of the difficulties associated with these measurements is the ability to isolate the effects of any systematic experimental errors from the physical phenomena that is being measured. Standard Bode plots, where the transfer function (such as $G$) between the input and output signals is plotted as a function of the frequency, provide meaningful representations of the circuit response when the circuit elements are known, but they are not well-suited for determining unknown elements of a circuit. As an example, consider Fig. 4.4 which contains a Bode plot comparing the actual measured values of the test cell gain and phase and the predicted response of a model assuming a resistor in parallel with the capacitor. From this plot, it is reasonable to assume that perturbing the values of $R_1$ and $C_1$ will give a better fit to the data, but this is not the case. Other types of plots, such as Cole-Cole plots, illustrate the structure of the unknown circuit impedance more clearly and are used in the fields of electrochemistry [79] and solid dielectrometry [80,81].

One type of Cole-Cole plot has the real component of the measured test cell impedance plotted on the horizontal axis and the negative of the imaginary component of the impedance plotted on the vertical axis. To create this plot for the parallel combination of $R_1$ and $C_1$ given in Fig. 4.2, the impedance can be written as

$$Z_1 = \frac{R_1}{1 + j\omega R_1 C_1} \quad \Rightarrow \quad \begin{cases} Z_{1r} &= \dfrac{R_1}{1 + (\omega R_1 C_1)^2} \\ -Z_{1i} &= \dfrac{\omega R_1^2 C_1}{1 + (\omega R_1 C_1)^2} \end{cases} \tag{4.13}$$

These expressions for the real and imaginary components of the impedance are parametric equations in terms of the frequency. By eliminating the frequency, the real and imaginary components are found to lie on a circle defined by

$$\left(Z_{1r} - \frac{R_1}{2}\right)^2 + (-Z_{1i})^2 = \left(\frac{R_1}{2}\right)^2 \tag{4.14}$$

as sketched in Fig. 4.5. Similar Cole-Cole plots use the effective material properties calculated from the test cell impedance. For example, with the material in the test cell represented by a complex permittivity, the real component can be plotted on the horizontal axis and the imaginary component plotted on the vertical axis [81].

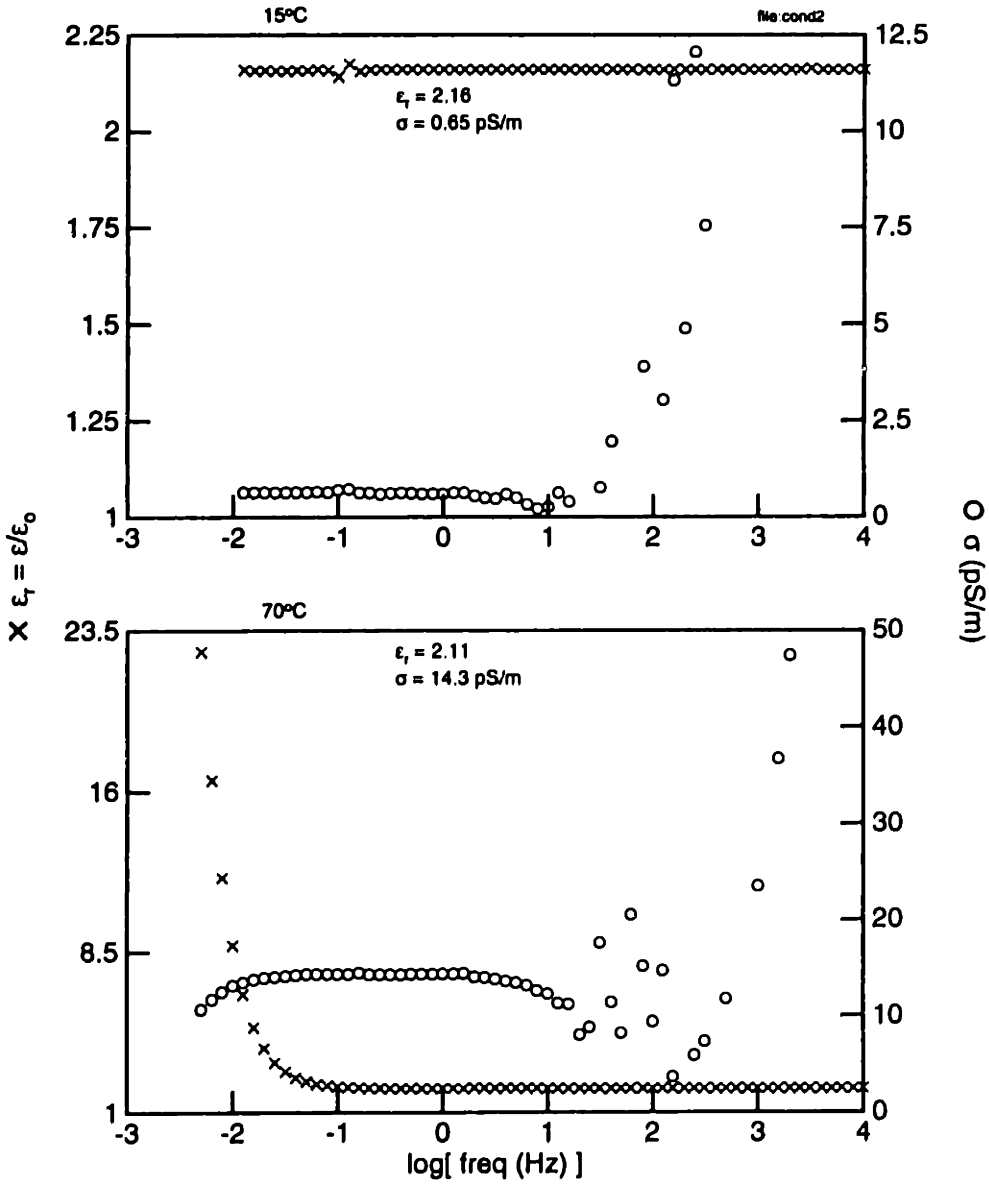


Figure 4.3: Representative effective dielectric response of oil at two temperatures. By immersing an air-gap capacitor in Shell Diala A transformer oil and measuring the impedance of the structure, the effective dielectric properties (relative permittivity and conductivity) of the oil can be determined. In these measurements, the capacitor was simply modeled as a resistor in parallel with a capacitor. The upper plot shows the dielectric properties at 15°C while the bottom plot is for 70°C. The low frequency variations in the estimation of the permittivity and conductivity from the mid-frequency response are probably caused by unmodeled effects of an electrical double layer at the electrode interfaces. The conductivity estimates showed a large variation at the high frequencies because errors in the phase measurement were comparable to the phase of the signal.

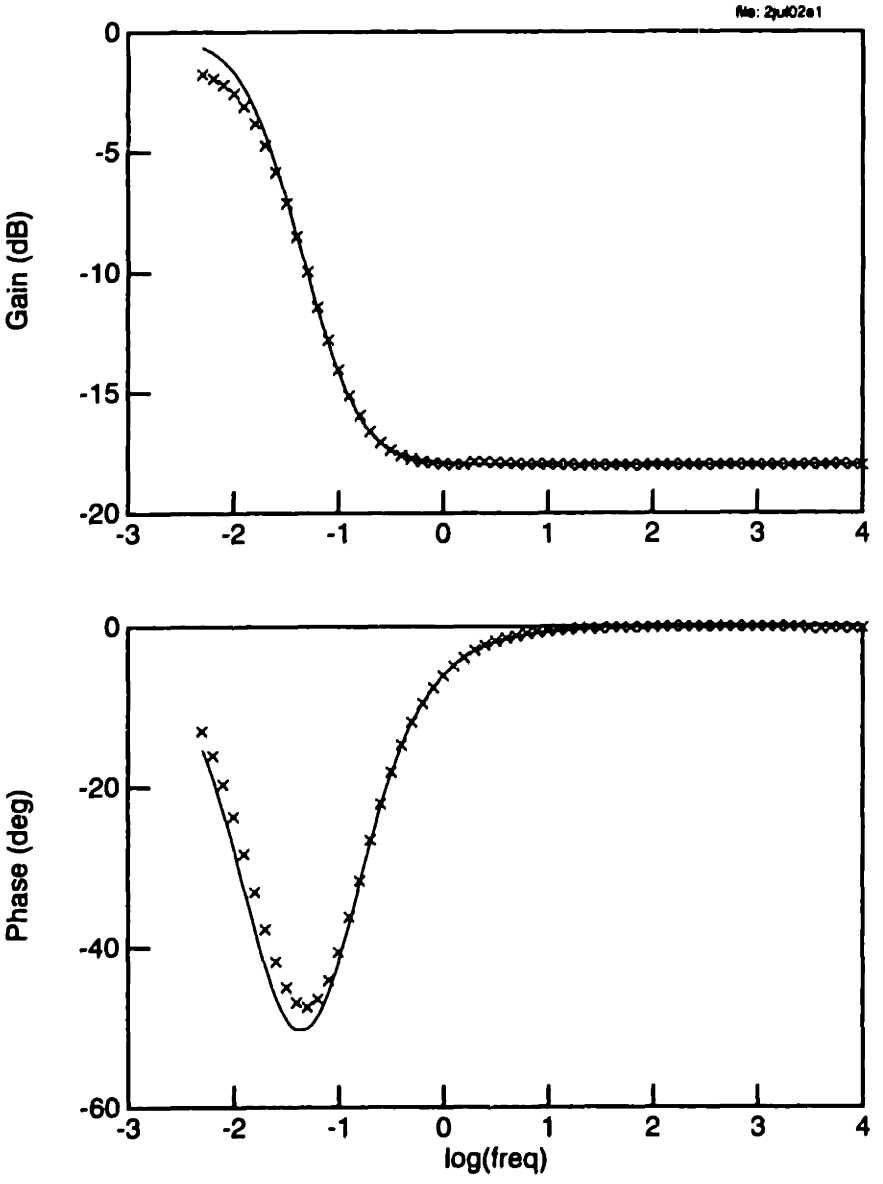


Figure 4.4: Actual measured values of the gain and the phase of the test cell in Shell Diala A transformer oil at 70°C. The solid line represents a fit to the data assuming the test cell is could be modeled as a resistor ($R_1$ = 12.0 GΩ) in parallel with a capacitor ($C_1$ = 108.9 pF), while the known load cell impedance consisted of a resistor ($R_2$ = 1000 GΩ) in parallel with a capacitor ($C_2$ = 753 pF).

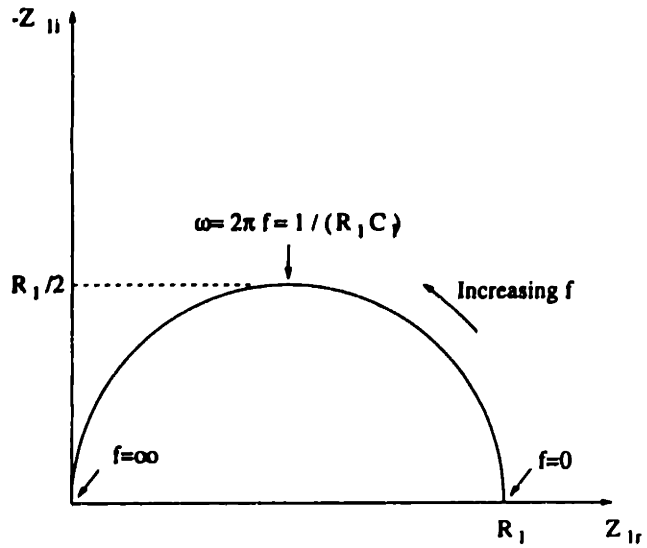


Figure 4.5: The ideal Cole-Cole plot for a resistor $R_1$ in parallel with a capacitor $C_1$. The real and imaginary components lie on a semi-circle of radius $R_1/2$. At a frequency $\omega = 2\pi f = 1/R_1C_1$, the imaginary component of the impedance is $-R_1/2$.

### 4.2.3 Lumped parameter *RC* model with double layer capacitance

When the effects of interfacial electrical double layers become significant the shape of the Cole-Cole plot changes dramatically. To see this, consider the lumped parameter model of Fig. 4.6, where all of the effects of the space-charge polarization associated with the electrical double layer are lumped into the capacitances $C_{dl}$ near the electrodes and the bulk properties of the liquid are given by $R_1$ and $C_1$. In this representation, the lumped elements are related to the dielectric properties of the liquid by

$$C_1 = \frac{\epsilon A}{d - 2\lambda_D} \quad ; \quad R_1 = \frac{d - 2\lambda_D}{\sigma A} \quad ; \quad C_{dl} = \frac{\epsilon A}{\lambda_D} \tag{4.15}$$

with $\lambda_D$ the characteristic Debye length over which the space-charge is distributed. For this model to be valid, the Debye length must be small compared to the plate spacing ($\lambda_D \ll d$), from which it follows that $C_{dl} \gg C_1$. For this model, the terminal impedance can be expressed as

$$Z_1 = \frac{R_1}{1 + j\omega R_1 C_1} + \frac{2}{j\omega C_{dl}} \Rightarrow \begin{cases} Z_{1r} &= \dfrac{R_1}{1 + (\omega R_1 C_1)^2} \\ -Z_{1i} &= \dfrac{\omega R_1^2 C_1}{1 + (\omega R_1 C_1)^2} + \dfrac{2}{\omega C_{dl}} \end{cases} \tag{4.16}$$

A Cole-Cole plot of this impedance is given in Fig. 4.7. At high frequencies, the impedance across the double layer capacitance is small and the dominant contribution to

the impedance comes from the parallel combination of $R_1$ and $C_1$. As the frequency is decreased, the impedance across the double layer capacitance becomes more significant until, at low enough frequencies, the series combination of $R_1$ and $C_{dl}$ provide the dominant contribution to the terminal impedance. Representative Cole-Cole plots for Shell Diala A transformer oil data, using the program **prcc.c** in Appendix E to process the data, are given in Fig. 4.8 for four temperatures. These plots indicate that double layer effects are being observed over the frequency range of these measurements as the temperature is increased.

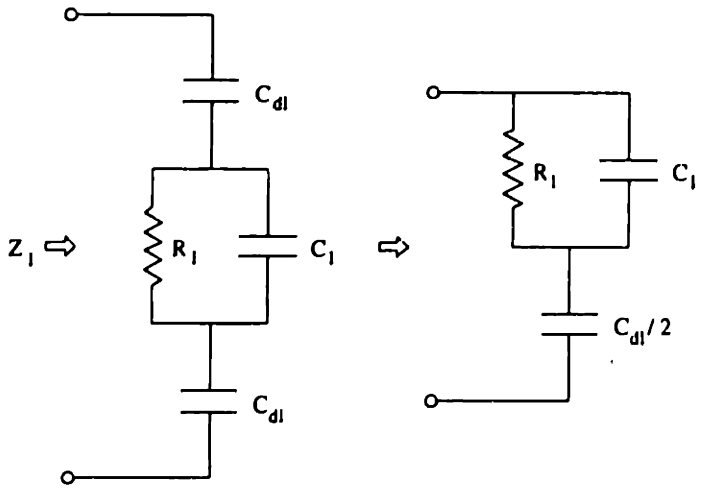


Figure 4.6: A lumped parameter model for the impedance of the fluid between the plates of the test cell including double layer capacitances at each electrode.

In this model, three material properties are unknown: the permittivity, the conductivity, and the Debye length. To estimate these properties the gain and phase from a minimum of two measurements are required. For example, if the fluid is insulating enough that the measured phase is near zero degrees at high frequencies, then the test cell acts as a capacitor and the permittivity of the fluid can be obtained from the high frequency limit of Eqs. 4.2, 4.3, 4.15, and 4.16 as

$$\epsilon_r = \frac{\epsilon}{\epsilon_o} = \frac{C_2}{C_{air}} \frac{|G|}{1 - |G|} \tag{4.17}$$

Then, at a sufficiently low frequency such that the double layer effects are becoming apparent, such as 10 mHz in the measurements discussed here, Eqs. 4.15 and 4.16 can be combined to give

$$\sigma = \frac{\epsilon_o}{C_{air} Z_{1r}^m} (1 + \omega \epsilon_r C_{air} Z_{1i}^m) \tag{4.18}$$

$$\frac{\lambda_D}{d} = -\frac{\omega \epsilon_r C_{air}}{2} \left( Z_{1i}^m + \frac{\omega \epsilon_r C_{air} Z_{1r}^{m2}}{1 + \omega \epsilon_r C_{air} Z_{1i}^m} \right) \tag{4.19}$$

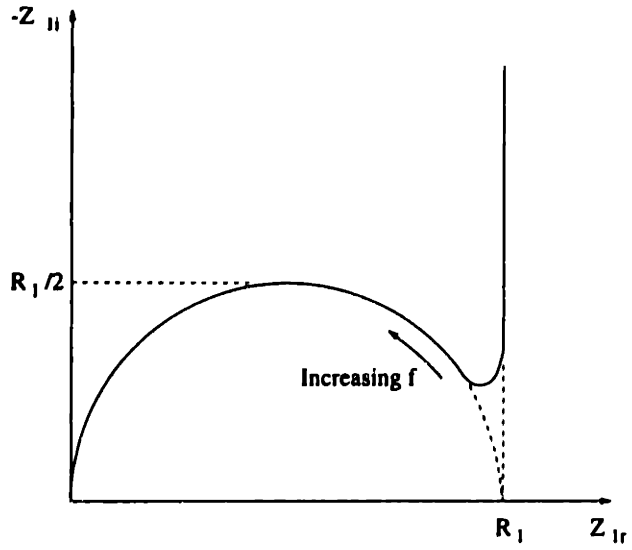


Figure 4.7: The ideal Cole-Cole plot for the lumped parameter model of Fig. 4.6. At high frequencies, the impedance is given by the parallel combination of $R_1$ and $C_1$. At low frequencies, the impedance is given by the series combination of $R_1$ and $C_{dl}$.

This approach was used to estimate the material properties and generate the solid lines given in Fig. 4.8. This relatively simple approach fits the data reasonably well.

### 4.2.4 Representative results

A comparison of the estimation techniques for the liquid conductivity is given in Table 4.1. In each technique, the permittivity is estimated from the high frequency gain because the liquids are insulating enough that the phase is approximately zero. In the "RC" techniques, the test cell is modeled as a resistance in parallel with a capacitance. The liquid conductivity is then estimated through a least squares fit between all of the measured data and Eq. 4.14, or using only the data at mid-band frequency (0.1 Hz) where the effects of the electrical double layers are not appreciable. In the "RCC" technique, the bulk region of the liquid is modeled as a resistance in parallel with a capacitance, but capacitances associated with the electrical double layer are also modeled. The bulk conductivity and Debye length are calculated from the measured gain and phase at a frequency of 10 mHz.

From the data in Table 4.1, it is clear that all three estimation techniques give essentially the same conductivity when the conductivity of the liquid is low enough that double layer effects are not present over the frequency range of the measurements. As the conductivity increases, the "RCC" model probably gives the most accurate conductivity measurements because it accounts for the double layers, at least in a simple manner. Furthermore, as the conductivity increases, the "RC" technique using all of the data begins to fail because it does not account for the double layers. The mid-frequency "RC" technique still successfully estimates the conductivity because the double layers do not

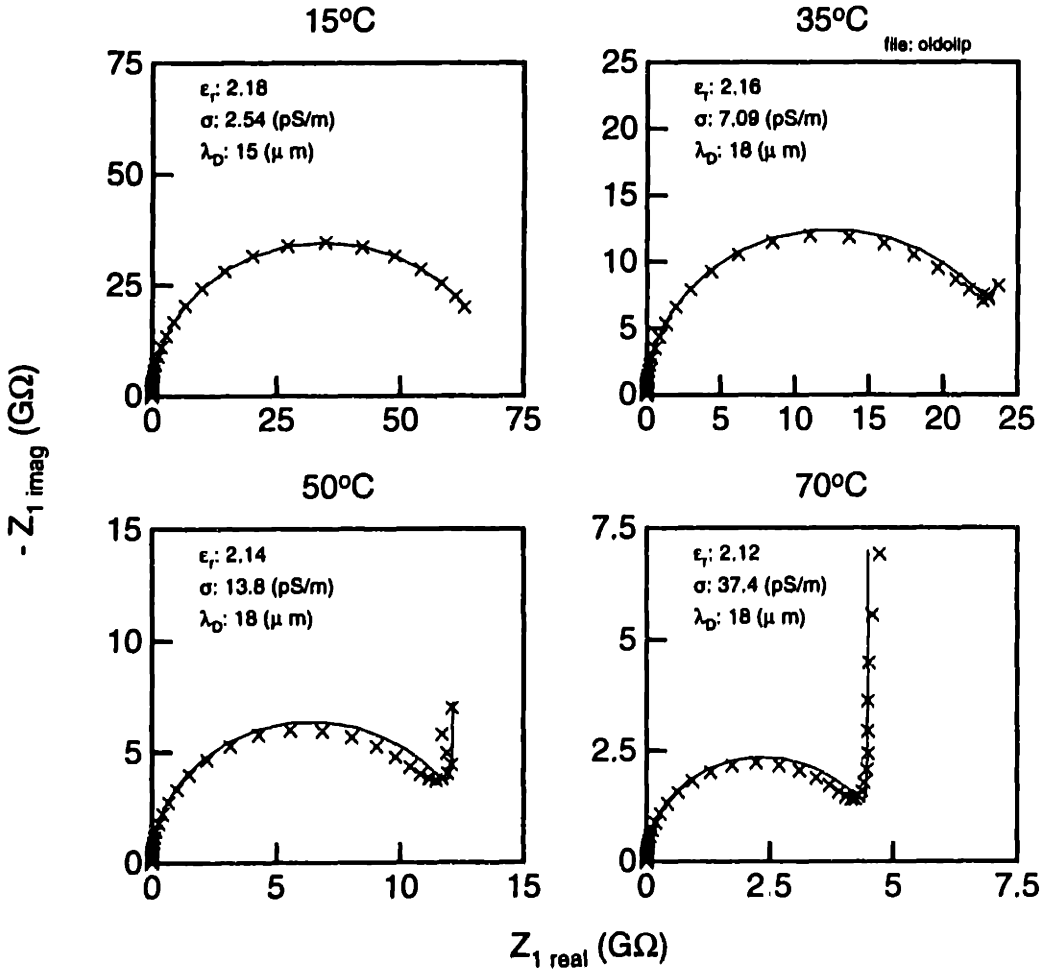


Figure 4.8: Representative data for impedance measurements of the conductivity test cell in Shell Diala A transformer oil at four temperatures. This data shows the presence of double layers at the electrode interfaces. The solid lines give the calculated impedances using a high frequency estimate of the permittivity (from Eq. 4.17 at 10 kHz) and estimates of the bulk conductivity (from Eq. 4.18) and Debye length (from Eq. 4.19) at 10 mHz.

| Run | Temp (°C) | $\epsilon_r$ (10kHz) | $\sigma$ (pS/m) | | | $\lambda_D$ ($\mu$m) | $D$ ($10^{-11}$m$^2$/s) |
|---|---|---|---|---|---|---|---|
| | | | RC (all) | RC (0.1Hz) | RCC (0.01Hz) | | |
| 2jun11f | 15 | 2.18 | 2.48 | 2.47 | 2.54 | 15 | 3.0 |
| 2jun12g | 35 | 2.16 | 6.90 | 7.13 | 7.09 | 18 | 12 |
| 2jun13d | 50 | 2.14 | 13.0 | 14.4 | 13.8 | 18 | 24 |
| 2jun14d | 70 | 2.12 | 26.5 | 38.0 | 37.4 | 18 | 65 |
| 2jun23b | 15 | 2.16 | 1.21 | 1.21 | 1.22 | 9.9 | 0.62 |
| 2jun25d | 70 | 2.10 | 12.1 | 12.9 | 13.0 | 20 | 28 |
| 2jun27a | 15 | 2.16 | 1.24 | 1.19 | 1.25 | 7.6 | 0.38 |
| 2jul01a | 35 | 2.14 | 3.42 | 3.43 | 3.48 | 17 | 5.3 |
| 2jul01i | 50 | 2.12 | 6.54 | 6.86 | 7.03 | 18 | 12 |
| 2jul02e | 70 | 2.11 | 13.1 | 14.3 | 14.5 | 19 | 28 |
| 3jan10a | 35 | 2.16 | 5.48 | 5.45 | 5.65 | 19 | 12 |
| 3jan11a | 50 | 2.14 | 9.82 | 10.6 | 10.4 | 20 | 22 |
| 3jan12a | 70 | 2.13 | 19.3 | 22.0 | 22.5 | 21 | 53 |
| 3jan12b | 15 | 2.18 | 2.07 | 1.90 | 2.15 | 17 | 3.2 |
| 3jan13a | 35 | 2.16 | 5.73 | 5.40 | 6.09 | 19 | 11 |

Table 4.1: Representative estimated properties comparing the simple RC model and the double layer model.

significantly affect the measured response in this frequency range.

The variation in the oil permittivity with temperature provides an indication for the accuracy of the measurements. The permittivity is expected to remain essentially constant at 2.2 over the temperature range of these measurements. The temperature variation in the measured values indicates that some relatively small parasitic capacitances are not being modeled. Nevertheless, the permittivity measurements are still within 4% of the accepted value. From this error, the measurement uncertainties, and the possible errors in modeling the effective test cell impedance, the overall measurement uncertainty is estimated to be less than 10%.

Also included in Table 4.1 are the estimated Debye lengths for the "RCC" model fit to the data and the associated values for the molecular diffusivity . These tabulated values show the Debye length and diffusivity increasing with temperature for a given oil sample. To check if this is reasonable, assume that the Debye length can be represented as

$$\lambda_D = \sqrt{\frac{\epsilon D}{\sigma}} \tag{4.20}$$

with $D$ the ion diffusivity. (The diffusivity was calculated from this expression, using the measured values for the permittivity, conductivity, and the Debye length.) The conductivity can be estimated as

$$\sigma = 2qbn_o \tag{4.21}$$

with $q = 1.6 \times 10^{-19}$ C the electronic charge, $b$ the ion mobility, and $n_o$ the number

density of the ions. Using Einstein's relation

$$\frac{D}{b} = \frac{kT}{q} \tag{4.22}$$

where $k = 1.38 \times 10^{-23}$ J/K= $8.62 \times 10^{-5}$ eV/K is Boltzmann's constant, and $T$ is the temperature in Kelvin, the Debye length can be expressed as

$$\lambda_D = \sqrt{\frac{\epsilon kT}{2q^2 n_o}} \tag{4.23}$$

If the trace impurities are fully ionized, then $n_o$ is a constant, independent of temperature, and $\lambda_D \sim \sqrt{T}$, consistent with the tabulated values. Unfortunately, the assumption of complete ionization is questionable because it depends greatly upon the impurity. Furthermore, the precise value of the Debye length may be in error because of fitting the data for a continuum phenomenon to a lumped parameter model and only using a single frequency for the estimation. Also, the fact that the Debye length is very small compared to the gap spacing between the plates makes it more sensitive than the conductivity to measurement error. Nevertheless, even though the precise quantitative values for the Debye length are questionable, it is still possible to conclude that the Debye length is on the order of 20 $\mu$m for the oils that were tested.

For the continuous conductivity measurements in the Couette Facility, the conductivity is calculated using the mid-frequency "RC" technique at a frequency of 0.1 Hz. This frequency lies in the mid-frequency range for most of the liquids used in the facility. Furthermore, since the period of this excitation is only 10 sec, measurements can be taken more frequently than if a relatively low frequency, such as 10 mHz, which has a period of 100 sec, is used.

The temperature dependence of the conductivity is shown in the Arrhenius plots of Fig. 4.9 for three samples of Shell Diala A transformer oil. The data shows that the conductivity is related to the temperature by

$$\sigma = \sigma_o e^{-W_a/kT} \tag{4.24}$$

where $\sigma_o$ is constant for each oil sample, $W_a$ is an activation energy, $k$ is Boltzmann's constant, and $T$ is the temperature in Kelvin. This relation can also be expressed as

$$\log_{10}\sigma = \log_{10}\sigma_o - \frac{W_a}{kT}\log_{10} e \tag{4.25}$$

so that a standard linear least squares estimations of the slope and intercept can be used to obtain the Arrhenius coefficients $\sigma_o$ and $W_a$. These oil samples had activation energies that varied between 0.38 eV and 0.42 eV, which is comparable to previously reported values for transformer oil of 0.408 eV [82] and 0.45 eV [23].

Since most failures of electric power transformers associated with flow electrification appear to have occurred under "dry" conditions, water has been implicated as a significant factor in the electrification process. One role that the water may play is in the creation of ionizable species in the bulk of the oil. If the water contained in the oil is

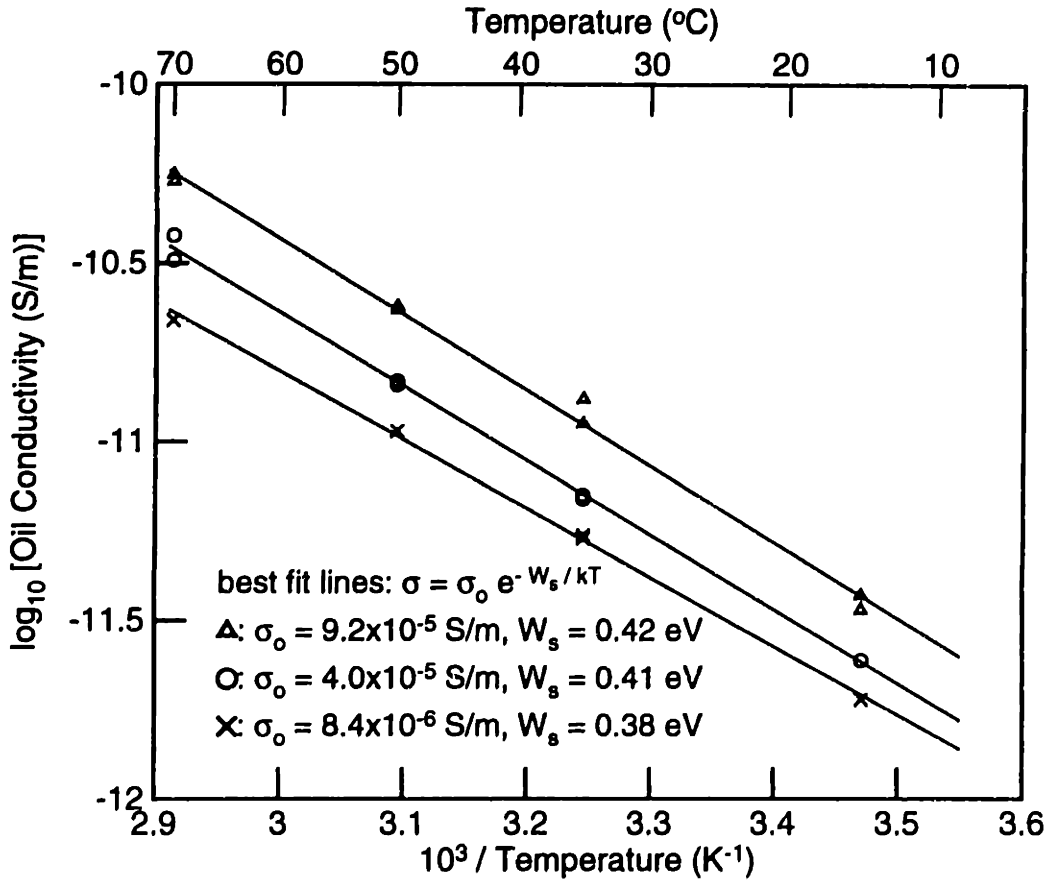


Figure 4.9: Sample conductivity measurements as a function of temperature for different batches of Shell Diala A transformer oil. The solid lines give linear least squares fit to the data.

the primary trace impurity that dissociates into ionized species, then the oil conductivity should increase as the moisture content increases.

To test if the oil moisture content affected the conductivity, an air gap capacitor (19.5 pF capacitance), a Harley moisture sensor [Model CT-880-BN-H (0/100%)-X], and a thermocouple probe were immersed in a beaker of Shell Diala A transformer oil. The oil was mixed by a magnetic stirrer and open to atmosphere at the top. Heating tape was wrapped around the beaker and an Omega CN 9000 temperature controller was used to maintain a constant temperature. The moisture content of the oil was varied by bubbling dry nitrogen gas through a porous plate diffuser immersed in the oil. After reaching a low moisture content, typically on the order of 1 ppm, the nitrogen gas was shut off and moisture from the air slowly raised the oil moisture content. The conductivity, oil moisture content, and temperature were measured as a function of time through the same computer controlled data acquisition program (**cf6.bas** in Appendix E) used in the electrification experiments.

A sample set of measurements of the oil moisture content and conductivity as a

function of time is given in Fig. 4.10 for a temperature of 27°C. In this experiment, the moisture content initially decreased as the relatively wet oil was dried by the atmosphere. At hour 35, dry nitrogen was bubbled through the oil which caused a more rapid decrease in moisture content. At hour 37, the nitrogen flow rate was increased, causing an even more rapid decrease in the moisture content. At hour 39, the nitrogen line was closed and the oil moisture content slowly increased as water from the atmosphere diffused into the oil. Throughout these moisture transients, the conductivity (measured at 0.1 Hz) remained essentially constant. These results are consistent with those of Li [31], in which the oil conductivity was found to be independent of the moisture content, but disagree with those of Higaki, et al [29], where the oil conductivity increased by a factor of 3 as the moisture content increased from 8 to 65 ppm. Since it is not clear how the moisture content was varied in the measurements of Higaki, et al and the oil was also in contact with vacuum dried pressboard, it is possible that the conductivity variations were the result of impurities in the system and not simply moisture.

Measurements of the conductivity as the moisture content was varied for several temperatures is shown in Fig. 4.11. For these higher temperature measurements, the oil was dried by bubbling dry nitrogen through the oil before starting the data acquisition program. The nitrogen supply was turned off prior to starting the indicated measurements. Again, these measurements show that the oil conductivity is essentially independent of the moisture content over this range of temperatures and moisture contents. The apparent increase in conductivity with moisture content at 70°C is probably due to oil oxidation, rather than moisture, since the oil was exposed to air.

Similar measurements were also performed with BTA, instead of moisture, added to the oil. With the oil at a temperature of 70°C and a moisture content of 17.8 ppm (5.2% of saturation), as BTA crystals were added to the oil, creating a 112 ppm BTA solution, the conductivity immediately decreased from 30 to 26 pS/m. Although it took a few hours for the BTA to dissolve completely, the conductivity remained essentially constant once the BTA was added.

## 4.3 Solid Properties

To determine the dielectric properties of the pressboard insulation, terminal measurements were made between the inner and outer cylinders of the Couette Charger. By applying a DC voltage between the cylinders and measuring the short-circuit terminal current or open-circuit voltage decay after the voltage source was disconnected, the effective dielectric properties of the pressboard could be estimated. This technique was also used to similarly determine the dielectric properties of teflon insulation as a proof-of-concept measurement.

### 4.3.1 Maxwell capacitor model

To develop relations between the dielectric properties of the materials contained by two cylindrical electrodes and the terminal measurements, consider the structure given in Fig. 4.12. For this analysis, the materials in both layers are assumed to behave as simple

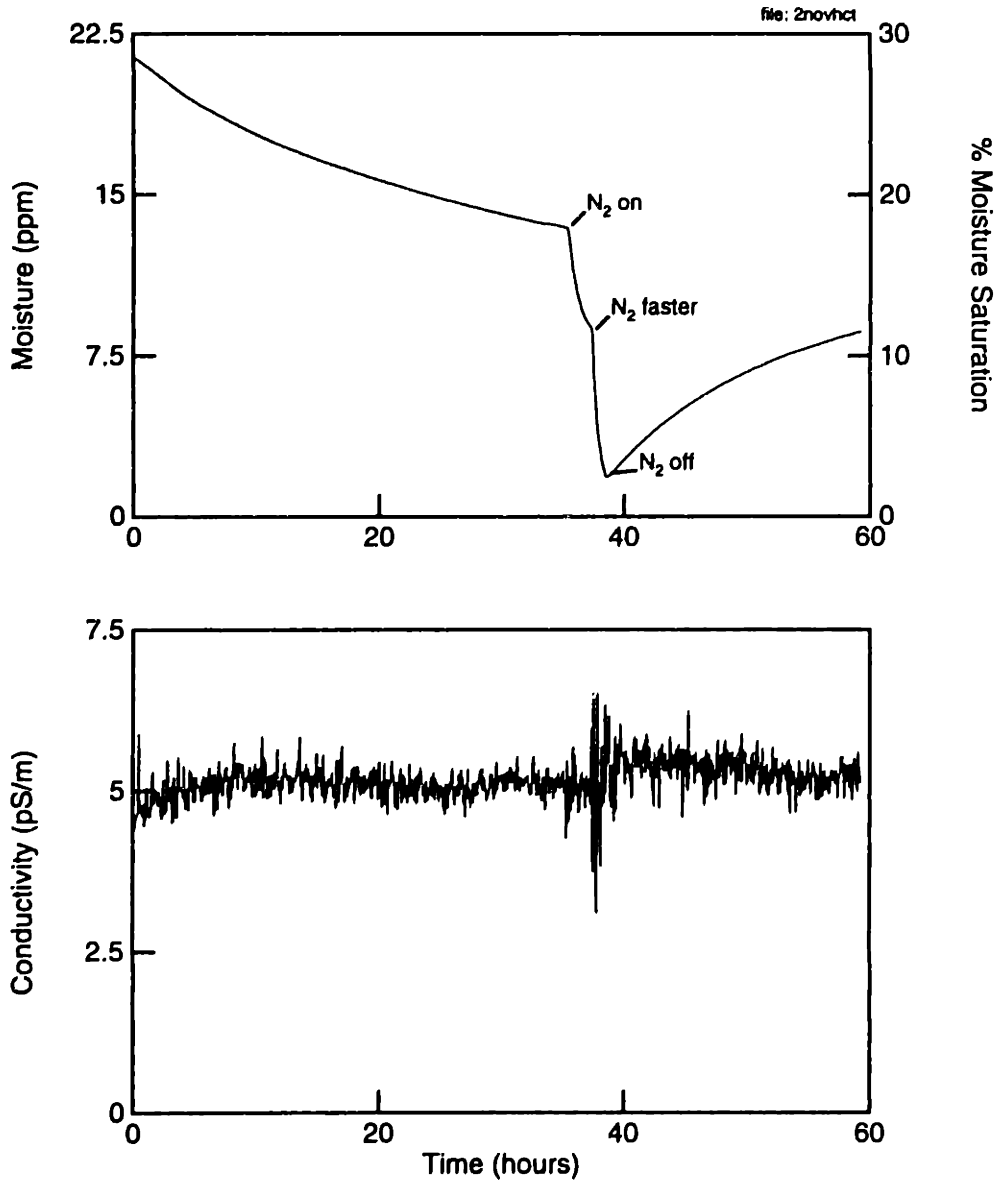


Figure 4.10: A representative set of measurements showing that the conductivity of Shell Diala A transformer oil is relatively independent of the moisture content at 27°C. The relatively wet oil was dried by exposure to the atmosphere and by bubbling dry nitrogen through the oil.

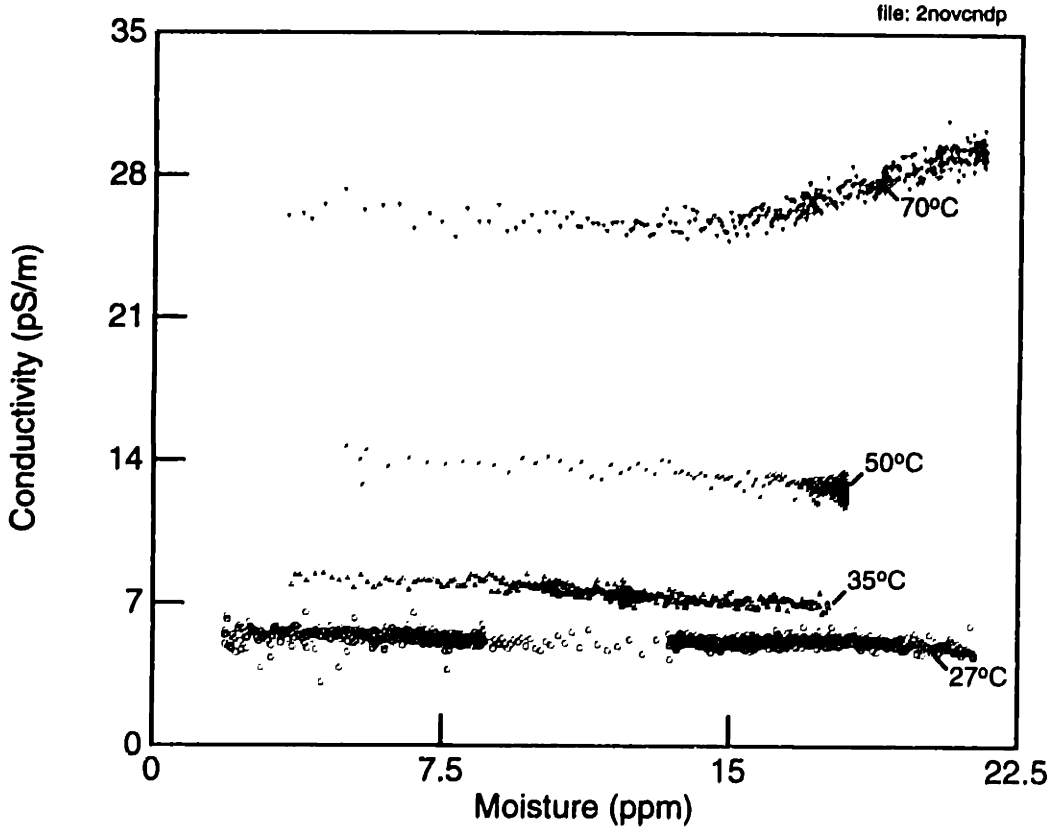


Figure 4.11: Electrical conductivity for Shell Diala A transformer oil as the moisture content and temperature are varied, showing the relative independence of the conductivity and moisture.

dielectrics having a single permittivity and conductivity. By neglecting end effects, such as fringing fields, the system can then be modeled electrically as a Maxwell capacitor in cylindrical coordinates [66: pp.184-188]. The corresponding lumped parameter representation, also given in Fig. 4.12, consists of a capacitor (for energy storage) and a resistor (for conduction losses) in parallel for each region, with the impedances of the regions in series with one another. The lumped element resistance $R$ and capacitance $C$ for each region can be defined in terms of the dielectric properties by

$$R_1 = \frac{\ln(c/a)}{2\pi\sigma_1 D} \quad ; \quad C_1 = \frac{2\pi\epsilon_1 D}{\ln(c/a)} \quad ; \quad R_2 = \frac{\ln(d/c)}{2\pi\sigma_2 D} \quad ; \quad C_2 = \frac{2\pi\epsilon_2 D}{\ln(d/c)} \qquad (4.26)$$

with $\sigma$ giving the conductivity of the layer, $\epsilon$ giving the permittivity of the the layer, $D$ the height of the cylinders, $a$ the inner cylinder radius, $d$ the outer cylinder radius, and $c$ the radius of the interface between the two dielectrics.

During the charging transient when the voltage source is applied, the field distribution

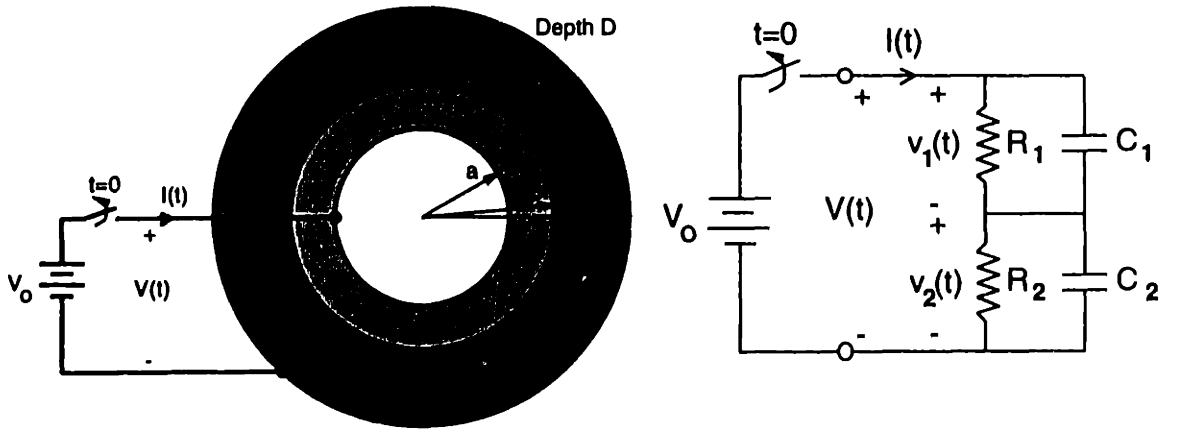


Figure 4.12: A schematic diagram of a cylindrical Maxwell capacitor containing two ohmic dielectric layers. The corresponding lumped element circuit diagram is given on the right.

is dominated by the permittivity (capacitance) of each region for short times and by the conductivity (resistance) for long times. If the system starts from an uncharged state in which the interface between the dielectrics is free of charge, then the application of a voltage $V_o$ will cause a current to flow through the system and a surface charge $\sigma_f$ to develop on the interface according to

$$\sigma_f = \frac{\epsilon_2\sigma_1 - \epsilon_1\sigma_2}{\sigma_1 \ln(d/c) + \sigma_2 \ln(c/a)} \frac{V_o}{c} \left(1 - e^{-t/\tau_c}\right) \tag{4.27}$$

where the charging time constant is given by

$$\tau_c \equiv \frac{C_1 + C_2}{\frac{1}{R_1} + \frac{1}{R_2}} = \frac{\epsilon_1 \ln(d/c) + \epsilon_2 \ln(c/a)}{\sigma_1 \ln(d/c) + \sigma_2 \ln(c/a)} \tag{4.28}$$

The corresponding voltage across each region can be expressed as

$$\frac{v_1(t)}{V_o} = \frac{C_2}{C_1 + C_2} e^{-t/\tau_c} + \frac{R_1}{R_1 + R_2} \left(1 - e^{-t/\tau_c}\right) \tag{4.29}$$

$$\frac{v_2(t)}{V_o} = \frac{C_1}{C_1 + C_2} e^{-t/\tau_c} + \frac{R_2}{R_1 + R_2} \left(1 - e^{-t/\tau_c}\right) \tag{4.30}$$

Notice that the total voltage between the electrodes, which is the sum of the voltages across each region, is $V_o$ for all time.

A very different transient results if the charging source is a constant current source. Then each region charges independently with the same current going through each region. If the current source has a magnitude $I$ then the surface charge at the dielectric interface

develops according to

$$\sigma_f = \frac{I}{2\pi cD}\left[\tau_2\left(1-e^{-t/\tau_2}\right)-\tau_1\left(1-e^{-t/\tau_1}\right)\right] \tag{4.31}$$

where the time constants are given by

$$\tau_1 = R_1C_1 = \frac{\epsilon_1}{\sigma_1} \quad ; \quad \tau_2 = R_2C_2 = \frac{\epsilon_2}{\sigma_2} \tag{4.32}$$

The corresponding voltage across each region can be expressed as

$$v_1(t) = IR_1\left(1-e^{-t/\tau_1}\right) = \frac{I\ln(c/a)}{2\pi\sigma_1 D}\left(1-e^{-t/\tau_1}\right) \tag{4.33}$$

$$v_2(t) = IR_2\left(1-e^{-t/\tau_2}\right) = \frac{I\ln(d/c)}{2\pi\sigma_2 D}\left(1-e^{-t/\tau_2}\right) \tag{4.34}$$

Thus, the temporal dynamics associated with the accumulation of surface charge at the dielectric interface depends upon the method of charging the interface. In both cases, when the conductivity of one of the layers is much smaller than the other layer (so that the geometric factors can be neglected), the electrical energy is essentially stored by the field inside that layer. In other words, when the layer next to the inner cylinder is more insulating than the layer next to the outer cylinder, the free surface charge at the dielectric interface is imaged to the inner cylinder. The free surface charge is imaged to the outer cylinder when the outer layer is much more insulating than the inner layer.

In a similar fashion, during the discharge transient after the source is disconnected, the decay of the surface charge depends upon the terminal connections. If the terminals are short-circuited by a current measuring electrometer, the current is the same through both regions and the decay time is the same as the voltage source charging time constant $\tau_c$. On the other hand, if the terminals are open-circuited then the fields in each region decay independently so that there isn't any current flow through the terminals. The open-circuit voltage decay can be expressed as

$$v_{oc}(t) = v_1(0^-)e^{-t/\tau_1} + v_2(0^-)e^{-t/\tau_2} \tag{4.35}$$

where $v_1(0^-)$ is the initial voltage across the pressboard region and $v_2(0^-)$ is the initial voltage across the oil region. The first term reflects the decay of the field stored in the layer next to the inner cylinder while the second term comes from the decay of the field across the layer next to the outer cylinder. When steady state conditions have been achieved during the charging transient, using a voltage source, the terminal current can be expressed as

$$\begin{aligned} I_{sc}(t) &= -\frac{V_o(\tau_2-\tau_1)^2}{R_1R_2(R_1+R_2)(C_1+C_2)^2}e^{-t/\tau_c} - \frac{C_1C_2V_o}{C_1+C_2}\delta(t) \\ &= -\frac{2\pi DV_o}{[\epsilon_1\ln(d/c)+\epsilon_2\ln(c/a)]}\left\{\frac{(\epsilon_2\sigma_1-\epsilon_1\sigma_2)^2\ln(d/c)\ln(c/a)}{[\sigma_1\ln(d/c)+\sigma_2\ln(c/a)]}e^{-t/\tau_c}+\epsilon_1\epsilon_2\delta(t)\right\} \end{aligned} \tag{4.36}$$

| Parameter | Couette Charger | |
|---|---|---|
| | Small | Large |
| $a$ | 2.54 cm | 7.62 cm |
| $c$ | 3.73 cm | 7.72 cm |
| $d$ | 3.81 cm | 10.16 cm |
| $D$ | 22.9 cm | 40.64 cm |
| Layer 1 | oil | pressboard |
| Layer 2 | teflon | oil |

Table 4.2: Geometry and materials tested the cylindrical electrode structures.

where $\delta(t)$ denotes the Dirac delta function and provides the impulse in current due to the instantaneous changes in the displacement fields as the terminals are short-circuited. The open-circuit terminal voltage can be expressed as

$$v_{oc}(t) = V_o\left[\frac{R_1 e^{-t/\tau_1} + R_2 e^{-t/\tau_2}}{R_1 + R_2}\right] = V_o\left[\frac{\sigma_2 \ln(c/a) e^{-t/\tau_1} + \sigma_1 \ln(d/c) e^{-t/\tau_2}}{\sigma_1 \ln(d/c) + \sigma_2 \ln(c/a)}\right] \qquad (4.37)$$

By relating these expressions to measurements of the short-circuit current or open-circuit voltage, the dielectric properties of the layers can be estimated. The following two subsections describe measurements of the dielectric properties for a system containing teflon and transformer oil and for a system containing pressboard insulation and transformer oil.

### 4.3.2 Sample teflon measurements

Consider first an electrode system that has teflon covering the outer cylinder and Shell Diala A transformer oil filling the remainder of the gap between the cylinders. These materials were placed into the small Couette Charger, which has the dimensions given in Table 4.2. A 22.5 V battery was used as the charging source and connected between the inner and outer cylinder electrodes for about 30 minutes to charge the system. The charging and discharging terminal currents were measured by a Keithley 617 electrometer connected to the outer cylinder, with the electrometer ground connected either to the battery or the inner cylinder. When measuring the open-circuit voltage decay, the electrometer was connected to the inner cylinder and the outer cylinder was grounded.

Representative room temperature measurements of the short-circuit current are given in Fig. 4.13. The solid lines are the result of a least squares fit to the expression

$$I_{sc}(t) = Ae^{-t/\tau_c} + B \qquad (4.38)$$

where $A$, $\tau_c$, and $B$ are estimated parameters and the program **pelexp.for** in Appendix E was used to process the data. The parameter $B$ was included so that a better estimate of the time constant could be obtained. Ideally $B$ is zero for ohmic materials, but small steady state galvanic currents were usually observed in the measurements. As expected from the analysis, the charging and discharging time constants are the same,

being roughly 400 sec, because a voltage source was applied. Similar measurements with the polarity of the battery reversed give the same time constant.

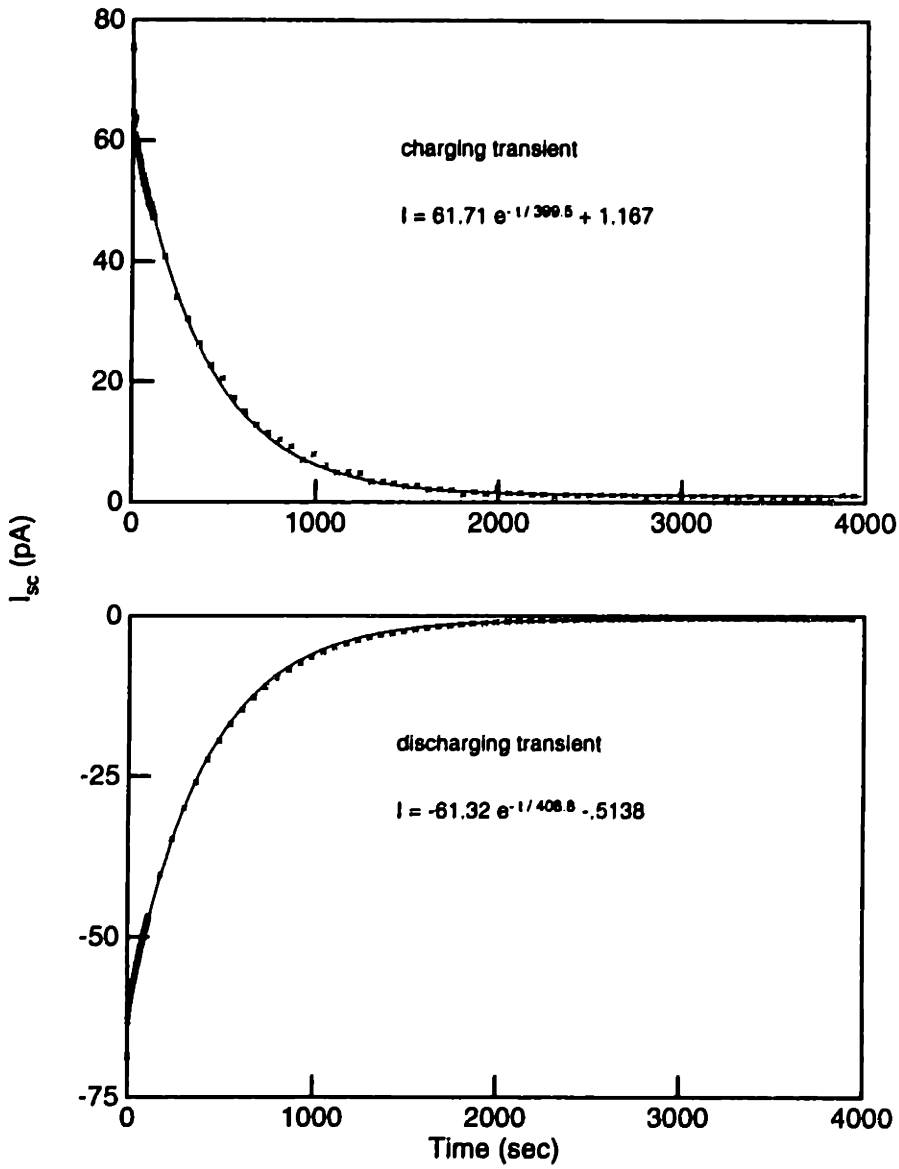


Figure 4.13: Short-circuit terminal current measurements for teflon and Shell Diala A transformer oil in the small Couette Charger. The upper plot gives the charging transient and the lower plot the discharging transient when a 22.5 V battery was connected to the inner cylinder. The temperature was 22°C. The solid lines are a least squares fit to the indicated expressions.

Typically, oil is much more conducting than teflon, and as given by Eq. 4.37, the open-circuit voltage should decay with two distinct time constants. A representative set of open-circuit voltage decay measurements, given in Fig. 4.14, confirms that the teflon

is indeed more insulating than the oil. Furthermore, over short time periods the voltage across the teflon does not decay appreciably and fitting the voltage decay to Eq. 4.38 gives the relaxation time for the field through the oil as $\tau_{oil} = 30.5$ sec. For long time periods, after a few oil relaxation times, only the voltage across the teflon remains. Assuming that the oil relaxation time is known, the teflon relaxation time $\tau_{teflon}$ can be obtained from the program **pe2exp.for** in Appendix E which fits the entire set of data to the expression

$$v_{oc}(t) = Ae^{-t/\tau_{teflon}} + Be^{-t/\tau_{oil}} \tag{4.39}$$

where $A$, $B$, and $\tau_{teflon}$ are estimated parameters. The teflon relaxation time was found to be 10.6 hrs, which was longer than the duration of the experiment. Another open-circuit voltage decay measurement, with the battery polarity reversed and performed over a 17 hour time period, gave 9.2 hrs for the teflon relaxation time. This was comparable to the previous value.

From the measured values of the time constants, the geometry, and an assumed permittivity for the oil, the dielectric properties for the teflon itself can be estimated. First, for the oil, using $\tau_{oil} = 30.5$ sec and assuming that $\epsilon_{oil} = 2.19\epsilon_o$, with $\epsilon_o = 8.854 \times 10^{-11}$ F/m, then Eq. 4.32 gives $\sigma_{oil} = 6.36 \times 10^{-13}$ S/m. To obtain the teflon conductivity, substitute Eq. 4.32 for the teflon permittivity into Eq. 4.28 to obtain

$$\frac{\sigma_{teflon}}{\sigma_{oil}} = \frac{(\tau_c - \tau_{oil})}{(\tau_{teflon} - \tau_c)} \frac{\ln(d/c)}{\ln(c/a)} \tag{4.40}$$

Using the values for the radii from Table 4.2, $\tau_c = 405$ sec, and $\tau_{teflon} = 38200$ sec, then $\sigma_{teflon} = 3.5 \times 10^{-16}$ S/m and the corresponding permittivity is $\epsilon_{teflon} = 1.5\epsilon_o$.

While this value for the teflon conductivity compares reasonably well to reported values of less than $10^{-16}$ S/m [83: p. 251], the permittivity is significantly less than the reported value of $2.1\epsilon_o$ [66: p. 147]. The major source of error in this measurement is probably the finite input impedance of the electrometer, which is approximately $2 \times 10^{14}$ $\Omega$. While the impedance of the oil layer is much smaller than the electrometer impedance, the estimated teflon conductivity gives a resistance of $4.2 \times 10^{13}$ $\Omega$ for the teflon layer, which is comparable to the electrometer impedance. This indicates that the short time constant response will not be affected by the electrometer impedance but the long time constant response will be shortened (the effective impedance for the 'RC' time constant will be reduced since the electrometer impedance is in parallel with the layer impedance). To get a better estimate of the teflon conductivity, *assume* that $\epsilon_{teflon} = 2.1\epsilon_o$. This then gives a capacitance of 1.26 nF for the teflon layer. Using the measured time constant (38200 sec) and assuming that the electrometer impedance is in parallel with the teflon layer resistance gives a resistance of $3.6 \times 10^{13}\Omega$ for the teflon layer. This corresponds to a conductivity of $\sigma_{teflon} \approx 6.1 \times 10^{-16}$ S/m which is still quite reasonable. Although the unmodeled capacitance of the electrical double layers on the oil side of each interface may also contribute to the error, the capacitance associated with the double layers (at this temperature) are much larger than the capacitances associated with each dielectric layer so that the correction will be minimal.

In summary, this decay measurement technique appears to provide representative values for the solid dielectric properties. While some of the details of the measurements

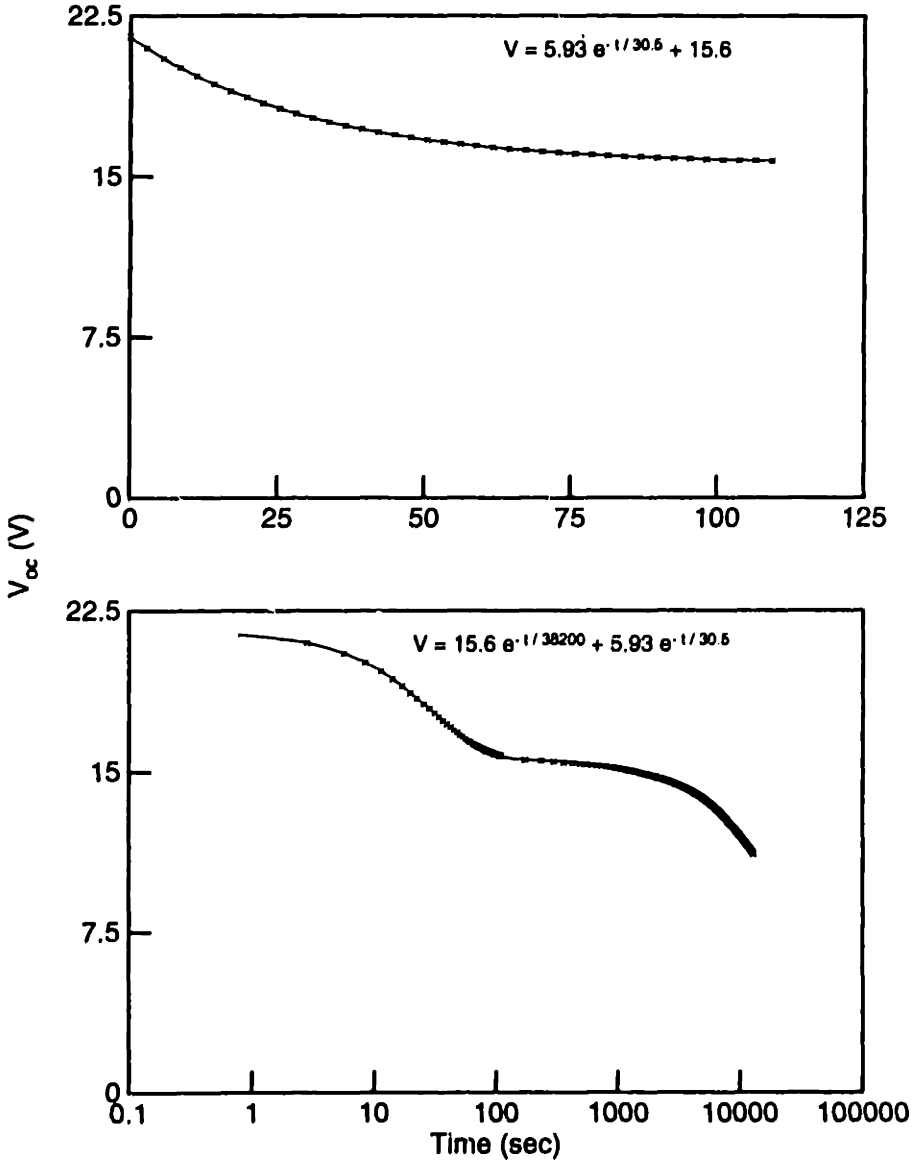


Figure 4.14: Open-circuit voltage decay for teflon and Shell Diala A transformer oil in the small Couette Charger. The upper plot gives the voltage decay for short times, which can be associated with the decay of the field through the oil. The lower plot gives the complete voltage decay, over both short and long time periods, and shows a long time transient decay that can be associated with the decay of the field through the teflon. The solid lines show the results of a least squares fit to the indicated expressions.

and the model can be brought into question, depending upon the relative impedances of the different layers and the electrometer itself, the basic idea remains that the measured time constants are indicative of the losses through the dielectrics.

### 4.3.3 Sample pressboard measurements

Consider next an electrode system that has EHV-Weidmann HiVal pressboard covering the inner cylinder and Shell Diala A transformer oil filling the remainder of the gap between the cylinders. In reference to Fig. 4.12, region 1 corresponds to the pressboard insulation and region 2 to the oil region. These materials were placed into the large Couette Charger, which has the dimensions given in Table 4.2, and were used in the flow electrification studies. The system was charged by applying a 22.5 V battery between the inner and outer cylinders or by rotating the inner cylinder to redistribute the charge by flow electrification. All terminal discharging measurements were performed with a stationary inner cylinder. The discharging current and open-circuit voltage decay were measured by a Keithley 614 or Keithley 617 electrometer connected from the inner cylinder to the grounded outer cylinder.

A representative set of measurements of the short-circuit terminal current, at two temperatures are given in Fig. 4.15. The dashed lines are the result of a least squares fit to Eq. 4.38 using **pe1exp.for** in Appendix E. The 15°C data shows the exponential decay that one would expect from an "ohmic" model during short times, but also contains another long time transient decay. This is more evident in the 70°C data, where the simple exponential expression does not provide a good fit to the data. As in the open-circuit voltage measurements, the loss increases (or the time constant for the decay decreases) as the temperature increases.

Representative measurements of the open-circuit voltage are given in Fig. 4.16 for two temperatures. The dashed lines are the result of a least squares fit (using **pe2exp.for** in Appendix E) to the expression

$$v_{oc}(t) = Ae^{-t/\tau_{pb}} + Be^{-t/\tau_{oil}} \tag{4.41}$$

where $A$, $B$, and $\tau_{pb}$ are estimated parameters and $\tau_{oil}$ is the oil relaxation time, assumed to be known from oil dielectric measurements. Since the oil dielectric measurements showed that the oil behaves "ohmically" and can be represented by a single permittivity and conductivity, except possibly at the higher temperatures, the relatively poor fit between the theoretical fit and the data can be attributed to the non-ohmic response of the pressboard. Nevertheless, these measurements show that the loss associated with the pressboard increases significantly with temperature, as given by the decrease in the effective pressboard relaxation time with increasing temperature. Reversing the polarity of the excitation does not appreciably affect the measured time constants.

While an effective permittivity and conductivity for the pressboard can be calculated from the terminal measurement time constants, the relatively poor fit between the theoretical expressions and the data indicates that the values would be questionable. In fact, it seems unreasonable to use a single permittivity and conductivity to represent the pressboard. One reason for this is that pressboard is dispersive in the sense that AC

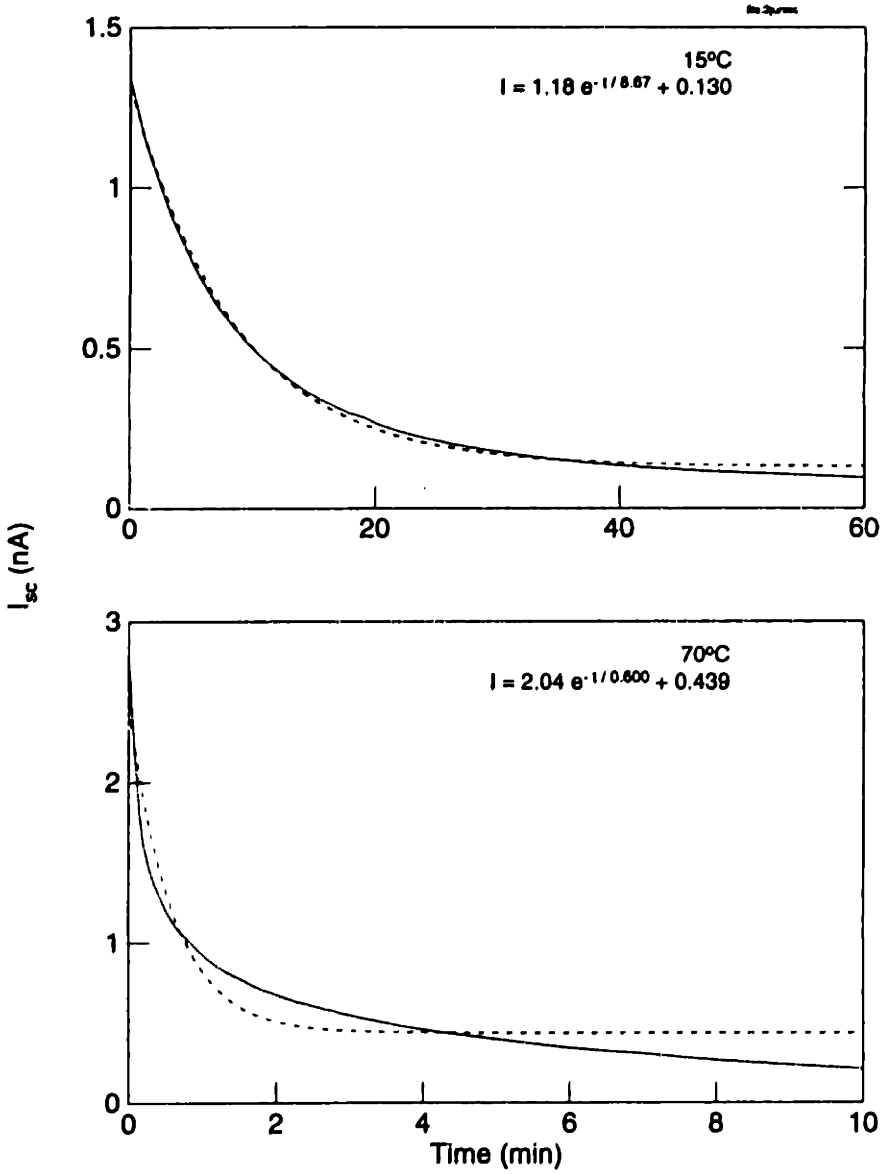


Figure 4.15: The short-circuit terminal current decay for HiVal pressboard covering the inner cylinder and Shell Diala A transformer oil filling the remainder of the annular gap. This data was taken immediately after stopping the rotation of the inner cylinder from a flow electrification measurement. The solid line is the measured data while the dashed line is a least squares fit to the indicated expression.

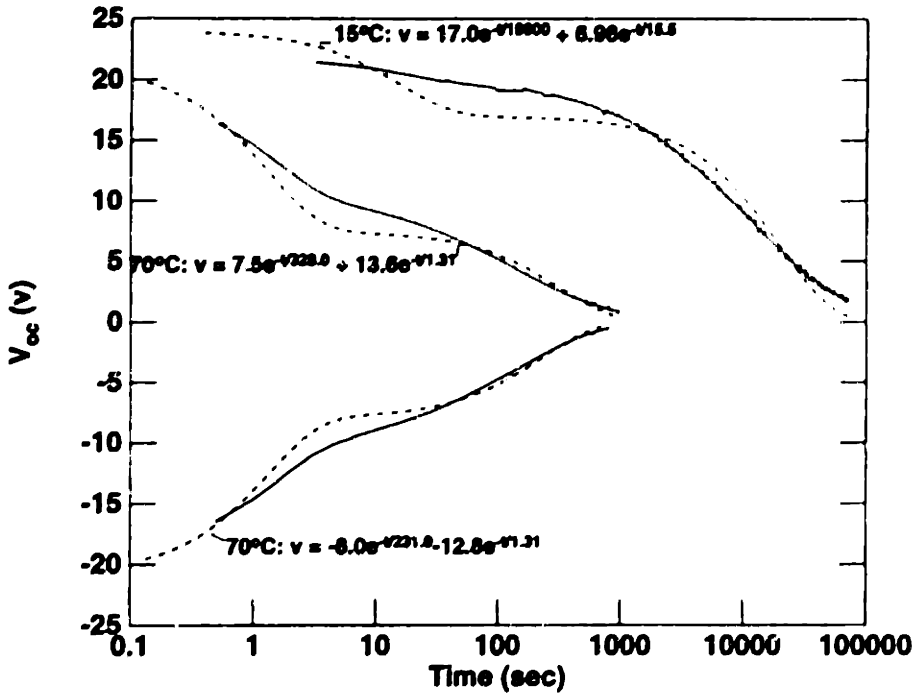


Figure 4.16: The open-circuit voltage decay for HiVal pressboard covering the inner cylinder and Shell Diala A transformer oil filling the remainder of the annular gap. To charge the system, a battery was connected between the cylinders and applied for approximately 30 minutes for the 15°C measurement and approximately 15 minutes for the 70°C measurement. The solid line is the measured data while the dashed line is a least squares fit to the indicated expression, where the smaller time constant is assumed to be known from separate oil dielectric measurements. The long time constant provides an indication of the loss through the pressboard.

measurements show the dielectric properties varying as a function of frequency [17,84,85]. Another reason is that the moisture content of the pressboard, which affects the dielectric properties, is probably non-uniform, especially at low temperatures [85-87]. This non-uniformity in the pressboard conductivity across the sample could then lead to a spectrum of relaxation times.

An adequate model for the dielectric properties of the pressboard insulation must be able to explain both the time domain transient measurements shown here and the frequency domain measurements showing the dispersive behavior of the insulation. In the absence of an adequate model, an ad-hoc expression for the time transient voltage decay through the pressboard was assumed and fit to the data (using **peept.for** in Appendix E). The expression had the form

$$v_{oc}(t) = \frac{A}{1 + t/\tau_{pb}} + Be^{-t/\tau_{oil}} \tag{4.42}$$

where $\tau_{oil}$ is the oil relaxation time and the factors $A$, $B$, and $\tau_{pb}$ are estimated parameters. This type of expression usually results from a unipolar migration model for charge transport that is dominated by the self-precipitation of the charged species [88]. As shown in Fig. 4.17, this expression provides a much better fit to the open-circuit voltage decay, particularly for times much greater than the oil relaxation time when the decay of the voltage across the pressboard is dominant. Additional voltage decays are shown in Fig. 4.18.

The exponential decay and the unipolar-type $1/(1 + t/\tau)$ decay are not always distinguishable by terminal measurements. For example, for short times, both vary essentially linearly with time. If the time constant associated with this decay is too large compared to the duration of the experiment, it would be hard to determine the dominant conduction law. Furthermore, the combination time constant obtained from the terminal current measurements may only reflect the dominant "ohmic" time constant at low temperatures, where the pressboard loss is low, and may reflect more of the true conduction behavior at the high temperatures where the pressboard loss is relatively high.

For reference, the results of numerous terminal decay measurements are summarized in Table 4.3. Also given is the moisture content of the oil in contact with the pressboard. One observation from this data is that the time constant for relaxation through the pressboard appears to become slower when electrification tests are performed, after the pressboard has been oil impregnated. This may be a result of the oil taking a long time to finish impregnating the pressboard, but increasing the equilibration times for the impregnation process and the subsequent reduction in temperature did not appear to affect this trend.

At a given temperature, the pressboard relaxation time appears to be relatively independent of the oil moisture content, probably because the bulk moisture content in the pressboard is essentially the same in each of the measurements. The oil moisture content only reflects the moisture content in the bulk of the pressboard at the higher temperatures where the diffusion time for water through oil impregnated pressboard is short compared to the duration time of the experiments [17]. From the Norris equilibrium curves, the moisture contents of the pressboard in the various measurements are not

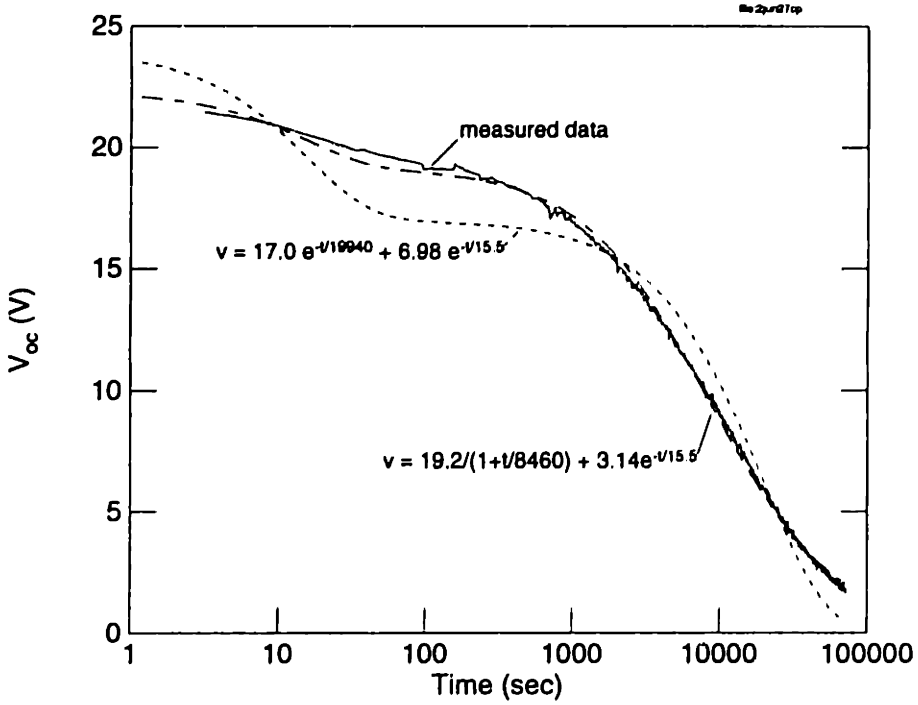


Figure 4.17: A better fit to the open-circuit voltage decay data, illustrated above (long dashes) for 15°C data, can be obtained by assuming an expression of the form $v_{oc}(t) = \frac{A}{1+t/\tau_{pb}} + Be^{-t/\tau_{oil}}$ where $\tau_{oil}$ is the oil relaxation time, the factors $A$, $B$, and $\tau_{pb}$ are estimated parameters. For comparison, the two exponential voltage decay associated with an "ohmic" conduction model is also plotted (short dashes).

significantly different. This is not surprising because essentially the same drying process was applied to each sample before oil impregnation. Furthermore, at low temperatures where the diffusion time for water across the pressboard is long compared to the duration of the experiments, the oil is only in moisture equilibrium with a thin layer at the pressboard/oil interface; even though the oil moisture content varies with time, the bulk of the pressboard remains essentially uniform and constant. These conclusions are consistent with AC dielectrometry measurements that have shown that the pressboard conduction tends to increase with the pressboard moisture content [84,86,87]

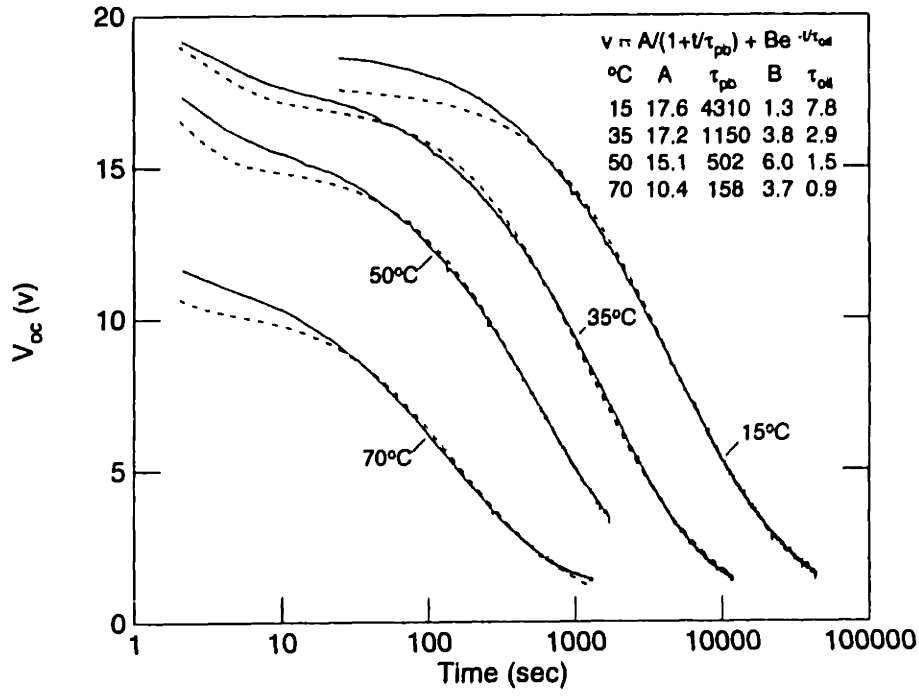


Figure 4.18: The open-circuit voltage decay at four temperatures. The solid lines give the measured data while the dashed lines give theoretical fits to the assumed relation of Eq. 4.42.

## 4.4 Summary

In this chapter, several experimental techniques for determining the dielectric properties of semi-insulating materials were described. In this application, impedance measurements at a single frequency (0.1 Hz) of a test cell containing insulating oils were used to estimate a bulk relative permittivity of 2.2 and a conductivity that varied between 0.1 pS and 100 pS. Choosing a lower frequency for the AC excitation allows lower conductivities to be measured. For higher conductivities, where double layer effects become important, multiple frequency measurements of the impedance, such as at a very high frequency and at a very low frequency, can be used to estimate the bulk liquid properties and an effective double layer thickness. Using this technique, the oil conductivity was found to be essentially independent of the oil moisture content over a moisture content range of 2 to 22 ppm and a temperature range of 27 to 70°C.

Also discussed in this chapter was the use of time domain measurements for determining the dielectric properties of solid insulation. These measurements showed that

| Date | Temp (°C) | Oil Moist. (ppm) | $\tau_{oil}$ (sec) | $\tau_c$ (sec) | $\tau_{pb}$ (sec) | |
|---|---|---|---|---|---|---|
| | | | | | $\exp(-t/\tau_{pb})$ | $1/(1+t/\tau_{pb})$ |
| 6-19-92* | 15 | 3.0 | 29.8 | — | — | — |
| 6-23-92 | 15 | 1.3 | 16.0 | — | 3740 | 2730 |
| 6-25-92 | 70 | 4.2 | 1.5 | — | 291 | 99.0 |
| 6-27-92 | 15 | 1.4 | 15.5 | — | 19900 | 8460 |
| 7-1-92 | 35 | 2.6 | 5.5 | — | 1854 | 753 |
| | 50 | 3.6 | 3.0 | — | 1018 | 496 |
| 7-2-92 | 70 | 5.8 | 1.5 | — | 310 | 106 |
| 6-1-93* | 15 | 3.4 | 16.4 | 531.9 | 3868 | 2140 |
| 6-2-93 | 15 | 1.5 | 15.8 | 520.2 | 28780 | 13200 |
| 6-4-93 | 15 | 1.4 | 16.4 | 544.4 | 41250 | 19700 |
| 6-8-93 | 70 | 7.0 | 1.34 | 36.0 | 444. | 108. |
| 6-14-93* | 15 | 0.70 | 12.2 | 475.1 | 3752 | 1650 |
| 6-15-93 | 15 | 0.46 | 13.6 | 420.7 | 6750 | 2430 |
| 6-17-93 | 70 | 1.9 | 1.46 | 81.6 | 364 | 89.1 |
| 6-23-93* | 15 | 0.6 | 12.8 | — | 7408 | 2810 |
| 6-24-93 | 15 | 0.45 | 13.3 | 517 | — | 8830 |
| 6-28-93 | 70 | 1.3 | 1.64 | 299 | 595 | 191 |
| 10-15-93* | 15 | 0.8 | 8.77 | 324 | 4250 | 1430 |
| 11-20-93 | 15 | 0.84 | 7.76 | 324 | 13980 | 4310 |
| 11-28-93 | 35 | 1.9 | 2.86 | 194 | 3194 | 1150 |
| 11-30-93 | 50 | 3.0 | 1.49 | 160 | 1074 | 502 |
| 12-01-93 | 70 | 5.2 | 0.91 | 100 | 501 | 158 |

Table 4.3: Summary of estimated relaxation times from terminal measurements for HiVal pressboard and Shell Diala A transformer oil. A superscript * indicates that the measurements were taken after oil impregnating the pressboard and lowering the temperature to the specified level, before any electrification measurements.

pressboard insulation does not act "ohmically" and cannot be represented by a single permittivity and conductivity. Although an ohmic model for the solid qualitatively predicts the temporal decay of fields in the pressboard, other ad-hoc models give better fits to some of the data. A self-consistent model for the conduction would have to be able to describe both these time domain measurements and AC frequency spectrum measurements, with the possible complication of inhomogeneous moisture distributions.

# Chapter 5

# Electrification Model using Postulated Interfacial Conditions

While the previous two chapters described experimental techniques for monitoring parameters critical to the electrification processes, a better understanding of the underlying physics requires physical models. In this chapter, a relatively simple model for flow electrification in a rotating cylindrical electrode structure is presented. The objectives of this analysis and the comparison to the experimental measurements are to determine how well previously postulated boundary conditions represent the interfacial charge transfer processes and how these conditions change as various parameters, such as the oil BTA concentration, are varied.

## 5.1 Introduction

In Chapter 3, electrification experiments were performed with a rotating cylindrical electrode and materials typically used in electric power apparatus. In addition to simulating the behavior of actual transformers, except for scale and geometry differences, these experiments also provide information about the fundamental electrification processes. In particular, by comparing the experimental data to a self-consistent flow electrification model, the charge transfer reaction at the liquid/solid interface can be explored.

The goal of this chapter is to develop a self-consistent steady state model for flow electrification in which the equations that describe the transport of the charged species in the bulk of the fluid are coupled to the chemical reactions describing the interfacial charge transfer. Since the impurities involved in creating the ionized species in flow electrification problems are usually unknown, the chemical reactions these impurities undergo are not known either. This ambiguity in the identity of the charged species significantly complicates the modeling of the charge separation process. Usually, generic chemical reactions are assumed for the bulk and at the interfaces, similar to Levich's approach to the various reactions that could occur with a rotating disk electrode in an aqueous solution [47]. This will also be the approach followed here.

In this model, it is assumed that the fluid flow causes a net charge density to develop in the bulk region of the liquid between the electrodes. This charge density is the result

of an interfacial chemical reaction that is driven out of equilibrium by the fluid motion. Since the chemical species involved in the reaction are not known, a simple form for the reaction, identical to that used by other researchers, will be assumed. While the terminal current or voltage from the electrode may be related to the parameters describing the interfacial reaction [48], direct measurements of the volume charge density are also possible for the semi-insulating materials of interest in electric power apparatus [2,10,11]. As a result, the focus of this model is the development of relations between the bulk charge density and the interfacial parameters for various imposed boundary conditions. Self-consistent relations between the terminal variables and the interfacial parameters will also be obtained.

In this presentation, Section 5.2 outlines the basic equations and fundamental physical processes involved in flow electrification. In Section 5.3, the equilibrium charge distribution is derived for an isolated interface without fluid motion. Section 5.4 then describes the basic geometry of the cylindrical electrode structure being modeled. Section 5.5 discusses the stationary, equilibrium distribution of the charge density in the cylindrical structure and the conditions under which a bipolar model for the charge species can be linearized so that only the net charge density in an ohmic fluid needs to be considered. Section 5.6 gives a summary of the hydrodynamics associated with the fluid motion. Section 5.7 presents the derivation of the electrification model and discusses several limiting cases. Section 5.8 compares the model to several experimental measurements. Section 5.9 provides a concluding summary.

## 5.2 Basic Formulation

Even in a highly purified state, the fluid will contain impurities that can undergo chemical reactions and have a significant effect on the charge generated by flow electrification. Since these impurities are usually present in trace amounts, their composition tends to be unknown. For the purposes of this model, a single ionizable impurity is assumed. A model for the chemical reaction involving this impurity is based on the assumption that there are three reacting species which obey the ionic equation [1: Appendix 1]

$$\gamma C \underset{k_r}{\overset{k_d}{\rightleftharpoons}} A^{+z} + B^{-z} \tag{5.1}$$

where $C$ dissociates into a positive ion $A$ and a negative ion $B$, $k_d$ is the dissociation rate constant, $k_r$ is the recombination rate constant, and $z$ is the valence charge of the ions. The factor $\gamma$ represents the molecularity of the reaction [89]. For example, with $\gamma$=1, the reaction is unimolecular when molecule $C$ decomposes into the products $A$ and $B$, but bimolecular when $A$ and $B$ combine to form $C$. When $\gamma$=2, both the forward and reverse reactions are bimolecular and 2 molecules of $C$ are involved in the reaction. The molecularity is an empirical result that depends upon the species actually involved in the chemical reaction and can be determined from the conductivity variation with the

concentration of $C$ [90].[1]

As a result of the chemical reactions, the concentrations of the species will change with time. The equations that describe these chemical kinetics for uniform concentrations are

$$\frac{d[A]}{dt} = \frac{d[B]}{dt} = -\frac{1}{\gamma}\frac{d[C]}{dt} = k_d[C]^\gamma - k_r[A^{+z}][B^{-z}] \tag{5.2}$$

where the $[X]$ symbols denote the molar concentration or number density of the species $X$. The first term on the right side of Eq. 5.2 gives the rate of generation of ions ($A^{+z}$ and $B^{-z}$) from the dissociating neutral molecule $C$, while the second term gives the rate of recombination of the ions to form the neutral molecule.

While this description of the chemical kinetics is valid for a fully mixed system, most systems have spatial variations. A more general formulation for the kinetics can be derived by balancing the time rate of change of the concentration of each species in a differential volume to the flux through the surface enclosing the volume and any chemical reactions inside the volume. This conservation equation can be written as [91: Section 5.2]

$$\frac{\partial n_i}{\partial t} + \nabla \cdot \vec{\Gamma}_i = G_i - R_i \tag{5.3}$$

where the subscript $i$ denotes the $i$th species, $n_i$ is the density, $\vec{\Gamma}_i$ is the flux, and $G_i$ and $R_i$ represent the generation and recombination due to the chemical reactions.

The flux term gives the transport of each species through the fluid. It is generally stipulated by a constitutive law that accounts for diffusion, convection, and drift if the species is charged. For the $i$th species, the flux can be expressed as [92]

$$\vec{\Gamma}_i = -D_i \nabla n_i + n_i \vec{v} + \frac{z_i}{|z_i|} b_i n_i \vec{E} \tag{5.4}$$

where $D_i$ is the diffusivity, $\vec{v}$ is the fluid velocity, $z_i$ is the valence number, $b_i$ is the ion mobility if the species is charged ($z_i \neq 0$) and $\vec{E}$ is the electric field. Typically, the

---

[1] To determine the molecularity of the reaction, a relation between the conductivity and the concentration of the ions or the neutrals must be obtained. In general the bulk conductivity $\sigma_b$ can be expressed as

$$\sigma_b \equiv qz(b_{A^+}[A^{+z}] + b_{B^-}[B^{-z}])$$

where $q$ is the elementary electronic charge and $b_i$ is the mobility for the $A^{+z}$ or $B^{-z}$ ions. The ion concentrations can be related to the neutral concentration through the kinetics equation, Eq. 5.2. In this case consider steady state conditions, so that the time derivatives are zero, and assume there aren't any other sources for the ions, so that the ion concentrations are equal ($[A^{+z}] = [B^{-z}]$). This implies that the ion concentrations are proportional to $[C]^{\gamma/2}$ and the conductivity can be expressed as

$$\sigma_b = \sigma_o[C]^{\gamma/2}$$

where $\sigma_o$ is a proportionality constant. If measurements of the conductivity show a linear variation with $[C]$, then $\gamma = 2$, but if there is a square-root dependence, $\gamma = 1$.

diffusivity and mobility are related through the Einstein relation

$$\frac{D_i}{b_i} = \frac{kT}{|z_i|q} \tag{5.5}$$

where $k = 1.38 \times 10^{-23}$ J/K is Boltzmann's constant, $T$ is the absolute temperature and $q = 1.6 \times 10^{-19}$ C is the elementary electronic charge. The diffusion flux is based on Fick's law and the assumption that the species are present in trace quantities so that each species diffuses independently [93]. Note that in this formulation a neutral ion (with $|z_i| = 0$) can be treated as an ion having zero mobility.

The generation and recombination terms in Eq. 5.3 can be expressed in a more explicit form when the chemical reactions in the bulk of the liquid are specified. As an example, consider the three species reaction given by Eq. 5.1. When the fluid is fully mixed so that there are no spatial gradients, Eqs. 5.2 and 5.3 have the same form. If the species are identified by

$$n_{A^+} = \left[A^{+z}\right] \quad ; \quad n_{B^-} = \left[B^{-z}\right] \quad ; \quad n_C = [C] \tag{5.6}$$

the generation and recombination terms can be expressed as

$$G_{A^+} = G_{B^-} = \frac{1}{\gamma} R_C = k_d n_C^{\gamma} \tag{5.7}$$

$$R_{A^+} = R_{B^-} = \frac{1}{\gamma} G_C = k_r n_{A^+} n_{B^-} \tag{5.8}$$

The terms $R_C$ and $G_C$ are divided by the factor $\gamma$ because it takes $\gamma$ moles of the neutral molecule $C$ to produce one mole of the ions $A^{+z}$ and $B^{-z}$.

To complete the description of the flux of the individual species both the electric field and the fluid velocity must be determined. To determine the electric field, first note that the system can be considered to be electroquasistatic [83]. This allows Faraday's law to be approximated by

$$\nabla \times \vec{E} \approx 0 \tag{5.9}$$

so that the electric field is given by

$$\vec{E} = -\nabla \Phi \tag{5.10}$$

where $\Phi$ is the scalar electric potential. The electric field is related to the net free charge in any region of space through Gauss' law

$$\nabla \cdot \epsilon \vec{E} = q \sum_i z_i n_i = \rho \tag{5.11}$$

where $\epsilon$ is the dielectric permittivity and $\rho$ is the net free volume charge density.

Determining the fluid velocity is more complicated. In general the fluid velocity depends upon the electrical forces on the charged species, as in electrophoresis and electroosmosis, even when the charged species are present in trace amounts. For the purposes of this model, the fluid is assumed to be an incompressible liquid with the flow imposed

by an external mechanical system. The fluid flow is then governed by [91: Section 7.16]

$$\rho_m \frac{D\vec{v}}{Dt} = -\nabla p + \eta \nabla^2 \vec{v} + \vec{F}_{ex} \tag{5.12}$$

where $\vec{v}$ is the fluid velocity, $\rho_m$ is the mass density, $D/Dt \equiv \partial/\partial t + \vec{v} \cdot \nabla$ denotes the convective derivative, $p$ is the pressure, $\eta$ is the dynamic viscosity, and $\vec{F}_{ex}$ denotes any external forces applied to the system. With the flow imposed mechanically, the electrical effects on the flow profile can be neglected so that the fluid mechanical laws are decoupled from the electrical laws and only the flow profile for the solvent needs to be determined. Once the geometry and the external source have been specified, the fluid velocity can be determined from Eq. 5.12 and used in Eq. 5.4 for the flux of each species.

In addition to the equations describing the dynamics of the charged species in the bulk of the fluid, the boundary conditions imposed by the interface between the solid and liquid phases must also be considered. Just as chemical reactions can be used to describe the generation and recombination of ionic species in the fluid bulk, a net current can pass between the fluid phase and the solid phase if a chemical (redox) reaction is occurring at the interface or if charge is accumulating at the interface. But chemical reactions for the adsorption, charge transfer, and desorption at the interface can only be specified if the identity of the constituents are known. Since the constituents are typically unidentified trace impurities, a generic, composite reaction is typically postulated. One example is to have the interfacial flux of each individual species linearly related to the difference between the volume density of the species near the interface and the equilibrium density. Considering again the chemical constituents of the case given by Eq. 5.1, general postulated conditions for two charged species can be written as

$$\hat{n}_s \cdot \vec{\Gamma}_{A^+} = k_+(n_{A^+} - n^w_{A^+}) \tag{5.13}$$

$$\hat{n}_s \cdot \vec{\Gamma}_{B^-} = k_-(n_{B^-} - n^w_{B^-}) \tag{5.14}$$

where $\hat{n}_s$ is a unit vector normal to the interface and pointing into the solid and the parameters $k_\pm$ and $n^w_{A^+,B^-}$ are constants for the interface at a given temperature [94-96]. With the charge transfer attributed to an oxidation-reduction process occurring at the interface, the $k$'s can be considered reaction velocities and the $n^w$'s can be considered the equilibrium carrier densities in the absence of any flow of current. These boundary conditions will be discussed in more detail in later sections.

Electrically, with the interface able to support a net surface charge, the normal component of the electric field can be discontinuous across the interface. Applying Gauss' law to the interface

$$\hat{n} \cdot [\![\vec{D}]\!] = q \sum_i z_i \sigma_i = \sigma_{su} \tag{5.15}$$

where $\hat{n}$ is a unit vector normal to the interface, $\vec{D}$ is the displacement field, $\sigma_i$ is the surface number density of the $i$th species, $\sigma_{su}$ is the free surface charge density and $[\![X]\!]$ denotes the jump discontinuity in $X$. When the surface charge is time varying, charge

conservation requires

$$\hat{n} \cdot [\![\vec{J}]\!] = \hat{n} \cdot q \sum_i z_i \vec{\Gamma}_i = -\frac{d\sigma_{su}}{dt} \tag{5.16}$$

where $\vec{J}$ is the net current density. This condition is redundant when all of the conservation equations for all of the species have been specified. For example, this condition is necessary if the solid is represented by a single conductivity $\sigma_1$ so that charge conservation at the interface can be expressed as

$$\hat{n}_s \cdot \left[\sigma_1 \vec{E}_1^b - qz\left(\vec{\Gamma}_{A+}^b - \vec{\Gamma}_{B-}^b\right)\right] = -\frac{d\sigma_{su}}{dt} \tag{5.17}$$

where $\hat{n}_s$ is again assumed to point into the solid and $\vec{E}_1^b$ denotes the electric field on the solid side of the interface. But this charge conservation condition is redundant if the holes and electrons responsible for the conduction through a semiconducting solid are modeled because the conservation of each individual species has already been expressed. The final condition is that the electric potential is continuous across the interfaces.

Fluid mechanically, for the viscous fluids assumed here, the fluid is not allowed to slip at the interface. This indicates that the interfacial tangential fluid velocity is zero. In addition, if the solid phase is non-porous or if a porous solid is backed by a non-porous structure, the flow of fluid through the solid must also be zero. This indicates that the normal component of the fluid velocity is also zero. Thus, the boundary condition for the fluid flow is that

$$\vec{v} = 0 \tag{5.18}$$

at the interface. Even though the velocity can be taken as zero at the interface, the roughness of the interface will also affect the fluid flow. Irregularly shaped interfaces can cause the flow to be unsteady and leads to turbulent flow at Reynold's number lower than when the surface is smooth [97].

## 5.3 Isolated Interface

Consider first the equilibrium case of a single liquid/solid interface that is far from all electrodes, as shown in Fig. 5.1. With the electrodes far from the interface, any preferential adsorption of one polarity of charge species onto the interface will be imaged by the mobile charge on the liquid side of the interface, assuming that the solid is an ohmic conductor represented by a single conductivity and permittivity. If there is a preferential adsorption, a potential difference will develop between the interface and the bulk region of the liquid. This interfacial potential is the zeta potential $\zeta$ if the liquid bulk is grounded. The corresponding distribution in mobile charge carriers is the electrical double layer. The objectives of this special case are to introduce the Debye length as the characteristic length scale over which a net space charge extends away from the interface and to relate the zeta potential to the parameters that have been postulated to describe the state of the interface.

In equilibrium, the flux of each individual species is zero everywhere. This specification has the effect of decoupling the distributions of the charged species from the

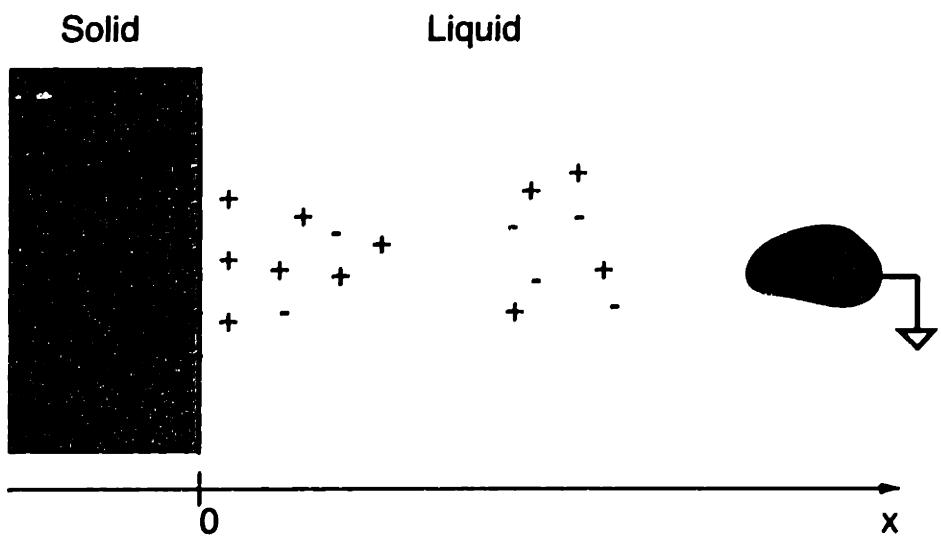


Figure 5.1: An isolated interface between solid and liquid dielectrics. The solid is assumed to be a homogeneous, ohmic conductor described by a single permittivity and conductivity. The liquid is assumed to have both positive and negative charges that have been created by the dissociation of a single ionizable constituent. The bulk of the liquid is grounded by a perfectly conducting electrode at $x = \infty$.

neutrals. In fact, Eq. 5.4 indicates that the neutral species have a uniform distribution. The steady state form of Eq. 5.3 then shows that generation balances recombination. Using Eqs. 5.7 and 5.8, the neutral concentration $n_C$ is given by

$$n_C = \left(\frac{k_r}{k_d}\right)^{1/\gamma} n_o^{2/\gamma} \tag{5.19}$$

where charge neutrality in the bulk region of the liquid ($n_{A^+} = n_{B^-} = n_o$), far from the electrodes, has been assumed. The distributions of the charged species can be obtained by setting the fluxes to zero in Eq. 5.4 to give

$$D_{A^+,B^-}\frac{dn_{A^+,B^-}}{dx} = \pm b_{A^+,B^-} n_{A^+,B^-} E_x \tag{5.20}$$

where, on the right side, the positive sign goes with $A^+$ and the negative sign goes with $B^-$. This can be rewritten by identifying

$$\frac{1}{n}\frac{dn}{dx} = \frac{d}{dx}(\ln n) \tag{5.21}$$

and using Einstein's relation (Eq. 5.5 with $z_{A^+} = -z_{B^-} \equiv z$) to give

$$\frac{d}{dx}(\ln n_{A^+,B^-}) = \pm\frac{qz}{kT}E_x \tag{5.22}$$

Replacing the electric field by $E_x = -d\Phi/dx$, where $\Phi$ is the electrical potential, and integrating from $x$ to $\infty$, the carrier densities can be expressed as

$$\ln\left[\frac{n_o}{n_{A^+,B^-}(x)}\right] = \pm\frac{qz}{kT}\Phi(x) \tag{5.23}$$

where boundary conditions at $x = \infty$ of charge neutrality ($n_{A^+} = n_{B^-} = n_o$) and zero potential have been imposed. Rearranging Eq. 5.23 gives

$$n_{A^+,B^-}(x) = n_o e^{\mp qz\Phi(x)/kT} \tag{5.24}$$

Note that the bulk charge carrier density $n_o$ can be determined from measurements of the bulk conductivity $\sigma_b$ defined as

$$\sigma_b \equiv qz(b_{A^+}n_o + b_{B^-}n_o) = qzn_o(b_{A^+} + b_{B^-}) \tag{5.25}$$

or

$$n_o = \frac{\sigma_b}{qz(b_{A^+} + b_{B^-})} \tag{5.26}$$

Thus, if the ion mobilities ($b_{A^+}$ and $b_{B^-}$) and the conductivity can be determined, the carrier density $n_o$ can be found.

To determine the potential, Gauss' law can be used. In this case, Eq. 5.11 becomes

$$-\epsilon\frac{d^2\Phi}{dx^2} = qz(n_{A^+} - n_{B^-}) = -2qzn_o\sinh\left(\frac{qz\Phi}{kT}\right) \tag{5.27}$$

or

$$\frac{d^2\Phi}{dx^2} = \frac{2qzn_o}{\epsilon}\sinh\left(\frac{qz\Phi}{kT}\right) \tag{5.28}$$

which is the Poisson-Boltzmann Equation. For convenience, normalize the parameters $\Phi$ and $x$ according to

$$\underline{\Phi} = \frac{qz\Phi}{kT} \quad ; \quad \underline{x} = \frac{x}{\lambda_D} \tag{5.29}$$

with the Debye length $\lambda_D$ defined by

$$\lambda_D = \sqrt{\frac{\epsilon kT}{2q^2z^2n_o}} \tag{5.30}$$

This gives Eq. 5.28 in normalized form as

$$\frac{d^2\underline{\Phi}}{d\underline{x}^2} = \sinh(\underline{\Phi}) \tag{5.31}$$

Multiplying both sides by $d\underline{\Phi}/d\underline{x}$, integrating from $\underline{x}$ to $\infty$, and assuming that $\underline{E}_x \to 0$ at $\infty$ gives

$$\left(\frac{d\underline{\Phi}}{d\underline{x}}\right)^2 = 4\sinh^2\left(\frac{\underline{\Phi}}{2}\right) \tag{5.32}$$

The normalized electric field is then given by

$$\underline{E}_x = -\frac{d\underline{\Phi}}{d\underline{x}} = 2\sinh\left(\frac{\underline{\Phi}}{2}\right) \tag{5.33}$$

where the negative root of Eq. 5.32 was chosen so that the electric field is positive for positive potentials. By integrating Eq. 5.33 from 0 to $\underline{x}$, the potential can be written as

$$\tanh\left(\frac{\underline{\Phi}}{4}\right) = \tanh\left(\frac{\underline{\zeta}}{4}\right)e^{-\underline{x}} \tag{5.34}$$

where $\underline{\zeta}$ is the normalized potential at $\underline{x} = 0$. Using the relation that

$$\tanh^{-1}(y) = \frac{1}{2}\ln\left(\frac{1+y}{1-y}\right) \qquad \text{for } y^2 < 1 \tag{5.35}$$

and noting that $\left[\tanh\left(\underline{\zeta}/4\right)e^{-\underline{x}}\right]^2 < 1$ because $\left|\tanh\left(\underline{\zeta}/4\right)\right| < 1$ and $|e^{-\underline{x}}| \leq 1$, then the potential can be solved explicitly as

$$\underline{\Phi} = 2\ln\left[\frac{1+\tanh(\underline{\zeta}/4)e^{-\underline{x}}}{1-\tanh(\underline{\zeta}/4)e^{-\underline{x}}}\right] \tag{5.36}$$

Note that for a weak double layer, $\underline{\zeta} \ll 1$ and the potential is given by

$$\underline{\Phi} \approx \underline{\zeta}e^{-\underline{x}} \tag{5.37}$$

This shows that the potential decays exponentially with distance away from the interface when the zeta potential is small.

Now that the potential and charge distributions have been determined everywhere in terms of the zeta potential, the interfacial parameters can be related to the zeta potential. With the interface assumed to be in an equilibrium state, there is no net flux of ionic species to the interface and Eqs. 5.13 and 5.14 indicate that the carrier densities have their equilibrium value of $n^w_{A^+,B^-}$. Using Eq. 5.24, these carrier densities are related to the zeta potential by

$$n^w_{A^+} = n_o e^{-qz\zeta/kT} \tag{5.38}$$

$$n^w_{B^-} = n_o e^{qz\zeta/kT} \tag{5.39}$$

Thus, $n^w_{A^+}$ and $n^w_{B^-}$ are not independent and the zeta potential will yield both quantities if the conductivity and temperature are known. One of the limitations of this representation is that the zeta potential is taken as a fundamental parameter of the interface, independent of the reaction velocities ($k_\pm$). While this is consistent with the hypothesis

that the reaction velocities are only involved in nonequilibrium conditions in which current flows across the interface, the zeta potential physically represents an imbalance in the interfacial reaction rates so that one charged species is preferentially adsorbed. In Chapter 6 this will be discussed in more detail.

## 5.4 Couette Geometry

For comparison to the experiments performed with a rotating cylindrical electrode experiment, consider the cylindrical geometry shown in Fig. 5.2. The gap between the cylinders is filled with a dielectric fluid having a permittivity $\epsilon_2$ and an ohmic conductivity $\sigma_2$. The cylinders themselves are considered to be perfectly conducting, but may be covered with solid dielectrics. For the case to be considered here, only the inner cylinder is covered and the solid dielectric has a permittivity of $\epsilon_1$ and a conductivity of $\sigma_1$. The radius of the inner cylinder is $R_1$, but the solid dielectric causes the effective radius of the inner cylinder in contact with the fluid to increase to $a$. The outer cylinder has an inside radius of $R_2$. The inner cylinder is electrically connected to the grounded outer cylinder through a load impedance $R_L$ and a voltage source $V_o$. In this analysis, the cylinders are assumed to have a height $H$, but no variations in the azimuthal or axial directions are considered.

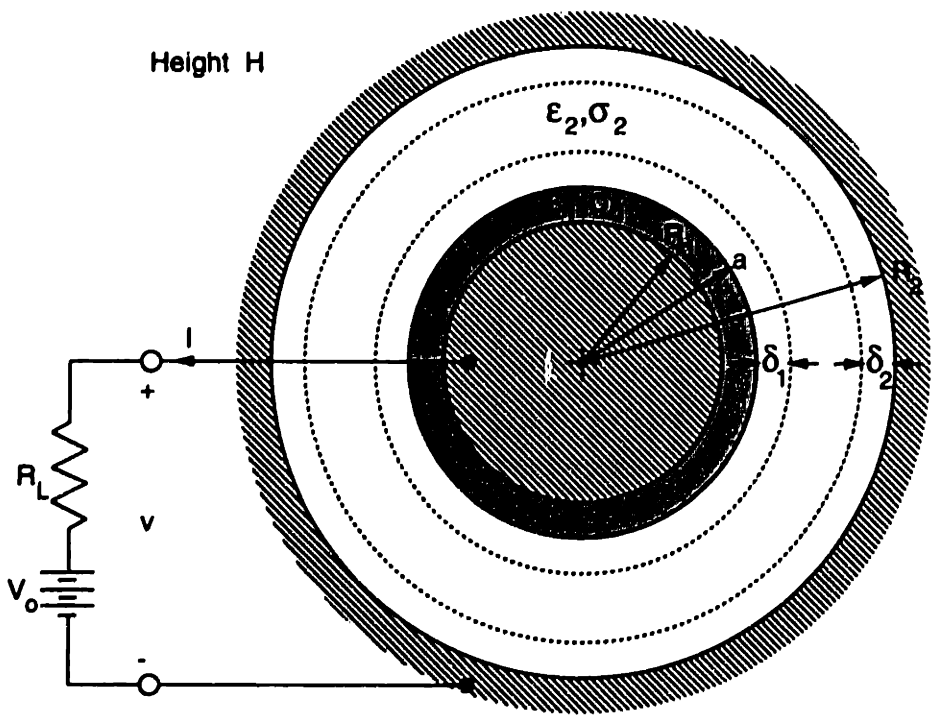


Figure 5.2: A model for the Couette charger experiment. The inner cylindrical electrode is assumed to be covered by a solid dielectric, the outer cylinder is a bare metal (perfectly conducting) electrode, and the remaining space is filled by a dielectric liquid.

## 5.5 Stationary Case

Consider first the case where both cylinders are stationary so that there isn't any imposed fluid motion. In this situation, the system will reach an equilibrium state depending upon the chemical kinetics of the ionizable impurities and the electrical forces acting upon these species.

In general, the potential distribution across the oil filled gap will be governed by the Poisson-Boltzmann equation (Eq. 5.28) in cylindrical coordinates. Since a simple analytic solution is currently not know to this equation, it is convenient to develop expressions in terms of measurable quantities, such as the net current density $\vec{J}$ and volume charge density $\rho$ associated with the chemical species given in Eq. 5.1. Assuming the valencies of the ions are given by $z_{A^+} = -z_{B^-} = z$ and defining $\vec{J} \equiv qz\left(\vec{\Gamma}_{A^+} - \vec{\Gamma}_{B^-}\right)$ and $\rho \equiv qz(n_{A^+} - n_{B^-})$, the conservation equation given by Eq. 5.3 can be summed for the positive and negative charge carriers to give

$$\frac{\partial \rho}{\partial t} + \nabla \cdot \vec{J} = 0 \tag{5.40}$$

This is the charge conservation equation written in terms of the net charge density and current density. Using Eq. 5.4, the net current density is

$$\vec{J} = -qz\left(D_{A^+}\nabla n_{A^+} - D_{B^-}\nabla n_{B^-}\right) + qz\left(n_{A^+} - n_{B^-}\right)\vec{v} + qz\left(b_{A^+}n_{A^+} + b_{B^-}n_{B^-}\right)\vec{E} \tag{5.41}$$

or

$$\begin{aligned} \vec{J} \;=\; & -qz\frac{(D_{A^+} + D_{B^-})}{2}\nabla\left(n_{A^+} - n_{B^-}\right) + qz\left(n_{A^+} - n_{B^-}\right)\vec{v} \\ & -qz\frac{(D_{A^+} - D_{B^-})}{2}\nabla\left(n_{A^+} + n_{B^-}\right) + qz\left(b_{A^+}n_{A^+} + b_{B^-}n_{B^-}\right)\vec{E} \end{aligned} \tag{5.42}$$

For simplicity, assume that the species satisfy

$$\left|\frac{(D_{A^+} + D_{B^-})}{(D_{A^+} - D_{B^-})}\frac{\nabla\left(n_{A^+} - n_{B^-}\right)}{\nabla\left(n_{A^+} + n_{B^-}\right)}\right| \gg 1 \tag{5.43}$$

This is the same as assuming that the diffusivities are essentially the same or, using Eq. 5.24 to approximate the carrier densities when a net current is flowing, the zeta potential is small and the carrier densities are only perturbed from the background concentrations. Then, defining a composite molecular diffusivity by $D_m \equiv (D_{A^+} + D_{B^-})/2$ and the fluid conductivity by $\sigma_2 \equiv qz(b_{A^+}n_{A^+} + b_{B^-}n_{B^-})$, Eq. 5.42 can be written as

$$\vec{J} = -D_m\nabla\rho + \rho\vec{v} + \sigma_2\vec{E} \tag{5.44}$$

As long as the contribution to the conductivity caused by the imbalance of charge carrier densities, as manifested by the net charge density, is small compared to the background conductivity, the use of a constant $\sigma_2$ is justified.

The limitation of the model created by the use of a uniform and constant conductivity

for the liquid can be explored by assuming that the bulk region of the stationary fluid contains an equal number of positive and negative charge carriers given by $n_o$. Due to interfacial effects, an applied voltage or fluid motion, the carrier densities $n_\pm$ are assumed to be perturbed from the equilibrium values such that

$$n_+ \equiv n_{A^+} = n_o + n'_+ \tag{5.45}$$

$$n_- \equiv n_{B^-} = n_o + n'_- \tag{5.46}$$

where the perturbation densities $n'_+$ and $n'_-$ are small compared to $n_o$. This is tantamount to assuming a zeta potential that is small compared to the thermal voltage ($kT/q$) so that the carrier densities are not too far from their equilibrium level, even in the double layer. The electric field can be written as the superposition of two fields

$$\vec{E} = \vec{E}_o + \vec{E}_s \tag{5.47}$$

where the terminal field $\vec{E}_o$ comes from the external terminal constraints, such as the applied voltage source, and the self-field $\vec{E}_s$ comes from the imbalance of charge carriers (the perturbation carrier densities) giving rise to a net charge density. The conduction term in Eq. 5.42 can then be expressed as

$$qzb(n_+ + n_-)\vec{E} = qzb\left(2n_o + n'_+ + n'_-\right)\left(\vec{E}_o + \vec{E}_s\right) \tag{5.48}$$

The uniform conductivity can be identified as $\sigma_2 = 2qzbn_o$. In order to neglect the perturbations in the carrier densities but include the effect these perturbations have on the charge density and the electric field $\vec{E}_s$ requires

$$\left|qzb(n'_+ + n'_-)\vec{E}_o\right| \ll \left|\sigma_2\vec{E}_s\right| \tag{5.49}$$

Approximating the applied (terminal) field as $|\vec{E}_o| = O(V_o/(R_2 - a))$[2], the product of the ionic charge and the carrier densities to be of the same order as the volume charge density $qz(n'_+ + n'_-) = O(\rho)$, and the self-field from Gauss' law $|\vec{E}_s| = O(\lambda_D\rho/\epsilon_2)$, with $\lambda_D$ the Debye length characterizing interfacial charge separation (Eq. 5.54), the applied potential must obey

$$V_o \ll \frac{(R_2 - a)}{\lambda_D}\frac{kT}{qz} \tag{5.50}$$

Taking $\lambda_D \approx 10\mu$m, $kT/qz \approx 0.025$ V, and $R_2 - a \approx 2.5$ cm as representative values gives $V_o \ll 62.5$ V. Thus, for applied potentials that are much smaller than about 100 V, the assumption of a uniform and constant conductivity can be considered reasonable. This constraint also satisfies the requirement that the applied field is small compared to the equilibrium field in the double layer. Indeed, with the terminal field given by $|\vec{E}_o| = O(V_o/(R_2 - a))$ and the double layer field of order $|\vec{E}_s| = O(\zeta/\lambda_D)$, then the

[2]This uses the notation where $f = O(x)$ means that $f$ is of the same order of magnitude as $x$ [98: p. 56].

applied potential must obey

$$V_o \ll \frac{(R_2 - a)}{\lambda_D}\zeta \tag{5.51}$$

Using the constraint $\zeta \ll kT/qz$ then gives the relation of Eq. 5.50.

To determine the steady state charge density without any fluid motion, substitute Eq. 5.44 into Eq. 5.40 with $\vec{v}$ set to zero to get

$$\nabla^2\rho - \frac{\sigma_2}{D_m}\nabla\cdot\vec{E} = 0 \tag{5.52}$$

(Note that this equation also applies when the charge density only varies in the radial direction and the velocity is only in the $\theta$ direction, as in laminar flow caused by a rotating inner cylinder.) The electric field can be replaced using Gauss' law (Eq. 5.11 with $\epsilon = \epsilon_2$) so that

$$\nabla^2\rho - \frac{\sigma_2}{D_m\epsilon_2}\rho = 0 \tag{5.53}$$

Neglecting any axial or azimuthal variations and defining the Debye length as

$$\lambda_D = \sqrt{\frac{D_m\epsilon_2}{\sigma_2}} \tag{5.54}$$

Eq. 5.53 can be written as

$$\frac{1}{r}\frac{\partial}{\partial r}\left(r\frac{\partial\rho}{\partial r}\right) - \frac{\rho}{\lambda_D^2} = 0 \tag{5.55}$$

This is a form of Bessel's equation having modified Bessel functions of order zero, $I_0(r/\lambda_D)$ and $K_0(r/\lambda_D)$, as solutions. With the volume charge density on the liquid side of the interfaces given by $\rho_1^b$ at the inner cylinder and $\rho_2^b$ at the outer cylinder, the charge density can be written as

$$\rho(r) = \rho_1^b\frac{f(R_2,r)}{f(R_2,a)} + \rho_2^b\frac{f(r,a)}{f(R_2,a)} \tag{5.56}$$

where

$$f(\alpha,\beta) \equiv I_0\left(\frac{\alpha}{\lambda_D}\right)K_0\left(\frac{\beta}{\lambda_D}\right) - K_0\left(\frac{\alpha}{\lambda_D}\right)I_0\left(\frac{\beta}{\lambda_D}\right) \tag{5.57}$$

The function $f(\alpha,\beta)$ is plotted in Fig. 5.3. In the limit when the Debye length is small compared to the radii of the cylinders ($\lambda_D \ll R_1, a, R_2$), the modified $m$th order Bessel functions can be approximated by [91: Section 2.16]

$$\lim_{u\to\infty} I_m(u) = \frac{1}{\sqrt{2\pi u}}e^u \tag{5.58}$$

$$\lim_{u\to\infty} K_m(u) = \sqrt{\frac{\pi}{2u}}e^{-u} \tag{5.59}$$

so that

$$f(\alpha,\beta) \approx \frac{\lambda_D}{\sqrt{\alpha\beta}}\sinh\left[\frac{(\alpha-\beta)}{\lambda_D}\right] \tag{5.60}$$

This gives the charge distribution in the fluid as

$$\rho(r) = \rho_1^b \sqrt{\frac{a}{r}} \frac{\sinh\left[\frac{(R_2-r)}{\lambda_D}\right]}{\sinh\left[\frac{(R_2-a)}{\lambda_D}\right]} + \rho_2^b \sqrt{\frac{R_2}{r}} \frac{\sinh\left[\frac{(r-a)}{\lambda_D}\right]}{\sinh\left[\frac{(R_2-a)}{\lambda_D}\right]} \tag{5.61}$$

The first term on the right side is non-negligible only when $r \approx a$ and the second term is non-negligible only when $r \approx R_2$. Away from the interfaces, the charge density decreases exponentially to zero so that the net charge density in the bulk region of the fluid is zero for a stationary fluid.

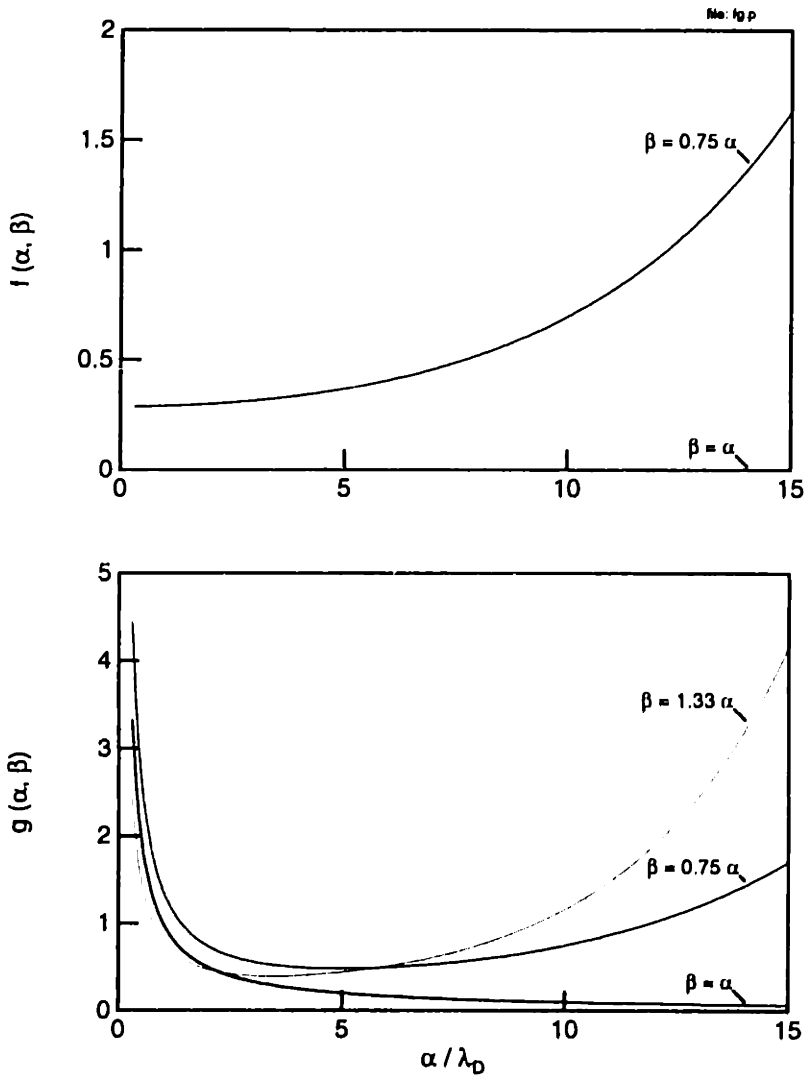


Figure 5.3: Plots of the functions $f(\alpha,\beta)$ (defined by Eq. 5.57) and $g(\alpha,\beta)$ (defined by Eq. 5.68). Note that $f(\alpha,\alpha)$ is zero while $g(\alpha,\alpha)$ can be appreciable when $\alpha/\lambda_D$ is small.

To determine the interfacial charge densities $\rho_1^b$ and $\rho_2^b$ the boundary condition im-

posed by the interface between the solid and liquid phases is used. Since the model being discussed here is concerned with the net charge density and current density, the simplified approach of Abedian and Sonin will be used in which the charge transfer from the liquid to the solid is taken as

$$\hat{n}_s \cdot \vec{J}^b_{1,2} = k_{1,2}(\rho^b_{1,2} - \rho^w_{1,2}) \tag{5.62}$$

where $\hat{n}_s$ is a unit vector normal to the interface and pointing into the solid, the subscript 1 denotes the inner cylinder interface, the subscript 2 denotes the outer cylinder interface, and the parameters $k_{1,2}$ (representing surface reaction velocities) and $\rho^w_{1,2}$ (representing the equilibrium wall charge densities in the absence of a current) are constants for the interface at a given temperature [99]. This condition can be obtained from Eqs. 5.13 and 5.14 by setting $k_+ = k_-$ and using the definition of the current density for the difference in the fluxes between the positive and negative charge carriers.

The current densities given by Eq. 5.62 *at* the interfaces must be balanced by the transport of charged species to the interface. With Eq. 5.44 for the current density on the liquid side of the interface, Eq. 5.62 implies that

$$k_1(\rho^b_1 - \rho^w_1) = -\left[-D_m \frac{\partial \rho}{\partial r} + \sigma_2 E_r\right]_{r=a^+} \tag{5.63}$$

$$k_2(\rho^b_2 - \rho^w_2) = \left[-D_m \frac{\partial \rho}{\partial r} + \sigma_2 E_r\right]_{r=R_2^-} \tag{5.64}$$

where the superscripts $\pm$ indicate the limit

$$X^{\pm} = \lim_{\delta \to 0}(1 \pm \delta)X \tag{5.65}$$

with $X$ taken as either $a$ or $R_2$, in this case, so that the limit is evaluated on the liquid side of the interfaces.

Equations 5.63 and 5.64 require a knowledge of the electric field distribution before $\rho^b_1$ and $\rho^b_2$ can be determined. With variations only in the radial direction, the electric field can be obtained from Eq. 5.11 by integrating

$$\frac{1}{r}\frac{\partial}{\partial r}(rE_r) = \frac{\rho}{\epsilon_2} \tag{5.66}$$

over the radial coordinate. Using the charge distribution from Eq. 5.56, the electric field can be written as

$$E_r = \frac{\lambda_D}{\epsilon_2 f(R_2, a)}\left[\rho^b_2 g(a, r) - \rho^b_1 g(R_2, r)\right] + \frac{A_3}{r} \qquad a < r < R_2 \tag{5.67}$$

where

$$g(\alpha, \beta) \equiv I_0\left(\frac{\alpha}{\lambda_D}\right) K_1\left(\frac{\beta}{\lambda_D}\right) + K_0\left(\frac{\alpha}{\lambda_D}\right) I_1\left(\frac{\beta}{\lambda_D}\right) \tag{5.68}$$

To obtain this result, the relations

$$\int r I_0\left(\frac{r}{\lambda_D}\right) dr = \lambda_D r I_1\left(\frac{r}{\lambda_D}\right) + \text{constant} \tag{5.69}$$

$$\int r K_0\left(\frac{r}{\lambda_D}\right) dr = -\lambda_D r K_1\left(\frac{r}{\lambda_D}\right) + \text{constant} \tag{5.70}$$

$$I_1\left(\frac{r}{\lambda_D}\right) = \lambda_D \frac{dI_0\left(\frac{r}{\lambda_D}\right)}{dr} \tag{5.71}$$

$$K_1\left(\frac{r}{\lambda_D}\right) = -\lambda_D \frac{dK_0\left(\frac{r}{\lambda_D}\right)}{dr} \tag{5.72}$$

were used [98]. A plot of $g(\alpha,\beta)$ is given in Fig. 5.3. In the limit when the Debye length is small compared to the radii of the cylinders ($\lambda_D \ll R_1, a, R_2$), the modified Bessel functions can be approximated using Eqs. 5.58 and 5.59 to give

$$g(\alpha,\beta) \approx \frac{\lambda_D}{\sqrt{\alpha\beta}} \cosh\left[\frac{(\alpha-\beta)}{\lambda_D}\right] \tag{5.73}$$

From Eqs. 5.56 and 5.67 it can be shown that

$$-D_m \frac{\partial \rho}{\partial r} + \sigma_2 E_r = \frac{\sigma_2 A_3}{r} \tag{5.74}$$

Substitution of Eq. 5.74 into Eqs. 5.63 and 5.64 yields

$$\rho_1^b = \rho_1^w - \frac{\sigma_2 A_3}{a k_1} \tag{5.75}$$

$$\rho_2^b = \rho_2^w + \frac{\sigma_2 A_3}{R_2 k_2} \tag{5.76}$$

The first term on the right hand side gives the equilibrium value for the charge density while the second term indicates the effect that the electric field in the fluid has on the charge density, assuming that the equilibrium values themselves are independent of the electric field.

Now, the remaining unknown is the field component $A_3$. This can be determined from the conservation of charge constraint at the $r = a$ interface and the terminal current and voltage. With the solid dielectric assumed to have an ohmic conductivity, the current density is given by

$$\vec{J} = \sigma_1 \vec{E} \tag{5.77}$$

Furthermore, assuming that the bulk of the solid is free of a net charge, the electric field in the solid is given by

$$E_r = \frac{A_1}{r} \qquad R_1 < r < a \tag{5.78}$$

Thus, steady state charge conservation at $r = a$ relates the chemical reaction current

density to the electric field in the solid dielectric and the fluid according to

$$-ak_1(\rho_1^b - \rho_1^w) = \sigma_1 A_1 = \sigma_2 A_3 \tag{5.79}$$

In addition, the terminal voltage is equal to the line integral of the radial component of the electric field between the cylinders

$$v = \int_{R_1}^{R_2} E_r \cdot dr \tag{5.80}$$

Carrying out the line integral yields

$$v = A_1 \ln\left(\frac{a}{R_1}\right) + A_3 \ln\left(\frac{R_2}{a}\right) + \frac{\lambda_D^2}{\epsilon_2}\left(\rho_2^b - \rho_1^b\right) \tag{5.81}$$

The terminal voltage can also be expressed as

$$v = V_o + R_L I \tag{5.82}$$

where the first term, $V_o$, is the voltage of the power supply and the second term gives the potential across the series resistance $R_L$ caused by the current $I$ flowing into the cylindrical electrodes. By applying charge conservation around the inner cylinder or the outer cylinder, the terminal current can be expressed as

$$I = -2\pi H\left(\sigma_1 A_1\right) = -2\pi H R_2 k_2\left(\rho_2^b - \rho_2^w\right) \tag{5.83}$$

with the first equality relating the current to the field passing through the solid dielectric on the inner cylinder and the second equality relating the current to the chemical reaction at the outer cylinder electrode. Because steady state conditions have been assumed, this current is also equal to that through the interface between the dielectric and the liquid, given by Eq. 5.79.

By combining Eqs. 5.75, 5.76, and 5.79 to 5.83, $A_3$ is found to be given by

$$A_3 = \frac{1}{B_0}\left[V_o + \frac{\lambda_D^2}{\epsilon_2}\left(\rho_1^w - \rho_2^w\right)\right] \tag{5.84}$$

where

$$B_0 = \frac{\sigma_2}{\sigma_1}\ln\left(\frac{a}{R_1}\right) + \ln\left(\frac{R_2}{a}\right) + D_m\left(\frac{1}{R_2 k_2} + \frac{1}{ak_1}\right) + 2\pi H R_L \sigma_2 \tag{5.85}$$

Substitution back into Eqs. 5.75 and 5.76 then gives

$$\rho_1^b = \frac{1}{B_0}\left[\left(B_0 - \frac{D_m}{ak_1}\right)\rho_1^w + \frac{D_m}{ak_1}\rho_2^w - \frac{\sigma_2}{ak_1}V_o\right] \tag{5.86}$$

$$\rho_2^b = \frac{1}{B_0}\left[\frac{D_m}{R_2 k_2}\rho_1^w + \left(B_0 - \frac{D_m}{R_2 k_2}\right)\rho_2^w + \frac{\sigma_2}{R_2 k_2}V_o\right] \tag{5.87}$$

for the charge densities on the liquid side of the interface at the inner and outer cylinders. Using these interfacial charge densities, the charge distribution throughout the fluid is

given by Eq. 5.56.

Several important conclusions can be reached from the charge density distribution results for the stationary case (Eqs. 5.56, 5.85, 5.86, and 5.87). First note that the application of an applied field doesn't affect the length scale over which the charge is distributed (the Debye length), but it does affect the magnitude of the charge density in the regions near the interfaces. Indeed, with positive applied voltages, the charge density on the liquid side of the inner cylinder interface ($\rho_1^b$) is decreased as negative charge accumulates to shield the applied field from the bulk of the fluid. At the same time, the charge density on the liquid side of the outer cylinder interface ($\rho_2^b$) is increased as positive charge accumulates to shield the applied field from the bulk of the fluid. Second, note that in the limit as the terminal resistance becomes infinite, the current flowing through the electrodes must go to zero. This implies that the current due to the chemical reactions at the interface must also go to zero and the charge densities on the liquid side of the interfaces go to their equilibrium values. Third, if the reaction velocities $k_{1,2}$ can be considered "infinite," the interfacial charge densities go to their equilibrium values and are independent of the applied voltage.

In addition, the terminal current can be written as

$$I = -\frac{2\pi H \sigma_2}{B_0}\left[V_o + \frac{\lambda_D^2}{\epsilon_2}(\rho_1^w - \rho_2^w)\right] \tag{5.88}$$

This expression suggests that the short-circuit current (or open-circuit voltage) can be used to obtain information about the interfacial parameters. When the voltage source is short-circuited ($V_o = 0$), the current is caused by the difference in equilibrium charge densities on the liquid side of the interface resulting from dissimilar materials bordering the fluid. The current is also shown to vary linearly with the applied potential, consistent with modeling both the liquid and the solid as ohmic conductors. As long as the self-induced electrohydrodynamic mixing of the fluid by the motion of the charged species is negligible, the slope of this linear variation can be related to the reaction velocities at the interface. Note also that as the terminal resistance $R_L$ becomes infinite (open-circuit), the current and the field terms $A_1$ and $A_3$ go to zero. In this case, the charge densities on the liquid side of the interface go to their equilibrium values.

A number of criteria can be used to determine the conditions under which the reaction velocities can be considered "infinite." One criterion can be obtained from Eq. 5.85. By assuming that $B_0 \sim O(\ln(R_2/a))$, the reaction velocity terms will have a negligible contribution to $B_0$ if

$$k_1 \gg \frac{D_m}{a \ln\left(\frac{R_2}{a}\right)} \quad , \quad k_2 \gg \frac{D_m}{R_2 \ln\left(\frac{R_2}{a}\right)} \tag{5.89}$$

Under this condition, the interfacial charge densities are given by their equilibrium values. Using representative values of $D_m \approx 2.5 \times 10^{-11}$ m$^2$/s, $a \approx 7.6$ cm, and $R_2 \approx 10.2$ cm, then $k_1 \gg 1.1 \times 10^{-9}$ m/s and $k_2 \gg 8.2 \times 10^{-10}$ m/s. In this limit, the reaction velocities are fast enough that the charge transfer processes are diffusion limited.

Another criterion can be obtained from Eqs. 5.86 and 5.87 by determining the conditions for neglecting the applied potential. Assuming again that $B_0 \sim O(\ln(R_2/a))$, then

the applied potential can be neglected with respect to the equilibrium charge densities when

$$k_1 \gg \frac{\sigma_2 V_o}{a\rho_1^w \ln\left(\frac{R_2}{a}\right)} \quad , \quad k_2 \gg \frac{\sigma_2 V_o}{R_2 \rho_2^w \ln\left(\frac{R_2}{a}\right)} \tag{5.90}$$

Using representative values of $\sigma_2 \approx 10^{-12}$ S/m, $\rho_{1,2}^w \approx 10^{-3}$ C/m$^3$, $V_o \approx 50$ V, and taking again $a \approx 7.6$ cm and $R_2 \approx 10.2$ cm, then $k_1 \gg 2.3 \times 10^{-6}$ m/s and $k_2 \gg 1.7 \times 10^{-6}$ m/s. Thus, being able to neglect the effects of the applied potential imposes a harsher criterion on the reaction velocities than if the reaction velocities are simply considered to happen quickly compared to the effective diffusion rates. This also indicates that experiments using modest applied voltages may be used to obtain information about the reaction velocities.

With the stationary case reasonably well understood, the redistribution of the charge due to the fluid flow can be considered.

## 5.6 Hydrodynamics

The fluid motion is created by rotation of the inner cylinder with the outer cylinder kept stationary. This rotation is at speeds that are high enough to provide turbulent mixing, creating a "core" region where the densities of the species of interest (neutrals, positive and negative charge carriers) can be taken as essentially uniform. At the edge of this region, near the boundaries, diffusion sublayers develop in which molecular diffusion and drift dominate the convective mixing by the turbulent flow. For the semi-insulating liquids of interest in electrification, the Debye length and the diffusion sublayer thickness are of the same order so both drift and diffusion contribute to the flux of the ions. On the other hand, in the relatively conducting aqueous solutions used in most mass transfer experiments, the Debye length is much smaller than the sublayer thickness and the flux contribution due to drift is negligible compared to diffusion. Including the drift contribution to the flux significantly complicates the model for the mass (and charge) transport; to reduce some of this complexity, the effects of the turbulence on the transport will be represented by a uniform molecular diffusivity in the sublayer region and a turbulent diffusivity outside the sublayer. The price paid for this assumption is that the sublayer thickness must be known reasonably accurately. Since the descriptions of the sublayer thickness near a rotating cylinder are relatively incomplete, this section will review some of the relevant experiments and models and then propose an equation for the sublayer thickness.

The thickness of the diffusion sublayer can be defined as the distance at which molecular diffusion balances the effective diffusivity caused by the convective mixing. In general, the sublayer thicknesses $\delta_{1,2}$ can be written as

$$\delta_{1,2} = \frac{k\nu}{Sc^{1/m}\sqrt{\tau_{w1,2}/\rho_m}} \quad ; \quad Sc \equiv \frac{\nu}{D_m} \tag{5.91}$$

where the subscript 1 denotes the inner cylinder sublayer and 2 denotes the outer cylinder sublayer, $\nu$ is the kinematic viscosity of the fluid, $\tau_w$ is the wall shear stress, $\rho_m$ is the

mass density of the fluid, $Sc$ is the Schmidt number of the fluid, and the empirical coefficients $k = 11.7$ and $m = 3$ are estimated from high Schmidt number pipe flow measurements [25,99]. The sublayer thickness near an interface can also be obtained by analogy with momentum transfer in which the turbulent motion leads to an effective turbulent diffusivity $D_T$, which is approximately the same as the turbulent viscosity $\nu_T$, that increases with distance away $y_+$ from the wall according to

$$\frac{D_T}{\nu} \approx \frac{\nu_T}{\nu} \approx C_1^3 y_+^3 \quad ; \quad y_+ \equiv \left(\frac{1}{\nu}\sqrt{\frac{\tau_{w1}}{\rho_m}}\right)(r-a) \tag{5.92}$$

where $r$ is the radius and $C_1$ is an empirical constant having been given values of 0.0747 [100] and 0.0866 [101]. Setting $D_T = D_m$ then leads to Eq. 5.91, with $m = 3$ and $k = C_1^{-1} = 13.4$ and 11.5, respectively.

The rotational speed of the inner cylinder affects the sublayer thicknesses through the wall shear stresses. When the rotation of the inner cylinder has reached a steady state, conservation of angular momentum requires that the torques on the inner and outer cylinders be equal and

$$2\pi H a^2 \tau_{w1} = 2\pi H R_2^2 \tau_{w2} \tag{5.93}$$

This indicates that the diffusion sublayer thicknesses are related by

$$\frac{\delta_1}{\delta_2} = \sqrt{\frac{\tau_{w2}}{\tau_{w1}}} = \frac{a}{R_2} \tag{5.94}$$

and a normalized sublayer thickness $\delta$ can be defined as

$$\delta \equiv \frac{\delta_1}{a} = \frac{\delta_2}{R_2} \tag{5.95}$$

In order to extend this derivation and develop an explicit relation between the sublayer thickness and the rotational speed, the interfacial shear stress must be specified. Unfortunately, the shear stress dependence on Reynolds number, cylinder radii, and surface roughness is not well understood, with various relations being reported in the literature [102]. For the purposes of this analysis, three of the relations used in the literature will be reviewed and contrasted. In order to facilitate the comparisons, all of the expressions will be written in terms of a non-dimensional drag coefficient $C_f$ and Reynolds number $R$ defined by

$$\frac{C_f}{2} \equiv \frac{\tau_{w1}}{\rho_m(\Omega a)^2} \quad ; \quad R \equiv \frac{2\Omega a^2}{\nu} \tag{5.96}$$

with $\Omega$ the cylinder angular velocity (rad/sec).

Some of the most extensive experiments for the shear stress were performed by Theodorsen and Regier [103], where the frictional drag on rotating cylinders in an essentially unbounded fluid was measured for a wide range of Reynolds numbers and surface roughnesses. An expression which combines the smooth cylinder results with the rough

cylinder results is

$$\frac{1}{\sqrt{C_f}} \approx -0.6 - 4.07 \log_{10}\left(\frac{2}{R\sqrt{C_f}} + 0.215\frac{e}{a}\right) \quad ; \quad 8 \times 10^2 < R < 8 \times 10^5 \qquad (5.97)$$

where $e$ is the surface roughness height. At high enough $R$, $C_f$ becomes independent of $R$ and depends only upon the surface roughness. For calculation purposes, the expression

$$\frac{C_f}{2} \approx 0.079 R^{-0.30} \qquad (5.98)$$

provides a good approximation to the smooth cylinder ($e/a = 0$) drag coefficient [104].

Another set of experiments was performed by Taylor [105], in which the wall shear stress on a stationary outer cylinder was related to the angular velocity of the inner cylinder over a range of gap thicknesses between the cylinders. These measurements can be used to determine the shear stress at the inner cylinder, and hence the drag coefficient, via Eq. 5.96. Representative results are

$$\frac{C_f}{2} \approx 0.48 R^{-0.5} \quad ; \quad 1.4 \times 10^4 < R < 1.4 \times 10^5 \qquad (5.99)$$

for a gap thickness $d \equiv (R_2 - a)$ satisfying $d/a$=0.1480 and

$$\frac{C_f}{2} \approx 0.72 R^{-0.5} \quad ; \quad 2.2 \times 10^4 < R < 4.7 \times 10^5 \qquad (5.100)$$

for $d/a$=0.0271.

Lastly, the drag coefficient can also be estimated from fluid velocity profile measurements reported by Smith and Townsend [106]. In these experiments, the gap between the cylinders was relatively wide with $d/a = 0.5$. By assuming that the shear stress was proportional to $R^{-0.25}$ and non-dimensionalizing the radial distance and velocity in the sublayers near the cylinder walls, the profile data was shown to collapse onto a single curve. With a reported drag coefficient of $2.2 \times 10^{-3}$ for $R = 182400$ and the assumed Reynolds number dependence, it follows that

$$\frac{C_f}{2} \approx 2.27 \times 10^{-2} R^{-0.25} \quad ; \quad 3.48 \times 10^4 < R < 2.00 \times 10^5 \qquad (5.101)$$

is another estimate of the shear stress.

These various expressions for the drag coefficient are plotted in Fig. 5.4. The spread in the curves illustrates the large variation in drag coefficients between the experiments, making it unclear as to which expression is appropriate for determining the sublayer thickness. One way to gain insight into, and possibly resolve, this issue is to use the results of mass (and heat) transfer studies involving rotating cylindrical electrodes. The mass transfer experiments typically related the terminal current between the electrodes to the transport of the reacting ions in an aqueous solution to the rotating inner cylinder under transport limited conditions (i.e. the rates associated with the interfacial chemical

reactions are fast compared to the transport time to the interface). The nondimensional mass transfer rate, the Sherwood number $Sh$, has been found to be related to the drag coefficient, Reynolds number and Schmidt number via

$$Sh \equiv \frac{2aJ_L}{zqc_oD_m} = \frac{C_f}{2} RSc^{0.356} \tag{5.102}$$

where $J_L$ is the limiting current density, $z$ is the valence of the reacting ion, $q$ is the charge of a single electron, and $c_o$ is the bulk concentration of the reacting species [71]. From these mass transfer studies, the drag coefficient has been found to be Eq. 5.98 for smooth cylinders [104] and

$$\frac{C_f}{2} \approx \left[1.25 + 5.76 \log_{10}\left(\frac{2a}{e}\right)\right]^{-2} \quad ; \quad R > R_{crit} = 41.7\left(\frac{a}{e}\right)^{1.18} \tag{5.103}$$

for fully rough conditions at high Reynolds numbers [71]. Notice that this is essentially identical with the results of Theodorsen and Regeir in Eq. 5.97. Although these empirical correlations are still being refined and there is some evidence that increased surface roughness may also change the dependence on the Schmidt number [101], numerous researchers have confirmed these basic results [48,49]. To now get an expression for the sublayer thickness at the inner cylinder, models must be used.

The goal of numerous mass and heat transfer models has been to derive Eq. 5.102 from basic principles. In the mass transfer experiments, a supporting electrolyte that does not enter into the interfacial chemical reactions is used to raise the conductivity of the liquid and reduce the electric field in the bulk of the fluid. With the field essentially confined to the Debye layer, the transport of the ions is dominated by the diffusion and convective mixing. It follows that the simplest models for the mass transfer use a Nernst layer approximation for the diffusion of the reacting species across the sublayer, such that [104,107]

$$J \approx zq\frac{D_m(c_o - c_s)}{\delta_1} \quad \Rightarrow \quad Sh \approx \frac{2a}{\delta_1} = \frac{2}{\delta} = C_1 RSc^{1/3}\sqrt{\frac{C_f}{2}} \tag{5.104}$$

where $c_s$ is the concentration of the reacting species at the interface and with the limiting current density being obtained when $c_s \rightarrow 0$. The rightmost equality comes from a substitution for $\delta$ using the normalized form of Eq. 5.91 as

$$\delta \approx \frac{2k\sqrt{2}}{Sc^{1/m}R\sqrt{C_f}} \tag{5.105}$$

Other models are based on the turbulent viscosity profile of Eq. 5.92 [100,102]. For high Schmidt number fluids, the diffusion sublayer is deep within the viscous sublayer and is in a region of approximately constant flux or shear. The concentration profile, and the flux, can then be found by integrating the reciprocal of the total diffusivity across the

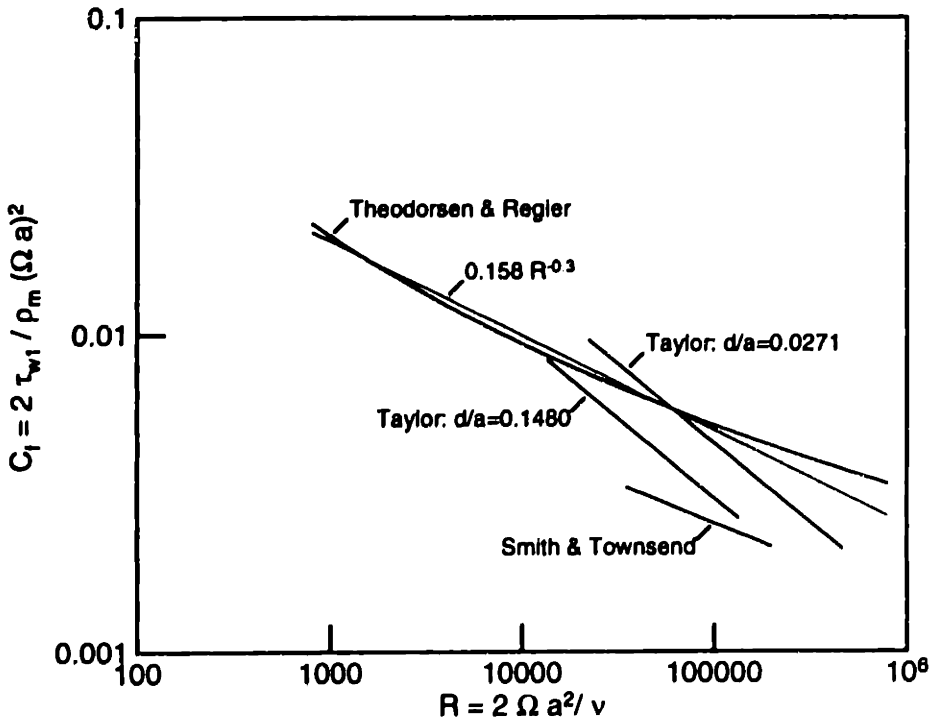


Figure 5.4: A comparison of the measured drag coefficients for a smooth rotating cylinder.

sublayer. Assuming $Sc_T = 1$ and $Sc\,C_1^3 \approx 1$, the integration leads to

$$Sh = \frac{2a}{qzD_m}\frac{J_L}{c_o} = \frac{3\sqrt{3}}{2\pi}C_1 RSc^{1/3}\sqrt{\frac{C_f}{2}} \approx \frac{1.65}{\delta} \tag{5.106}$$

Except for the numerical coefficient, this is the same as the result obtained with the Nernst layer approximation in Eq. 5.104.

Comparing these turbulent model results for the Schmidt number with the experimental result in Eq. 5.102, it is clear that the Schmidt number dependence is predicted quite well ($m$=3), but the Reynolds number dependence (through the drag coefficient) is in error. Over the range in Reynolds number in which Eq. 5.97 is valid, the model and experimental Sherwood numbers only differ significantly in the high and low Reynolds number regimes. Other than using different shear stress measurements, attempts have not been made to improve the fit at the high Reynolds numbers [101]. To improve the fit at low Reynolds numbers though, Smith and Greif suggested using an enhanced turbulent

viscosity (or enhanced mixing length) due to the curvature of the flow, such that

$$C_{1c} = C_1 \left(1 + \frac{8\beta}{RC_f}\right)^{2/3} \tag{5.107}$$

where $C_{1c}$ is a corrected coefficient for the turbulent viscosity and the empirical constant $\beta = 5$ [100]. The correction factor is based on an analogy between buoyancy forces and the effects of curvature or rotation on the turbulent mixing via the Richardson number. It is most important at low Reynolds number and gradually decreases as the Reynolds number increases, consistent with the observations that the effects of curvature are not significant at large Reynolds numbers [106]. The net result is that the turbulent viscosity is enhanced, increasing more rapidly with distance from the wall, and the effective sublayer thickness is smaller than that given by Eq. 5.91, with

$$\delta_c \approx \frac{2k\sqrt{2}}{Sc^{1/m}R\sqrt{C_f}} \left(1 + \frac{8\beta}{RC_f}\right)^{-2/3} \tag{5.108}$$

giving the corrected normalized sublayer thickness.

Another formulation for the sublayer thickness is based on the Sherwood number measurements. Since the Sherwood number appears to be well-represented, at least at low Reynolds numbers, by a constant divided by the normalized sublayer thickness, solving for the sublayer thickness between the empirical result of Eq. 5.102 and the model result of Eq. 5.106 gives

$$\delta_e = \frac{3.3}{Sc^{0.356}RC_f} \tag{5.109}$$

This is the proposed formula for the sublayer thickness, with the drag coefficient given in general by Eq. 5.97, but approximated by Eq. 5.98 for smooth cylinders. A plot of this equation, assuming the cylinders are smooth, is given in Fig. 5.5. The sublayer thickness $\delta_c$, calculated from Eq. 5.108 using $k$=13.4, $m$=3, $\beta = 5$, and Eq. 5.98, is also plotted. As expected, the sublayer thicknesses are reasonably close, with $\delta_c$ smaller than $\delta_e$ at the higher Reynolds numbers; this is where the turbulence model overestimates the Sherwood number.

The third curve plotted in Fig. 5.5 (at each Schmidt number) is an estimate of the sublayer thickness incorporated into electrification [25] and moisture transfer models [17] involving transformer oil and pressboard insulation. This estimate uses an "average" drag coefficient, based on Taylor's measurements [105], giving

$$\frac{C_f}{2} \approx 0.67R^{-0.5} \quad ; \quad 1.4 \times 10^3 < R < 4.5 \times 10^4 \tag{5.110}$$

for $d/a$=0.33. Using this drag coefficient in the uncorrected equation for the sublayer thickness (Eq. 5.105) and the empirical coefficients of $k$=11.7 and $m$=3 gives the sublayer thickness $\delta_m$. This estimate is consistently higher than that proposed in Eq. 5.108 and helps to explain why the molecular diffusivity or the shear stresses typically had to be larger than expected in order to fit the models to the data [17,25]; using the simplified

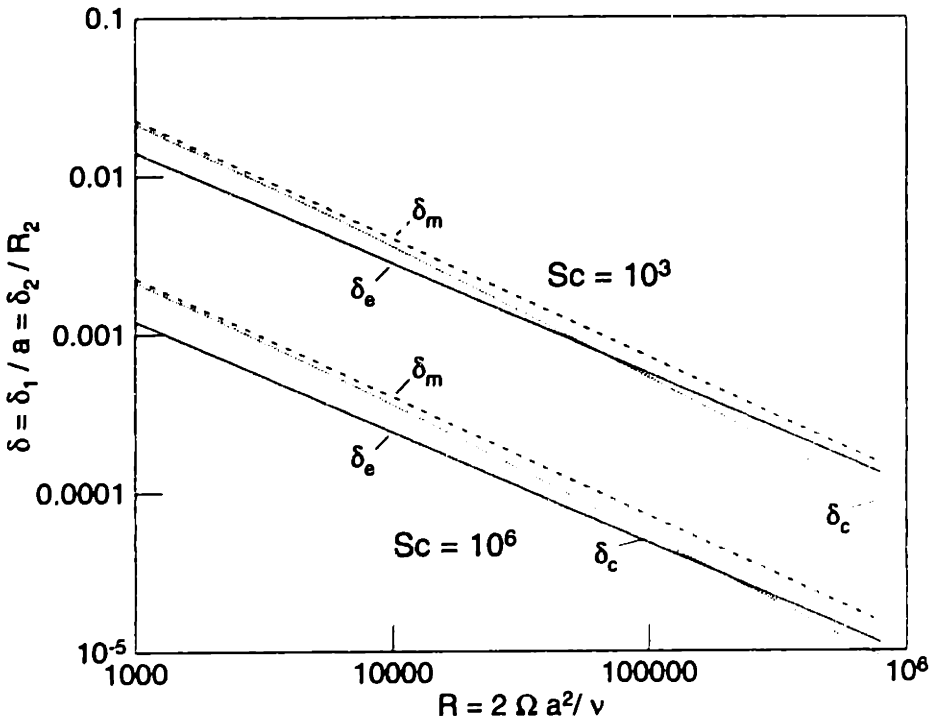


Figure 5.5: A comparison of the normalized sublayer thicknesses for a smooth rotating cylinder ($e/a = 0$). $\delta_e$ denotes the proposed empirical estimate of the sublayer thickness; $\delta_c$ denotes the turbulent viscosity model estimate of the sublayer thickness; and $\delta_m$ denotes the sublayer thickness used in electrification and mass transfer models for electrical insulation. The Schmidt numbers for each set of curves are indicated.

current density of Eq. 5.104, if the sublayer thickness is too large then maintaining the same current density requires the molecular diffusivity and the shear stress to be increased. Furthermore, the difference between $\delta_e$ and $\delta_m$ increases with the Schmidt number because $\delta_e/\delta_m \propto Sc^{-0.023}$ and can become appreciable at very large Schmidt numbers. Indeed, for $R = 10^4$ and $Sc = 7.2 \times 10^5$, $\delta_e/\delta_m \approx 0.6$, which would lead to an overestimate of the molecular diffusivity by a factor of 1.67.

Fig. 5.5 also shows that the sublayer thickness decreases as the Schmidt number increases. While most of the relations that have been discussed were determined for relatively low Schmidt number fluids ($10^3 < Sc < 10^4$) [101], they are also assumed to apply to higher Schmidt number fluids, such as transformer oil ($10^4 < Sc < 10^6$ in this case).

Surface roughness may also play a role in explaining the observed enhanced diffusivities; it has been observed to greatly increase the mass transfer once a critical Reynolds

number has been attained [71,101]. Physically, the surface roughness increases the drag coefficient and decreases the sublayer thickness. Thus, smooth cylinder expressions again overestimate the sublayer thickness. In the Couette apparatus, the stainless steel metal surfaces are relatively smooth but contain numerous feedthroughs for instrument probes and the calendered dielectric surfaces are known to have roughness and periodicities that are comparable to and even larger than the diffusion sublayer thickness [26].

This completes the discussion of the basic ideas and concepts involved in describing mass transfer in turbulent flow between rotating cylinders. In summary, an equation (Eq. 5.109) relating the diffusion sublayer thicknesses to the Schmidt number of the fluid, the Reynolds number, and the drag coefficient was proposed, using measurements of the Sherwood number and the drag coefficient (Eq. 5.97). These results can be incorporated into an electrification model.

## 5.7 Non-stationary case

Consider now the non-stationary case in which the inner cylinder is rotating and causing turbulent fluid motion. The motion of the fluid redistributes the chemical species, carrying charge from the double layers at the interfaces into the core region of the fluid flow. In this section, relations between the measurable quantities (volume charge density in the core region, terminal current, terminal voltage, and the rate of change in the core charge density with respect to an imposed DC terminal voltage) and the interfacial and bulk parameters are derived. For the purposes of this initial analysis, only steady state relations are to be obtained.

To simplify the analysis, several assumptions will be made. First, assume that turbulent mixing causes the species densities to be independent of the axial and azimuthal directions and approximately uniform in the core region. In terms of the net charge density, a uniform charge density across the core region is a valid assumption when the fluid is insulating enough that the turbulent Debye length, based upon the turbulent diffusivity instead of the molecular diffusivity, is large compared to the gap thickness.

Second, treat the system as being quasi-unipolar so that only the net charge density and net current density must be determined, not the individual carrier dynamics associated with two (or more) charged species. This could be restated as assuming that the positive and negative carriers have equal diffusivities (and mobilities) or that only one charged species is mobile and the other is immobile. For highly insulating hydrocarbon liquids, the mobility of the negative ions is roughly twice the mobility of the positive ions [91: Section 5.2], so an assumption of nearly equal mobilities should be reasonable.

Third, as in the stationary case of Section 5.5, assume that the carrier densities near the solid/liquid interfaces are not significantly different than the bulk densities so that a region of enhanced conductivity near the interfaces does not have to be modeled. This is tantamount to assuming small zeta potentials for the interfaces. In addition, assume that the applied voltage is small enough that the conduction through the liquid can be represented by the bulk ohmic conductivity of the liquid.

Finally, assume that the net charge density varies across the diffusion sublayers according to Eq. 5.56. Inside the sublayers, the effective turbulent diffusivity is small

compared to the molecular diffusivity and the charge distribution reflects the contributions of diffusion and migration to the flux. A linear variation across the sublayer is not assumed, even when the sublayer thickness is small compared to the Debye length, because this leads to an inconsistency in the charge conservation equations, as discussed later. It follows that the charge distribution can be expressed as

$$\rho = \begin{cases} 0 & \text{(I)}: \quad R_1 < r < a \\ \dfrac{1}{f(a+\delta_1, a)}\left[\rho_1^b f(a+\delta_1, r) + \rho_o f(r, a)\right] & \text{(II)}: \quad a < r < a+\delta_1 \\ \rho_o & \text{(III)}: \quad a+\delta_1 < r < R_2 - \delta_2 \\ \dfrac{1}{f(R_2, R_2-\delta_2)}\left[\rho_o f(R_2, r) + \rho_2^b f(r, R_2-\delta_2)\right] & \text{(IV)}: \quad R_2 - \delta_2 < r < R_2 \end{cases} \tag{5.111}$$

where $\rho$ is the volume charge density, $\rho_o$ is the charge density in the turbulent core region and the charge densities on the liquid side of the solid/liquid interface are given by $\rho_1^b$ for the inner cylinder interface and $\rho_2^b$ for the outer cylinder interface. The roman numerals are used to identify the regions of applicability for each expression. This distribution is shown schematically in Fig. 5.6.

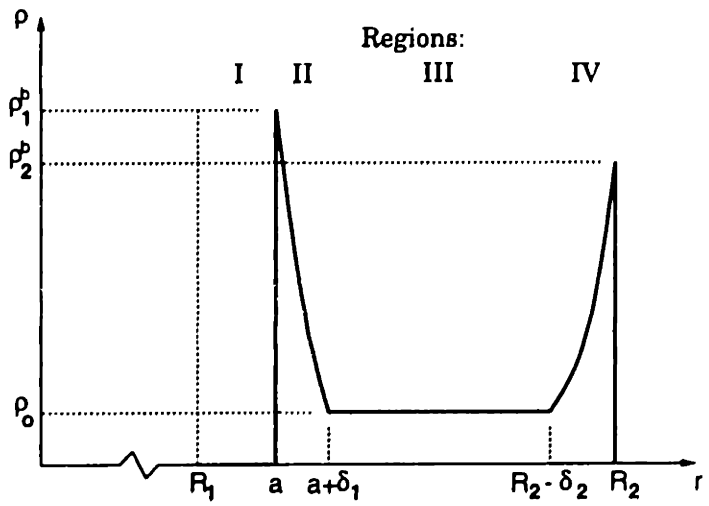


Figure 5.6: A schematic representation of the charge distribution between the Couette cylinders. Rotation of the inner cylinder creates turbulent flow that carries the charged species from the fluid/solid interfaces into a well-mixed core region. The charge density is assumed to be uniform in this core region and varies with distance across the diffusion sublayer regions.

The electric field distribution corresponding to this charge distribution can be obtained from the differential form of Gauss' law

$$\frac{1}{r}\frac{\partial}{\partial r}(rE_r) = \frac{\rho}{\epsilon} \tag{5.112}$$

Integrating over the radial coordinate gives

$$E_r = \begin{cases} \dfrac{A_1}{r} & \text{(I)} \\ \dfrac{A_2}{r} + \dfrac{\lambda_D}{\epsilon_2 f(a+\delta_1, a)}\left[-\rho_1^b g(a+\delta_1, r) + \rho_o g(r,a)\right] & \text{(II)} \\ \dfrac{A_3}{r} + \dfrac{\rho_o r}{2\epsilon_2} & \text{(III)} \\ \dfrac{A_4}{r} + \dfrac{\lambda_D}{\epsilon_2 f(R_2, R_2-\delta_2)}\left[-\rho_o g(R_2, r) + \rho_2^b g(r, R_2-\delta_2)\right] & \text{(IV)} \end{cases} \tag{5.113}$$

where the $A_i$ are constants of integration. Note also that the radial variation in the charge density can be expressed as

$$\frac{\partial \rho}{\partial r} = \begin{cases} \dfrac{1}{\lambda_D f(a+\delta_1, a)}\left[-\rho_1^b g(a+\delta_1, r) + \rho_o g(r,a)\right] & \text{(II)} \\ 0 & \text{(I), (III)} \\ \dfrac{1}{\lambda_D f(R_2, R_2-\delta_2)}\left[-\rho_o g(R_2, r) + \rho_2^b g(r, R_2-\delta_2)\right] & \text{(IV)} \end{cases} \tag{5.114}$$

Similarly, by combining Eqs. 5.113 and 5.114, the radial current density in the diffusion sublayers is given by

$$J_r = -D_m \frac{\partial \rho}{\partial r} + \sigma_2 E_r = \begin{cases} \dfrac{\sigma_2 A_2}{r} & \text{(II)} \\ \dfrac{\sigma_2 A_4}{r} & \text{(IV)} \end{cases} \tag{5.115}$$

Note that the current density in the core region could not be obtained this way because even though the gradient in the charge density goes to zero, the turbulent diffusivity is being taken as infinite and the product is a finite quantity.

The next step is to determine the governing equations relating the unknown parameters to the measurable quantities. Begin by applying the integral form of charge conservation to a surface just inside the diffusion sublayer regions [at an inner radius of $r = (a+\delta_1)^-$ and an outer radius of $r = (R_2 - \delta_2)^+$] so that

$$\frac{d}{dt}\int_V \rho dV + \oint_S \vec{J} \cdot d\vec{a} = 0 \tag{5.116}$$

In this case, the left hand quantity is zero because steady state conditions are being considered. Using Eq. 5.115, it follows that

$$A_4 = A_2 \tag{5.117}$$

Note also that applying charge conservation to each of the diffusion sublayers [regions (II) and (IV)] give an identity ($0 = 0$) and don't provide any new information. This is consistent with the understanding that in the steady state, the net charge in the sublayers does not vary with time and the total current into the sublayers due to diffusion and migration must be zero. If a linear charge density profile across the sublayer was assumed,

then the current densities due to diffusion on each side of the sublayer would have opposite polarities and essentially identical magnitudes, thereby canceling one another. But the current densities due to migration will not cancel one another because the charge present in the double layer causes the electric fields at each sublayer surface to be different. (This can be seen more clearly in a parallel plate geometry with a turbulent core region bounded on each side by diffusion sublayers. In that case, the current density due to diffusion on each side of the sublayer regions would exactly cancel one another, but the migration terms would not.) Even though the assumption of linear profiles does not self-consistently describe the system, reasonable results have been obtained for relatively simple boundary conditions [25]. When using other boundary conditions, a self-consistent model becomes necessary.

Charge conservation can also be applied to the interfaces between the materials. In the steady state, this gives

$$\sigma_1 A_1 = \sigma_2 A_2 \tag{5.118}$$

at $r = a$ and

$$A_4 = -\frac{I}{2\pi H \sigma_2} \tag{5.119}$$

at $r = R_2$. A similar relation is obtained for the interface at $r = R_1$, except it does not provide any new information. Thus, of the seven possible charge conservation equations [for the interfaces at $r = R_1, a, R_2$ and for the regions (I),(II), (III), and (IV)], only three of the equations are independent.

Additional independent information can be obtained from the continuity of the electric field in the liquid volume and the terminal constraints. Surface charge cannot accumulate at the interfaces between the turbulent core and the diffusion sublayer fluid flow regions and the turbulent mixing should only have a weak effect, if any, on the dielectric permittivity. As a result, the electric field is subject to the constraints

$$E_r|_{r=(a+\delta_1)^+} = E_r|_{r=(a+\delta_1)^-} \tag{5.120}$$

$$E_r|_{r=(R_2-\delta_2)^+} = E_r|_{r=(R_2-\delta_2)^-} \tag{5.121}$$

It follows that

$$A_2 = A_3 + \frac{\rho_o}{2\epsilon_2}(a+\delta_1)^2 - \frac{\lambda_D(a+\delta_1)}{\epsilon_2 f(a+\delta_1, a)}\left[\rho_o g(a+\delta_1, a) - \rho_1^b g(a+\delta_1, a+\delta_1)\right] \tag{5.122}$$

$$A_4 = A_3 + \frac{\rho_o}{2\epsilon_2}(R_2-\delta_2)^2 - \frac{\lambda_D(R_2-\delta_2)}{\epsilon_2 f(R_2, R_2-\delta_2)}\left[\rho_2^b g(R_2-\delta_2, R_2-\delta_2) - \rho_o g(R_2, R_2-\delta_2)\right] \tag{5.123}$$

The electric field is related to the terminal variables by Eqs. 5.80 and 5.82. Taking the line integral of the radial component of the electric field between the electrodes gives

$$\begin{aligned} V_o + R_L I = {} & A_1 \ln\left(\frac{a}{R_1}\right) + A_2 \ln\left(\frac{a+\delta_1}{a}\right) + A_3 \ln\left(\frac{R_2-\delta_2}{a+\delta_1}\right) + A_4 \ln\left(\frac{R_2}{R_2-\delta_2}\right) \\ & + \frac{\rho_o}{4\epsilon_2}\left[(R_2-\delta_2)^2 - (a+\delta_1)^2\right] + \frac{\lambda_D^2}{\epsilon_2}\left(\rho_2^b - \rho_1^b\right) \end{aligned} \tag{5.124}$$

Note that the terminal voltage can be obtained from the terminal current after the current is found.

At this point there are eight unknowns ($\rho_o$, $\rho_1^b$, $\rho_2^b$, $A_1$, $A_2$, $A_3$, $A_4$, and $I$) but only six equations (Eqs. 5.117, 5.118, 5.119, 5.122, 5.123, and 5.124). The remaining equations come from the constitutive laws for the interfacial dynamics, such as Eq. 5.62, for each interface. This then gives an equal number of equations and unknowns and the system of equations can be solved. Before solving the equations though, it is convenient to simplify them further.

The experiment that this model represents contains very different length scales which allow the governing equations to be greatly simplified. For example, in the experiment, the cylinder radii scale as $a/R_2 = O(1)$, the non-dimensional sublayer thickness scales as $\delta = o(1)$, and the Debye length is small compared to the cylinder radii $[\lambda_D/R_2 = o(1)]$[3]. These approximations allow the simplified expressions for $f$ (Eq. 5.60) and $g$ (Eq. 5.73) to be used. Eliminating the variables $A_1$, $A_2$, $A_3$, and $A_4$ and non-dimensionalizing according to Tables 5.1 and 5.2 then gives the governing equations (without the postulated boundary conditions) as

$$\rho_o = \frac{2\lambda_D\left[\operatorname{acsch}\left(\frac{a\delta}{\lambda_D}\right)\rho_1^b + \operatorname{csch}\left(\frac{\delta}{\lambda_D}\right)\rho_2^b\right]}{1-a^2+2\lambda_D\left[a\coth\left(\frac{a\delta}{\lambda_D}\right)+\coth\left(\frac{\delta}{\lambda_D}\right)\right]} \qquad (\underline{5.125})$$

$$\begin{aligned} V_o = {} & \frac{\rho_o}{\lambda_D^2}\left\{\frac{(1-a^2)}{4}+\ln(a)\left[\frac{1}{2}-\lambda_D\coth\left(\frac{\delta}{\lambda_D}\right)\right]\right\}-\rho_1^b \\ & +\rho_2^b\left[1-\frac{\ln(a)}{\lambda_D}\operatorname{csch}\left(\frac{\delta}{\lambda_D}\right)\right]-\frac{I}{2}\left[R_L+\frac{1}{\sigma_1}\ln\left(\frac{a}{R_1}\right)-\ln(a)\right] \end{aligned} \qquad (\underline{5.126})$$

where the underscore beneath the equation number indicates an equation containing non-dimensional variables. These two equations can be simplified further by assuming that the sublayer thicknesses have values that are limited on the upper side by the Debye length $[\delta/\lambda_D = O(1)]$ and on the lower side by $\delta \gg \lambda_D^2$. Then, the governing equations are reduced to the boundary conditions at the solid/liquid interfaces and

$$\begin{aligned} V_o = {} & \frac{\rho_1^b a}{\lambda_D}\operatorname{csch}\left(\frac{a\delta}{\lambda_D}\right)\left[\frac{1}{2}+\frac{\ln(a)}{1-a^2}\right]+\frac{\rho_2^b}{\lambda_D}\operatorname{csch}\left(\frac{\delta}{\lambda_D}\right)\left[\frac{1}{2}+a^2\frac{\ln(a)}{1-a^2}\right] \\ & -\frac{I}{2}\left[R_L+\frac{1}{\sigma_1}\ln\left(\frac{a}{R_1}\right)-\ln(a)\right] \end{aligned} \qquad (\underline{5.127})$$

The unknowns to be determined first are then the terminal current $I$ and the interfacial volume charge densities $\rho_1^b$ and $\rho_2^b$. Once these are known, the core charge density can be obtained from

$$\rho_o = \frac{2\lambda_D}{1-a^2}\left[\operatorname{acsch}\left(\frac{a\delta}{\lambda_D}\right)\rho_1^b+\operatorname{csch}\left(\frac{\delta}{\lambda_D}\right)\rho_2^b\right] \qquad (\underline{5.128})$$

[3]This uses the notation where $f = O(x)$ means that $f$ is of the same order of magnitude as $x$ and $f = o(x)$ means that $f$ is negligibly small compared to $x$ [98: p. 56].

| Variable | Normalization |
|---|---|
| Lengths ..... | $(x, y, z) = (\underline{x}, \underline{y}, \underline{z})R_2$ |
| Charge density ..... | $\rho_i^j = \underline{\rho}_i^j \sigma_2 / b$ |
| Electric potential ..... | $v = \underline{v} D_m / b$ |
| Terminal resistance ..... | $R_L = \underline{R}_L / 2\pi H \sigma_2$ |
| Terminal current ..... | $I = \underline{I} \pi H \sigma_2 D_m / b$ |
| Terminal voltage ..... | $V_o = \underline{V}_o D_m / b$ |
| Solid conductivity ..... | $\sigma_1 = \underline{\sigma}_1 \sigma_2$ |
| Solid relaxation time ..... | $\tau_1 = \underline{\tau}_1 \tau_2$ |
| Reaction velocity ..... | $k_i = \underline{k}_i D_m / R_2$ |
| Charge density gradient ..... | $\alpha_i = \underline{\alpha}_i \sigma_2 / b R_2$ |
| Effective charge density ..... | $\xi_i = \underline{\xi}_i \sigma_2 / b$ |

Table 5.1: Normalizations for the electrification model variables.

and the terminal voltage can be obtained from

$$v = \frac{\rho_1^b a}{\lambda_D} \operatorname{csch}\left(\frac{a\delta}{\lambda_D}\right)\left[\frac{1}{2} + \frac{\ln(a)}{1-a^2}\right] + \frac{\rho_2^b}{\lambda_D} \operatorname{csch}\left(\frac{\delta}{\lambda_D}\right)\left[\frac{1}{2} + a^2\frac{\ln(a)}{1-a^2}\right] - \frac{I}{2}\left[\frac{1}{\sigma_1}\ln\left(\frac{a}{R_1}\right) - \ln(a)\right] \quad (5.129)$$

These equations are to be solved for open-circuit ($R_L \to \infty$), short-circuit ($V_o = 0$, $R_L \to 0$), and applied DC voltage ($V_o \neq 0$, $R_L \to 0$) conditions.

### 5.7.1 Imposed interfacial current density (Abedian-Sonin)

The first boundary condition to be considered proposes that the current densities at the interfaces are given by Eq. 5.62. Although Abedian and Sonin further restricted themselves to the case of $k_i \to \infty$, the more general case of finite $k_i$ is considered here. Using Eq. 5.115 for the current densities on the liquid side of the interfaces, it follows that normalized volume charge densities near the interface can be written as

$$\rho_1^b - \frac{I}{2ak_1} = \rho_1^w \quad (5.130)$$

$$\rho_2^b + \frac{I}{2k_2} = \rho_2^w \quad (5.131)$$

Then, by using Eq. 5.127, the current can be solved as

$$I = -\frac{2}{\gamma}\left\{V_o - \frac{a\rho_1^w}{\lambda_D}\operatorname{csch}\left(\frac{a\delta}{\lambda_D}\right)\left[\frac{1}{2} + \frac{\ln(a)}{1-a^2}\right] - \frac{\rho_2^w}{\lambda_D}\operatorname{csch}\left(\frac{\delta}{\lambda_D}\right)\left[\frac{1}{2} + a^2\frac{\ln(a)}{1-a^2}\right]\right\} \quad (5.132)$$

| Parameter | Definition |
|---|---|
| Sublayer thickness ..... | $\delta = \delta_1/a = \delta_2/R_2$ |
| Liquid relaxation time ..... | $\tau_2 = \epsilon_2/\sigma_2$ |
| Debye length ..... | $\lambda_D = \sqrt{D_m \tau_2}$ |
| Effective rate constant ..... | $K_i^e = k_i^f/\lambda_D k_i^r$ |
| Effective reverse reaction rate . | $K_i^r = 1/\tau_2 k_i^r$ |

Table 5.2: Summary of parameters used in the electrification model.

where

$$\gamma \equiv \frac{1}{\lambda_D}\left\{\frac{1}{k_2}\mathrm{csch}\left(\frac{\delta}{\lambda_D}\right)\left[\frac{1}{2}+a^2\frac{\ln(a)}{1-a^2}\right]-\frac{1}{k_1}\mathrm{csch}\left(\frac{a\delta}{\lambda_D}\right)\left[\frac{1}{2}+\frac{\ln(a)}{1-a^2}\right]\right\} + R_L+\frac{1}{\sigma_1}\ln\left(\frac{a}{R_1}\right)-\ln(a) \qquad (5.133)$$

is a positive definite quantity (since $a < 1$). It then follows that the core charge density can be obtained from Eq. 5.128 as

$$\rho_o = \frac{2\lambda_D}{\gamma(1-a^2)}\left\{\left[R_L+\frac{1}{\sigma_1}\ln\left(\frac{a}{R_1}\right)-\ln(a)\right]\left[\rho_1^w a\,\mathrm{csch}\left(\frac{a\delta}{\lambda_D}\right)+\rho_2^w\mathrm{csch}\left(\frac{\delta}{\lambda_D}\right)\right] -\frac{\ln(a)}{\lambda_D}\left[\frac{a\rho_1^w}{k_2}+\frac{\rho_2^w}{k_1}\right]\mathrm{csch}\left(\frac{a\delta}{\lambda_D}\right)\mathrm{csch}\left(\frac{\delta}{\lambda_D}\right) +V_o\left[\frac{1}{k_2}\mathrm{csch}\left(\frac{\delta}{\lambda_D}\right)-\frac{1}{k_1}\mathrm{csch}\left(\frac{a\delta}{\lambda_D}\right)\right]\right\} \qquad (5.134)$$

and the terminal voltage comes from Eq. 5.129 as

$$v = V_o\left[1-\frac{R_L}{\gamma}\right]+\frac{R_L}{\gamma}\left\{\frac{a\rho_1^w}{\lambda_D}\mathrm{csch}\left(\frac{a\delta}{\lambda_D}\right)\left[\frac{1}{2}+\frac{\ln(a)}{1-a^2}\right]+\frac{\rho_2^w}{\lambda_D}\mathrm{csch}\left(\frac{\delta}{\lambda_D}\right)\left[\frac{1}{2}+a^2\frac{\ln(a)}{1-a^2}\right]\right\} \qquad (5.135)$$

The significance of these results can be explored through several limiting cases.

First consider the open-circuit ($R_L \to \infty$) case in which there isn't any external current. Even though the liquid is in motion, the charge densities on the liquid side of the interface remain at their equilibrium levels. The charge density in the core region becomes

$$\rho_o^{oc} = \frac{2\lambda_D}{1-a^2}\left[\frac{\rho_2^w}{\sinh\left(\frac{\delta}{\lambda_D}\right)}+\frac{\rho_1^w a}{\sinh\left(\frac{a\delta}{\lambda_D}\right)}\right] \qquad (5.136)$$

and the terminal voltage is

$$v^{oc} = \frac{1}{\lambda_D}\left\{\frac{\rho_2^w}{\sinh\left(\frac{\delta}{\lambda_D}\right)}\left[\frac{1}{2}+a^2\frac{\ln(a)}{1-a^2}\right]+\frac{\rho_1^w a}{\sinh\left(\frac{a\delta}{\lambda_D}\right)}\left[\frac{1}{2}+\frac{\ln(a)}{1-a^2}\right]\right\} \qquad (5.137)$$

Because there isn't any net current flow across the interface, these results are independent

of the reaction velocities $k_i$. Notice that the core charge density involves the weighted sum of the equilibrium interfacial volume charge densities, while the terminal voltage involves the weighted difference (through the geometric factors which cause the first bracketed term to be positive and the second to be negative). This can be seen more clearly by considering identical bare metal electrodes ($\rho_1^w = \rho_2^w$). Then the core charge density has the same polarity as the volume charge densities on the liquid side of the metal/liquid interfaces and the open-circuit voltage always has a polarity opposite that of the core charge density.

Representative plots of the open-circuit core charge density and voltage are given in Fig. 5.7. As the rotation rate of the inner cylinder increases, the sublayer thickness decreases and the core charge density and voltage tend to increase in magnitude. Physically, as the sublayer thickness decreases *relative to the Debye length*, an increasing fraction of the charge in the electrical double layers is swept into the turbulent core region. These plots show that the polarity of the voltage, relative to that of the charge density, depends upon the relative magnitudes of the wall charge densities at the cylinder interfaces. In particular, if the wall charge density at the outer cylinder interface is equal to, or smaller than, the wall charge density on the inner cylinder interface, the charge density and voltage have the opposite polarity. But if the wall charge density on the outer cylinder is much larger than that on the inner cylinder, they have the same polarity. In the intermediate regime (determined by the value of $\underline{a}$ being used), when the wall charge density at the outer cylinder is slightly larger than that at the inner cylinder, the polarity of the voltage can change with the sublayer thickness. In these simulations, the wall charge densities at the inner and outer cylinders were assumed to have the same polarity. Similar results can be obtained when they have opposite polarities, except the polarity effects on the charge density and voltage are reversed.

Next, consider the short-circuit ($R_L \to 0$) case in which the current flowing across the solid/liquid interfaces will perturb the volume charge densities away from their equilibrium levels. The current can be expressed as

$$I^{sc} = \frac{2}{\gamma_{R_L=0}} (v^{oc} - V_o) \qquad (\underline{5.138})$$

and the charge density is given by

$$\rho_o^{sc} = \rho_o^{oc} + \frac{\lambda_D}{(1-a^2)} \left[ \frac{1}{k_1 \sinh\left(\frac{a\delta}{\lambda_D}\right)} - \frac{1}{k_2 \sinh\left(\frac{\delta}{\lambda_D}\right)} \right] I^{sc} \qquad (\underline{5.139})$$

where the superscript 'oc' denotes "open-circuit" and 'sc' denotes "short-circuit" quantities. In the absence of an applied voltage ($V_o = 0$), the charge density and current are due entirely to flow electrification. When the reaction velocities become fast compared to the relaxation time ($\underline{k}_i \to \infty$), the short-circuit and open-circuit core charge densities become equal because the interfacial volume charge densities maintain their equilibrium value. The discussion for open-circuit conditions then applies to short-circuit conditions as well. In particular, for identical bare metal electrodes, the current always has a polarity opposite that of the core charge density. Also, the ratio of the open-circuit voltage to

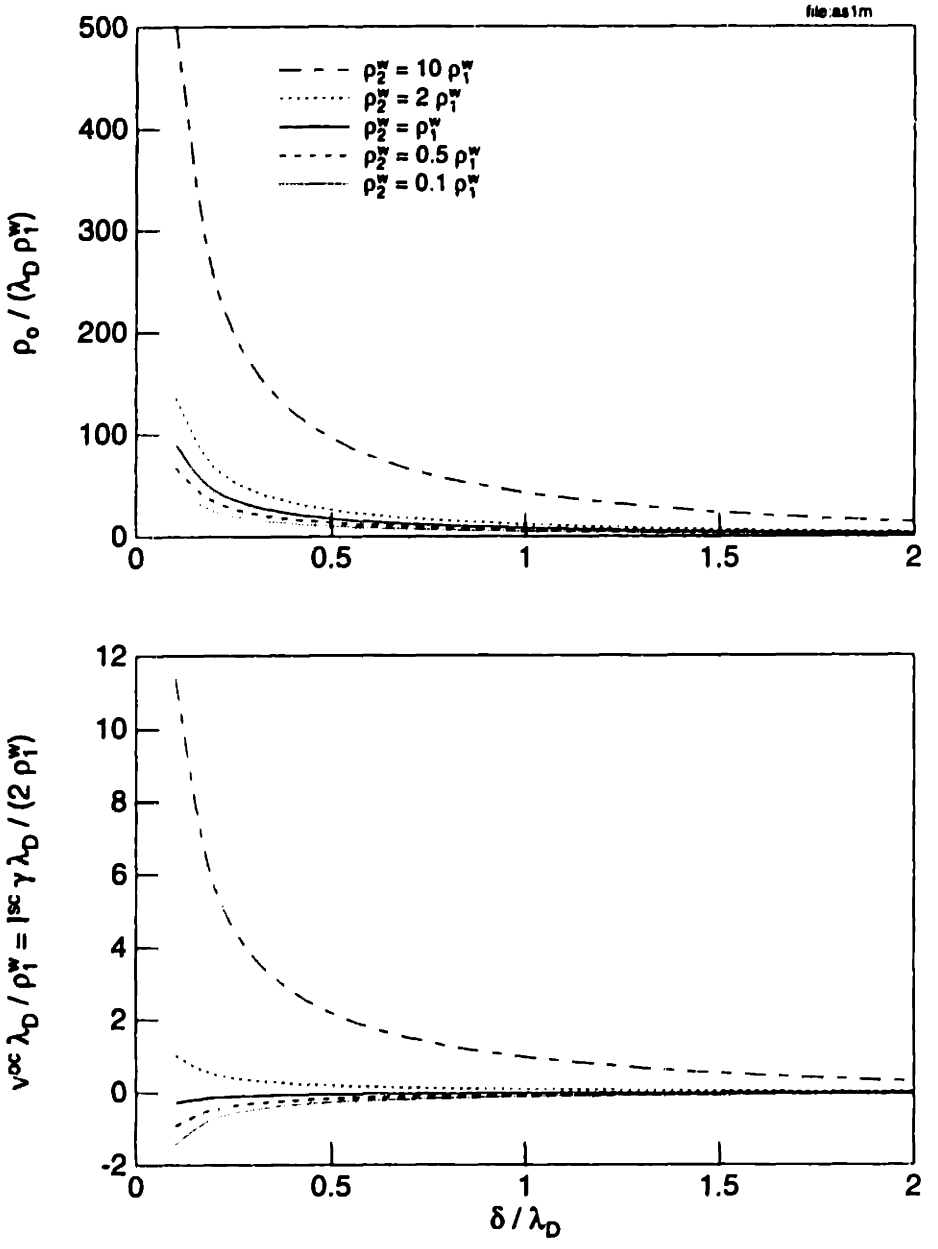


Figure 5.7: Sample normalized open-circuit simulation results from the electrification model. The charge density and voltage are plotted against the sublayer thickness. These simulations assumed $\underline{a} = 0.763$, which is appropriate for pressboard covering a copper sleeve on the inner cylinder. The product of the short-circuit current and the effective cell impedance can also be obtained from the open-circuit voltage.

short-circuit current gives the normalized "ohmic" resistance between the cylinders. For small reaction velocities ($\underline{k}_i \to 0$) the short-circuit current goes to zero, keeping the same polarity as the open-circuit voltage. In addition, the short-circuit core charge density will be different than the open-circuit core charge density. For identical metal electrodes having a negative open-circuit voltage, the short-circuit charge density will always be slightly less than the open-circuit charge density. For comparison, the product of the short-circuit current and the effective resistance between the cylinders, which is related to the open-circuit voltage, is plotted in Fig. 5.7.

With an applied voltage, the measured terminal current includes the current due to flow electrification and the imposed current through the bulk of the liquid and the interfaces. The core charge density is also affected by the applied voltage, either increasing or decreasing as the voltage is increased, depending upon the relative magnitudes of the reaction rates at each solid/liquid interface. If the $\underline{k}_i$ and $\underline{\rho}_i^w$ are taken to be independent of the applied voltage, then the rate of change of the core charge density with respect to the applied voltage, denoted by $D_v\rho_o$, is given by

$$D_v\rho_o \equiv \frac{\partial \rho_o}{\partial V_o} = \frac{2\lambda_D}{\gamma_{R_L=0}(1-a^2)}\left[\frac{1}{k_2 \sinh\left(\frac{\delta}{\lambda_D}\right)} - \frac{1}{k_1 \sinh\left(\frac{a\delta}{\lambda_D}\right)}\right] \qquad (5.140)$$

This shows that the polarity of $D_v\rho_o$ depends intimately upon the relative magnitudes of the reaction velocities. As a special case, for identical bare metal electrodes ($\underline{k}_1 = \underline{k}_2$), $D_v\rho_o < 0$ always. Furthermore, as the reaction velocities become fast the effect of the applied voltage on the charge density decreases. In the limit as $\underline{k}_i \to \infty$, the core charge density is not affected by the applied voltage.

As another limiting case, the steady state results of Morin, et al. can also be obtained [25]. In the limit of fast reaction velocities ($\underline{k}_i \gg 1$) and small sublayer thicknesses ($\underline{\lambda}_D^2 \ll \delta \ll \underline{\lambda}_D$), the core charge density, short-circuit terminal current, and open-circuit terminal voltage become

$$\rho_o \approx \frac{2\lambda_D^2}{\delta(1-a^2)}\left[\rho_1^w + \rho_2^w + \frac{V_o\left(\frac{1}{k_2} - \frac{1}{ak_1}\right)}{R_L - \ln(a) + \frac{1}{\sigma_1}\ln\left(\frac{a}{R_1}\right)}\right] \qquad (5.141)$$

$$v^{oc} \approx \frac{1}{\delta}\left[\frac{1}{2}\left(\rho_1^w + \rho_2^w\right) + \left(\rho_1^w + a^2\rho_2^w\right)\frac{\ln(a)}{(1-a^2)}\right] \qquad (5.142)$$

$$I^{sc} \approx \frac{2}{\left[\frac{1}{\sigma_1}\ln\left(\frac{a}{R_1}\right) - \ln(a)\right]}\left(v^{oc} - V_o\right) \qquad (5.143)$$

Setting the applied voltage to zero and neglecting the effects of the conduction through the solid dielectric layer (by setting $a = R_1$) yields Morin's results when the diffusion times across the sublayers are much smaller than the charge relaxation time.

While quantitative estimates of the boundary condition parameters are provided in the next section, some qualitative conclusions can be reached by comparing the model to the experimental data. Consider first identical, bare metal electrodes. The $\rho^w$ are positive because the charge density was positive, as shown in Figs. 3.9, 3.12, and 3.28.

Consistent with the positive $\rho^w$, the charge density also increased with rotation rate. The open-circuit voltage and short-circuit current are then predicted to be negative with a magnitude that increases with the rotation rate, but the steady state values tended to be positive. Several experiments gave terminal currents and voltages that were negative, as shown in Figs. 3.12 and 3.11, and during an initial "conditioning" phase or at low rotation rates, as shown in Fig. 3.28. But those experiments also showed polarity reversals as the rotation rate was varied, which suggests that the wall charge densities were different at each interface (see Fig. 5.7). Thus, although the cylinders were nominally the same in the experiments, the actual interfacial parameters were probably different. In addition, the measured core charge density usually increased with applied voltage, but the model only predicts a decrease for interfacial reaction velocities, as given by Eq. 5.140.

With pressboard covering the inner cylinder, as in Fig. 3.10, the charge density was still positive, indicating that both $\rho_1^w$ and $\rho_2^w$ are positive, but the voltage and current were negative. These results are consistent with the model for $\rho_1^w$ larger than $\rho_2^w$, as illustrated in Fig. 5.7, otherwise the terminal variables have the wrong polarity. In this case, the measured slope of the charge density variation with applied voltage was temperature dependent, being positive or negative. This is reasonable, according to the model, because the reaction rates at each interface probably had different temperature coefficients, which then led to different polarity slopes. Also, the relatively small values for the measured slopes are consistent with the open and short-circuit charge densities being essentially the same; from Eq. 5.139, the difference between open and short-circuit charge densities is the product of the slope and the open-circuit voltage, which is usually small compared to the open-circuit charge density.

### 5.7.2 Imposed charge density gradient (Gavis-Koszman)

Another boundary condition has attempted to relate the electrification charge density to an actual chemical reaction at the interface [108–110]. In this subsection, the derivation of an imposed charge density gradient boundary condition will be reviewed and then the boundary condition will be incorporated into the flow electrification model. The criteria under which this boundary condition gives results similar to those obtained with the Abedian-Sonin boundary condition are also examined.

To derive the boundary condition first assume that only negative ions react at the interface so that the flux of positive ions is zero. Although it was not expressed explicitly, a chemical reaction for the ionizable species $B^{-z}$ can be written as

$$B^{-z} \underset{k_r}{\overset{k_f}{\rightleftharpoons}} D^{x-z} + xe \tag{5.144}$$

where $k_f$ and $k_r$ are rate constants, $x$ is the number of electrons $e$ transferred in the reaction, and $D$ denotes the product of the reaction, possibly being an ion adsorbed onto the surface or a new constituent resulting from an interfacial redox reaction. Assuming that the reverse reaction is negligible, then the interfacial flux of negative ions ($\vec{\Gamma}_-^b$) from

the liquid to the solid can be expressed as

$$-\frac{1}{qz}\hat{n}_s \cdot \vec{J}^b = \hat{n}_s \cdot \vec{\Gamma}_-^b \approx k_f n_-^b \tag{5.145}$$

where $\hat{n}_s$ is a unit vector normal to the interface, pointing into the solid, and $n_-^b$ is the number density or concentration of negative ions on the liquid side of the interface. This is the starting point of Gavis' derivation of the boundary condition [110]. This flux must be balanced by the transport of the ions through the fluid (Eq. 5.4) so that

$$\hat{n}_s \cdot \vec{\Gamma}_+^b = -D_+\frac{\partial n_+}{\partial r} + b_+ n_+^b E_r = 0 \tag{5.146}$$

$$\hat{n}_s \cdot \vec{\Gamma}_-^b = -D_-\frac{\partial n_-}{\partial r} - b_- n_-^b E_r = k_f n_-^b \tag{5.147}$$

where the radial components of the vectors were chosen in order to be consistent with the cylindrical geometry being described in this chapter.

To determine $n_-^b$ and the current density at the interface, three assumptions are made. First, assume a linear variation in the species densities over a diffusion sublayer thickness $d$ so that

$$\frac{\partial n_-}{\partial r} \approx \frac{(n_-^b - n_{-o})}{d} \tag{5.148}$$

with $n_{-o}$ the negative ion density in the core region of the fluid. Second, assume that the bulk carrier densities are only perturbed from their equilibrium levels so that $n_{-o} \approx n_o$. Lastly, it is assumed that the portion of the current due to conduction of the negative ions can be expressed as the transference number $t_-$. From Eq. 5.147, this implies that

$$-D_-\frac{\partial n_-}{\partial r} = (1 - t_-)k_f n_-^b = t_+ k_f n_-^b \tag{5.149}$$

While the transference number was not specified in this paper, the usual definition of the transference number for binary electrolytes

$$t_\pm \equiv \pm\frac{z_\pm b_\pm}{z_+ b_+ - z_- b_-} \tag{5.150}$$

with $z_- = -z$ and $z_+$ a positive number, yields the last equality. While the transference number usually represents the fraction of the current carried by each species *in the absence of concentration gradients*, in this case, it essentially represents the ratio of the mobilities [111: Section 5]. This is an inappropriate use of the transference number, though, because it leads to an inconsistency; from Eqs. 5.147 and 5.149, the transference number should depend upon the electric field and not simply the properties of the ions. Furthermore, while this derivation is similar to that used to relate the interfacial current of a single reacting species in an aqueous solution to the ion properties, the assumptions used in the aqueous solution derivation are quite different; electroneutrality is assumed, so that there isn't a significant net charge in the bulk of the fluid.

Despite the inconsistency inherent in the transference number assumption, it is in-

structive to continue the derivation of the boundary condition. Substituting for the gradient in the negative ion carrier density and solving for the volume density near the interface gives

$$n_-^b \approx \frac{D_- n_o}{D_- + t_+ k_f d} \tag{5.151}$$

It then follows that the interfacial current density is given by

$$\hat{n}_s \cdot \vec{J}^b \approx \frac{-qzD_- k_f n_o}{D_- + t_+ k_f d} \tag{5.152}$$

While this is similar in form to the Abedian-Sonin boundary condition (Eq. 5.62) if $\rho^b \ll \rho^w$, the physical interpretation is completely different due to the assumptions involved in the derivation. To obtain the final form of the boundary condition, it is assumed that this current density must be augmented by ohmic conduction. Comparing this result with Eq. 5.44 then indicates that the above current density is due to diffusion and the gradient in the net charge density at the interface can be expressed as

$$\vec{n}_s \cdot \nabla \rho \equiv \alpha \approx \frac{qzD_- k_f n_o}{D_m(D_- + t_+ k_f d)} \tag{5.153}$$

For slow reaction rates such that $t_+ k_f d \ll D_-$, $\alpha$ is essentially independent of the sublayer thickness. For fast reaction rates such that $t_+ k_f d \gg D_-$, $\alpha$ varies with the inverse of the sublayer thickness as

$$\alpha \approx \frac{qzD_- n_o}{D_m t_+ d} \tag{5.154}$$

where the numerator on the right side is a fluid dependent constant, independent of the flow rate. Note that in this limit $\alpha$ is independent of the solid in contact with the fluid. This is the boundary condition derived, and used, by Gavis [110].

Before proceeding further it is important to identify the fundamental shortcomings of this boundary condition. The first one was the use of the transference number which was already discussed. The second is that the current density expressed by Eq. 5.152 only leads to a current passing from the solid into the liquid because only negative ions were assumed to react at the interface and the reverse reaction of negative ions going from the solid into the liquid was neglected. While this may have been a reasonable assumption for pipe flow, in which there was only a single solid/liquid interface, this leads to inconsistencies when applied to the flow between rotating, identical, bare metal cylinders. For example, applying Eq. 5.152 to Eq. 5.115 indicates that $R_2 A_2 = -a A_4$, which contradicts Eq. 5.117 unless the current density is zero. Thirdly, Eq. 5.152 describes a current density that is *independent of the terminal constraints.* If the terminals are open-circuited, rather than short-circuited, the interfacial current density should go to zero, but that is not possible with this boundary condition. A fourth shortcoming is in the assumption that the ohmic contribution must be added to the current density in Eq. 5.152. This effectively double counts the ohmic contribution because the use of transference numbers already accounts for the conduction current. While it is clear that the underlying physics incorporated into this boundary condition are questionable,

reasonable results can be obtained when incorporating boundary conditions that have the form of an imposed charge density gradient into the electrification model.

To apply this boundary condition to the electrification model, the general normalized equations of Eqs. 5.127, 5.128, and 5.129 will be used. To this end, the boundary conditions for the charge transfer are related to the transport of charge to the interface by Eq. 5.153 or

$$\frac{\partial \rho}{\partial r} = \begin{cases} -\alpha_1 & r = a \\ \alpha_2 & r = R_2 \end{cases} \tag{5.155}$$

Using Eq. 5.114, it follows that

$$-\rho_1^b g(a+\delta_1, a) + \rho_o g(a,a) = -\alpha_1 \lambda_D f(a+\delta_1, a) \tag{5.156}$$

$$\rho_2^b g(R_2, R_2-\delta_2) - \rho_o g(R_2, R_2) = \alpha_2 \lambda_D f(R_2, R_2-\delta_2) \tag{5.157}$$

Again, using the normalizations of Tables 5.1 and 5.2 and taking the limit as the cylinder radii become large compared to the diffusion sublayer thicknesses and the Debye length gives

$$\rho_1^b \coth\left(\frac{a\delta}{\lambda_D}\right) - \rho_o \operatorname{csch}\left(\frac{a\delta}{\lambda_D}\right) \approx \alpha_1 \lambda_D \tag{5.158}$$

$$\rho_2^b \coth\left(\frac{\delta}{\lambda_D}\right) - \rho_o \operatorname{csch}\left(\frac{\delta}{\lambda_D}\right) \approx \alpha_2 \lambda_D \tag{5.159}$$

where the underscore beneath the equation number indicates that the equation contains non-dimensional variables. To be consistent with the assumption of $\delta \gg \underline{\lambda}_D^2$ and with Eq. 5.128 indicating $\underline{\rho}_o \ll \underline{\rho}_{1,2}^b$, it follows that

$$\rho_1^b \approx \alpha_1 \lambda_D \tanh\left(\frac{a\delta}{\lambda_D}\right) \tag{5.160}$$

$$\rho_2^b \approx \alpha_2 \lambda_D \tanh\left(\frac{\delta}{\lambda_D}\right) \tag{5.161}$$

Substitution into Eq. 5.128 then gives the charge density as

$$\rho_o = \frac{2\lambda_D^2}{1-a^2}\left[a\alpha_1 \operatorname{sech}\left(\frac{a\delta}{\lambda_D}\right) + \alpha_2 \operatorname{sech}\left(\frac{\delta}{\lambda_D}\right)\right] \tag{5.162}$$

which is independent of the terminal constraints. Eq. 5.129 then gives the open-circuit voltage as

$$v^{oc} = a\alpha_1 \operatorname{sech}\left(\frac{a\delta}{\lambda_D}\right)\left[\frac{1}{2} + \frac{\ln(a)}{1-a^2}\right] + \alpha_2 \operatorname{sech}\left(\frac{\delta}{\lambda_D}\right)\left[\frac{1}{2} + a^2\frac{\ln(a)}{1-a^2}\right] \tag{5.163}$$

and Eq. 5.127 then gives the short-circuit current as

$$I = -\frac{2}{-\ln(a) + \frac{1}{\sigma_1}\ln\left(\frac{a}{R_1}\right)}\left(v^{oc} - V_o\right) \qquad (5.164)$$

Notice that if the sublayer thickness is further constrained by $\delta \ll \underline{\lambda}_D$, then all of the $\mathrm{sech}(\delta/\underline{\lambda}_D)$ and $\mathrm{sech}(\underline{a}\delta/\underline{\lambda}_D)$ terms go to one. In this limit, the only possible way that the charge density or terminal variables can depend upon the flow rate is through the boundary condition parameters $\alpha_1$ and $\alpha_2$.

As in the previous subsection, the effects of the reaction rate can be explored through limiting cases. When the interfacial charge transfer is reaction limited ($t_+ k_f d \ll D_-$), $\alpha_1$ and $\alpha_2$ are constants, independent of the flow rate. If the sublayer thicknesses are also small compared to the Debye length, then the charge density and terminal variables are independent of the flow rate. In the transport limited case ($t_+ k_f d \gg D_-$), $\underline{\alpha}_2 = \underline{\alpha}_1 \,/\, \underline{a} = \beta/\delta$ with $\beta$ a non-dimensional parameter that is dependent upon the fluid properties but not the flow rate and the solid materials. If the sublayer thicknesses are small compared to the Debye length, results similar to Morin et al. are obtained. Note also that for this boundary condition, the core charge density is found to be independent of the applied voltage because the interfacial current density is independent of the terminal constraints.

Now consider identical bare metal cylinders having a radii ratio of $\underline{a} = 0.75$. The positive charge densities and the increase in charge density with rotation rate, shown in Figs. 3.9, 3.12, and 3.28, indicate that the $\alpha$ in Eq. 5.162 are positive.[4] The variation in open-circuit voltage and short-circuit current with rotation rate then provides information about the reaction rates at the interface. When the reaction rate is fast ($t_+ k_f d \gg D_-$), the core charge density and the terminal variables ($v$ and $i$) always have opposite polarities. In contrast, when the reaction rate is slow ($t_+ k_f d \ll D_-$), the charge density and the terminal variables have the *same* polarity for $\delta \lesssim 0.7\underline{\lambda}_D$ but *opposite* polarities if $\delta \gtrsim 0.7\underline{\lambda}_D$. This is significant because it indicates that the polarity of the terminal variables can change with the flow rate. While this type of polarity reversal, shown in Figs. 3.12 and 3.11, is consistent with the reaction rates being considered slow, the opposite variation (slightly negative voltage and current at low rotation rates but positive at high rotation rates), shown in Fig. 3.28, is not predicted.

With pressboard covering the inner cylinder the charge densities are slightly larger than the bare metal cylinder charge densities (see Figs. 3.9 and 3.10), indicating that $\alpha_1$ is larger than $\alpha_2$ in Eq. 5.162. From Eqs. 5.163 and 5.164, this is consistent with the measured voltage and current being negative at each rotation rate and temperature while the charge densities are positive. According to the model (Eq. 5.153), this condition is satisfied as long as the inner cylinder reaction rate is faster than that on the outer cylinder.

In summary, the derivation of this boundary conditioned had several fundamental shortcomings, but the use of a boundary condition having the *form* of an imposed charge

[4]Strictly speaking, the $\alpha$ must be positive for the reactions that were assumed in the derivation of the boundary condition. If positive ions were assumed to transfer charge at the interface, a similar derivation of the boundary condition would show that the $\alpha$ become negative.

density gradient was able to describe some of the experimental observations.

## 5.8 Comparison to Experiments

In this section, several sets of experimental measurements are used to estimate the values of the interfacial parameters. In this analysis, the model incorporating the Abedian-Sonin boundary condition is used because it does not have the flaws inherent in the Gavis-Koszman boundary condition.

In order to compare the model to the experimental data, the kinematic viscosity of the oil and the molecular diffusivity of the charged species must be known as a function of temperature ($T$ in K). For this work, the kinematic viscosity $\nu$ of the oil is assumed to be given by

$$\nu = \nu_o e^{W_\nu/kT} \tag{5.165}$$

where $k = 1.38 \times 10^{-23}$ J/K$= 8.6167 \times 10^{-5}$ eV/K is Boltzmann's constant, $\nu_o = 3.956 \times 10^{-10}$ m$^2$/s and $W_\nu = 0.2725$ eV [23]. Since the ionic species are not known, the ionic diffusivity must be estimated. Empirically, the ion mobility $b$ (SI units of m$^2$/volt-sec) in hydrocarbon liquids is related to the viscosity $\eta$ (SI units of kg/m-sec) by Walden's rule as [72]

$$b\eta \approx 2 \times 10^{-11} \tag{5.166}$$

with $\eta = \rho_m \nu$ the dynamic viscosity of the liquid and $\rho_m \approx 886$ kg/m$^3$ the oil mass density [73]. The molecular diffusivity $D_m$ can then be obtained from Einstein's relation

$$\frac{D_m}{b} = \frac{kT}{q} \tag{5.167}$$

with $q$ the charge of the ion. Thus, the temperature sets the viscosity of the oil and the ionic diffusivity can be estimated from the calculated mobility and the Einstein relation. For the experiments, the diffusion sublayer thicknesses and Debye lengths are estimated to be roughly the same, varying from a few microns up to about 50 $\mu$m. In terms of the normalized variables, $\delta \approx \lambda_D$.

Representative plots of the normalized electrification data are given in Fig. 5.8 for bare metal cylinders and in Fig. 5.9 for pressboard covering the inner cylinder. The plots on the left side of each figure show the electrification data plotted against the Reynolds number and the plots on the right side show the same data plotted against the ratio of the diffusion sublayer thickness to the Debye length, using the correlation of Eqs. 5.109 and 5.97. As expected from the model, the critical parameter for the electrification is not simply the Reynolds number but the relative thickness of the sublayer to the Debye length. These figures clearly show that once the sublayer thickness becomes smaller than the Debye length, the electrification becomes larger.

The lines in both figures were obtained from the model after estimating for the values of the interfacial parameters (using the program **mod2est.for** in Appendix E). A good fit was obtained for the charge density and voltage, but the fit to the current and $D_v\rho_o$ was relatively poor due to the nature of the measurements and the estimation. In general, simultaneously fitting parameters to multiple types of measurements of the same data is

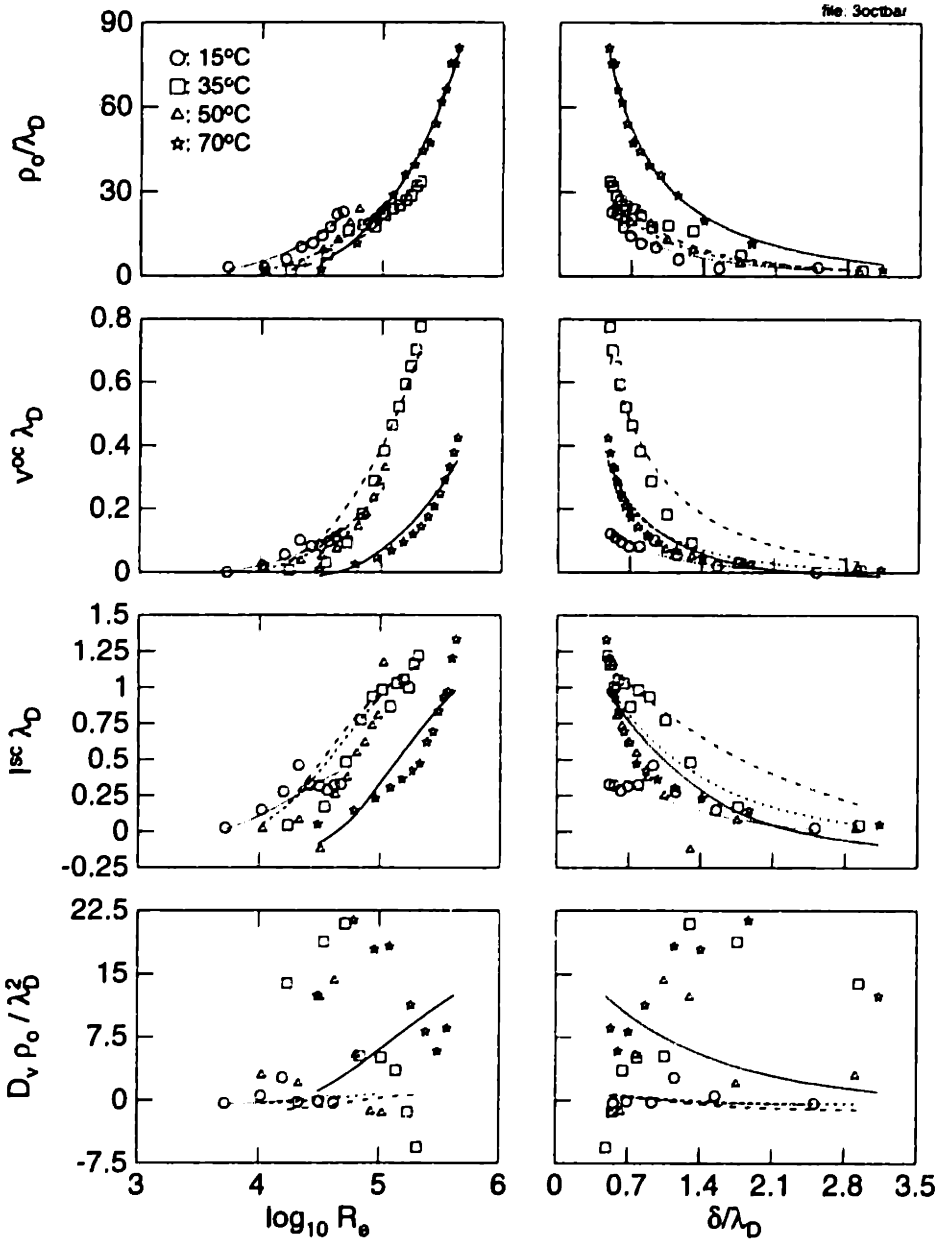


Figure 5.8: Normalized plots of the electrification data from Fig. 3.9 for bare stainless steel cylinders. At each temperature, the electrification increases dramatically as the Reynolds number $R_e$ increases and the sublayer thickness $\delta$ becomes small compared to the Debye length $\lambda_D$. The lines are obtained from fits to the electrification model, with the dimensional values for the wall charge densities and reaction velocities given in Table 5.3.

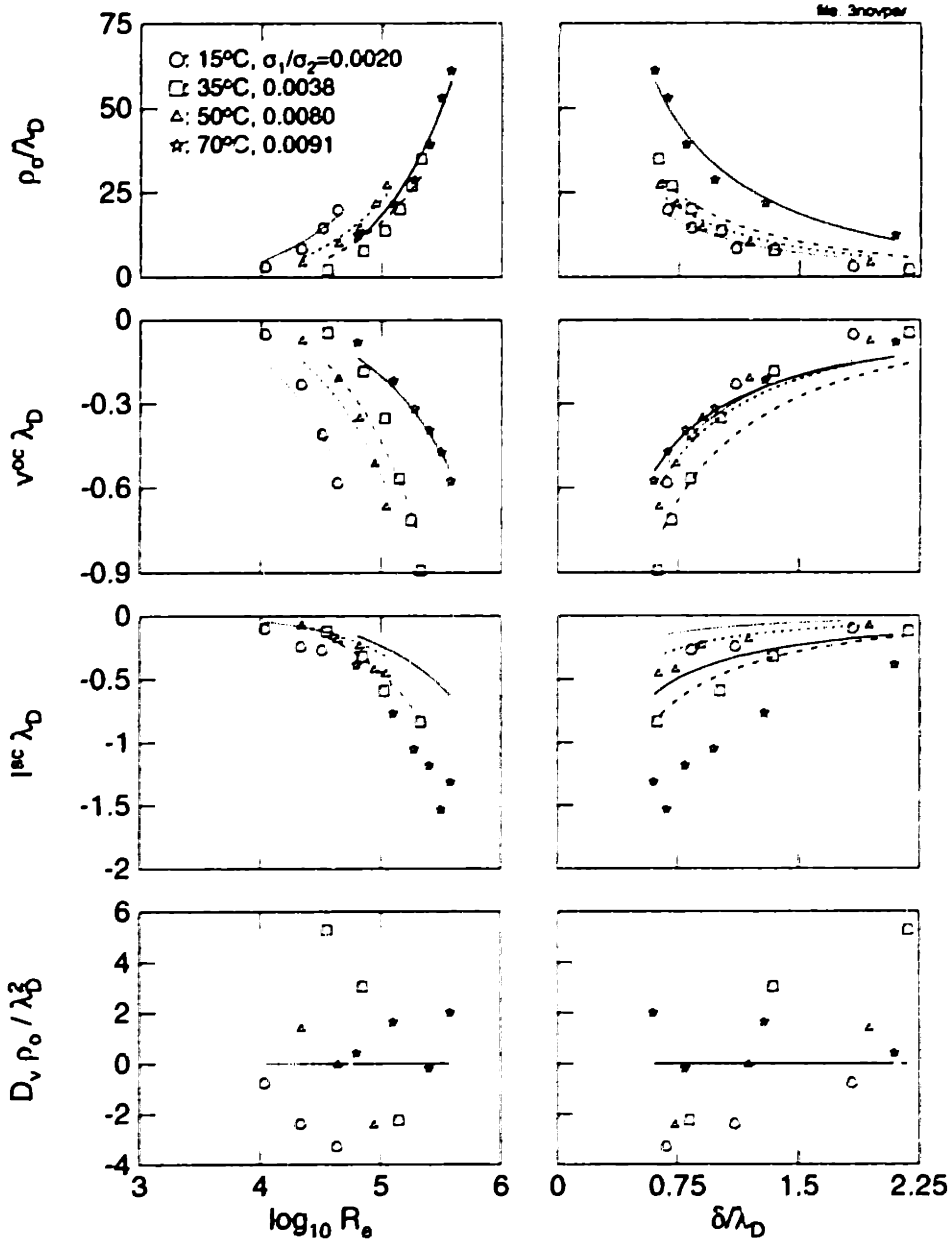


Figure 5.9: Normalized plots of the electrification data from Figs. 3.13 and 3.15 for pressboard covering the inner cylinder and a bare stainless steel outer cylinder. At each temperature, the electrification increases dramatically as the Reynolds number $R_e$ increases and the sublayer thickness $\delta$ becomes small compared to the Debye length $\lambda_D$. The lines are obtained from fits to the electrification model, with the dimensional values for the wall charge densities and reaction velocities given in Table 5.3. The relative pressboard conductivity at each temperature is indicated.

complicated, but the task is greatly simplified under open-circuit conditions. Then, the voltage and the charge density are *independent* of the reaction velocities ($\underline{k_i}$) and only the $\underline{\rho_i^w}$ need to be determined. Furthermore, the equations for the open-circuit voltage and charge density can be inverted to give

$$P_1 = \frac{a\rho_1^w}{\sinh\left(\frac{a\delta}{\lambda_D}\right)} = \frac{v^{oc}\lambda_D}{\ln(a)} - \frac{1}{2}\frac{\rho_o^{oc}}{\lambda_D}\left[a^2 + \frac{(1-a^2)}{2\ln(a)}\right] \qquad (\underline{5.168})$$

$$P_2 = \frac{\rho_2^w}{\sinh\left(\frac{\delta}{\lambda_D}\right)} = -\frac{v^{oc}\lambda_D}{\ln(a)} + \frac{1}{2}\frac{\rho_o^{oc}}{\lambda_D}\left[1 + \frac{(1-a^2)}{2\ln(a)}\right] \qquad (\underline{5.169})$$

where $P_1$ and $P_2$ are parameters for describing the contributions of each interface. This allows the values of $\underline{\rho_i^w}$ at each interface to be determined at a given rotation rate and temperature. A least-squares fit then gives the best value for the $\underline{\rho_i^w}$ at each temperature. As part of this estimation a "goodness-of-fit" number $\chi^2$, defined as

$$\chi^2_{P_i} \equiv \sum_{n=1}^{N}\left[\frac{P_i^{measured} - P_i^{calculated}}{P_i^{calculated}}\right]^2 \qquad (5.170)$$

for $N$ data points, was calculated. Typically, good fits had $\chi^2 \lesssim 1$ while poor fits had $\chi^2 \gg 1$.

To obtain information about the reaction velocities, data taken under short-circuited or applied voltage conditions must be used. For example, Eq. 5.133 shows that $\gamma$, the effective impedance between the cylinders and, from Eq. 5.138, the ratio of the open-circuit voltage to the short-circuit current, depends upon the flow rate through the sublayer thicknesses. While others have *assumed* that the reaction velocities are large enough to make the interfacial charge transfer limited by the charge transport from the fluid bulk [25,99], Fig. 5.10 shows the cell impedance varying with sublayer thickness, which suggests that the reaction velocities are "finite." Unfortunately, simultaneously estimating the velocities for both interfaces is difficult.

Several different approaches for estimating the reaction velocities were tried. The first was to find the reaction velocities which minimized the least-squares error between the short-circuit current measurements and Eq. 5.132, but any errors in estimating the $\underline{\rho_i^w}$ contributed to errors in estimations of the reaction velocities. The second method was to simultaneously use measurements of the open-circuit voltage and the short-circuit current to calculate $\gamma$. Minimizing the error between these values of $\gamma$ and Eq. 5.133 eliminated the dependence on the $\underline{\rho^w}$ estimation, but the current occasionally reversed polarity, passing through zero, which caused the estimation to be sensitive to noise in the current measurement. Furthermore, both of these approaches relied upon the slightly different flow rate dependence of the contributions from each interface. The third, and final approach, was similar to that used to obtain $P_1$ and $P_2$. Combining Eqs. 5.133,

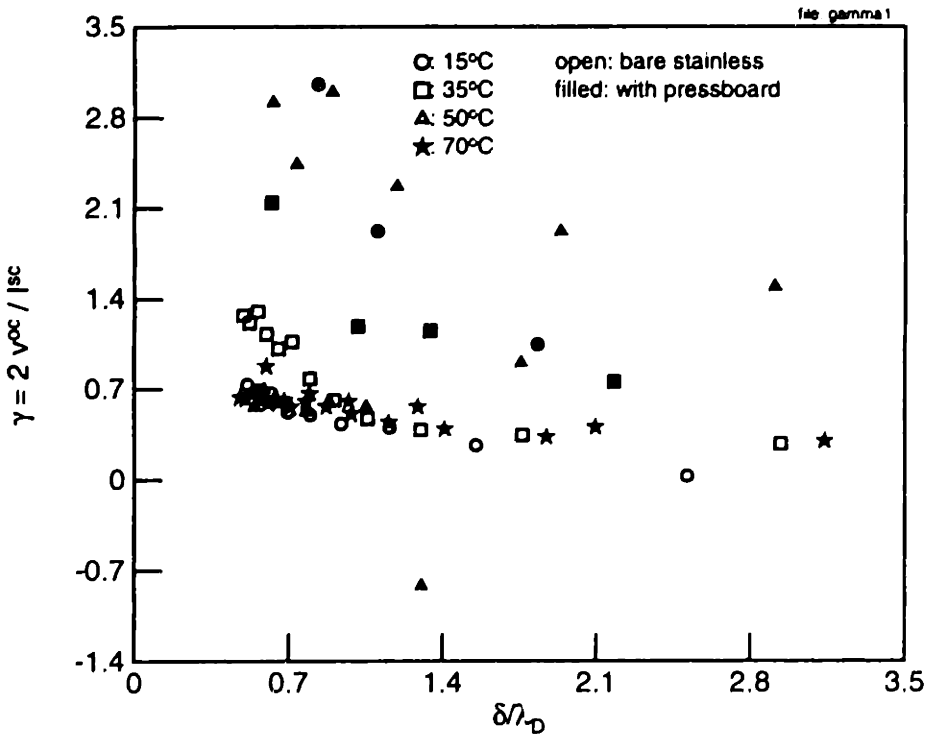


Figure 5.10: Normalized plot of $\gamma$, the ratio of the open-circuit voltage to the short-circuit current electrification data, for the data from Figs. 5.8 and 5.9. The value of $\gamma$ changes with the sublayer thickness, indicating that the interfacial reaction velocities cannot be taken as "infinite."

5.138, and 5.140 gives

$$P_3 = \frac{1}{k_1 \lambda_D \sinh\left(\frac{a\delta}{\lambda_D}\right)} = -1 + \frac{\ln\left(\frac{a}{R_1}\right)}{\sigma_1 \ln(a)} + \frac{v^{oc}}{I^{sc}} \left\{ a^2 D_v \rho_o + \frac{\left[-2 + \frac{1}{2}(1-a^2) D_v \rho_o\right]}{\ln(a)} \right\} \quad (5.171)$$

$$P_4 = \frac{1}{k_2 \lambda_D \sinh\left(\frac{\delta}{\lambda_D}\right)} = -1 + \frac{\ln\left(\frac{a}{R_1}\right)}{\sigma_1 \ln(a)} + \frac{v^{oc}}{I^{sc}} \left\{ D_v \rho_o + \frac{\left[-2 + \frac{1}{2}(1-a^2) D_v \rho_o\right]}{\ln(a)} \right\} \quad (5.172)$$

where $P_3$ and $P_4$ provide the contributions from each interface. A least-squares fit then gives the best value for the $\underline{k}_i$ at each temperature, with the $\underline{k}_i$ constrained to be positive. A representative plot of the measured and estimated values of the $P_i$ are given in Fig. 5.11. The relatively large variation in the measured values of $P_3$ and $P_4$ is indicative of the uncertainty in the measurements of $I^{sc}$ and $D_v \rho_o$. In Fig. 5.9, $D_v \rho_o$ was calcu-

lated to be zero because the conductivity of the pressboard, estimated from transient decay measurements, was not known accurately and the reaction velocities could not be determined accurately.

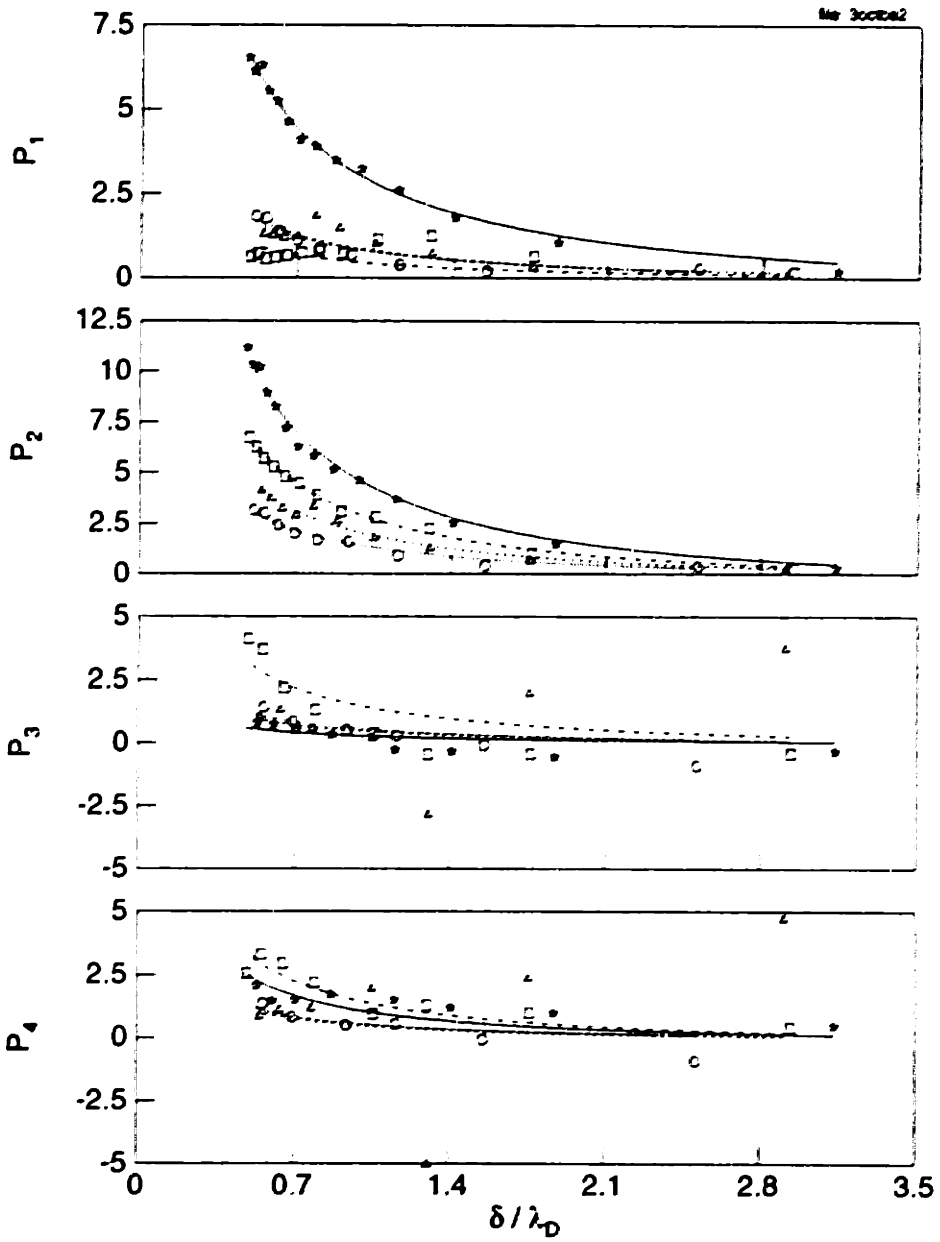


Figure 5.11: Plots of the $P_i$ used in the parameter estimation of the bare stainless steel cylinder data in Fig. 5.8.

A representative listing of the estimated parameters is given in Table 5.3. The first set of data with stainless steel cylinders shows that the $\rho_i^*$ and the $k_i$ tend to increase with

temperature. The $\rho^w$ is also larger on the outer cylinder, consistent with Fig. 3.9 showing positive measured charge densities and negative terminal measurements. The second set of data shows the $\rho^w$ being essentially the same, at least for the lower temperatures. As observed in the plots on the left side of Fig. 3.28, the charge densities were positive and the open-circuit voltage tended to be negative. After reaching 70°C the $\rho^w$ on the outer cylinder became significantly larger than that on the inner cylinder, and the voltage had the same polarity as the charge density. Subsequent measurements, given by the third set of stainless steel cylinder data and the plots on the right side of Fig. 3.28, show that this "conditioned" behavior of the system persisted. This analysis also showed that copper tends to have a slightly lower $\rho^w$ than the stainless steel. In contrast, pressboard tended to have a slightly larger $\rho^w$ than the stainless steel. Quantitatively, these results are consistent with past estimates of the $\rho^w$ [2,25,112]. These measurements are also comparable to recent pipe flow measurements and analysis that have shown a $\rho^w$ of 5 mC/m$^3$ and a reaction velocity of $3.8\times10^{-6}$ m/s for room temperature pressboard [113].

Using these estimated values for the wall charge density and assuming an Arrhenius temperature dependence, the activation energy associated with the wall charge density could be calculated. More specifically, it was assumed that $\rho_i^w$ obeyed the relation

$$\ln(\rho_i^w) = c_i - \frac{W_i}{kT} \tag{5.173}$$

where $c_i$ is a scaling coefficient, $W_i$ is the activation energy, $k$ is Boltzmann's constant, and $T$ is the temperature in Kelvin. A least-squares fit was then performed to determine the $c_i$ and $W_i$ for both interfacial materials in each experiment. A summary of the estimated activation energies, given in Table 5.4, indicates that the copper and the stainless steel interfaces tend to have larger activation energies ($\sim$ 0.25 eV) than the pressboard interface ($\sim$ 0.16 eV). The values for the $c_i$ are not listed because they had large uncertainties.

Estimations were also performed on the electrification data of Figs. 3.40, 3.41, and 3.42, where the additive BTA was added to the oil. Good estimates of the volume charge densities on the liquid side of the interfaces were obtained, but the uncertainty in the pressboard conductivity prevented an accurate determination of the reaction velocities. Fig. 5.12 shows the estimated $\rho^w$ as the BTA concentration was varied. In general, the BTA reduced the $\rho^w$ for both the pressboard/oil and the stainless steel/oil interfaces with approximately 7 ppm BTA being a critical concentration for the reduction. Increasing the concentration beyond this yielded slight further reductions in $\rho^w$. From Table 5.4, the BTA did not appear to significantly affect the temperature dependence of the wall charge densities.

An implicit assumption in these estimates of the wall charge densities is that the mobility of the ions is not affected by the BTA. After all, the mobility was assumed to be determined from Eqs. 5.165 and 5.166, independent of the BTA concentration. With the mobility held constant, in order for the BTA to reduce the oil conductivity, the number density of the ions had to be reduced by the BTA. In the opposite limit, it can be assumed that the number density of the ions is held constant and the BTA affects the

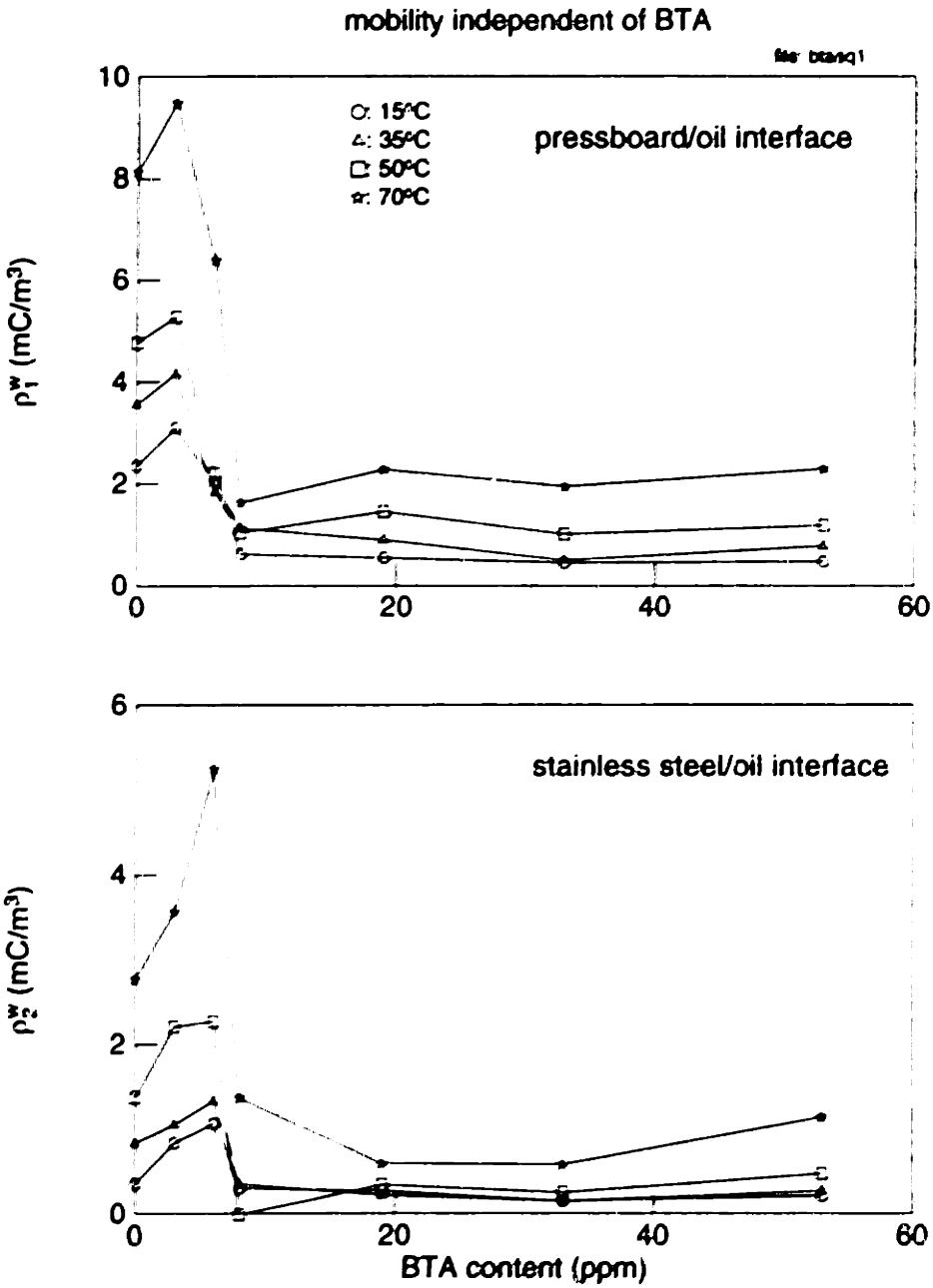


Figure 5.12: Estimated volume charge densities on the liquid side of each interface as the BTA concentration varied. These estimations used the open-circuit data and were independent of the reaction rates. These plots show that the BTA reduced the charge density at both the pressboard and metal interfaces.

| Cylinders Inner | Cylinders Outer | Figure | Temp. °C | $\rho_1^w$ mC/m$^3$ | $k_1$ $10^{-6}$ m/s | $\rho_2^w$ mC/m$^3$ | $k_2$ $10^{-6}$ m/s |
|---|---|---|---|---|---|---|---|
| stainless | stainless | 3.9, 5.8 | 15 | 1.53 | 3.23 | 2.83 | 2.23 |
| | | | 35 | 2.22 | 9.29 | 5.57 | 6.15 |
| | | | 50 | 1.22* | 5.00 | 8.37 | 3.49 |
| | | | 70 | 9.54 | 53.6 | 15.7 | 9.36 |
| | | 3.28 (left) | 15 | 1.82 | 1.21 | 1.93 | 0.91 |
| | | | 35 | 2.99 | — | 3.21 | — |
| | | | 50 | 4.61 | — | 5.25 | — |
| | | | 70 | 7.27 | — | 12.8 | — |
| | | 3.28 (right) | 15 | 1.54 | — | 2.63 | — |
| | | | 35 | 2.64 | 92.6 | 4.26 | 67.0 |
| | | | 50 | 3.49 | 22.3 | 5.76 | — |
| | | | 70 | 5.81 | 89.2 | 10.4 | 43.5 |
| copper | stainless | 3.33 | 15 | 0.35 | — | 0.58 | — |
| | | | 35 | 0.77 | — | 1.46 | — |
| | | | 50 | 1.27 | — | 2.43 | — |
| | | | 70 | 2.18 | — | 4.29 | — |
| HiVal | stainless | 3.13, 3.15, 5.9 | 15 | 7.11 | — | 0.45* | — |
| | | | 35 | 10.1 | — | 1.58 | — |
| | | | 50 | 15.0 | — | 1.61 | — |
| | | | 70 | 17.6 | — | 11.2 | — |
| HiVal (over copper) | stainless | 3.10 | 15 | 3.4 | 0.03 | 0.02* | 0.04 |
| | | | 70 | 10.2 | — | 3.58 | — |
| | | | 15 | 3.56 | — | 0.13* | — |
| | | | 35 | 5.96 | — | 0.89 | — |
| | | | 50 | 7.71 | 2.84 | 1.84 | 3.12 |
| | | | 70 | 9.43 | — | 3.66 | — |

Table 5.3: Representative estimated values for the interfacial parameters using the Abedian-Sonin boundary condition. Asterisked values indicate a poor fit in the estimation, as calculated from Eq. 5.170.

mobility. The BTA then changes the conductivity by changing the mobility. Assuming the viscosity is independent of the BTA concentration [69], then the ion mobility can be expressed in terms of the measured conductivities as

$$b_{(\text{with BTA})} = b_{(\text{no BTA})} \frac{\sigma_{2\ (\text{with BTA})}}{\sigma_{2\ (\text{no BTA})}} \tag{5.174}$$

At the low BTA concentrations, where the oil conductivity actually increased, the mobility is calculated to increase as well. From Eq. 5.167, the molecular diffusivity is also affected by the BTA and the reduced mobility does not affect the normalizations for the Debye length, the open-circuit voltage, or the short-circuit current. Instead, the reduced mobility causes a decrease in the normalized volume charge density, which increases the sensitivity of the $\rho_i^w$ estimation to the terminal voltage. As shown in Fig. 5.13, the $\rho_1^w$ tends to decrease as the BTA concentration increases, but the decrease is not as dramatic

| Inner cylinder | $W_1$ (eV) | Outer cylinder | $W_2$ (eV) | Figure |
|---|---|---|---|---|
| stainless | 0.29±0.07 | stainless | 0.26±0.01 | 3.9, 5.8 |
| | 0.22±0.01 | | 0.29±0.04 | 3.28 (left) |
| | 0.20±0.01 | | 0.21±0.02 | 3.28 (right) |
| copper | 0.28±0.01 | stainless | 0.31±0.02 | 3.33 |
| HiVal | 0.15±0.02 | stainless | 0.53±0.26 | 3.13, 3.15, 5.9 |
| HiVal | 0.16±0.01 | stainless | 0.36±0.02 | 3.10 |
| (over copper) | 0.19±0.02 | | 0.32±0.01 | 3.40 (0 ppm BTA) |
| | 0.17±0.03 | | 0.24±0.05 | 3.40 (3 ppm BTA) |
| | 0.17±0.10 | | 0.25±0.06 | 3.40 (6 ppm BTA) |
| | 0.15±0.08 | | 0.14±0.38 | 3.41 (4 ppm BTA) |
| | 0.14±0.04 | | 0.24±0.09 | 3.41 (8 ppm BTA) |
| | 0.22±0.01 | | 0.13±0.07 | 3.41 (19 ppm BTA) |
| | 0.24±0.06 | | 0.21±0.07 | 3.42 (33 ppm BTA) |
| | 0.23±0.03 | | 0.23±0.05 | 3.42 (52 ppm BTA) |
| | 0.24±0.02 | | 0.26±0.06 | 3.42 (53 ppm BTA) |

Table 5.4: Calculated activation energies for the estimated wall charge densities of Table 5.3 and Fig. 5.12, assuming an Arrhenius temperature dependence.

as that shown in Fig. 5.12. This suggests that either operational mechanism for the BTA, reducing the ion number density or the ion mobility, leads to a reduction in $\rho_1^w$. While Fig. 5.13 also shows the $\rho_2^w$ reversing polarity as the BTA concentration increases, the numerical fit to the data was relatively poor. This, coupled with the observation that the wall charge densities do not always monotonically increase with temperature, suggests that the simple model for a BTA dependent mobility is probably not reasonable. Undoubtedly, the BTA affects both the number density of the ions and the ion mobility, but the results obtained with the mobility independent of the BTA concentration appeared to be more physically reasonable.

## 5.9 Discussion

The primary objectives of this chapter were to outline an electrification model in its most general sense and to determine if the commonly postulated boundary conditions for the interfacial redox reactions accurately represent the interface. It was found that under some limiting conditions, both the Abedian-Sonin and the Gavis-Koszman boundary conditions give similar results, but the Abedian-Sonin condition is more general and does not have the theoretical flaws inherent in the Gavis-Kosman model.

Using the Abedian-Sonin boundary condition, the model was able to explain a wide range of operating conditions. Under open-circuit conditions, without current flowing across the interfaces, estimates of the volume charge densities on the liquid side of the interfaces, provide good fits between the model and the measured data. Under short-circuit and applied voltage conditions, when current flows across the interfaces, the fits

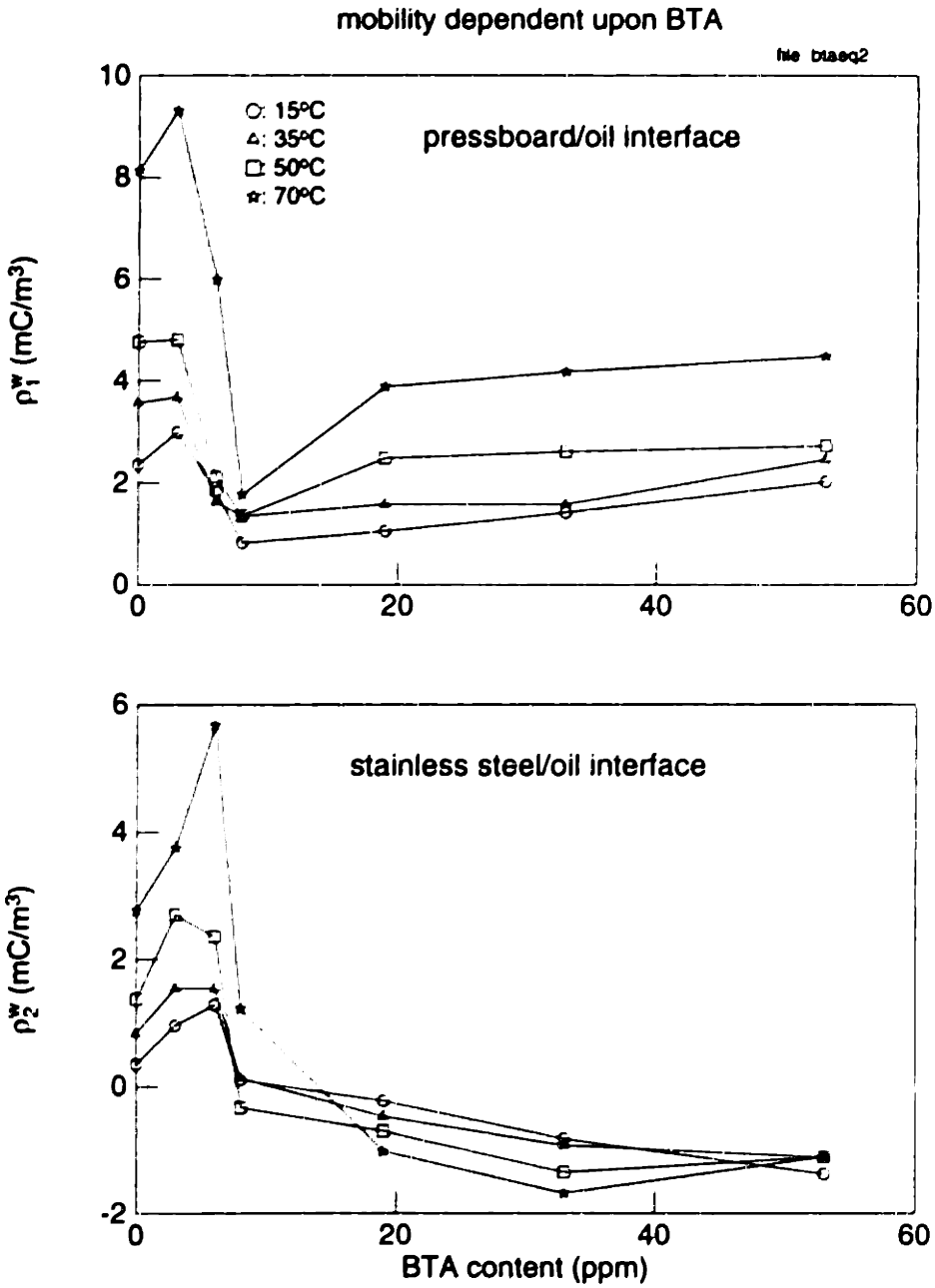


Figure 5.13: Estimated volume charge densities on the liquid side of each interface as the BTA concentration varied, assuming that the BTA affected the ionic mobility. These estimations used the open-circuit data and were independent of the reaction rates. These plots show that the BTA tended to decrease the wall charge densities, similar to those in Fig. 5.12, and also caused a polarity reversal for the stainless steel/oil interface.

were poor and the measured data indicated that the reaction velocities for the interfacial charge transfer could not be taken as "infinite." Indeed, it is evident that the passage of current through the interface can affect the charge density measurements, indicating that the chemical reactions at the interface cannot maintain the equilibrium charge density.

One of the short-comings of this model is the ability to describe the effects of an applied voltage or accumulated surface charge on the volume charge density. More specifically, since the measured slope of the charge density variation with applied voltage for bare metal electrodes was positive, the reaction velocities cannot be considered identical, large and finite since that leads to a negative slope. Even though some of the experimental measurements show the slope becoming negative for high rotation rates, when the slope reverses polarity it is usually of a small magnitude and may be the result of inaccuracies in the measurements. The only way to explain this variation, is to assume that the bare metal interfaces are not the same, only being nominally "identical." With different reaction rates at each interface, positive slopes are then possible. While this reasoning was used to explain how the volume charge density and terminal measurements had the same polarity, positive slopes were also obtained when the interfaces were apparently "identical," having the same $\rho^w$'s so that the charge density and terminal measurements had the opposite polarity. As a result, the model has trouble self-consistently describing all of the electrification behavior.

It is not surprising that these initial attempts to describe the field dependence of the charge density are unsatisfactory. Part of the reason is that the boundary conditions were initially developed for flow in conducting, not insulating, pipes and it is reasonable to expect the interfacial charge transfer to be affected by the accumulation of charge on an insulating surface. In addition, these postulated conditions do not appear to account for the desorption of charged species from the solid into the liquid. One way of seeing this is to consider the system shown in Fig. 5.14. When a positive voltage is applied, it is reasonable to assume that a current flows through the liquid with the interfacial current density going from the metal electrode into the liquid. Using the general form of the postulated boundary conditions given by Eqs. 5.13 and 5.14, the interfacial fluxes of each species can be expressed as

$$\Gamma_{\pm}^{b} = -k_{\pm}(n_{\pm}^{b} - n_{\pm}^{w}) = \pm \Upsilon V_o \tag{5.175}$$

where $\Upsilon$ is a positive constant. Solving for the volume carrier density near the interface gives

$$n_{\pm}^{b} = n_{\pm}^{w} \mp \frac{\Upsilon V_o}{k_{\pm}} \tag{5.176}$$

For positive applied voltages, the surface charge $\sigma_{ru}$ is also positive but $n_{+}^{b} < n_{+}^{w}$ and $n_{-}^{b} > n_{-}^{w}$, indicating that only the shielding effect of the bipolar medium is predicted, never desorption. A similar conclusion can be reached for negative applied voltages.

An alternative to the postulated boundary conditions presented here is to build upon the approach outlined in Subsection 5.7.2 without making all of the limiting assumptions. In particular, by starting with interfacial chemical reactions and including the reverse reactions so that desorption from the solid to the liquid is possible, a more physical boundary condition that applies to both open and short-circuit conditions and both

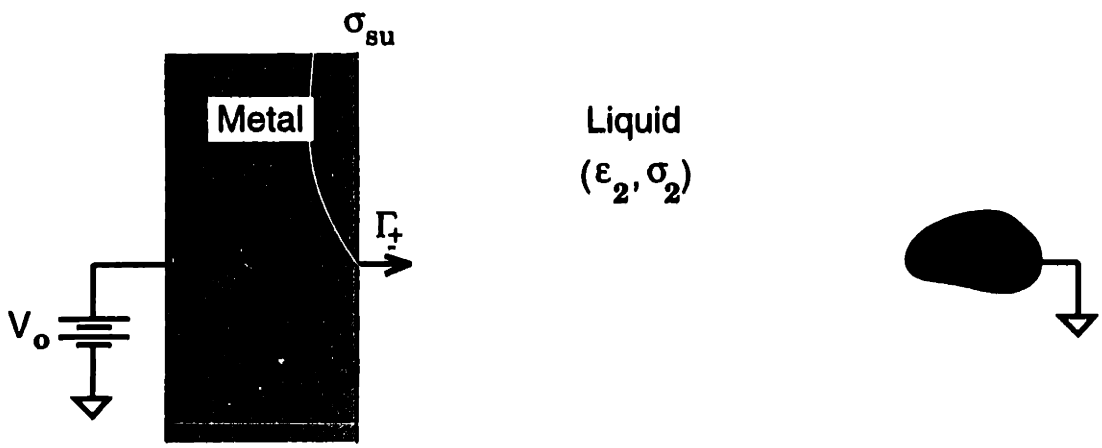


Figure 5.14: A simplified schematic of an isolated interface between a metal and a liquid dielectric having permittivity $\epsilon_2$ and conductivity $\sigma_2$. By applying a voltage $V_o$, a surface charge $\sigma_{su}$ develops and current flows through the liquid. The interfacial fluxes of the ionized species in the liquid are given by $\Gamma_\pm$. The bulk of the liquid is grounded by a perfectly conducting electrode far from the interface.

conducting and insulating solids can be obtained.

# Chapter 6

# Electrification Model using Interfacial Chemical Reactions

One of the fundamental unknowns in models for flow electrification by insulating liquids is the boundary condition for charge transfer at the interface. With the ions responsible for the conduction in the liquid usually unknown and present in trace quantities, the boundary conditions must be postulated, as in the models of the previous chapter. In an attempt at developing a more fundamental understanding of this boundary condition, this chapter develops a chemical reaction based boundary condition for charge transfer at the interface between the solid and liquid phases. This boundary condition is then used in an electrification model for comparison to the steady state data.

## 6.1 Introduction

In the last chapter an electrification model which used an interfacial "wall" charge density $\rho^w$ boundary condition (Eq. 5.62) was correlated to a wide range of experimental measurements. Generally, this model was in reasonable agreement with the data and significant results were obtained, such as the temperature and BTA dependence of the $\rho^w$. Despite its successes, this model was also incomplete. It could not explain the accumulated surface charge effects on the volume charge density and required different interfacial material properties on the nominally identical inner and outer cylinders in order to describe both the increases in core charge density with applied voltage and the situations in which the charge density and terminal quantities had the same polarity. Part of this shortcoming is due to the boundary condition being postulated, so that there isn't a good physical model for the charge transfer. Even though a physicochemical derivation of the boundary condition has recently been published [114], important physical mechanisms, such as charge desorption off of the interface, were omitted. Here, a physicochemical approach is used to develop an alternative derivation for the charge transfer boundary condition. This improved boundary condition is an extension of the postulated condition, in the sense that it includes the effects of charge desorption through the presence of a surface charge density.

The main objective of this chapter is to propose and develop a chemical reaction based

boundary condition. Section 6.2 provides a general discussion of the chemical boundary conditions pertinent to flow electrification processes, while subsequent sections provide simplified example applications of the boundary conditions. For example, Section 6.3 applies the boundary condition to a single, isolated interface and relates interfacial reaction rates to the commonly referenced zeta potential. Also in this section is a justification for simplifying the interfacial reactions of two individual ionic species in terms of the net current density and charge density. Building upon the formulations for the bulk response between concentric electrodes discussed in the previous chapter, Section 6.4 is an application of the boundary conditions to the case of stationary electrodes while Section 6.5 relates the flow induced volume charge density and terminal quantities to the interfacial parameters. The model is compared to several sets of experimental data in Section 6.6, with estimation techniques for determining values for the interfacial parameters also described. Finally, Section 6.7 provides a concluding discussion.

## 6.2 Improved Boundary Conditions

This section gives a general description for charge transfer at an interface. Just as Section 5.2 gave an overview of the fundamental relations for the chemical, electrical, and mechanical dynamics in the fluid bulk, this section gives an overview of the chemical dynamics at the interface. Only the interfacial chemical dynamics are emphasized because the interfacial constraint on the electrical and fluid mechanical dynamics were discussed in Section 5.2. In this description, the interface between the liquid and the solid phases is taken to be an infinitely thin region (in the continuum sense) which imposes boundary conditions on the bulk relations of the chemical species. The constraints described in this section assume a specific set of interfacial chemical reactions for the ionic species.

In order for a net current to pass between the fluid phase and the solid phase and an external circuit, a chemical (redox) reaction must occur at the interface or charged species must accumulate at the interface. Both of these processes can be described as heterogeneous reactions because they occur between two different phases. The following steps have been outlined for describing heterogeneous reactions [115]

1. Transport of reactants to the surface
2. Adsorption of reactants onto the surface
3. Reaction on the surface
4. Desorption of reactants (products) off of the surface
5. Transport of reactants (products) away from the surface

The transport mechanism in steps 1 and 5 is usually taken to be diffusion, but fluid convection and the migration of charged species also serve as transport mechanisms as given by Eq. 5.4. Steps 2 and 4 lead to boundary conditions on the flux of species to the interface. Step 3 is the stage where the charge transfer actually occurs.

This section is concerned with the roles of steps 2, 3, and 4 on the charged species. Since the actual chemical constituents are typically not known when impurities are important, the case given by Eq. 5.1 will be treated. Consider first the adsorption of reactants to the interface, step 2. The species can be adsorbed from the liquid side of the interface into vacancies on the interface according to the ionic equations

$$A^{+z} + V_+ \underset{k_+^r}{\overset{k_+^f}{\rightleftharpoons}} SA^{+z} \tag{6.1}$$

$$B^{-z} + V_- \underset{k_-^r}{\overset{k_-^f}{\rightleftharpoons}} SB^{-z} \tag{6.2}$$

$$C + V \underset{k_C^r}{\overset{k_C^f}{\rightleftharpoons}} SC \tag{6.3}$$

where $V_+$, $V_-$, and $V$ are the vacant sites available to each respective species, $SA^{+z}$, $SB^{-z}$, and $SC$ are the adsorbed species at the interface and $k_i^j$ denote reaction rates for the forward ($j = f$) and reverse ($j = r$) reactions for the $i$th species ($+, -, C$). The vacant sites represent the microscopic locations where the chemical reactions occur. Related examples are the diffusion of calcium through muscle, in which the calcium ions react with specific binding sites in the tissue [92,116], the surface states associated with the triboelectric contact charging of toner particles [117] and the surface states that can be present at semiconductor interfaces [118].

Once at the interface, the species can be involved in a redox reaction, typically transferring electrons, but proton transfer may also occur [1: p. A-3]. Assuming, for simplicity, that only electron transfer occurs and that the adsorbed neutral $SC$ is not involved in these redox reactions, the ionic equations corresponding to step 3 are

$$SA^{+z} + ze^- \underset{k_{SA}^r}{\overset{k_{SA}^f}{\rightleftharpoons}} SA \tag{6.4}$$

$$SB^{-z} \underset{k_{SB}^r}{\overset{k_{SB}^f}{\rightleftharpoons}} SB + ze^- \tag{6.5}$$

where $SA$ and $SB$ denote adsorbed neutral species at the interface. These new constituents can be desorbed from the interface to the liquid side of the interface in step 4 according to

$$SA \underset{k_A^r}{\overset{k_A^f}{\rightleftharpoons}} A + V_+ \tag{6.6}$$

$$SB \underset{k_B^r}{\overset{k_B^f}{\rightleftharpoons}} B + V_- \tag{6.7}$$

Thus, in addition to the three original reacting species in the bulk ($A^{+z}$, $B^{-z}$, and $C$) two more neutral species ($A$ and $B$) are also present.

Associated with each of the chemical reactions is a kinetic equation. For example, the kinetic equations for the surface states involved in the adsorption processes can be

expressed as

$$\frac{d[SA^{+z}]}{dt} = -\frac{d[V_+]}{dt} = -\frac{d[A^{+z}]^b}{dt} = k_+^f[A^{+z}]^b[V_+] - k_+^r[SA^{+z}] \quad (6.8)$$

$$\frac{d[SB^{-z}]}{dt} = -\frac{d[V_-]}{dt} = -\frac{d[B^{-z}]^b}{dt} = k_-^f[B^{-z}]^b[V_-] - k_-^r[SB^{-z}] \quad (6.9)$$

$$\frac{d[SC]}{dt} = -\frac{d[V]}{dt} = -\frac{d[C]^b}{dt} = k_C^f[C]^b[V] - k_C^r[SC] \quad (6.10)$$

where the concentrations of species at the liquid side of the interface have the superscript $b$ to indicate the concentration at the liquid boundary. In order to couple these kinetic equations to the conservation equations for the species in the bulk regions, conservation equations can also be written for the species at the surface. Similar to Eq. 5.3, the conservation equation for the surface density $\sigma_i$ of the $i$th species can be written as

$$\frac{d\sigma_i}{dt} + \hat{n}_s \cdot [\![\vec{\Gamma}]\!] = G_i' - R_i' \quad (6.11)$$

where the symbol $[\![\vec{\Gamma}]\!]$ denotes the difference in fluxes on either side of the interface, $\hat{n}_s$ is the unit vector normal to the interface and pointing from the liquid into the solid, and $G_i'$ and $R_i'$ are the surface generation and recombination rates due to the redox reactions. Letting the surface density $\sigma_X$ denote the surface concentration $[SX]$ and using the notation of Section 5.5, the conservation equations for the surface densities become

$$\frac{d\sigma_{A^+}}{dt} - \hat{n}_s \cdot \vec{\Gamma}_{A^+}^b = -(k_{SA}^f\sigma_{A^+} - k_{SA}^r\sigma_A) \quad (6.12)$$

$$\frac{d\sigma_{B^-}}{dt} - \hat{n}_s \cdot \vec{\Gamma}_{B^-}^b = -(k_{SB}^f\sigma_{B^-} - k_{SB}^r\sigma_B) \quad (6.13)$$

$$\frac{d\sigma_C}{dt} - \hat{n}_s \cdot \vec{\Gamma}_C^b = 0 \quad (6.14)$$

where the fluxes $\hat{n}_s \cdot \vec{\Gamma}_i^b$ give the flux of the species *from* the liquid phase *into* the solid phase as

$$\hat{n}_s \cdot \vec{\Gamma}_{A^+}^b = k_+^f n_{A^+}^b \sigma_{V^+} - k_+^r \sigma_{A^+} \quad (6.15)$$

$$\hat{n}_s \cdot \vec{\Gamma}_{B^-}^b = k_-^f n_{B^-}^b \sigma_{V^-} - k_-^r \sigma_{B^-} \quad (6.16)$$

$$\hat{n}_s \cdot \vec{\Gamma}_C^b = k_C^f n_C^b \sigma_V - k_C^r \sigma_C \quad (6.17)$$

These fluxes are the boundary conditions for the equations describing the species densities in the bulk region.

In this formulation, it is assumed that the reaction rates $k_i^j$ are independent of time and dependent upon the temperature, obeying an Arrhenius equation

$$k_i^j = A_i^j e^{-E_i^j/kT} \quad (6.18)$$

where $A_i^j$ is a constant, $E_i^j$ is an activation energy, and $k$ is Boltzmann's constant. The

activation energy represents the energy that the reactants require to change states and form the products. For this work, the activation energies are assumed to be independent of the applied voltage. While this may be a weak assumption, small electric fields are considered in most of this analysis and large fields are usually necessary for voltage dependent reaction rates, as in Onsager field enhanced dissociation [119]. On the other hand, it has been shown that externally applied electrical potentials influence the activation energy of some aqueous electrolytic reactions, as in the Tafel equation [64]. Since the potential difference that enters into the Tafel equation is essentially that across the thin interfacial "Stern" layer, which is relatively large compared to the diffuse portion of the double layer in aqueous solutions but small in the nonaqueous semi-insulating solutions of interest here, it appears reasonable to assume that the dynamics will be dominated by the diffuse portion of the double layer and the interfacial reaction rates can be taken as independent of the applied potential. While this may be a weak assumption, it provides a starting point for the analysis.

While the primary purpose of this subsection was to introduce the basic concepts that need to be included in a self-consistent description of the interfacial boundary condition, the general results need to be made more specific to be useful in the electrification model. Indeed, a formidable number of parameters have been introduced for describing the charge transfer at the interface which, when coupled with the model for the charge dynamics in the bulk of the liquid and solid, exceeds the ability of experimentally determining all of the parameters uniquely. As a result, additional simplifying assumptions will be made. These are discussed in more detail in the next subsection.

## 6.3 Isolated Interface

Before getting immersed in the details of the electrification model, it is useful to explore some of the implications of these chemical reaction based boundary conditions. As in Section 5.3, consider the equilibrium case of a single liquid/solid interface that is far from all electrodes, as shown in Fig. 5.1. The analysis deriving the carrier densities and potential distribution in Section 5.3 is still applicable. The only difference comes in the relation between the zeta potential and the interfacial parameters.

### 6.3.1 Statics

In this case, the zeta potential is related to the interfacial reaction rates for each charge carrier. To obtain this relation, first notice that the electric field on the liquid side of the interface is

$$\epsilon E_z|_{z=0} = qz(\sigma_{A^+} - \sigma_{B^-}) \tag{6.19}$$

as long as the electric field inside the solid is negligibly small, which for example would be the case for a solid that is perfectly conducting or an ohmic conductor. With the equilibrium assumption requiring the flux of each species to be zero at the interface, the species densities on the liquid side of the interface can be related to the surface densities

according to Eqs. 6.15 and 6.16, as

$$k_+^r \sigma_{A+} = k_+^f n_{A+}^b \sigma_{V+} \tag{6.20}$$

$$k_-^r \sigma_{B-} = k_-^f n_{B-}^b \sigma_{V-} \tag{6.21}$$

In principle, the surface densities of the vacant sites for the charged species ($\sigma_{V\pm}$) are related to the charge transfer and desorption reactions. Since little is known about these reactions, an approach used in modeling the diffusion of calcium ions through muscle [92] will be applied, where it is assumed that the surface densities can be written as

$$\sigma_{V_+} \equiv \sigma_+^s - \sigma_{A+} \tag{6.22}$$

$$\sigma_{V_-} \equiv \sigma_-^s - \sigma_{B-} \tag{6.23}$$

where $\sigma_+^s$ is the surface saturation density for $A^+$ and $\sigma_-^s$ is the surface saturation density for $B^-$. Physically, this implies that the total number of states (filled and unfilled) for each species remains constant. This allows the bulk-phase species density near the interface to be related to the surface density on the interface by

$$K_+ n_{A+}^b = \frac{\sigma_{A+}}{\sigma_+^s - \sigma_{A+}} \tag{6.24}$$

$$K_- n_{B-}^b = \frac{\sigma_{B-}}{\sigma_-^s - \sigma_{B-}} \tag{6.25}$$

with $K_+ \equiv k_+^f / k_+^r$ and $K_- \equiv k_-^f / k_-^r$ defined as the equilibrium rate constants for the positive and negative charge carriers. These expressions are in the form of the classical Langmuir isotherm for the equilibrium adsorption of species onto an interface [120: Section 5.3]. Solving for the carrier surface densities in Eqs. 6.24 and 6.25 and substituting the unnormalized form of Eq. 5.33 into Eq. 6.19 then gives

$$\frac{2\epsilon kT}{qz\lambda_D} \sinh\left(\frac{qz\zeta}{2kT}\right) = qz\left(\frac{K_+ n_{A+}^b \sigma_+^s}{1 + K_+ n_{A+}^b} - \frac{K_- n_{B-}^b \sigma_-^s}{1 + K_- n_{B-}^b}\right) \tag{6.26}$$

Substitution for the interfacial carrier densities from Eq. 5.24 and normalizing the variables according to

$$\underline{\zeta} = \frac{qz\zeta}{kT} \quad ; \quad \underline{K}_\pm = K_\pm n_o \quad ; \quad \underline{\sigma}_\pm^s = \frac{\sigma_\pm^s}{\lambda_D n_o} \tag{6.27}$$

then gives

$$\sinh\left(\frac{\underline{\zeta}}{2}\right) = \frac{1}{4}\left(\frac{K_+ e^{-\zeta} \sigma_+^s}{1 + K_+ e^{-\zeta}} - \frac{K_- e^{\zeta} \sigma_-^s}{1 + K_- e^{\zeta}}\right) \tag{6.28}$$

where $\lambda_D$ was defined by Eq. 5.30 and the underscore beneath the equation number indicates an equation containing non-dimensional variables. This result is an implicit relation between the zeta potential, the reaction rate constants and the saturation surface densities. An explicit solution can be found for small zeta potentials ($\underline{\zeta} \ll 1$). Then

linearizing Eq. 6.28 gives

$$\zeta \approx \frac{\frac{K_+\sigma_+^s}{1+K_+} - \frac{K_-\sigma_-^s}{1+K_-}}{2 + \frac{K_+\sigma_+^s}{(1+K_+)^2} + \frac{K_-\sigma_-^s}{(1+K_-)^2}} \tag{6.29}$$

As an example, consider $\sigma_\pm^s = \sigma^s$ so that the positive and negative saturation surface densities are equal. Then if $K_+ = K_-$ there isn't any preferential adsorption of either charged species and $\zeta = 0$. If there is a preferential adsorption of the positive charged carrier then $K_+ > K_-$ and $\zeta > 0$. If the negative charge carrier is preferentially adsorbed, then $K_+ < K_-$ and $\zeta < 0$.

Another simplification is that the availability of surface sites can be neglected when the density of occupied sites is small compared to the available number of sites. While the densities of the surface states are not known, reasonable estimates can be obtained so that the negligible occupied state assumption can be checked. For example, assume that only one polarity carrier accumulates at the interface so that the surface density $\sigma_\pm$ can be estimated from Gauss' law as

$$\sigma_\pm \approx \frac{\epsilon E}{q} \tag{6.30}$$

with $\epsilon$ a representative permittivity and $E$ the magnitude of the electric field on one side of the interface and zero on the other side. The magnitude of the electric field can be approximated by

$$E \sim \frac{\zeta}{\lambda_D} \tag{6.31}$$

where the zeta potential $\zeta$ describes the equilibrium potential of the interface. With $\zeta$ on the order of the thermal voltage ($kT/q = 25$ mV at room temperatures), $\lambda_D \approx 10$ $\mu$m, and $\epsilon \approx 10^{-11}$ F/m, then $E \sim 2500$ V/m and $\sigma_\pm \sim 1.6 \times 10^{11}$ m$^{-2}$. The surface density at saturation (when the electric field reaches the breakdown strength of the medium) can be approximated from Eq. 6.30 as $\sigma^s \approx 6.3 \times 10^{14}$ m$^{-2}$ for a breakdown field of $E = 10^7$ V/m. This compares favorably with measurements of the surface state densities on semiconducting materials of $\sigma \sim 10^{14} - 10^{15}$ m$^{-2}$ [118: Table 9.1]. When the surface is saturated with charge, the approximate distance between the charges can be calculated from the surface density as 40 nm. This is greater than the size of most molecules and suggests that all of the vacant sites are probably not filled before breakdown occurs. In summary, with $\sigma_\pm \ll \sigma^s$, typical surface densities are much smaller that the saturation densities and it is reasonable to neglect the availability of surface sites, thereby keeping the number density of vacant sites ($\sigma_{V\pm}$) essentially constant.

The effect of the vacant surface sites remaining constant is essentially contained in the equilibrium rate constant. To see this, first note that Eqs. 6.24 and 6.25 can be simplified to

$$\sigma_{A^+} \approx K_+ n_{A^+}^b \sigma_+^s \tag{6.32}$$

$$\sigma_{B^-} \approx K_- n_{B^-}^b \sigma_-^s \tag{6.33}$$

It then follows that the (normalized) transcendental equation for the zeta potential can

be written as

$$\sinh\left(\frac{\zeta}{2}\right) = \frac{1}{4}\left(K'_+ e^{-\zeta} - K'_- e^{\zeta}\right) \qquad (6.34)$$

with $K'_\pm \equiv K_\pm \sigma^s_\pm / \lambda_D$ defined as modified equilibrium rate constants. Again, an explicit solution can be found for small zeta potentials ($\zeta \ll 1$) as

$$\zeta \approx \frac{K'_+ - K'_-}{2 + K'_+ + K'_-} \qquad (6.35)$$

The discussion in Section 5.3 regarding the effect of the relative magnitudes of these modified rate constants on the zeta potential still holds.

### 6.3.2 Dynamics

While that completes the discussion of the equilibrium static distribution of charged species near the interface, of interest in electrification problems is the dynamic or kinetic description of the interface. The goal of this next discussion is to derive a boundary condition suitable for use in the electrification model. Using the fluxes for the positive and negative carriers in Eqs. 6.15 and 6.16 and the assumption that the surface sites are essentially empty ($\sigma^s_+ \gg \sigma_{A+}$, $\sigma^s_- \gg \sigma_{B-}$), the current density at the interface is given by

$$\hat{n}_s \cdot \vec{J} = qz\left[k^f_+ \sigma^s_+ n^b_{A+} - k^f_- \sigma^s_- n^b_{B-} + k^r_- \sigma_{B-} - k^r_+ \sigma_{A+}\right] \qquad (6.36)$$

Furthermore, assuming that the effective reaction rates for the charged carriers are not too different so that

$$k^f_\pm \sigma^s_\pm \equiv k^f \pm dk^f \quad ; \quad \left|dk^f\right| \ll k^f \qquad (6.37)$$

$$k^r_\pm \equiv k^r \pm dk^r \quad ; \quad |dk^r| \ll k^r \qquad (6.38)$$

the interfacial current density can then be expressed as

$$\hat{n}_s \cdot \vec{J} = k^f \rho^b - k^r \sigma_{su} + qz\left[dk^f\left(n^b_{A+} + n^b_{B-}\right) - dk^r\left(\sigma_{A+} + \sigma_{B-}\right)\right] \qquad (6.39)$$

where $\rho^b$ is the net charge density on the liquid side of the interface and $\sigma_{su}$ is the net surface charge density on the interface. For small perturbations away from equilibrium, the last term on the right side (in square brackets) will be essentially constant. Then the current density can be expressed as

$$\hat{n}_s \cdot \vec{J} = k^f \rho^b - k^r \sigma_{su} - k^f \xi \qquad (6.40)$$

with $\xi$ a constant having the units of a volume charge density and caused by the difference in reaction rates between the positive and negative charged carriers. To see how $\xi$ is related to the reaction rates and hence the zeta potential, consider the equilibrium case of $\hat{n} \cdot \vec{J} = 0$. Then

$$\xi = \rho^{b,e} - \frac{k^r}{k^f}\sigma^e_{su} \qquad (6.41)$$

where the superscript $e$ denotes equilibrium. Substituting for the volume and surface charge densities in terms of the zeta potential then gives

$$\xi = 2qzn_o \left[ \frac{1}{K^e} \sinh\left(\frac{\underline{\zeta}}{2}\right) - \sinh\left(\underline{\zeta}\right) \right] \tag{6.42}$$

with $K^e \equiv k^f/(\lambda_D k^r)$. Notice that for small zeta potentials, this can be expressed more simply as

$$\xi \approx 2qzn_o \underline{\zeta} \left( \frac{1}{2K^e} - 1 \right) \tag{6.43}$$

But the zeta potential is related to the reaction rates through Eq. 6.35. Since the modified reaction rates can be approximated by

$$\underline{K}'_{\pm} = \frac{k^f_{\pm}\sigma^e_{\pm}}{\lambda_D k^r_{\pm}} \approx K^e \left[ 1 \pm \left( \frac{dk^f}{k^f} - \frac{dk^r}{k^r} \right) \right] \tag{6.44}$$

the zeta potential is approximately

$$\underline{\zeta} \approx \frac{K^e}{2} \left( \frac{dk^f}{k^f} - \frac{dk^r}{k^r} \right) \tag{6.45}$$

and

$$\xi \approx qzn_o (1 - 2K^e) \left( \frac{dk^f}{k^f} - \frac{dk^r}{k^r} \right) \tag{6.46}$$

The rightmost term in parenthesis gives the difference in reaction rates between the carriers. If there isn't any difference, the zeta potential and $\xi$ go to zero. From this analysis, it is clear that $\xi$ plays a role similar to $\rho^w$ in Eq. 5.62. Indeed, with $k^r = 0$, the Abedian-Sonin boundary condition is obtained and $\xi = \rho^w$. Since $k^r$ is the desorption rate for ions off of the interface, setting it to zero implies the absence of desorption. This confirms the qualitative argument given in Section 5.9 that the Abedian-Sonin model doesn't predict desorption. Consistent with the Abedian-Sonin condition, if the ion mobility is constant, then $\xi \propto \sigma_2$ (when $K^e \ll 1$) [112]. The boundary condition derived here, though, also predicts that other variations with the liquid conductivity can be present, such as $\xi \propto \sigma_2^{3/2}$ when $K^e \gg 1$.

## 6.4 Stationary Case

In the last subsection, the static and dynamic boundary conditions at a single interface were discussed. In this subsection, the simplified chemical reaction based boundary condition is applied to a liquid bounded by two concentric cylinders. This is a continuation of the stationary case of the linear bipolar model discussed in Section 5.5. For the geometry described in Section 5.4, the general solutions for the volume charge density and the electric field, derived in Section 5.5, still apply. For example, the governing equation for

the charge density in the liquid, is still Eq. 5.56,

$$\rho(r) = \rho_1^b \frac{f(R_2,r)}{f(R_2,a)} + \rho_2^b \frac{f(r,a)}{f(R_2,a)} \tag{6.47}$$

and the electric field is given by

$$E_r = \begin{cases} \dfrac{A_1}{r} & R_1 < r < a \\ \dfrac{A_3}{r} + \dfrac{\lambda_D}{\epsilon_2}\left[\dfrac{\rho_2^b g(a,r) - \rho_1^b g(R_2,r)}{f(R_2,a)}\right] & a < r < R_2 \end{cases} \tag{6.48}$$

where $A_1$ and $A_3$ are integration constants determined by the boundary conditions, $\rho_1^b$ is the liquid charge density at the inner electrode interface, $\rho_2^b$ is the charge density at the outer interface, $f(\alpha,\beta)$ is defined in Eq. 5.57, and $g(\alpha,\beta)$ is defined in Eq. 5.68. Notice that once the interfacial charge densities have been determined, the charge density profile is known.

To determine the interfacial charge densities, the boundary conditions describing the interfacial charge transfer must be specified. In Section 6.3 the boundary condition was given by Eq. 6.40 which is expressed here as

$$\hat{n}_s \cdot \vec{J}_i = k_i^f \rho_i^b - k_i^r \sigma_{su,i} - k_i^f \xi_i \tag{6.49}$$

with the subscript $i = 1$ denoting the inner interface and the subscript $i = 2$ denoting the outer interface, $\sigma_{su}$ the surface charge density at the interface, $\xi$ an effective volume charge density, and $k^f$ and $k^r$ reaction rate coefficients. Since $\xi$ reflects the differences in adsorption and desorption rates for the charge carriers, just as $\rho^w$ did in the analysis of Section 5.5, the discussion regarding $\rho^w$ in that section is applicable here as well. For this analysis, the $\xi_i$ will be included in the general solution, but the focus will be on exploring the effect of the applied potential on the interfacial volume charge densities in the liquid.

The current densities at the inner and outer interfaces must be balanced by the transport of charge through the liquid to the interface. Using Eq. 5.74, these conditions can be expressed as

$$k_1^f(\rho_1^b - \xi_1) - k_1^r \sigma_{su,1} = -\left[-D_m \frac{\partial \rho}{\partial r} + \sigma_2 E_r\right]_{r=a^+} = -\frac{\sigma_2 A_3}{a} \tag{6.50}$$

$$k_2^f(\rho_2^b - \xi_2) - k_2^r \sigma_{su,2} = \left[-D_m \frac{\partial \rho}{\partial r} + \sigma_2 E_r\right]_{r=R_2^-} = \frac{\sigma_2 A_3}{R_2} \tag{6.51}$$

The surface charge densities for the ionic species are related to the electric fields on either side of the interfaces according to

$$\sigma_{su,1} = \epsilon_2 E_r\,|_{a^+} - \epsilon_1 E_r\,|_{a^-} = \lambda_D\left[\frac{\rho_2^b g(a,a) - \rho_1^b g(R_2,a)}{f(R_2,a)}\right] + \frac{(\epsilon_2 A_3 - \epsilon_1 A_1)}{a} \tag{6.52}$$

$$\sigma_{su,2} = -\epsilon_2 E_r\,|_{R_2^-} = -\lambda_D\left[\frac{\rho_2^b g(a,R_2)-\rho_1^b g(R_2,R_2)}{f(R_2,a)}\right]-\frac{\epsilon_2 A_3}{R_2} \tag{6.53}$$

Substituting into Eqs. 6.50 and 6.51 gives

$$\left[K_1^e+\frac{g(R_2,a)}{f(R_2,a)}\right]\rho_1^b-\frac{g(a,a)}{f(R_2,a)}\rho_2^b = \frac{\epsilon_2 A_3}{a\lambda_D}(1-K_1^r)-\frac{\epsilon_1 A_1}{a\lambda_D}+K_1^e\xi_1 \tag{6.54}$$

$$-\frac{g(R_2,R_2)}{f(R_2,a)}\rho_1^b+\left[K_2^e+\frac{g(a,R_2)}{f(R_2,a)}\right]\rho_2^b = \frac{\epsilon_2 A_3}{R_2\lambda_D}(K_2^r-1)+K_2^e\xi_2 \tag{6.55}$$

with $K_i^e \equiv k_i^f/(\lambda_D k_i^r)$ and $K_i^r \equiv 1/(k_i^r\tau_2)$. In the steady state, the current flowing through the dielectric is equal to that going through the interface and the liquid to the interface. This condition can be expressed as

$$k_1^f(\rho_1^b-\xi_1)-k_1^r\sigma_{su,1} = -\frac{\sigma_2 A_3}{a} = -\frac{\sigma_1 A_1}{a} \tag{6.56}$$

As a final constraint, the terminal voltage is given by Eqs. 5.81 and 5.82 as

$$v = V_o + R_L I = A_1\ln\left(\frac{a}{R_1}\right)+A_3\ln\left(\frac{R_2}{a}\right)+\frac{\lambda_D^2}{\epsilon_2}\left(\rho_2^b-\rho_1^b\right) \tag{6.57}$$

with

$$I = -2\pi H\sigma_1 A_1 \tag{6.58}$$

giving the current density to the inner electrode. Combining Eqs. 6.54 to 6.58 gives

$$A_3 = \frac{V_o+\frac{\lambda_D^2}{\epsilon_2}\left(K_1^e\xi_1 B_{43}-K_2^e\xi_2 B_{42}\right)}{\frac{\sigma_2}{\sigma_1}\ln\left(\frac{a}{R_1}\right)+\ln\left(\frac{R_2}{a}\right)+2\pi H R_L\sigma_2+\frac{\lambda_D}{R_2}\left(K_2^r-1\right)B_{42}-\frac{\lambda_D}{a}\left(1-\frac{\tau_1}{\tau_2}-K_1^r\right)B_{43}} \tag{6.59}$$

$$\begin{aligned}\rho_1^b = {} & \frac{\epsilon_2 A_3}{a\lambda_D B_{41}}\left\{\left(1-\frac{\tau_1}{\tau_2}-K_1^r\right)\left[K_2^e+\frac{g(a,R_2)}{f(R_2,a)}\right]+\frac{a}{R_2}\left(K_2^r-1\right)\frac{g(a,a)}{f(R_2,a)}\right\} \\ & +\frac{K_1^e\xi_1}{B_{41}}\left[K_2^e+\frac{g(a,R_2)}{f(R_2,a)}\right]+\frac{K_2^e\xi_2}{B_{41}}\frac{g(a,a)}{f(R_2,a)}\end{aligned} \tag{6.60}$$

$$\begin{aligned}\rho_2^b = {} & \frac{\epsilon_2 A_3}{R_2\lambda_D B_{41}}\left\{\left(K_2^r-1\right)\left[K_1^e+\frac{g(R_2,a)}{f(R_2,a)}\right]+\frac{R_2}{a}\left[1-\frac{\tau_1}{\tau_2}-K_1^r\right]\frac{g(R_2,R_2)}{f(R_2,a)}\right\} \\ & +\frac{K_2^e\xi_2}{B_{41}}\left[K_1^e+\frac{g(R_2,a)}{f(R_2,a)}\right]+\frac{K_1^e\xi_1}{B_{41}}\frac{g(R_2,R_2)}{f(R_2,a)}\end{aligned} \tag{6.61}$$

where

$$B_{41} = \left[K_1^e+\frac{g(R_2,a)}{f(R_2,a)}\right]\left[K_2^e+\frac{g(a,R_2)}{f(R_2,a)}\right]-\frac{g(a,a)g(R_2,R_2)}{f^2(R_2,a)} \tag{6.62}$$

$$B_{42} = \frac{1}{B_{41}}\left\{K_1^e + \frac{[g(R_2,a) - g(a,a)]}{f(R_2,a)}\right\} \tag{6.63}$$

$$B_{43} = \frac{1}{B_{41}}\left\{K_2^e + \frac{[g(a,R_2) - g(R_2,R_2)]}{f(R_2,a)}\right\} \tag{6.64}$$

These equations indicate that the applied voltage can **increase or decrease** the charge density on the liquid side of each interface, depending upon the reaction rates at the interface and the relative relaxation times in the solid and liquid dielectrics. This provides a degree of freedom that was not available in the postulated boundary conditions discussed in the previous chapter, where the interfacial charge density was either independent of the applied voltage or decreased with increasing voltage on the inner electrode and increased on the outer electrode.

The interfacial charge density variation with the applied voltage can be explored further by taking partial derivatives with respect to the applied voltage. For this work, the cylinder radii are much larger than the Debye length so the electrical double layers are non-interacting. With $(R_2 - a) \gg \lambda_D$, the approximate expressions for $f$ and $g$, given by Eqs. 5.60 and 5.73, apply and

$$g(R_2,a) \approx g(a,R_2) \approx f(R_2,a) \approx \frac{\lambda_D}{2\sqrt{aR_2}} e^{(R_2-a)/\lambda_D} \tag{6.65}$$

$$ag(a,a) \approx R_2 g(R_2,R_2) \approx \frac{\lambda_D}{2} \tag{6.66}$$

Defining $D_v X$ as the partial derivative of $X$ with respect to the applied voltage and taking $R_L \to 0$, it follows that

$$D_v\rho_1^b \approx \frac{\epsilon_2}{a\lambda_D} \frac{(1 - K_1^r - \frac{\tau_1}{\tau_2})}{(1+K_1^e)\left[\ln\left(\frac{R_2}{a}\right) + \frac{\sigma_2}{\sigma_1}\ln\left(\frac{a}{R_1}\right) + \frac{\lambda_D}{R_2}\frac{(K_2^r-1)}{1+K_2^e} - \frac{\lambda_D}{a}\frac{(1-K_1^r-\frac{\tau_1}{\tau_2})}{(1+K_1^e)}\right]} \tag{6.67}$$

$$D_v\rho_2^b \approx \frac{\epsilon_2}{R_2\lambda_D} \frac{(K_2^r - 1)}{(1+K_2^e)\left[\ln\left(\frac{R_2}{a}\right) + \frac{\sigma_2}{\sigma_1}\ln\left(\frac{a}{R_1}\right) + \frac{\lambda_D}{R_2}\frac{(K_2^r-1)}{1+K_2^e} - \frac{\lambda_D}{a}\frac{(1-K_1^r-\frac{\tau_1}{\tau_2})}{(1+K_1^e)}\right]} \tag{6.68}$$

In this approximation, it was assumed that the Debye length was small enough compared to the cylinder gap that all of the exponential terms could be neglected. This also requires that any terms multiplying the exponentials, such as the relative reaction rates between the interfaces or the relative dielectric time constants, to also be negligible.

As an initial case study take $\tau_1 \to 0$ ($\sigma_1 \to \infty$), which is applicable to the case of bare metal electrodes or when the solid dielectric is very conducting with respect to the liquid dielectric, as for wet pressboard. For convenience, assume that the electrodes are the same so that $K_1^r = K_2^r \equiv K_m^r$ and $K_1^e = K_2^e \equiv K_m^e$. This allows Eqs. 6.59 to 6.64 to be combined to give

$$D_v\rho_1^b \approx -\frac{R_2}{a} D_v\rho_2^b \approx \frac{\epsilon_2}{a\lambda_D}\left[\frac{(1 - K_m^r)}{(1+K_m^e)\ln\left(\frac{R_2}{a}\right) - \frac{\lambda_D}{a}\left(1+\frac{a}{R_2}\right)(1-K_m^r)}\right] \tag{6.69}$$

This indicates that the polarity of the interfacial charge density variation with the applied voltage depends upon the interfacial reaction rates, with opposite effects always occurring at the inner and outer interfaces. If the left term in the denominator is larger than the right term, then the field across the fluid is dominated by the "ohmic" contribution rather than the interfacial charge dynamics and charge diffusion. The polarity is then determined by the quantity $(1 - K_m^r)$, with $D_v\rho_1^b$ positive for $K_m^r < 1$ but negative for $K_m^r > 1$. On the other hand, if the left term in the denominator is smaller than the right term then the "ohmic" contribution to the field is dominated by the interfacial charge dynamics and charge diffusion and $D_v\rho_1^b$ is always negative. Implicit to this last condition is the constraint of $K_m^r > 1$ so that charge relaxation is fast compared to interfacial desorption.

Physically, $K_m^r = 1/(k_m^r\tau_2)$ describes the competition between charge desorption from the interface and charge relaxation in the liquid bulk as the mobile ions redistribute themselves to shield the bulk of the liquid from any applied fields. For $K_m^r > 1$, the charge desorption is slow compared to charge relaxation and the volume charge density near the inner cylinder interface becomes negative (for positive applied voltages) while near the outer cylinder the charge density becomes positive. This is the case of heterocharge because the volume charge on the liquid side of the interface has a polarity opposite that of the surface charge on the interface. For $K_m^r < 1$, charge desorption is fast compared to charge relaxation and the volume charge density near the inner cylinder interface increases while near the outer cylinder the charge density decreases for positive applied voltages. This is a case of homocharge because the volume charge density on the liquid side of the interface and the surface charge at the interface have the same polarity. The parameter $K_m^e$ contains the adsorption rate constant and can influence whether the "ohmic" contribution or the charge dynamics are dominant.

Next, consider the case of a solid dielectric that is very insulating with respect to the fluid, such that $\tau_1 \gg \tau_2$. Once again, the interfacial charge densities depend upon desorption rates at each interface. In the limit that $k_i^r\tau_1 \gg 1$ (or $\tau_1/\tau_2 \gg K_i^r$), conduction through the solid is slow compared to the interfacial desorption rates and the interfacial charge densities are given by

$$D_v\rho_1^b \approx -\frac{\epsilon_1}{a\lambda_D}\frac{1}{\left[(K_1^e+1)\ln\left(\frac{a}{R_1}\right)+\frac{\lambda_D}{a}\frac{\epsilon_1}{\epsilon_2}\right]} \tag{6.70}$$

$$D_v\rho_2^b \approx 0 \tag{6.71}$$

The electric field resulting from the applied voltage is primarily contained inside the solid dielectric and charge accumulates in the double layer at the inner interface to shield the applied field from the fluid volume. As the factor $K_1^e$ increases, adsorption onto the interface increases so that the interfacial surface charge accumulates (becomes more negative) and less charge is necessary in the double layer to shield the applied field. The result is a volume charge density near the interface that decreases in magnitude. The volume charge density near the outer cylinder interface is essentially unaffected because the field is nearly zero there. In the limit that $k_i^r\tau_1 \ll 1$ (or $\tau_1/\tau_2 \ll K_i^r$), conduction through the solid is fast compared to the interfacial desorption rates and the interfacial

charge densities are given by

$$D_v\rho_1^b \approx -\frac{\epsilon_2}{a\lambda_D}\frac{1}{\frac{\lambda_D}{a}+k_1^r\tau_1\frac{\epsilon_2}{\epsilon_1}(K_1^e+1)\ln\left(\frac{a}{R_1}\right)+\frac{\lambda_D}{R_2}\frac{k_1^r}{k_2^r}\left(\frac{K_1^e+1}{K_2^e+1}\right)} \tag{6.72}$$

$$D_v\rho_2^b \approx \frac{\epsilon_2}{R_2\lambda_D}\frac{1}{\frac{\lambda_D}{R_2}+k_2^r\tau_1\frac{\epsilon_2}{\epsilon_1}(K_2^e+1)\ln\left(\frac{a}{R_1}\right)+\frac{\lambda_D}{a}\frac{k_1^r}{k_1^r}\left(\frac{K_1^e+1}{K_1^e+1}\right)} \tag{6.73}$$

In this case, while some of the electric field is contained inside the solid dielectric, an appreciable field can also be found throughout the fluid volume. The interfacial volume charge densities depend primarily upon the reaction rates and not the conduction through the solid, indicating that the reaction rates are the rate limiting processes in this case.

This analysis for the stationary electrodes is summarized in Fig. 6.1. This figure shows the regimes of the different limiting cases and shows the variation in the interfacial charge densities with respect to the applied voltage. In most situations, the charge density near the inner interface decreases while that near the outer interface increases with increasing applied voltage. However, there are conditions under which those variations are reversed, with the charge density near the inner interface increasing and that near the outer interface decreasing for increasing applied voltage.

With respect to flow electrification, since the inner cylinder interface is subjected to a field that is larger than the outer cylinder interface, the inner interface has a slightly larger contribution to the electrification charge density. Since the variation of the inner cylinder charge density with respect to the applied voltage depends upon the interfacial reaction kinetics and the relative relaxation times in the solid and the liquid phases, extending this model to include fluid motion should allow a wider range of electrification data, especially that which includes applied voltages, to be explained.

## 6.5 Non-stationary Case

As in Section 5.7, when the inner cylinder is set into motion, the charge in the fluid is redistributed, with some of the charge from the diffuse portion of the electrical double layers carried into the turbulent core. The objective of this section is to derive expressions for the core charge density, terminal current and terminal voltage in terms of the interfacial parameters, the material properties, and the system geometry. Since the only difference between this analysis and that presented in Section 5.7 is the boundary condition used to represent the interfacial charge transfer, many of the basic equations and concepts previously discussed are directly applicable. For example, Eqs. 5.127, 5.128, and 5.129 still apply and the boundary conditions must be imposed before solving the system of equations.

In this case, the boundary conditions for the charge transfer are related to the transport of charge to the interface by Eq. 6.40. With the free surface charge density at each solid/liquid interface determined by the electric field (of Eq. 5.113) as

$$\sigma_{sul} = \epsilon_2\frac{A_2}{a}+\lambda_D\left[-\rho_1^b\frac{g(a+\delta_1,a)}{f(a+\delta_1,a)}+\rho_o\frac{g(a,a)}{f(a+\delta_1,a)}\right]-\epsilon_1\frac{A_1}{a} \tag{6.74}$$

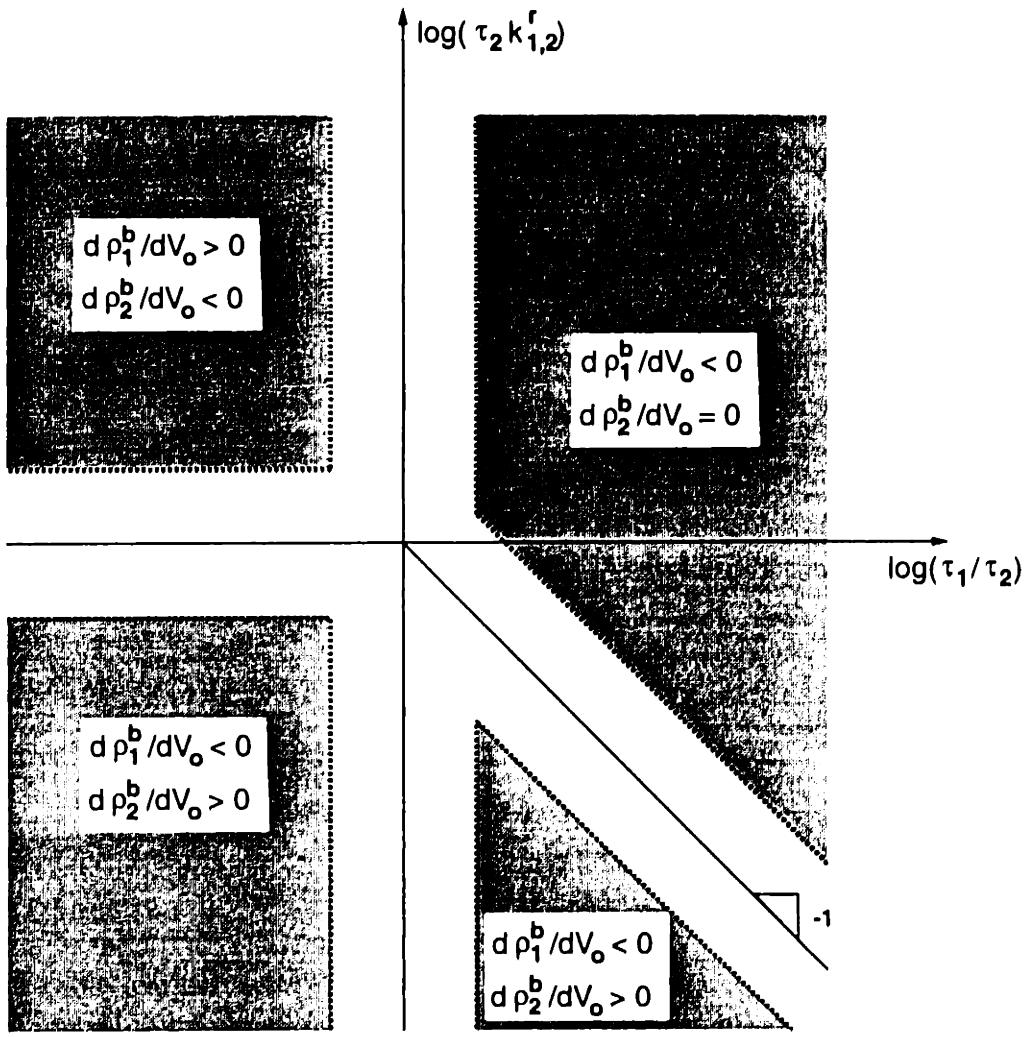


Figure 6.1: Regions of applicability for the approximate expressions for the effects of the applied potential on the volume charge densities near the inner and outer interfaces without fluid flow.

$$\sigma_{su2} = -\epsilon_2 \frac{A_4}{R_2} - \lambda_D \left[ -\rho_o \frac{g(R_2, R_2)}{f(R_2, R_2 - \delta_2)} + \rho_2^b \frac{g(R_2, R_2 - \delta_2)}{f(R_2, R_2 - \delta_2)} \right] \tag{6.75}$$

and the transport of the charge to the interface given by Eq. 5.115, the boundary conditions become

$$\rho_1^b \left[ K_1^e + \frac{g(a+\delta_1, a)}{f(a+\delta_1, a)} \right] - \rho_o \frac{g(a,a)}{f(a+\delta_1, a)} - (1 - K_1^r) \frac{\epsilon_2 A_2}{a\lambda_D} + \frac{\epsilon_1 A_1}{a\lambda_D} = K_1^e \xi_1 \tag{6.76}$$

$$\rho_2^b \left[ K_2^e + \frac{g(R_2, R_2 - \delta_2)}{f(R_2, R_2 - \delta_2)} \right] - \rho_o \frac{g(R_2, R_2)}{f(R_2, R_2 - \delta_2)} + (1 - K_2^r) \frac{\epsilon_2 A_4}{R_2 \lambda_D} = K_2^e \xi_2 \tag{6.77}$$

Using Eqs. 5.117, 5.118, and 5.119 to substitute for the $A_i$, taking the limit as the cylinder radii become large compared to the Debye length so that the simplified expressions for $f$ (Eq. 5.60) and $g$ (Eq. 5.73) can be used, and using the normalizations of Tables 5.1 and 5.2 gives

$$\rho_1^b\left[K_1^e+\coth\left(\frac{a\delta}{\lambda_D}\right)\right]-\rho_o\sqrt{1+\delta}\,\mathrm{csch}\left(\frac{a\delta}{\lambda_D}\right)+(1-K_1^r-\tau_1)\frac{\lambda_D}{2a}I = K_1^e\xi_1 \quad (\underline{6.78})$$

$$\rho_2^b\left[K_2^e+\coth\left(\frac{\delta}{\lambda_D}\right)\right]-\rho_o\sqrt{1-\delta}\,\mathrm{csch}\left(\frac{\delta}{\lambda_D}\right)-(1-K_2^r)\frac{\lambda_D}{2}I = K_2^e\xi_2 \quad (\underline{6.79})$$

where the underscore beneath the equation number indicates that the equation contains non-dimensional variables. Finally, to be consistent with Eqs. 5.127, 5.128, and 5.129 requires $\underline{\lambda}_D^2 \ll \delta \lesssim \underline{\lambda_D}$ so that the boundary condition equations can be reduced to

$$\rho_1^b \approx \frac{1}{K_1^e+\coth\left(\frac{a\delta}{\lambda_D}\right)}\left\{K_1^e\xi_1-(1-K_1^r-\tau_1)\frac{\lambda_D I}{2a}\right.$$
$$\left.-\frac{2\lambda_D\,\mathrm{csch}\left(\frac{a\delta}{\lambda_D}\right)\mathrm{csch}\left(\frac{\delta}{\lambda_D}\right)}{(1-a^2)\left[K_2^e+\coth\left(\frac{\delta}{\lambda_D}\right)\right]}\left[K_2^e\xi_2+(1-K_2^r)\frac{\lambda_D I}{2}\right]\right\} \quad (\underline{6.80})$$

$$\rho_2^b \approx \frac{1}{K_2^e+\coth\left(\frac{\delta}{\lambda_D}\right)}\left\{K_2^e\xi_2+(1-K_2^r)\frac{\lambda_D I}{2}\right.$$
$$\left.+\frac{2a\lambda_D\,\mathrm{csch}\left(\frac{a\delta}{\lambda_D}\right)\mathrm{csch}\left(\frac{\delta}{\lambda_D}\right)}{(1-a^2)\left[K_1^e+\coth\left(\frac{a\delta}{\lambda_D}\right)\right]}\left[K_1^e\xi_1-(1-K_2^r-\tau_1)\frac{\lambda_D I}{2a}\right]\right\} \quad (\underline{6.81})$$

Substitution into Eq. 5.129 gives the open-circuit voltage as

$$v^{oc}=\frac{1}{\lambda_D}\left\{\frac{a\xi_1\,\mathrm{csch}\left(\frac{a\delta}{\lambda_D}\right)}{1+\frac{1}{K_1^e}\coth\left(\frac{a\delta}{\lambda_D}\right)}\left[\frac{1}{2}+\frac{\ln(a)}{1-a^2}\right]+\frac{\xi_2\,\mathrm{csch}\left(\frac{\delta}{\lambda_D}\right)}{1+\frac{1}{K_2^e}\coth\left(\frac{\delta}{\lambda_D}\right)}\left[\frac{1}{2}+a^2\frac{\ln(a)}{1-a^2}\right]\right\} \quad (\underline{6.82})$$

and the general terminal voltage as

$$v=V_o\left[1-\frac{R_L}{\gamma_1}\right]+\frac{R_L}{\gamma_1}v^{oc} \quad (\underline{6.83})$$

with

$$\gamma_1 \equiv R_L+\frac{1}{\sigma_1}\ln\left(\frac{a}{R_1}\right)-\ln(a)+\frac{(1-K_1^r-\tau_1)}{K_1^e\sinh\left(\frac{a\delta}{\lambda_D}\right)+\cosh\left(\frac{a\delta}{\lambda_D}\right)}\left[\frac{1}{2}+\frac{\ln(a)}{1-a^2}\right]$$
$$-\frac{(1-K_2^r)}{K_2^e\sinh\left(\frac{\delta}{\lambda_D}\right)+\cosh\left(\frac{\delta}{\lambda_D}\right)}\left[\frac{1}{2}+a^2\frac{\ln(a)}{1-a^2}\right] \quad (\underline{6.84})$$

Mathematically, it is possible for $\gamma_1$ to be zero. This requires $v^{oc}$ to also be zero if

the current is to remain finite; otherwise, an "infinite" current would be generated, but no physical mechanisms leading to such a current are apparent. Alternatively, if $v^{oc}$ is nonzero, then constraining $\gamma_1 > 0$ leads to a finite current. This constraint is guaranteed to be satisfied if each of the individual terms in $\gamma_1$ is positive, or

$$K_2^r > 1 \quad ; \quad K_1^r + \tau_1 > 1 \tag{6.85}$$

These are sufficient, but *not* necessary for a finite current. Depending upon the magnitudes of the $K_1^e$ and the sublayer thicknesses, these conditions can be relaxed. For example, if $K_2^e \gg 1$ then $K_2^r$ can be smaller than one. The final result is that the terminal current can be expressed as

$$I = \frac{2}{\gamma_1}(v^{oc} - V_o) \tag{6.86}$$

and the charge density is given by

$$\rho_o = \frac{2\lambda_D}{(1-a^2)}\left[\frac{a\xi_1 \operatorname{csch}\left(\frac{a\delta}{\lambda_D}\right)}{1+\frac{1}{K_1^e}\coth\left(\frac{a\delta}{\lambda_D}\right)} + \frac{\xi_2 \operatorname{csch}\left(\frac{\delta}{\lambda_D}\right)}{1+\frac{1}{K_2^e}\coth\left(\frac{\delta}{\lambda_D}\right)} + \lambda_D \frac{\gamma_2}{\gamma_1}(v^{oc} - V_o)\right] \tag{6.87}$$

with

$$\gamma_2 \equiv \frac{(1-K_2^r)}{K_2^e \sinh\left(\frac{\delta}{\lambda_D}\right) + \cosh\left(\frac{\delta}{\lambda_D}\right)} - \frac{(1-K_1^r-\tau_1)}{K_1^e \sinh\left(\frac{a\delta}{\lambda_D}\right) + \cosh\left(\frac{a\delta}{\lambda_D}\right)} \tag{6.88}$$

It follows that the rate of change of the charge density with respect to the applied voltage can be expressed as

$$D_v\rho_o \equiv \frac{\partial \rho_o}{\partial V_o} = -\frac{2\lambda_D^2}{(1-a^2)}\frac{\gamma_2}{\gamma_1} \tag{6.89}$$

As before, some of the aspects of this model can be explored through limiting cases.

Consider first a system that has identical bare metal electrodes. The unknown interfacial parameters are then $K_1^e$, $K_1^r$, and $\xi_1$. The effects of these parameters can be explored by fixing two of them and letting the third vary. For example, consider Fig. 6.2 in which $K_1^r$ is varied for a given $K_1^e$ and $\xi_1$, whose values were chosen to give magnitudes that are comparable to those observed in the experiments. This figure shows that the open-circuit voltage is independent of $K_1^r$, as expected from Eq. 6.82. The sublayer thickness that led to an open-circuit voltage of zero also led to a short-circuit current of zero, independent of $K_1^r$, as expected from Eq. 6.86. While it follows from Eq. 6.87 that $\rho_o^{oc}$ is also independent of $K_1^r$, $\rho_o^{sc}$ is seen to be only weakly dependent on $K_1^r$. In contrast, the short-circuit current and $D_v\rho_o$ depend strongly on $K_1^r$. In particular, for $K_1^r < 1$, $D_v\rho_o > 0$, but for $K_1^r > 1$, $D_v\rho_o < 0$. Also note that the terminal quantities (voltage and current) can have polarity changes that are dependent only upon the rotation rate. This is reasonable because the terminal quantities depend upon the difference in effects occurring at each interface and would be zero for a parallel plate geometry. Since the interfaces are curved in this system, the sublayer thicknesses are different at each interface and small changes in the thickness of the sublayer, relative to the Debye length, can

have significant effects on the terminal quantities.

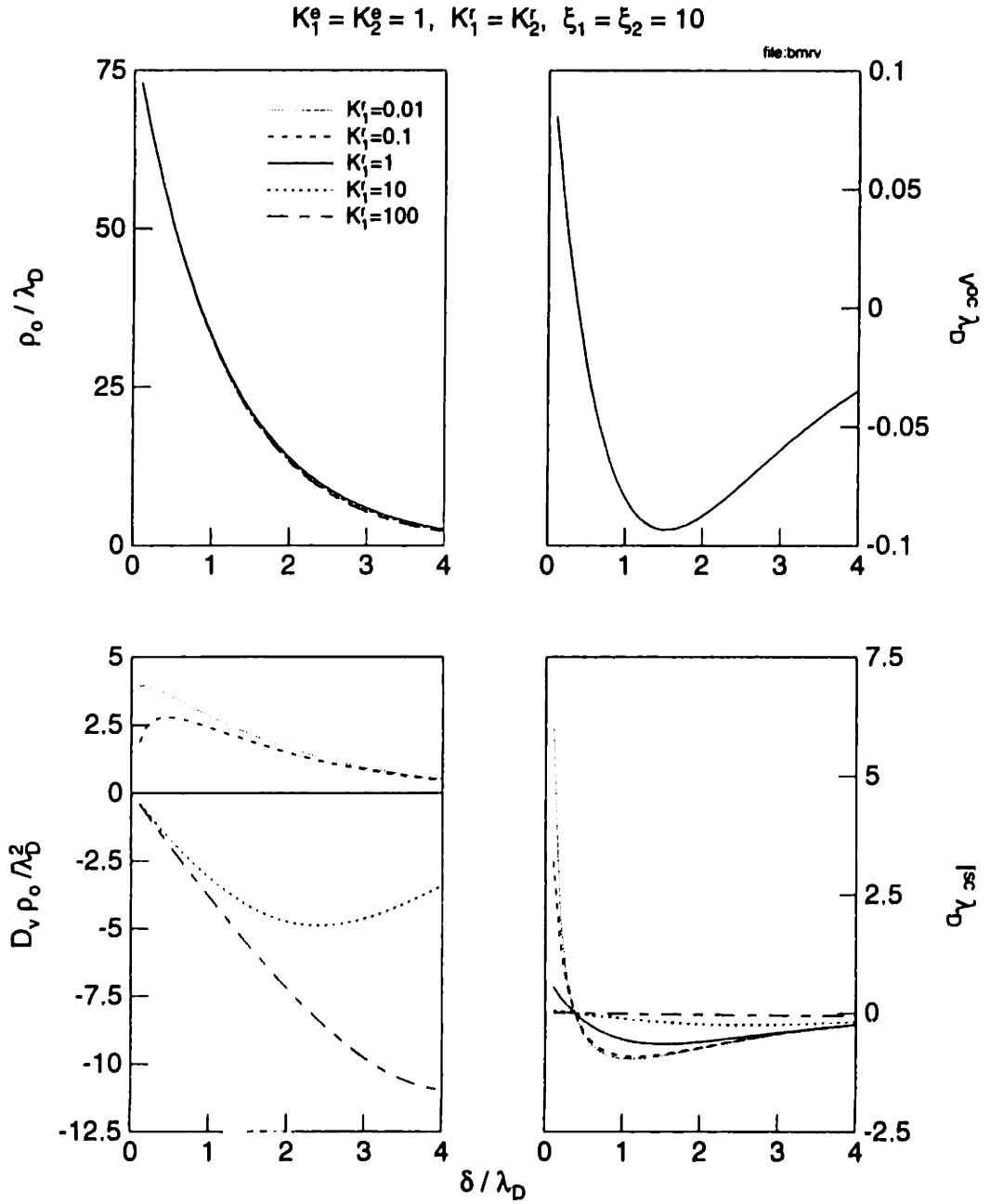


Figure 6.2: Calculated response for identical bare metal cylinders with $K_1^r$ varied. This simulation assumed $\underline{a} = 0.75$, which is appropriate for the large Couette. All of the variables are expressed in normalized form. Both the open-circuit and short-circuit charge densities are plotted. The $v^{oc}$ is independent of $K_1^r$ while $\rho_o$ has only a slight dependence. In contrast, $I^{sc}$ and $D_v\rho_o$ are strongly dependent on $K_1^r$, with $D_v\rho_o > 0$ for $K_1^r < 1$ and $D_v\rho_o < 0$ for $K_1^r > 1$.

As another example, consider Fig. 6.3 in which $K_1^r$ and $\xi_1$ are fixed and $K_1^e$ varies. All of the electrification variables depend strongly on $K_1^e$. For $K_1^e$ large, the reaction rates can be considered "fast," the charge density has a polarity opposite that of the terminal quantities and the voltage and current are linearly related to one another. This matches the predictions of the "constant wall charge density" model [25]. As $K_1^e$ becomes smaller, the polarity of the terminal quantities depends upon the sublayer thickness and the voltage and current are no longer linearly related to one another. $D_v\rho_o$ is always positive in this example, because $K_1^r < 1$. If $K_1^r > 1$ is chosen, as would be appropriate for the Abedian-Sonin type boundary condition [99], $D_v\rho_o$ is always negative. As a final note, the magnitude of $\xi_1$ affects the scaling of the charge density, the open-circuit voltage, and the short-circuit current, similar to $K_1^e$, but does not affect $D_v\rho_o$.

In most situations, the interfaces are not identical. Occasionally this is intentional, such as when copper is used to cover the inner cylinder. Other times it can be unintentional, such as when the cylinders are both bare stainless steel but the cleaning of the cylinders or the past history of an experiment causes the interfaces to be slightly different. For example, the passage of current through the interfaces may cause the thickness of a thin oxide region to be different on one interface versus the other.

When the $\xi_i$ are different, as shown in Fig. 6.4, the scaling of the charge density is affected but the $K_1^r$ still does not affect the charge density appreciably. The relative values of the $\xi_i$ affect the transition of the open-circuit voltage polarity from positive to negative. Similarly, the short-circuit current has a polarity reversal as $\xi_2$ becomes large compared to $\xi_1$. This is analogous to the plot in Fig. 5.7. This highlights the sensitivity of the terminal quantities to slight differences in the interfacial properties; a factor of four in $\xi$ can lead to polarity changes at a given sublayer thickness (or rotational speed). Again, $D_v\rho_o$ is independent of the $\xi_i$.

Similar results for the charge density, voltage and current can be obtained when the $K_i^e$ are different, as shown in Fig. 6.5. Because these results are so similar to those of Fig. 6.4, separately estimating the effects of variations in $K_i^e$ and $\xi_i$ can be difficult. For example, when $K_i^e \gg 1$, the polarity of the voltage and the current are not as sensitive to the relative values of the $K_i^e$ on the inner and outer interfaces and variations in the polarity of the terminal quantities are estimated as relative differences in the $\xi_i$. When $K_i^e \ll 1$, the product $\xi_i K_i^e$ at each interface becomes important and the two parameters are not easily separated. In contrast to Fig. 6.4, $D_v\rho_o$ is strongly affected by the $K_i^e$ variation, suggesting that it can be used to estimate the $K_i^e$. Unfortunately, the measurement of $D_v\rho_o$ is more prone to error than the other electrification quantities. More is said about these estimations in the next subsection.

As discussed previously, variations in $K_i^r$ do not affect the open-circuit voltage and have a minimal effect on the charge density, but can greatly affect the short-circuit current and $D_v\rho_o$. Fig. 6.6 shows the effect of different interfacial $K_i^r$ on the current and $D_v\rho_o$. In this case, the magnitude of the current is increased slightly as $K_2^r$ is decreased, but the effect on $D_v\rho_o$ is much more noticeable. This suggests again that $D_v\rho_o$ is more sensitive to the interfacial dynamics than the charge density or even the voltage and current.

The effects of an insulating dielectric layer on the inner cylinder can also be explored. In Fig. 6.7, it was assumed that the interfacial parameters were the same at the inner and outer interfaces and the relative conductivity (and relaxation time) of the solid was varied.

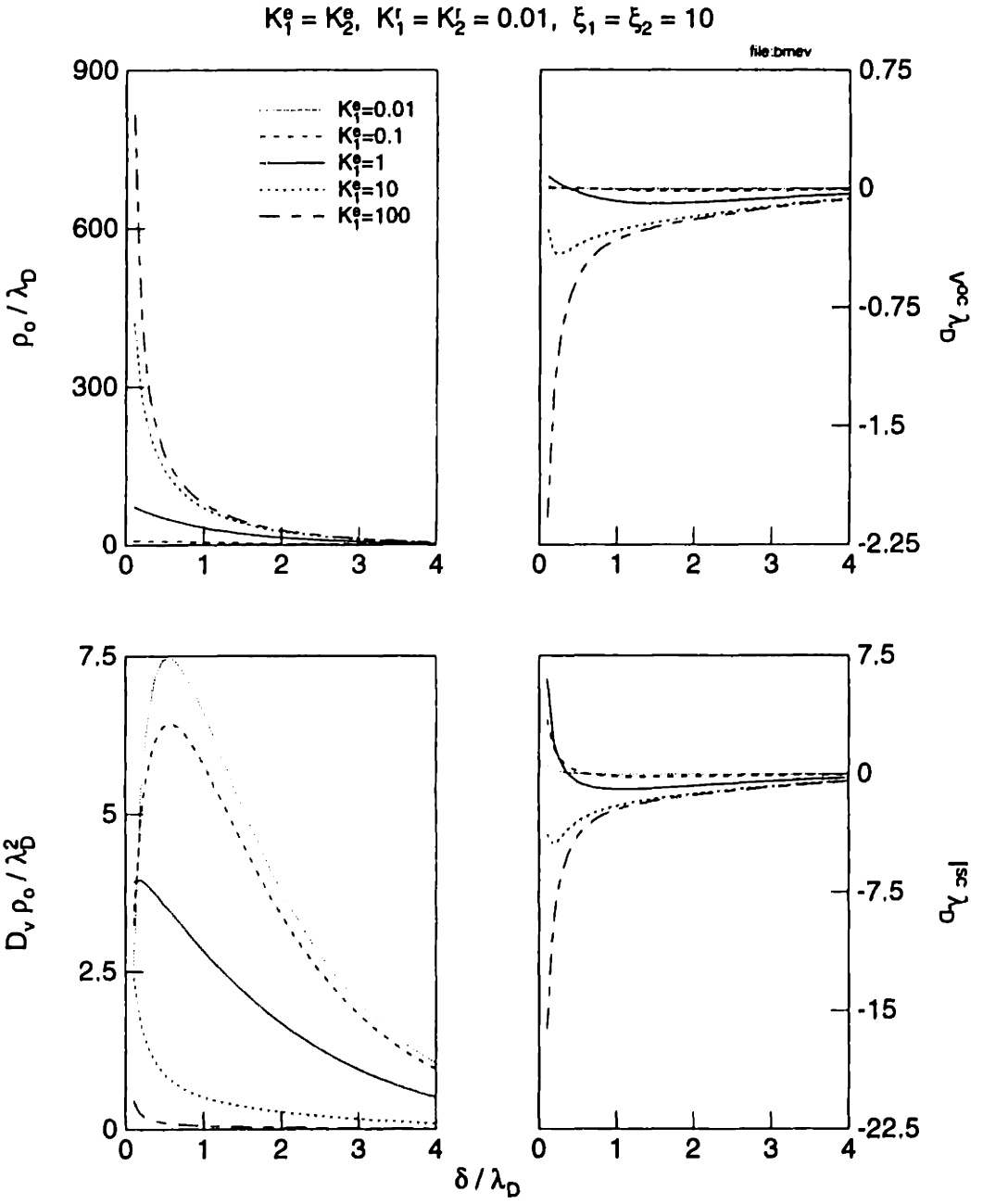


Figure 6.3: Calculated response for identical bare metal cylinders with $K_i^e$ varied. This simulation assumed $\underline{a} = 0.75$. All of the variables are expressed in normalized form. Both the open-circuit and short-circuit charge densities are plotted. For $K_i^e$ large, the results of the model using the generalized Abedian-Sonin boundary condition are obtained. For $K_i^e$ small, the polarity of $v^{oc}$ and $I^{sc}$ depends upon the flow rate.

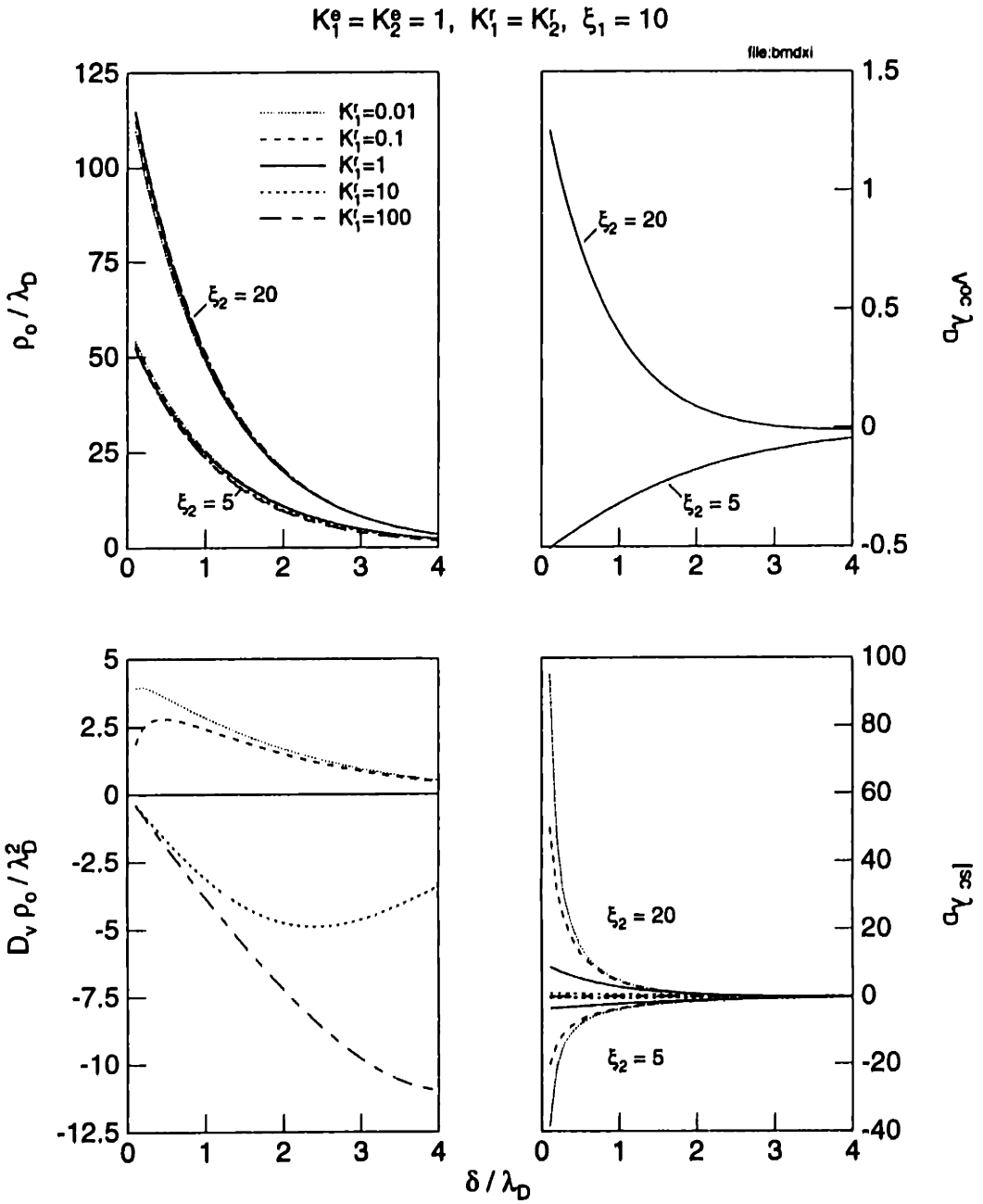


Figure 6.4: Calculated response for bare metal cylinders with $\xi_2$ varied. This simulation assumed $\underline{a} = 0.75$. All of the variables are expressed in normalized form. Both the open-circuit and short-circuit charge densities are plotted. Slight relative changes between the $\xi_i$ affect the polarity of $v^{oc}$ and $I^{sc}$ but only the magnitude of $\rho_o$.

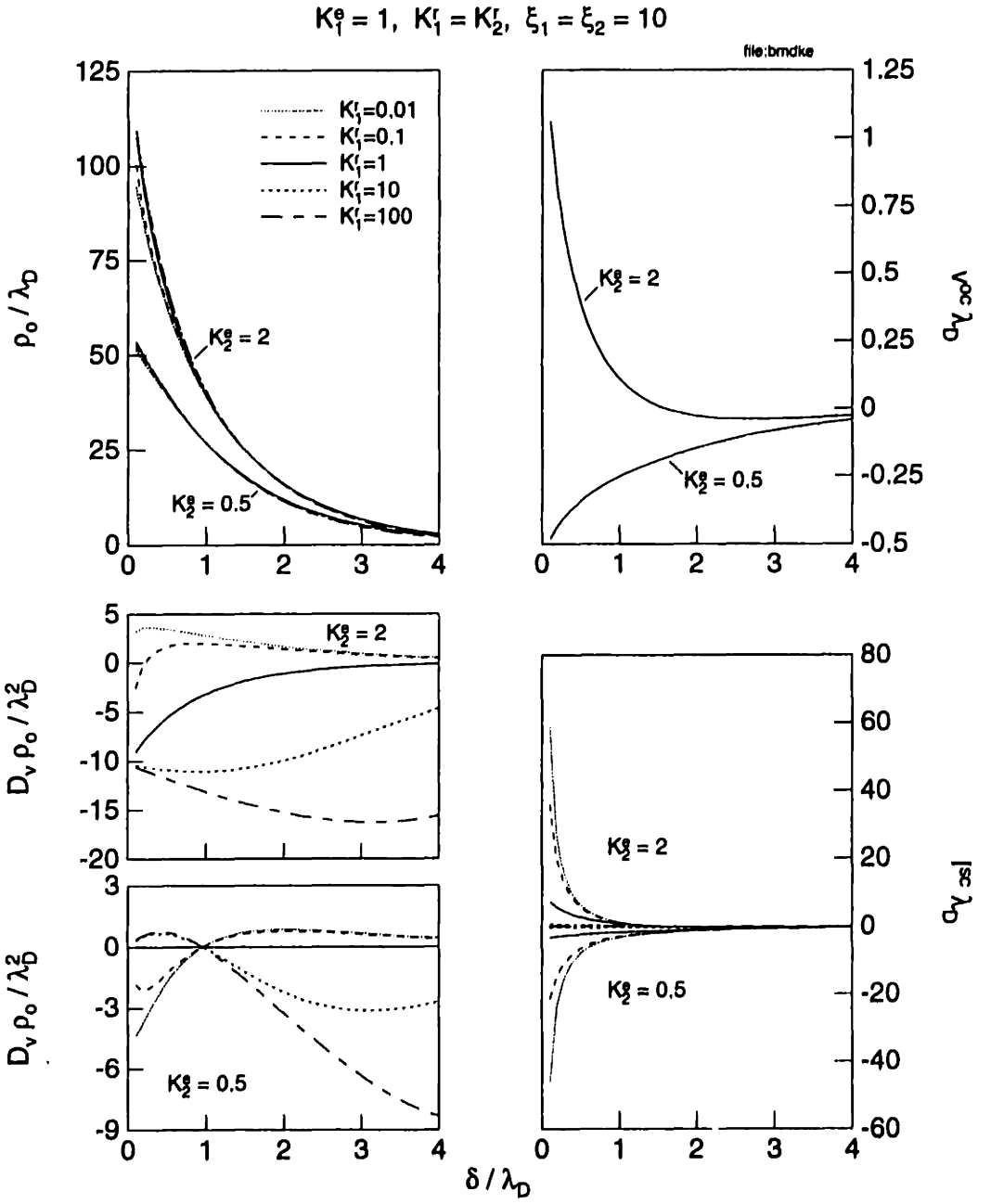


Figure 6.5: Calculated response for bare metal cylinders with $K_2^e$ varied. This simulation assumed $\underline{a} = 0.75$. All of the variables are expressed in normalized form. Both the open-circuit and short-circuit charge densities are plotted. Slight relative changes between the $K_i^e$ affect the polarity of $v^{oc}$ and $I^{sc}$ but only the magnitude of $\rho_o$. The variation of $D_v\rho_o$ with sublayer thickness is very sensitive to relative values of $K_i^e$.

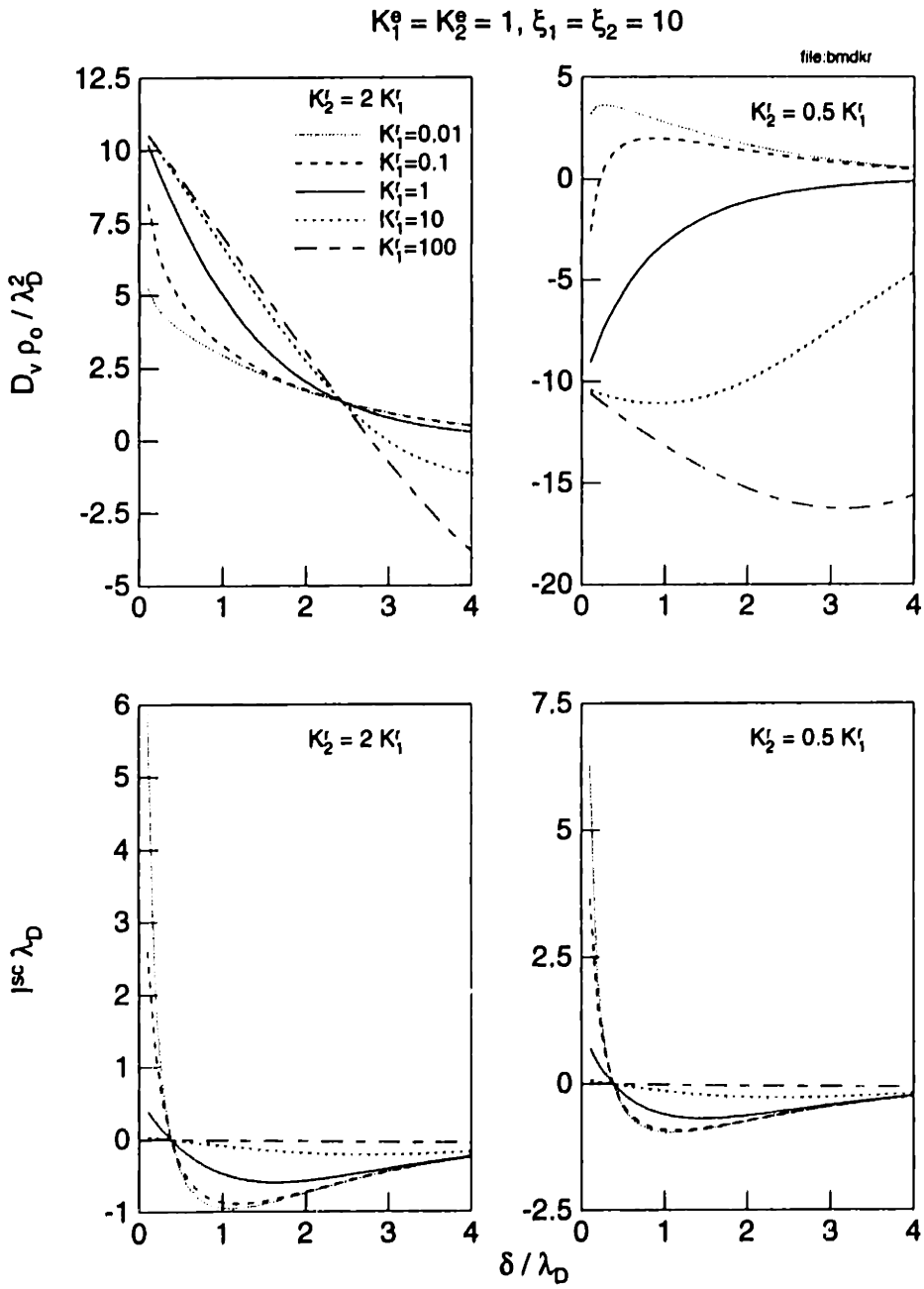


Figure 6.6: Calculated response for bare metal cylinders with $K_2^r$ varied. This simulation assumed $a = 0.75$. All of the variables are expressed in normalized form. While the charge density and voltage are unaffected by changes in $K_i^r$, the amplitude of the $I^{sc}$ and the flow rate dependence of $D_v \rho_o$ are sensitive to changes in $K_i^r$.

As expected from Eq. 6.82, the conductivity does not affect the open-circuit voltage or the open-circuit charge density. While the short-circuit charge density is only slightly affected by the decreasing conductivity, the magnitude of the current decreases strongly with the decreasing conductivity. $D_v\rho_o$ is negative, similar to the case of $K_1^r = 1, K_2^r = 0.5$, because $\tau_1$ always enters the equations with $K_1^r$ and effectively increases $K_1^r$, as shown in Eqs. 6.84 and 6.88. As the pressboard becomes more insulating, $I^{sc}$ decreases, as expected, but $D_v\rho_o$ increases, indicating that a given applied voltage will lead to *larger charge densities*. Under the dry conditions in actual transformers, the pressboard may be insulating enough to lead to these enhanced charge densities.

## 6.6 Comparison to Experiments

Following the structure of Chapter 5, several sets of experimental measurements are used to estimate the values of the interfacial parameters in this section. In this estimation, the governing equations are written in a general form as

$$v^{oc}\lambda_D = \left\{ P_1 \left[ \frac{1}{2} + \frac{\ln(a)}{1-a^2} \right] + P_2 \left[ \frac{1}{2} + a^2 \frac{\ln(a)}{1-a^2} \right] \right\} \tag{6.90}$$

for the open-circuit voltage,

$$I^{sc}\lambda_D = \frac{2}{\gamma_1}(v^{oc}\lambda_D) \tag{6.91}$$

$$\gamma_1 \equiv \frac{1}{\sigma_1}\ln\left(\frac{a}{R_1}\right) - \ln(a) - P_3\left[\frac{1}{2} + \frac{\ln(a)}{1-a^2}\right] + P_4\left[\frac{1}{2} + a^2\frac{\ln(a)}{1-a^2}\right] \tag{6.92}$$

for the short-circuit current,

$$\frac{\rho_o^{oc}}{\lambda_D} = \frac{2}{(1-a^2)}\left[P_1 + P_2\right] \tag{6.93}$$

for the open-circuit charge density,

$$\frac{\rho_o^{sc}}{\lambda_D} = \frac{\rho_o^{oc}}{\lambda_D} + \frac{1}{(1-a^2)}\left[P_3 - P_4\right] I^{sc}\lambda_D \tag{6.94}$$

for the short-circuit charge density, and

$$\frac{D_v\rho_o}{\lambda_D^2} = \frac{2}{(1-a^2)}\frac{1}{\gamma_1}\left(P_4 - P_3\right) \tag{6.95}$$

for the rate of change of the charge density with applied voltage. The parameters $P_i$ describe the contributions of each interface and are given, in general, as case 3 in Table 6.1. These are the same equations that were used in the estimations of Section 5.7; only the functional form of the $P_i$ has changed. When written in this manner, it becomes clear that the only differences between this model and the model of the last chapter are the

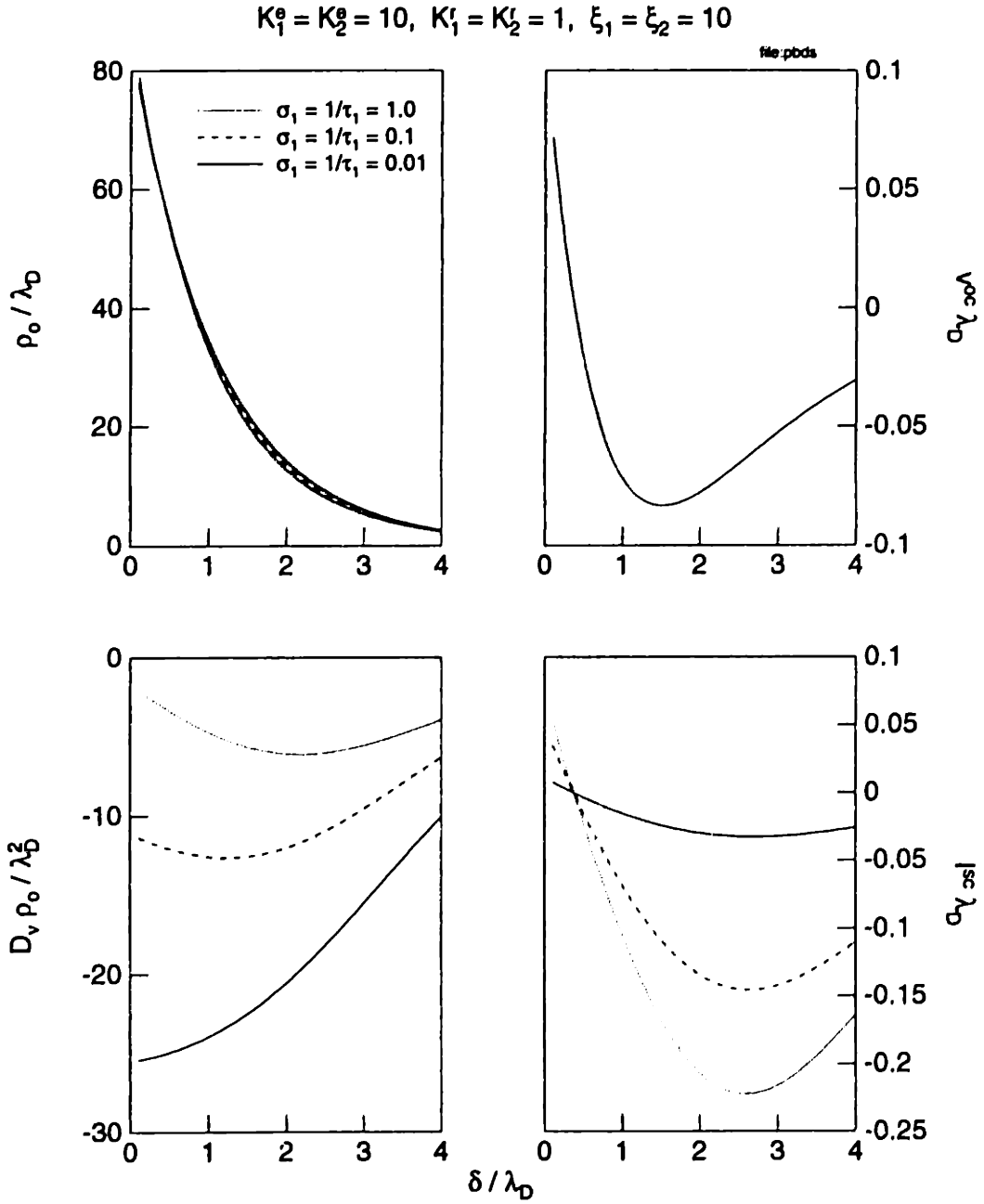


Figure 6.7: Calculated response for an insulating layer on the inner cylinder and a bare metal outer cylinder with $\underline{\tau}_1$ varied. This simulation assumed $\underline{R}_1 = 0.753$ (as when copper covers the inner cylinder) and $\underline{a} = 0.763$ (as when HiVal pressboard covers the copper sheet). All of the variables, are expressed in normalized form. Both the open-circuit and short-circuit charge densities are plotted, but only the short-circuit charge density showed a variation with the pressboard conductivity. As the pressboard becomes more insulating, the $I^{sc}$ decreases and $D_v \rho_o$ increases, which suggests that energization can lead to enhanced charge densities under dryer conditions.

contributions from the interfaces. In particular, the model using the generalized Abedian-Sonin ("wall" charge density) boundary condition is obtained in the limit of $K_i^e \gg 1$, which is given as case 1 in Table 6.1. Surprisingly enough, expressions similar in form to the model using the Gavis-Koszman boundary condition are obtained in the limit of $K^e \ll 1$, which is given as case 2. This indicates that similar functional forms of the equations can be obtained for different physical interpretations of the interfacial dynamics. For the parameter estimations, the data was normalized as described in Section 5.7.

| Parameter | Limiting Cases | | |
|---|---|---|---|
| | 1 ($K_i^e \gg 1$) | 2 ($K_i^e \ll 1$) | 3 ($K_i^e \sim 1$) |
| $P_1$ | $\dfrac{a\rho_1^w}{\sinh\left(\frac{a\delta}{\lambda_D}\right)}$ | $\dfrac{a\xi_1 K_1^e}{\cosh\left(\frac{a\delta}{\lambda_D}\right)}$ | $\dfrac{a\xi_1}{\sinh\left(\frac{a\delta}{\lambda_D}\right) + \frac{1}{K_1^e}\cosh\left(\frac{a\delta}{\lambda_D}\right)}$ |
| $P_2$ | $\dfrac{\rho_2^w}{\sinh\left(\frac{\delta}{\lambda_D}\right)}$ | $\dfrac{\xi_2 K_2^e}{\cosh\left(\frac{\delta}{\lambda_D}\right)}$ | $\dfrac{\xi_2}{\sinh\left(\frac{\delta}{\lambda_D}\right) + \frac{1}{K_2^e}\cosh\left(\frac{\delta}{\lambda_D}\right)}$ |
| $P_3$ | $\dfrac{1}{k_1\lambda_D}\dfrac{1}{\sinh\left(\frac{a\delta}{\lambda_D}\right)}$ | $\dfrac{(K_1^r + \tau_1 - 1)}{\cosh\left(\frac{a\delta}{\lambda_D}\right)}$ | $\dfrac{\frac{1}{K_1^e}(K_1^r + \tau_1 - 1)}{\sinh\left(\frac{a\delta}{\lambda_D}\right) + \frac{1}{K_1^e}\cosh\left(\frac{a\delta}{\lambda_D}\right)}$ |
| $P_4$ | $\dfrac{1}{k_2\lambda_D}\dfrac{1}{\sinh\left(\frac{\delta}{\lambda_D}\right)}$ | $\dfrac{(K_2^r - 1)}{\cosh\left(\frac{\delta}{\lambda_D}\right)}$ | $\dfrac{\frac{1}{K_2^e}(K_2^r - 1)}{\sinh\left(\frac{\delta}{\lambda_D}\right) + \frac{1}{K_2^e}\cosh\left(\frac{\delta}{\lambda_D}\right)}$ |

Table 6.1: Limiting cases for the parameter estimation of $P_i$ in the electrification model.

The complicated nature of the estimation, where multiple parameters ($\xi$, $K^e$, and $K^r$ at each interface) are used to fit several types of measurements (charge density and terminal data), required the two-step approach outlined in Section 5.8. The first step was to invert the equations for the open-circuit measurements and calculate $P_1$ and $P_2$ (from Eqs. 5.168 and 5.169) at each flow rate or sublayer thickness. Ideally, the $\xi$ and $K^e$ at each interface could then be calculated from a least-squares fit to the data. This did not always work though, because the estimation routine could not always separate the variables. For example, Table 6.1 gives the general form for the $P_i$, as well as two limiting cases, for $K_i^e$ large or small compared to one. In the limit of $K_i^e \gg 1$, only the product of $\xi_i K_i^e$ can be estimated from $P_i$, not each one individually. To resolve this issue, a least-squares fit was performed using each of the three cases defined in Table 6.1. The fit that led to the smallest "goodness-of-fit" number $\chi^2$, defined by Eq. 5.170, was then denoted as the best case for each interface. When the goodness-of-fit number was similar between the general case (3) and either of the limiting cases (1 or 2), the limiting case was taken as the best case, because that estimation required fewer free variables.

The second step in this approach was to invert the short-circuit equations and calculate $P_3$ and $P_4$ (from Eqs. 5.171 and 5.172) at each flow rate. Then, using the case determined from the open-circuit measurements, a least-squares fit was performed with the corresponding expression. In this approach, it was *assumed* that the open-circuit data is more reliable, at least in determining the appropriate case for each interface,

because open-circuit results do not depend upon the conduction through the interface or the dielectric materials.

When actually applying this estimation approach to the experimental data, the model incorporating the generalized Abedian-Sonin boundary condition usually gave the best fit to the data. Then, the comparisons from Section 5.8 still hold. One notable exception was the data taken as BTA was added to the CF. In that case, the Abedian-Sonin condition (limiting case 1) almost always gave the best fit to the open-circuit data for the *inner* cylinder (the pressboard/oil) interface, but usually **did not** give the best fit to the data for the *outer* cylinder (the stainless steel/oil) interface.

A summary of the estimation result for the outer cylinder interface are given in Table 6.2; the results for the inner cylinder interface were essentially described in Section 5.8. The most consistent results appeared at 35°C in which the estimation showed a gradual transition from $K_2^s \gg 1$ to $K_2^s \ll 1$ with the addition of BTA. Since the value of $k_2^f/k_2^r$ did not appear to change appreciably, it appears that this transition was caused by the decreasing oil conductivity. Reasonable results were not obtained for the estimations on the parameters $P_3$ and $P_4$ for two reasons. First, the uncertainty in the pressboard conductivity was large and if the $K_i^r$ are small then uncertainties in $\underline{\sigma}_1$ or $\underline{\tau}_1$ can lead to negative values for the $K_i^r$, which are not physically reasonable. Second, the measurements of $D_v\rho_o$ are noisy, which again can lead to non-physical (negative) values for the $K_i^r$.

The difference between models incorporating the Abedian-Sonin ($\rho^w$) boundary condition and the more general boundary condition derived here is illustrated in Fig. 6.8. For this particular set of data, the Abedian-Sonin condition underestimates the value of $P_2$ at low flow rates (large sublayer thicknesses), but overestimates the $P_2$ at high flow rates (small sublayers). The more general boundary condition describes the flow rate dependence better. Although the data points used in the estimations show considerable scatter, the trends are quite clear. While the better fit by the general model can be attributed to the extra parameter $K_2^s$ being determined by the flow rate dependence, the final fit for each temperature above 15°C only had one free parameter $\xi_2 k_2^f/k_2^r$ in the estimation, which is equivalent to fitting to only $\rho_2^w$ in the Abedian-Sonin condition.

## 6.7 Discussion

In this chapter, an improved boundary condition for interfacial charge transport was developed. This boundary condition reduces to the general $\rho^w$ boundary condition proposed by Abedian and Sonin in the limit of no desorption off of the interface. The derivation itself provides a more physical model for the interfacial charge transfer. One result of this is that the "wall" volume charge density $\rho^w$, on the liquid side of the interface, is not simply a postulated parameter, but actually determined by the difference in adsorption and desorption rates for the individual ionic species.

This new boundary condition was also incorporated into an electrification model and techniques were developed for estimating the interfacial properties. These techniques yielded mixed results, though similar to the estimations of the last chapter. In particular, since the boundary condition developed here is an extension of the $\rho^w$ boundary

| Temp. °C | BTA ppm | $\sigma_{oil}$ pS/m | $\sigma_{pressboard}$ $10^{-15}$ S/m | Estimation limit | $\xi_2$ mC/m$^3$ | $k_2^f/k_2^r$ $10^{-4}$ m | $\xi_2 k_2^f/k_2^r$ $10^{-8}$ Cm |
|---|---|---|---|---|---|---|---|
| 15 | 0 | 1.0 | 2.1 | 2 | — | — | 1.59 |
| | 3 | 1.1 | 3.2 | 3 | 0.10 | 2.09 | 2.11 |
| | 6 | 1.5 | 5.4 | 1 | 1.06 | — | — |
| | 4 | — | — | — | — | — | — |
| | 8 | 0.50 | 1.8 | 2 | — | — | 2.55 |
| | 19 | 0.27 | 12. | 3 | 0.04 | 4.41 | 1.62 |
| | 33 | 0.15 | 0.53 | 3 | 0.06 | 0.99 | 0.59 |
| | 52 | 0.10 | 0.83 | 2 | — | — | 1.62 |
| | 53 | 0.096 | 0.96 | 3 | 0.01 | 0.11 | 0.01 |
| 35 | 0 | 2.2 | 7.0 | 1 | 0.83 | — | — |
| | 3 | 3.0 | 30. | 1 | 1.05 | — | — |
| | 6 | 4.3 | 15. | 1 | 1.33 | — | — |
| | 4 | 3.4 | 21. | 3 | 0.16 | 1.18 | 1.83 |
| | 8 | 1.5 | 3.7 | 3 | 0.12 | 3.01 | 3.55 |
| | 19 | 0.80 | 11. | 3 | 0.08 | 0.47 | 0.39 |
| | 33 | 0.35 | 3.7 | 3 | 0.05 | 1.37 | 0.66 |
| | 52 | 0.35 | 2.3 | 2 | — | — | 2.47 |
| | 53 | 0.34 | 4.5 | 2 | — | — | 1.36 |
| 50 | 0 | 4.2 | 20. | 3 | 0.17 | 2.23 | 3.79 |
| | 3 | 5.6 | 56. | 3 | 0.46 | 3.59 | 16.5 |
| | 6 | 7.8 | 26. | 2 | — | — | 6.04 |
| | 4 | 6.4 | 34. | 2 | — | — | 1.42 |
| | 8 | 2.7 | 23. | 2 | — | — | 1.72 |
| | 19 | 1.6 | 19. | 3 | 0.15 | 0.38 | 0.55 |
| | 33 | 0.90 | 12. | 3 | 0.06 | 1.67 | 0.98 |
| | 52 | 0.85 | 12. | 3 | 0.14 | 0.43 | 0.61 |
| | 53 | 0.92 | 21. | 2 | — | — | 2.24 |
| 70 | 0 | 9.5 | 93. | 2 | — | — | 10.7 |
| | 3 | 10.0 | 110 | 2 | — | — | 13.2 |
| | 6 | 14.8 | 140 | 2 | — | — | 14.8 |
| | 4 | 11.4 | 130 | 3 | 0.22 | 1.95 | 4.37 |
| | 8 | 6.2 | 160 | 2 | — | — | 8.28 |
| | 19 | 3.6 | 71. | 3 | 0.08 | 2.76 | 2.33 |
| | 33 | 2.5 | 160 | 3 | 0.08 | 5.13 | 3.88 |
| | 52 | 2.8 | 87. | 3 | 0.25 | 0.77 | 1.95 |
| | 53 | 2.4 | 40. | 2 | — | — | 4.96 |

Table 6.2: General estimation results for the outer cylinder (stainless steel/oil) interface as BTA was added to the CF. For reference, the oil and pressboard conductivities at each condition are indicated.

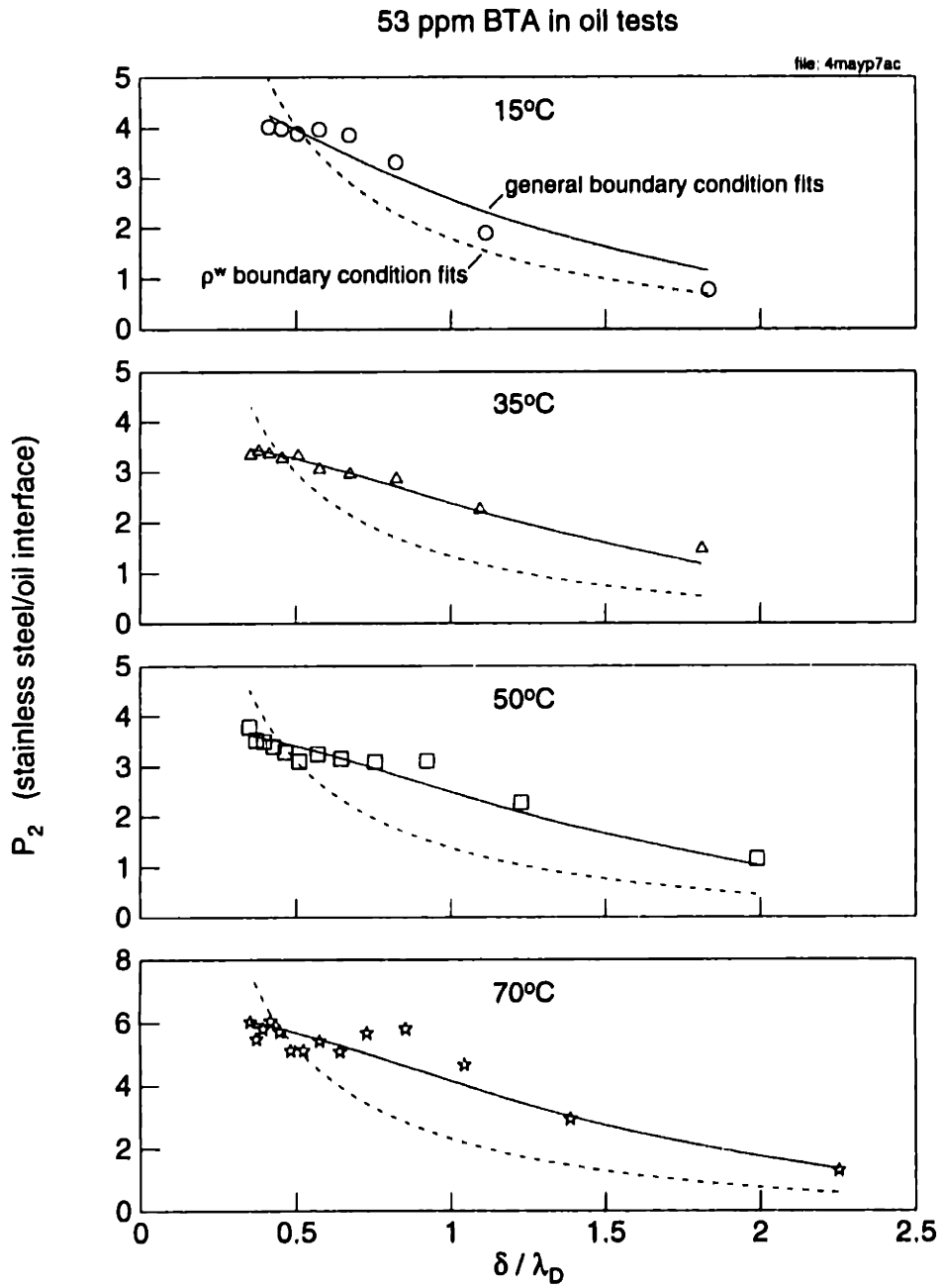


Figure 6.8: A comparison of the estimated fits to $P_2$ at four temperatures for the 53 ppm electrification data of Fig. 3.42. The fits to the Abedian-Sonin $\rho^w$ boundary condition are given by the dashed lines. The solid lines show that the general model, in which $k^r$ is nonzero, gives a better fit to this data.

condition, a wider range of data could be qualitatively and quantitatively described. The results are not always as clean as those of the simpler models, though, and require additional interpretation. In summary, while the uncertainties and noise in the data prevent estimations of all of the interfacial parameters and rate constants, this new boundary condition provides additional insight into the interfacial charge transfer processes.

# Chapter 7

# Charge Density Enhancement due to Recirculatory Flow

The four previous chapters described experimental and analytical techniques for exploring the charge generation stage of flow electrification. While the other electrification stages were also present, the generation stage was the primary one being explored. In a similar fashion, this chapter isolates the charge accumulation stage by investigating the enhancement of volume charge densities as a result of flow recirculation. In this investigation, a model is developed for a recirculatory flow loop which is similar to that found in electric power transformers and also in automotive fuel systems. The predictions of this model are then compared to measurements in a flow loop experiment in which the charge source was a cellulose paper filter.

## 7.1 Introduction

Flow electrification can become a hazard whenever a moving liquid transports charge to a downstream location where the charge can accumulate. If the field due to the accumulated charge exceeds the breakdown strength of the materials, spark discharges may occur. These discharges can then lead to the failure of the system. The charge itself comes from the interface between the liquid and its boundary, where there is usually a preferential adsorption of one charge carrier at the interface, with the other carrier diffusely distributed into the liquid. As the liquid flows by this boundary, some of the distributed charge is convected along with the liquid, resulting in a net charge being entrained in the liquid flow. This charge will then either accumulate in the liquid volume or leak away to the liquid/solid boundary, where it can still accumulate if the solid structure can rise in potential.

Numerous catastrophic failures of large scale systems appear to have followed this flow electrification scenario. Several explosions and fires in the petroleum industry during the transfer, processing, and storage of various hydrocarbon distillates have been attributed to charge accumulation in the fluid volume and at the interface between the fluid and the vapor space [4]. If enough charge accumulates, the resulting electric field can discharge through the vapor, igniting it and causing an explosion.

Numerous failures of very large forced-oil-cooled electric power transformers have also been attributed to flow electrification [13,14]. While the actual failure usually involves a discharge from the high-voltage windings to the low-voltage windings in the header region of the transformer, the sequence of events leading to the failure condition is not well understood. One proposed scenario is that the flowing oil carries charge from the ducts through the transformer windings up to the header region above the windings where the charge can accumulate in the oil or at the pressboard surfaces at the top of the ducts. When the transformer is energized, the applied AC field is superimposed on the DC field associated with the volume space charge and the total field may exceed the breakdown strength of the dielectric insulation between the windings [63,121]. Support for this scenario comes from the observation that most failures appear to occur during the start-up transient when the transformer is being brought on-line. Under these conditions, when the transformer is at low temperatures, the temperature dependent conductivity of the oil is also low, resulting in a long dielectric relaxation time. If the residence time in the header region is small compared to the relaxation time, significant volume charge can accumulate. In addition, if the residence time in the pipes and heat exchanger outside the transformer is small compared to the relaxation time, the oil re-entering the transformer can be significantly charged. This feedback of charged fluid can result in an enhancement of the oil volume charge densities, possibly leading to the eventual discharge and failure.

Another sequence of events that can lead to the electrification failure of a transformer begins with charge accumulating on the surface of the solid insulation in the plenum or entrance region to the winding ducts [122,123]. This surface charge can be the result of flow electrification in the pumps and heat exchangers so that the charge in the oil entering the plenum region relaxes to the solid insulation or the flowing oil entrains charge at the entrance region to the winding ducts, leaving behind image charge on the solid insulation. If the solid is very insulating, enough charge can accumulate that the total field formed by the superposition of the DC field and the energization AC field can exceed the breakdown strength of the solid insulation. Indeed, several failed transformers have shown discharge patterns ("wormholes") near the surface of the solid insulation at the entrance region to the windings [14]. It is probably not coincidental that this is a region where high DC fields can occur and significant eddies in the oil flow are created by the duct geometry. While it is unlikely that a single discharge in this region has sufficient energy to cause the transformer to fail, repeated discharges can create gas bubbles [82] and possibly particulates that can be transported by the oil up to the region between the high and low voltage windings. If enough gas or particulates accumulate, the dielectric strength of the insulation is sufficiently reduced that a discharge may occur.

This chapter investigates the concept of flow recirculation leading to enhanced volume charge densities. Until the development of sensors that unambiguously measure the local charge density, such as the Absolute Charge Sensor [11] or the Tandem Charge Monitor [10], enhanced charge densities could not be measured. Other charge density sensors could not separate the effects of flow electrification through the sensor from the desired charge density to be measured [30]. Furthermore, experiments based upon streaming current measurements could not show the charge density enhancement because the streaming current results from the difference in convection currents between charged fluid entering or exiting a structure. Because the difference is required, absolute values for the charge

density can only be obtained if the charge density is known to be zero somewhere in the system, implying no significant recirculation of charged fluid.

In this investigation, a "system" approach is used to model flow electrification by combining the contributions from several different components to determine the conditions leading to charge density enhancement. While it is well known that individual components can have dramatically different effects on the charge density, as shown by experiments in which varying the flow rate between components that charge the fluid with opposite polarities can change the net charge density of the fluid [124,125], most work has considered systems in which the flow was not recirculated or the fluid entering the charge source was essentially uncharged. An exception is the work of Roach and Templeton that developed a system model for the flow recirculation in a transformer and the accumulation of volume charge in the transformer header region, but those conditions did not lead to an enhanced charge density by the flow recirculation [121].

This chapter begins with the development of a model for a recirculatory flow loop in Section 7.2 that is similar to flow loops found in electric power transformers and automotive fuel systems. According to the model, the charge density will be enhanced if the charge does not relax completely before being returned to the entrance region of a charge source. This enhanced charge density was also verified in a flow loop experiment in which the charge source was a cellulose paper filter, as described in Section 7.3. Section 7.4 provides a summary and discusses the application of these results to an electric power transformer.

## 7.2 Recirculatory Flow Model

A schematic diagram for a generic flow loop is shown in Fig. 7.1. The recirculatory flow is driven by a pump (region 1). As the fluid flows through the loop, charge can be added to the fluid volume by the charge source (region 3), a paper filter in our case, and the charge can relax in the expansion volumes on either side of the charge source (regions 2 and 4). Charge can also relax in the pipes (region 5) which connect the various parts of the system or other expansion volumes (region 6) in the system. In this model, all of the charge entrained in the fluid flow comes from the charge source; only charge relaxation occurs in the other components of the system. Even though other regions may generate some charge, these contributions are assumed to be negligible in comparison to the charge provided by the charge source. This assumption can be tested by verifying that the charge density of the fluid exiting each region is less than that entering or by measuring the charge density in the loop with the charge source bypassed to verify that it is small compared to the charge densities obtained with the source present. To prevent ohmic conduction through the fluid from system components rising in potential, each region is assumed to be grounded or virtually grounded through a current measuring electrometer.

This type of flow loop can be found in electric power apparatus, such as a transformer, where oil is used for both electrical insulation and heat transfer. The oil is circulated through the system by a series of pumps (region 1). The oil then enters a plenum region (region 2) and passes into the insulation duct between the transformer windings. This

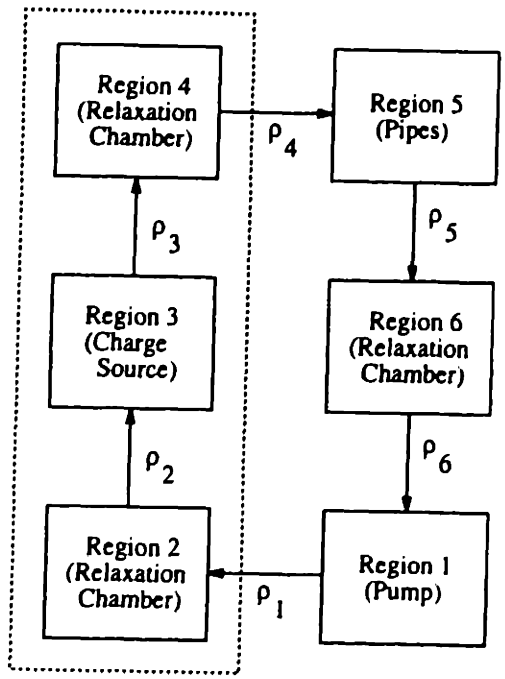


Figure 7.1: A schematic diagram for a recirculatory flow loop. The fluid flow is driven by a pump in region 1 into region 3 where charge can be entrained in the fluid volume. As the fluid flows through the other regions (2, 4, 5, and 6) the charge is allowed to relax. Regions 2, 4, and 6 are expansion regions while region 5 represents the pipes connecting the different regions. The regions enclosed within the box with dashed lines could correspond to a filter, with the filter paper acting as the charge source, or a transformer, with the pressboard ducts through the windings acting as the charge source.

duct is the charge source (region 3) because a charge separation process takes place in which charge (generally positive) on the liquid side of the interface is entrained in the oil flow with the opposite polarity charge remaining on the oil/pressboard insulation interface. The charged liquid then flows into the header region (region 4) where charge relaxation can occur. The oil is then recirculated back to the pump through a pipe network (region 5) and a heat exchanger (region 6).

Some fuel transfer systems, such as those supplying gasoline to the engine of an automobile, can also be considered recirculatory flow loops. The pressure for driving the fuel through the lines is created by a pump (region 1). The fuel then goes through some tubing into a filter, which strains fine particulate matter from the fuel so that the fuel injection ports will not get blocked. The filter material is typically a paper cellulose with small pores through which the fluid must pass. If the fluid is relatively insulating, the Debye length over which charge is distributed in the fluid volume is large compared to the pore radius and the pores are essentially uniformly filled with charge. As the fuel flows through the pores, some of this charge is entrained in the fuel flow and the

filter acts as a charge source. In most filters, the fluid flows through a small expansion volume (region 2), the filter paper itself (region 3), and then through another expansion volume (region 4). After the filter, the fluid flows through additional tubing (region 5) to either be injected for combustion or returned to the fuel tank (region 6). In typical polymeric (nylon) fuel systems, the conductivity of the tubing is low enough that various components in the system can rise in potential and ohmic conduction through the fluid becomes important.

## 7.2.1 Component models

To model the accumulation of charge in the fluid volume, the charge dynamics of each component will be modeled first. Then the net charge in the volume will be obtained by coupling the components together into a system.

### Expansion regions (2, 4, and 6)

To model the charge dynamics inside the relaxation regions, charge conservation can be applied. Consider a volume containing a fluid which has a uniform conductivity $\sigma$ and permittivity $\epsilon$. Also, let the fluid be circulated through the volume at a volume flow rate $Q$, where the fluid entering the volume has a charge density $\rho_i$ while the exiting fluid has a charge density $\rho_o$. The charge density of the exiting fluid will be the same as the bulk fluid charge density inside the volume if the fluid can be considered well-mixed. Inside this volume, charge must be conserved.

For a region with surface area $S$ and volume $V$, charge conservation can be written as

$$\oint_S (\vec{J} + \rho\vec{u}) \cdot d\vec{a} + \frac{d}{dt}\int_V \rho dV = 0 \tag{7.1}$$

where $\vec{J}=\sigma\vec{E}$ is an ohmic current density in the electric field $\vec{E}$ and $\rho\vec{u}$ is the convection current density for a fluid having a volume charge density $\rho$ and moving at a velocity $\vec{u}$. Assuming that the charge density is uniform over the fluid cross-section at the inlet and outlet, Eq. 7.1 gives

$$\oint_S \sigma\vec{E} \cdot d\vec{a} + (\rho_o - \rho_i)Q + V\frac{d\rho_o}{dt} = 0 \tag{7.2}$$

Since the fluid has homogeneous properties, the leftmost term can be rewritten using Gauss' law as the total charge in the volume $\rho_o V$, divided by the dielectric relaxation time $\tau_e = \epsilon/\sigma$. The charge density inside a well-mixed volume with ohmic relaxation and charge convection is then given by

$$\frac{d\rho_o}{dt} + \left(\frac{1}{\tau_e} + \frac{1}{\tau_r}\right)\rho_o = \frac{1}{\tau_r}\rho_i \tag{7.3}$$

where $\tau_r = V/Q$ is the residence time of charge in the fluid volume. As an example, when $\rho_i$ is a constant, the outlet charge density goes as

$$\rho_o(t) = \frac{\rho_i}{1 + \frac{\tau_r}{\tau_e}}\left(1 - e^{-t/\tau}\right) \quad ; \quad \frac{1}{\tau} \equiv \frac{1}{\tau_e} + \frac{1}{\tau_r} \tag{7.4}$$

for an initial charge density of zero. This will be contrasted with the pipe flow regions where the average charge density decays *exponentially* with the residence time. More generally, $\rho_i$ is a function of time and the charge densities for the expansion regions 2, 4 and 6 are governed by

$$\frac{d\rho_2}{dt} + \left(\frac{1}{\tau_e} + \frac{1}{\tau_{r2}}\right)\rho_2 = \frac{1}{\tau_{r2}}\rho_1 \tag{7.5}$$

$$\frac{d\rho_4}{dt} + \left(\frac{1}{\tau_e} + \frac{1}{\tau_{r4}}\right)\rho_4 = \frac{1}{\tau_{r4}}\rho_3 \tag{7.6}$$

$$\frac{d\rho_6}{dt} + \left(\frac{1}{\tau_e} + \frac{1}{\tau_{r6}}\right)\rho_6 = \frac{1}{\tau_{r6}}\rho_5 \tag{7.7}$$

In this formulation, it is assumed that the fluid properties are uniform throughout the system ($\tau_{e2} = \tau_{e4} = \tau_{e6} \equiv \tau_e$).

### Charge source region (3)

The most general description of the charge source would take into account a large number of parameters including, but not limited to, the fluid properties, such as the conductivity, permittivity, ion mobilities, trace impurities, temperature and self-fields from charge already entrained in the fluid, and the properties of the charging element itself. In a transformer, the ducts for oil flow through the windings would be considered the charging element. The volume charge density generated by the fluid flow would depend upon the flow rate, the applied fields, and probably the conductivity and moisture content associated with the pressboard insulation.

In the case being considered here, the charging element is a paper cellulose filter, composed of a matrix of paper fibers with small pores through which the fluid must pass. As the oil flows through the pores, some of the volume charge distributed across the pores is entrained in the oil flow and the filter paper acts as a charge source (region 3). Thus, the charge density of the fluid exiting the filter paper will depend upon the paper material.

A model for the charge entrained by the flow of hydrocarbon liquids through filter paper has been developed by Huber and Sonin [126]. In this model, the solid matrix of the filter paper (having permittivity $\epsilon_s$) is assumed to be much more insulating than the liquid flowing through it and the liquid enters the paper uncharged but leaves the paper charged. An analytical expression for the charge densities exiting the paper was derived for the case of small charge densities, such that the additional conductivity due to net mobile volume charge is negligible compared to the equilibrium ohmic conductivity, and for Peclet numbers ($uh/D_m$) based on the average axial fluid velocity $u$ in the pores, filter paper thickness $h$ and ion diffusivity $D_m$ much larger than unity. By extending this derivation to include a charge density $\rho_2$ for the fluid entering the filter paper, the charge density of the fluid exiting the paper can be written as

$$\rho_3 \simeq \frac{\epsilon_p \rho_f}{\epsilon P}\left(1 - e^{-1/R_e}\right) + \rho_2 e^{-1/R_e} \tag{7.8}$$

where $P$ is the paper porosity or the volume fraction occupied by the fluid, $\rho_f$ is the fixed charge density associated with the filter paper and the fluid, $\epsilon_p = P\epsilon + (1-P)\epsilon_s$ is the effective permittivity of the fluid-solid composite, and $R_e$ is an electric Reynolds number given by

$$R_e = \frac{\epsilon_p u}{P^2 \sigma h} \tag{7.9}$$

The electric Reynolds number is the ratio of the dielectric relaxation time to the fluid transport time through the filter paper. This can be seen more clearly by rewriting Eq. 7.9 as

$$R_e = \left(\frac{\epsilon_p}{P\sigma}\right)\left(\frac{\tau u}{P}\right)\left(\frac{1}{\tau h}\right) = \frac{\tau_{ep}}{\tau_{rp}} \tag{7.10}$$

where $\tau$ is the tortuosity of the pores through the filter paper, $\tau_{ep} = \epsilon_p/(P\sigma)$ is an effective relaxation time, $\tau u/P$ is the average fluid volume flow rate over the cross sectional area of the filter, $\tau h$ is an effective pore length, and $\tau_{rp} = Ph/u = V_p/Q$ is a residence time for fluid in filter paper having an effective volume $V_p$. Thus, the charge density exiting the filter paper can be expressed as

$$\rho_3 \simeq \rho_d \left(1 - e^{-\tau_{rp}/\tau_{ep}}\right) + \rho_2 e^{-\tau_{rp}/\tau_{ep}} \tag{7.11}$$

where $\rho_d \equiv \epsilon_p \rho_f/(P\epsilon)$ is a material dependent constant that is independent of flow rate. The analytical expression developed by Huber and Sonin can be obtained by setting $\rho_2$ to zero.

The charge density exiting the filter consists of the contribution from the paper itself plus the charge density entering the paper modified by a decay associated with the time the charge spends in the paper. This superposition of the contributions to the exiting charge is consistent with the small charge density constraint. In this formulation, the parameter $\rho_d$ is an effective charge "difference" for charge added to the fluid as it passes though the filter paper. Note that for low flow rates such that $\tau_{rp} \gg \tau_{ep}$, $\rho_3 \approx \rho_d$ and the filter paper acts as a constant charge density source. On the other hand, for high flow rates such that $\tau_{rp} \ll \tau_{ep}$, the influent and effluent charge densities are related to the current from the paper $I_{fp}$ by

$$I_{fp} = (\rho_2 - \rho_3)Q \approx -\frac{\rho_d V_p}{\tau_{ep}} \tag{7.12}$$

and the filter paper acts as a constant current source.

### Pipe region (5)

In order to complete the flow loop, pipes will be present. In these flow sections, the volume is not necessarily well-mixed so Eq. 7.3 does not hold over the pipe length. Even in turbulent flow, the fluid is only considered well-mixed at a given pipe cross-section; the charge density is taken as uniform over a cross-section, but can vary over the pipe length. A relation describing the relaxation of charge in the pipes is given by

$$\rho_5 = \alpha \rho_4 \tag{7.13}$$

where the relaxation parameter $\alpha$ reflects the amount of charge relaxation in this region and will, in general, be different for laminar and turbulent flow. The relaxation parameter must satisfy $\alpha \leq 1$ to be consistent with the assumption of only charge relaxation in this region.

The relaxation parameter depends upon the flow rate, the fluid properties, and the system geometry through the Reynolds number for the fluid flow. For pipe flow, the Reynolds number $R$ can be defined as

$$R = \frac{4Q}{\pi D \nu} \tag{7.14}$$

with $D$ the pipe diameter and $\nu$ the fluid kinematic viscosity. For fully developed flow, the flow can be considered laminar if $R \lesssim 2000$ and the flow can be considered turbulent if $R \gtrsim 2000$. These different flow regimes will result in different relaxation parameters, but, if the flow is developing because of short pipe lengths and numerous bends or protuberances (such as valves) as in the experiment to be discussed in Section 7.3, the flow can be considered well mixed with an essentially uniform velocity profile. Thus, even though the flow in the experiment varies from laminar to turbulent because of the different flow rates and pipe diameters, we assume that the flow is fully mixed so that the charge density $\rho(z)$ and fluid velocity $u$ are uniform across the pipe cross-section. If we write charge conservation over a differential pipe length $dz$ and take the limit as $dz$ goes to zero, the steady state charge density is found to vary with position as

$$\rho(z) = \rho_i e^{-1/R_e(z)} \tag{7.15}$$

where $\rho_i$ is the charge density at the inlet to the pipe section and $R_e(z) = u\tau_e/z$ is an electric Reynolds number giving the ratio of the dielectric relaxation time to the fluid transport time over a length $z$. With the average fluid velocity related to the volume flow rate by $u = 4Q/\pi D^2$, a comparison of Eqs. 7.13 and 7.15 gives the relaxation parameter as

$$\alpha = e^{-\tau_{r5}/\tau_e} \tag{7.16}$$

where $\tau_{r5}$ is the residence time in region 5. Appendix D shows that this is also a reasonably accurate representation for the relaxation parameter in laminar flow.

## Pump region (1)

The pump for driving the flow is in region 1. The volume in this region may be considered well-mixed so Eq. 7.3 applies. If the volume is considered to be small so that the residence time is negligible in comparison to the dielectric relaxation time, the charge density exiting is essentially that entering, or

$$\rho_1 = \rho_5 \tag{7.17}$$

In any real pump, both charge relaxation and generation will be taking place; these effects are assumed to be negligible in this analysis.

### 7.2.2 System model

To obtain a relation describing the steady state charge densities in terms of the properties of each region, the charge dynamic equations for each region must be combined. In the experiment to be discussed in Section 7.3, the inlet and outlet of the charge source (filter paper) are not readily accessible and expansion volumes are present on either side of the source. As a result, the charge densities at the filter outlet ($\rho_4$) and inlet ($\rho_1$) are measured, and these are the charge densities to be determined. Note that the largest charge densities will occur in region 4 because it is immediately after the charge source and the other regions are assumed to only have charge relaxation, not generation.

The governing equation for the charge density in the fluid exiting region 4 can be obtained by combining Eqs. 7.5 to 7.7, 7.11, 7.13, and 7.17 to yield

$$\begin{aligned}
\frac{d^3\rho_4}{dt^3} &+ \left[\frac{3}{\tau_e}+\frac{1}{\tau_{r2}}+\frac{1}{\tau_{r4}}+\frac{1}{\tau_{r6}}\right]\frac{d^2\rho_4}{dt^2} \\
&+ \left[\left(\frac{1}{\tau_e}+\frac{1}{\tau_{r4}}\right)\left(\frac{2}{\tau_e}+\frac{1}{\tau_{r2}}+\frac{1}{\tau_{r6}}\right)+\left(\frac{1}{\tau_e}+\frac{1}{\tau_{r2}}\right)\left(\frac{1}{\tau_e}+\frac{1}{\tau_{r6}}\right)\right]\frac{d\rho_4}{dt} \\
&+ \left[\left(\frac{1}{\tau_e}+\frac{1}{\tau_{r2}}\right)\left(\frac{1}{\tau_e}+\frac{1}{\tau_{r4}}\right)\left(\frac{1}{\tau_e}+\frac{1}{\tau_{r6}}\right)-\frac{\alpha}{\tau_{r2}\tau_{r4}\tau_{r6}}e^{-\tau_{rp}/\tau_{ep}}\right]\rho_4 \\
&= \frac{\left(1-e^{-\tau_{rp}/\tau_{ep}}\right)}{\tau_{r4}}\left[\frac{d^2\rho_d}{dt^2}+\left(\frac{2}{\tau_e}+\frac{1}{\tau_{r2}}+\frac{1}{\tau_{r6}}\right)\frac{d\rho_d}{dt}\right. \\
&\qquad \left.+\left(\frac{1}{\tau_e}+\frac{1}{\tau_{r2}}\right)\left(\frac{1}{\tau_e}+\frac{1}{\tau_{r6}}\right)\rho_d\right] \qquad (7.18)
\end{aligned}$$

Since this is a third order differential equation in the charge density, it is difficult to determine the stability from the roots of the characteristic polynomial. Instead, the equation can be shown to be stable with the Routh test [127: pp. 174-175] or by considering the homogeneous solutions of the differential equations given in Eqs. 7.5 to 7.7. The homogeneous solutions correspond to exponentials that decay with time. As long as the "source" charge density ($\rho_d$ in this case) does not increase indefinitely with time, the charge densities throughout the system will also be bounded and not increase indefinitely with time.

For the filter paper being considered here, assume that $\rho_d$ can be taken to be a constant with respect to time. The steady state charge densities at the outlet and inlet of the filter are then given by

$$\rho_{4ss} = \rho_d\left[\frac{\left(1+\frac{\tau_{r2}}{\tau_e}\right)\left(1+\frac{\tau_{r6}}{\tau_e}\right)\left(1-e^{-\tau_{rp}/\tau_{ep}}\right)}{\left(1+\frac{\tau_{r2}}{\tau_e}\right)\left(1+\frac{\tau_{r4}}{\tau_e}\right)\left(1+\frac{\tau_{r6}}{\tau_e}\right)-\alpha e^{-\tau_{rp}/\tau_{ep}}}\right] \qquad (7.19)$$

$$\rho_{1ss} = \frac{\alpha\rho_{4ss}}{1+\frac{\tau_{r6}}{\tau_e}} \qquad (7.20)$$

The steady state charge density in region 4 can also be written as

$$\rho_{4ss} = \rho_d\frac{\left(1-e^{-\tau_{rp}/\tau_{ep}}\right)}{1-G} \qquad (7.21)$$

where $G$ is a feedback coefficient defined by

$$G \equiv \frac{\alpha e^{-\tau_{rp}/\tau_{ep}}}{\left(1+\frac{\tau_{r2}}{\tau_e}\right)\left(1+\frac{\tau_{r4}}{\tau_e}\right)} - \frac{\tau_{r4}}{\tau_e} \tag{7.22}$$

Note that the magnitude of $G$ is always less than one. In the limit where the system does not have any loss elements, $G$ approaches $e^{-\tau_{rp}/\tau_{ep}}$ and the maximum possible charge density is $\rho_4 = \rho_d$.

A limiting case for this model occurs when the relaxation parameter is zero ($\alpha = 0$) or the residence time for the fluid in region 6 is long compared to the relaxation time. Under these conditions, all of the charge relaxes before the fluid returns to the charge source. Then $G = -\tau_{r4}/\tau_e$ and the steady state charge density is

$$\rho_{4ss} = \rho_d \frac{\left(1 - e^{-\tau_{rp}/\tau_{ep}}\right)}{1+\frac{\tau_{r4}}{\tau_e}} \tag{7.23}$$

This result is consistent with previously published results for charge relaxation inside a well-mixed charge trap [2]. Furthermore, if the residence times are small compared to the relaxation times ($\tau_{r4}/\tau_e \ll 1$, $\tau_{rp}/\tau_{ep} \ll 1$), Eq. 7.23 approximately reduces to

$$\rho_{4ss} \approx \rho_d \frac{\tau_{rp}}{\tau_{ep}}\left(1 - \frac{\tau_{r4}}{\tau_e}\right) = \rho_d \frac{P\sigma V_p}{Q\epsilon_p}\left(1 - \frac{V_4\sigma}{Q\epsilon}\right) \tag{7.24}$$

Thus, when the flow rates are large or the fluids are insulating, these residence times are small compared to the relaxation times and the charge density in the fluid volume decreases as the flow rate increases.

Another limiting case occurs when the relaxation parameter is one ($\alpha = 1$) or the residence time for expansion region 6 is small compared to the relaxation time. In this case, the charge only relaxes in the expansion volumes on the inlet and outlet sides of the (filter paper) charge source and the fluid entering the charge source can still contain a significant charge. Assuming, for simplicity, that $\tau_{r2} = \tau_{r4}$, a first order approximation to $G$ is

$$G \simeq \left(1 - \frac{\tau_{r4}}{\tau_e}\right) e^{-\tau_{rp}/\tau_{ep}} - \frac{\tau_{r4}}{\tau_e} \tag{7.25}$$

For low flow rates, the exponential goes to zero and the steady state charge density will be the same as the $\alpha = 0$ case. For high flow rates, the steady state charge density becomes

$$\rho_{4ss} \approx \rho_d \left[1 + 2\frac{\epsilon_p}{P\epsilon}\frac{V_4}{V_p}\right]^{-1} \tag{7.26}$$

which is a constant, independent of flow rate. Thus, if the flow rate is high enough, the steady state charge density is enhanced compared to the non-recirculating ($\alpha = 0$) charge case. Conceptually, this enhancement can be interpreted as charge accumulating in the fluid with each pass through the filter, reaching a steady state when charge leakage just balances charge generation.

The limiting cases illustrating the enhancement of volume charge densities can be

related to the electrification processes inside a transformer where failures have generally occurred when the transformer is being re-energized after being out of service. When in operation, the temperature of a transformer is elevated and the temperature dependent oil conductivity is relatively large. Then, the $\alpha = 0$ limiting case applies and the charge relaxes without any significant accumulation of charge in the oil volume. On the other hand, when first being brought on-line, transformers are typically at a low temperature so the oil conductivity is low. It is then possible for the residence times and dielectric relaxation times to be comparable so that the $\alpha = 1$ limiting case applies and significant charge can accumulate in the oil volume.

By substituting for the relaxation parameter from Eq. 7.16 into Eqs. 7.19 and 7.20, the steady state charge densities relative to $\rho_d$ can be written as

$$\frac{\rho_{4ss}}{\rho_d} = \frac{\left(1 + \frac{V_2}{V_4}\frac{\tau_{r4}}{\tau_e}\right)\left(1 + \frac{V_3}{V_4}\frac{\tau_{r4}}{\tau_e}\right)\left(1 - e^{-\frac{V_p}{V_4}\frac{\rho_s}{\epsilon_p}\frac{\tau_{r4}}{\tau_e}}\right)}{\left(1 + \frac{V_2}{V_4}\frac{\tau_{r4}}{\tau_e}\right)\left(1 + \frac{V_3}{V_4}\frac{\tau_{r4}}{\tau_e}\right)\left(1 + \frac{\tau_{r4}}{\tau_e}\right) - e^{-\left(\frac{V_3}{V_4} + \frac{V_p}{V_4}\frac{\rho_s}{\epsilon_p}\right)\frac{\tau_{r4}}{\tau_e}}} \tag{7.27}$$

$$\frac{\rho_{1ss}}{\rho_d} = \frac{\left(1 + \frac{V_2}{V_4}\frac{\tau_{r4}}{\tau_e}\right)\left(1 - e^{-\frac{V_p}{V_4}\frac{\rho_s}{\epsilon_p}\frac{\tau_{r4}}{\tau_e}}\right)e^{-\frac{V_3}{V_4}\frac{\tau_{r4}}{\tau_e}}}{\left(1 + \frac{V_2}{V_4}\frac{\tau_{r4}}{\tau_e}\right)\left(1 + \frac{V_3}{V_4}\frac{\tau_{r4}}{\tau_e}\right)\left(1 + \frac{\tau_{r4}}{\tau_e}\right) - e^{-\left(\frac{V_3}{V_4} + \frac{V_p}{V_4}\frac{\rho_s}{\epsilon_p}\right)\frac{\tau_{r4}}{\tau_e}}} \tag{7.28}$$

When written in this form, the steady state charge densities depend upon the flow rate through the parameter $\tau_{r4}/\tau_e$ and upon the relative volumes of the other regions (except the filter paper region, which also has a contribution due to the differences in permittivities).

A plot of the theoretical relative charge density at the outlet of the filter and the inlet to the filter as a function of flow rate is given in Fig. 7.2 for representative parameters from the experiments. In the experiments, two flow conditions are considered: reservoir and bypass. In the reservoir flow condition, the fluid flows through an expansion volume (drum) near the pump inlet. By making the residence time in this region large compared to the relaxation time, the fluid is essentially uncharged as it exits this region and goes toward the filter inlet. In the bypass flow condition, the fluid flows through a pipe that bypasses the expansion volume. The volume of this pipe section is much smaller than the expansion volume so significantly less charge relaxation occurs. As a result, the fluid entering the filter has a significant charge density.

For very low flow rates ($\tau_{rp} \gg \tau_{ep}$), the fluid leaving the filter paper has approached $\rho_d$ and the charge density is determined by the residence time for charge relaxation in the expansion volumes; as the flow rate increases, the residence time decreases and the charge density increases. At high flow rates, the contribution to the volume charge density from the filter paper decreases with increasing flow rate but the residence time for charge relaxation in the expansion volumes also decreases. At the higher flow rates, the decrease in charge density from the filter paper source dominates the reduced charge relaxation, causing a net decrease in the charge density as the flow rate increases.

When the residence time in the pipe region and expansion region 6 are small compared to the dielectric relaxation time, charged fluid enters the filter and the charge density

is enhanced with respect to the case when the fluid enters the filter uncharged. This enhancement is most evident at the higher flow rates. The results for complete charge relaxation in the loop ($V_6/V_4 \rightarrow \infty$) are essentially the same as shown in Fig. 7.2 for reservoir flow.

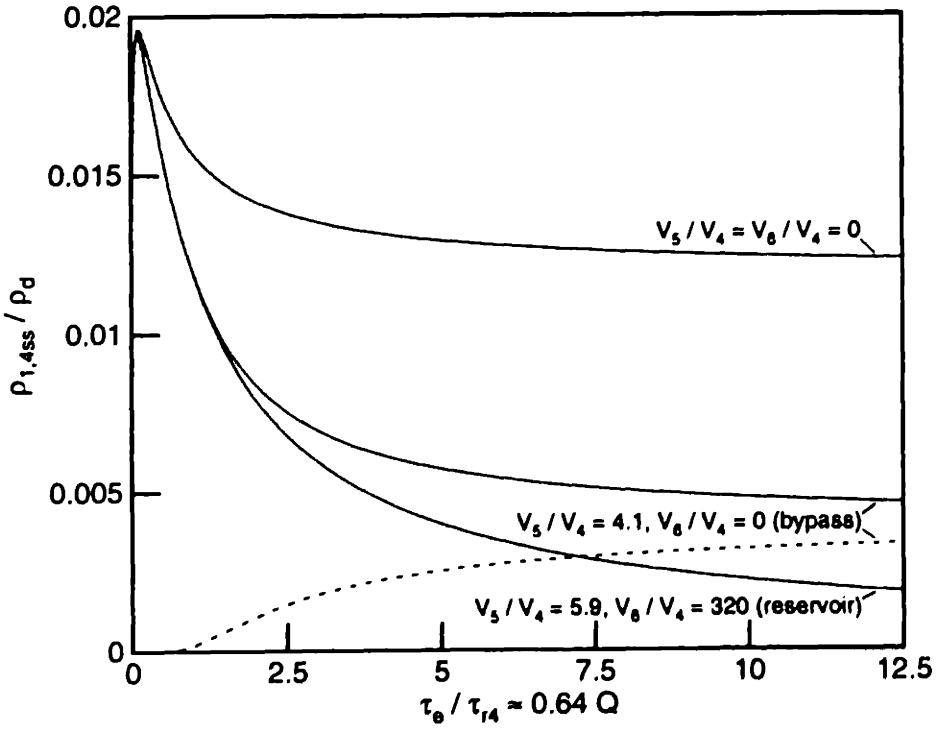


Figure 7.2: The theoretical filter outlet (solid) and inlet (dashed) steady state charge densities as a function of the fluid volume flow rate with representative parameters $V_2 = V_4$ and $V_p P \epsilon / V_4 \epsilon_p = 0.024$. In the $V_5 = V_6 = 0$ case, the inlet and outlet charge densities are the same. For the $V_6/V_4 = 320.0$ case of flow through the reservoir, the filter inlet charge density is near zero. For comparison to the experiment, it was assumed that $\tau_e/\tau_{r4}$ is approximately 0.64 times the flow rate $Q$ in GPM.

## 7.3 Flow Loop Experiment

To test the model and show that charge densities can be enhanced by flow recirculation, a flow loop experiment was developed. The experimental facility itself is a much smaller version of the facility used by Cooper Power Systems [128,129] for studying electrification. In the basic experiment, the charge density is measured at the inlet and outlet of a paper

filter for various flow rates. In addition to showing the charge density enhancement, the charge generated or relaxed by various components in the system can be determined. Another experiment, with the charge densities measured at the inlet and outlet to the drum reservoir, showed the charge density variation with temperature and other, as yet undetermined, parameters.

### 7.3.1 Apparatus

A closed flow loop facility for testing the enhancement of charge densities is shown in Fig. 7.3. In this loop, transformer oil flow is driven by a pump through standard iron piping (4.13 cm I.D.) to an oil filter and a 208 l (55 gal) drum reservoir. The oil filter was connected to the flow loop through short sections of copper tubing (2.00 cm I.D.) but electrically isolated from the grounded pipes through two nylon joints and virtually grounded through a current measuring electrometer [Keithley 614]. The filter was a ZINGA AE-10, which is a 10 $\mu$m paper cellulose filter. The reservoir was electrically isolated from the grounded pipes by PVC tubing but grounded with an external wire. A low pass electronic filter was attached to the electrometer input to prevent AC electrical noise from saturating the electrometer.

To measure the charge densities, Absolute Charge Sensors (ACS's) were installed at the filter inlet and outlet [11]. The ACS's sampled oil from the center of the pipes; charge density profile measurements have shown a uniform charge density across the pipe so the exact position of the sampling probe was not critical [11]. Gate valves allow the reservoir to be bypassed so that the residence time for charge relaxation in the flow loop could be greatly reduced and the enhancement of the charge density due to the recirculation of the fluid flow could be determined.

The oil temperature was monitored with an Omega model 747 digital thermometer and a thermocouple probe at the pump inlet and found to vary from 27.4°C to 32.2°C when the flow went through the bypass. When the flow went through the reservoir, the temperature varied from 29.9°C to 30.8°C. The impeller speed of the pump was controlled using an AC motor controller to give flow rates between 0.063 and 1.26 l/s (1 and 20 GPM). When the fluid flows through the bypass, the volume of oil for dissipating the heat generated by the flow is greatly decreased and the oil temperature increases more rapidly than when the flow is through the reservoir. The temperature increase was not a problem at the lower flow rates, but did become a problem at the higher flow rates because the measured charge densities increased with temperature. To prevent the oil temperature from increasing too much, after each measurement with bypass flow, the flow was valved through the reservoir to return the oil to near its ambient temperature.

In these measurements, the oil had a relative permittivity of $\epsilon/\epsilon_o$=2.2. The oil moisture content and conductivity were determined at the end of the experiment from samples of oil withdrawn from the system. The moisture content was measured to be 34 ppm with a Mitsubishi Moisture Meter, which performs a Karl-Fischer titration. This is a relatively high moisture content (about 40% of saturation) because the oil was readily available and no attempts were made to vacuum process or dry it. The conductivity was measured with an interdigital electrode structure (flex sensor), which has one set of electrodes driven at a 1 V peak AC signal that could be varied in frequency from 5 mHz

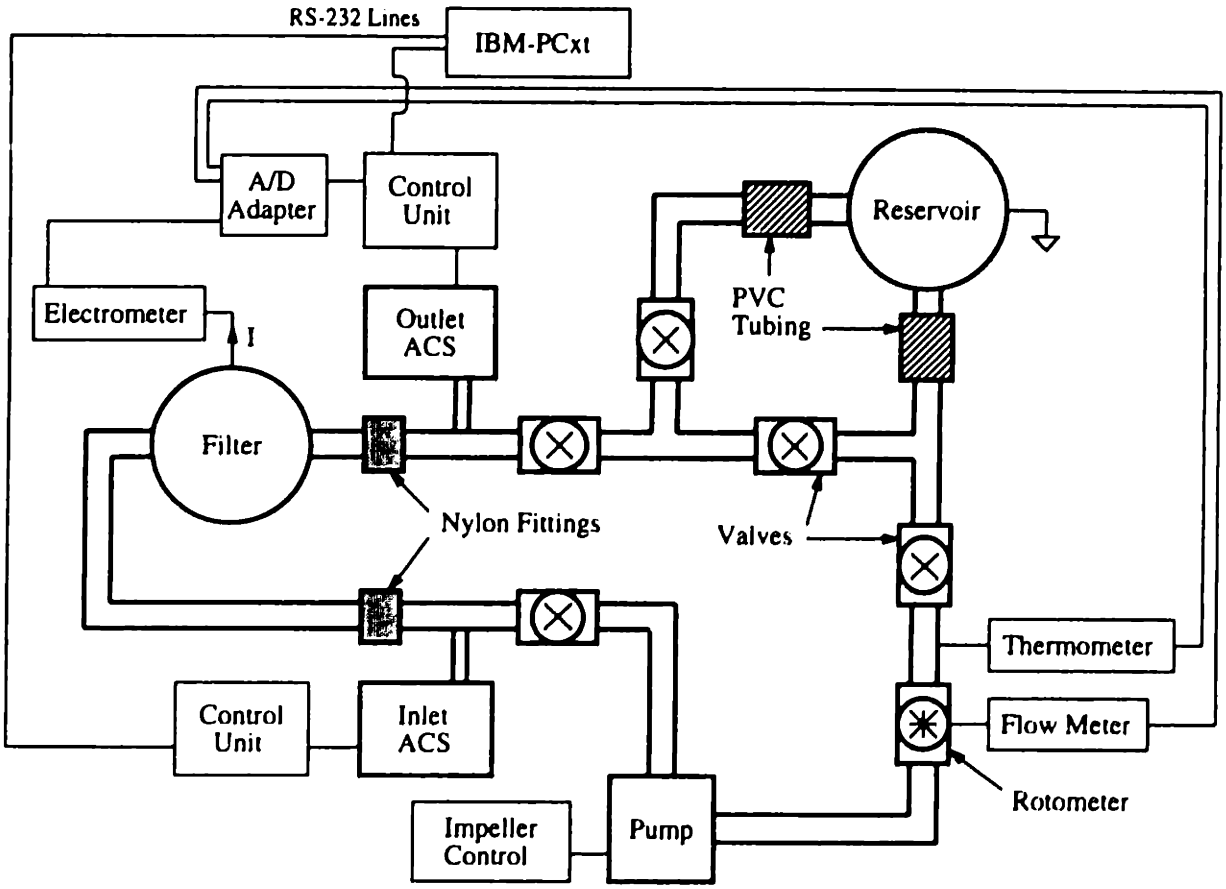


Figure 7.3: The flow loop experiment. The fluid is circulated between a filter, which contains cellulose paper and acts as a charge source, and a reservoir, which acts as a charge relaxation chamber. The charge density was measured at the inlet and the outlet to the filter. The reservoir can be bypassed using the valves.

to 10 kHz [17]. The other set of electrodes were sensing electrodes, with the output signal attenuated and phase delayed with respect to the driven signal. A parameter estimation algorithm was then used to process these measured signals and gave an ohmic conductivity of $\sigma$=3 pS/m at 25°C [58].

The system was filled with as much oil as possible to minimize the air content and the effects of bubbles. The inlet pipe to the reservoir extended to the end opposite the reservoir outlet so that any charged oil entering the reservoir spent a full residence time in the reservoir before exiting. The residence time for oil in the reservoir at the highest flow rate of 1.26 l/s (20 GPM) was about 165 s. Since the oil dielectric relaxation time was on the order of 6.5 s, the oil leaving the reservoir should have been essentially uncharged. On the other hand, when the reservoir was bypassed, the volume of the pipes for recirculating the flow (region 5 of the model) was on the order of $V_5$=2.6 l (0.7 gal), giving a reduced residence time of about 2.1 s at the highest flow rate. With this reduced residence time,

the charge did not have sufficient time to completely relax before re-entering the paper filter. For comparison to the model, a complete set of the flow loop parameters are given in Table 7.1.

| Structure | Parameter | Flow Condition | |
|---|---|---|---|
| | | Bypass | Reservoir |
| Pump volume | $V_1$ | 1.25 l (0.33 gal) | |
| Filter (inlet) volume | $V_2$ | 0.64 l (0.17 gal) | |
| Filter (paper) volume | $V_p$ | 0.026 l (0.007 gal) | |
| Filter (outlet) volume | $V_4$ | 0.64 l (0.17 gal) | |
| Pipe volume | $V_5$ | 2.6 l (0.7 gal) | 3.8 l (1.0 l) |
| Expansion volume | $V_6$ | 0.0 l (0.0 gal) | 208 l (55 gal) |
| Fluid permittivity | $\epsilon/\epsilon_o$ | 2.2 | |
| Fluid conductivity | $\sigma$ (pS/m) | 3 (at 25°C) | |
| Paper permittivity | $\epsilon_s/\epsilon_o$ | 3.5 | |
| Paper porosity | $P$ | 0.7 | |

Table 7.1: Nominal experimental parameters for the flow loop. The values given for volumes $V_2$ and $V_4$ include the volumes of the pipe sections between the filter itself and the locations where the ACS's sampled the fluid.

The current measured by the filter electrometer should be equal to the difference between the convection currents at the inlet and the outlet. If the charge density and fluid flow rate can be taken as uniform over the cross section of the pipe, the electrometer current $i_E$ is given by

$$i_E = (\rho_i - \rho_o)Q \tag{7.29}$$

with $Q$ the volume flow rate. In the experiment, the flow rate varied between 0.063 and 1.26 l/s (1 and 20 GPM). Using a representative oil kinematic viscosity of $\nu = 1.8 \times 10^{-5}\text{m}^2/\text{s}$, the Reynolds number varied from 108 to 2160 in the iron piping and from 225 to 4500 in the copper piping. The development length $L_e$ for fully developed flow at the entrance of a duct of diameter $D$ is given by [97: pp.312-313]

$$\frac{L_e}{D} \approx \begin{cases} 0.06R & \text{laminar} \\ 4.4R^{1/6} & \text{turbulent} \end{cases} \tag{7.30}$$

where $R$ is the Reynold's number defined in Eq. 7.14. This gives a minimum development length (for laminar flow at 0.063 l/s) of 13 cm for the copper tubing and 27 cm for the iron piping. This indicates that the flow may have been fully developed in some sections of the pipe network at the lower flow rates. At the higher flow rates, where most of the measurements were performed, the flow was developing because of the short sections of pipes and the numerous bends. For the analysis presented here, even when the flow was not turbulent, the velocity profile was taken as uniform over the pipe cross section.

### 7.3.2 Results

To test for the enhancement of charge densities due to recirculatory flow, the charge densities at the inlet and outlet to the filter were measured as a function of flow rate. A representative set of data is shown in Fig. 7.4. With flow through the reservoir, the charge density at the filter outlet is seen to decrease as the flow rate increases. The charge density at the inlet is small compared to that at the outlet, thereby confirming that the charge generated external to the paper filter source is negligible. With the reservoir bypassed so that the charge is not completely relaxed before entering the filter, the charge density at the outlet tends to be enhanced with respect to the reservoir flow case.

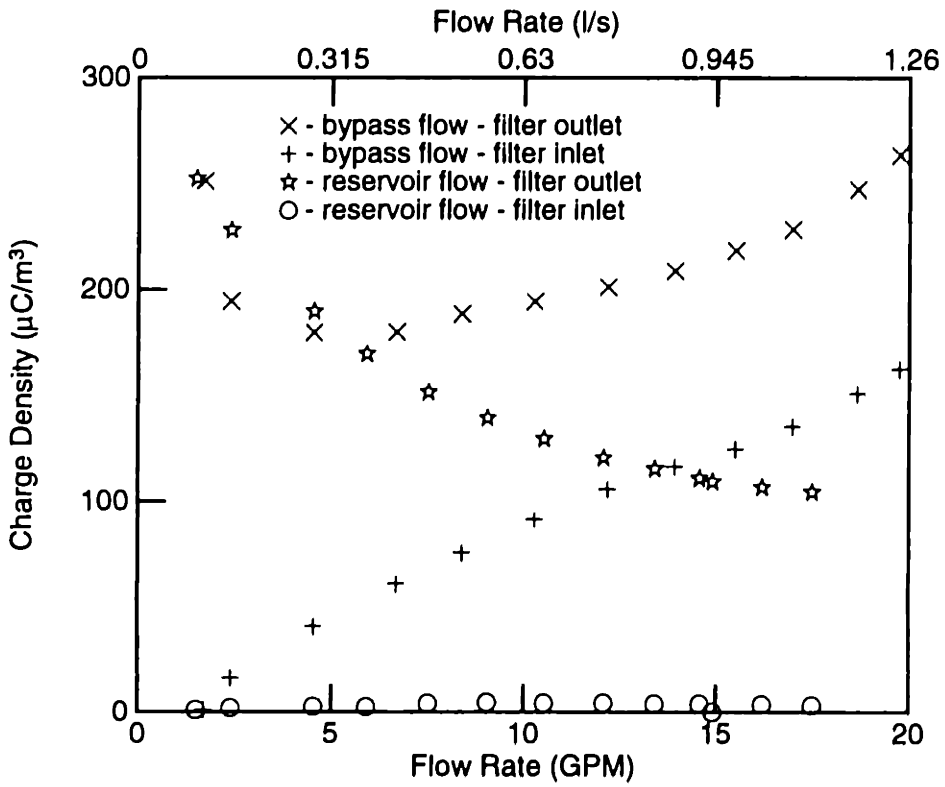


Figure 7.4: Measured charge densities at the filter inlet and outlet as the fluid flow rate and relaxation volume vary. The oil temperature varied from 27.4°C to 32.2°C when the flow was through the bypass and varied from 29.9°C to 30.8°C when the flow was through the reservoir. The oil moisture level was 34 ppm and the conductivity was 3 pS/m.

During these measurements, it was found that the ACS required a correction factor whenever the hydrodynamic pressure became greater than about 5 psi gauge. To describe this correction factor and how it was obtained, some background on the operation of the

ACS is necessary. The ACS determines the volume charge density by drawing a sample of oil into a Faraday cage, measuring the current going to the cage, and then dividing this current by the flow rate of fluid into the cage. The fluid flow into the Faraday cage is driven by a stepper motor expanding a bellows, with the flow rate related to the step rate of the stepper motor by a calibration constant (the effective area of the bellows). This calibration constant was determined at ambient pressures. At the higher flow rates through the flow loop, the pressure at the inlet to the filter was found to be appreciable, on the order of 5–15 psi gauge. This resulted in a "squirming" of the bellows and an increase in the effective area of the bellows and the calibration constant.

An empirical correction factor was used to account for the increased flow rate into the ACS. This correction factor was found by measuring the change in bellows volume between pressurized and ambient conditions for the bellows in its initial position at the start of an ACS measurement cycle and at the position of maximum extension during a cycle. The difference between these volumes is the contribution to the volume of the bellows during the ACS measurement cycle. Assuming that this excess volume divided by the duration of the sampling cycle of the ACS gives the flow rate correction, the net flow rate into the ACS is the sum of the original flow rate and the flow rate caused by the hydrodynamic pressure. A plot of the correction factor for the charge density as a function of flow rate for both bypass and reservoir flow is given in Fig. 7.5. In summary, the charge densities at the high pressures, which occurred at the filter inlet during the higher flow rates through the flow loop, required this correction; at the filter outlet, the correction was usually not significant because of the large pressure drop across the filter.

The data in Fig. 7.4 tends to be consistent with the model and shows the enhancement of the charge density at the higher flow rates. The main discrepancy between the model and the experiment occurs at the higher flow rates with bypass flow where the filter outlet charge density increases with flow rate. In the model, a constant or slowly decreasing outlet charge density is predicted for increasing flow rates. This increase in charge density with flow rate can be attributed to a slight increase in oil temperature; the charge density is sensitive to temperature changes through the oil conductivity and $\rho_d$. The inlet charge density increased with flow rate as the residence time in the bypass section decreased.

At the lowest flow rate, the difference in inlet charge densities between the bypass flow case and the reservoir flow case is small, so the outlet charge densities should be about the same, with the reservoir flow charge density smaller. The small increase in outlet charge density between the bypass flow case and the reservoir flow case can be attributed to an increase in the oil temperature; the measurements through the bypass were made before those through the reservoir, so the reservoir flow measurements were made at a slightly higher temperature. At the lower flow rates, the increase in charge density due to temperature variations dominated the enhancement due to smaller residence times with the flow bypass.

The difference in convection currents at the inlet and outlet to the filter should be balanced by the electrometer current. Plots of these currents, given in Figs. 7.6 and 7.7, show relatively good agreement between the calculated convection current and the measured electrometer current. Without the pressure correction factor for the flow rate into the ACS at the filter inlet, the currents would not compare favorably for high flow rates through the bypass [130]. For any given flow rate, the magnitude of the current

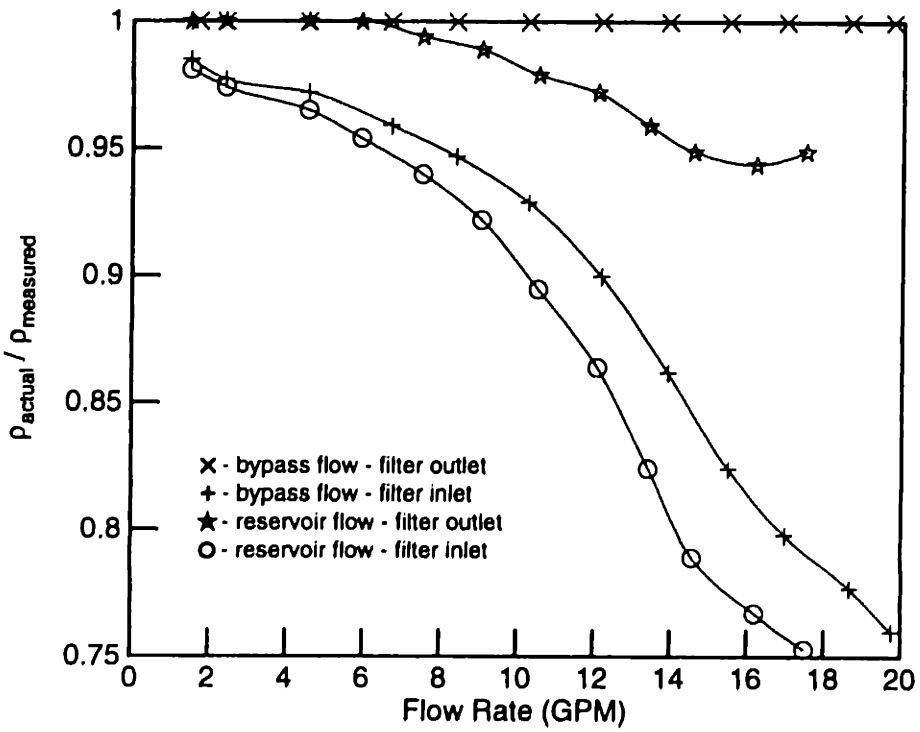


Figure 7.5: ACS calibration correction. At the higher flow rates, the hydrodynamic pressure caused an increase in the effective area of the ACS bellows. The resulting charge density then measured by the instrument was too large. To obtain the correct charge density, the calibration correction lines given above were used.

when the flow is through the reservoir is larger than when the flow is through the bypass. This is consistent with the analysis of the previous section in which the filter paper acts as a constant current source ($\tau_{rp} \ll \tau_{ep}$). In this flow regime, the relaxation of the charge entering the filter results in less current being drawn from the external circuit, through the electrometer. This indicates that charged fluid entering the filter affects the terminal measurement of the current but it doesn't affect the charging process of the filter paper itself. While this conclusion is reasonable for these measurements, it is unlikely that this is true in general. Indeed, the model used to describe the charging of the fluid by the filter paper is only valid for small charge densities. At the low flow rates, the calculated difference in convection currents and the measured currents do not agree as well, probably because the flow is nearly fully developed in some sections of the pipes, giving non-uniform velocity and charge density profiles so that Eq. 7.29 is no longer

accurate. Then the more general expression for the electrometer current

$$i_E = \int_{A_o} \rho_o v_z da - \int_{A_i} \rho_i v_z da \tag{7.31}$$

must be used, with $v_z$ the axially directed fluid velocity, and $A_o$ and $A_i$ the respective cross-sectional areas at the outlet and the inlet.

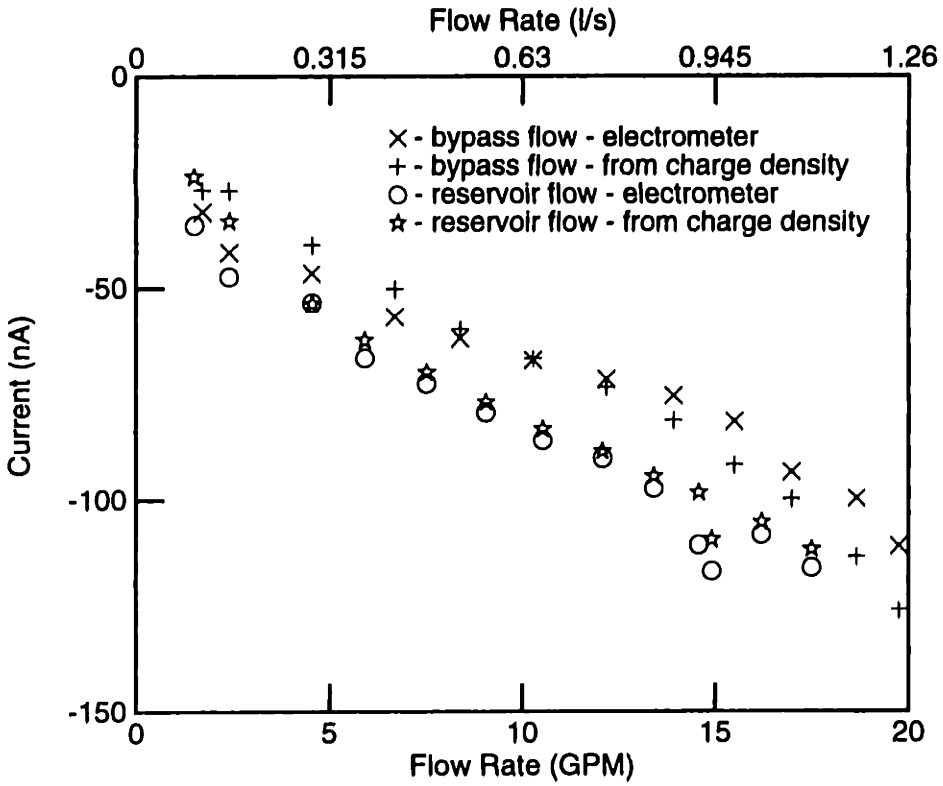


Figure 7.6: Measured electrometer current and the difference in convection currents calculated from the measured charge densities for flow through the bypass and the reservoir.

Various experiments have shown that the electrification charge density is strongly temperature dependent [23,63,122]. One set of charge density measurements showing this temperature dependence in the flow loop facility had the ACS's positioned at the inlet and the outlet of the reservoir. The filter was grounded externally with a wire while the electrometer and low pass filter were connected to the drum reservoir. The flow still went through the filter so that large charge densities would be measured. With the pump running at its maximum speed, the flow rate through the reservoir was measured to be about 1.14 l/s (18 GPM). At this flow rate, the heat generated by the pump took about 12 hours to raise the temperature of the oil from an ambient temperature of

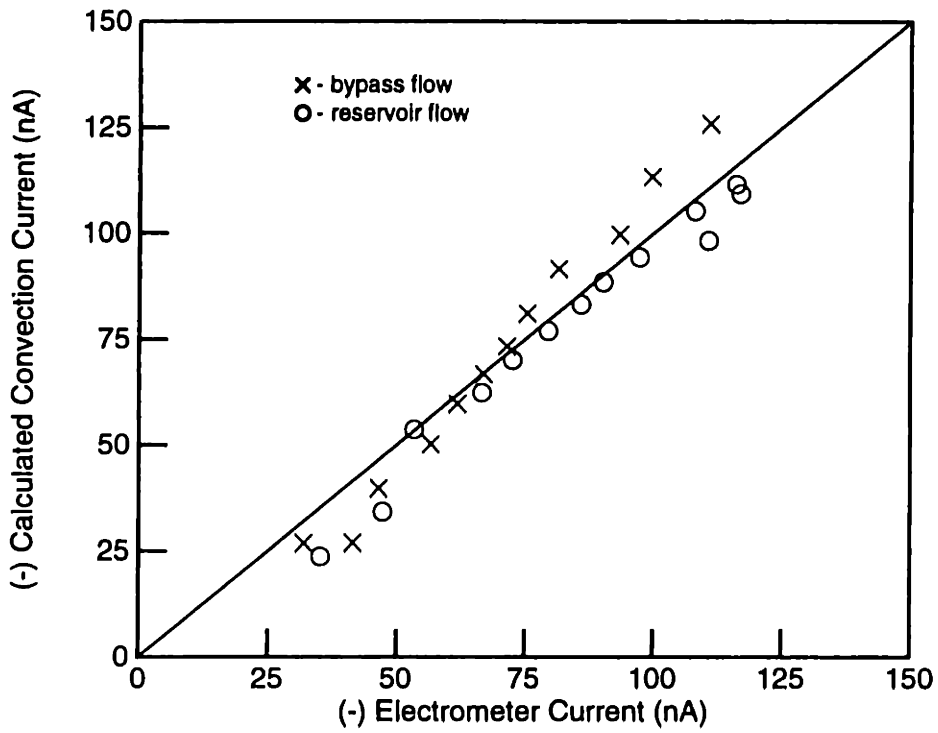


Figure 7.7: An alternative method for comparing the measured filter and reservoir electrometer currents with the convection current calculated from the difference in the inlet and outlet charge densities. Ideally, each data point would lie on the solid line where the currents are equal.

18°C to about 38°C. The charge density at the inlet to the reservoir is plotted against the oil temperature in Fig. 7.8(a). The oil temperature initially increased with time, but then decreased slightly later in the day, as the ambient temperature in the room decreased. While the charge density also decreased, it did not follow the same curve as the temperature increase, indicating some type of hysteresis. Thus, it can be concluded that, in addition to the temperature, some other parameter, such as moisture or trace impurities, has a small effect on the charge density. The charge density at the outlet of the reservoir increased from an initial level of 9 $\mu C/m^3$ to 17 $\mu C/m^3$ at the end of the experiment.

To get a better understanding of the charge density temperature dependence, the natural logarithm of the charge density was plotted against the inverse of the oil temperature, as shown in the lower plot of Fig. 7.8(b). Because the data lie along a straight line, the charge density has an Arrhenius type temperature dependence, with an activa-

tion temperature of 6675 K or an activation energy (activation temperature multiplied by Boltzmann's constant) of 0.58 eV. If the pipe volume between the filter outlet and the reservoir inlet can be neglected so that the charge relaxation between these points is negligible, then Eq. 7.24 describes the charge density variation at the reservoir inlet and indicates that the total activation energy should be the sum of the activation energies for the oil conductivity and for $\rho_d$. Other research has shown that the activation energy for temperature variations in the oil conductivity is about 0.45 eV [22]. Thus, the activation energy associated with $\rho_d$ is estimated to be 0.13 eV. This is consistent with the estimates of the activation energy for the wall charge density at the oil/pressboard interfaces in Section 5.8.

### 7.3.3 Comparisons with the model

Strict comparisons between the model and the experiments are complicated by the temperature variations in the system and the possibility that some of the assumptions in the model are not strictly valid. For example, the fluid is not necessarily well-mixed in the various expansion volumes or pipe sections and the Huber and Sonin model for charging from filter paper may require additional modifications (for the filter geometry or non-uniform flow across the entire face of the filter) when being applied to an actual filter assembly. Nonetheless, some comparisons can be made.

First consider the reservoir flow data of Fig. 7.4, where Eq. 7.24 describes the charge density on the outlet of the filter. To obtain a quantitative fit between the model and the experiment, it was assumed that $\rho_d$ obeyed

$$\rho_d = c_1 e^{-W_r/kT} \tag{7.32}$$

with $W_r = 0.13$ eV and the conductivity obeyed

$$\sigma = \sigma_o e^{-W_s/kT} \tag{7.33}$$

with $\sigma_o = 1.21 \times 10^{-4}$ S/m and $W_s = 0.45$ eV. Since the temperature variations in the system were small (less than one degree Celsius), both $\rho_d$ and $\sigma$ could almost be taken as constants. By using the experimental values for the various parameters and varying $c_1$ until the least squares error between the data and the model was minimized, the light line in Fig. 7.9 was obtained. With $c_1$ found to be 3.31 C/m$^3$, $\rho_d$ is calculated to be 22.9 mC/m$^3$ at 30°C. Using the nominal parameters from Table 7.1 of $P = 0.7$, $\epsilon_s/\epsilon_o = 3.5$, and $\epsilon/\epsilon_o = 2.2$, it follows that the fixed charge density on the filter paper can be approximated from

$$\rho_f = \frac{\rho_d}{1 + \frac{\epsilon_s}{\epsilon}\left(\frac{1}{P} - 1\right)} \approx 0.59\rho_d \tag{7.34}$$

as 14.1 mC/m$^3$. This is slightly larger than the values obtained for $\rho^w$ in Section 5.8, but compares favorably with the value of 12.6 mC/m$^3$estimated by Huber and Sonin [74].

The value of $\rho_d$ is only as accurate as the estimates of $P$, $\sigma$, $V_p$, and $\epsilon_p$ because all of these parameters affect the scaling of the charge density. On the other hand, the shape of

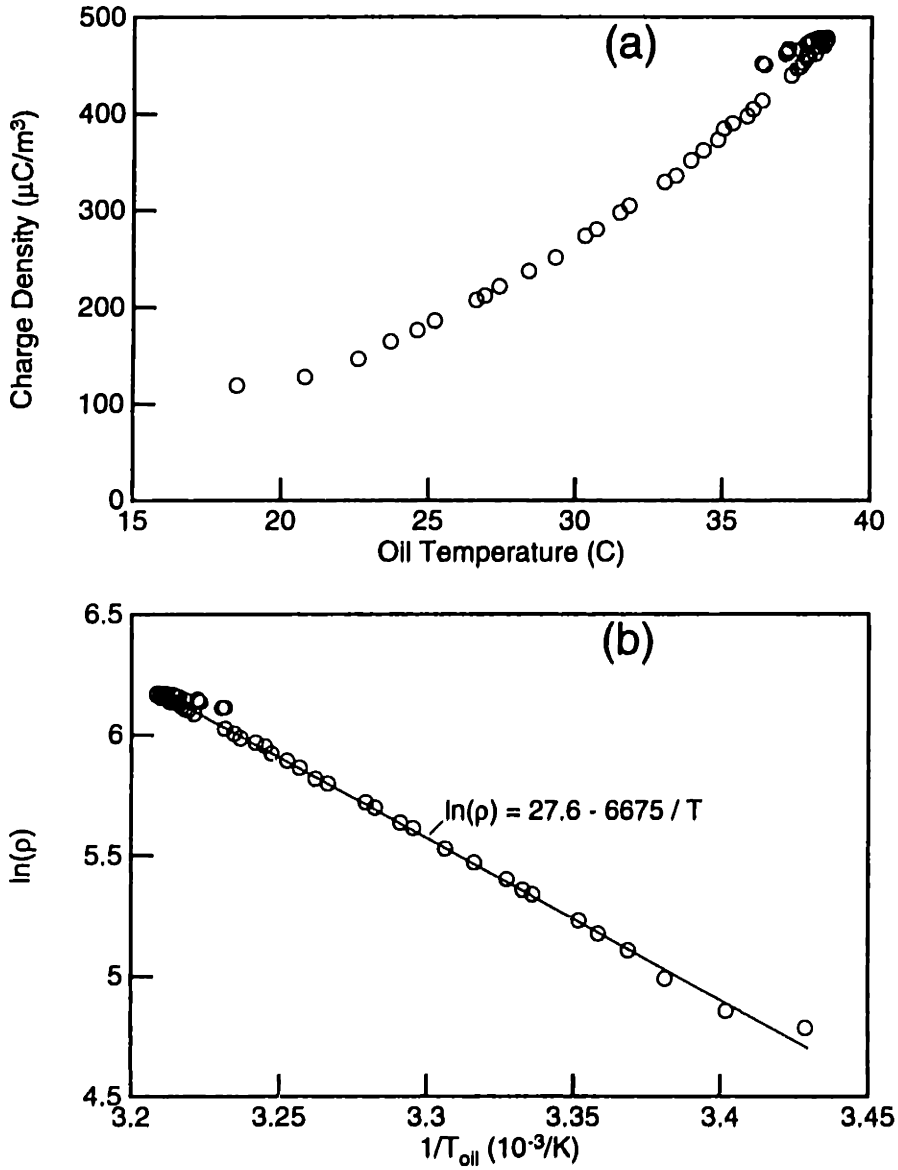


Figure 7.8: (a) Charge density variations with temperature at a flow rate of 1.14 l/s (18 GPM). The charge densities were measured at the inlet to the reservoir as the heat generated by the pump slowly raised the system temperature over a 24 hour period of time. The "hysteresis" in charge density at the higher temperatures indicates that some other parameter, in addition to the temperature, has an effect on the charge density. The straight line relating the logarithm of the charge density to the inverse of the temperature in plot (b) indicates that the charge density has an Arrhenius type dependence, with an activation temperature of 6675 K equal to an activation energy of 0.58 eV.

the charge density curve with respect to flow rate is essentially determined by the product $V_4\sigma$ in Eq. 7.24 if the permittivity of the fluid is known accurately. Since the conductivity was measured, it can be assumed that it was known accurately. While the volume $V_4$ can also be measured, it includes a pipe volume that runs between the filter and the location where the charge density was measured. For a given volume, relaxation in pipes is more complete than in well-mixed expansion volumes (compare for example Eqs. 7.4 and 7.16). This indicates that it is reasonable for $V_4$ to be larger than its nominal value. In fact, if $V_4$ is increased from 0.64 to 2.27 l (0.17 to 0.6 gal) and a best fit estimation to $c_1$ is again performed, the bold line in Fig. 7.9 is obtained. This line corresponds to a $c_1$ of 6.48 C/m$^3$ and a $\rho_d$ of 44.8 mC/m$^3$ at 30°C. Thus, it appears that the effective volume $V_4$ is larger than its nominal value.

Next, consider both the reservoir flow case and the bypass flow case together. The only differences between these two cases are the temperature and the volumes associated with the pipe region and the expansion volume in region 6; all of the other parameters should be the same. In the reservoir flow case, the volume $V_4$ was found to have an effective volume of 2.27 l (0.6 gal). A similar analysis can be used to determine the effective volume $V_5$ in the bypass flow case. By taking the ratio of the measured charge densities at the filter inlet and outlet and comparing this result to Eqs. 7.27 and 7.28, the effective volume for $V_5$ is found to vary between 2.04 and 3.37 l (0.54 and 0.87 gal), with an average of 2.54 l (0.67 gal). This corresponds very well to the nominal measured value of 2.65 l (0.7 gal). The other volumes $V_p$ and $V_2$ cannot be determined simply and are assumed to have their nominal values.

With the volumes known, the only remaining unknown is $\rho_d$. In Section 7.3.2 it was observed that the measured charge density exhibited an Arrhenius temperature dependence and also some hysteresis as the temperature was lowered. In the bypass flow experiment, attempts were made to maintain a constant temperature by valving relatively cool oil from the reservoir through the bypass loop between measurements. Thus, it is reasonable to assume that the charge densities for the bypass flow measurements will have a similar temperature and hysteretic effect. As a result, $\rho_d$ was assumed to obey

$$\rho_d = c_1 e^{-W_r/kT} + c_2 \tag{7.35}$$

where $W_r$=0.13 eV and parameters $c_1$ and $c_2$ are to be estimated. In this expression, the first term gives the temperature dependence and the second term gives the effect due to the hysteresis. Using the effective volume $V_4$=2.27 l (0.6 gal) and the original values for the other volumes, filter paper permittivity, and fluid properties, a least squares estimation gives $c_1$=41.9 C/m$^3$ and $c_2$=-0.236 C/m$^3$ and the lines in Fig. 7.10. At 30°C, this gives $\rho_d$=52.4 mC/m$^3$. While the fit is not perfect, it is reasonable for the variation in conditions. It appears that the increase in charge density at the higher flow rates can be described by the increase in temperature.

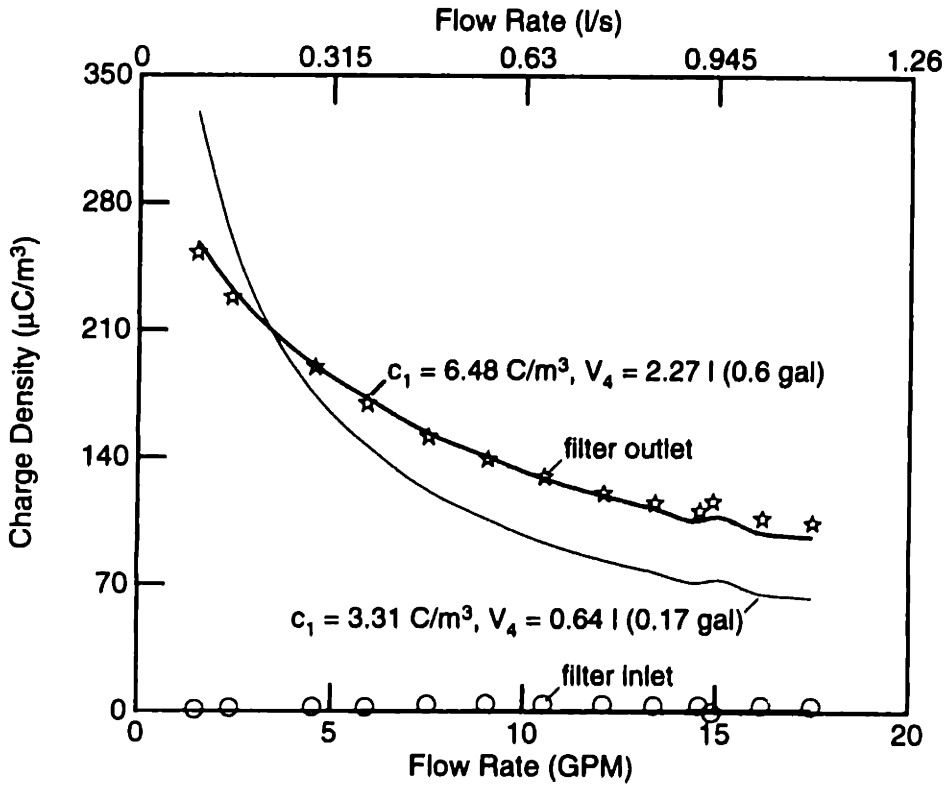


Figure 7.9: Measured charge densities at the filter inlet and outlet as the flow rate through the reservoir is varied. According to the model, the parameter $\rho_d = c_1 e^{-W_r/kT}$, with $W_r$ = 0.13 eV, affects the amplitude of the charge density, while the parameter $\tau_{r4}/\tau_e = V_4\sigma/\epsilon Q$ essentially affects the shape of the curve. The solid lines give the theoretical charge densities for two different values of $V_4$, with $c_1$ estimated to minimize the error between the data and the model. The charge density at the inlet to the filter was measured and calculated to be essentially zero.

## 7.4 Discussion

In this chapter, it has been shown that the volume charge densities can be enhanced by recirculated flow if the charge is not allowed to significantly relax before re-entering a paper filter charge source. While the enhancement was qualitatively predicted by a simple model and verified in an experiment, quantitative comparisons between the model and the experiment were complicated by uncontrolled parameters, such as the temperature, moisture content, conductivity, and trace impurities. Experimental measurements with this filter and other filters were repeatable at any given time, with similar trends observed for the charge density and electrometer current variations with flow rate, but the levels were found to vary on a daily basis; the best experimental results were obtained when all

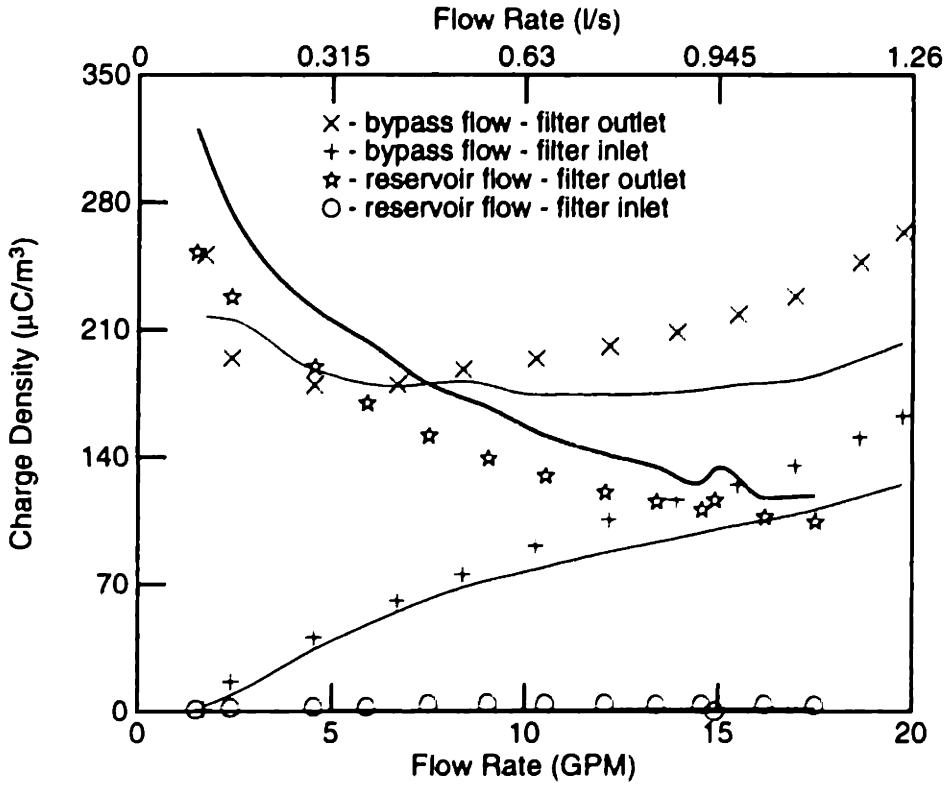


Figure 7.10: A comparison between the experimental charge densities of Fig. 7.4 and those predicted by the model. The bold line corresponds to the reservoir flow case. The light lines correspond to the bypass flow case.

of the measurements were obtained in a single day and the temperature variations were kept to a minimum.

After accounting for the limitations of the experiment and the model, a reasonable fit between them was obtained. Ideally, a single set of model parameters, such as $\rho_d$, the volumes, fluid properties, and filter paper permittivity, would describe all of the data. Attempts to improve the fit from that shown in Fig. 7.10 were unsuccessful. It appears that the model is too simple to describe all of the data. A better model would more accurately describe the physics of the charge generation process, such as the dependence on temperature, so that the observed hysteresis in the charge density variation with temperature (in Fig. 7.8) could be explained. Additionally, relaxing some of the assumptions made for the other components, such as allowing charge generation from regions other than the charge source, could also improve the model. In some situations, charge generation from regions other than the charge source may also be significant, but that did not appear to be the case in this experiment.

In any physical system, the degree to which the volume charge density is enhanced depends upon the losses in the system and the nature of the charge source. One basic criterion for flow recirculation to enhance the charge density is that the residence time in the loop must be comparable to or smaller than the dielectric relaxation time for the fluid. As to the charge source, the manner in which the source charges the fluid must also be considered. For example, if the charge source provides a constant charge density, then the charge density exiting the source is independent of the residence time in the loop. On the other hand, if the source provides a constant current, then the charge density of any fluid element entering the source is augmented with each pass through the loop and the steady state charge density will be enhanced if the residence time is not large compared to the relaxation time.

As an example application of this analysis for an actual system, consider an oil-cooled transformer. These transformers typically contain about 38,000 l (10,000 gal) of oil and have a bank of pumps, typically around four in number, each of which has a maximum flow rate near 50 l/s (800 GPM). If all of the pumps are running, the residence time in the system is 190 sec. When in operation, the temperature in the transformer is high enough that the dielectric relaxation time is a fraction of a second and there won't be an enhancement of the charge density. On the other hand, during the start-up transient when the transformer is still cold (near 0°C), the relaxation time is on the order of tens of seconds. Even though this is still small compared to the residence time, some enhancement of the charge density can occur. While it is unlikely that this is the primary mechanism for failure in an actual transformer, it may still play a role.

# Chapter 8

# Conclusions and Future Work

While this thesis was made as complete as possible, there are numerous opportunities for extending and improving this work. This chapter attempts to put this work in perspective by summarizing the major results obtained in this thesis and providing recommendations for future work.

## 8.1 Rotating Cylindrical Electrode Experiments

A rotating cylindrical electrode experimental apparatus, the Couette facility, was used to study flow electrification over a wide range of conditions. The compact size and relatively well-defined nature of the fluid flow between the cylinders made this experiment well-suited for the study of charge and mass transfer dynamics. Measurements of the steady state and time transient volume charge density, terminal current, and terminal voltage as the system was driven out of equilibrium by changes in the inner cylinder rotation rate, temperature, moisture content, applied voltage, and BTA concentration, were used to provide insight into the fundamental electrification mechanisms.

Similar to pipe flow experiments and other measurement techniques, the electrification tended to increase with the flow rate and the temperature. Unlike those other techniques though, the electrification was monitored in several different ways, with each method providing complementary information about the interfacial kinetics. As an example, measurements of the volume charge density showed a variation with open-circuit, short-circuit, and applied voltage conditions. This indicated that the volume charge densities on the liquid side of the solid/liquid interfaces could not be taken as constant at their equilibrium value for a given flow rate and temperature.

A detailed study of the effects of the additive 1,2,3 benzotriazole (BTA), a proposed electrification suppressant, showed that the BTA caused a reduction in both the electrification and the oil conductivity. While the decreasing conductivity leads to an increase in the electrification, the long term effect was a reduction in the electrification. The balance between these competing effects showed that an oil BTA concentration of 5-8 ppm led to the greatest reduction in the electrification. Even after the oil BTA concentration decreased (slightly) below this level, the reduction in the electrification remained.

While these measurements with BTA provide convincing evidence in support of the

use of BTA as an electrification suppressant in transformer, other possible effects of the BTA still need to be investigated. One is the stability of the BTA in the oil since measurements show it disappearing from the oil volume. If the BTA is actually decomposing, the products of the decomposition need to be identified to ensure that they do not pose a hazard to the transformer. If the BTA is being partitioned between the pressboard and the oil, equilibrium measurements of the BTA content in each phase should be performed, so that relations similar to the Norris curves for the equilibrium moisture concentrations between the paper and the oil are obtained. Knowledge of these relations may help determine the amount of BTA necessary for reducing the electrification in a transformer. The effects of the BTA on the pressboard itself, if any, should also be studied. Since the BTA has been shown to reduce the oil conductivity, the effective conductivity of the pressboard, which includes a contribution due to the absorbed oil, should be reduced, but other possible side effects should be identified.

One of the significant observations from these experiments was the apparent importance of initial conditions. The electrification appeared to be greatest during an initial equilibrium period after the system had been filled with oil. This type of information is not captured in many experiments because it is difficult to obtain reproducible results and most of the measurements are taken in the steady state, after the system has become conditioned. An exception to this appears to be the ministatic tester measurements which show short-time transient behavior as the filter and oil become charged and also long-time transient behavior as the materials become passivated [68]. Similar transients were observed in the Couette facility. Other measurements with duct flow also show significant currents during the initial transient as the flow is started [131]. These initial transient observations are significant because most transformer failures appear to have occurred during the startup transient or immediately after reprocessing. To help eliminate the flow electrification hazard in the electric power transformers, these "initial" conditions need to be understood better, and avoided.

Another variable that was not thoroughly explored was the condition of the oil. Most of the Couette measurements were performed with fresh oil directly out of a drum, but the oil from in-service transformers ages and changes with time. As the properties change, the charging tendency of the oil changes as well. This suggests that a comprehensive set of measurements with aged oil should be performed. These tests should also include monitoring the effects as BTA is added to the oil, to ensure that the electrification suppressing behavior of the BTA is maintained.

## 8.2 Dielectric Property Measurements

In order to develop a better understanding of the electrification processes, it was important to measure as many of the relevant material properties as possible. One such set of properties, the dielectric properties of the materials, which determine the charge accumulation and leakage rates, play a critical role in the electrification process and need to be monitored. To this end, AC and time transient techniques for monitoring the dielectric properties of insulating liquids and solids were developed.

For the dielectric measurements of transformer oil, AC impedance measurements of

parallel plate electrodes immersed in the oil showed that the bulk response of the oil could be represented with a single frequency independent permittivity and conductivity and could be considered "ohmic". Deviations from this "ohmic" behavior at low frequencies were consistent with polarization effects at the electrodes, with the impedance across the interfacial electrical double layers becoming comparable to the impedance across the bulk region of the oil. These measurements also provide convincing evidence that the oil conductivity is relatively independent of the moisture content of the oil. In addition, time transient measurements of the terminal voltage gave results consistent with an "ohmic" response for the oil, where the voltage decayed with a single exponential time constant.

On the other hand, these same time transient measurements showed that the pressboard insulation did not behave as an "ohmic" material. Some of this can be associated with the pressboard conduction being moisture dependent so that a non-uniform moisture distribution across the pressboard leads to a distribution of pressboard conductivities. For the voltage measurements, this can lead to a non-exponential decay with time, but the terminal current would still have a single exponential time constant, even for multiple layers of "ohmic" materials. But AC frequency spectrum measurements show that dry pressboard itself does not have an "ohmic" response either, indicating that the pressboard is not an "ohmic" material. An alternative formulation for the time transient response of the pressboard, based on a space-charge conduction model, gave a reasonably good fit to the data, but has not yet been correlated with the AC measurements. Ideally, one could obtain the time transient response from the frequency response, and vice versa. Since the pressboard is not "ohmic" and not well-understood, it is difficult to interpret all of the electrification measurements involving the pressboard insulation. The effects of the pressboard on the electrification should become more clear once conduction models for the pressboard, including temperature and moisture effects, become better established.

Other techniques can also be used to obtain more information about the state of the pressboard insulation. In contrast to the time transient technique, which was only performed periodically, flexible sensors which conform to the pressboard surfaces have become developed to the point that they can be incorporated into the Couette facility so that the pressboard dielectric properties can be monitored continuously [17,85]. This would allow for the charge and mass transfer effects, driven by the flowing fluid, to be characterized. Furthermore, when the sensor is placed behind the pressboard, it is possible for these flexible sensors to see through the pressboard itself so that the sensors will respond to the dielectric properties of the oil, the pressboard, *and the interface*. Since the charge entrained by the flowing liquid comes from the interfaces, these sensors may provide another tool for monitoring the electrification process.

## 8.3 Electrification Models

A self-consistent model was developed for the electrification between the rotating cylindrical electrodes. The first version of this model used an established ("wall" charge density) boundary condition for the interfacial charge transfer. The steady state electrification data was fit to the model and the interfacial parameters were estimated. These estimates showed that the interfacial "wall" charge density obeyed an Arrhenius temper-

ature dependence and tended to be largest for the pressboard, smallest for the copper, and intermediate for the stainless steel. In some cases, estimates of the charger transfer rate constants were obtained. Even when the rate constants were not estimated, it was clear that they could not be taken as "infinite". When BTA was added to the oil, the "wall" charge density was shown to decrease by a factor of four. It also appeared that the BTA reduced the oil conductivity by reducing the number density of ions in the oil and not simply the mobility of the ions.

The second version of the model used a newly developed boundary condition. This boundary condition added the effects of surface charge accumulation to the "wall" charge density boundary condition. In addition, the derivation provides a more physical basis for the boundary condition. This version of the model allowed a wider range of observations to be described. As part of the electrification model, a general methodology was also developed for combining the volume and terminal measurements so that the parameters describing the interfacial charge transfer kinetics could be estimated.

Although the model was formulated for both time varying and steady state conditions, only the steady state solutions were derived. While several qualitative arguments for the time transient response were given, the emphasis was on the steady state. Since these steady state results showed that the more general boundary conditions with finite rate constants are necessary, models for the time transient evolution of the charge and fields should also use these more general boundary conditions. This would extend the work of other time transient models that used overly simplified boundary conditions [25,132,133].

These more general boundary conditions can also be incorporated into other electrification models, such as the flow through pipes, ducts or filters. Since these boundary conditions include terms for the non-equilibrium processes associated with the passage of current across the interfaces, both the time transient and steady state results would be modified. The formulation of these boundary conditions also makes them suitable for describing the effects of energization on the electrification. While additional physical processes, such as high-field charge injection, are undoubtably significant in actual systems, these boundary conditions provide a step toward the development of a self-consistent model that can describe electrification both with and without energization.

## 8.4 Electrification in Systems

Some of the "systems" aspects of flow electrification were studied through a flow loop experiment and model. In the experiment, transformer oil was charged by a paper filter and convected through several types of relaxation regions. The recirculation of the flow and the nature of the charge source led to enhanced volume charge densities when the residence time for the oil in the relaxation regions was comparable to the dielectric relaxation time. This experiment relied upon newly developed sensors that could measure the volume charge density, separate from any flow electrification through the sensor itself. Prior to the development of these sensors, this type of enhancement could not be measured since previous sensors required the complete relaxation of charge somewhere in the loop.

The model for this experiment superimposed the electrification contributions from

each of the separate components into a "system" response. In this model, the volume charge density output from each component was used as the input to the downstream component. Comparing the model to the experimental data led to insight about the electrification processes, including estimates of the temperature dependence of the (paper filter) charge source being comparable to those measured in the Couette facility and effective volumes for the charge relaxation regions.

One idea that was not explored was the possibility of developing a "feedback" mechanism, by which the charge density could continuously increase until a discharge occurred. In many physical situations, such as the flow loop here, the accumulated charge and fields were found to be self-limiting, with the leakage of charge from the oil volume or surfaces increasing as the charge accumulates. It may be possible to configure the system to make it unstable, where for example the voltage rise in one component in the system is used to drive the charge source so that the system has positive feedback. The motivation behind such a test is that similar regenerative mechanisms may be involved in the electrification failures of complex systems, such as transformers.

# Appendix A

# BTA Measurements using Ultraviolet Spectrophotometry

## A.1 Introduction

This appendix describes an experimental procedure for determining the concentration of 1,2,3 benzotriazole (BTA) in a background oil using an ultraviolet (UV) spectrophotometer. The basic procedure follows the Japanese standard on BTA measurement [134]. The main differences with this standard are the mixing process for the BTA extraction from the oil and the calculated corrections for the sample sizes used in the analysis.

## A.2 Basic Equipment

- Mixing machine (e.g. Fisher Vortex Genie 2, model 12-812, or Lab-Line Instruments orbital shaker table, model 3520)
- UV spectrophotometer (e.g. Perkin-Elmer Lambda 3B UV/VIS Spectrophotometer)
- Centrifuge (e.g. Sorvall RT 6000 refrigerated centrifuge)
- Balance (e.g. Allied Electronic Balance, Model 7301A)
- 1,2,3-Benzotriazole (greater than 98% pure, such as Fisher Scientific, Reagent Grade)
- 0.5N Potassium bicarbonate ($KHCO_3$) solution (e.g add 1 l of distilled water to 50 g of $KHCO_3$)
- 0.001N Silver Nitrate ($AgNO_3$) solution (e.g add 200 ml of distilled water to 34 mg of $AgNO_3$)

## A.3 Sample Preparation

Samples of oil with known BTA concentrations are used for developing calibration curves relating the oil BTA content to the spectrophotometer absorbance and for mixing with the oil in the Couette facility. In preparing these samples, it is important to consider the solubility of BTA in transformer oil. Although information is limited, the solubility apparently depends upon the composition of the oil and the temperature. For example, the solubility of BTA approximately halves as the percentage of aromatic carbons (%Ca) in the oil is halved, and, for an oil with %Ca = 8, the BTA solubility varies from near 100 ppm at 20°C to about 1000 ppm at 80°C [134]. For comparison, Shell Diala A oil has a %Ca of 7 [73] and should have similar BTA solubilities.

For this work, standard solutions were made by adding approximately 100 mg of BTA to a beaker containing approximately 900 g of Shell Diala A oil. To prepare accurate standards, the BTA mass was measured with an accuracy of less than 1 mg while the oil was measured to within 1 g. The oil was mixed with a stirring bar and the temperature was kept constant at 70°C by means of heating tape wrapped around the beaker. A thermocouple probe was used to monitor the temperature and a Harley moisture sensor [model CT-880-BN-H(0/100%)-X] indicated an oil moisture content of 16–25 ppm (4.7–7.3% of saturation). The BTA took a few hours to dissolve in the oil, which is consistent with reported difficulties in dissolving BTA in oil at near-ambient temperatures [39].

## A.4 Methods

The procedure for determining the BTA concentration in the oil is relatively straightforward. The first step is to extract the BTA from the oil and measure the absorbance of the extract. This step is necessary because the oil contains compounds which absorb in the UV range and dominate the response of the BTA, which is only present in trace amounts. The same extraction can be performed on the base oil, to which the BTA was originally added, in order to get a base line absorbance. The effect of the BTA is then the difference in these two absorbances and the BTA concentration can be obtained from a calibration curve. If the base oil is not available or if the oil has been aged, a base line response cannot be obtained and a second extraction step is required. In this step, the BTA is precipitated out of the extract from the first step and the absorbance of the final solution is measured. The difference in absorbances again gives the BTA response.

With that as an overview of the experimental method, the details of each experimental procedure are listed below:

1. **BTA extraction**

   (a) From the oil phase: Measure the mass and then combine approximately equal portions (about 25 g) of the oil sample and the 0.5N $KHCO_3$ in a sealable test tube. Shake the test tube with the vortexer for about 1 min, pausing occasionally to also shake the test tube by hand. This creates a fine dispersion between the two phases. Allow the tube to stand still until the oil and water

phases separate (typically 60 min). The BTA is then contained in the lower aqueous layer and can be pipetted out of the test tube. To minimize the amount of oil in the extract, air should be expelled out of the pipette while it is passed through the oil layer and the pipette should be wiped cleaned after obtaining the extract sample.

An alternative mixing process is to combine the oil sample and the 0.5N $KHCO_3$ in a separatory funnel, and then place the funnel on a shaker table for 10 min, with the table shaking more than 150 times/min. Set the funnel aside and let the layers separate (about 30 to 60 min). Again, the BTA is in the lower aqueous layer. Although the Japanese standard recommends using the shaking machine, probably to reduce the amount of oil contained in the extract solution, it did not extract as much of the BTA from the oil, as will be shown in the results section. Thus, with the tradeoff being a more complete removal of BTA from the oil versus the possibility of some oil in the extract and somewhat longer settling times, the prior (vortex) method was used.

The final step is to centrifuge the aqueous extract for 10 min at 1500 rpm. This helps to further separate any trace amounts of oil from the water phase. The lower layer (if there are two layers) is the BTA extract solution. When pipetting this solution, be careful not to include any oil.

(b) From the aqueous phase: Measure and combine approximately 10 ml of the BTA extract solution and 5 ml of the 0.001N $AgNO_3$ in a sealable centrifuge tube. Shake the solution well by hand and place the tube in a dark place for 1 hr. The silver salt of BTA should then precipitate out of solution as a fine white salt. Centrifuge the test tube for 15 min at 2500 rpm.

2. **UV absorbance measurement**

While BTA absorbs at wavelengths between 230 nm and 300 nm, the absorption is greatest near 270 nm. Thus, for single wavelength measurements, the absorbance should be measured near 270 nm. The sample to be measured, whether it is the BTA extract or the extract after the silver salt has been precipitated, is to be placed in a quartz cuvet. (Note that other cuvet materials, such as polysulfone, have high absorbances in the UV range and should not be used.) A second cuvet containing 0.5N $KHCO_3$ is to be used as a reference. To obtain an absorbance that is independent of the sample size, the following corrections were performed:

(a) After extracting the BTA from the oil: the extract absorbance $A^e$ can be expressed as

$$A^e = \frac{m_{KHCO_3}}{m_{oil}} A^m \qquad (A.1)$$

where $m_{KHCO_3}$ is the mass of the $KHCO_3$ used, $m_{oil}$ is the mass of the oil sample, and $A^m$ is the measured absorbance. The physical reason for this correction is that the measured absorbance from the extract will not reflect the actual BTA concentration in the oil if the masses are different. For example, increasing the BTA concentration in the extract by using a large mass of oil

relative to the mass of $KHCO_3$ would result in an artificially high absorbance. To minimize the effect of the correction, approximately equal amounts of oil and $KHCO_3$ should be used.

(b) After precipitating the BTA from the extract solution: the solution absorbance $A^s$ can be expressed as

$$A^c = \left(1 + \frac{m_{AgNO_3}}{m_{extract}}\right) A^m \tag{A.2}$$

where $m_{AgNO_3}$ is the mass of the $AgNO_3$ used, $m_{extract}$ is the mass of the extract sample, and $A^m$ is the measured absorbance. In this case, since the mass densities of each of the solutions is essentially that of water, the volume of each solution can be used. Again, the physical reason for this correction is that the amount of each solution affects the measured absorbance.

### 3. Calibration curves

The calibration curves are generated by slightly different procedures, depending upon whether or not the base oil is present. In both cases, at least three stand samples containing known BTA concentrations are necessary. After performing the BTA extraction procedure and measuring the absorbance, the calibration absorbance $A^c$ can be obtained from

$$A^c = A^e - A_{back} \tag{A.3}$$

where $A^e$ is the extract absorbance and the background absorbance $A_{back}$ is either the base oil absorbance $A^e_{base}$, if the base oil is available, or the solution absorbance $A^s$ after the BTA has been precipitated, if the base oil is not available. This data provides a calibration curve which is essentially a line passing through the origin. The slope of this line ($\Delta A^c_i$) has units of absorbance per ppm of BTA and can be determined by a least squares fit to the data, assuming that the curve passes identically through the origin.

### 4. Determining the BTA concentration

As with the calibration curves, the first step in determining the BTA concentration is to perform the BTA extraction procedure and measure the absorbance. The sample absorbance $A^i$ can be obtained from

$$A^i = A^e - A_{back} \tag{A.4}$$

where $A^e$ is the extract absorbance and the background absorbance $A_{back}$ is either the base oil absorbance $A^e_{base}$, if the base oil is available, or the solution absorbance $A^s$ after the BTA has been precipitated, if the base oil is not available. The BTA concentration $S^i$ is then obtained graphically from the calibration curve or from

$$S^i = \frac{A^i}{\Delta A^c_i} \tag{A.5}$$

when the slope of the line relating the absorbance to the BTA concentration has been determined.

## A.5 Representative Results

For reference, representative results from some of the measurements are given. Fig. A.1 contains a representative plot of the absorbance as the wavelength of the excitation and the BTA concentration are varied. While the absorbance spectrum is quite broad over the entire wavelength range, it exhibits a peak near 270 nm and increases with BTA concentration. The absorbance of the 0 ppm (weight/weight) oil is small and relatively independent of the wavelength, indicating that the extraction procedure was effective at separating the BTA from the oil. The machine is only rated for absorbances between -0.3 and 3.000 so the data showing absorbances greater than 3.0 are not accurate.[1]

Fig. A.2 contains a representative plot of the corrected absorbance, where the absorbances come from Fig. A.1 and the correction accounts for the difference in the oil and $KHCO_3$ sample masses and subtracts off the absorbance of the base oil (0 ppm BTA). The plot also shows that mixing for 1 min or 10 min in the vortexer does not appear to make a difference in the amount of BTA that is extracted, but the shaker table does not appear to extract as much of the BTA from the oil. All of these measurements were done at ambient temperature.

Once the corrected absorbances are obtained, the BTA concentration of the oil can be obtained from calibration data. Table A.1 lists a least squares fit to the calibration slopes at each wavelength. In principle, each of these slopes can be used to calculate the BTA concentration in the oil, but the measurement is most sensitive near 270 nm. In practice, to determine the concentration from the absorbance measurements, a computer program (**btacal.c** in Appendix E) was written. This program automatically compensates for any differences in sample masses, subtracts off the base oil response, and averages the BTA concentration over the 260–280 nm wavelength range. Based on the standard calibration solutions, the concentration measurement is estimated to be accurate to within 5%. This uncertainty includes errors in the measurements of the masses, incomplete mixing, and drift in the spectrophotometer absorbance.

For comparison, several samples were also analyzed using high performance liquid chromatography (HPLC). As shown in Table A.2, the two methods are in reasonable agreement. Since BTA is sensitive to sunlight [134], the samples were stored in Nalgene amber high-density polyethylene bottles at room temperature. During the time period between measurements (about six weeks and 12 weeks), the BTA concentration decreased. While it is possible that the BTA adsorbed onto the walls of the container, only a small

[1]The absorbance $A$, a dimensionless quantity, is defined by

$$A \equiv \log \frac{P_o}{P}$$

where $P$ is the radiant power in the beam of light transmitted by the solution and $P_o$ is the radiant power in the incident beam of light [135]. This indicates that an absorbance of 3.0 only has 1/1000th of the power in the incident light beam being transmitted.

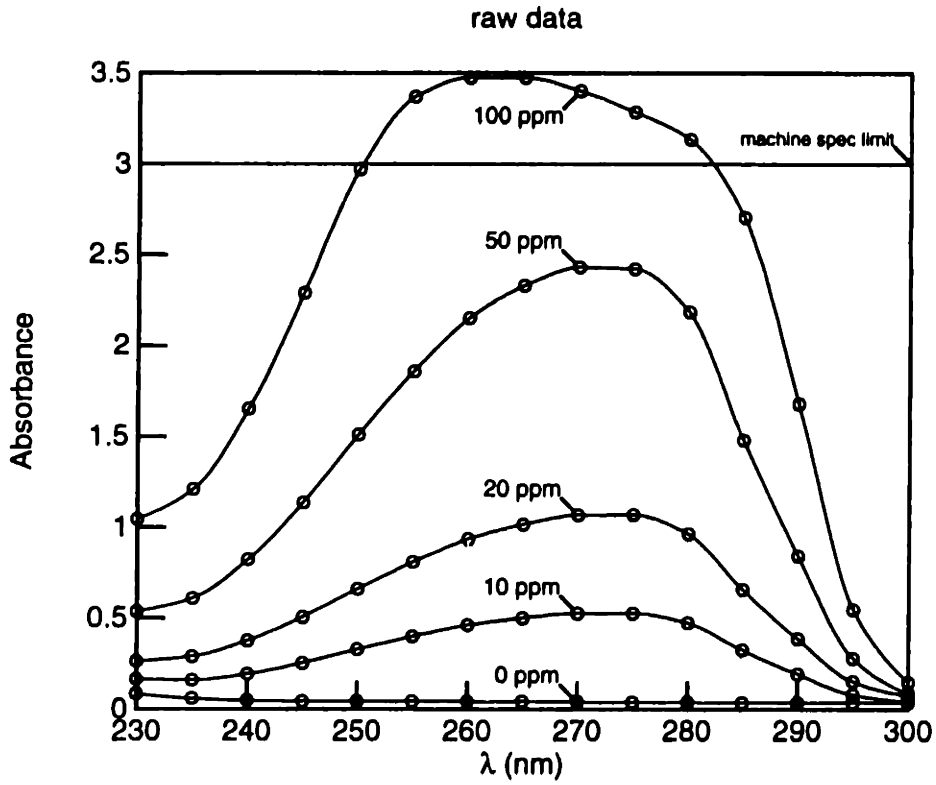


Figure A.1: Sample absorption curves for various BTA concentrations using roughly equal portions of oil and $KHCO_3$. The sample was mixed for 10 min in the vortexer when extracting the BTA from the oil.

fraction of the BTA in solution is necessary to create a monolayer of BTA along the surface. Unless relatively thick layers (many molecules in thickness) were formed, adsorption is unlikely to explain the concentration decrease. On the other hand, another possibility is that the BTA was decomposing. Since the fractional decrease in concentration was 30 to 50% over a wide range of initial concentrations, it seems plausible that a volume effect, such as molecular decomposition, instead of a surface effect, was occurring.

Attempts were also made to measure the BTA concentration of the pressboard insulation used in the Couette facility (CF) experiments. The extraction procedure was to slice apart 2-5 g of pressboard and then mix the pressboard pieces with the $KHCO_3$. This was similar to the procedure for extracting the BTA from the oil. It was found that cutting and peeling the pressboard, followed by the vortex mixing, caused some discoloration of the $KHCO_3$ solution and some cellulose fibers to fall off from the pressboard into the solution. Subsequent centrifuging caused the particulates to settle, but the discolored solution gave a broad absorbance in the UV range, as shown in Fig. A.3. These

| Wavelength $\lambda$ (nm) | $\Delta A_i^c$ (A/ppm BTA) |
|---|---|
| 300 | 0.0012 |
| 295 | 0.0049 |
| 290 | 0.0175 |
| 285 | 0.0322 |
| 280 | 0.0499 |
| 275 | 0.0562 |
| 270 | 0.0570 |
| 265 | 0.0542 |
| 260 | 0.0495 |
| 255 | 0.0422 |
| 250 | 0.0339 |
| 245 | 0.0252 |
| 240 | 0.0178 |
| 235 | 0.0126 |
| 230 | 0.0102 |

Table A.1: Calibration slopes between the corrected absorbance ($A$) and the BTA concentration.

| Sample ID | UV Spectrophotometry | | | HPLC[136] |
|---|---|---|---|---|
| | 3/31/94 | 5/13/94 | 8/10/94 | 4/94 |
| Blank | 0 | 0 | 0 | <0.010 |
| 10 ppm | 9.2 | 7.1 | 4.7 | 7 |
| 20 ppm | 19 | 15 | 8.7 | 16 |
| 50 ppm | 47 | 41 | 28 | 42 |
| 106 ppm | 92 | 92 | 61 | 87 |

Table A.2: A comparison of BTA concentrations (in ppm weight/weight), in Shell Diala A oil, measured by UV spectrophotometry and high performance liquid chromatography (HPLC). The nominal concentrations of the solutions are used for sample identification. The approximate dates of the measurements are given; the BTA was added to the oil on 3/30/94.

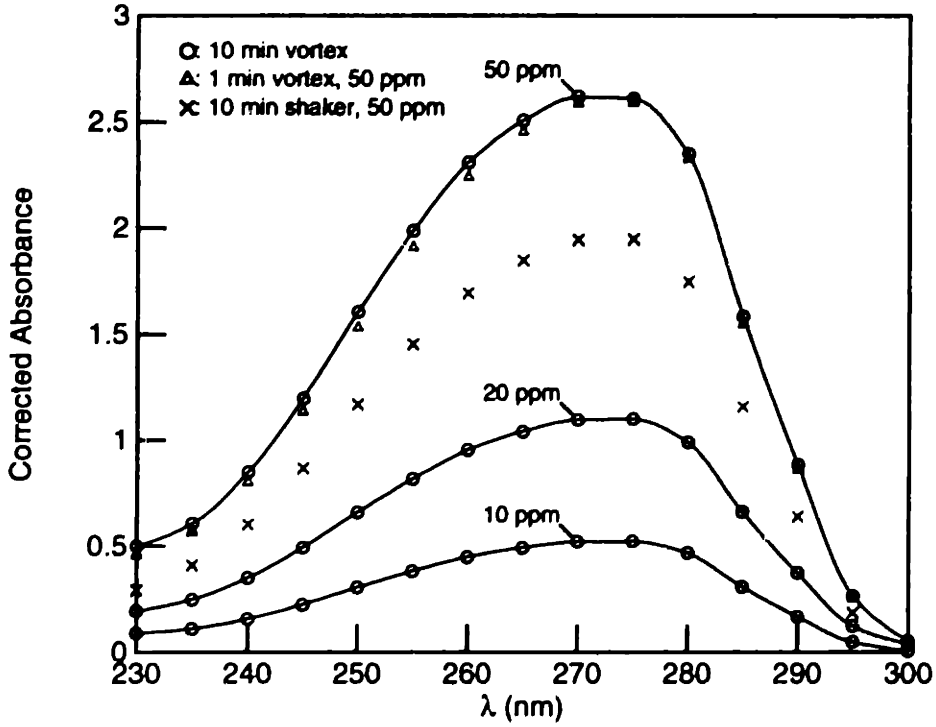


Figure A.2: Sample corrected absorption curves for various BTA concentrations. The correction accounts for the difference in masses of the oil and $KHCO_3$ solutions and subtracts off the response of the base oil (0 ppm BTA).

baseline measurements were taken on old oil-impregnated samples from the CF which had not been exposed to BTA. Clearly, excessive mixing with the vortexer enhanced the degradation of the pressboard.

To separate the effects of the pressboard degradation from the BTA in the absorbance measurement, it was observed that the shapes of the absorbance curves were roughly the same, only scaled differently. By fitting a quadratic function of the wavelength to the absorbance data and dividing by the absorbance at 300 nm, a "shape" function for the pressboard absorbance was obtained. An approximate expression for the absorbance of the pressboard samples was obtained as

$$A_{pb} \approx A^m_{pb}\big|_{\lambda=300\text{ nm}} \left[1.85 \times 10^{-4}(\lambda - 300\text{ nm})^2 - 3.2 \times 10^{-3}(\lambda - 300\text{ nm}) + 1.05\right] \quad \text{(A.6)}$$

where $A^m_{pb}$ is the measured absorbance at a wavelength of 300 nm. The solid lines in Fig. A.3 show that this expression gives a reasonably good fit to the data. The lower curve in Fig. A.3 shows the absorbance of a pressboard sample that had been exposed

to BTA. In this case, the BTA absorption peak is hidden by the broad absorbance of the pressboard. To isolate the BTA peak, the approximate expression for the pressboard absorbance, given in Eq. A.6, was subtracted from the measured absorbance. This seemed reasonable since the absorption due to the BTA at 300 nm is usually relatively small compared to the peak value. After subtracting the pressboard response, the BTA peak is seen much more clearly.

Using the relative masses of the pressboard and $KHCO_3$ and assuming that the calibration data from the BTA in oil measurements still apply, the BTA concentration in the bulk or on the surface of the pressboard can be estimated. In this case, the pressboard BTA concentration is estimated to be 140 ppm ($\mu$g BTA / g pressboard). Measurements of other samples that did not have the pressboard peeled and only vortexed for 15 sec indicated a BTA concentration of only 60 ppm, probably because less BTA was removed from the bulk of the pressboard. In summary, while the extraction procedure and the assumed use of the BTA in oil calibration may not be strictly valid, these measurements indicated that significant amounts of BTA were present in (or on) the pressboard.

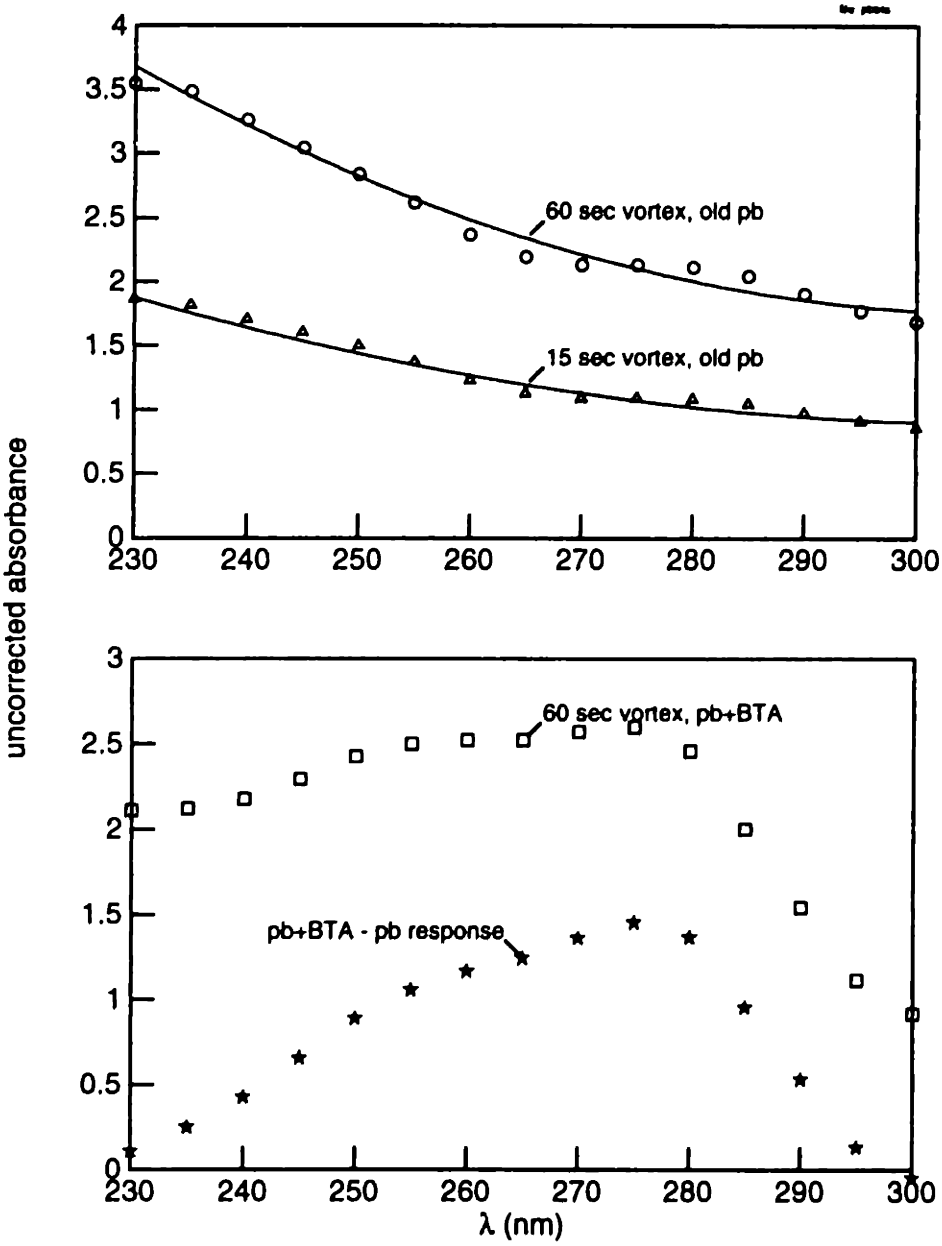


Figure A.3: Sample absorption curves (not mass corrected) for oil impregnated HiVal pressboard used in the Couette facility. The upper plot shows the response of old pressboard samples that had not been exposed to BTA. The vortex mixing appears to cause degradation of the pressboard and a release of molecules that absorb in the UV range. The solid lines are a fit to a quadratic "shape" function. The lower plot was obtained from pressboard that had been exposed to BTA. To highlight the BTA peak, the absorbance from the pressboard was subtracted.

# Appendix B

# A Model for the Nilsson Plate Charge Monitor

## B.1 Introduction

The Absolute Charge Sensor (ACS) has been tested under laboratory conditions and has been found to give charge density values similar to those measured by a continuous flow sampling system [11]. Even though there is good agreement between these measurements, the lack of a known charge source for calibration purposes leaves the validity of these measurements in question. With the placement of ACS's on transformers, a suggestion has been made to insert a current measuring probe – a flat plate within a shielded structure – inside one of the manhole covers on top of a transformer, next to an ACS. This current measuring structure has been called the Nilsson Plate.[1] If a relation between the current from the Nilsson Plate and the charge density inside the structure can be determined, this would provide another comparison for the charge densities as measured by the ACS. In this document, an analytical expression is derived for the current in terms of the charge density near the Nilsson Plate. A back-of-the-envelope calculation is then shown to be in good agreement with this analytical expression.

## B.2 Problem Statement

Assume that the shielded Nilsson plate can be modeled as a hemisphere of radius $a$ filled uniformly with a charge density $\rho_o$, as shown in Fig. B.1. The flat side of the hemisphere is virtually grounded through a current measuring electrometer and the curved side consists of a grounded wire mesh. The hole size of the mesh is assumed to be large enough to allow fluid convection without introducing appreciable electrification but small enough to shield the volume from any external fields. While more recent versions of this plate have been made without the curved screen [137], this analysis applies when the screen is present.

[1]The plate was named after Stig Nilsson of EPRI, who had originally promoted the use of a current measuring plate.

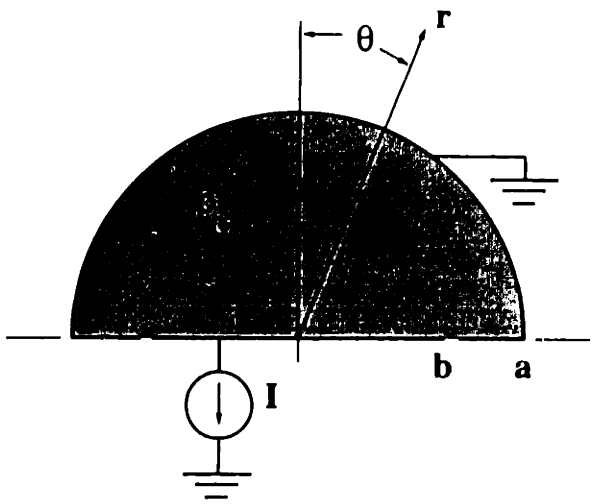


Figure B.1: A model for the Nilsson Plate. This is a cross-sectional view of the grounded hemisphere which is filled with a uniform charge density of $\rho_o$.

The liquid is considered to be ohmic with permittivity $\epsilon$ and conductivity $\sigma$. In order to support the uniform charge density assumed in this model, any charge that decays through ohmic relaxation to the grounded walls must be replaced by charge being convected into the volume through the mesh. With these assumptions, the charge density inside the hemisphere can be related to the current going through the bottom plate. The approach will be to solve for the field distribution inside the hemisphere first. Once the field distribution has been determined, the current will be related to the electric field at the bottom surface.

To simplify the problem and allow for an analytical description for the field distribution inside the hemisphere, consider the image problem shown in Fig. B.2. The problem then requires solving for the field distribution inside of a grounded sphere with a charge density given by

$$\rho = \begin{cases} +\rho_o & 0 \leq \theta < \frac{\pi}{2}, \quad r < a \\ -\rho_o & \frac{\pi}{2} < \theta \leq \pi, \quad r < a \end{cases} \tag{B.1}$$

The potential at $\theta = \pi/2$ is zero for this charge distribution. The field distribution of interest is in the upper hemisphere.

## B.3 Basic Equations

This problem is electro-quasistatic, so the electric field is irrotational and can be represented by a scalar potential

$$\vec{E} = -\nabla\Phi \tag{B.2}$$

Gauss' law can be written as

$$\nabla \cdot \vec{D} = \rho \tag{B.3}$$

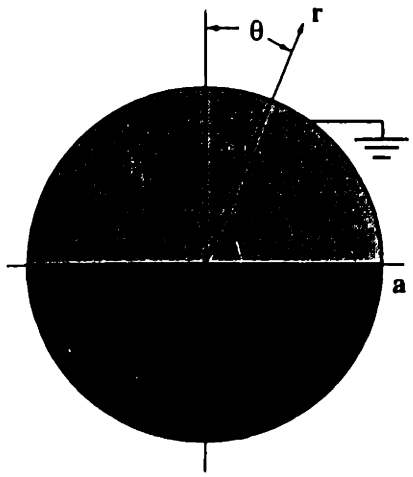


Figure B.2: The image problem for the grounded hemisphere. The structure is a grounded sphere with a charge density of $+\rho_o$ in the upper hemisphere and $-\rho_o$ in the lower hemisphere.

where the displacement field and the electric field are related by the constitutive relation

$$\vec{D} = \epsilon \vec{E} \tag{B.4}$$

The governing equation for the potential field distribution is then Poisson's equation

$$\nabla^2 \Phi = -\frac{\rho}{\epsilon} \tag{B.5}$$

This problem requires solving Eq. B.5 for the potential in terms of the charge density inside the sphere. Once the potential is known, the electric field and current density can be determined.

## B.4 General Potential Distribution

In spherical coordinates, Eq. B.5 can be written as

$$\frac{1}{r^2}\frac{\partial}{\partial r}\left[r^2\frac{\partial \Phi}{\partial r}\right] + \frac{1}{r^2 \sin\theta}\frac{\partial}{\partial \theta}\left[\sin\theta\frac{\partial \Phi}{\partial \theta}\right] + \frac{1}{r^2 \sin^2\theta}\frac{\partial^2 \Phi}{\partial \phi^2} = -\frac{\rho}{\epsilon} \tag{B.6}$$

Since there is no angular dependence in the $\phi$ direction, Eq. B.6 becomes

$$\frac{1}{r^2}\frac{\partial}{\partial r}\left[r^2\frac{\partial \Phi}{\partial r}\right] + \frac{1}{r^2 \sin\theta}\frac{\partial}{\partial \theta}\left[\sin\theta\frac{\partial \Phi}{\partial \theta}\right] = -\frac{\rho}{\epsilon} \tag{B.7}$$

The general approach for solving a non-homogeneous differential equation is to find a

homogeneous solution and a particular solution. The constants obtained from the homogeneous solution are then used to fit the solution to the specified boundary conditions. If that approach is naively used here, it will be found that the boundary conditions cannot be met, at least with any obvious choice of particular solution.

To solve Eq. B.7, the standard technique of separation of variables will be used. (Incidently, this is the approach one would use when determining the homogeneous solution.) Thus, try a series solution to Eq. B.7 of the form

$$\Phi = \sum_{l=0}^{\infty} R_l(r) P_l(\cos\theta) \tag{B.8}$$

This form of $\Phi$ reduces Eq. B.7 to

$$\sum_{l=0}^{\infty} P_l(\cos\theta) \left[ \frac{1}{r^2} \frac{d}{dr} \left( r^2 \frac{dR_l(r)}{dr} \right) - \frac{l(l+1)}{r^2} \right] = -\frac{\rho}{\epsilon} \tag{B.9}$$

where the $P_l(\cos\theta)$ are the Legendre functions of order $l$ and are defined by

$$\frac{1}{\sin\theta} \frac{d}{d\theta} \left[ \sin\theta \frac{dP_l(\cos\theta)}{d\theta} \right] = -l(l+1) P_l(\cos\theta) \tag{B.10}$$

Note that $l$ is a nonnegative integer. Legendre functions satisfy the orthogonality condition [98]

$$\int_{-1}^{1} P_n(x) P_l(x) dx = \begin{cases} 0 & l \neq n \\ \frac{2}{2l+1} & l = n \end{cases} \tag{B.11}$$

Looking ahead, in order to match the boundary conditions in a convenient form, the source term will also be expanded into a series. In this case, it is desirable to express the charge density in terms of an infinite series of Legendre functions. With this objective, express the charge density as

$$\rho = \sum_{l=0}^{\infty} \alpha_l P_l(\cos\theta) \tag{B.12}$$

where the $\alpha_l$ are constants. With this form of the charge density, Eq. B.9 can be expressed as

$$\sum_{l=0}^{\infty} P_l(\cos\theta) \left[ \frac{1}{r^2} \frac{d}{dr} \left( r^2 \frac{dR_l(r)}{dr} \right) - l(l+1) \frac{R_l(r)}{r^2} \right] = \sum_{l=0}^{\infty} \left( \frac{-\alpha_l}{\epsilon} \right) P_l(\cos\theta) \tag{B.13}$$

Multiplying both sides of Eq. B.13 by $P_n(\cos\theta)\sin\theta$ then integrating $\theta$ from 0 to $\pi$ and using the orthogonality condition gives

$$\frac{1}{r^2} \frac{d}{dr} \left( r^2 \frac{dR_l(r)}{dr} \right) - l(l+1) \frac{R_l(r)}{r^2} = \frac{-\alpha_l}{\epsilon} \tag{B.14}$$

For the homogeneous solution to Eq. B.14 look for solutions of the form $R_l(r) = r^n$. The

result is

$$[n(n+1) - l(l+1)]r^{n-2} = 0 \tag{B.15}$$

which requires $n = l$ or $n = -(l+1)$. The homogeneous solution then is

$$R_l(r) = b_l r^l + c_l r^{-(l+1)} \tag{B.16}$$

where $b_l$ and $c_l$ are constants. For the particular solution, recall that the $\alpha_l$ are constants so try $R_l(r) = d_l r^p$ with $d_l$ a constant. Then, Eq. B.14 gives

$$d_l \left[p(p+1) - l(l+1)\right] r^{p-2} = -\frac{\alpha_l}{\epsilon} \tag{B.17}$$

The only way this equation can be satisfied for all $r$ is if $p = 2$. Then,

$$d_l = \frac{\alpha_l}{\epsilon[l(l+1) - 6]} \qquad l \geq 0, l \neq 2 \tag{B.18}$$

The case of $l = 2$ is special because it corresponds to a homogeneous solution of Eq. B.14. For this case, the governing equation for the particular solution is

$$\frac{1}{r^2}\frac{d}{dr}\left[r^2 \frac{dR_2}{dr}\right] - 6\frac{R_2}{r^2} = -\frac{\alpha_2}{\epsilon} \tag{B.19}$$

To solve this equation, let $R_2(r) = r^2 f(r)$ where $f(r)$ is some function of $r$ which is to be determined. Substitution into Eq. B.19 results in

$$r^2 \frac{d^2 f}{dr^2} + 6r\frac{df}{dr} = -\frac{\alpha_2}{\epsilon} \tag{B.20}$$

Letting $y = df/dr$ gives

$$\frac{dy}{dr} + \frac{6}{r}y = -\frac{\alpha_2}{\epsilon}\frac{1}{r^2} \tag{B.21}$$

which can be solved using an integrating factor of $r^6$. The solution is

$$y = \frac{df}{dr} = -\frac{\alpha_2}{5\epsilon r} + \frac{e_a}{r^6} \tag{B.22}$$

or

$$f(r) = -\frac{\alpha_2}{5\epsilon}\ln r - \frac{1}{5}\frac{e_a}{r^5} + e_b \tag{B.23}$$

The constants $e_a$ and $e_b$ correspond to the homogeneous solution and are not included in the particular solution. Thus, the particular solution for the case of $l = 2$ is

$$R_2(r) = -\frac{\alpha_2}{5\epsilon} r^2 \ln r \tag{B.24}$$

Superimposing the homogeneous and particular solutions gives the general solution

$$\Phi(r,\theta) = \sum_{l=0,l\neq 2}^{\infty} \left[b_l r^l + c_l r^{-(l+1)} + d_l r^2\right] P_l(\cos\theta) + \left[b_2 r^2 + c_2 r^{-3} + d_2 r^2 \ln r\right] P_2(\cos\theta) \tag{B.25}$$

where

$$d_l = \begin{cases} \frac{\alpha_l}{\epsilon[l(l+1)-6]} & l \geq 0, l \neq 2 \\ -\frac{\alpha_2}{5\epsilon} & l = 2 \end{cases} \tag{B.26}$$

This solution for the potential distribution is valid for any problem in spherical coordinates which only has charge density variations in the $\theta$ direction. In the next section, the $\alpha_l$ are determined in terms of the original charge density and the boundary conditions are applied.

## B.5 Particular Potential Distribution

To find the potential distribution for the Nilsson Plate structure, the series coefficients for the charge density defined in Eq. B.12 must be found. To determine these $\alpha_l$, exploit the orthogonality condition of the Legendre functions by multiplying both sides of Eq. B.12 by $P_n(\cos\theta)\sin\theta$ and then integrating $\theta$ from 0 to $\pi$. This gives

$$\begin{aligned} \frac{2}{2n+1}\alpha_n &= \int_0^{\pi} \rho P_n(\cos\theta)\sin\theta d\theta \\ &= \int_0^{\frac{\pi}{2}} \rho_o P_n(\cos\theta)\sin\theta d\theta - \int_{\frac{\pi}{2}}^{\pi} \rho_o P_n(\cos\theta)\sin\theta d\theta \\ &= \rho_o\left[-\int_1^0 P_n(x)dx + \int_0^{-1} P_n(x)dx\right] \\ &= \rho_o\left[2\int_0^1 P_n(x)dx - \int_{-1}^1 P_n(x)dx\right] \end{aligned} \tag{B.27}$$

Letting $l = 0$ in Eq. B.11 gives

$$\int_{-1}^1 P_n(x)dx = \int_{-1}^1 P_n(x)P_0(x)dx = \begin{cases} 0 & n \neq 0 \\ 2 & n = 0 \end{cases} \tag{B.28}$$

Also, [98]

$$\int_0^1 P_n(x)dx = \begin{cases} 1 & n = 0 \\ 0 & n \text{ even} \\ (-1)^{(n-1)/2}\frac{1}{n(n+1)}\frac{(1\cdot 3\cdot 5\cdots n)^2}{n!} & n \text{ odd} \end{cases} \tag{B.29}$$

Substituting Eqs. B.28 and B.29 into Eq. B.27 gives

$$\alpha_n = \begin{cases} \rho_o(-1)^{(n-1)/2}\frac{2n+1}{n(n+1)}\frac{(1\cdot 3\cdot 5\cdots n)^2}{n!} & n \text{ odd} \\ 0 & n = 0, \text{ even} \end{cases} \tag{B.30}$$

Now that the $\alpha_l$ have been determined, the next step is to apply the boundary con-

ditions to Eq. B.25. The boundary conditions are

$$\begin{array}{lll} \text{(i)} & \Phi \text{ finite} & \text{as } r \to 0 \\ \text{(ii)} & \Phi = 0 & \text{at } r = a \\ \text{(iii)} & \Phi = 0 & \text{at } \theta = \frac{\pi}{2} \end{array} \tag{B.31}$$

The first condition requires $c_l = 0$. The second condition gives

$$\sum_{l=0, l\neq 2}^{\infty} \left[b_l a^l + d_l a^2\right] P_l(\cos\theta) + \left[b_2 a^2 + d_2 a^2 \ln a\right] P_2(\cos\theta) = 0 \tag{B.32}$$

This condition must hold for all $\theta$, so make

$$b_l = \begin{cases} -d_l a^{2-l} & l \neq 0 \\ -d_2 \ln a & l = 2 \end{cases} \tag{B.33}$$

The final result is

$$\Phi(r,\theta) = \sum_{l=0, l\neq 2}^{\infty} d_l a^2 \left[\left(\frac{r}{a}\right)^2 - \left(\frac{r}{a}\right)^l\right] P_l(\cos\theta) + d_2 r^2 \ln\left(\frac{r}{a}\right) P_2(\cos\theta) \tag{B.34}$$

The third boundary condition is a consistency check on the solution. It requires that

$$\Phi(r, \theta = \frac{\pi}{2}) = \sum_{l=0, l\neq 2}^{\infty} d_l a^2 \left[\left(\frac{r}{a}\right)^2 - \left(\frac{r}{a}\right)^l\right] P_l(0) + d_2 r^2 \ln\left(\frac{r}{a}\right) P_2(0) = 0 \tag{B.35}$$

It can be shown that [138]

$$\begin{aligned} P_{2j+1}(0) &= 0 \\ P_{2j}(0) &= \frac{(-1)^j (2j)!}{2^{2j} (j!)^2} \end{aligned} \tag{B.36}$$

where $j$ is a nonnegative integer. Eq. B.35 then implies that $d_l \neq 0$ only for $l$ odd. This is the same as the constraints on $\alpha_l$ from Eq. B.30, so the solution of Eq. B.34 is consistent with the boundary condition at $\theta = \frac{\pi}{2}$.

Since only the $l$ odd terms are nonzero, Eq. B.34 can be rewritten by substituting for $d_l$ and letting $l = 2k + 1$. The final result for the electric potential inside the sphere is

$$\Phi(r,\theta) = \frac{\rho_o a^2}{\epsilon} \sum_{k=0}^{\infty} \gamma_k \left[\left(\frac{r}{a}\right)^2 - \left(\frac{r}{a}\right)^{2k+1}\right] P_{2k+1}(\cos\theta) \tag{B.37}$$

where

$$\gamma_k \equiv \frac{(-1)^k (4k+3)}{(k+1)(2k-1)(k+2)} \frac{(2k)!}{2^{2k+2}(k!)^2} \tag{B.38}$$

## B.6 Current Calculation

Assume that only a portion of the current flowing through the bottom surface will be measured. More specifically, assume that the current is measured over a radius $r = b$, where $b \leq a$. This current can be expressed in terms of the electric field by

$$I = \int_0^{2\pi} \int_0^b [\sigma E_\theta]|_{\theta=\frac{\pi}{2}} r dr d\phi \tag{B.39}$$

The electric field can be determined from Eq. B.2. For the $\theta$ component

$$E_\theta = -\frac{1}{r\sin\theta}\frac{\partial\Phi}{\partial\theta} = -\frac{1}{r\sin\theta}\frac{\rho_o a^2}{\epsilon}\sum_{k=0}^{\infty}\gamma_k\left[\left(\frac{r}{a}\right)^2 - \left(\frac{r}{a}\right)^{2k+1}\right]\frac{d}{d\theta}\left[P_{2k+1}(\cos\theta)\right] \tag{B.40}$$

One form of the recurrence relation for Legendre functions is [138]

$$(1-x^2)\frac{dP_l(x)}{dx} = (l+1)[xP_l(x) - P_{l+1}(x)] \tag{B.41}$$

Let $x = \cos\theta$. Then

$$\frac{d[P_{2k+1}(\cos\theta)]}{d\theta} = -\sin\theta\frac{d[P_{2k+1}(x)]}{dx} = -(\sin\theta)(2k+2)\frac{[xP_{2k+1}(x) - P_{2k+2}(x)]}{(1-x^2)} \tag{B.42}$$

Thus,

$$E_\theta = \frac{\rho_o a}{\epsilon}\sum_{k=0}^{\infty}(2k+2)\frac{\gamma_k}{a}\left[\left(\frac{r}{a}\right) - \left(\frac{r}{a}\right)^{2k}\right]\left[\frac{(\cos\theta)P_{2k+1}(\cos\theta) - P_{2k+2}(\cos\theta)}{\sin^2\theta}\right] \tag{B.43}$$

and

$$I = \frac{-2\pi\sigma\rho_o a}{\epsilon}\int_0^b r dr\sum_{k=0}^{\infty}(2k+2)\gamma_k\left[\left(\frac{r}{a}\right) - \left(\frac{r}{a}\right)^{2k}\right]P_{2k+2}(0) \tag{B.44}$$

The general equation for the current flowing through a section of radius $b$ on the bottom surface is

$$I = \frac{-2\pi\sigma\rho_o a^3}{\epsilon}\sum_{k=0}^{\infty}\gamma_k(2k+2)\left[\frac{1}{3}\left(\frac{b}{a}\right)^3 - \frac{1}{(2k+2)}\left(\frac{b}{a}\right)^{2k+2}\right]P_{2k+2}(0) \tag{B.45}$$

where $\gamma_k$ is defined by Eq. B.38 and $P_{2k+2}(0)$ can be determined from Eq. B.36. The final result is

$$\frac{I}{\frac{2}{3}\pi\rho_o a^3\frac{\sigma}{\epsilon}} = \sum_{k=0}^{\infty}\frac{1}{2^{4k+2}}\frac{(4k+3)(k+1)(2k+1)}{(2k-1)(k+2)}\left[\frac{(2k)!}{k!(k+1)!}\right]^2\left[\left(\frac{b}{a}\right)^3 - \frac{3}{(2k+2)}\left(\frac{b}{a}\right)^{2k+2}\right] \tag{B.46}$$

This normalized current is plotted as a function of the ratio $b/a$ in Fig. B.3.

Some typical values are a charge density of $\rho_o = 10\ \mu C/m^3$, $a = 0.22$ m, $b = 0.11$ m, and $\tau_e = \epsilon/\sigma = 3$ sec. This gives a ratio of b/a = 0.5 and $I = 12.9$ nA, which is an

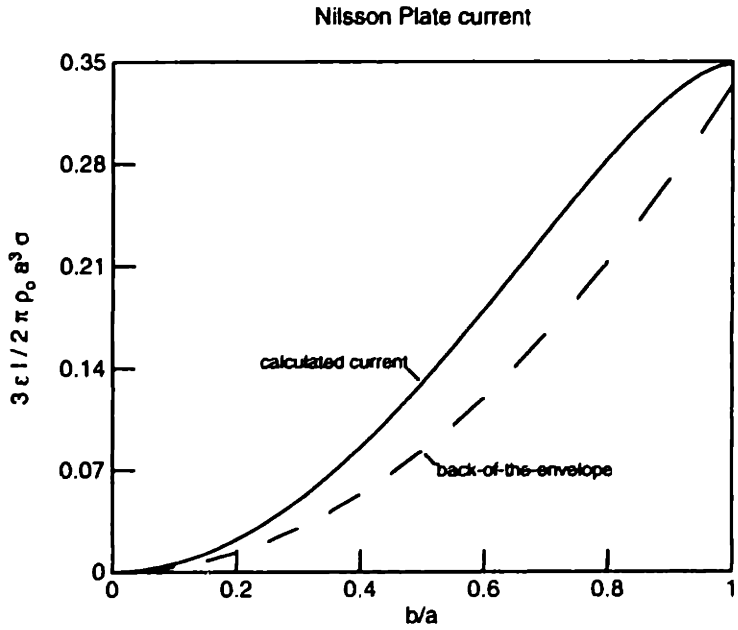


Figure B.3: The short circuit current passing through the Nilsson Plate as a function of $b/a$, where $b$ is the radius of the current measuring plate and $a$ is the radius of the grounded hemisphere. The solid line corresponds to the exact analysis while the dashed line is obtained from the back-of-the envelope calculation.

appreciable current. If the measured current is much larger than this, the assumptions neglecting electrification from the grounded shield and the plate itself are likely to be invalid.

## B.7 Back-of-the-Envelope Calculation

An excellent estimate of the current can be obtained using a rather crude model. Again, assume that all of the current flowing through the bottom surface is caused by ohmic relaxation of charge in the fluid volume. Also assume that only a fraction of this relaxation current is measured by an electrometer, where the fraction is determined by the ratio of the area of the current measuring plate to the total surface area of the shell. The current can then be written as

$$I = \frac{\frac{2}{3}\pi a^3 \rho_o}{\frac{\epsilon}{\sigma}} \frac{\pi b^2}{3\pi a^2} \tag{B.47}$$

where $\frac{2}{3}\pi a^3 \rho_o$ is the volume of charge enclosed in the hemisphere, $\frac{\epsilon}{\sigma}$ is the relaxation time of the fluid, and $\frac{\pi b^2}{3\pi a^2}$ is the ratio of the surface area of the current measuring plate

to the total surface area of the hemisphere. This gives a current of

$$\frac{I}{\frac{2}{3}\pi\rho_o a^3 \frac{\sigma}{\epsilon}} = \frac{1}{3}\left(\frac{b}{a}\right)^2 \tag{B.48}$$

This current is plotted as the dashed line in Fig. B.3. This analysis shows that an accurate estimate for the current can be obtained from a purely physical approach.

# Appendix C

# Two-point Calibration Technique

Many instruments have an output response that is linearly related to a measurable physical parameter through a calibration. To calibrate the instrument, two adjustments are usually provided: a zero (offset) and a span (gain). Typically, manufacturers recommend providing the instrument with a known load and adjusting the zero until the output gives the correct response. Then a different load must be added and the span adjusted until the output is correct. This process of adjusting the zero and the span is then repeated until the correct output, without any adjustments, is obtained for each load. While this method is necessary if the zero and the span adjustments are strongly coupled so that one affects the other, it is inefficient if the zero and the span are essentially independent. This appendix gives a more efficient calibration technique for setting the zero and the span. If the zero and the span are independent, only two initial data points (known loads) are required for the calibration.

The goal of this calibration is to adjust the instrument settings so that the ideal response of the instrument is obtained with the fewest number of adjustments. The ideal relation between the input parameter $x$ and the output signal $y$ is

$$y = a_i x + b_i \tag{C.1}$$

where $a_i$ is desired span and $b_i$ is the desired zero. To use this technique, it is assumed that the output response varies linearly with the input, the zero and the span adjustments are independent, and the zero and the span adjustments are at a "mid-range" level so that the output signal does not saturate when the known loads are applied. The technique is illustrated in Figure C.1, where the initial instrument response is to be shifted to the ideal response.

The technique is as follows:

1. First measure the output response $y_1$ for a given load $x_1$. Repeat the measurement for output $y_2$ and load $x_2$. To increase the sensitivity of the adjustments to the zero and the span, use $|x_2| > |x_1|$. From these measurements, the initial response of the instrument can be expressed as

$$y = a_o x + b_o \tag{C.2}$$

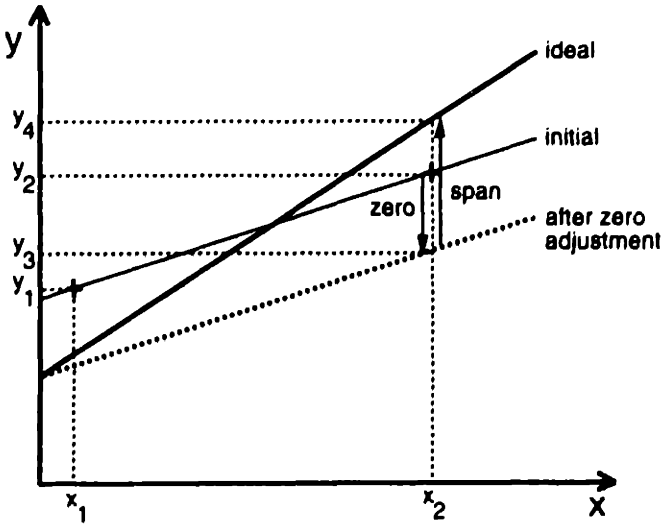


Figure C.1: Calibration of an instrument having a linear variation in output signal $y$ for a load $x$. By measuring two initial data points $(x_1,y_1)$ and $(x_2,y_2)$, the ideal zero setting can be obtained by adjusting the output to $(x_2,y_3)$ and then adjusting the span to the output $(x_2,y_4)$. If the adjustments of the zero and the span are not independent, the process must be repeated.

where the initial settings for the span $a_o$ and zero $b_o$ are given by

$$a_o = \frac{y_2 - y_1}{x_2 - x_1} \tag{C.3}$$

$$b_o = y_2 - \frac{x_2}{(x_2 - x_1)}(y_2 - y_1) \tag{C.4}$$

2. With the load kept at $x_2$, adjust the zero so that the output response has the ideal zero setting. This is accomplished by setting $b_o = b_i$ in Eq. C.2 and setting the output to $y_3$ given by

$$y_3 = a_o x_2 + b_i = \frac{x_2}{(x_2 - x_1)}(y_2 - y_1) + b_i \tag{C.5}$$

As long as the zero and the span adjustments are independent, the slope (span) does not change.

3. With the load still kept at $x_2$, adjust the span so that the output response has the ideal span setting. This is accomplished by setting the output to $y_4$ given by

$$y_4 = a_i x_2 + b_i \tag{C.6}$$

This is the ideal response to the input $x_2$.

4. A third data point should be taken to confirm the calibration. The load used in

the first measurement ($x_1$) may be used again, but it is not necessary. If this check point does not lie on the calibration line, it indicates an error in the previous measurements or that the zero and the span adjustments are not truly independent. By repeating the previous three steps, a more accurate calibration can then be obtained. The corrections should be significantly smaller with each successive measurement.

As an example, consider the calibration of a moisture sensor where the output response is the voltage of the instrument and the input load is the relative humidity (in percent) for the vapor above a saturated salt solution. The ideal response of the instrument is an output signal that varies from 1 to 5 volts as the relative humidity changes from 0 to 100%. The relative humidities associated with four salt solutions are given in Table C.1.

| Salt | Notation | %rH | Ideal Output (V) |
|---|---|---|---|
| Lithium Chloride | LiCl | 11.3 | 1.452 |
| Potassium Acetate | $KC_2H_3O_2$ | 22.7 | 1.908 |
| Sodium Chloride | NaCl | 75.3 | 4.012 |
| Potassium Sulfate | $K_2SO_4$ | 97.0 | 4.880 |

Table C.1: Relative humidities for the vapor above several saturated salt solutions. These relative humidities are accurate to about ±1% (between various measured values) at 75°F. The output voltage is the ideal response of the moisture sensor assuming an output of 1 to 5 volts over an input range of 0 to 100% relative humidity.

The first data point was taken using the LiCl solution ($x_1$=11.3%) with a measured output of $y_1$=1.420 V. Next, using an NaCl solution, ($x_2$=75.3%), the output was measured to be $y_2$=4.21 V. Continuing with the NaCl solution, the zero was adjusted until the output voltage (calculated from Eq. C.5 with $b_i$=1 V) was $y_3$=4.28 V. Finally, the span was adjusted until the output voltage was $y_4$=4.01 V. As a check, the instrument was then used to measure the relative humidities of the three other salt solutions. For the LiCl solution, the measured voltage was 1.455 V (an error of -0.2%), for the $KC_2H_3O_2$ solution the output was 1.893 V (an error of 0.8%), and for the $K_2SO_4$ solution the output was 4.76 V (an error of 2.5%). These errors are reasonable considering that the calibration was performed at a room temperature of 70°F instead of the 75°F associated with the tabulated values. This temperature difference suggests that the actual relative humidities of the vapor above the salt solutions were slightly different than the referenced values. Also, the manufacturer of the instrument quotes an accuracy (including repeatability and linearity) of ±2.5 %rH or 0.1 V. This calibration was within that accuracy.

# Appendix D

# Charge Relaxation in Pipe Flow

## D.1 Introduction

The flow of insulating fluid through pipes tends to result in a net charge being convected downstream. The volume charge in the fluid is typically attributed to either the fluid flow stripping charge away from the pipe wall or an upstream source that creates the charge. The first case (charge generation in the pipe) has been treated in detail [94,95,99,108–110,139] and will not be considered here. Rather, this appendix focuses on the second case, charge relaxation in the pipe flow. The amount of charge relaxation is determined for well-mixed, turbulent flow and for laminar flow through the pipe.

## D.2 Analysis

Consider the flow of a charged fluid through a pipe of radius $a$ at a volume flow rate $Q$. The fluid is assumed to have a kinematic viscosity $\nu$, permittivity $\epsilon$, and ohmic conductivity $\sigma$. To be consistent with this definition of the conductivity, any contributions to the conductivity caused by the imbalance of the charge carrier densities are assumed to be negligible. In addition, it is assumed that the fluid contains a uniform charge density $\rho_i$ as it enters the pipe.

In the models discussed below, the flow is always considered to be fully developed. Any entrance effects associated with the development of the fluid velocity profile are assumed to be negligible. While analytical methods for treating the hydrodynamic development of the flow profile and the associated pressure gradient at the entrance region to a pipe are available [140], their inclusion would significantly complicate this analysis and prevent a relatively simple comparison of charge relaxation between the cases of well-mixed and laminar flow. The applicability of the fully developed flow assumption is discussed in Section D.3

As the fluid flows through the pipe, the charge initially contained in the fluid volume will leak away to the pipe walls. A general description for the relaxation of the volume charge density along the length of the pipe can be written as

$$\rho(z) = \alpha(z)\rho_i \tag{D.1}$$

where $\rho(z)$ is the charge density at axial position $z$ and $\alpha$ is a relaxation parameter. The relaxation parameter reflects the amount of charge relaxation that has taken place inside the pipe and must satisfy $\alpha \leq 1$ to be consistent with the assumption of only charge relaxation.

The relaxation parameter depends upon the flow rate, the fluid properties, and the pipe size through the Reynolds number. For pipe flow, the Reynolds number $R$ can be defined as

$$R = \frac{2Q}{\pi a \nu} \tag{D.2}$$

For fully developed flow, the flow is laminar if $R < 2300$ and the flow is turbulent if $R > 4000$ [141: p. 407]. For intermediate Reynolds numbers, the flow is considered transitional. These different flow regimes will result in different relaxation parameters, but if the flow is developing because of short pipe lengths and numerous bends or protuberances (such as valves), the flow can be considered well-mixed with an essentially uniform velocity profile. The relaxation parameter will be derived for the cases of well-mixed (turbulent) and laminar flow.

### D.2.1 Well-mixed flow

For well-mixed flow through the pipe, the fluid velocity $u_o = Q/(\pi a^2)$ and the charge density profiles can be taken as essentially uniform over the cross-section of the pipe. The axial variation in the charge density can be determined by applying charge conservation over a differential pipe length $dz$ and taking the limit as $dz$ goes to zero. The resulting expression for the charge density is

$$\frac{\partial \rho}{\partial t} + u_o \frac{\partial \rho}{\partial z} = -\frac{\rho}{\tau_e} \tag{D.3}$$

where $\tau_e = \epsilon/\sigma$ is the dielectric relaxation time [1]. With the fluid entering the pipe charged at a constant level $\rho_i$, the general solution for the charge density can be written as

$$\rho(z) = \rho_i e^{-z/(u_o \tau_e)} u_{-1}(u_o t - z) \tag{D.4}$$

where $u_{-1}(z)$ is the unit step function. This indicates that at any axial position $z$ the fluid is uncharged until time $t = z/u_o$ when the charged fluid reaches that position. After this time, the charge density has its steady state value determined by

$$\frac{\rho(z)}{\rho_i} = e^{-1/R_e(z)} \tag{D.5}$$

where

$$R_e(z) = \frac{u_o \tau_e}{z} \tag{D.6}$$

is an electric Reynolds number, expressing the ratio of the dielectric relaxation time to a fluid transport time over a length $z$. This shows that the charge density and the relaxation parameter decay exponentially along the length of the pipe for well-mixed or turbulent flow.

In most pipe flow experiments the volume charge density was not measured directly. Rather, the leakage current from an isolated segment of the pipe (or the entire pipe itself) was measured by a current measuring electrometer that virtually grounded the isolated pipe segment. The charge density could then be inferred from the leakage current if the fluid velocity profile was known. With the objective of deriving a relation between the electrometer current and the volume charge density, apply charge conservation to a surface enclosing the isolated pipe segment. The electrometer current $I_e$ to ground is equal to the difference in convection currents $I_c$ due to the volume charge entering and leaving the pipe segment as

$$I_e = I_c(z) - I_c(z + L) \tag{D.7}$$

where $z$ indicates the axial distance that the isolated pipe segment is from the entrance to the pipe itself and $L$ is the length of the isolated pipe segment. The convection current can be expressed as

$$I_c(z) = Q\rho(z) \tag{D.8}$$

because the charge density and fluid velocity are assumed to be essentially uniform over the pipe cross-section, which indicates that the electrometer current can be written as

$$I_e = \pi a^2 \rho_i e^{-z/u_o\tau_e}(1 - e^{-L/u_o\tau_e}) \tag{D.9}$$

The exponential in front of the term in parentheses indicates the decay of charge in the pipe before reaching the pipe segment that is connected to the electrometer. The term in parentheses gives the fraction of the entering charge that decays in the volume of the pipe segment where the current is measured. For example, as $L$ goes to $\infty$, the term in parenthesis goes to one, indicating that all of the charge entering the isolated pipe segment relaxes to the wall before the fluid is convected out of the segment. Furthermore, when expressed in this form, the axial dependence of the current due to charge relaxation is identical to that of the streaming current due to charge generation in the pipe [99]. This is consistent with the understanding that the axial development of the charge profile is independent of the current density at the interface between the pipe wall and the fluid, with charge relaxation leading to a current out of the pipe segment and charge generation leading to a current into the pipe segment for positive charge entrained in the fluid.

The corresponding current density at the pipe wall can be obtained by setting $L = dz$ and taking the limit as $dz$ goes to zero. The result is

$$J_e = -\frac{1}{2\pi a}\frac{dI_c}{dz} \tag{D.10}$$

For well-mixed flow, substitution of Eqs. D.5 and D.8 then gives the current density as

$$J_e = \frac{a\rho_i}{2\tau_e} e^{-1/R_e(z)} \tag{D.11}$$

which is identical to the axial dependence of the charge density. Physically, the current density at the wall is due to the relaxation of charge in a volume $\pi a^2 dz$ over a surface area of $2\pi a dz$ with a time constant $\tau_e$. Thus, the current density and the charge density are expected to have the same axial dependence.

### D.2.2 Laminar flow

Next, consider the case of fully developed laminar flow in which the fluid enters the pipe with a uniform charge density $\rho_i$. In this case, the fluid velocity is in the axial direction but has a parabolic profile in the radial direction [141: p. 417]

$$u(r) = 2u_o\left(1 - \frac{r^2}{a^2}\right) \tag{D.12}$$

Even though the charge density is not uniform over the cross-section of the pipe, charge conservation can be applied to a differential volume element along a streamline so that Eqs. D.3 and D.4 are still valid. Thus, the steady state charge density as a function of both the radial and axial position can be expressed as

$$\rho(r,z) = \rho_i e^{-a^2/\left[2R_e(z)(a^2-r^2)\right]} \tag{D.13}$$

While this expression describes the local charge density in the fluid and, in principle, can be measured by some instruments [10,11], mixing of the fluid by the insertion of probes into the pipe, the sampling of the fluid by the instruments, pumps between the pipe section of interest and the measurement probe, or bends and protuberances typically result in an *average* charge density being measured. To obtain an expression for the average charge density $\rho_{av}(z)$, the charge density can be integrated over the cross-section of the pipe

$$\rho_{av}(z) = \frac{2\pi\int_0^a \rho(r,z)r\,dr}{\pi a^2} = \frac{2}{a^2}\int_0^a \rho_i e^{-a^2/\left[2R_e(z)(a^2-r^2)\right]} r\,dr \tag{D.14}$$

To evaluate this integral, make the substitution

$$w = \frac{a^2}{a^2 - r^2} \tag{D.15}$$

so that the average charge density can be expressed as

$$\frac{\rho_{av}(z)}{\rho_i} = \int_1^\infty \frac{1}{w^2} e^{-w/2R_e(z)}\,dw \tag{D.16}$$

This integral is a special case $[n = 2,\ y = 1/2R_e(z)]$ of the more general exponential integral given by [142: Eq. 5.1.4]

$$E_n(y) = \int_1^\infty \frac{1}{w^n} e^{-yw}\,dw \qquad \Re(y) > 0, n \text{ a positive integer} \tag{D.17}$$

Exponential integrals can be expressed as an infinite series by using the recursive relation [142: Eq. 5.1.14]

$$E_n(y) = \frac{1}{n-1}\left[e^{-y} - yE_{n-1}(y)\right] \tag{D.18}$$

and the relation [142: Eq. 5.1.11]

$$E_1(y) = -\gamma - \ln(y) - \sum_{j=1}^{\infty} \frac{(-1)^j y^j}{j(j!)} \tag{D.19}$$

The parameter $\gamma$ is Euler's constant and numerically equal to 0.5772156649. For the case of $n = 2$, substitution of Eq. D.19 into Eq. D.18 gives

$$E_2(y) = e^{-y} + y\left[\gamma + \ln(y) + \sum_{j=1}^{\infty} \frac{(-1)^j y^j}{j(j!)}\right] \tag{D.20}$$

so that the average charge density in the fluid is given by

$$\begin{aligned} \frac{\rho_{av}(z)}{\rho_i} &= E_2\left[\frac{1}{2R_e(z)}\right] \\ &= e^{-1/2R_e(z)} + \frac{1}{2R_e(z)}\left\{\gamma + \ln\left[\frac{1}{2R_e(z)}\right] + \sum_{j=1}^{\infty} \frac{(-1)^j}{j(j!)}\left[\frac{1}{2R_e(z)}\right]^j\right\} \end{aligned} \tag{D.21}$$

This is the relaxation parameter for laminar flow through the pipe. The first term is similar to the exponential decay found in turbulent flow. While the effect of the term in brackets is not clear for $R_e(z)$ large, as $R_e(z)$ becomes small it decays exponentially. Indeed, the exponential integral asymptotically approaches [143: pp. 575–576]

$$E_n(y) \sim \frac{e^{-y}}{y}\left[1 - \frac{n}{y} + \frac{n(n+1)}{y^2}\right] \qquad y \to \infty \tag{D.22}$$

so the relaxation parameter is larger in the laminar flow case than the turbulent flow case when $R_e(z)$ is small.

As in the case of well-mixed flow, the leakage current that would be measured by a current measuring electrometer virtually grounding an isolated pipe segment can be calculated. In this case convection current can be expressed as

$$\begin{aligned} I_c(z) &= 2\pi \int_0^a \rho(r,z)u(r)r\,dr \\ &= 2\pi \int_0^a 2u_o\rho_i\left(1 - \frac{r^2}{a^2}\right) e^{-a^2/2R_e(z)(a^2-r^2)} r\,dr \end{aligned} \tag{D.23}$$

Using the substitution of Eq. D.15 gives

$$I_c(z) = 2Q\rho_i \int_1^{\infty} \frac{1}{w^3} e^{-w/2R_e(z)}\,dw \tag{D.24}$$

so that

$$I_c(z) = 2Q\rho_i E_3\left[\frac{1}{2R_e(z)}\right] \tag{D.25}$$

The exponential integral $E_3(y)$ can be evaluated by substituting Eq. D.20 into Eq. D.18.

Taking the difference in convection currents entering and exiting the pipe section then gives the electrometer current as

$$I_e = 2Q\rho_i \left\{ E_3\left[\frac{1}{2R_e(z)}\right] - E_3\left[\frac{1}{2R_e(z+L)}\right] \right\} \tag{D.26}$$

This expression for the laminar flow leakage current is analogous to Eq. D.9 for well-mixed flow. The corresponding current density at the wall can be obtained from Eqs. D.10, D.25 and the relation [142: Eq. 5.1.26]

$$\frac{dE_n(y)}{dz} = -E_{n-1}(y) \tag{D.27}$$

as

$$J_e = \frac{a\rho_i}{2\tau_e} E_2\left[\frac{1}{2R_e(z)}\right] \tag{D.28}$$

Similar to the well-mixed flow case, the current density has the same axial dependence as the average charge density because the current density is determined by the total charge enclosed within a differential pipe segment.

## D.3 Discussion

The relaxation parameters are plotted as a function of the electric Reynolds number (or axial position) in Fig. D.1. The relaxation parameter is larger for laminar flow than turbulent flow for $R_e(z)$ small. But for $R_e(z)$ large, the turbulent flow relaxation parameter is larger. This comparison can be physically motivated by considering charge relaxation along the streamlines for the fluid flow. In the laminar flow case, when the streamlines are near the pipe walls, the charged fluid relaxes before it can travel a significant distance and the average charge density is smaller than the turbulent flow case. Once this charge has decayed, it no longer has an effect on the average charge density. When the streamlines are near the center of the pipe, the fluid moves faster than in the well-mixed flow case and the charged fluid can travel further downstream. Thus, once the fluid has traveled far enough downstream, the average charge density in the laminar flow case is higher than the well-mixed case.

Also shown in Fig. D.1 is a comparison of the decay rates for well-mixed and laminar flow, assuming that each decays exponentially with distance. It has been reported that the current density to the wall obeys the relation

$$J_e = J_o e^{-m/R_e(z)} \tag{D.29}$$

with $J_o$ is the current density at the pipe entrance and the decay coefficient $m$ is one for turbulent flow but varies between three and ten for laminar flow [123]. Figure D.1 shows that the $m$ for laminar flow is larger than that of turbulent flow when the electric Reynolds number is large, but it becomes smaller when the electric Reynolds number is small. Indeed, in the limit as the electric Reynolds number goes to infinity, Eq. D.28

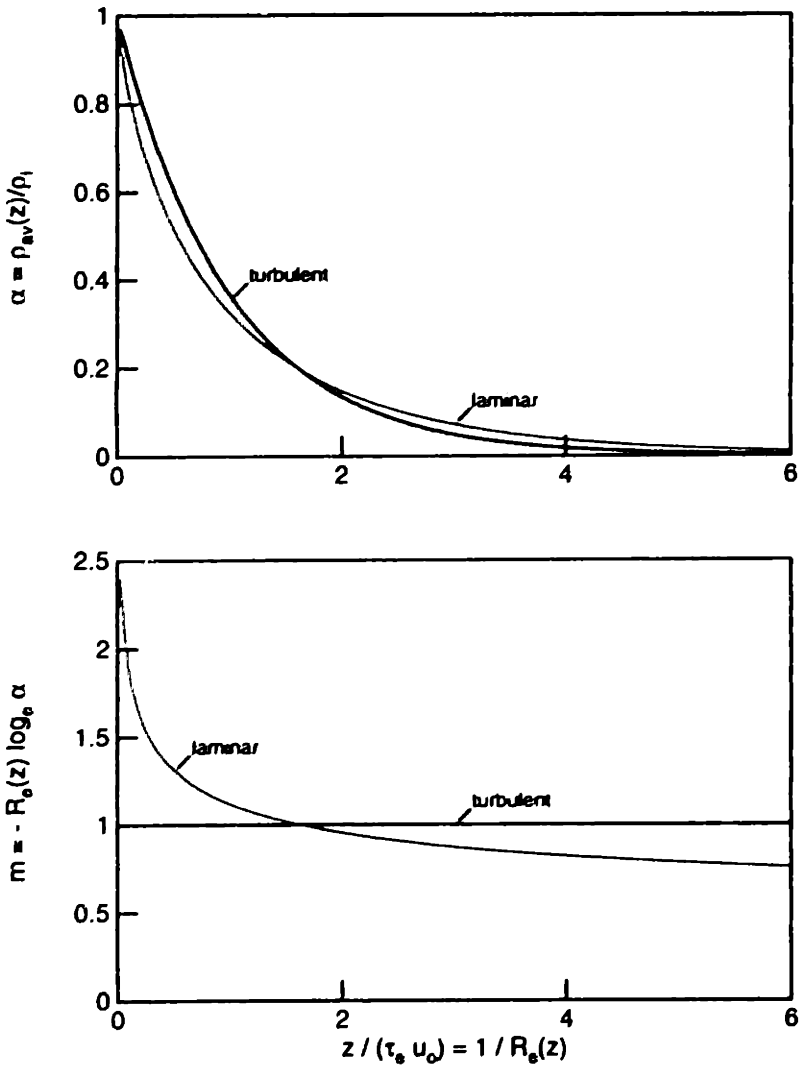


Figure D.1: The upper plot gives the relaxation parameter $\alpha$, the ratio of the average charge density to the charge density at the pipe entrance as a function of the electric Reynolds number. The second plot is a comparison of the decay factor $m$ for the cases of well-mixed and laminar flow, assuming an exponential dependence on the electric Reynolds number of the form $\alpha = e^{-m/R_e(z)}$.

gives the laminar flow decay coefficient as

$$\lim_{\nu \to 0} m = \lim_{\nu \to 0} -\frac{\ln\left[E_2(y/2)\right]}{y} = \lim_{\nu \to 0} -\frac{E_1(y/2)}{2E_2(y/2)} = \infty \tag{D.30}$$

where $y = 1/R_e(z)$ and L'Hôpital's Rule was used. Even though this analysis does not apply for very large $R_e(z)$, as discussed at the end of this section, it does indicate that observed decay coefficients in the range from three to ten are reasonable.

The leakage current for an isolated pipe section is plotted in Fig. D.2. A number of fundamental features are evident from the plot. First, when the electric Reynolds number based on the isolated segment length $R_e(L)$ is large, the current is small because the residence time for charge relaxation in the pipe segment is small. Second, the current decays exponentially with $1/R_e(z)$ for turbulent flow and decays roughly exponentially for laminar flow, but *less* rapidly than in the turbulent flow case. This is a result of the charge that was entrained in the fluid flow near the center of the pipe being convected at a rate higher than the average fluid velocity. Third, the current is smaller for laminar flow when $R_e(z)$ is large, because the charge being carried by the fluid near the center of the pipe does not relax significantly before being convected out of the pipe segment. On the other hand, in the turbulent case the mixing of the fluid causes a larger portion of the charge to relax before exiting the segment. When $R_e(z)$ is small, the turbulent flow current is smaller because most of the charge has already relaxed while the fluid moving at higher than average velocities still contains charge in the case of laminar flow.

One of the assumptions for this analysis was that any entrance effects due to the development of the fluid velocity flow profile were negligible. One criterion for neglecting these entrance effects is based on the observation that little charge relaxation occurred when the electric Reynolds number was much larger than one. Under this condition the charge density is essentially unchanged from its inlet value. Applying this result to the development region, if the electric Reynolds number based on the length of the development region $L_e$ is much larger than one, or

$$R_e(L_e) \gg 1 \quad \Rightarrow \quad \frac{2aL_e}{\nu\tau_e} \ll R \tag{D.31}$$

the entrance effects on the charge density can be neglected. The development length for fully developed flow at the entrance of a circular duct of radius $a$ can be taken as [141: p. 407]

$$\frac{L_e}{2a} \approx \begin{cases} 0.06R & \text{laminar flow} \\ 4.4R^{1/6} & \text{turbulent flow} \end{cases} \tag{D.32}$$

Note that the longest development length corresponds to laminar flow with $R \approx 2300$ so that $L_{e\max} \approx 276a$. Combining Eqs. D.31 and D.32 then gives a criterion for neglecting the entrance effects as

$$\frac{a^2}{\tau_e\nu} \ll \begin{cases} 4.17 & \text{laminar flow} \\ 0.057R^{5/6} & \text{turbulent flow} \end{cases} \tag{D.33}$$

As an example, let the fluid of interest be transformer oil at room temperature, with

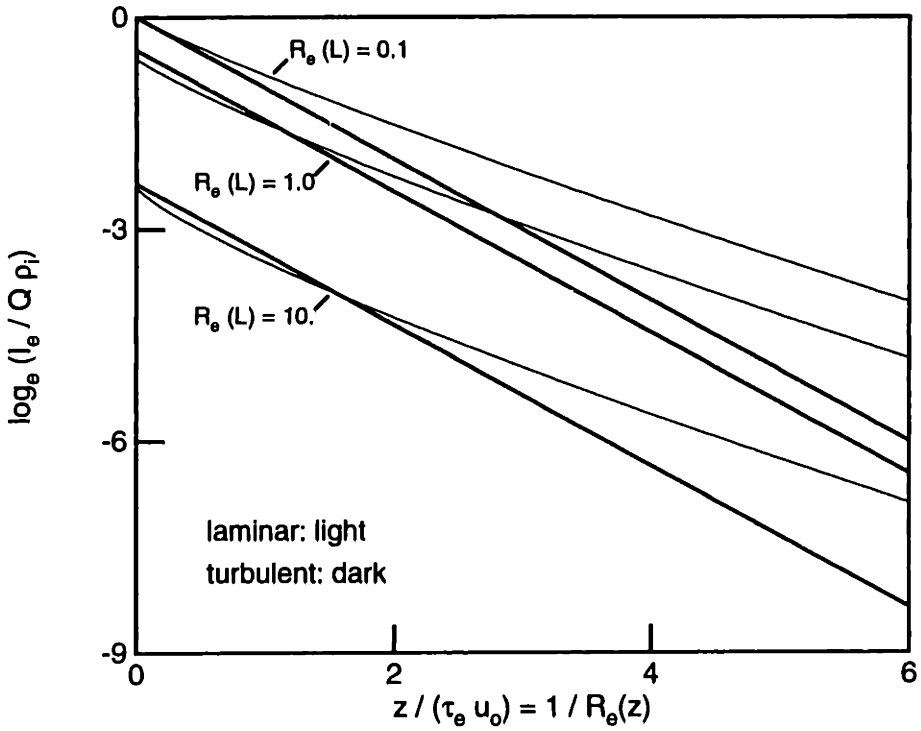


Figure D.2: Calculated leakage current from an isolated pipe segment as a function of the electric Reynolds numbers $R_e(z)$ based on the axial distance the isolated pipe segment is from the entrance to the pipe and $R_e(L)$ based on the length of the isolated pipe segment.

$\nu = 1.8 \times 10^{-5}$ m$^2$/s, and $\tau_e = 20$ s. For laminar flow, the pipe radius must satisfy $a \ll 3.9$ cm to neglect the development length. For turbulent flow, the radius must satisfy $a \ll 0.0045 R^{5/12}$ m. With a nominal turbulent Reynolds number of $R = 4000$, this gives $a \ll 14.3$ cm, which is less strict than the laminar flow criterion. Indeed, neglecting the entrance effects becomes a better approximation for a pipe of a given radius as the Reynolds number increases in turbulent flow.

## D.4 Conclusions

In this analysis, the charge density variation with position was derived for a fluid having a constant charge density inlet to a pipe. The functional form of the charge density is different between well-mixed and laminar flows, but the average charge density at any axial position is not significantly different between the two cases. The leakage current from an isolated pipe segment was calculated and found to decay essentially exponentially

with distance, for a given flow rate, with the decay rate smaller for laminar flow.

# Appendix E

# Program Listings

This appendix lists the main programs, in alphabetical order, used in this thesis. The following table gives each program name and a brief description. The program listings themselves follow the table.

**btacal.c** This C program takes wavelength scan data for the ultraviolet spectrophotometer and converts it into BTA oil concentrations.

**cf6.bas** This QuickBasic™ data acquisition program measures the terminal voltages and charge density in the Couette Charger as a function of time. The rotational speed is held constant or can vary during the run. The voltage of the cylinder can also be varied. The moisture is measured with the temperatures in the Couette (two locations), hood and ambient, outside the hood. Conductivity measurements from a conductivity cell are also made at a single frequency.

**filter.bas** This QuickBasic™ data acquisition program is for the Flow Loop Facility. This program writes all of the necessary initialization information to two controllers and then performs ACS measurements for the inlet charge density and the outlet charge density. The program also monitors the data logger line to retrieve information about the temperature, flow rate, and short circuit current.

**lmdif1.for** This Fortran subroutine performs a nonlinear least-squares minimization using the Levenberg-Marquardt algorithm. It is a standard MINPACK subroutine and is not listed here [144].

**lmdif1o.for** This Fortran subroutine provides diagnostic information about the parameter estimations. It is used in conjunction with **lmdif1.for**.

**pcf6.c** This C program plots most of the the data generated by the data acquisition program **cf6.bas**. Most of the data is unprocessed and displayed in "raw" form, but some data is also processed, such as the oil moisture content and the oil conductivity.

**pelexp.for** This parameter estimation program, written in Fortran, fits data to the relation

$$y = ae^{-t/\tau} + b$$

where $a$, $b$, and $\tau$ are to be determined. This program uses **lmdif1o.for** and **lmdif1.for**.

**pe2exp.for** This parameter estimation program, written in Fortran, fits data to the relation

$$y = ae^{-t/\tau_1} + be^{-t/\tau_2}$$

where $a$, $b$, and $\tau_1$ are to be determined. It is assumed that $\tau_2$ has been determined by some other method. This program uses **lmdif1o.for** and **lmdif1.for**.

**peept.for** This parameter estimation program, written in Fortran, fits data to the relation

$$y = \frac{a}{1 + t/\tau_1} + be^{-t/\tau_2}$$

where $a$, $b$, and $\tau_1$ are to be determined. It is assumed that $\tau_2$ has been determined by some other method. This program uses **lmdif1o.for** and **lmdif1.for**.

**perho.for** This program, written in Fortran, performs a parameter estimation on the outlet charge density from the recirculatory flow loop apparatus. This program uses **lmdif1o.for** and **lmdif1.for**.

**prc.c** This C program is used to calculate the effective impedance of a test cell from a frequency scan of the gain and phase as measured by the Otten box and logged through kermit. The resistance and capacitance at each frequency is calculated and an effective resistance and capacitance are also estimated. Given the capacitance of the test cell in air, the permittivity and conductivity of the test medium is also calculated.

**prcc.c** This C program is used to calculate the effective impedance of a test cell from a frequency scan of the gain and phase as measured by the Otten box and logged through kermit. The impedance is fit to a three element lumped parameter circuit, composed of a capacitor in series with the parallel combination of a resistor and capacitor. The medium permittivity is estimated from the high frequency gain (capacitance) assuming the phase is zero. The medium conductivity and Debye length are then calculated at a low frequency. The permittivity, conductivity, and Debye length are then used to calculated the effective resistances and capacitances.

```
/*****************************************************************

                        btacal.c

                        05/11/93

This program takes wavelength scan data for the ultraviolet
spectrophotometer and converts it into BTA oil concentrations.
Inputs are:
        base oil scan(s)
        BTA extracted from oil phase scan(s)
        and the masses of the samples and solutions.
When more than one scan is performed, the same mixture is assumed
to be used. The scans are assumed to go for wavelengths from 300 to
225 nm in steps of 5 nm. Because of an apparent ''shift'' in the
indexing by the data acquisition software, the 290 to 225 nm are
wavelength shifted to 295 to 230 nm.

        Usage: btacal

*****************************************************************/

# include       <stdio.h>
# define        EOL     '\n'    /* end of line definition */
# define        NMAX    16      /* number of wavelengths */
# define        WCAL    0.2668  /* sum of calibration absorbances */
# define        WCALA   0.4645  /* sum of calibration absorbances */

float   wave[NMAX] = {300.,295.,290.,285.,280.,275.,270.,265.,
        260.,255.,250.,245.,240.,235.,230.,225.};
/*float         calabs[NMAX] = {0.0012,0.0054,0.0177,0.0317,0.0471,0.0523,
        0.0524,0.0501,0.0461,0.0397,0.0320,0.0239,0.0169,0.0121,0.0099};*/
float   calabs[NMAX] = {0.0012,0.0049,0.0175,0.0322,0.0499,0.0562,
        0.0570,0.0542,0.0495,0.0422,0.0339,0.0252,0.0178,0.0126,0.0102};

main()
{
        int     n;
        float   *babs,*oabs,ppm[NMAX],ave,wgave;
        void    getdata(char *, float *);
        printf("This program assumes that the base oil is present\n");
        for (n=0;n<NMAX;++n) babs[n] = oabs[n] = 0.;
        getdata("base oil",babs);
        getdata("oil extract",oabs);
        printf("\n");
        for (ave=0.,wgave=0.,n=0;n<NMAX-1;++n) {
           ppm[n] = (oabs[n] - babs[n]) / calabs[n];
           printf("%f\t%f\n",wave[n],ppm[n]);
           ave += ppm[n] / (float) (NMAX - 1);
           wgave += calabs[n] * ppm[n] / WCALA ;
           }
        printf("(230-300 nm) average = %f ",ave);
        printf("weighted average = %f ppm\n",wgave);
```

```
        for (ave=0.,wgave=0.,n=4;n<NMAX-7;++n) {
           ave += ppm[n] / (float) (NMAX - 11);
           wgave += calabs[n] * ppm[n] / WCAL ;
           }
        printf("(260-280 nm) average = %f ",ave);
        printf("weighted average = %f ppm\n",wgave);
        printf("btacal finished\n");
        fflush(stdout);
}

void    getdata(char titl[], float dum[]) {
        int     i,ib,n;
        float   abs,jk,moil,mkhco;
        char    fileses[9];
        FILE    *fpses,*fopen();
        printf("\n Enter the number of %s scans: ",titl);
        scanf("%d",&ib);
        printf("\n Enter the KHCO3 mass: ");
        scanf("%f",&mkhco);
        printf("\n Enter the oil mass: ");
        scanf("%f",&moil);
        for(i=1;i<=ib;++i) {
           printf("\n Enter scan %d file name: ",i);
           scanf("%s",fileses);
           if ((fpses = fopen(fileses,"r")) == NULL) {
              printf("Error: cannot open %s\n",fileses);
              exit(1);
              }
           for(n=0;n<NMAX;++n) {
                fscanf(fpses,"%f %f\n",&jk,&abs);
                dum[n] += mkhco * abs / ((float) ib * moil);
                }
           fclose(fpses);
           }
        for(n=0;n<NMAX-1;++n) dum[n] = dum[n+1];
        }
```

```
'       program cf6.bas made 9-30-93 (modified version of CF5.bas)
'               moisture sensor calibration as of 01/28/93
'
'       This program measures the terminal voltages and charge density in the
'       Couette Charger as a function of time.  The rotational speed is held
'       constant or can vary during the run.  The voltage of the
'       inner cylinder can also be varied.  The moisture is measured
'       along with the temperatures in the Couette (two locations),
'       the hood and ambient, outside the hood. Conductivity measurements from
'       a conductivity cell are also made at a single frequency.
'       During the initializing stage, several high frequency readings are
'       taken to determine the capacitance of the cell.  It is
'       assumed that Moisture Charge Meter software version 1.4 is used.
'
'       The old values for the parameters are displayed along with
'       the new ones.  The old values are stored in vector OLD with
'               OLD(1) =        Time
'               OLD(2) =        CC Temperature at top
'               OLD(3) =        CC Temperature at side
'               OLD(4) =        Hood Air Temperature
'               OLD(5) =        Ambient Temperature
'               OLD(6) =        Low voltage (Trek) Signal, when TREK used
'               OLD(7) =        Electrometer 1 voltage
'               OLD(8) =        Electrometer 2 voltage
'               OLD(9) =        Rotation
'               OLD(10) =       TH5 Temperature
'               OLD(11) =       ACS offset
'               OLD(12) =       ACS current
'               OLD(13) =       ACS overshoots
'               OLD(15) =       ACS charge density
'               OLD(17) =       Moisture sensor 37 (air) voltage
'               OLD(18) =       Moisture sensor 37 (air) rH
'               OLD(20) =       Moisture sensor 35 (CC) voltage
'               OLD(21) =       Moisture sensor 35 (CC) rS
'               OLD(22) =       Moisture sensor 35 (CC) moisture
'               OLD(23) =       RC cell frequency
'               OLD(24) =       RC cell gain
'               OLD(25) =       RC cell phase
'               OLD(26) =       RC cell offset
'               OLD(27) =       oil conductivity
'
' 9/21/94 modification (APW)
'       The electrometer is assumed to be connected through the HPIB.
'       Using the autoscaling feature of the Keithley 617
'       electrometer, the scale factors do NOT have to be entered for
'       the voltage or the current.  The scale factors are set to 1
'       for this option.
'
'10/27/94
'       Options 2 and 4 also changed to use HPIB for current
'       measurement.  All measurements from electrometer 1 are taken
'       over the HPIB and not the analog outputs.
'
```

```
DIM SHARED OLD(30),MRPM(30),MV(50)
        ON ERROR GOTO 10
10      RESUME NEXT
        CLS: PRINT "CF6.BAS STARTED ..."
        PRINT: PRINT "INITIALIZING HPIB ..."
100     REM INCLUDE: 'QBSETUP'
        CALL INITIALIZE
        GOSUB 1400
        GOSUB 500
        GOSUB 1400
'*************************************************************************
'       USER PROGRAM STARTS HERE:
'*************************************************************************
        GOSUB 600
        print ROT
        IF (ROT=0 or ROT=1) THEN
          IF (ROT=0) THEN
            NE=0
            CALL SETELEC(NE)
          ELSE
            NE=1
            CALL SETELEC(NE)
          END IF
          FOR IPO=1 TO IPN
            IF (2*INT(IPO/2) <> IPO) THEN CMC2$="Y" ELSE CMC2$="N"
            GOSUB 40
          NEXT IPO
        ELSEIF (ROT=2 or ROT=3) THEN
          IF (ROT=2) THEN
            NE=0
            CALL SETELEC(NE)
          ELSE
            NE=1
            CALL SETELEC(NE)
          END IF
          FOR IRPM=1 TO IRSPD STEP 1
            RPM=IRMIN + (IRMAX-IRMIN)*(IRPM-1.)/(IRSPD-1.) : GOSUB 1500
            FOR LPJK=1 TO IRMEAS
              IF (LPJK = 1) THEN CMC2$="Y" ELSE CMC2$="N"
              GOSUB 40
            NEXT LPJK
          NEXT IRPM
        ELSEIF (ROT=4) THEN
          FOR IV=1 TO IVLT STEP 1
            VOLT=VLTMIN + (VLTMAX-VLTMIN)*(IV-1.)/(IVLT-1.) : GOSUB 1600
            FOR IRPM=1 TO IRSPD STEP 1
              IF (IRPM = 1) THEN CMC2$="Y" ELSE CMC2$="N"
              RPM=IRMIN + (IRMAX-IRMIN)*(IRPM-1.)/(IRSPD-1.) : GOSUB 1500
              FOR LPJK=1 TO IRMEAS
                GOSUB 40
              NEXT LPJK
            NEXT IRPM
          NEXT IV
```

```
ELSEIF (ROT=5 or ROT=6) THEN
  MV(1) = 0.
  MV(2) =-40.
  MV(3) =+40.
  MV(4) =-20.
  MV(5) =+20.
  IF (ROT=5) THEN
    MRPM(1) = 100
    MRPM(2) = 200
    MRPM(3) = 300
    MRPM(4) = 400
    MRPM(5) = 600
    MRPM(6) = 800
    MRPM(7) = 1000
    MRPM(8) = 1200
    MRPM(9) = 1400
  ELSE '(ROT=6)
    MRPM(1) = 200
    MRPM(2) = 400
    MRPM(3) = 800
    MRPM(4) = 1200
    MRPM(5) = 1600
    MRPM(6) = 600
    MRPM(7) = 1000
    MRPM(8) = 1400
    MRPM(9) = 100
  END IF
  FOR IRPM=1 TO MRPMX STEP 1
    RPM = MRPM(IRPM): GOSUB 1500
    FOR IV=1 TO MVX STEP 1
      VOLT = MV(IV): GOSUB 1600
      FOR LPJK=1 TO IRMEAS
        IF (IV=1 and LPJK=1) THEN CMC2$="Y" ELSE CMC2$="N"
        GOSUB 40
      NEXT LPJK
    NEXT IV
  NEXT IRPM
  FOR IRPM=MRPMX TO 1 STEP -1
    RPM = MRPM(IRPM): GOSUB 1500
    GOSUB 1300:TW#=RTIME#+20#: GOSUB 1100
    FOR IV=MVX TO 1 STEP -1
      VOLT = MV(IV): GOSUB 1600
      FOR LPJK=1 TO IRMEAS
        IF (IV=MVX and LPJK=1) THEN CMC2$="Y" ELSE CMC2$="N"
        GOSUB 40
      NEXT LPJK
    NEXT IV
  NEXT IRPM
ELSEIF (ROT=7) THEN
  FOR IDUM=1 TO IRMEAS
    FOR IRPM=1 TO IRSPD STEP 1
      FOR LPJK=1 TO IRMEAS
        RPM=IRMIN + (IRMAX-IRMIN)*(IRPM-1.)/(IRSPD-1.)
```

```
            GOSUB 1500
            GOSUB 40
          NEXT LPJK
          RPM = 0
          FOR LPJK=1 TO IRMEAS
            GOSUB 1500
            GOSUB 40
          NEXT LPJK
        NEXT IRPM
      NEXT IDUM
    ELSE '(ROT=9)
      MRPM(1) = 100
      MRPM(2) = 200
      MRPM(3) = 300
      MRPM(4) = 400
      MRPM(5) = 600
      MRPM(6) = 800
      MRPM(7) = 1000
      MRPM(8) = 1200
      MRPM(9) = 1400
      FOR IRPM=1 TO MRPMX STEP 1
        RPM = MRPM(IRPM): GOSUB 1500
        FOR IV=1 TO MVX STEP 1
          NE = IV MOD 2
          CALL SETELEC(NE)
          FOR LPJK=1 TO IRMEAS
            IF (IV=1 and LPJK=1) THEN CMC2$="Y" ELSE CMC2$="N"
            GOSUB 40
          NEXT LPJK
        NEXT IV
      NEXT IRPM
    END IF
    GOTO 99
40  KKK$=INKEY$: IF (KKK$ = "Q" OR KKK$ = "q") THEN GOTO 99
    PRINT "setting rotation ...": GOSUB 1500
    IF (ROT=4 or ROT=5 or ROT=6) THEN
      PRINT "amplifier voltage ... ": GOSUB 2100
    END IF
    IF (ROT<7 OR ROT=9) THEN
      PRINT "charge density ... ": GOSUB 1700 'RES$ = "D"
    END IF
    PRINT "terminal data ... ": GOSUB 1880
    PRINT "temperatures ... ": GOSUB 2000
    IF (ROT<7 OR ROT=9) THEN
      PRINT "moisture content ... ": GOSUB 2300
    END IF
    IF ((ROT<7 OR ROT=9) and (CMC$ <> "N" or CMC2$ <> "N")) THEN
      PRINT "conductivity ... ": GOSUB 2350
    END IF
    PRINT "writing output ... ": GOSUB 1900
    RETURN
'*************************************************************************
99  'END OF USER PROGRAM
```

```
        VOLT=0.0: GOSUB 1600: RPM=0: GOSUB 1600
        END


500     ' GET INITIAL PROGRAM INFORMATION FROM USER
        DTT$=DATE$
        PRINT "Today's date is ";DTT$
        INPUT "What is the name of the output file? ",DNAM$ : PRINT
              DNAMA$="A:"+DNAM$: DNAM$="C:\DATA\"+DNAM$
        PRINT
        PRINT "Types of possible measurements:"
        PRINT "     0: rotation rate constant and terminal current measured"
        PRINT "     1: rotation rate constant and terminal voltages measured"
        PRINT "     2: rotation rate varied and terminal current measured"
        PRINT "     3: rotation rate varied and terminal voltages measured"
        PRINT "     4: rotation rate and applied voltage varied"
        PRINT "     5: rotation rate and applied voltage varied in set (1)"
        PRINT "     6: rotation rate and applied voltage varied in set (2)"
        PRINT "     7: rotation rate varied, open circuit voltage only"
'       PRINT "     8: rotation rate varied, short circuit current only"
        PRINT "     9: rotation varied, current / voltage measured"
505     INPUT "Enter the coefficient of the desired measurement: ",ROT
        '
        '       GET THE ROTATION RATE INFORMATION
        '
        IF (ROT=0 or ROT=1) THEN
          CALL GETRPM(RPM)
          INPUT "What is the approximate experiment run time? (hours) ",TRUN
          'calculate the counter accordingly assuming 4 minutes per scan
          IPN = CINT(TRUN*15)
        ELSEIF (ROT=2 or ROT=3 or ROT=4 or ROT=7) THEN
          PRINT "Minimum rotation rate: ";
          CALL GETRPM(IRMIN)
          PRINT "Maximum rotation rate: ";
          CALL GETRPM(IRMAX)
          INPUT "How many different rotation rates do you want? "; IRSPD
        ELSEIF (ROT=5 or ROT=6) THEN
506       INPUT "What is the number of rotation rates? "; MRPMX
          IF (MRPMX > 9 or MRPMX < 0) THEN
                PRINT "That is not a valid option." : GO TO 506
          END IF
507       INPUT "What is the number of voltages? "; MVX
          IF (MVX > 7 or MVX < 0) THEN
                PRINT "That is not a valid option." : GO TO 507
          END IF
        ELSEIF (ROT=9) THEN
516       INPUT "What is the number of rotation rates? "; MRPMX
          IF (MRPMX > 9 or MRPMX < 0) THEN
                PRINT "That is not a valid option." : GO TO 516
          END IF
517       INPUT "What is the number of voltage/current changes? "; MVX
          IF (MVX < 0) THEN
                PRINT "That is not a valid option." : GO TO 517
```

```
        END IF
      ELSE
        PRINT "That is not a valid option." : GOTO 505
      END IF
'
'     GET THE APPLIED VOLTAGE INFORMATION
'
      IF (ROT=4) THEN
        PRINT "Minimum voltage: ";
        CALL GETVOLT(VLTMIN)
        PRINT "Maximum voltage: ";
        CALL GETVOLT(VLTMAX)
        INPUT "How many different voltages do you want? "; IVLT
      END IF
      IF (ROT > 1) THEN
        INPUT "How many measurements are to be at each setting? ",IRMEAS
      END IF
'
'     dimension storage array for measurements and zero accumulators
'
      DIM CV(1000)
      PZEROC=0 : PZEROS=0
'
'     set the averaging time for terminal and moisture measurements
'
      DEL# = 5#
'
'     THIS IS THE ELECTROMETER SETUP
'
      VEMAX = 20000.
      SCALE1=1.
      IF (ROT=1 OR (ROT>2 AND ROT<7)) THEN
        INPUT "What is the electrometer (#2) scale? (V/V) ",SCALE2
      ELSE
        SCALE1=1.
        SCALE2=1.
      END IF
'
'     THIS IS THE CONDUCTIVITY CELL SETUP
'
      EO = 8.854E-12
      PI = 3.1415927
      'INPUT "What is the conductivity cell load resistance? (Go) ", R2
            R2= 1000.
            R2=R2*1.E9
      'INPUT "What is the conductivity cell load capacitance? (pF) ", C2
            C2= 753.
            C2=C2*1E-12
      'INPUT "What is the conductivity cell capacitance in air? (pF) ", CAIR
            CAIR=50.03
            'CAIR = 19.52
            CAIR=CAIR*1E-12
      'INPUT "What's log(freq) for the HIGH freq. permittivity data? ",HF
```

```
        HF=3
'INPUT "What's log(freq) for the LOW freq. conductivity data? ",LOGF
        LOGF=-1
'
'       GET EXPERIMENT INFORMATION
'
IF (ROT<7 OR ROT=9) THEN
 INPUT "Do you want continnous conductivity measurements? [y/n] ",CMC$
   IF (CMC$="N" or CMC$="n") THEN CMC$="N"
 INPUT "Do you want to purge the acs bellows? [y/n] ",ACSP$
ELSE
 ACSP$="N"
END IF
'
'       START THE OUTPUT FILE
'
OPEN DNAM$ FOR OUTPUT AS #1
  DTT$=DATE$:TMM$=TIME$
  PRINT #1,"PROGRAM CF6.BAS MADE 09/24/94"+" DATA FILE IS: "+DNAM$
  PRINT #1,DTT$, " ... DATE"
  PRINT #1,TMM$, " ... TIME"
  CLOSE #1
RETURN


600     'SET PARAMETERS AND MAKE INITIAL MEASUREMENTS
        '
        PRINT
        PRINT "CALLING MCM INITIALIZATION PROGRAM ... "
        REM $INCLUDE: 'INIMCM14.BAS'
        IF (ACSP$ = "Y" or ACSP$ = "y") THEN
          PRINT "PURGING BELLOWS ...                "
          CALL DPRINT("[PB]"):INPUT #2,JUNK$
628       CALL DPRINT("[CS]")
          INPUT #2,JUNK$,JUNK$,BM$,JUNK$,JUNK$,JUNK$,JUNK$,JUNK$
          IF BM$="E" THEN 628
        END IF
        '
        IF (ROT<7 or ROT=9) THEN
        CALL DPRINT("[CM]"):INPUT #2,JUNK$
        PRINT "MEASURING ZERO ROTATION CHARGE DENSITY ... "
        CALL DPRINT("[TA]"):INPUT #2,JUNK$
630     CALL DPRINT("[CS]")
          INPUT #2,JUNK$,JUNK$,JUNK$,JUNK$,ACSM$,JUNK$,JUNK$,JUNK$
          IF ACSM$="E" THEN 630
        CALL DPRINT("[AD]")
          INPUT #2,JUNK$,JNK,JNK,AVCGA,JNK,JNK,JUNK$,JNK,JNK,JNK,JNK,JNK,JUNK$
          INPUT #2,JUNK$
        PRINT USING "   Zero rotation charge density: ####.## (uC/m3)"; AVCGA
        '
        END IF
        PRINT "MEASURING ZERO ROTATION TERMINAL DATA ... "
        IF (ROT=9) THEN
```

```
  NE=1
  CALL SETELEC(NE)
  GOSUB 1800
  PRINT USING " Zero rotation response: ####.#### (V)"; AVCG1
ELSE
  IF (ROT=0 or ROT=2) THEN
    NE=0
    CALL SETELEC(NE)
    GOSUB 1800
    PRINT USING " Zero rotation current: ####.#### (pA)"; AVCG1*1.E+12
  ELSE
    NE=1
    CALL SETELEC(NE)
    GOSUB 1800
    PRINT USING " Zero rotation voltages: 1) ####.#### (V)"; AVCG1;
    PRINT USING "   2) ####.#### (V)"; AVCG2;
  END IF
END IF
'
'GET CONDUCTIVITY CELL DATA AFTER ACS FINISHED
IF (ROT<7 or ROT=9) THEN
PRINT "MEASURING HIGH FREQUENCY RCCELL STUFF ...   "
  'SET UP GPM PARAMETERS
  EXL=1.0                 'EXITATION LEVEL
  C1$="E"                 'CHANNEL 1 ENABLE
  C2$="D"                 'CHANNEL 2 ENABLE
  C3$="D"                 'CHANNEL 3 ENABLE
  C4$="D"                 'CHANNEL 4 ENABLE
  DI$="D"                 'DIAGNOSTIC ENABLE
  AT$="D"                 'AUTO TRIGGER ENABLE
  DUM$=STR$(EXL)+","+C1$+","+C2$+","+C3$+","+C4$+","+DI$+","+AT$+"]"
  'Get the high frequency data first
    C$="[GP,"+STR$(HF)+","+STR$(HF)+","+DUM$
    CALL DPRINT(C$):INPUT #2,JUNK$
    GOSUB 2350
    PRINT USING "  log(f)=##.###  gain=###.###";GPF;GPG;
    PRINT USING " phase=###.### offset=##.###";GPP;GPO
    PRINT USING "  C1=%#.###^^^^ perm=##.###^^^^";C1;PERM;
    PRINT USING " R1=##.###^^^^ COND=##.###^^^^";R1;COND
  '      Set the low frequency scan info
    C$="[GP,"+STR$(LOGF)+","+STR$(LOGF)+","+DUM$
    CALL DPRINT(C$):INPUT #2,JUNK$
END IF
OPEN DNAM$ FOR APPEND AS #1
  PRINT #1,R2*1.E-9, " ... conductivity cell load resistance"
  PRINT #1,C2*1.E12, " ... conductivity cell load capacitance"
  PRINT #1,CAIR*1.E12, " ... conductivity cell air capacitance"
  PRINT #1,AVCGA, " ... zero rotation charge density"
  PRINT #1,ROT, " ... type of measurement"
  IF (ROT=0 or ROT=2) THEN
    PRINT #1,SCALE1, " ... scale factor for current"
    PRINT #1,AVCG1*1.E12, " ... zero rotation current"
  ELSE
```

```
        PRINT #1,SCALE1, " ... scale factor for #1"
        PRINT #1,AVCG1, " ... zero rotation terminal voltage (1)"
        PRINT #1,SCALE2, " ... scale factor for #2"
        PRINT #1,AVCG2, " ... zero rotation terminal voltage (2)"
      END IF
      PRINT #1,HF," ... log(HIGH frequency) RC cell"
      PRINT #1,GPF, GPG " ... log(actual f) gain"
      PRINT #1,GPP, GPO " ... phase offset"
      PRINT #1,C1, PERM " ... C1 permit"
      PRINT #1,R1, COND " ... R1 sigma"
      PRINT #1,LOGF " ... log(LOW frequency) RC cell"
      PRINT #1,"-------------------------------------------"
    CLOSE #1
    PRINT: PRINT "Starting measurements ..."
    GOSUB 1500
    RETURN


1000  'DELAY OF TD
      '
      GOSUB 1300:TTIME#=RTIME#
1001  GOSUB 1300
      DTIME=RTIME#-TTIME#
      IF DTIME > TD THEN RETURN
      GOTO 1001


1100  'WAIT UNTIL TW#
      '
      GOSUB 1300:IF RTIME# > TW# THEN BEEP
1101  GOSUB 1300
      IF RTIME# > TW# THEN RETURN
      GOTO 1101


1200  'GETS THE TIME PRTIME# (NICE)
      '
      GOSUB 1300
      PRTIME#=INT(RTIME#*100+.5)/100
      RETURN


1300  'GETS THE TIME RTIME#
      '
      CTIME=TIMER
      IF CTIME < OTIME THEN KTD=KTD+1
      RTIME#=CTIME-STIME+KTD*86400!
      OTIME=CTIME
      RETURN


1400  'RESET TIME
      '
```

```
        KTD=0
        STIME=TIMER
        OTIME=STIME
        RETURN


1500    'SET RPM
        '
        CALL OUTPUTS("FRQ03")
        CALL ENTER(RPMO)
        IF ABS(RPM-RPMO) > 50 THEN VOFF=.002472*RPM+.0624 ELSE VOFF=VOFF+.002472*&
(RPM-RPMO)
        IF RPM < 50 THEN VOFF=.002472*RPM+.0624
        IF RPM=0 THEN VOFF=0.0
        C$="D"+STR$(VOFF)+"I"
        CALL GEN2(C$)
        RETURN


1600    'SET VOLTAGE
        '
        IF (VOLT < -VEMAX) THEN VOLT = -VEMAX
        IF (VOLT > VEMAX)  THEN VOLT = VEMAX
        ' this is when the TREK is being used
        ' VIN = (VOLT +1.311) / 4127.
        ' this is when the HEATH is being used
        VIN = (VOLT + 0.06257) / (-20.06)
        C$="D"+STR$(VIN)+"I"
        CALL GEN(C$)
        RETURN


1700    'ACS SUBROUTINE
        '
        CALL DPRINT("[CM]"):INPUT #2,JUNK$
        CALL DPRINT("[TA]"):INPUT #2,JUNK$
1730    CALL DPRINT("[CS]")
        INPUT #2,JUNK$,JUNK$,JUNK$,JUNK$,ACSM$,JUNK$,JUNK$,JUNK$
        IF ACSM$="E" THEN 1730
        CALL DPRINT("[AD]")
        INPUT #2,JUNK$,AVCO,AVCA,AVCGA,SCA,OVER,RES$,JNK,JNK,JNK,JNK,JNK,JUNK$
        INPUT #2,JUNK$
        AVCGA=AVCGA/1E6
        RETURN


1800    'TERMINAL DATA SUBROUTINE
        '
        GOSUB 1880
        IF (ROT=7 OR ROT=0 OR ROT=2 OR ROT=9) THEN GO TO 1825
        NNCF=0: AVCG2=0.
        GOSUB 1300:CTW#=RTIME#+DEL#
        CALL OUTPUTS("TO LS04;F1 RA1 Z0 N3 T3"):CALL ENTER(JUNK)
```

```
1811    GOSUB 1300:IF RTIME# >= CTW# THEN GO TO 1812
        NNCF=NNCF+1
        CALL TRIGGER:CALL ENTER(CV(NNCF))
        GOTO 1811
1812    FOR II=1 TO NNCF
          AVCG2=AVCG2+CV(II)*SCALE2/NNCF
        NEXT II
        AVCG2=-AVCG2     'INVERT FOR VOLTAGES
1825    RETURN


1880    'TERMINAL DATA SUBROUTINE FOR HPIB ELECTROMETER CONNECTION
        '
        NNCF=20:AVCG1=0.
        FOR II=1 TO NNCF
          CALL OUTELEC("T4 X"): CALL ENTELEC(FOO)
          AVCG1=AVCG1+FOO/NNCF
        NEXT II
1890    RETURN


1900    'WRITE TO THE OUTPUT FILE AND SCREEN
        '
        OPEN DNAM$ FOR APPEND AS #1
        GOSUB 1200
        PRINT #1, USING "######.# #### ##.#### ##.##";PRTIME#;RPMO;VTREK;TCCT;
        PRINT #1, USING " ##.## ##.## ##.## ##.##";TCCS;THD;TAIR;TH5
        PRINT #1, USING " ##.#### ##.## ##.#### ##.##";AVPA;RHA;AVP5;PPM5
        PRINT #1, USING " ### ### !  ####.###";SCA;OVER;RES$;AVCO;
        PRINT #1, USING " ####.### ##.####^^^^";AVCA;AVCGA
        IF (ROT<9) THEN
          PRINT #1, USING " ##.####^^^^ ##.####^^^^";AVCG1;AVCG2
        ELSE '(ROT=9)
          PRINT #1, USING " ###  ##.####^^^^";NE;AVCG1
        END IF
        PRINT #1, USING " ##.### ###.## ###.## ##.###";GPF;GPG;GPP;GPO;
        PRINT #1, USING " ##.##^^^^ ##.##^^^^";PERM;COND
        CLOSE#1
        GOSUB 2500
        RETURN

2000    'MEASURE OTHER SYSTEM TEMPERATURES (HOOD AND AMBIENT)
        '
        CALL OUTPUTS("TEM14")
        CALL ENTER(THD)
        CALL OUTPUTS("TEM15")
        CALL ENTER(TAIR)
        RETURN

2100    'LOW VOLTAGE TREK OUTPUT
        '
        NNCF=0: VTREK=0
        GOSUB 1300:CTW#=RTIME#+DEL#
```

```
        CALL OUTPUTS("TO LS02;F1 RA1 Z0 N3 T3"):CALL ENTER(JUNK)
2101    GOSUB 1300:IF RTIME# >= CTW# THEN GO TO 2102
          NNCF=NNCF+1
          CALL TRIGGER:CALL ENTER(CV(NNCF))
        GOTO 2101
2102    FOR II=1 TO NNCF
          VTREK=VTREK+CV(II)/NNCF
        NEXT II
        RETURN


2300    'MEASURE MOISTURE FOR SENSOR #36
        '
        NNCF=0: AVP5=0
        'A = -0.2857#    : B = 0.2500#     : C = 0.004226# : TR = 24.00
        'A35 = 0.00#     : B35 = 0.2500#     'for number 35 (air)
        A = -0.0311#     : B = 0.2258#     'for number 35
        'A = -0.0176#    : B = 0.2730#     'for number 60
        'A = -0.0077#    : B = 0.2446#     'for number 36 old
        'A = -0.0744#    : B = 0.2388#     'for number 36
        'A = -0.0322#    : B = 0.2333#     'for number 37
        Aa = -0.0902#    : Ba= 0.2615#     'for number 37 (air)
        EA = 3677.5# : SO=15.568E+06:  TABS = 273.15
        GOSUB 1300:CTW#=RTIME#+DEL#
        CALL OUTPUTS("TO LS07;F1 RA1 Z1 N5 T3"):CALL ENTER(JUNK)
2310    GOSUB 1300:IF RTIME# >= CTW# THEN GO TO 2320
          NNCF=NNCF+1
          CALL TRIGGER:CALL ENTER(CV(NNCF))
        GOTO 2310
2320    FOR II=1 TO NNCF
          AVP5=AVP5+CV(II)/NNCF
        NEXT II
        'Get the temperatures for the moisture measurement
        CALL OUTPUTS("TEM12")
        CALL ENTER(TCCT)
        CALL OUTPUTS("TEM13")
        CALL ENTER(TCCS)
        'CALL OUTPUTS("TEM17")
        'CALL ENTER(TH5)
        TH5=0.
        RS5 = (A + B * (AVP5 - 1.0))
        PPM5 = RS5 * SO* EXP(-EA / (TCCT + TABS))
        'Now get the rH of the hood
        NNCF=0: AVPA=0
        GOSUB 1300:CTW#=RTIME#+DEL#
        CALL OUTPUTS("TO LS06;F1 RA1 Z1 N5 T3"):CALL ENTER(JUNK)
2330    GOSUB 1300:IF RTIME# >= CTW# THEN GO TO 2340
          NNCF=NNCF+1
          CALL TRIGGER:CALL ENTER(CV(NNCF))
        GOTO 2330
2340    FOR II=1 TO NNCF
          AVPA = AVPA+CV(II)/NNCF
        NEXT II
```

```
        RHA = (Aa + Ba * (AVPA-1.0))
        RETURN


2350    'RC CELL SUBROUTINE
        '
        CALL DPRINT("[CM]"):INPUT #2,JUNK$
        CALL DPRINT("[TG]"):INPUT #2,JUNK$
2360    CALL DPRINT("[CS]")
          INPUT #2,JUNK$,JUNK$,JUNK$,JUNK$,JUNK$,GPM$,JUNK$,JUNK$
          IF GPM$="E" THEN 2360
        CALL DPRINT("[GD]")
          INPUT #2,JUNK$,JNK,JNK,JNK,JNK,JNK,JNK,JUNK$
          INPUT #2,JUNK$,JNK,GPF,GPG,GPP,GPO,JUNK$
          INPUT #2,JUNK$
        CALL ESTRC(R2, C2, CAIR, EO, PI, GPF, GPG, GPP, R1, C1, PERM, COND)
        RETURN


2500    'PRINT OUT DATA TO THE DISPLAY
        '
        '       WRITE OUT THE DATA TO THE SCREEN
        '
        TMM$ = TIME$
        AVCGA = AVCGA*1.E6
        CLS: BEEP
        PRINT USING "Time:\          \";TMM$
        PRINT USING "Run Time:       (######.#) ";OLD(1);
        PRINT USING "      ######.#     (sec)";PRTIME#
        PRINT USING "Rotation/Trak:(####/##.####) ";OLD(9);OLD(6);
        PRINT USING "    ####/##.#### (RPM/V)";RPMO;VTREK
        PRINT USING "CC top/side:   (##.#/##.#) ";OLD(2);OLD(3);
        PRINT USING "     ##.#/##.#      (C)";TCCT;TCCS
        PRINT USING "Hood/ambient:  (##.#/##.#) ";OLD(4);OLD(5);
        PRINT USING "     ##.#/##.#      (C)";THD;TAIR
        PRINT USING "Moist:       (##.##/#.####)";OLD(10);OLD(20);
        PRINT USING "    ##.##/#.####  (C/V)";TH5;AVP5
        PRINT USING "              (#.###/##.##) ";OLD(21);OLD(22);
        PRINT USING "    #.###/##.##  (rS/ppm)";RS5;PPM5
        PRINT USING "Hood:       (#.####/#.###) ";OLD(17);OLD(18);
        PRINT USING "   #.####/#.###    (V/rH)";AVPA;RHA
        PRINT USING "ACS:             [  (###) ] ";OLD(13);
        PRINT USING "       (###)   !   (over)";OVER;RES$
        PRINT USING "               (##.##/##.##)";OLD(11);OLD(12);
        PRINT USING "    ##.##/##.##     (pA)";AVCO;AVCA
        PRINT USING "                (#####.##) ";OLD(15);
        PRINT USING "     #####.##     (uC/m3)";AVCGA
        IF (ROT<9) THEN
          PRINT USING "Terminal   (##.###/##.###) ";OLD(7);OLD(8);
          IF (ROT=0 or ROT=2) THEN
                AVCG1 = AVCG1*1.E9
                AVCG2 = AVCG2*1.E9
                PRINT USING "   ##.###/##.###    (nA)";AVCG1,AVCG2
```

```
        ELSE
              PRINT USING "   ####.#/####.#    (V)";AVCG1,AVCG2
        END IF
      ELSE '(ROT=9) THEN
        PRINT USING "Terminal     (##.###^^^^)  ";OLD(7);
        IF (NE=0) THEN
              PRINT USING "     ##.###^^^^     (A)";AVCG1
        ELSE
              PRINT USING "     ##.###^^^^     (V)";AVCG1
        END IF
      END IF
      PRINT USING "RC cell:   (##.###/###.##) ";OLD(23);OLD(24);
      PRINT USING "  ##.###/###.##    (-/db)";GPF;GPG
      PRINT USING "           (###.##/##.###) ";OLD(25);OLD(26);
      PRINT USING "  ###.##/##.###   (deg/V)";GPP,GPO
      PRINT USING "             (##.###^^^^) ";OLD(27);
      PRINT USING "    ##.###^^^^     (S/m)";COND
      '
      '       Now replace the old values
      '
      OLD(1) = PRTIME# : OLD(9) = RPMO : OLD(6) = VTREK
      OLD(2) = TCCT: OLD(3) = TCCS: OLD(4) = THD: OLD(5) = TAIR
      OLD(10) = TH5: OLD(20) = AVP5: OLD(21) = RS5: OLD(22) = PPM5
      OLD(17) = AVPA: OLD(18) = RHA
      OLD(13) = OVER: OLD(11) = AVCO: OLD(12) = AVCA: OLD(15) = AVCGA
      OLD(7) = AVCG1: OLD(8) = AVCG2: OLD(23) = GPF: OLD(24) = GPG
      OLD(25) = GPP: OLD(26) = GPO: OLD(27) = COND
      RETURN


SUB INITIALIZE STATIC
SHARED PCIB.ERR,PCIB.BASERR,NOERR
      ISC=7
      CALL IORESET(ISC)
      IF PCIB.ERR <> NOERR THEN ERROR PCIB.BASERR
      CALL IOTIMEOUT(ISC,60.0)
      IF PCIB.ERR <> NOERR THEN ERROR PCIB.BASERR
      CALL IOCLEAR(ISC)
      IF PCIB.ERR <> NOERR THEN ERROR PCIB.BASERR
      CALL OUTPUTS("CLS20;CLS22;CLS24;CLS26")
      CALL GEN("IQ0")
      CALL GEN("C4F1.0A0.005D0.0I")
      CALL GEN2("IQ0")
      CALL GEN2("C4F1.0A0.005D0.0I")
END SUB


SUB AMPL(AMP) STATIC
      C$="A"+STR$(AMP)+"I"
      CALL GEN(C$)
END SUB
```

```
SUB FREQ(FRQ) STATIC
        FRR=FRQ*2048
        C$="F"+STR$(FRR)+"I"
        CALL GEN(C$)
END SUB


SUB GEN(C$) STATIC
SHARED PCIB.ERR,PCIB.BASERR,NOERR
        FEQ=711
        LENG=LEN(C$)
        CALL IOOUTPUTS(FEQ,C$,LENG)
        IF PCIB.ERR <> NOERR THEN ERROR PCIB.BASERR
END SUB


SUB GEN2(C$) STATIC
SHARED PCIB.ERR,PCIB.BASERR,NOERR
        FEQ=712
        LENG=LEN(C$)
        CALL IOOUTPUTS(FEQ,C$,LENG)
        IF PCIB.ERR <> NOERR THEN ERROR PCIB.BASERR
END SUB


SUB OUTPUTS(C$) STATIC
SHARED PCIB.ERR,PCIB.BASERR,NOERR
        AQS=709
        LENG=LEN(C$)
        CALL IOOUTPUTS(AQS,C$,LENG)
        IF PCIB.ERR <> NOERR THEN ERROR PCIB.BASERR
END SUB


SUB TRIGGER STATIC
SHARED PCIB.ERR,PCIB.BASERR,NOERR
        AQS=709
        CALL IOTRIGGER(AQS)
        IF PCIB.ERR <> NOERR THEN ERROR PCIB.BASERR
END SUB


SUB ENTER(X) STATIC
SHARED PCIB.ERR,PCIB.BASERR,NOERR
        AQS=709
        CALL IOENTER(AQS,X)
        IF PCIB.ERR <> NOERR THEN ERROR PCIB.BASERR
END SUB

SUB DPRINT(D$) STATIC
'
'       DELAYED PRINT STATEMENT FOR MCM COMMUNICATION
'
```

```
        DT = 0.25               'EMPIRICAL TIME CONSTANT
        PRINT #2, D$
        TIME1 = TIMER
        TIME2 = TIME1
        WHILE ((TIME1 - TIME2) < DT)
                IF (TIME1 < TIME2) THEN TIME2 = TIME1
                TIME1 = TIMER
        WEND
END SUB


SUB GETRPM(RPMF) STATIC
9750    INPUT "What is the rotational speed? ",RPMF
        IF RPMF > 2001 OR RPMF < 0 THEN
                PRINT "That is not a valid option."
                GO TO 9750
        END IF
END SUB


SUB GETVOLT(VOLT) STATIC
        INPUT "What is the applied voltage? ",VOLT
END SUB


SUB ESTRC (R2, C2, CAIR, EO, PI, GPF, GPG, GPP, R1, C1, PERM, COND) STATIC
'       This subroutine inverts the gain-phase measurement into the
'       corrseponding resistance-capacitance and conductivity-permittivity
        O = (2! * PI * 10! ^ GPF)* R2 * C2
        G = 10! ^ (GPG / 20!)
        P = GPP * PI / 180!
        DUM1 = 1 + G^2 - 2 * G * COS(P)
        C1 = C2 * G * (COS(P) - G + SIN(P)/O) / DUM1
        R1 = R2 * DUM1 / (G * (COS(P) - G - O * SIN(P)))
        PERM = C1 / CAIR
        COND = EO / (R1 * CAIR)
END SUB



SUB OUTELEC(C$) STATIC
SHARED PCIB.ERR,PCIB.BASERR,NOERR
        AQS=728
        LENG=LEN(C$)
        CALL IOOUTPUTS(AQS,C$,LENG)
        IF PCIB.ERR <> NOERR THEN ERROR PCIB.BASERR
END SUB


SUB ENTELEC(X) STATIC
SHARED PCIB.ERR,PCIB.BASERR,NOERR
        AQS=728
        CALL IOENTER(AQS,X)
```

```
        IF PCIB.ERR <> NOERR THEN ERROR PCIB.BASERR
END SUB


SUB SETELEC(NE) STATIC
' set the electrometer to voltage mode (NE=1) or current mode (NE=0)
        IF (NE=1) THEN
                CALL OUTELEC("F0 R0 C0 Z0 N0 D0 B0 Q6 G1 X")
        ELSE
                CALL OUTELEC("F1 R0 C0 Z0 N0 D0 B0 Q6 G1 X")
        END IF
END SUB
```

```
'*************************************************************************
'
'                        Program FILTER.BAS
'                           09 June 1990
'
'       This is the data acquisition program for the Flow Loop Facility.
'       This program writes all of the necessary initialization
'       information to both ACM's then performs ACS measurements
'       for the inlet charge density (com1) and the outlet charge
'       density (com2).  With the flow meter/data logger box connected
'       to the second port of the outlet ACM (com2), the program
'       monitors the data logger line to retrieve information about
'       the temperature (line 1), flow rate (line 5), and short circuit
'       current (line 6).   In this program, it is assumed that the ACM
'       software is version 0.98 or lower.
'
'*************************************************************************
DECLARE SUB ACM (I(), O())
DECLARE SUB DLM (NUMAVG, DV())
DECLARE SUB DPRINT (C%, D$)
DECLARE SUB FIRST (ONAM$, SCLIE, NUMAVG, YR, MON, DY, HR, MN, SC)
DECLARE SUB OUTPUT2 (I(), O(), DV(), SCLIE, ONAM$)
DECLARE SUB PSUB ()
DECLARE SUB SETUP (YR, MON, DY, HR, MN, SC)
DIM DV(10), I(11), O(11), DUM(10)
        OPEN "COM1:9600,N,8,1,RS,CS0,DS0,CD0" FOR RANDOM AS #1
        OPEN "COM2:9600,N,8,1,RS,CS0,DS0,CD0" FOR RANDOM AS #2
        CLS
        CALL SETUP(YR, MON, DY, HR, MN, SC)
        CALL FIRST(ONAM$, SCLIE, NUMAVG, YR, MON, DY, HR, MN, SC)
5       'MAKE A DATA LOGGER SCAN
                CALL DLM(NUMAVG, DV())
                FOR I = 1 TO 10: DUM(I) = DV(I): NEXT I
        'MAKE AN ACS MEASUREMENT
                CALL ACM(I(), O())
        'MAKE A DATA LOGGER SCAN
                CALL DLM(NUMAVG, DV())
                FOR I = 1 TO 10: DV(I) = (DUM(I) + DV(I)) / 2!: NEXT I
        CALL OUTPUT2(I(), O(), DV(), SCLIE, ONAM$)
        KK$ = INKEY$
        IF (KK$ = "q" OR KK$ = "Q") THEN 10
        IF (KK$ = "p" OR KK$ = "P") THEN CALL PSUB
        GOTO 5
10      PRINT : PRINT "Program FILTER.BAS is finished": PRINT
        CLOSE #2
        CLOSE #1
END

SUB ACM (I(), O()) STATIC
        'PERFORM AN ACS TEST
        CALL DPRINT(2, "[TA]"): INPUT #2, JK$
        CALL DPRINT(1, "[TA]"): INPUT #1, JK$
100     'READ STATUS OF OUTLET ACS
```

```
        CALL DPRINT(2, "[CS]")
        INPUT #2, JK$, MAT$, BM$, DM$, AM$, GM$, BP$, VP$
        IF AM$ = "E" THEN 100
101     'READ STATUS OF INLET ACS
        CALL DPRINT(1, "[CS]")
        INPUT #1, JK$, MAT$, BM$, DM$, AM$, GM$, BP$, VP$
        IF AM$ = "E" THEN 101
        'GET THE CHARGE DENSITY
        CALL DPRINT(2, "[AD]")
        INPUT #2, JK$,O(1),O(2),O(3),O(4),O(5),O(6),O(7),O(8),O(9),O(10),SC2$
        INPUT #2, JK$
        O(11) = VAL(SC2$)
        CALL DPRINT(1, "[AD]")
        INPUT #1, JK$,I(1),I(2),I(3),I(4),I(5),I(6),I(7),I(8),I(9),I(10),SC2$
        INPUT #1, JK$
        I(11) = VAL(SC2$)
        CALL DPRINT(1, "[CM]"): INPUT #1, JK$
        CALL DPRINT(2, "[CM]"): INPUT #2, JK$

END SUB

SUB DLM (NUMAVG, DV()) STATIC
        DIM D(10), S(10)
        FOR I = 1 TO 7
                DV(I) = 0
        NEXT I
        'PERFORM DATA LOGGER MEASUREMENT
        FOR J = 1 TO NUMAVG
                CALL DPRINT(2, "[TL]"): INPUT #2, JK$
                'READ STATUS
150             CALL DPRINT(2, "[CS]")
                INPUT #2, JK$, MAT$, BM$, DM$, AM$, GM$, BP$, VP$
                IF DM$ = "E" THEN GOTO 150
                'GET THE DATA LOGGER VALUES
                CALL DPRINT(2, "[LD]")
                INPUT #2, JK$,D(1),D(2),D(3),D(4),D(5),D(6),D(7),JK$,JK$,JK$,JK$,&
JK$,JK$
                INPUT #2, JK$
                FOR I = 1 TO 7
                        DV(I) = DV(I) + D(I)
                NEXT I
                CALL DPRINT(2, "[CM]"): INPUT #2, JK$
        NEXT J
        'GET SCALE FACTORS AND CONVERT DATA LOGGER VALUES TO VOLTAGES
        CALL DPRINT(2, "[LP]")
        INPUT #2, JK$, S(1), S(2), S(3), S(4), S(5), S(6), S(7), JK$, JK$
        FOR I = 1 TO 7
                DV(I) = DV(I) * 5! / (20.47 * (2! ^ S(I)) * NUMAVG)
        NEXT I
END SUB

SUB DPRINT (C%, D$) STATIC
        DT = .2
```

```
        PRINT #C%, D$
        STIME = TIMER
        OTIME = STIME
        WHILE ((STIME - OTIME) < DT)
                STIME = TIMER
        WEND
END SUB

SUB FIRST (ONAM$, SCLIE, NUMAVG, YR, MON, DY, HR, MN, SC) STATIC
        PRINT
        INPUT "What is the output file name? ", ONAM$
        INPUT "What is the scale factor for the current (nA/V)? ", SCLIE
        INPUT "How many data logger measurments for the average? ", NUMAVG
        'PRINT OUT THE HEADER INFORMATION FOR THE OUTPUT FILE AND SCREEN
        OPEN ONAM$ FOR OUTPUT AS #3
        PRINT #3, "FILTER.BAS MADE 07/09/90." + " DATA FILE: " + ONAM$
        PRINT #3, "Date: "; MON; "/"; DY; "/"; YR
        PRINT #3, "Start: "; HR; ":"; MN; ":"; SC
        PRINT #3, "  TIME    GAIN  OVER    OFFC     AVCU     AVCH";
        PRINT #3, "     TEMP    FLOW      IE"
        PRINT #3, "                          (pA)     (pA)   (uC/m3)";
        PRINT #3, "     (C)    (GPM)    (nA)"
        CLOSE #3
        CLS
        PRINT "FILTER.BAS MADE 07/09/90." + " DATA FILE IS: " + ONAM$
        PRINT "Date: "; MON; "/"; DY; "/"; YR
        PRINT "Start: "; HR; ":"; MN; ":"; SC
        PRINT "  TIME    GAIN  OVER    OFFC     AVCU     AVCH";
        PRINT "     TEMP    FLOW      IE"
        PRINT "                          (pA)     (pA)   (uC/m3)";
        PRINT "    (C)     (GPM)    (nA)"
END SUB

SUB OUTPUT2 (I(), O(), DV(), SCLIE, ONAM$) STATIC
        'PRINT OUT THE DATA TO THE OUTPUT FILE AND SCREEN
        'FIRST CONVERT THE DATA LOGGER VOLTAGES TO PHYSICAL VALUES
        TM = (DV(1) + .0004337) / (.008938)
        FL = (DV(5) - .0113) / .1931
        IE = DV(6) * SCLIE
        OPEN ONAM$ FOR APPEND AS #3
        PRINT #3, USING "## ## ##"; O(9); O(10); O(11);
        PRINT #3, USING "   ###  ###  ####.##"; O(4); O(5); O(1);
        PRINT #3, USING "  ####.## #####.##"; O(2); O(3);
        PRINT #3, USING "    ###.#  ###.##  #####.#"; TM; FL; IE
        PRINT #3, USING "--------   ###  ###  ####.##"; I(4); I(5); I(1);
        PRINT #3, USING "  ####.## #####.##"; I(2); I(3)
        CLOSE #3
        PRINT USING "## ## ##"; O(9); O(10); O(11);
        PRINT USING "   ###  ###  ####.##"; O(4); O(5); O(1);
        PRINT USING "  ####.## #####.##"; O(2); O(3);
        PRINT USING "    ###.#  ###.##  #####.#"; TM; FL; IE
        PRINT USING "--------   ###  ###  ####.##"; I(4); I(5); I(1);
        PRINT USING "  ####.## #####.##"; I(2); I(3)
```

```
END SUB

SUB PSUB STATIC
        PRINT "Program paused ... Hit c or C to continue"
15      KK$ = INKEY$
        IF (KK$ = "c" OR KK$ = "C") THEN 20 ELSE 15
20      PRINT "Program execution resumed ..."
END SUB

SUB SETUP (YR, MON, DY, HR, MN, SC) STATIC
        PRINT "Inlet ACS: now sending ... [MD]"
        CALL DPRINT(1, "[MD]"): INPUT #1, JK$ 'MASTER AUTO TRIGGER DISABLE
        PRINT "Outlet ACS: now sending ... [MD]"
        CALL DPRINT(2, "[MD]"): INPUT #2, JK$ 'MASTER AUTO TRIGGER DISABLE
        PRINT "Inlet ACS: now sending ... [AM]"
        CALL DPRINT(1, "[AM]"): INPUT #1, JK$  'ABORT MEASUREMENT IN PROGRESS
        PRINT "Outlet ACS: now sending ... [AM]"
        CALL DPRINT(2, "[AM]"): INPUT #2, JK$ 'ABORT MEASUREMENT IN PROGRESS
        PRINT "Inlet ACS: now sending ... [CM]"
        CALL DPRINT(1, "[CM]"): INPUT #1, JK$ 'CLEAR MEMORY BUFFER
        PRINT "Outlet ACS: now sending ... [CM]"
        CALL DPRINT(2, "[CM]"): INPUT #2, JK$  'CLEAR MEMORY BUFFER

        'SET UP ACS PARAMETERS
        OAT = 96                'OFFSET AVERAGING TIME        96
        DLT = 192                'DELAY TIME                  192
        CAT = 96                'CURRENT AVERAGING TIME       96
        CUC = .98               'CURRENT CALIBRATION CONSTANT
        CHC = 61.5              'CHARGE CALIBRATION CONSTANT
        CLR = 10                'CLOCK RATE                   10
        MIG = 8                'MANUAL/INITIAL GAIN
        AAS$ = "E"              'AUTO-SCALE ENABLE
        AVA$ = "D"              'VALVE ENABLE
        ADI$ = "D"              'DIAGNOSTIC ENABLE
        AAT$ = "D"              'AUTO TRIGGER ENABLE
        C$ = "[AP," + STR$(OAT) + "," + STR$(DLT) + "," + STR$(CAT) + ","
        C$ = C$ + STR$(CUC) + "," + STR$(CHC) + "," + STR$(CLR) + ","
        C$ = C$ + STR$(MIG) + "," + AAS$ + "," + AVA$ + ","
        C$ = C$ + ADI$ + "," + AAT$ + "]"
        PRINT "Inlet ACS: now sending ... "; C$
        CALL DPRINT(1, C$): INPUT #1, JK$
        PRINT "Outlet ACS: now sending ... "; C$
        CALL DPRINT(2, C$): INPUT #2, JK$

        'SET UP GPM PARAMETERS
        STF = 4!                'STARTING FREQUENCY
        EDF = -2.3              'ENDING FREQUENCY
        EXL = 1!                'EXITATION LEVEL
        GC1$ = "E"              'CHANNEL 1 ENABLE
        GC2$ = "D"              'CHANNEL 2 ENABLE
        GC3$ = "D"              'CHANNEL 3 ENABLE
        GC4$ = "D"              'CHANNEL 4 ENABLE
```

```
GDI$ = "D"                'DIAGNOSTIC ENABLE
GAT$ = "D"                'AUTO TRIGGER ENABLE
C$ = "[GP," + STR$(STF) + "," + STR$(EDF) + "," + STR$(EXL) + ","
C$ = C$ + GC1$ + "," + GC2$ + "," + GC3$ + "," + GC4$ + ","
C$ = C$ + GDI$ + "," + GAT$ + "]"
PRINT "Inlet ACS: now sending ... "; C$
CALL DPRINT(1, C$): INPUT #1, JK$
PRINT "Outlet ACS: now sending ... "; C$
CALL DPRINT(2, C$): INPUT #2, JK$

'SET UP DATA LOGGER PARAMETERS
DC1 = 2                   'CHANNEL 1 GAIN
DC2 = 7                   'CHANNEL 2 GAIN
DC3 = 7                   'CHANNEL 3 GAIN
DC4 = 7                   'CHANNEL 4 GAIN
DC5 = 0                   'CHANNEL 5 GAIN
DC6 = 1                   'CHANNEL 6 GAIN
DC7 = 7                   'CHANNEL 7 GAIN
DAZ$ = "E"                'AUTO ZERO ENABLE
DAT$ = "D"                'AUTO TRIGGER ENABLE
C$ = "[LP," + STR$(DC1) + "," + STR$(DC2) + "," + STR$(DC3) + ","
C$ = C$ + STR$(DC4) + "," + STR$(DC5) + "," + STR$(DC6)
C$ = C$ + "," + STR$(DC7) + "," + DAZ$ + "," + DAT$ + "]"
PRINT "Inlet ACS: now sending ... "; C$
CALL DPRINT(1, C$): INPUT #1, JK$
PRINT "Outlet ACS: now sending ... "; C$
CALL DPRINT(2, C$): INPUT #2, JK$

'SET UP COMMUNICATION PARAMETERS
BAUD = 9600               'RS-232 BAUD RATE
TEL$ = "253-4691"         'TELEPHONE NUMBER
DSE = 120                 'DATA STORAGE INTERVAL (SECONDS)
MTC = 40                  'MEASUREMENTS UNTIL CALL IS MADE
CL$ = "D"                 'CALL ENABLE
C$ = "[CP," + STR$(BAUD) + "," + TEL$ + "," + STR$(DSE)
C$ = C$ + "," + STR$(MTC) + "," + CL$ + "]"
PRINT "Inlet ACS: now sending ... "; C$
CALL DPRINT(1, C$): INPUT #1, JK$
PRINT "Outlet ACS: now sending ... "; C$
CALL DPRINT(2, C$): INPUT #2, JK$

'SET UP TIME AND DATE
CALL DPRINT(2, "[DT]")
INPUT #2, JK$, YR, MON, DY, HR, MN, SC2$
SC = VAL(SC2$)
PRINT "     The date is"; MON; "-"; DY; "-"; YR
PRINT "     The time is"; HR; ":"; MN; ":"; SC
INPUT "Change the time and date (Y/N)"; Q$
IF Q$ = "Y" OR Q$ = "y" THEN
   INPUT "MONTH,DAY,YEAR"; MON, DY, YR
   INPUT "HOUR,MINUTE,SECOND"; HR, MN, SC
END IF
C$ = "[DT," + STR$(YR) + "," + STR$(MON) + "," + STR$(DY) + ","
```

```
        C$ = C$ + STR$(HR) + "," + STR$(MN) + "," + STR$(SC) + "]"
        IF Q$ = "Y" OR Q$ = "y" THEN
           PRINT "Outlet ACS: now sending ... "; C$
           CALL DPRINT(2, C$): INPUT #2, JK$
        END IF
        PRINT "Inlet ACS: now sending ... "; C$
        CALL DPRINT(1, C$): INPUT #1, JK$

END SUB
```

```
      subroutine lmdif1o(info,n,x)
      integer info,n
      real*8 x(10)
c
c     this subroutine returns the diagnostic message for lmdif1.for
c     then prints out the estimate for the variables
c
      write (*,*)
      if (info.eq.0) write (*,200)
      if (info.eq.1) write (*,201)
      if (info.eq.2) write (*,202)
      if (info.eq.3) then
         write (*,203)
         write (*,201)
         write (*,202)
      endif
      if (info.eq.4) write (*,204)
      if (info.eq.5) write (*,205)
      if (info.eq.6) write (*,206)
      if (info.eq.7) write (*,207)
      write(*,250) (i,x(i),i=1,n)
  200 format (' info= 0, improper input parameters',/)
  201 format (' info= 1, algorithm estimates that the relative error ',
     &       /,'          in the sum of squares is at most tol',/)
  202 format (' info= 2, algorithm estimates that the relative error ',
     &       /,'          between x and the solution is at most tol',/)
  203 format (' info= 3, conditions for info=1 and info=2 both hold',/)
  204 format (' info= 4, fvec is orthogonal to the columns of the',
     &       /,'          jacobian to machine precision',/)
  205 format (' info= 5, number of calls to fcn has reached or ',
     &       /,'          exceeded 200*(n+1)',/)
  206 format (' info= 6, tol is too small. no further reduction in ',
     &       /,'          the sum of squares is possible',/)
  207 format (' info= 7, tol is too small. no further improvement in ',
     &       /,'          the approximate solution x is possible',/)
  250 format ((' x(',I2,')= ',G15.6,/))
      return
      end
```

```
c               mod2est.for     10-19-94
c
c       This program plots the normalized data versus the Reynolds number
c       and then the sublayer thickness. It is assumed that the data has been
c       normalized and is in the standard parameter estimation format:
c
c               number of data sets
c               schmidt number
c               debye length (L)
c               oil conductivity (NOT normalized)
c               relative pressboard conductivity (-1.0 if metal)
c               for each data set:
c                       number of data flow rates
c               for each flow rate:
c                       Reyn. No.   rho/L   v^{oc}L   I^{sc}L   D_v rho/L^2
c
c       This program also does up to a six parameter estimation of
c       electrification data from the CF.  It is assumed that the
c       short-circuit and open-circuit charge densities are
c       essentially the same.  First the open-circuit data is used
c       to determine the best representation (case) for each interface.
c       Then the short-circuit data is used to get the remainder of the
c       parameters.  For the simple cases, an Arrhenius temperature
c       dependence is assumed and activation energies are calculated.
c
c       In this program, the interfacial parameter information is stored in
c       the array u(i,j,k), with
c                       k = data set number
c                       j = interface number
c                                       case number
c                                1              2              3
c                           1   rho^w          xi * K^e       xi
c                       i = 2   1/(k * L)      K^r - 1 + tau  K^e
c                           3    ---           ---            (K^r-1+tau)/K^e
c       with the case number stored in ichoic(j,k)
c
      program mod2est
      implicit real*8 (a-h,q-z)
      implicit integer (i-p)
      character*10 fname,oname
      real*8 u(9,9,9)
      real*8 dl(9),ds(9,99),r(9,99),ch(9,99),voc(9,99),sci(9,99),sc(9)
      real*8 drdv(9,99),dsig1(9),cond2(9)
      integer nd(99)
      integer it,mt,ichoic(9,9),mvec(99)
      common /data/nt,nd,ds,r,ch,voc,sci,drdv,sc,dl,dsig1,cond2
      common /outp/fname,oname
      common /param/r1,a,ea,tol,u,dmin,dmax,eps1,ntype
      common /testt/it,mt,ichoic,mvec,chi2
      external fcncf,fp1m,fp2m,fp3m,fp4m,rocc,vocc,scic,gam1,drdvc
c
c       read in the plot file name and system constants
c
```

```
      call inpar
c
c     read in the electrification data
c
      call gdata
c
c     calculate the sublayer thicknesses
c
      call subthick
c
c     parameter estimate the boundary condition parameters
c
      call estpar
c
c     calculate the output information and send it to the plot file
c
      call outpl
c
c     end the program
c
      print*, 'Program complete'
      STOP
      END

      SUBROUTINE inpar
      implicit real*8 (a-h,p-z)
      real*8 u(9,9,9)
      character*10 fname,oname
      common /param/r1,a,ea,tol,u,dmin,dmax,eps1,ntype
      common /outp/fname,oname
      print*, 'What is the input (data) filename?  '
      read (*,99) fname
      ia = index(fname,' ') - 1
      if (ia.LT.0) ia = 9
      oname = fname(:ia)//'.r'
 99   format (a9)
c
c     Enter (assumed) known system constants
c
      print*, 'What are the relative cylinder radii (inner,solid)? '
      read (*,*) r1,a
      print*, 'What is the relative roughness height? '
      read (*,*) ea
      print*, 'What is the tolerance for the calculation? '
      read (*,*) tol
c
c     Enter initial guesses for unknown parameters
c
      print*, 'Enter initial guess for rho^w_1 / Xi_1: '
      read (*,*) u(1,1,1)
      print*, 'Enter initial guess for k_1 lamda_D / K^e_1: '
      read (*,*) u(2,1,1)
      print*, 'Enter initial guess for (K^r_1+t1-1)/K^e_1: '
```

```
      read (*,*) u(3,1,1)
      print*, 'Enter initial guess for rho^w_2 / Xi_2: '
      read (*,*) u(1,2,1)
      print*, 'Enter initial guess for k_2 lambda_D/ K^e_2: '
      read (*,*) u(2,2,1)
      print*, 'Enter initial guess for (K^r_2-1)/K^e_2: '
      read (*,*) u(3,2,1)
   61 print*, 'Enter the type of estimation: '
      print*, ' 1: A-S model only '
      print*, ' 2: general model'
      print*, ' 3: A-S model with mobility normalizations'
      print*, ' 4: general model with mobility normalizations'
      print*, ' 5: A-S model, no rate estimations'
      print*, ' 6: A-S model, p3 and p4 used for estimations'
      read (*,*) ntype
      if (ntype.LT.1 .or. ntype.GT.6) goto 61
      RETURN
      END

      SUBROUTINE gdata
      implicit real*8 (a-h,q-z)
      implicit integer (i-p)
      character*10 fname,oname
      real*8 u(9,9,9)
      real*8 dl(9),ds(9,99),r(9,99),ch(9,99),voc(9,99),sci(9,99),sc(9)
      real*8 drdv(9,99),dsig1(9),cond2(9)
      integer nd(99)
      integer it,mt,ichoic(9,9),mvec(99)
      common /param/r1,a,ea,tol,u,dmin,dmax,eps1,ntype
      common /data/nt,nd,ds,r,ch,voc,sci,drdv,sc,dl,dsig1,cond2
      common /outp/fname,oname
      common /testt/it,mt,ichoic,mvec,chi2
c
c     set min and max for numerical work
c
      dmin = dsqrt(tol)
      dmax = 1.0/dmin
c
c     set the ratio of pressboard to oil permittivity
c
      eps1= 1.6
c
c     read in the number of temperatures
c             then the Schmidt number, normalized Debye length,
c             oil conductivity, relative pressboard conductivity
c             (-1.0 for bare metal),
c             and the number of data points, for each temperature
c
      open (unit=5, file=fname)
      read (5,*) nt
      do 50 i=1,nt
        do 45 k1=1,9
          ichoic(k1,i)=1
```

```
          do 45 k2=1,2
45          u(k1,k2,i)=u(k1,k2,1)
        read (5,*) sc(i),dl(i),cond2(i),dsig1(i),nd(i)
        do 50 j=1,nd(i)
          read (5,*) r(i,j),ch(i,j),voc(i,j),sci(i,j),drdv(i,j)
50    continue
      close (unit=5)
      if (ntype.EQ.3 .or. ntype.EQ.4) then
        do 63 i=1,nt
          if (sc(i).GT.950000.) then
            temp=1.0D-12
          elseif (sc(i).GT.200000.) then
            temp=2.2D-12
          elseif (sc(i).GT.70000.) then
            temp=4.2D-12
          elseif (sc(i).GT.20000.) then
            temp=9.5D-12
          endif
          do 63 j=1,nd(i)
            ch(i,j)=ch(i,j)/(temp/cond2(i))
            drdv(i,j)=drdv(i,j)/(temp/cond2(i))
63      continue
      endif
      RETURN
      END

      SUBROUTINE subthick
      implicit real*8 (a-h,q-z)
      implicit integer (i-p)
      real*8 u(9,9,9)
      real*8 dl(9),ds(9,99),r(9,99),ch(9,99),voc(9,99),sci(9,99),sc(9)
      real*8 drdv(9,99),dsig1(9),cond2(9)
      integer nd(99)
      common /data/nt,nd,ds,r,ch,voc,sci,drdv,sc,dl,dsig1,cond2
      common /param/r1,a,ea,tol,u,dmin,dmax,eps1,ntype
      do 50 i=1,nt
        do 50 j=1,nd(i)
          x1=2.516D0*r(i,j)**0.15
          do while ((fcncf(x1,r(i,j),ea)-x1).GT.tol)
            slop=-1.-8.14/(dlog(10.D0)*(0.215*ea*r(i,j)+2.*x1))
            x1=x1-(fcncf(x1,r(i,j),ea)-x1)/slop
          end do
          ds(i,j)=3.3*(x1**2)/(dl(i)*sc(i)**0.356*r(i,j))
50    continue
      RETURN
      END

      real*8 function fcncf(x,ry,ea)
      real*8 x,ry,ea
      fcncf=-0.6-4.07*dlog10(0.215*ea+2.*x/ry)
      end

      SUBROUTINE estpar
```

```
      implicit real*8 (a-h,q-z)
      implicit integer (i-p)
      integer iwa(10),infoa(9)
      real*8 fvec(500),x(10),wa(5550),ut(9),ct(9)
      real*8 u(9,9,9)
      real*8 dl(9),ds(9,99),r(9,99),ch(9,99),voc(9,99),sci(9,99),sc(9)
      real*8 drdv(9,99),dsig1(9),cond2(9)
      integer nd(99)
      integer it,mt,ichoic(9,9),mvec(99)
      common /data/nt,nd,ds,r,ch,voc,sci,drdv,sc,dl,dsig1,cond2
      common /param/r1,a,ea,tol,u,dmin,dmax,eps1,ntype
      common /testt/it,mt,ichoic,mvec,chi2
      external fp1,fp2,fp3,fp4,fpi,fae
c
c     perform estimation for each data set
c
      print*, 'ESTIMATION TYPE: ',ntype
      do 400 i=1,nt
        print*, 'data set: ',i
        it=i
        m=0
        do 311 j=1,nd(i)
          if (dabs(ch(i,j)).GT.dmin.AND.dabs(voc(i,j)).GT.dmin) then
            m=m+1
            mvec(m)=j
          endif
311     continue
        if (m.GT.0) then
          do 314 ki=1,2
            do 312 jm=1,3
              mt=jm
              x(1)=u(1,ki,i)
              if (jm.LT.3) then
                n=1
              else
                n=2
                x(2)=u(2,ki,i)
              endif
              lwa = m*n+5*n+m
              if (ki.EQ.1) then
                call lmdif1(fp1,m,n,x,fvec,tol,info,iwa,wa,lwa)
              else
                call lmdif1(fp2,m,n,x,fvec,tol,info,iwa,wa,lwa)
              endif
              ut(jm)=x(1)
              ct(jm)=chi2
              infoa(jm)=info
312         continue
            if (ntype.EQ.1 .or. ntype.EQ.3 .or. ntype.EQ.5 .or.
     &          ntype.EQ.6) then
              ichoic(ki,i)=1
            else
              ichoic(ki,i)=3
```

```
              if (((ct(1)-ct(2)).LT.dmin).and.((ct(1)-ct(3)).LT.dmin))
     &          ichoic(ki,i)=1
              if (((ct(2)-ct(1)).LT.dmin).and.((ct(2)-ct(3)).LT.dmin))
     &          ichoic(ki,i)=2
             endif
             jm=ichoic(ki,i)
             u(1,ki,i)=ut(jm)
             if (ichoic(ki,i).EQ.3) then
               u(2,ki,i)=x(2)
               write (*,401) jm,infoa(jm),u(1,ki,i),u(2,ki,i),ct(jm)
             else
               write (*,401) jm,infoa(jm),u(1,ki,i),ct(jm)
             endif
  314      continue
           else
             write (*,*) 'no p1 and p2 estimate ...'
             u(1,1,i)=0.D0
             u(1,2,i)=0.D0
           endif
c
c       finally, estimate on the last two parameters
c
c       The ichoic parameter determined from the oc case is used
c
           m=0
           if (ntype.EQ.5) then
             do 281 j=1,nd(i)
               if (dabs(sci(i,j)).GT.dmin) then
                 m=m+1
                 mvec(m)=j
               endif
  281        continue
             if (m.GT.0) then
               n=2
               lwa = m*n+5*n+m
               do 284 ki=1,2
                 ichoic(ki+2,i)=ichoic(ki,i)
                 if (ichoic(ki,i).LT.3) then
                   x(ki)=u(2,ki,i)
                 else
                   x(ki)=u(3,ki,i)
                 endif
  284          continue
               call lmdif1(fpi,m,n,x,fvec,tol,info,iwa,wa,lwa)
               do 294 ki=1,2
               if (ichoic(ki,i).LT.2) then
                 if (x(ki).GT.0.D0) then
                   u(2,ki,i)=x(ki)
                 else
                   u(2,ki,i)=0.D0
                 endif
                 x(ki)=u(2,ki,i)
               else
```

```
            if ((ki.EQ.1).AND.(dsig1(i).GT.0.D0)) then
              t1=eps1/dsig1(i)-1.D0
            else
              t1=-1.D0
            endif
            if (ichoic(ki,i).LT.3) then
              if (x(ki).GT.t1) then
                u(2,ki,i)=x(ki)
              else
                u(2,ki,i)=t1
              endif
              x(ki)=u(2,ki,i)
            else
              if ((u(2,ki,i)*x(ki)).GT.t1) then
                u(3,ki,i)=x(ki)
              else
                u(3,ki,i)=t1/u(2,ki,i)
              endif
              x(ki)=u(3,ki,i)
            endif
          endif
294         continue
            write(*,401) 0,info,x(1),x(2),chi2
        endif
      else
        do 321 j=1,nd(i)
          if (dabs(sci(i,j)).GT.dmin.AND.dabs(voc(i,j)).GT.dmin
     &      .AND.dabs(drdv(i,j)).GT.dmin) then
            m=m+1
            mvec(m)=j
         endif
321     continue
        if (m.GT.0) then
          do 324 ki=1,2
            ichoic(ki+2,i)=ichoic(ki,i)
            n=1
            if (ichoic(ki,i).LT.3) then
              x(1)=u(2,ki,i)
            else
              x(1)=u(3,ki,i)
            endif
            lwa = m*n+5*n+m
            if (ki.EQ.1) then
              call lmdif1(fp3,m,n,x,fvec,tol,info,iwa,wa,lwa)
              if (ichoic(1,i).LT.2) then
                if (x(1).LT.0.D0) x(1)=0.D0
              else
                if (dsig1(i).GT.0.D0) then
                  t1=eps1/dsig1(i)
                else
                  t1=0.D0
                endif
                if (ichoic(3,i).LT.3) then
```

```
                    if (x(1).LT.(t1-1.D0)) x(1)=t1-1.D0
                  else
                    if ((u(2,1,i)*x(1)).LT.(t1-1.D0)) x(1)=(t1-1.D0)/u(2,1,i)
                  endif
                endif
              else
                call lmdif1(fp4,m,n,x,fvec,tol,info,iwa,wa,lwa)
                if (ichoic(2,i).LT.2) then
                  if (x(1).LT.0.D0) x(1)=0.D0
                else if (ichoic(2,i).LT.3) then
                  if (x(1).LT.(-1.D0)) x(1)=-1.D0
                else
                  if (x(1).LT.(-1.D0/u(2,2,i))) x(1)=-1.D0/u(2,2,i)
                endif
              endif
              if (ichoic(ki,i).LT.3) then
                u(2,ki,i)=x(1)
              else
                u(3,ki,i)=x(1)
              endif
  324         write(*,401) ichoic(ki,i),info,x(1),chi2
            endif
          endif
          if (m.EQ.0) then
            write (*,*) 'no p3 and p4 estimate ...'
            do 326 ki=1,2
              if (ichoic(ki,i).LT.3) then
                u(2,ki,i)=0.D0
              else
                u(3,ki,i)=0.D0
              endif
  326       continue
          endif
          call outpr(i)
  400   continue
c
c       estimate activation energies for the simple parameter fits
c
        if (ntype.EQ.1.or.ntype.EQ.5.or.ntype.EQ.6) then
          write(*,*) 'Interface ',' Amplitude ',' Activation Energy (eV)'
          do 510 ki=1,2
            m=nt
            it=ki
            n=2
            lwa = m*n+5*n+m
            x(1)=1.0D2
            x(2)=0.3D0
            do 505 i=1,nt
              if (sc(i).GT.950000.) then
                u(9,ki,i)=15.D0
              elseif (sc(i).GT.200000.) then
                u(9,ki,i)=35.D0
              elseif (sc(i).GT.70000.) then
```

```
              u(9,ki,i)=50.D0
            else
              u(9,ki,i)=70.D0
            endif
            u(9,ki,i)=8.6167D-5 * (u(9,ki,i)+273.15D0)
            print*, -1.D0/u(9,ki,i), dlog(u(8,ki,i))
505         continue
          call lmdif1(fae,m,n,x,fvec,tol,info,iwa,wa,lwa)
          write(*,401) ki,info,x(1),x(2)
510     continue
      endif
401   format (' Choice: ',I2,' Info: ',I2,' ... ',3G10.3)
      RETURN
      END

      SUBROUTINE outp1
      implicit real*8 (a-h,q-z)
      implicit integer (i-p)
      character*10 fname,oname,symb,lcolor
      real*8 dp(9),u(9,9,9)
      real*8 dl(9),ds(9,99),r(9,99),ch(9,99),voc(9,99),sci(9,99),sc(9)
      real*8 drdv(9,99),dsig1(9),cond2(9)
      integer nd(99)
      common /data/nt,nd,ds,r,ch,voc,sci,drdv,sc,dl,dsig1,cond2
      common /outp/fname,oname
      common /param/r1,a,ea,tol,u,dmin,dmax,eps1,ntype
c
c     start the output file
c
      print*, 'Creating plot file ...'
      open (unit=6, file=oname)
        write(6,210) oname
c
c     print out normalized information in plot form
c     versus Reynolds number first
c
        write(6,213) 'bottom',-0.4,'right',0.2
        write(6,218) -0.3,'\circle: 15^oC'
        write(6,218) -0.5,'\square: 35^oC'
        write(6,218) -0.7,'\triangle: 50^oC'
        write(6,218) -0.9,'\star: 70^oC'
        write(6,212) 'left','\rho_o/\lambda_D'
        write(6,215) 'w','log scale 1000. 1000000. suppress ticks 3'
        write(6,215) 'x','scale 3. 6. suppress ticks 3'
        do 165 i=1,nt
          call symcol(sc(i),symb,lcolor)
          write(6,221) symb,'use w'
          do 163 j=1,nd(i)
            if (dabs(ch(i,j)).GT.dmin) then
              write(6,222) r(i,j),ch(i,j)
            endif
163       continue
          write(6,220) lcolor,'use w'
```

```
            do 164 j=1,nd(i)
              call getdp(i,ds(i,j),dp)
  164         write(6,222) r(i,j),rocc(a,dp)
  165       continue
c
            write(6,213) 'top',0.7,'bottom',0.15,'right',0.2
            write(6,212) 'left','v^{oc} \lambda_D'
            write(6,215) 'w','log scale 1000. 1000000. suppress ticks 3'
            write(6,215) 'x','scale 3. 6. suppress ticks 3'
            do 185 i=1,nt
              call symcol(sc(i),symb,lcolor)
              write(6,221) symb,'use w'
              do 182 j=1,nd(i)
                if (dabs(voc(i,j)).GT.dmin) then
                  write(6,222) r(i,j),voc(i,j)
                endif
  182         continue
              write(6,220) lcolor,'use w'
              do 184 j=1,nd(i)
                call getdp(i,ds(i,j),dp)
  184           write(6,222) r(i,j),vocc(a,dp)
  185       continue
c
            write(6,213) 'top',0.15,'bottom',0.7,'right',0.2
            write(6,212) 'left','I^{sc} \lambda_D'
            write(6,215) 'w','log scale 1000. 1000000. suppress ticks 3'
            write(6,215) 'x','scale 3. 6. suppress ticks 3'
            do 195 i=1,nt
              call symcol(sc(i),symb,lcolor)
              write(6,221) symb,'use w'
              do 192 j=1,nd(i)
                if (dabs(sci(i,j)).GT.dmin) then
                  write(6,222) r(i,j),sci(i,j)
                endif
  192         continue
              write(6,220) lcolor,'use w'
              do 194 j=1,nd(i)
                call getdp(i,ds(i,j),dp)
  194           write(6,222) r(i,j),scic(r1,a,dp,dsig1(i))
  195       continue
c
            write(6,213) 'top',-0.4,'right',0.2
            write(6,212) 'left','D_v \rho_o / \lambda_D^2'
            write(6,212) 'bottom','log_{10} R_e'
            write(6,215) 'w','log scale 1000. 1000000. suppress ticks 3'
            write(6,215) 'x','scale 3. 6. ticks 3'
            do 175 i=1,nt
              call symcol(sc(i),symb,lcolor)
              write(6,221) symb,'use w'
              do 172 j=1,nd(i)
                if (dabs(drdv(i,j)).GT.dmin) then
                  write(6,222) r(i,j),drdv(i,j)
                endif
```

```
 172       continue
           write(6,220) lcolor,'use w'
           do 174 j=1,nd(i)
             call getdp(i,ds(i,j),dp)
 174         write(6,222) r(i,j),drdvc(r1,a,dp,dsig1(i))
 175     continue
c
c       now print out vs sublayer thickness
c
         write(6,213) 'bottom',-0.4,'left',0.2
         write(6,215) 'y','suppress'
         write(6,215) 'x','suppress'
         do 365 i=1,nt
           call symcol(sc(i),symb,lcolor)
           write(6,221) symb,' '
           do 363 j=1,nd(i)
             if (dabs(ch(i,j)).GT.dmin) then
               write(6,222) ds(i,j),ch(i,j)
             endif
 363       continue
           write(6,220) lcolor,' '
           do 364 j=1,nd(i)
             call getdp(i,ds(i,j),dp)
 364         write(6,222) ds(i,j),rocc(a,dp)
 365     continue
c
         write(6,213) 'top',0.7,'bottom',0.15,'left',0.2
         write(6,215) 'y','suppress'
         write(6,215) 'x','suppress'
         do 385 i=1,nt
           call symcol(sc(i),symb,lcolor)
           write(6,221) symb,' '
           do 382 j=1,nd(i)
             if (dabs(voc(i,j)).GT.dmin) then
               write(6,222) ds(i,j),voc(i,j)
             endif
 382       continue
           write(6,220) lcolor,' '
           do 384 j=1,nd(i)
             call getdp(i,ds(i,j),dp)
 384         write(6,222) ds(i,j),vocc(a,dp)
 385     continue
c
         write(6,213) 'top',0.15,'bottom',0.7,'left',0.2
         write(6,215) 'y','suppress'
         write(6,215) 'x','suppress'
         do 395 i=1,nt
           call symcol(sc(i),symb,lcolor)
           write(6,221) symb,' '
           do 392 j=1,nd(i)
             if (dabs(sci(i,j)).GT.dmin) then
               write(6,222) ds(i,j),sci(i,j)
             endif
```

```
  392       continue
            write(6,220) lcolor,' '
            do 393 j=1,nd(i)
              call getdp(i,ds(i,j),dp)
  393         write(6,222) ds(i,j),scic(r1,a,dp,dsig1(i))
  395     continue
c
          write(6,213) 'top',-0.4,'left',0.2
          write(6,212) 'bottom','\delta/\lambda_D'
          write(6,215) 'y','suppress'
          write(6,215) 'x'
          do 375 i=1,nt
            call symcol(sc(i),symb,lcolor)
            write(6,221) symb,' '
            do 372 j=1,nd(i)
              if (dabs(drdv(i,j)).GT.dmin) then
                write(6,222) ds(i,j),drdv(i,j)
              endif
  372       continue
            write(6,220) lcolor,' '
            do 374 j=1,nd(i)
              call getdp(i,ds(i,j),dp)
  374         write(6,222) ds(i,j),drdvc(r1,a,dp,dsig1(i))
  375     continue
c
c       now create another output page with diagnostic information
c       such as the fits to the actual parameters p1 ... p4
c
          write(6,*) 'page'
          write(6,213) 'bottom',-0.4,'right',0.2
          write(6,212) 'left','P_1'
          write(6,215) 'x','suppress '
          do 565 i=1,nt
            call symcol(sc(i),symb,lcolor)
            write(6,221) symb,' '
            do 563 j=1,nd(i)
              if (dabs(ch(i,j)).GT.dmin.AND.dabs(voc(i,j)).GT.dmin) then
                write(6,222) ds(i,j),fp1m(a,voc(i,j),ch(i,j))
              endif
  563       continue
            write(6,220) lcolor,' '
            do 564 j=1,nd(i)
              call getdp(i,ds(i,j),dp)
  564         write(6,222) ds(i,j),dp(1)
  565     continue
c
          write(6,213) 'top',0.7,'bottom',0.15,'right',0.2
          write(6,212) 'left','P_2'
          write(6,215) 'x','suppress'
          do 585 i=1,nt
            call symcol(sc(i),symb,lcolor)
            write(6,221) symb,' '
            do 582 j=1,nd(i)
```

```
            if (dabs(ch(i,j)).GT.dmin.AND.dabs(voc(i,j)).GT.dmin) then
              write(6,222) ds(i,j),fp2m(a,voc(i,j),ch(i,j))
            endif
  582       continue
            write(6,220) lcolor,' '
            do 584 j=1,nd(i)
              call getdp(i,ds(i,j),dp)
  584         write(6,222) ds(i,j),dp(2)
  585     continue
c
          write(6,213) 'top',0.15,'bottom',0.7,'right',0.2
          write(6,212) 'left','P_3'
          write(6,215) 'x','suppress'
          do 595 i=1,nt
            call symcol(sc(i),symb,lcolor)
            write(6,221) symb,' '
            do 592 j=1,nd(i)
              if (dabs(sci(i,j)).GT.dmin.AND.dabs(voc(i,j)).GT.dmin
     &          .AND.dabs(drdv(i,j)).GT.dmin) then
                uc= fp3m(a,voc(i,j),sci(i,j),drdv(i,j),r1,dsig1(i))
                write(6,222) ds(i,j),uc
              endif
  592       continue
            write(6,220) lcolor,' '
            do 594 j=1,nd(i)
              call getdp(i,ds(i,j),dp)
  594         write(6,222) ds(i,j),dp(3)
  595     continue
c
          write(6,213) 'top',-0.4,'right',0.2
          write(6,212) 'left','P_4'
          write(6,212) 'bottom','\delta / \lambda_D'
          write(6,215) 'x',' '
          do 575 i=1,nt
            call symcol(sc(i),symb,lcolor)
            write(6,221) symb,' '
            do 572 j=1,nd(i)
              if (dabs(sci(i,j)).GT.dmin.AND.dabs(voc(i,j)).GT.dmin
     &          .AND.dabs(drdv(i,j)).GT.dmin) then
                uc= fp4m(a,voc(i,j),sci(i,j),drdv(i,j),r1,dsig1(i))
                write(6,222) ds(i,j),uc
              endif
  572       continue
            write(6,220) lcolor,' '
            do 574 j=1,nd(i)
              call getdp(i,ds(i,j),dp)
  574         write(6,222) ds(i,j),dp(4)
  575     continue
c
          write(6,213) 'bottom',-0.4,'left',0.2
          write(6,212) 'right','\gamma_1'
          write(6,215) 'x','suppress'
          do 655 i=1,nt
```

```
            call symcol(sc(i),symb,lcolor)
            write(6,221) symb,'use z '
            do 652 j=1,nd(i)
              if (dabs(sci(i,j)).GT.dmin.AND.dabs(voc(i,j)).GT.dmin) then
                uc= 2.D0*voc(i,j)/sci(i,j)
                write(6,222) ds(i,j),uc
              endif
  652       continue
            write(6,220) lcolor,'use z '
            do 654 j=1,nd(i)
              call getdp(i,ds(i,j),dp)
  654         write(6,222) ds(i,j),gam1(r1,a,dp,dsig1(i))
  655     continue
c
c       all done so close up the file
c
        close (unit=6)
  210   format (' device color format \ ',/,
     &       '  "CheckPath [ %d dup 1 le { pop } { dup mul dup ',/,
     &       '  dup 16 gt {2 div dup dup} if } ifelse ] 0 setdash\n"',/,
     &       ' window',/,' frame suppress',/,
     &       ' text over 0.05 right 0.1 size 0.07 "file: ',A,'"',/)
  212   format (' label ',A,' "',A,'"')
  213   format (' window vertical 1/4 horizontal 1/2',/,
     &          ' margin ',4(A,F6.3,' '))
  215   format (' ',A,' axis ',A)
  218   format (' text over ',F6.3,' left .2 size .1 "',A,'"')
  220   format (' plot ',A,' spline ',A)
  221   format (' plot ',A,' marker 0.07 ',A)
  222   format (2G15.6)
        RETURN
        END

        SUBROUTINE symcol(sch,symb,lcolor)
        character*10 symb,lcolor
        real*8 sch
        if (sch.GT.950000.) then
          symb='circles'
          lcolor='red'
        elseif (sch.GT.200000.) then
          symb='triangles'
          lcolor='green'
        elseif (sch.GT.70000.) then
          symb='squares'
          lcolor='blue'
        elseif (sch.GT.20000.) then
          symb='stars'
          lcolor=' '
        else
          symb='dots'
          lcolor='yellow'
        endif
        end
```

```
      real*8 function fp1m(ae,ve,ce)
      real*8 ae,ve,ce
        fp1m=ve/dlog(ae)-0.5D0*(ae**2+(1.D0-ae**2)/(2.D0*dlog(ae)))*ce
      end

      real*8 function fp2m(ae,ve,ce)
      real*8 ae,ve,ce
        fp2m=-ve/dlog(ae)+0.5D0*(1.D0+(1.D0-ae**2)/(2.D0*dlog(ae)))*ce
      end

      real*8 function fp3m(ae,ve,sce,de,r1e,ds1)
      real*8 ae,ve,sce,de,r1e,ds1
        fp3m=-1.D0+(ve/sce)*(ae**2*de+(-2.D0+
     &       de*(1.D0-ae**2)/2.D0)/dlog(ae))
        if (ds1.GT.0.D0) fp3m = fp3m + dlog(ae/r1e)/(ds1*dlog(ae))
      end

      real*8 function fp4m(ae,ve,sce,de,r1e,ds1)
      real*8 ae,ve,sce,de,r1e,ds1
        fp4m=-1.D0+(ve/sce)*(de+(-2.D0+
     &       de*(1.D0-ae**2)/2.D0)/dlog(ae))
        if (ds1.GT.0.D0) fp4m = fp4m + dlog(ae/r1e)/(ds1*dlog(ae))
      end

      real*8 function vocc(ae,dp)
      real*8 ae,dp(9)
        vocc=dp(1)*(0.5D0+dlog(ae)/(1.D0-ae**2))
     &       +dp(2)*(0.5D0+ae**2*dlog(ae)/(1.D0-ae**2))
      end

      real*8 function rocc(ae,dp)
      real*8 ae,dp(9)
        rocc=2.D0*(dp(1)+dp(2))/(1.D0-ae**2)
      end

      real*8 function gam1(r1e,ae,dp,ds1)
      real*8 ae,dp(9),ds1,r1e
        gam1=-dlog(ae)-dp(3)*(0.5D0+dlog(ae)/(1.D0-ae**2))
     &       +dp(4)*(0.5D0+ae**2*dlog(ae)/(1.D0-ae**2))
        if (ds1.GT.0.D0) gam1 = gam1 + dlog(ae/r1e)/ds1
      end

      real*8 function drdvc(r1e,ae,dp,ds1)
      implicit real*8 (a-h,q-z)
      real*8 ae,dp(9),ds1,r1e
        drdvc=2.D0*(dp(4)-dp(3))/(gam1(r1e,ae,dp,ds1)*(1.D0-ae**2))
      end

      real*8 function scic(r1e,ae,dp,ds1)
      implicit real*8 (a-h,q-z)
      real*8 ae,dp(9),ds1,r1e
        scic=2.D0*vocc(ae,dp)/gam1(r1e,ae,dp,ds1)
```

```
      end

      SUBROUTINE getdp(k,ad,dp)
      implicit real*8 (a-h,q-z)
      implicit integer (i-p)
      real*8 dp(9),u(9,9,9)
      real*8 dl(9),ds(9,99),r(9,99),ch(9,99),voc(9,99),sci(9,99),sc(9)
      real*8 drdv(9,99),dsig1(9),cond2(9)
      integer nd(99)
      integer it,mt,ichoic(9,9),mvec(99)
      common /data/nt,nd,ds,r,ch,voc,sci,drdv,sc,dl,dsig1,cond2
      common /param/r1,a,ea,tol,u,dmin,dmax,eps1,ntype
      common /testt/it,mt,ichoic,mvec,chi2
      if (ichoic(1,k).EQ.1) then
        dp(1)=a*u(1,1,k)/dsinh(a*ad)
      elseif (ichoic(1,k).EQ.2) then
        dp(1)=a*u(1,1,k)/dcosh(a*ad)
      else
        dp(1)=a*u(1,1,k)/(dsinh(a*ad)+dcosh(a*ad)/u(2,1,k))
      endif
      if (ichoic(2,k).EQ.1) then
        dp(2)=u(1,2,k)/dsinh(ad)
      elseif (ichoic(2,k).EQ.2) then
        dp(2)=u(1,2,k)/dcosh(ad)
      else
        dp(2)=u(1,2,k)/(dsinh(ad)+dcosh(ad)/u(2,2,k))
      endif
      if (ichoic(3,k).EQ.1) then
        dp(3)=u(2,1,k)/dsinh(a*ad)
      elseif (ichoic(3,k).EQ.2) then
        dp(3)=u(2,1,k)/dcosh(a*ad)
      else
        dp(3)=u(3,1,k)/(dsinh(a*ad)+dcosh(a*ad)/u(2,1,k))
      endif
      if (ichoic(4,k).EQ.1) then
        dp(4)=u(2,2,k)/dsinh(ad)
      elseif (ichoic(4,k).EQ.2) then
        dp(4)=u(2,2,k)/dcosh(ad)
      else
        dp(4)=u(3,2,k)/(dsinh(ad)+dcosh(ad)/u(2,2,k))
      endif
      end

      subroutine fp1(m,n,x,fvec,iflag)
      implicit real*8 (a-h,q-z)
      implicit integer (i-p)
      real*8 x(n),fvec(m),u(9,9,9)
      real*8 dl(9),ds(9,99),r(9,99),ch(9,99),voc(9,99),sci(9,99),sc(9)
      real*8 drdv(9,99),dsig1(9),cond2(9)
      integer nd(99),it,mt,ichoic(9,9),mvec(99)
      common /data/nt,nd,ds,r,ch,voc,sci,drdv,sc,dl,dsig1,cond2
      common /param/r1,a,ea,tol,u,dmin,dmax,eps1,ntype
      common /testt/it,mt,ichoic,mvec,chi2
```

```
      chi2=0.D0
      do 900 j=1,m
        um=fp1m(a,voc(it,mvec(j)),ch(it,mvec(j)))
        ad= ds(it,mvec(j))
        if (mt.EQ.1) then
          uc= a*x(1)/dsinh(a*ad)
        elseif (mt.EQ.2) then
          uc= a*x(1)/dcosh(a*ad)
        else
          uc= a*x(1)/(dsinh(a*ad)+dcosh(a*ad)/x(2))
        endif
        fvec(j)=um-uc
        chi2=chi2+(fvec(j)/uc)**2
900   continue
      return
      end

      subroutine fp2(m,n,x,fvec,iflag)
      implicit real*8 (a-h,q-z)
      implicit integer (i-p)
      real*8 x(n),fvec(m),u(9,9,9)
      real*8 dl(9),ds(9,99),r(9,99),ch(9,99),voc(9,99),sci(9,99),sc(9)
      real*8 drdv(9,99),dsig1(9),cond2(9)
      integer nd(99),it,mt,ichoic(9,9),mvec(99)
      common /data/nt,nd,ds,r,ch,voc,sci,drdv,sc,dl,dsig1,cond2
      common /param/r1,a,ea,tol,u,dmin,dmax,eps1,ntype
      common /testt/it,mt,ichoic,mvec,chi2
      chi2=0.D0
      do 900 j=1,m
        um=fp2m(a,voc(it,mvec(j)),ch(it,mvec(j)))
        ad=ds(it,mvec(j))
        if (mt.EQ.1) then
          uc= x(1)/dsinh(ad)
        elseif (mt.EQ.2) then
          uc= x(1)/dcosh(ad)
        else
          uc= x(1)/(dsinh(ad)+dcosh(ad)/x(2))
        endif
        fvec(j)=um-uc
        chi2=chi2+(fvec(j)/uc)**2
900   continue
      return
      end

      subroutine fp3(m,n,x,fvec,iflag)
      implicit real*8 (a-h,q-z)
      implicit integer (i-p)
      real*8 x(n),fvec(m),u(9,9,9)
      real*8 dl(9),ds(9,99),r(9,99),ch(9,99),voc(9,99),sci(9,99),sc(9)
      real*8 drdv(9,99),dsig1(9),cond2(9)
      integer nd(99),it,mt,ichoic(9,9),mvec(99)
      common /data/nt,nd,ds,r,ch,voc,sci,drdv,sc,dl,dsig1,cond2
      common /param/r1,a,ea,tol,u,dmin,dmax,eps1,ntype
```

```
      common /testt/it,mt,ichoic,mvec,chi2
      chi2=0.D0
c
c     first check to ensure that the reaction rates are postive
c
      if (ichoic(3,it).LT.2) then
        if (x(1).LT.0.D0) x(1)=0.D0
      else
        if (dsig1(it).GT.0.D0) then
          t1=eps1/dsig1(it)
        else
          t1=0.D0
        endif
        if (ichoic(3,it).LT.3) then
          if (x(1).LT.(t1-1.D0)) x(1)=t1-1.D0
        else
          if ((u(2,1,it)*x(1)).LT.(t1-1.D0)) x(1)=(t1-1.D0)/u(2,1,it)
        endif
      endif
      do 900 j=1,m
        jd=mvec(j)
        um=fp3m(a,voc(it,jd),sci(it,jd),drdv(it,jd),r1,dsig1(it))
        ad=ds(it,jd)
        if (ichoic(3,it).EQ.1) then
          uc= x(1)/dsinh(a*ad)
        elseif (ichoic(3,it).EQ.2) then
          uc= x(1)/dcosh(a*ad)
        else
          uc= x(1)/(dsinh(a*ad)+dcosh(a*ad)/u(2,1,it))
        endif
        fvec(j)=um-uc
        if (dabs(x(1)).GT.dmin) chi2=chi2+(fvec(j)/uc)**2
  900 continue
      return
      end

      subroutine fp4(m,n,x,fvec,iflag)
      implicit real*8 (a-h,q-z)
      implicit integer (i-p)
      real*8 x(n),fvec(m),u(9,9,9)
      real*8 dl(9),ds(9,99),r(9,99),ch(9,99),voc(9,99),sci(9,99),sc(9)
      real*8 drdv(9,99),dsig1(9),cond2(9)
      integer nd(99),it,mt,ichoic(9,9),mvec(99)
      common /data/nt,nd,ds,r,ch,voc,sci,drdv,sc,dl,dsig1,cond2
      common /param/r1,a,ea,tol,u,dmin,dmax,eps1,ntype
      common /testt/it,mt,ichoic,mvec,chi2
      chi2=0.D0
      if (ichoic(4,it).LT.2) then
        if (x(1).LT.0.D0) x(1)=0.D0
      else if (ichoic(4,it).LT.3) then
        if (x(1).LT.(-1.D0)) x(1)=-1.D0
      else
        if (x(1).LT.(-1.D0/u(2,2,it))) x(1)=-1.D0/u(2,2,it)
```

```
      endif
      do 900 j=1,m
        jd=mvec(j)
        um=fp4m(a,voc(it,jd),sci(it,jd),drdv(it,jd),r1,dsig1(it))
        ad=ds(it,jd)
        if (ichoic(4,it).EQ.1) then
          uc= x(1)/dsinh(ad)
        elseif (ichoic(4,it).EQ.2) then
          uc= x(1)/dcosh(ad)
        else
          uc= x(1)/(dsinh(ad)+dcosh(ad)/u(2,2,it))
        endif
        fvec(j)=um-uc
        if (dabs(x(1)).GT.dmin) chi2=chi2+(fvec(j)/uc)**2
900   continue
      return
      end

      subroutine fpi(m,n,x,fvec,iflag)
      implicit real*8 (a-h,q-z)
      implicit integer (i-p)
      real*8 x(n),fvec(m),u(9,9,9),dp(9)
      real*8 dl(9),ds(9,99),r(9,99),ch(9,99),voc(9,99),sci(9,99),sc(9)
      real*8 drdv(9,99),dsig1(9),cond2(9)
      integer nd(99),it,mt,ichoic(9,9),mvec(99)
      common /data/nt,nd,ds,r,ch,voc,sci,drdv,sc,dl,dsig1,cond2
      common /param/r1,a,ea,tol,u,dmin,dmax,eps1,ntype
      common /testt/it,mt,ichoic,mvec,chi2
      chi2=0.D0
      do 344 ki=1,2
        if (ichoic(ki,it).LT.2) then
          if (x(ki).GT.0.D0) then
            u(2,ki,it)=x(ki)
          else
            u(2,ki,it)=0.D0
          endif
        else
          if ((ki.EQ.1).AND.(dsig1(it).GT.0.D0)) then
            t1=eps1/dsig1(it)-1.D0
          else
            t1=-1.D0
          endif
          if (ichoic(ki,it).LT.3) then
            if (x(ki).GT.t1) then
              u(2,ki,it)=x(ki)
            else
              u(2,ki,it)=t1
            endif
          else
            if ((u(2,ki,it)*x(ki)).GT.t1) then
              u(3,ki,it)=x(ki)
            else
              u(3,ki,it)=t1/u(2,ki,it)
```

```
            endif
          endif
        endif
  344   continue
        do 900 j=1,m
          call getdp(it,ds(it,j),dp)
          uc=scic(r1,a,dp,dsig1(it))
          fvec(j)=sci(it,j)-uc
          chi2=chi2+(fvec(j)/uc)**2
  900   continue
        return
        end

        SUBROUTINE outpr(i)
        implicit real*8 (a-h,q-z)
        implicit integer (i-p)
        real*8 u(9,9,9)
        real*8 dl(9),ds(9,99),r(9,99),ch(9,99),voc(9,99),sci(9,99),sc(9)
        real*8 drdv(9,99),dsig1(9),cond2(9)
        integer nd(99)
        integer it,mt,ichoic(9,9),mvec(99)
        common /data/nt,nd,ds,r,ch,voc,sci,drdv,sc,dl,dsig1,cond2
        common /param/r1,a,ea,tol,u,dmin,dmax,eps1,ntype
        common /testt/it,mt,ichoic,mvec,chi2
c
c       print out dimensional values
c
          er2=2.19*8.854D-12
          r2=0.1016D0
          bk=8.6167D-5
          vo=3.956D-10
          Ev=0.2725D0
          wc=2.D-11
          To=273.15D0
          rhom=886.D0
          if (sc(i).GT.950000.) then
            temp=15.D0+To
            tsig=1.0D-12
          else if (sc(i).GT.200000.) then
            temp=35.D0+To
            tsig=2.2D-12
          else if (sc(i).GT.70000.) then
            temp=50.D0+To
            tsig=4.2D-12
          else if (sc(i).GT.20000.) then
            temp=70.D0+To
            tsig=9.5D-12
          else
            stop
          endif
          v=vo*dexp(Ev/(bk*temp))
          b=wc/(rhom*v)
          if ((ntype.EQ.3) .or. (ntype.EQ.4)) b=b*cond2(i)/tsig
```

```
        D=b*bk*temp
        do 410 ki=1,2
          if (ichoic(ki,i).EQ.1) then
            u(8,ki,i)=u(1,ki,i)*cond2(i)/b
            print*, 'rho^w_',ki,' = ',u(8,ki,i)
            if (u(2,ki,i).GT.0.D0) then
              print*, 'k_',ki, ' = ',D/(r2*dl(i)*u(2,ki,i))
            endif
          else if (ichoic(ki,i).EQ.2) then
            print*, 'xi k^f / k^r at ',ki,' = ',
     &        u(1,ki,i)*cond2(i)*dl(i)*r2/b
            if (ki.EQ.1 .and. dsig1(i).GT.0.D0) then
              t1=eps1/dsig1(i)-1.D0
            else
              t1=-1.D0
            endif
            if ((u(2,ki,i)-t1).GT.dmin) then
              print*, 'K^r_',ki, ' = ',u(2,ki,i)-t1
              print*, '   k^r_',ki, ' = ',cond2(i)/((u(2,ki,i)-t1)*er2)
            endif
          else
            print*, 'xi_',ki,' = ', u(1,ki,i)*cond2(i)*r2/b
            print*, 'k^f / k^r at ',ki,' = ', dl(i)*r2*u(2,ki,i)
            if (ki.EQ.1 .and. dsig1(i).GT.0.D0) then
              t1=eps1/dsig1(i)-1.D0
            else
              t1=-1.D0
            endif
            dum = u(2,ki,i)*u(3,ki,i)
            if ((dum-t1).GT.dmin) then
              print*, 'K^r_',ki, ' = ',dum-t1
              print*, '   k^r_',ki, ' = ',cond2(i)/((dum-t1)*er2)
            endif
          endif
410     continue
        print*, ' '
      return
      end

      subroutine fae(m,n,x,fvec,iflag)
      implicit real*8 (a-h,q-z)
      implicit integer (i-p)
      real*8 x(n),fvec(m),u(9,9,9)
      integer it,mt,ichoic(9,9),mvec(99)
      common /param/r1,a,ea,tol,u,dmin,dmax,eps1,ntype
      common /testt/it,mt,ichoic,mvec,chi2
      do 900 j=1,m
        fvec(j) = x(1)*dexp(-x(2)/u(9,it,j)) - u(8,it,j)
900   continue
      return
      end
```

```
/*****************************************************************

                          pcf6.c

                          09/30/93

This program plots most of the the data generated by the data
acquisition program cf6.bas.  Moisture values are calculated from the
measured output voltage of the moisture sensors.  The oil conductivity
is also calculated. It is assumed in this program that the software
for the MCM is Version 1.4.

Calibrations used:
   Harley Moisture Sensor (35) used to measure air rH.
   Harley Moisture Sensor (37) used in the top, cal on 01/28/93.
   RC cell calibration as of 6/15/92.

Usage: pcf6 [filein]

Output files:
   filein.o1    Contains six plots versus time.  The first plot
                contains the outer cylinder and oil temperature.
                The second contains the charge density.  The third
                contains the terminal current or the terminal voltages
                (inner cylinder voltage, amplifier input voltage,
                amplifier output voltage).  The fourth contains the
                oil moisture data, giving the relative saturation of
                moisture and the absolute moisture content. The fifth
                gives the oil conductivity data in absolute terms and
                a coefficient that is independent of temperature.
                The sixth plot gives the rotational speed of the inner
                cylinder.

   filein.o2    Contains six plots of diagnostic information versus
                time.  The first plot contains the currents (offset
                and measurement) from the ACS measurement cycle.  The
                second displays the overshoots from the ACS measurement
                cycle.  The third gives the relative humidity of the
                air, the relative satuation of moisture in the oil, and
                the output voltage of the oil moisture sensor.  The
                fourth plot gives the gain and phase of the conductivity
                sensor.  The fifth gives the offset voltage of the
                conductivity sensor.  The sixth plot gives the room
                temperature and the hood temperature.

   filein.o3    Contains two plots.  The first plot gives the charge
                density and terminal current versus the rotational speed.
                The second plot gives the charge density and terminal
                current versus the terminal voltage.

*****************************************************************/

# include       <stdio.h>
```

```
# include       <math.h>
# define        A35       0.0000          /* calibration a for sensor 35-air*/
# define        B35       0.2500          /* calibration b for sensor 35-air*/
# define        A36      -0.0744          /* calibration a for sensor 36*/
# define        B36       0.2388          /* calibration b for sensor 36*/
# define        A37      -0.0322          /* calibration a for sensor 37*/
# define        B37       0.2333          /* calibration b for sensor 37*/
# define        C37       0.00275         /* calibration c for sensor 37*/
# define        R2        1000.e9         /* RCcell load resistor calibration*/
# define        C2        753.e-12        /* RCcell load capacitor calibration*/
# define        CAIR      50.03e-12       /* RCcell air capacitance calibration*/
# define        COFF      0.40e-12        /* RCcell CC offset air capacitance*/
# define        E1OFF     0.000           /* Electrometer 1 output offset*/
# define        E2OFF     0.000           /* Electrometer 2 output offset*/
# define        PI        3.14159265      /* PI */
# define        SOO       15.6e+6         /* Oil solubility saturation constant*/
# define        EA        3678.           /* Oil solubility activation temp */
# define        ESIGMA    5220.           /* conductivity activation temp */
# define        Eo        8.854e-12       /* permittivity of free space*/
# define        EOL       '\n'    /* end of line definition */
# define        LBLL      "label left"    /* plop label header */
# define        LBLR      "label right"   /* plop label header */
# define        LBLW      "window vertical 1/3 horizontal 1/2"    /* plop head */
# define        TXT       "text green over .1 right .35 size .08" /*label head*/
# define        TXTL      "text over .1 left 0. size .1"  /*label head*/
# define        TXTR      "text over .1 right 0. size .1" /*label head*/
# define        MAX       10000           /* maximum number of data points */
# define        RL        9.773e+09       /* load resistance for I-V curve */
# define        STOH      3600.   /* conversion for seconds in an hour */
# define        TABS      273.15  /* conversion for absolute zero in Kelvin */
# define        TREF      24.30   /* reference temp for Harley compensation */

char    fileses[9];
float   tme[MAX],rpm[MAX],trk[MAX],tcct[MAX],tccs[MAX];
float   thd[MAX],tai[MAX],th5[MAX],avp5[MAX],ppm5[MAX],avhd[MAX],rshd[MAX];
float   over[MAX],avco[MAX],avca[MAX],trm1[MAX],trm2[MAX],avcga[MAX];
float   lfg[MAX],lfp[MAX],lfo[MAX],perm[MAX],cond[MAX],rs[MAX];
float   icurr[MAX];

main(argc, argv)
int     argc;
char    *argv[];

{
        int     dskip,i,imin,j,nd,ndo,mumovr,rot;
        float   pzs,sca,offtme,c1,r1,scale1,scale2,pzc1,pzc2;
        float   doo,dg,dp,d1,hfperm,hf,hfg,hfp,hfo,lff,jk;
        float   mid,low,upp,tst;
        char    date[11],head[7],junk,time[11];
        char    fout1[12],fout2[12],fout3[12];
        char    protec[21],rst,harc,subo;
        FILE    *fpses,*fopen(),*fpo1,*fpo2,*fpo3;
/*
```

```
        open files
*/
        if (argc > 1) {
           strcpy(fileses,argv[1]);
           if ((fpses = fopen(fileses,"r")) == NULL) {
              printf("Error: cannot open %s\n",fileses);
              exit(1);
              }
           }
        else {
           if ((fpses = fopen(fileses,"r")) == NULL) {
              printf("Enter data file name: ");
              scanf("%s",fileses);
              }
           if ((fpses = fopen(fileses,"r")) == NULL) {
              printf("Error: cannot open %s\n",fileses);
              exit(1);
              }
           }
/*
        determine the output file names and check if they are valid
*/
        chkfil(fileses,fout1,".o1");
        chkfil(fileses,fout2,".o2");
        chkfil(fileses,fout3,".o3");
        fflush(stdout);
/*
        get the header data from the input file
*/
        while (junk=fgetc(fpses) != EOL);
        fscanf(fpses,"%s \n",date);
        while (junk=fgetc(fpses) != EOL);
        fscanf(fpses,"%s \n",time);
        while (junk=fgetc(fpses) != EOL);
        printf("Input file: %s \n",fileses);
        printf("\tDate: %s \n \tTime: %s \n",date,time);
        printf("Enter offset time (hours): ");
        scanf("%f",&offtme);
        for(nd=0;(nd!=3);nd++)
                while (junk=fgetc(fpses) != EOL);
        fscanf(fpses,"%f \n",&pzs);
        while (junk=fgetc(fpses) != EOL);
        fscanf(fpses,"%d \n",&rot);
        while (junk=fgetc(fpses) != EOL);
        fscanf(fpses,"%f \n",&scale1);
        while (junk=fgetc(fpses) != EOL);
        fscanf(fpses,"%f \n",&pzc1);
        while (junk=fgetc(fpses) != EOL);
        if(rot != 0 && rot != 2) {
                fscanf(fpses,"%f \n",&scale2);
                while (junk=fgetc(fpses) != EOL);
                fscanf(fpses,"%f \n",&pzc2);
                while (junk=fgetc(fpses) != EOL);
```

```
        }
    while (junk=fgetc(fpses) != EOL);
    fscanf(fpses,"%f %f \n",&hf,&hfg);
    while (junk=fgetc(fpses) != EOL);
    fscanf(fpses,"%f %f \n",&hfp,&hfo);
    while (junk=fgetc(fpses) != EOL);
/*
    get the high frequency permittivity
*/
    doo = 2.*PI*pow(10,hf)*R2*C2;
    dg = pow(10,hfg/20.);
    dp = hfp*PI/180.;
    c1 = C2*dg*(cos(dp)-dg+sin(dp)/doo)/(1+dg*dg-2*dg*cos(dp));
    hfperm = (c1-COFF)/(CAIR-COFF);
    for(nd=0;(nd!=4);nd++)
        while (junk=fgetc(fpses) != EOL);
/*
    get the bulk of the data
*/
    numovr = 0;
    for(nd=0;((junk=fgetc(fpses))!=EOF) && (nd!=MAX);++nd) {
        ungetc(junk,fpses);
        fscanf(fpses,"%f %f %f",&tme[nd],&rpm[nd],&trk[nd]);
        fscanf(fpses,"%f",&tcct[nd]);
        fscanf(fpses,"%f %f %f",&tccs[nd],&thd[nd],&tai[nd]);
        fscanf(fpses,"%f \n",&th5[nd]);
        fscanf(fpses,"%f %f %f %f \n",&avhd[nd],&jk,&avp5[nd],&jk);
        fscanf(fpses,"%f %f %s",&sca,&over[nd],&rst);
        fscanf(fpses,"%f %f %f\n",&avco[nd],&avca[nd],&avcga[nd]);
        fscanf(fpses,"%f %f\n",&trm1[nd],&trm2[nd]);
        fscanf(fpses,"%f %f %f %f\n",&lff,&lfg[nd],&lfp[nd],&lfo[nd]);
        fscanf(fpses,"%f %f\n",&jk,&jk);
/*
        check reset flag for ACS measurement
*/
        if(rst == 'E')  over[nd]=over[nd]+1;
        if(over[nd] > 0) numovr = numovr +1;
        }
    fclose(fpses);
    printf("\t %d sets of data points\n",nd);
    printf("\t initial charge density is %f uC/m3\n",pzs);
    printf("\t initial terminal data is %f ",pzc1);
    if (rot == 0 || rot ==2)
        printf(" pA\n");
    else {
        printf(" V\n");
        printf("\t initial terminal data is %f V\n",pzc2);
        }
/*
    average the data
*/
    if(numovr > 0)
        printf("\t %d bad ACS data points \n",numovr);
```

```
printf("Number of data points for averaging (1=none): ");
scanf("%d",&dskip);
if (dskip>1) {
        printf("Averaging the data ...");
        fflush(stdout);
        imin=0;
        nd /= dskip;
        for(i=0;i<nd; ++i) {
                ndo = 0;
                for(j=imin; j < (imin+dskip); ++j)
                        if (over[j]>0) ++ndo;
                tme[i] = tme[imin]/dskip;
                rpm[i] = rpm[imin]/dskip;
                trk[i] = trk[imin]/dskip;
                tcct[i]= tcct[imin]/dskip;
                tccs[i]= tccs[imin]/dskip;
                thd[i] = thd[imin]/dskip;
                tai[i] = tai[imin]/dskip;
                th5[i] = th5[imin]/dskip;
                avhd[i]= avhd[imin]/dskip;
                avp5[i]= avp5[imin]/dskip;
                if (over[imin]==0) {
                        over[i]= 0;
                        avco[i]= avco[imin]/(dskip-ndo);
                        avca[i]= avca[imin]/(dskip-ndo);
                        avcga[i]=avcga[imin]/(dskip-ndo);
                        }
                else    {
                        over[i]= 0;
                        avco[i]= avca[i]= avcga[i]= 0.;
                        }
                trm1[i]= trm1[imin]/dskip;
                trm2[i]= trm2[imin]/dskip;
                lfg[i] = lfg[imin]/dskip;
                lfp[i] = lfp[imin]/dskip;
                lfo[i] = lfo[imin]/dskip;
                for(j=imin+1; j < (imin+dskip); ++j) {
                        tme[i] += tme[j]/dskip;
                        rpm[i] += rpm[j]/dskip;
                        trk[i] += trk[j]/dskip;
                        tcct[i]+= tcct[j]/dskip;
                        tccs[i]+= tccs[j]/dskip;
                        thd[i] += thd[j]/dskip;
                        tai[i] += tai[j]/dskip;
                        th5[i] += th5[j]/dskip;
                        avhd[i]+= avhd[j]/dskip;
                        avp5[i]+= avp5[j]/dskip;
                        if (over[j]==0) {
                                avco[i]+= avco[j]/(dskip-ndo);
                                avca[i]+= avca[j]/(dskip-ndo);
                                avcga[i]+=avcga[j]/(dskip-ndo);
                                }
                        trm1[i]+= trm1[j]/dskip;
```

```
                                trm2[i]+= trm2[j]/dskip;
                                lfg[i] += lfg[j]/dskip;
                                lfp[i] += lfp[j]/dskip;
                                lfo[i] += lfo[j]/dskip;
                                }
                        imin += dskip;
                        }
                printf(" done\n");
                fflush(stdout);
                }
/*
        perform conversions on the data
*/
        printf("Subtract offset for charge density? ");
        scanf("%s",&subo);
        printf("Compensate moisture for hood temperature effect? ");
        scanf("%s",&harc);
        for(i=0;i<nd; ++i) {
/*              convert time to hours           */
                tme[i] = (tme[i]/STOH) + offtme;
/*              convert charge densities to XX uC/m^3   */
                avcga[i] *= 1.e6;
/*              calculate the corrected moisture levels
                Harley sensor no. 37 is in the CC top (avp5).
                Harley sensor 35 is in the hood measuring the air.      */
                rshd[i] = A35+B35*(avhd[i]-1.);
                if (harc=='Y' || harc=='y') {
                        rs[i] = A37+B37*(avp5[i]+C37*(thd[i]-TREF)-1.);
                        }
                else {
                        rs[i] = A37+B37*(avp5[i]-1.);
                        }
                ppm5[i]=rs[i]*SOO*exp(-EA/(tcct[i]+TABS));
/*              calculate the terminal current in nA    */
                if (rot != 0 && rot != 2)
                        icurr[i] = 1.e9 * (trm2[i]-trm1[i]) / RL;
/*              estimate the conductivity and the permittivity  */
                if(lfg[i]<-0.5) {
                        doo = 2.*PI*pow(10,lff)*R2*C2;
                        dg = pow(10,lfg[i]/20.);
                        dp = lfp[i]*PI/180.;
                        d1 = 1.+dg*dg-2.*dg*cos(dp);
                        c1 = C2*dg*(cos(dp)-dg+sin(dp)/doo)/d1;
                        r1 = R2*d1/(dg*(cos(dp)-dg-doo*sin(dp)));
                        perm[i] = (c1-COFF)/(CAIR-COFF);
                        cond[i] = Eo / (r1*(CAIR-COFF));
                        }
                else
                        cond[i] = 0.;
                if (subo=='Y' || subo=='y') avcga[i] -=pzs;
                }
/*
        begin with the main output file: CC temp, moisture, charge,
```

```
        conductivity, terminal data and rotation
*/
        printf("Writing %s ...",fout1); fflush(stdout);
        fpo1 = fopen(fout1,"w");
        fprintf(fpo1,"window\n frame suppress \n");
        fprintf(fpo1,"title top \"Date: %s Start Time: %s\" \n",date,time);
        fprintf(fpo1,"%s \"file: %s\" \n",TXT,fout1);
        fprintf(fpo1,"label bottom \"Time (hours)\" \n");
/*
        write out the temperature data
*/
        fprintf(fpo1,"%s\n",LBLW);
        fprintf(fpo1,"%s \"Oil Temp. (^{o}C)\" \n",LBLL);
        fprintf(fpo1,"plot red line\n");
        for (i=0;i<nd;++i)
                fprintf(fpo1," %f %f \n",tme[i], tcct[i]);
        fprintf(fpo1,"%s \"Side\"\n",TXTL);
        fprintf(fpo1,"plot blue line\n");
        for (i=0;i<nd;++i)
                fprintf(fpo1," %f %f \n",tme[i], tccs[i]);
/*
        write out the charge density information
*/
        fprintf(fpo1,"%s\n",LBLW);
        fprintf(fpo1,"%s \"\\rho_{0 rpm}=%2.2f\"\n",TXT,pzs);
        if (subo=='Y' || subo=='y')
                fprintf(fpo1,"%s \"\\rho - \\rho_{0 rpm} \" \n",LBLL);
        else
                fprintf(fpo1,"%s \"charge density (\\muC/m^{3})\" \n",LBLL);
        fprintf(fpo1,"plot red line  \n");
        for (i=0;i<nd;++i) {
                if(over[i] == 0)
                        fprintf(fpo1," %f %f \n",tme[i], avcga[i]);
                else {
                        fprintf(fpo1," \n");
                        }
                }
/*
        write out the terminal information
*/
        fprintf(fpo1,"%s\n",LBLW);
        if(rot == 0 || rot == 2) {
                fprintf(fpo1,"%s \"I_{0 rpm}= %2.2f pA\" \n",TXT,pzc1);
                fprintf(fpo1,"%s \"Term. Current (nA)\" \n",LBLL);
                fprintf(fpo1,"plot red line \n");
                for (i=0;i<nd;++i)
                        fprintf(fpo1," %f %f \n",tme[i], trm1[i]*1.E+9);
                }
        else {
                fprintf(fpo1,"%s \"V1_{0 rpm}= %2.2f V\" \n",TXT,pzc1);
                fprintf(fpo1,"%s \"Term. Voltages (V)\" \n",LBLL);
                fprintf(fpo1,"plot red line \n");
                for (i=0;i<nd;++i)
```

```
                fprintf(fpo1," %f %f \n",tme[i], trm1[i]);
        fprintf(fpo1,"%s \"Elec 2\"\n",TXTL);
        fprintf(fpo1,"plot blue line\n");
        for (i=0;i<nd;++i)
                fprintf(fpo1," %f %f \n",tme[i], trm2[i]);
        if (rot == 4 || rot == 5) {
                fprintf(fpo1,"%s \"V_{trek}\"\n",TXTR);
                fprintf(fpo1,"plot green line use z\n");
                for (i=0;i<nd;++i)
                        fprintf(fpo1," %f %f \n",tme[i], trk[i]);
                }
        }
/*
        write out the moisture for CC
*/
        fprintf(fpo1,"%s\n",LBLW);
        fprintf(fpo1,"%s \"Oil Moisture (ppm)\" \n",LBLR);
        fprintf(fpo1,"plot green line use z\n");
        for (i=0;i<nd;++i)
                fprintf(fpo1," %f %f \n",tme[i], ppm5[i]);
        fprintf(fpo1,"%s \"rS (\%\%)\"\n",TXTL);
        fprintf(fpo1,"plot blue line\n");
        for (i=0;i<nd;++i)
                fprintf(fpo1," %f %f \n",tme[i], 100.*rs[i]);
/*
        write out the conductivity data
*/
        fprintf(fpo1,"%s\n",LBLW);
        fprintf(fpo1,"%s \" high freq. \\epsilon_{r}=%2.2f \" \n",TXT,hfperm);
        fprintf(fpo1,"%s \"Conductivity (pS/m)\" \n",LBLR);
        fprintf(fpo1,"plot green line use z\n");
        for (i=0;i<nd;++i) {
                if(cond[i] >= 0)
                        fprintf(fpo1," %f %f \n",tme[i], cond[i]*1e12);
                }
        fprintf(fpo1,"%s \"\\sigma_o(10^{-4}S/m)\"\n",TXTL);
        fprintf(fpo1,"plot blue line\n");
        for (i=0;i<nd;++i) {
                if(cond[i] >= 0) {
                        jk = 1.e+4*cond[i]*exp(ESIGMA/(tcct[i]+TABS));
                        fprintf(fpo1," %f %f \n",tme[i], jk);
                        }
                }
        fprintf(fpo1,"%s\n",LBLW);
        fprintf(fpo1,"%s \"Rotation (RPM)\" \n",LBLR);
        fprintf(fpo1,"plot green line use z\n");
        for (i=0;i<nd;++i)
                fprintf(fpo1," %f %f \n",tme[i], rpm[i]);
/*
        this file is done so close it up and
        print out the diagnostic information for the ACS data
*/
        fclose(fpo1);
```

```
        printf(" done\n");
/*
        write out the ACS diagnostic and RC cell information
*/
        printf("Writing %s ...",fout2); fflush(stdout);
        fpo2 = fopen(fout2,"w");
        fprintf(fpo2,"window\n frame suppress \n");
        fprintf(fpo2,"title top \"Date: %s Start Time: %s\" \n",date,time);
        fprintf(fpo2,"%s \"file: %s\" \n",TXT,fout2);
        fprintf(fpo2,"label bottom \"Time (hours)\" \n\n");
/*
        the ACS information
*/
        fprintf(fpo2,"%s\n",LBLW);
        fprintf(fpo2,"%s \"ACS Current (pA)\" \n",LBLL);
        fprintf(fpo2,"plot red line  \n");
        for (i=0;i<nd;++i)
                fprintf(fpo2," %f %f \n",tme[i], avca[i]);
        fprintf(fpo2,"plot blue line\n");
        fprintf(fpo2,"%s \"Offset\" \n",TXTL);
        for (i=0;i<nd;++i)
                fprintf(fpo2," %f %f \n",tme[i], avco[i]);
        fprintf(fpo2,"%s\n",LBLW);
        fprintf(fpo2,"%s \"ACS Overshoots\" \n",LBLL);
        fprintf(fpo2,"plot red line  \n");
        for (i=0;i<nd;++i)
                fprintf(fpo2," %f %f \n",tme[i], over[i]);
/*
        diagnostic for moisture sensor
*/
        fprintf(fpo2,"%s\n",LBLW);
        fprintf(fpo2,"%s \"rH (\%\%)\" \n",LBLL);
        fprintf(fpo2,"plot red line  \n");
        for (i=0;i<nd;++i)
                fprintf(fpo2," %f %f \n",tme[i], 100.*rshd[i]);
        fprintf(fpo2,"%s \"rS (\%\%)\" \n",TXTL);
        fprintf(fpo2,"plot blue line  \n");
        for (i=0;i<nd;++i)
                fprintf(fpo2," %f %f \n",tme[i], 100.*rs[i]);
        fprintf(fpo2,"%s \"V_{moist} (V)\" \n",TXTR);
        fprintf(fpo2,"z axis scale 1.0 1.0  \n");
        fprintf(fpo2,"plot green line use z\n");
        for (i=0;i<nd;++i)
                fprintf(fpo2," %f %f \n",tme[i], avp5[i]);
/*
        write out the gain, phase and offset data
*/
        fprintf(fpo2,"%s\n",LBLW);
        fprintf(fpo2,"label top \"RC data (log(f)=%2.2f)\" \n",lff);
        fprintf(fpo2,"%s \"Gain (dB)\" \n",LBLR);
        fprintf(fpo2,"plot green line use z\n");
        for (i=0;i<nd;++i)
                fprintf(fpo2," %f %f \n",tme[i], lfg[i]);
```

```
        fprintf(fpo2,"%s \"Phase (deg)\" \n",TXTL);
        fprintf(fpo2,"plot blue line\n");
        for (i=0;i<nd;++i)
                fprintf(fpo2," %f %f \n",tme[i], lfp[i]);
        fprintf(fpo2,"%s\n",LBLW);
        fprintf(fpo2,"%s \"RC Cell Offset (V)\" \n",LBLR);
        fprintf(fpo2,"plot green line use z\n");
        for (i=0;i<nd;++i)
                fprintf(fpo2," %f %f \n",tme[i], lfo[i]);
/*
        write out the hood and room temperatures
*/
        fprintf(fpo2,"%s\n",LBLW);
        fprintf(fpo2,"%s \"Hood Temp. (^{o}C)\" \n",LBLR);
        fprintf(fpo2,"plot green line  use z\n");
        for (i=0;i<nd;++i)
                fprintf(fpo2," %f %f \n",tme[i], thd[i]);
        fprintf(fpo2,"%s \"Room\" \n",TXTL);
        fprintf(fpo2,"plot blue line\n");
        for (i=0;i<nd;++i)
                fprintf(fpo2," %f %f \n",tme[i], tai[i]);
/*
        this file is done so close it up
*/
        fclose(fpo2);
        printf(" done\n");
/*
        now write out the charge density versus rotation and voltage
*/
        printf("Writing %s ...",fout3); fflush(stdout);
        fpo3 = fopen(fout3,"w");
        fprintf(fpo3,"window\n frame suppress \n");
        fprintf(fpo3,"title top \"Date: %s Start Time: %s\" \n",date,time);
        fprintf(fpo3,"%s \"file: %s\" \n",TXT,fout3);
/*
        charge density/current versus rotation rate
*/
        fprintf(fpo3,"window vertical 1/2\n");
        fprintf(fpo3,"label bottom \"Rotation Rate (RPM)\" \n");
        if (subo=='Y' || subo=='y')
                fprintf(fpo3,"%s \"\\rho - \\rho_{0 rpm} \" \n",LBLL);
        else
                fprintf(fpo3,"%s \"charge density (\\muC/m^{3})\" \n",LBLL);
        fprintf(fpo3,"plot green cross marker 0.07\n");
        for (i=0;i<nd;++i) {
                if(over[i] == 0)
                   fprintf(fpo3,"%f %f #V=%f\n",rpm[i],avcga[i],trm1[i]);
                else
                   fprintf(fpo3," \n");
                }
        fprintf(fpo3,"label right \"Terminal Current (nA)\" \n");
        fprintf(fpo3,"plot green plus marker 0.07 use z\n");
        for (i=0;i<nd;++i) {
```

```
                if(rot==0 || rot == 2)
                        fprintf(fpo3,"%f %f\n",rpm[i],1.E+9*trm1[i]);
                else
                        fprintf(fpo3,"%f %f #V=%f\n",rpm[i],icurr[i],trm1[i]);
                }
/*
        charge density/current versus applied voltage
*/
        fprintf(fpo3,"window vertical 1/2\n");
        fprintf(fpo3,"label bottom \"Terminal Voltage (V)\" \n");
        if (subo=='Y' || subo=='y')
                fprintf(fpo3,"%s \"\\rho - \\rho_{0 rpm} \" \n",LBLL);
        else
                fprintf(fpo3,"%s \"charge density (\\muC/m^{3})\" \n",LBLL);
        fprintf(fpo3,"plot green cross marker 0.07\n");
        for (i=0;i<nd;++i) {
                if(over[i] == 0)
                        fprintf(fpo3,"%f %f #R=%f\n",trm1[i],avcga[i],rpm[i]);
                else
                        fprintf(fpo3," \n");
                }
        fprintf(fpo3,"label right \"Terminal Current (nA)\" \n");
        fprintf(fpo3,"plot green plus marker 0.07 use z\n");
        for (i=0;i<nd;++i)
                fprintf(fpo3,"%f %f #R=%f\n",trm1[i],icurr[i],rpm[i]);
/*
        this file is done so close it up
*/
        fclose(fpo3);
        printf(" done\n");
/*
        write protect the output files
*/
        clsfil(fout1);
        clsfil(fout2);
        clsfil(fout3);
        printf("pcf6 finished\n");
        fflush(stdout);
}


chkfil(fs,fout,ftail)
char    fs[],fout[],ftail[];
{
        FILE    *fopen(),*fpo;
        strcpy(fout, fs);
        strcat(fout, ftail);
        if ((fpo = fopen(fout,"r")) != NULL) {
              printf("\nDanger: File %s already exists\n",fout);
              exit(1);
              }
}
```

```
clsfil(fout)
char    fout[];
{
        char    protec[21];
        sprintf(protec, "chmod a=r %s", fout);
        system(protec);
        fflush(stdout);
}
```

```
ccccccccccccccccccccccccccccccccccccccccccccccccccccccccccccccccccccccc
c
c                       pe1exp.for
c
c       In this program, a parameter estimation is performed to the
c       relation
c               y = a e^(-t/t1) + b
c       where a, b, and t1 are to be determined.
c
        program pe1exp
        implicit real*8 (a-h,q-z)
        parameter (ISTOP = 200)
        parameter (MMAX = 5000)
        parameter (NMAX = 10)
        parameter (LWAMAX= MMAX*(NMAX+1)+5*NMAX)
        integer iwa(NMAX)
        real*8 fvec(MMAX),x(NMAX),wa(LWAMAX)
        character*9 fname
        character*11 oname
        real*8 t(MMAX),y(MMAX)
        common /data/ t,y
        external fcn
c
c       read in the data file name and the data from the file
c
        print*, 'One exponential estimation program'
        print*, '  y = a e^(-t/t1) + b'
        print*, '********************************** '
c
c       read in the initial guesses for the variables
c
        print*, 'What is the initial guess for a? '
        read*, x(1)
        print*, 'What is the initial guess for t1? '
        read*, x(2)
        print*, 'What is the initial guess for b? '
        read*, x(3)
        print*, 'What is the tolerance for the calculation? '
        read*, tol
        print*, 'What is the input (data) filename?  '
        read (*,100) fname
        ia = index(fname,' ') - 1
        if (ia.LT.0) ia = 9
        oname = fname(:ia)//'.p'
        open (unit=5, file=fname(:ia))
        do 40 m=1,MMAX
   40     read (5,*,err=60,end=60) t(m),y(m)
        close (unit=5)
c
c       set the value of the number of unknowns
c
   60   m = m - 1
        n = 3
```

```
      toff = t(1)
      do 65 i=1,m
   65   t(i) = t(i) - toff
cccccccccccccccccccccccccccccccccccccccccccccccccccccccccccccccccccccccc
c
c     call the minimization subroutine LMDIF1 to find the best fit
c
      lwa = m*n+5*n+m
      call lmdif1(fcn,m,n,x,fvec,tol,info,iwa,wa,lwa)
c
c     now print out the results of the calculation
c
      call lmdif1o(info,n,x)
c
cccccccccccccccccccccccccccccccccccccccccccccccccccccccccccccccccccccccc
c
c     create a plot for comparing the data and the fit
c
      open (unit=7, file=oname)
      write (7,200) oname,(x(i),i=1,n)
c
c     write out the initial data first
c
      write (7,206) "red"
      do 55 i=1,m
        write (7,210) t(i), y(i)
   55 continue
c
c     start the computation of the plot vector
c     generate the curve using the parameters given above
c
      write (7,206) "green"
      do 80 i=1,ISTOP
         dt = real(i-1)*t(m)/real(ISTOP-1)
         dv = x(1)*dexp(-dt/x(2)) + x(3)
   80    write(7,210) dt,dv
      close (unit=7)
  100 format (a9)
  200 format ('text green over .1 right .5 size .05 "file:',A11,'"',/,
     &    'label left "y(t)"',/,'label bottom "t"',/,
     &    'text red over -.3 right 1. size .1 "y = ',G10.4,
     &    ' e^{- t / ', G10.4,' } + ',G10.4,'"')
  206 format ('plot ',A6,' spline ')
  210 format (2G20.8)
      print*, ' program complete'
      stop
      end

      subroutine fcn(m,n,x,fvec,iflag)
c
c     this subroutine returns the function values for lmdif1
c     the format is return value = data value - model value
c
```

```
      integer m,n,iflag
      real*8 x(n),fvec(m)
      real*8 t(5000),y(5000)
      common /data/ t,y
      do 300 i=1,m
            fvec(i) = x(1)*dexp(-t(i)/x(2)) + x(3) - y(i)
300   continue
      return
      end
```

```
ccccccccccccccccccccccccccccccccccccccccccccccccccccccccccccccccccccccc
c
c                       pe2exp.for
c
c       In this program, a parameter estimation is performed to the
c       relation
c               y = a e^(-t/t1) + b e^(-t/t2)
c       where a, b, and t1 are to be determined.  It is assumed that
c       the value of t2 has been determined via another method.
c
        program pe2exp
        implicit real*8 (a-h,q-z)
        parameter (ISTOP = 200)
        parameter (MMAX = 5000)
        parameter (NMAX = 10)
        parameter (LWAMAX= MMAX*(NMAX+1)+5*NMAX)
        integer iwa(NMAX)
        real*8 fvec(MMAX),x(NMAX),wa(LWAMAX)
        character*9 fname
        character*11 oname
        real*8 t(MMAX),y(MMAX)
        common /data/ t,y,t2
        external fcn
c
c       read in the data file name and the data from the file
c
        print*, 'Two exponential estimation program'
        print*, '  y = a e^(-t/t1) + b e^(-t/t2)'
        print*, '********************************** '
c
c       read in the initial guesses for the variables
c
        print*, 'What is the initial guess for a? '
        read*, x(1)
        print*, 'What is the initial guess for t1? '
        read*, x(2)
        print*, 'What is the initial guess for b? '
        read*, x(3)
        print*, 'What is the initial guess for t2? '
        read*, t2
        print*, 'What is the tolerance for the calculation? '
        read*, tol
        print*, 'What is the input (data) filename?  '
        read (*,100) fname
        ia = index(fname,' ') - 1
        if (ia.LT.0) ia = 9
        oname = fname(:ia)//'.p'
        open (unit=5, file=fname(:ia))
        do 40 m=1,MMAX
   40     read (5,*,err=60,end=60) t(m),y(m)
        close (unit=5)
c
c       set the value of the number of unknowns
```

```
c
   60   m = m - 1
        n = 3
        toff = t(1)
        do 65 i=1,m
   65     t(i) = t(i) - toff
ccccccccccccccccccccccccccccccccccccccccccccccccccccccccccccccccccccccc
c
c       call the minimization subroutine LMDIF1 to find the best fit
c
        lwa = m*n+5*n+m
        call lmdif1(fcn,m,n,x,fvec,tol,info,iwa,wa,lwa)
c
c       now print out the results of the calculation
c
        call lmdif1o(info,n,x)
c
ccccccccccccccccccccccccccccccccccccccccccccccccccccccccccccccccccccccc
c
c       create a plot for comparing the data and the fit
c
        open (unit=7, file=oname)
        write (7,200) oname,(x(i),i=1,n),t2
c
c       write out the initial data first
c
        write (7,206) "red"
        do 55 i=1,m
          write (7,210) t(i), y(i)
   55   continue
c
c       start the computation of the plot vector
c       generate the curve using the parameters given above
c
        if (x(2).LT.t2) then
          tint = 5.*x(2)
        else
          tint = 5.*t2
        endif
        write (7,206) "green"
        do 75 i=1,ISTOP
           dt = real(i-1)*tint/real(ISTOP-1)
           dv = x(1)*dexp(-dt/x(2)) + x(3)*dexp(-dt/t2)
   75      write(7,210) dt,dv
        do 80 i=1,ISTOP
           dt = tint + real(i)*(t(m)-tint)/real(ISTOP)
           dv = x(1)*dexp(-dt/x(2)) + x(3)*dexp(-dt/t2)
   80      write(7,210) dt,dv
        close (unit=7)
  100   format (a9)
  200   format ('text green over .1 right .5 size .05 "file:',A11,'"',/,
     &     'label left "y(t)"',/,'label bottom "t"',/,
     &     'text red over -.3 right 1. size .1 "y = ',G10.4,
```

```
     &     ' e^{- t / ', G10.4,' } + ',G10.4,' e^{- t / ', G10.4,' }"')
  206   format ('plot ',A6,' spline ')
  210   format (2G20.8)
        print*, ' program complete'
        stop
        end

        subroutine fcn(m,n,x,fvec,iflag)
c
c       this subroutine returns the function values for lmdif1
c       the format is return value = data value - model value
c
        integer m,n,iflag
        real*8 x(n),fvec(m)
        real*8 t(5000),y(5000),t2
        common /data/ t,y,t2
        do 300 i=1,m
              fvec(i) = x(1)*dexp(-t(i)/x(2)) + x(3)*dexp(-t(i)/t2) - y(i)
  300   continue
        return
        end
```

```
ccccccccccccccccccccccccccccccccccccccccccccccccccccccccccccccccccccccc
c
c                       peept.for
c
c       In this program, a parameter estimation is performed to the
c       relation
c               y = (a /(1+t/t1)) + b e^(-t/t2)
c       where a, b, and t1 are to be determined.  It is assumed that
c       the value of t2 has been determined via another method.
c
        program peept
        implicit real*8 (a-h,q-z)
        parameter (ISTOP = 200)
        parameter (MMAX = 5000)
        parameter (NMAX = 10)
        parameter (LWAMAX= MMAX*(NMAX+1)+5*NMAX)
        integer iwa(NMAX)
        real*8 fvec(MMAX),x(NMAX),wa(LWAMAX)
        character*9 fname
        character*11 oname
        real*8 t(MMAX),y(MMAX)
        common /data/ t,y,t2
        external fcn
c
c       read in the data file name and the data from the file
c
        print*, 'Ohmic and migration estimation program'
        print*, ' y = (a /(1+t/t1)) + b e^(-t/t2)'
        print*, '********************************** '
c
c       read in the initial guesses for the variables
c
        print*, 'What is the initial guess for a? '
        read*, x(1)
        print*, 'What is the initial guess for t1? '
        read*, x(2)
        print*, 'What is the initial guess for b? '
        read*, x(3)
        print*, 'What is the initial guess for t2? '
        read*, t2
        print*, 'What is the tolerance for the calculation? '
        read*, tol
        print*, 'What is the input (data) filename?  '
        read (*,100) fname
        ia = index(fname,' ') - 1
        if (ia.LT.0) ia = 9
        oname = fname(:ia)//'.p'
        open (unit=5, file=fname(:ia))
        do 40 m=1,MMAX
   40     read (5,*,err=60,end=60) t(m),y(m)
        close (unit=5)
c
c       set the value of the number of unknowns
```

```
c
   60   m = m - 1
        n = 3
        toff = t(1)
        do 65 i=1,m
   65     t(i) = t(i) - toff
ccccccccccccccccccccccccccccccccccccccccccccccccccccccccccccccccccccccc
c
c       call the minimization subroutine LMDIF1 to find the best fit
c
        lwa = m*n+5*n+m
        call lmdif1(fcn,m,n,x,fvec,tol,info,iwa,wa,lwa)
c
c       now print out the results of the calculation
c
        call lmdif1o(info,n,x)
c
ccccccccccccccccccccccccccccccccccccccccccccccccccccccccccccccccccccccc
c
c       create a plot for comparing the data and the fit
c
        open (unit=7, file=oname)
        write (7,200) oname,(x(i),i=1,n),t2
c
c       write out the initial data first
c
        write (7,206) "red"
        do 55 i=1,m
          write (7,210) t(i), y(i)
   55   continue
c
c       start the computation of the plot vector
c       generate the curve using the parameters given above
c
        if (x(2).LT.t2) then
          tint = 5.*x(2)
        else
          tint = 5.*t2
        endif
        write (7,206) "green"
        do 75 i=1,ISTOP
           dt = real(i-1)*tint/real(ISTOP-1)
           dv = (x(1)/(1.+dt/x(2))) + x(3)*dexp(-dt/t2)
   75      write(7,210) dt,dv
        do 80 i=1,ISTOP
           dt = tint + real(i)*(t(m)-tint)/real(ISTOP)
           dv = (x(1)/(1.+dt/x(2))) + x(3)*dexp(-dt/t2)
   80      write(7,210) dt,dv
        close (unit=7)
  100   format (a9)
  200   format ('text green over .1 right .5 size .05 "file:',A11,'"',/,
     &     'label left "y(t)"',/,'label bottom "t"',/,
     &     'text red over -.3 right 1. size .1 "y = ',G10.3,
```

```
     &     ' / ( 1 + t / ', G10.3,' ) + ',G10.3,' e^{- t / ', G10.3,' }"')
  206   format ('plot ',A6,' spline ')
  210   format (2G20.8)
        print*, ' program complete'
        stop
        end

        subroutine fcn(m,n,x,fvec,iflag)
c
c       this subroutine returns the function values for lmdif1
c       the format is return value = data value - model value
c
        integer m,n,iflag
        real*8 x(n),fvec(m)
        real*8 t(5000),y(5000),t2
        common /data/ t,y,t2
        do 300 i=1,m
           fvec(i) = (x(1)/(1.+t(i)/x(2))) + x(3)*dexp(-t(i)/t2)-y(i)
  300   continue
        return
        end
```

```
c
c               perho.for
c
c       This program computes a parameter estimate of the outlet charge
c       density from the flowloop apparatus, satisfying the equation
c               ro = rd * (1.+a/q)*(1.+c/q)*(1.-exp(-(d*e/q)))/
c               ((1.+a/q)*(1.+c/q)*(1.+1./q) - exp(-(b+d*e)/q))
c               rd = c1 * exp(c3/kT) + c2
c               q = te/tr4
c       where the possible unknowns are c1, c2, and c3
c               a = V2/V4
c               b = V5/V4
c               c = V6/V4
c               d = Vp/V4
c               e = P epsilon / epsilon_p
c       All of the volume inputs are in m3.
c       The program normalizes the variables appropriately.
c       The conductivity is assumed to vary with
c       temperature according to K = Ko e(-W/kT).
c
        program perho
        integer info,iwa(10),lwa,m,n
        integer mdata,m1,iout
        real*8 fvec(500),x(10),wa(5550),tol,rc,v5(500),v6(500),v(8)
        character*16 oname
        real*8 ro(500),ri(500),q(500),tem(500),a5(500),a6(500)
        real*8 a(8),b,c(3),w,kb
        common /ins/ a,b,c,w,kb
        common /data/ ro,ri,q,tem,a5,a6,mdata
        external fcn,yeqn
        perm=2.2*8.854e-12
        kb=8.6167e-5
        tabs=273.15
c
c       read in the data file name and the data from the file
c
        print*, 'Estimation Program - for C1 to C3'
        print*, '****************************************** '
c
c       read in the initial guesses for the variables
c
        print*, 'How many unknowns to be estimated (0, 1, 2, or 3)?'
        read*, n
        if (n.gt.3) then
           print*, 'Invalid number of of unknowns.'
           stop
        else
           print*, 'What is the initial guess for C(1)? '
           read*, x(1)
           c(1)=x(1)
           if (n.gt.1) then
              print*, 'What is the initial guess for C(2)? '
              read*, x(2)
```

```
            else
               print*, 'What is C(2)? '
               read*, C(2)
            endif
            if (n.eq.3) then
               print*, 'What is the initial guess for C(3)? '
               read*, x(3)
            else
               print*, 'What is C(3)? '
               read*, C(3)
            endif
         endif
c
c        set the other variables for the program
c
         print*, 'What is the tolerance for the calculation? '
         read*, tol
         print*, 'What is the output data filename?  '
         read (*,50) oname
   50    format (a16)
         print*, 'Output data versus Q (1) or temperature (2)?  '
         read (*,*) iout
         print*, 'Enter the volumes for the first four regions (gal).'
         read*, (v(i),i=1,4)
         do 52 i=1,4
            a(i) = v(i)/ v(4)
            print*, 'a(',i,') = ',a(i)
   52    continue
c        get the oil properties
         print*, 'Enter the paper (solid) relative permittivity.'
         read*, perms
         perms = perms*8.854e-12
         print*, 'Enter the paper porosity.'
         read*, poro
         permp = poro*perm + (1.-poro)*perms
         a(7) = poro*perm/permp
         print*, 'permp = ',permp, '   a(7) =',a(7)
         print*, 'Enter the measured conductivity and temperature (pS/m, C)'
         read*, sigma,otemp
         print*, 'What is the activation energy for the conductivity (eV)?'
         read*, w
c        calculate the coefficient for the flow rate
         b = v(4) * 60. *sigma * 1.e-12 * exp(w/(kb*(otemp+tabs))) /perm
         print*, 'b = ',b
         print*, 'How many data points? '
         read*, mdata
         print*, 'How many data drum flow points? '
         read*, m1
         print*, 'Enter the data as q, ri, ro, temp, vol 5, vol 6.'
         read*, (q(i),ri(i),ro(i),tem(i),v5(i),v6(i),i=1,mdata)
c        convert the temperature to kelvin
         do 45 i=1,mdata
            tem(i) = tem(i) + tabs
```

```
            a5(i) = v5(i)/v(4)
            a6(i) = v6(i)/v(4)
   45    continue
c
c        set the value of the number of unknowns
c
         m = 2*mdata
c
ccccccccccccccccccccccccccccccccccccccccccccccccccccccccccccccccccccccccc
         if (n.gt.0) then
c
c           call the minimization subroutine LMDIF1 to find the best fit
c
            lwa = m*n+5*n+m
            call lmdif1(fcn,m,n,x,fvec,tol,info,iwa,wa,lwa)
c
c           now print out the results of the calculation
c
            call lmdif1o(info,n,x)
         endif
ccccccccccccccccccccccccccccccccccccccccccccccccccccccccccccccccccccccccc
c
c        set the final values into the constants array
c
         do 53 i=1,n
            c(i) = x(i)
   53    continue
c
c        write the header information for the plot file
c
         open (unit=7, file=oname)
         if (iout.eq.1) then
            write (7,200) oname, (c(i),i=1,3)
         else
            write (7,201) oname, (c(i),i=1,3)
         endif
  200    format (' title top " file: ',A16,'"',/
     &      ' label top "C1: ',G15.5,' C2: ',G15.5,' C3: ',G15.5,'"',/,
     &      ' label left " Charge density (\muC/m^3) "',/
     &      ' label bottom " Q (GPM) "')
  201    format (' title top " file: ',A16,'"',/
     &      ' label top "C1: ',G15.5,' C2: ',G15.5,' C3: ',G15.5,'"',/,
     &      ' label left " ln(\rho) (\muC/m^3) "',/
     &      ' label bottom " 1/T_{oil} (1/K) "')
c
c        print the original data first
c        begin with the filter outlet charge density
c
         write (7,*) "plot green stars size 0.08"
         if (iout.eq.1) then
            write(7,210) (q(i),ro(i), i=1,m1)
         else
            write(7,210) (1/tem(i),dlog(ro(i)), i=1,m1)
```

```
      endif
      if (iout.eq.1) then
         write (7,*) "plot green cross size 0.08"
         write(7,210) (q(i),ro(i), i=m1+1,mdata)
      endif
c     next do the filter inlet charge density
      write (7,*) "plot green circles size 0.08"
      if (iout.eq.1) then
         write(7,210) (q(i),ri(i), i=1,m1)
      else
         write(7,210) (1/tem(i),ri(i), i=1,m1)
      endif
      if (iout.eq.1) then
         write (7,*) "plot green plus size 0.08"
         write(7,210) (q(i),ri(i), i=m1+1,mdata)
      endif
c
c     start the best fit calculation using the parameters given above
c     begin with the filter outlet charge density
c
      write (7,60)
   60 format (/,' plot green line')
      do 85 i=1,m1
         rc = yeqn(q(i),tem(i),a5(i),a6(i))
         if (iout.eq.1) then
            write(7,210) q(i),rc
         else
            write(7,210) 1/tem(i),dlog(rc)
         endif
   85 continue
      if (iout.eq.1) then
         write (7,60)
         do 86 i=m1+1,mdata
            rc = yeqn(q(i),tem(i),a5(i),a6(i))
            write(7,210) q(i),rc
   86    continue
      endif
c        next do the filter inlet charge density
      write (7,60)
      do 125 i=1,m1
         qx = q(i) * exp(w/(kb*tem(i)))/b
         rc=exp(-(a5(i)/qx))*yeqn(q(i),tem(i),a5(i),a6(i))/(1.+a6(i)/qx)
         if (iout.eq.1) then
            write(7,210) q(i),rc
         else
            write(7,210) 1/tem(i),rc
         endif
  125 continue
      if (iout.eq.1) then
         write (7,60)
         do 126 i=m1+1,mdata
            qx = q(i) * exp(w/(kb*tem(i)))/b
            rc=exp(-(a5(i)/qx))*yeqn(q(i),tem(i),a5(i),a6(i))/(1.+a6(i)/qx)
```

```
            write(7,210) q(i),rc
  126       continue
        endif
        close (unit=7)
  210   format (2F15.7)
c
c       end the program
c
        print*, ' program complete'
        stop
        end


        subroutine fcn(m,n,x,fvec,iflag)
c
c       this subroutine returns the function values for lmdif1
c       the format is return value = data value - model value
c       bounds are also placed on the parameters for physical reasons
c
        integer m,n,iflag
        integer mdata
        real*8 x(n),fvec(m),rc
        real*8 ro(500),ri(500),q(500),tem(500),a5(500),a6(500)
        real*8 a(8),b,c(3),w,kb
        common /ins/ a,b,c,w,kb
        common /data/ ro,ri,q,tem,a5,a6,mdata
        external yeqn
        do 299 i=1,n
           c(i) = x(i)
  299   continue
        print*, (c(i), i=1,3)
        do 300 i=1,mdata
           rc= yeqn(q(i),tem(i),a5(i),a6(i))
           fvec(i) = ro(i) - rc
           qx = q(i) * exp(w/(kb*tem(i))) / b
           fvec(i+mdata) = ri(i)- exp(-(a5(i)/qx))*rc/(1.+a6(i)/qx)
  300   continue
        return
        end


        real*8 function yeqn(qc,tc,apc,arc)
c
        real*8 G,qc,tc,apc,arc,qx
        real*8 a(8),b,c(3),w,kb
        common /ins/ a,b,c,w,kb
           qx = qc * exp(w/(kb*tc))/b
           yeqn = (c(1)*exp(-c(3)/(kb*tc))+c(2))*(1.+a(2)/qx)*(1.+arc/qx)
     &          *(1.-exp(-(a(3)*a(7)/qx)))/ ((1.+a(2)/qx)*(1.+arc/qx)*
     &          (1.+1./qx) - exp(-(apc+a(3)*a((7)))/qx))
        return
        end
```

```
/*****************************************************************

                          prc.c

                         3/20/92

This program is used to calculate the effective impedance of a test
cell from a frequency scan of the gain and phase as measured by the
Otten box and logged through kermit.  The resistance and capacitance
at each frequency is calculated and an effective resistance and
capacitance are also estimated.  Given the capacitance of the test
cell in air, the permittivity and conductivity of the test medium is
also calculated. The effects of lead wire capacitances can be
subtracted from the test cell impedance through the offset
capacitance. It is assumed in this program that the software for the
MCM is Version 1.4.

Usage: prc [filein]

Output files:
   filein.p1    Plots the raw data (gain, phase, and offset voltage)
                versus the freuquency.  Also plotted is the model
                response using the estimated resistance and
                capacitance.
   filein.p2    Plots the real and imaginary parts of the measured
                impedance in the form of a Col-Cole plot.  Also
                plotted is the model response using the estimated
                resistance and capacitance.
   filein.p3    Plots the calculated resistance and capacitance at
                each frequency, as well as the estimated effective
                resistance and capacitance.  The permittivity and
                conductivity are also plotted.

 *****************************************************************/

# include       <stdio.h>
# include       <math.h>
# define        PI       3.14159265     /* PI */
# define        Eo       8.854e-12      /* permittivity of free space*/
# define        EOL     '\n'            /* end of line definition */
# define        MAX     5000            /* maximum number of data points */

char    fileses[] = "session.log";
float   f[MAX],g[MAX],p[MAX],o[MAX];
float   c1[MAX],r1[MAX];

main(argc, argv)
int     argc;
char    *argv[];

{
        int     i,j,n,ni,nmax;
        int     year,month,day,hour,minute;
```

```
        float   ch,d,dt,jk,minph;
        float   c2,coff,cair,r2,d1,d2,dg,dp,x,y,z1i,z1r;
        float   a,da,dn,nm,fi,dfida,tol,dd,ddx,ddy;
        char    head[5],fout1[11],fout2[11],fout3[11],protec[21],junk;
        FILE    *fpses,*fopen(),*fpo1,*fpo2,*fpo3;
/*
        open files
*/
        if (argc > 1) {
           strcpy(fileses,argv[1]);
           if ((fpses = fopen(fileses,"r")) == NULL) {
              printf("Error: cannot open %s\n",fileses);
              exit(1);
              }
           }
        else {
           if ((fpses = fopen(fileses,"r")) == NULL) {
              printf("Enter data file name: ");
              scanf("%s",fileses);
              }
           if ((fpses = fopen(fileses,"r")) == NULL) {
              printf("Error: cannot open %s\n",fileses);
              exit(1);
              }
           }
/*
        determine the output file names and check if they are valid
*/
        strcpy(fout1, fileses);
        strcat(fout1, ".p1");
        strcpy(fout2, fileses);
        strcat(fout2, ".p2");
        strcpy(fout3, fileses);
        strcat(fout3, ".p3");
        if ((fpo1 = fopen(fout1,"r")) != NULL ||
            (fpo2 = fopen(fout2,"r")) != NULL ||
            (fpo3 = fopen(fout3,"r")) != NULL) {
              printf("\nDanger: One of the plot files already exists\n");
              exit(1);
              }
        fflush(stdout);
/*
        get the calibration information
*/
        printf("Enter the load resistance (Gohms): \n");
                scanf("%f",&r2);
                a = r2;
        printf("Enter the load capacitance (pF): \n");
                scanf("%f",&c2);
        printf("Enter the air capacitance (pF): \n");
                scanf("%f",&cair);
        printf("Enter the offset capacitance (pF): \n");
                scanf("%f",&coff);
```

```
        printf("Enter the tolerance for the parameter estimation: \n");
                scanf("%f",&tol);
        printf("Enter the maximum number of iterations: \n");
                scanf("%d",&nmax);
        printf("Minimum phase required for conductivity: \n");
                scanf("%d",&minph);
/*
        get the header data from the input file
*/
        while((junk=fgetc(fpses)!=','));
        fscanf(fpses,"%f,%d,%d,%d,%d,%d",&ch,&year,&month,&day,&hour,&minute);
        while((junk=fgetc(fpses))!=EOL);
        for(n=0;((junk=fgetc(fpses))!=EOF) && (n!=MAX);++n) {
                junk=fgetc(fpses);
                while((junk!=',') && (junk!=']')) {
                        junk=fgetc(fpses);
                        }
                if (junk==',') {
                fscanf(fpses,"%f,%f,%f,%f,%f",&ch,&f[n],&g[n],&p[n],&o[n]);
                }
                while((junk=fgetc(fpses))!=EOL);
                }
        n-=1;
        fclose(fpses);
        printf("Done reading the input file ... %d data points.\n",n);
        fflush(stdout);
/*
        perform a parameter estimation for a parallel R1 C1
        assumes a functional form of f = (Zr-a)^2 + (Zi-b)^2 - c^2
        where Zr and Zi are measured values and the estimation is for
        a, b, and c.  Ideally, b=0 and c=a.  Then a=r1/2.
                ONLY a ESTIMATED NOW.
        The value of C1 is obtained from the high frequency gain,
        assuming that the phase is near zero.
*/
        printf("Performing parameter estimation for the data ... \n");
        fflush(stdout);
        ni = 0;
        do {
                nm = dn = 0.;
                for (i=0;i<n;++i) {
                        dt = 2.*PI*pow(10,f[i])*r2*c2*1.e-3;
                        dg = pow(10,-g[i]/20.);         /* dg is inverse*/
                        dp = p[i]*PI/180.;
                        z1r = r2*(dg*cos(dp)-1-dt*dg*sin(dp))/(1+dt*dt);
                        z1i = -r2*(dt*(dg*cos(dp)-1)+dg*sin(dp))/(1+dt*dt);
                        fi = (z1r-a)*(z1r-a) + z1i*z1i - a*a;
                        dfida = -2.*z1r;
                        nm+= dfida * fi;
                        dn+= dfida * dfida ;
                        }
                da = -nm/dn;
                a+=da;
```

```
                printf("Iteration %d: a= %f, da= %f\n",++ni,a,da);
                fflush(stdout);
                }
                while (fabs(da/a) > tol && ni < nmax);
        d = c2/(pow(10,-g[1]/20.)-1.);
        printf(" ... estimation done \n");
        fflush(stdout);
/*
        write out the raw data
*/
        printf("Writing %s ...",fout1);
        fflush(stdout);
        fpo1 = fopen(fout1,"w");
        fprintf(fpo1,"window \n frame suppress \n");
        fprintf(fpo1,"title top \"Raw gain-phase data\"\n");
        fprintf(fpo1,"label top \"date: %d/%d/%d \"\n ",month,day,year);
        fprintf(fpo1,"text over 0.1 right 0.3 size 0.07 \"file: %s\"\n",fout1);
        fprintf(fpo1,"label bottom \"log(freq)\"\n");
        fprintf(fpo1,"window vertical 1/3 horizontal 135/140\n");
        fprintf(fpo1,"label left \" Gain (dB)\" \n");
        fprintf(fpo1,"label right \"R1: %2.2f (G\\Omega)\"\n",2*a);
        fprintf(fpo1,"plot green cross marker 0.08\n");
        for (i=0;i<n;++i)
                fprintf(fpo1," %f %f \n",f[i], g[i]);
        fprintf(fpo1,"plot green spline\n");
        x = 2*a/r2;
        y = d/c2;
        for (i=0;i<n;++i) {
                dt = 2.*PI*pow(10,f[i])*r2*c2*1.e-3;
                d1 = 1+x+dt*dt*x*x*y*(1+y);
                d2 = dt*x*(x*y-1);
                dn = (1+x)*(1+x)+dt*dt*x*x*(1+y)*(1+y);
                nm = sqrt(d1*d1+d2*d2);
                fprintf(fpo1," %f %f \n",f[i],20*log10(nm/dn));
                }
        fprintf(fpo1,"window vertical 1/3 horizontal 135/140\n");
        fprintf(fpo1,"label left \" Phase (deg)\" \n");
        fprintf(fpo1,"label right \"C1: %2.2f (pf)\"\n",d);
        fprintf(fpo1,"plot green cross marker 0.08\n");
        for (i=0;i<n;++i)
                fprintf(fpo1," %f %f \n",f[i], p[i]);
        fprintf(fpo1,"plot green spline\n");
        for (i=0;i<n;++i) {
                dt = 2.*PI*pow(10,f[i])*r2*c2*1.e-3;
                d1 = 1+x+dt*dt*x*x*y*(1+y);
                d2 = dt*x*(x*y-1);
                dn = (1+x)*(1+x)+dt*dt*x*x*(1+y)*(1+y);
                nm = sqrt(d1*d1+d2*d2);
                fprintf(fpo1," %f %f \n",f[i],180*atan(d2/d1)/PI);
                }
        fprintf(fpo1,"window vertical 1/3 horizontal 135/140\n");
        fprintf(fpo1,"label left \" Offset (mV)\" \n");
        fprintf(fpo1,"plot green cross marker 0.08 \n");
```

```
        for (i=0;i<n;++i)
                fprintf(fpo1," %f %f \n",f[i], 1000.*o[i]);
        fclose(fpo1);
        printf(" done\n");
        fflush(stdout);
/*
        write out the imaginary vs real part of impedance for test cell
*/
        printf("Writing %s ...",fout2);
        fflush(stdout);
        fpo2 = fopen(fout2,"w");
        fprintf(fpo2,"window \n frame suppress \n");
        fprintf(fpo2,"title top \"Test cell impedance (real,-imaginary)\"\n");
        fprintf(fpo2,"label top \"date: %d/%d/%d \"\n ",month,day,year);
        fprintf(fpo2,"text over 0.1 right 0.3 size 0.07 \"file: %s\"\n",fout2);
        fprintf(fpo2,"window vertical 1/2 horizontal 3/4\n");
        fprintf(fpo2,"label left \" - Z_{imag} (G\\Omega)\" \n");
        fprintf(fpo2,"label bottom \" Z_{real} (G\\Omega)\" \n");
        fprintf(fpo2,"label right \"R1: %2.2f (G\\Omega)\"\n",2*a);
        fprintf(fpo2,"x axis hard scale 0.0 %2.2f \n",2*a);
        fprintf(fpo2,"y axis hard scale 0.0 %2.2f \n",2*a);
        fprintf(fpo2,"plot green cross marker 0.08 \n");
        for (i=0;i<n;++i) {
                dt = 2.*PI*pow(10,f[i])*r2*c2*1.e-3;
                dg = pow(10,-g[i]/20.);         /* dg is inverse*/
                dp = p[i]*PI/180.;
                z1r = r2*(dg*cos(dp)-1-dt*dg*sin(dp))/(1+dt*dt);
                z1i = -r2*(dt*(dg*cos(dp)-1)+dg*sin(dp))/(1+dt*dt);
                fi = (z1r-a)*(z1r-a) + z1i*z1i - a*a;
                fprintf(fpo2," %f %f \n",z1r,-z1i);
                }
        fprintf(fpo2,"plot green spline \n");
        for (i=0;i<50;++i) {
                z1r = a+a*cos(PI*i/50.);
                z1i = sqrt(a*a - (z1r-a)*(z1r-a));
                fprintf(fpo2," %f %f \n",z1r,z1i);
                }
        fclose(fpo2);
        printf(" done\n");
        fflush(stdout);
/*
        write to the resistance and capacitance file
*/
        for (i=0;i<n;++i) {
                dt = 2.*PI*pow(10,f[i])*r2*c2*1.e-3;
                dg = pow(10,g[i]/20.);
                dp = p[i]*PI/180.;
                c1[i] = c2*dg*(cos(dp)-dg+sin(dp)/dt)/(1+dg*dg-2*dg*cos(dp));
/*
        assume low conductivities so that high frequency phase should be zero
*/
                if (fabs(p[i]) > minph)
                  r1[i]=r2*(1+dg*dg-2*dg*cos(dp))/(dg*(cos(dp)-dg-dt*sin(dp)));
```

```
        else
          r1[i] = 0.;
        }
    d1 = cair - coff;
    printf("   high freq. permittivity: %3.2f\n",(d-coff)/d1);
    printf("   all data conductivity: %3.2f pS/m\n",0.5e15*Eo/(a*d1));
    printf("   0.1 Hz conductivity:   %3.2f pS/m\n",1.e15*Eo/(r1[50]*d1));
    printf("Writing %s ...",fout3);
    fflush(stdout);
    fpo3 = fopen(fout3,"w");
    fprintf(fpo3,"window \n frame suppress \n");
    fprintf(fpo3,"title top \"Calculated impedance parameters\"\n");
    fprintf(fpo3,"label top \"date: %d/%d/%d \"\n ",month,day,year);
    fprintf(fpo3,"text over 0.1 right 0.3 size 0.07 \"file: %s\"\n",fout3);
    fprintf(fpo3,"label bottom \"log(freq)\"\n");
    fprintf(fpo3,"window vertical 1/2 horizontal 135/140\n");
    fprintf(fpo3,"label left \" \\cross  C1 (pF)\" \n");
    fprintf(fpo3,"label right \" \\circle  R1 (G\\Omega)\" \n");
    fprintf(fpo3,"plot green cross marker 0.08 \n");
    for (i=0;i<n;++i)
        if (c1[i] > 0.)
            fprintf(fpo3," %f %f \n",f[i], c1[i]);
    fprintf(fpo3,"plot green line \n");
        fprintf(fpo3," %f %f \n",f[0],d);
        fprintf(fpo3," %f %f \n",f[n-1],d);
    fprintf(fpo3,"plot green circles marker 0.08 use right \n");
    for (i=0;i<n;++i)
        if (r1[i] > 0.)
            fprintf(fpo3," %f %f \n",f[i], r1[i]);
    fprintf(fpo3,"plot green line use right\n");
        fprintf(fpo3," %f %f \n",f[0],2*a);
        fprintf(fpo3," %f %f \n",f[n-1],2*a);
/*
    the permittivity and conductivity section
*/
    fprintf(fpo3,"window vertical 1/2 horizontal 135/140\n");
    fprintf(fpo3,"label left \" \\cross  \\epsilon/\\epsilon_o\" \n");
    fprintf(fpo3,"label right \" \\circle  \\sigma (pS/m) \" \n");
    fprintf(fpo3,"text over -0.2 right 0.5 size 0.09");
    fprintf(fpo3," \"\\epsilon_r = %2.2f\"\n",(d-coff)/d1);
    fprintf(fpo3,"text over -0.4 right 0.5 size 0.09");
    fprintf(fpo3," \"\\sigma = %2.2f pS/m\"\n",0.5e15*Eo/(a*d1));
    fprintf(fpo3,"y axis scale 1. 1. \n");
    fprintf(fpo3,"plot green cross marker 0.08 \n");
    for (i=0;i<n;++i)
        if (c1[i] > 0.)
            fprintf(fpo3,"%f %f\n",f[i], (c1[i]-coff)/d1);
    fprintf(fpo3,"plot green circles marker 0.08 use right \n");
    for (i=0;i<n;++i)
        if (r1[i] > 0. && r1[i] > 0.1*a)
            fprintf(fpo3,"%f %f\n",f[i], 1.e15*Eo/(r1[i]*d1));
    fclose(fpo3);
    printf(" done\n");
```

```
        fflush(stdout);
/*
        write protect the output files
*/
        sprintf(protec, "chmod a=r %s", fout1);
        system(protec);
        fflush(stdout);
        sprintf(protec, "chmod a=r %s", fout2);
        system(protec);
        fflush(stdout);
        sprintf(protec, "chmod a=r %s", fout3);
        system(protec);
        fflush(stdout);
        printf("prc finished\n");
        fflush(stdout);
}
```

```
/*****************************************************************

                          prcc.c

                          3/20/92


This program is used to calculate the effective impedance of a test
cell from a frequency scan of the gain and phase as measured by the
Otten box and logged through kermit.  The impedance is fit to a three
element lumped parameter circuit, composed of a capacitor in series
with the parallel combination of a resistor and capacitor.  For
example, the parallel elements could correspond to the bulk properties
of a fluid while the series capacitor would be the double layer
capacitance.  The medium permittivity is estimated from the high
frequency gain (capacitance) assuming the phase is zero.  The medium
condnctivity and Debye length are then calculated at a low frequency
(the third to last frequency taken, typically 0.01 Hz).  The
permittivity, conductivity, and Debye length are then used to
calculated the effective resistances and capacitances.  It is assumed
in this program that the software for the MCM is Version 1.4.

Usage: prcc [filein]

Outpnt files:
   filein.p1    Plots the raw data (gain, phase, and offset voltage)
                versus the freuquency.  Also plotted is the model
                response using the estimated resistance and
                capacitances.
   filein.p2    Plots the real and imaginary parts of the measured
                impedance in the form of a Col-Cole plot.  Also
                plotted is the model response using the estimated
                resistance and capacitances. The estimated resistance,
                capacitances, permittivity, conductivity, and Debye
                length are also listed. A second plot gives the
                calculated conductivity and Debye length at each
                frequency.

 *****************************************************************/

# include       <stdio.h>
# include       <math.h>
# define        GAP       1.52E-3         /* air-gap capacitor plate spacing */
# define        PI        3.14159265      /* PI */
# define        Eo        8.854e-12       /* permittivity of free space*/
# define        EOL      '\n'             /* end of line definition */
# define        MAX      5000             /* maximum number of data points */

char    fileses[] = "session.log";
float   f[MAX],g[MAX],p[MAX],o[MAX];
float   sig[MAX],lam[MAX];

main(argc, argv)
```

```
int     argc;
char    *argv[];

{
        int     i,j,n,ni,nmax;
        int     year,month,day,hour,minute;
        float   ch,dt,jk,minph;
        float   sigma,perm,lambda,c2,cair,r2,d1,d2,dg,dp,z1i,z1r;
        float   fr,r1t,c1t,cdlt;
        char    head[5],fout1[11],fout2[11],fout3[11],protec[21],junk;
        FILE    *fpses,*fopen(),*fpo1,*fpo2,*fpo3;
/*
        open files
*/
        if (argc > 1) {
           strcpy(fileses,argv[1]);
           if ((fpses = fopen(fileses,"r")) == NULL) {
              printf("Error: cannot open %s\n",fileses);
              exit(1);
              }
           }
        else {
           if ((fpses = fopen(fileses,"r")) == NULL) {
              printf("Enter data file name: \n");
              scanf("%s",fileses),
              }
           if ((fpses = fopen(fileses,"r")) == NULL) {
              printf("Error: cannot open %s\n",fileses);
              exit(1);
              }
           }
/*
        determine the output file names and check if they are valid
*/
        strcpy(fout1, fileses);
        strcat(fout1, ".p1");
        strcpy(fout2, fileses);
        strcat(fout2, ".p2");
        if ((fpo1 = fopen(fout1,"r")) != NULL ||
            (fpo2 = fopen(fout2,"r")) != NULL) {
              printf("\nDanger: One of the plot files already exists\n");
              exit(1);
              }
        fflush(stdout);
/*
        get the calibration information
*/
        printf("Enter the load resistance (Gohms): \n");
                scanf("%f",&r2);
                r2 *= 1.e9;
        printf("Enter the load capacitance (pF): \n");
                scanf("%f",&c2);
                c2 *= 1.e-12;
```

```
        printf("Enter the air capacitance (pF): \n");
                scanf("%f",&cair);
                cair *= 1.e-12;
        printf("Minimum phase required for conductivity and lambda: \n");
                scanf("%f",&minph);
/*
        get the header data from the input file
*/
        while((junk=fgetc(fpses)!=','));
        fscanf(fpses,"%f,%d,%d,%d,%d,%d",&ch,&year,&month,&day,&hour,&minute);
        while((junk=fgetc(fpses))!=EOL);
        for(n=0;((junk=fgetc(fpses))!=EOF) && (n!=MAX);++n) {
                junk=fgetc(fpses);
                while((junk!=',') && (junk!=']')) {
                        junk=fgetc(fpses);
                        }
                if (junk==',') {
                fscanf(fpses,"%f,%f,%f,%f,%f",&ch,&f[n],&g[n],&p[n],&o[n]);
                }
                while((junk=fgetc(fpses))!=EOL);
                }
        n-=1;
        fclose(fpses);
        printf("Done reading the input file ... %d data points.\n",n);
        fflush(stdout);
/*
        get high frequency permittivity and low frequency Debye
        length and conductivity
*/
        dg = pow(10,-g[1]/20.);
        perm = c2 / (cair * (dg - 1.));
        dg = pow(10,-g[n-4]/20.);
        dp = PI * p[n-4] / 180.;
        dt = 2.*PI*pow(10,f[n-4])*r2*c2;
        z1r = r2* ( (dg*cos(dp)-1.) - dt*dg*sin(dp)) / (1. + dt*dt);
        z1i = -r2*(dg*sin(dp) + dt*(dg*cos(dp)-1.)) / (1. + dt*dt);
        dt = 2.*PI*pow(10,f[n-4])*perm*cair;
        sigma = (1. + dt*z1i) * Eo / (z1r * cair);
        lambda = - dt * (z1i + dt*z1r*z1r / (1.+dt*z1i)) / 2.;
        printf(" permittivity: %3.2f\n",perm);
        printf(" conductivity: %3.2f\n",sigma*1.e12);
        printf(" lambda_D    : %3.2f\n",GAP*lambda*1.e6);
        c1t = cair * perm / (c2*(1. - 2. * lambda));
        cdlt = cair * perm / (c2* lambda);
        r1t = Eo * (1. - 2. * lambda) / (r2 * sigma * cair);
/*
        write out the raw data
*/
        printf("Writing %s ...",fout1);
        fflush(stdout);
        fpo1 = fopen(fout1,"w");
        fprintf(fpo1,"window \n frame suppress \n");
        fprintf(fpo1,"title top \"Raw gain-phase data\"\n");
```

```
        fprintf(fpo1,"label top \"date: %d/%d/%d \"\n ",month,day,year);
        fprintf(fpo1,"text over 0.1 right 0.3 size 0.07 \"file: %s\"\n",fout1);
        fprintf(fpo1,"label bottom \"log(freq)\"\n");
        fprintf(fpo1,"window vertical 1/3 horizontal 135/140\n");
        fprintf(fpo1,"label left \"Gain (dB)\" \n");
        fprintf(fpo1,"plot green cross marker 0.08\n");
        for (i=0;i<n;++i)
                fprintf(fpo1," %f %f \n",f[i], g[i]);
        fprintf(fpo1,"plot green spline\n");
        for (i=0;i<n;++i) {
                dt = 2.*PI*pow(10,f[i])*r2*c2;
                d1 = 1.+pow(dt*r1t*c1t,2);
                d2 = pow(1.+r1t+2*(1.+r1t*c1t)/cdlt,2) +
                pow(dt*r1t*(1.+c1t)+2.*(dt*dt*r1t*c1t-1)/(dt*cdlt),2);
                fprintf(fpo1," %f %f \n",f[i],10*log10(d1/d2));
                }
        fprintf(fpo1,"window vertical 1/3 horizontal 135/140\n");
        fprintf(fpo1,"label left \"Phase (deg)\" \n");
        fprintf(fpo1,"plot green cross marker 0.08\n");
        for (i=0;i<n;++i)
                fprintf(fpo1," %f %f \n",f[i], p[i]);
        fprintf(fpo1,"plot green spline\n");
        for (i=0;i<n;++i) {
                dt = 2.*PI*pow(10,f[i])*r2*c2;
                d1 = dt*r1t*c1t;
                d2 = (dt*r1t*(1.+c1t)+2.*(dt*dt*r1t*c1t-1)/(dt*cdlt))/(1.+r1t+2*(&
1.+r1t*c1t)/cdlt);
                fprintf(fpo1," %f %f \n",f[i],180.*(atan(d1)-atan(d2))/PI);
                }
        fprintf(fpo1,"window vertical 1/3 horizontal 135/140\n");
        fprintf(fpo1,"label left \"Offset (mV)\" \n");
        fprintf(fpo1,"plot green cross marker 0.08 \n");
        for (i=0;i<n;++i)
                fprintf(fpo1," %f %f \n",f[i], 1000.*o[i]);
        fclose(fpo1);
        printf(" done\n");
        fflush(stdout);
/*
        write out the imaginary vs real part of impedance for test cell
*/
        printf("Writing %s ...",fout2);
        fflush(stdout);
        fpo2 = fopen(fout2,"w");
        fprintf(fpo2,"window \n frame suppress \n");
        fprintf(fpo2,"title top \"Test cell impedance (real,-imaginary)\"\n");
        fprintf(fpo2,"label top \"date: %d/%d/%d \"\n ",month,day,year);
        fprintf(fpo2,"text over 0.1 right 0.3 size 0.07 \"file: %s\"\n",fout2);
        fprintf(fpo2,"window vertical 1/2 \n");
        fprintf(fpo2,"label left \" - Z_{imag} (G\\Omega)\" \n");
        fprintf(fpo2,"label bottom \" Z_{real} (G\\Omega)\" \n");
        fprintf(fpo2,"text over -0.2 left 1. size 0.1 ");
        fprintf(fpo2,"\"R1: %4.2f (G\\Omega)\"\n",r1t*r2*1.e-9);
        fprintf(fpo2,"text over -0.4 left 1. size 0.1 ");
```

```
        fprintf(fpo2,"\"C1: %4.2f (pF)\"\n",c1t*c2*1.e12);
        fprintf(fpo2,"text over -0.6 left 1. size 0.1 ");
        fprintf(fpo2,"\"C_{dl}: %4.2f (pF)\"\n",cdlt*c2*1.e12);
        fprintf(fpo2,"text over -0.8 left 1. size 0.1 ");
        fprintf(fpo2,"\"\\epsilon_r: %6.2f \"\n",perm);
        fprintf(fpo2,"text over -1.0 left 1. size 0.1 ");
        fprintf(fpo2,"\"\\sigma: %6.2f (pS/m)\"\n",1.e12*sigma);
        fprintf(fpo2,"text over -1.2 left 1. size 0.1 ");
        fprintf(fpo2,"\"\\lambda_D: %6.2f (\\mu m)\"\n",1.e6*GAP*lambda);
        fprintf(fpo2,"x axis hard scale 0.0 %2.2f \n",r1t*r2*1.e-9);
        fprintf(fpo2,"y axis hard scale 0.0 %2.2f \n",r1t*r2*1.e-9);
        fprintf(fpo2,"plot green cross marker 0.08 \n");
        for (i=0;i<n;++i) {
                dt = 2.*PI*pow(10,f[i])*r2*c2;
                dg = pow(10,-g[i]/20.);         /* dg is inverse*/
                dp = p[i]*PI/180.;
                z1r = r2*1.e-9*(dg*cos(dp)-1-dt*dg*sin(dp))/(1+dt*dt);
                z1i = -r2*1.e-9*(dt*(dg*cos(dp)-1)+dg*sin(dp))/(1+dt*dt);
                fprintf(fpo2," %f %f \n",z1r,-z1i);
                }
        fprintf(fpo2,"plot green line \n");
        for (i=0;i<n;++i) {
                fr = -2.3 + i/10.;
                dt = 2.*PI*pow(10,fr)*r2*c2;
                d1 = dt*r1t*c1t;
                z1r = r2*1.e-9*r1t/(1.+d1*d1);
                z1i = -r2*1.e-9*(2./(dt*cdl*) + r1t*d1/(1.+d1*d1));
                fprintf(fpo2," %f %f \n",z1r,-z1i);
                }
/*
        calculate the conductivity and Debye length data at each
        frequency and then write the information to the file.
        this calculation assumes that the permittivity is 2.19 for the oil
*/
        for (i=0;i<n;++i) {
                if (fabs(p[i]) > minph){
                        dg = pow(10,-g[i]/20.);
                        dp = PI * p[i] / 180.;
                        dt = 2.*PI*pow(10,f[i])*r2*c2;
                        z1r = r2*((dg*cos(dp)-1.)-dt*dg*sin(dp)) / (1.+dt*dt);
                        z1i = -r2*(dg*sin(dp)+dt*(dg*cos(dp)-1.)) / (1.+dt*dt);
                        dt = 2.*PI*pow(10,f[i])*perm*cair;
                        sig[i] = (1. + dt*z1i) * Eo / (z1r * cair);
                        lam[i] = - GAP*dt* (z1i+dt*z1r*z1r/(1.+dt*z1i)) / 2.;
                        }
                else {
                        sig[i] = 0.;
                        lam[i] = 0.;
                        }
                }
/*
        write to the file
*/
```

```
        fprintf(fpo2,"window vertical 1/2 horizontal 135/140\n");
        fprintf(fpo2,"label left \" \\cross  \\lambda_D (\\mu m)\" \n");
        fprintf(fpo2,"label right \" \\circle  \\sigma (pS/m) \" \n");
        fprintf(fpo2,"label bottom \"log(freq)\"\n");
        fprintf(fpo2,"y axis log\n z axis log\n");
        fprintf(fpo2,"plot green cross marker 0.08 \n");
        for (i=0;i<n;++i)
                if (lam[i] > 0. && lam[i] < 100.*lambda)
                        fprintf(fpo2,"%f %f\n",f[i], 1.e6*lam[i]);
        fprintf(fpo2,"plot green circles marker 0.08 use right \n");
        for (i=0;i<n;++i)
                if (sig[i] > 0. && sig[i] < 100.*sigma)
                        fprintf(fpo2,"%f %f\n",f[i], 1.e12*sig[i]);
        fclose(fpo2);
        printf(" done\n");
        fflush(stdout);
/*
        write protect the output files
*/
        sprintf(protec, "chmod a=r %s", fout1);
        system(protec);
        fflush(stdout);
        sprintf(protec, "chmod a=r %s", fout2);
        system(protec);
        fflush(stdout);
        printf("prcc finished\n");
        fflush(stdout);
}
```

# Bibliography

[1] S.M. Gasworth, J.R. Melcher, and M. Zahn, "Electrification Problems Resulting From Liquid Dielectric Flow," EL-4501, Project 1536-7, Electric Power Research Institute, April 1986.

[2] D.J. Lyon, J.R. Melcher, and M. Zahn, "Couette charger for measurement of equilibrium and energization flow electrification parameters: application to transformer insulation," *IEEE Transactions on Electrical Insulation*, Vol. 23, No. 1, pp. 159–176, February 1988.

[3] R.F. Probstein, *Physicochemical Hydrodynamics*, Butterworths, Boston, MA, 1989.

[4] Editors A. Klinkenberg and J.L. van der Minne, *Electrostatics in the Petroleum Industry*, Elsevier Publishing Company, New York, New York, 1958.

[5] J.T. Leonard, "Generation of Electrostatic Charge in Fuel Handling Systems: A Literature Survey," *NRL Report 8484*, September 1981.

[6] J.T. Leonard and H.F. Bogardus, "Pro-static Agents in Jet Fuels," *NRL Report 8021*, August 1976.

[7] A. Klinkenberg and B.V. Poulston, "Antistatic Additives in the Petroleum Industry," *Journal of the Institute of Petroleum*, Vol. 44, No. 419, pp. 379–389, November 1958.

[8] I. Ginsburgh, "The Static Charge Reducer," *Journal of Colloid and Interface Science.*, Vol. 32, No. 3, pp. 424–432, March 1970.

[9] N. Denbow and A.W. Bright, "The design and performance of novel on-line electrostatic charge-density monitors, injectors, and neutralisers for use in fuel systems," in *Electrostatics 1979*, The Institute of Physics, Techno House, Redcliffe Way, Bristol, England, 1979, pp. 171–180, Conference Series Number 48, Papers from the Fifth Conference on Electrostatic Phenomena.

[10] J.K. Nelson and M.J. Lee, "Tandem-chamber Charge Density Monitor," *IEEE Transactions on Electrical Insulation*, Vol. 25, No. 2, pp. 399–404, 1990.

[11] A.J. Morin II, M. Zahn, J.R. Melcher, and D.M. Otten, "An Absolute Charge Sensor for Fluid Electrification Measurements," *IEEE Transactions on Electrical Insulation*, Vol. 26, No. 2, pp. 181–199, 1991.

[12] A. Sierota and J. Rungis, "Electrostatic Charging Tendency in Transformer Oils: Testing and Assessment," *IEEE Transactions on Dielectrics and Electrical Insulation*, Vol. 1, No. 5, pp. 840–870, October 1994.

[13] D.W. Crofts, "The static electrification phenomena in power transformers," *IEEE Transactions on Electrical Insulation*, Vol. 23, No. 1, pp. 137–146, February 1988.

[14] S.R. Lindgren, A.P. Washabaugh, P.A. von Guggenberg, M. Zahn, M. Brubaker, and J.K. Nelson, "Temperature and Moisture Transient Effects on Flow Electrification in Power Transformers," in *Proceeding of the 1992 International Conference on Large High Voltage Electric Systems (CIGRE)*, 1992, Paris, France. Paper 15/12-02.

[15] L.J. Savio, "Ramapo Substation Westinghouse 500/345 kV, 1000 MVA Autotransformer Failure," in *EPRI Workshop Proceedings; Static Electrification in Power Transformers*, September 26–28, 1994.

[16] G. Arndt, "EPRI helps APS avoid Generator Step-Up Transformer Failures," Innovators with EPRI technology IN-101286, Electric Power Research Institute, January 1993.

[17] P.A. von Guggenberg, *Applications of Interdigital Dielectrometry to Moisture and Double Layer Measurements in Transformer Insulation*, PhD thesis, EECS Department, M.I.T., Cambridge, Mass., June 1993.

[18] D.W. Crofts, "Static Electrification Testing of Texas Utilities 345-20.9 kV, 650 MVA Generator Step-Up Transformer Under Controlled Factory Conditions," in *EPRI Workshop Proceedings; Static Electrification in Power Transformers*, September 26–28, 1994.

[19] W.N. Kennedy, "Examination of DC Stress Distribution due to Static Charge Accumulation in a Shell-Form Transformer," in *EPRI Workshop Proceedings; Static Electrification in Power Transformers*, September 26–28, 1994.

[20] Electric Power Research Institute, "Mini-Workshop on Static Electrification in Transformers," ABB Power T&D Company, Inc., Muncie, Indiana, Feb. 1993.

[21] H.R. Moore, "Review of recent transformer failures," preliminary report, Nov. 1992.

[22] T.V. Oommen, "Static Electrification Control in Power Transformers," Research Project 1499-7, Final Report EPRI EL-6081, Electric Power Research Institute, Dec. 1988.

[23] T.V. Oommen, "Static Electrification Properties of Transformer Oil," *IEEE Transactions on Electrical Insulation*, Vol. 23, No. 1, pp. 123–128, Feb. 1988.

[24] M.J. Lee, J.K. Nelson, and M.A. Franchek, "Electrification in Transformer Model Structures," in *EPRI Workshop Proceedings; Static Electrification in Power Transformers*, July 1990, pp. 4-1-1-4-1-12, EPRI EL-6918.

[25] A.J. Morin II, M. Zahn, and J.R. Melcher, "Fluid Electrification Measurements of Transformer Pressboard/Oil Insulation in a Couette Charger," *IEEE Transactions on Electrical Insulation*, Vol. 26, No. 5, pp. 870-901, 1991.

[26] H.P. Moser, Ch. Krause, G. Praxl, G. Spandonis, R. Stonitsch, and H. Brechna, "Influence of Transformerboard and Nomex Board on the Electrification of Power Transformers," in *EPRI Workshop Proceedings; Static Electrification in Power Transformers*, June 1993, pp. 2-2-1—2-2-18, EPRI TR-102480.

[27] P.J. Griffin and J. Christie, "Effects of Water and Benzotriazole on Electrostatic Charge Generation in Mineral Oil. Cellulose Systems," in *EPRI Workshop Proceedings; Static Electrification in Power Transformers*, June 1993, pp. 3-3-1—3-3-26, EPRI TR-102480.

[28] Aug. 1990, Personal communication, discussing papers only available in Japanese, between M. Higaki of The 2nd Dept., Hitachi Research Laboratory, Hitachi Ltd. and S. Lindgren of EPRI and forwarded to M. Zahn of MIT.

[29] M. Higaki, Y. Tsutsumi, H. Ohtani, and H. Tsukioka, "Consideration of the Measurement of Static Charges in Insulating Oil and the Influence of Oil Conductivity on the Charges," *Electrical Engineering in Japan*, Vol. 104, No. 5, pp. 9-17, 1984.

[30] M. Ieda, T. Yanari, T. Miyamoto, and M. Higaki, "Investigation of Static Electrification in Large Power Transformers in Japan," in *EPRI Workshop Proceedings; Static Electrification in Power Transformers*, June 1993, pp. 2-3-1—2-3-31, EPRI TR-102480.

[31] P. Li, *Low Frequency, Millimeter Wavelength, Interdigitated Dielectrometry of Insulating Media in a Transformer Environment*, Master's thesis, Department of Electrical Engineering, M.I.T., Cambridge, Mass., June 1987.

[32] P.A. von Guggenberg and J.R. Melcher, "Moisture Dynamics in Paper/Oil Systems Subject to Thermal Transients," in *PSE&G/EPRI Workshop Proceedings: Static Electrification in Transformers*, July 1990, pp. 3-4-1—3-4-16, (Nov. 15-17, 1989, Princeton, NJ). EPRI Technical Report EL-6918.

[33] H. Miyao, M. Higaki, and Y. Kamata, "Influence of ac and dc fields on streaming electrification of transformer oil," *IEEE Transactions on Electrical Insulation*, Vol. 23, No. 1, pp. 129-135, February 1988.

[34] A. Kishi and Y. Miura, "Influence of AC Stress on Static Electrification in High Voltage Power Transformer," in *EPRI Workshop Proceedings; Static Electrification in Power Transformers*, June 1993, pp. 2-4-1—2-4-14, EPRI TR-102480.

[35] S. Mukherji, A.K. Adikesavulu, R. Rajaraman, D. Suryanarayana, T.S.R. Murthy, and K.N. Labh, "The Influence of Electrical Field on Flow Electrification of Transformer Oil," in *7th BEAMA International Electrical Insulation Conference*, Brighton, England, May 23–26 1994.

[36] Ch. Krause, E. Knoll, R. Stonitsch, and J-J. Alff, "Measurements Showing the Enhancement of Electrostatic Charging by AC-Voltage in a Duct Model and Full-Scale Power Transformer," in *EPRI Workshop Proceedings; Static Electrification in Power Transformers*, September 26–28, 1994.

[37] T. Miyamoto, A. Kishi, and Y. Miura, "Effect of Insulating Oils on Streaming Electrification in Transformer," in *EPRI Workshop Proceedings; Static Electrification in Power Transformers*, July 1990, pp. 3-2-1—3-2-12, EPRI EL-6918.

[38] A.J. Morin II, *Fluid Electrification Measurements of Transformer Pressboard/Oil Insulation in a Couette Charger Using an Absolute Charge Sensor*, Master's thesis, EECS Department, M.I.T., Cambridge, Mass., Sept. 1989.

[39] D.W. Crofts, "Addition of 'BTA' to Transformer Oil for Control of Static Electrification," in *EPRI Workshop Proceedings; Static Electrification in Power Transformers*, June 1993, pp. 3-4-1—3-4-4, EPRI TR-102480.

[40] P.J. Griffin and E. Finnan, "Assessment of Laboratory-Aged Insulating Materials using the Mini-Static Tester," in *EPRI Workshop Proceedings; Static Electrification in Power Transformers*, September 26–28, 1994.

[41] M.A. Sens, J.B. Fernandez, and R. Ficara, "Benzotriazol Effects in Electrostatic Kraft Paper/Oil Flow Model Experiments," in *EPRI Workshop Proceedings; Static Electrification in Power Transformers*, September 26–28, 1994.

[42] T.S.R. Murthy, Meenakshi, P.G. Agashe, and K.M. Kamath, "Studies of Electrostatic Charge Suppressants for Paraffinic Transformer Oils," in *7th BEAMA International Electrical Insulation Conference*, Brighton, England, May 23–26 1994.

[43] J.C. Dean, G.M. Williams, and J. DeGiovanni, "Analysis of Flow Electrification in Fuel Distribution Systems," *IEEE Transactions on Industry Applications*, Vol. 29, No. 3, May/June 1993.

[44] "Ford Must Correct 'World Cars' Problem Days Before Launch," The Wall Street Journal, B10:4, September 23, 1994.

[45] S.R. Foster and D.R. Capriotti, "A Survey of Performance Elastomers – Meeting Automotive Requirements of the '80s," *Society of Automotive Engineers*, 1984, Report 840408.

[46] M.J. Harrigan, "Design Considerations for Plastic Fuel Lines," *Society of Automotive Engineers*, 1988, Report 880683.

[47] V.G. Levich, *Physicochemical Hydrodynamics*, Prentice-Hall, New York, NY, 1962.

[48] D.R. Gabe, "The rotating cylinder electrode," *Journal of Applied Electrochemistry*, Vol. 4, pp. 91–108, 1974.

[49] D.R. Gabe and F.C. Walsh, "The rotating cylinder electrode: a review of development," *Journal of Applied Electrochemistry*, Vol. 13, pp. 3–22, 1983.

[50] J. Kedzia, "Measurement of the Electrification of Liquids in the Rotating Cylinder System," *Journal of Electrostatics*, Vol. 20, pp. 305–312, 1988.

[51] J. Kedzia, "Investigation of Transformer Oil Electrification in a Spinning Disk System," *IEEE Transactions on Electrical Insulation*, Vol. 24, No. 1, pp. 59–65, February 1989.

[52] R.M. Radwan, R.M. El-Dewieny, and I.A. Metwally, "Investigation of Static Electrification Phenomenon due to Transformer Oil Flow in Electric Power Apparatus," *IEEE Transactions on Electrical Insulation*, Vol. 27, No. 2, pp. 278–286, April 1992.

[53] J. Kedzia and B. Willner, "Electrification Current in the Spinning Disk System," *IEEE Transactions on Dielectrics and Electrical Insulation*, Vol. 1, No. 1, pp. 58–62, February 1994.

[54] P.K. Poovamma and R. Jagadish, "Influence of Surface Roughness and Thickness of Pressboard on the Charging Characteristics of Transformer Oil," in *Conference Record of the 1994 IEEE International Symposium on Electrical Insulation*, June 1994, pp. 5–8.

[55] K. Dwarakanath P.K. Poovamma, R. Jagadish, "Investigation on static electrification characteristics of transformer oil," *Journal of Electrostatics*, Vol. 33, pp. 1–14, 1994.

[56] J. Rungis, R.G. Heydon, and A. Sierota, "Electrostatic Charging Tendency of Aged Transformer Oils," in *EPRI Workshop Proceedings; Static Electrification in Power Transformers*, September 26–28, 1994.

[57] F.M. White, *Viscous Fluid Flow*, McGraw-Hill Book Company, New York, NY, 1974.

[58] M.C. Zaretsky, L. Mouayad, and J.R. Melcher, "Continuum Properties from Interdigital Dielectrometry," *IEEE Trans. on Elec. Ins.*, Vol. 23, No. 6, pp. 897–917, December 1988.

[59] P.A. von Guggenberg and J.R. Melcher, "An Immersible Relative Saturation Moisture Sensor with Application to Transformer Oil," in *Proceedings of the 3rd International Conference on Properties and Applications of Dielectric Materials*, July 1991, pp. 1258–1261.

[60] J.A. Kalt, *Absolute Charge Sensor Measurements of Flow Electrification in a Couette Charger*, Bachelor's thesis, EECS Department, M.I.T., Cambridge, Mass., May 1990.

[61] E.T. Norris, "High Voltage Power Transformer Insulation," *Proceedings IEE*, Vol. 110, No. 2, Feb. 1963.

[62] S.D. Foss, "Power Transformer Drying Model, Report DS-002-87," Technical Report, Dynamic Systems, Inc., Oittsfield, MA, October 1987, Prepared for the General Electric Company and the Consolidated Edison Corporation.

[63] R. Tamura, Y. Miura, T. Watanabe, T. Ishii, N. Yamada, and T. Nitta, "Static electrification by forced oil flow in large power transformers," *IEEE Trans. Power Apparatus and Systems*, Vol. 99, No. 1, pp. 335–343, 1980.

[64] J.O'M. Bockris and A.K.N. Reddy, *Modern Electrochemistry 2*, Third Edition, Plenum Publication Corp., New York, NY, 1970.

[65] W. Kennedy, "Resistivity of oil and pressboard insulation and their effect on transformer design," in *EPRI Workshop Proceedings; Static Electrification in Power Transformers*, June 1993, pp. 1-4-1—1-4-13, EPRI TR-102480.

[66] M. Zahn, *Electromagnetic Field Theory: a problem solving approach*, Reprint Edition, Kreiger, Malabar, Florida, 1987.

[67] R.G. Heydon, J. Rungis, and R. Sheehy, "The Use of Sintered Metal Filters in the Study of ECT in Transformer Oils," in *1992 Annual Report, Conference on Electrical Insulation and Dielectric Phenomena*, Oct. 1992, pp. 275–280.

[68] M.E. Furey, J.A. Palmer, and J.K. Nelson, "A New Reciprocating Apparatus for the Measurement of Electrostatic Charging Tendency of Transformer Oil," in *EPRI Workshop Proceedings; Static Electrification in Power Transformers*, Sept. 28–30 1994.

[69] M. Yasuda, K. Goto, H. Okubo, T.Ishii, E. Mori, and M. Masunaga, "Suppression of Static Electrification of Insulating Oil for Large Power Transformers," *IEEE Transactions on Power Apparatus and Systems*, Vol. 101, No. 11, pp. 4272–4280, Nov. 1982.

[70] Sept. 1994, Personal communication with N. Hosokawa of the Mitsubishi Electric Corp.

[71] R. Kappesser, I. Cornet, and R. Greif, "Mass Transfer to a Rough Rotating Cylinder," *Journal of the Electrochemical Society*, Vol. 118, No. 12, pp. 1957–1959, Dec. 1971.

[72] I. Adamczewski, *Ionization, Conduction, and Breakdown In Dielectric Liquids*, Taylor and Francis, London, 1969, pp. 224–225.

[73] "Diala A oil, Diala AX oil: Electrical insulating oils for rapid heat transmission with high oxidation stability," Technical Bulletin SOC:39-85, Shell Oil Company.

[74] P.W. Huber and A.A. Sonin, "Electric Charging in Liquid Hydrocarbon Filtration: A Comparison of Theory and Experiments," *Journal of Colloid and Interface Science*, Vol. 61, No. 1, pp. 126–145, 1977.

[75] G. Chiodelli and P. Lupotto, "Experimental Approach to the Impedance Spectroscopy Technique," *J. Electrochem. Soc.*, Vol. 138, No. 9, pp. 2703–2711, September 1991.

[76] U. Gafvert, H. Kols, and J. Marinko, "Simple method for determining the electric conductivity of dielectric liquids," in *Conf. Record of Nordic Insulation Conference*, June 9–11 1986, pp. 23:1–23:5, Helsinki, Finland.

[77] J.W. Lou, *Conduction and Electrification in Semi-Insulating Liquids*, Bachelor's thesis, EECS Department, M.I.T., Cambridge, Mass., June 1993.

[78] M. Zahn, *Dielectric Physics: Polarization, Conduction, and Electrical Breakdown*, Notes for MIT Course 6.973, 1987.

[79] P. Vanýsek, *Electrochemistry on Liquid/Liquid Interfaces*, Springer-Verlag, Berlin, 1985.

[80] A.K. Jonscher, *Dielectric Relaxation in Solids*, Chelsea Dielectrics Press, London, 1983.

[81] D.R. Day, T.J. Lewis, H.J. Lee, and S.D. Senturia, "The Role of Boundary Layer Capacitance at Blocking Electrodes in the Interpretation of Dielectric Cure Data in Adhesives," *J. Adhesion*, Vol. 18, pp. 73–90, 1985.

[82] T. Tanaka, Y. Yasojima, N. Yamada, A. Kishi, and T. Nitta, "Model approach to the static electrification phenomena induced by the flow of oil in large power transformers," *IEEE Trans. Power Apparatus and Systems*, Vol. 99, No. 3, pp. 1097–1105, 1980.

[83] H.A. Haus and J.R. Melcher, *Electromagnetic Fields and Energy*, Prentice Hall, Englewood Cliffs, New Jersey, 1989.

[84] Y. Sheiretov and M. Zahn, "A Study of the Temperature and Moisture Dependent Dielectric Properties of Oil-Impregnated Pressboard," in *Proceedings of the 1993 Conference on Electrical Insulation and Dielectric Phenomena*, Oct. 1993, pp. 487–492.

[85] Y. Sheiretov, *Dielectrometry Measurements of Moisture Dynamics in Oil-Impregnated Pressboard*, Master's thesis, EECS Department, M.I.T., Cambridge, Mass., May 1994.

[86] U. Gafvert and B. Nettelblad, "Measurement techniques for dielectric response characterisation at low frequencies," in *Conf. Record of Nordic Insulation Conference*, 1990, pp. 7.1:1–7.1:10.

[87] B. Nettelblad, "Effect of moisture content on the dielectric properties of cellulose," in *Conf. Record of Nordic Insulation Conference*, 1992.

[88] M. Zahn, "Drift-dominated conduction within an Ohmic medium," *J. Appl. Phys.*, Vol. 47, No. 7, pp. 3122–3126, Jul 1976.

[89] D.D. Ebbing, *General Chemistry, Second Edition*, Houghton Mifflin Company, Boston, MA, 1987, Chapter 15.

[90] J.C. Devins and S.J. Rzad, "Additive Solution to Electrification Problem in Astoria Station," Technical Report No. 81CRD149, General Electric Company, July 1981.

[91] J.R. Melcher, *Continuum Electromechanics*, M.I.T. Press, Cambridge, Mass., 1981.

[92] A.J. Grodzinsky, *Fields, Forces and Flows in Biological Tissues and Membranes*, Notes for MIT course 6.651, 1991.

[93] R.B. Bird, W.E. Stewart, and E.N. Lightfoot, *Transport Phenomena*, John Wiley & Sons, New York, NY, 1960.

[94] H.L. Walmsley and G. Woodford, "The generation of electric currents by the laminar flow of dielectric liquids," *J. Phys. D: Appl. Phys.*, Vol. 14, pp. 1761–1782, 1981.

[95] H.L. Walmsley, "The generation of electric currents by the turbulent flow of dielectric liquids: II. Pipes of finite length," *J. Phys. D: Appl. Phys.*, Vol. 16, pp. 553–572, 1983.

[96] E.I. Nikiforovich, V.V. Tolmachev, and G.A. Shaposhnikova, "Charging of a Low-Conductivity Liquid Flowing Through a Cylindrical Pipe with Allowance for the Finite Rate of a Surface Electrochemical Reaction," *Fluid Dynamics*, Vol. 18, No. 1, pp. 59–63, January-February 1983, Published by Plenum Publishing Corporation.

[97] F.M. White, *Fluid Mechanics*, McGraw-Hill Book Company, New York, NY, 1979.

[98] F.B. Hildebrand, *Advanced Calculus for Applications, Second Edition*, Prentice-Hall, Inc., Englewood Cliffs, N.J., 1976, Sections 4.12 and 5.14.

[99] B. Abedian and A.A. Sonin, "Theory for electric charging in turbulent pipe flow," *J. Fluid Mech.*, Vol. 120, pp. 199–217, 1982.

[100] R.N. Smith and R. Greif, "Turbulent Transport to a Rotating Cylinder for Large Prandtl or Schmidt Numbers," *J. Heat Trans.*, pp. 594–597, Nov. 1975.

[101] J. Grifoll, X. Farriol, and F. Giralt, "Mass transfer at smooth and rough surfaces in a circular Couette flow," *Int. J. Heat Mass Transfer*, Vol. 29, No. 12, pp. 1911–1918, 1986.

[102] T.K. Sherwood and J.M. Ryan, "Mass transfer to a turbulent fluid with and without chemical reaction," *Chemical Engineering Science*, Vol. 11, No. 2, pp. 81–91, 1959.

[103] T. Theodorsen and A. Regier, "Experiments on drag of revolving disks, cylinders, and streamline rods at high speeds," Technical Report 793, NACA, 1944.

[104] M. Eisenberg, C.W. Tobias, and C.R. Wilke, "Ionic Mass Transfer and Concentration Polarization at Rotating Electrodes," *Journal of the Electrochemical Society*, Vol. 101, No. 6, pp. 306–319, June 1954.

[105] G.I. Taylor, "Fluid Friction Between Rotating Cylinders, Part I. Torque Measurements," *Proceedings of the Royal Society*, Vol. CLVII, pp. 546–564, 1936.

[106] G.P. Smith and A.A. Townsend, "Turbulent Couette flow between concentric cylinders at large Taylor numbers," *J. Fluid Mech.*, Vol. 123, pp. 187–217, 1982.

[107] D.R. Gabe and D.J. Robinson, "Mass transfer in a rotating cylinder cell – II. turbulent flow," *Electrochimica Acta*, Vol. 17, pp. 1129–1137, 1972.

[108] J. Gavis and I. Koszman, "Development of charge in low-conductivity liquids flowing past surfaces: a theory of the phenomenon in tubes," *J. Colloid Science*, Vol. 16, pp. 375–391, 1961.

[109] I. Koszman and J. Gavis, "Development of charge in low-conductivity liquids flowing past surfaces," *Chem. Eng. Sci.*, Vol. 17, pp. 1013–1022, 1962.

[110] J. Gavis, "Transport of electric charge in low dielectric constant fluids," *Chem. Eng. Sci.*, Vol. 19, pp. 237–252, 1964.

[111] J.S. Newman, *Electrochemical Systems*, Prentice-Hall, Inc., Englewood Cliffs, N.J., 1973.

[112] B. Abedian and A.A. Sonin, "Electric Currents Generated by Turbulent Flows of Liquid Hydrocarbons in Smooth Pipes: Experiment vs. Theory," *Chemical Engineering Science*, Vol. 41, No. 12, pp. 3183–3189, 1986.

[113] H. Romat, G. Touchard, and O. Moreau, "Flow electrification in power transformers," in *EPRI Workshop Proceedings; Static Electrification in Power Transformers*, September 26–28, 1994.

[114] G.G. Touchard, T.W. Patzek, and C.J. Radke, "A Physicochemical explanation for flow electrification in low conductivity liquids," in *Proceedings of the 1994 IEEE Industry Application Society meeting*, October 2–6 1994.

[115] G.W. Castellan, *Physical Chemistry*, Addison Wellesley, Reading, MA, 1983, Chapter 34.

[116] R.E. Safford and J.B. Bassingthwaighte, "Calcium Diffusion in Transient and Steady States in Muscle," *Biophysical Journal*, Vol. 20, 1977.

[117] L.B. Schein, *Electrophotography and Development Physics*, Springer-Verlag, New York, NY, 1992.

[118] A. Many, Y. Goldstein, and N.B. Grover, *Semiconductor Surfaces*, North-Holland Publishing Company, Amsterdam, 1965.

[119] L. Onsager, "Deviations from Ohm's Law in Weak Electrolytes," *Journal of Chemical Physics*, Vol. 2, pp. 599–615, 1934.

[120] D.A. Edwards, H. Brenner, and D.T. Wasan, *Interfacial Transport Processes and Rheology*, Butterworth-Heinemann, Boston, MA, 1991.

[121] J.F. Roach and J.B. Templeton, "An Engineering Model for Streaming Electrification in Power Transformers," in *Electrical Insulating Oils, STP 998*, H.G. Erdman, Editor, American Society for Testing and Materials, Philadelphia, 1988, pp. 119–135.

[122] M. Higaki, Y. Kako, M. Moriyama, M. Hirano, K. Hiraishi, and K. Kurita, "Static electrification and partial discharges caused by oil flow in forced oil cooled core type transformers," *IEEE Trans. Power Apparatus and Systems*, Vol. 98, No. 4, pp. 1259–1267, 1979.

[123] M. Higaki, H. Miyao, K. Endou, and H. Ohtani, "A calculation of potential distribution caused by static electrification owing to oil flow in a oil-paper insulation system and it's application to partial discharge phenomena in oil," *IEEE Trans. Power Apparatus and Systems*, Vol. 98, No. 4, pp. 1275–1282, 1979.

[124] J.T. Leonard and H.W. Carhart, "Effect of Conductivity on Charge Generation in Hydrocarbon Fuels Flowing through Fiber Glass Filters," *Journal of Colloid and Interface Science*, Vol. 32, No. 3, pp. 383–394, March 1970.

[125] M. Arimoto, A. Ohashi, and M. Ueda, "A New Method for Reduction of Static Charge in Oil Flowing in Pipeline," *Electrical Engineering in Japan*, Vol. 106, No. 2, pp. 31–37, 1986.

[126] P.W. Huber and A.A. Sonin, "Theory for Electric Charging in Liquid Hydrocarbon Filtration," *Journal of Colloid and Interface Science*, Vol. 61, No. 1, pp. 109–125, 1977.

[127] W.M. Siebert, *Circuits, Signals, and Systems*, McGraw-Hill, New York, NY, 1986.

[128] E. Howells, M. Zahn, and S.R. Lindgren, "Static Electrification Effects in Transformer Oil Circulating Pumps," *IEEE Trans. Power Devices*, Vol. 5, pp. 1000–1006, April 1990.

[129] E. Howells, "External Static Electrification in Power Transformers," in *EPRI Workshop Proceedings; Static Electrification in Power Transformers*, July 1990, pp. 4-4-1—4-4-6, EPRI EL-6918.

[130] A.P. Washabaugh, M. Zahn, and J.R. Melcher, "Enhanced Electrification Charge Densities due to Recirculatory Flow," in *Proceedings of the 3rd International Conference on Properties and Applications of Dielectric Materials*, July 1991, pp. 272–275.

[131] M.A. Brubaker and J.M. Walden, "A Methodology for Quantifying Streaming Electrification Based on the Charging Tendency of Solid/Liquid Insulation Combinations," in *EPRI Workshop Proceedings; Static Electrification in Power Transformers*, September 26–28, 1994.

[132] A.P. Washabaugh and M. Zahn, "Flow Electrification Measurements in a Couette Flow Facility," in *IEEE International Symposium on Electrical Insulation*, June 1994, Pittsburgh, PA.

[133] A.P. Washabaugh and M. Zahn, "Terminal Voltage and Current Measurements due to Flow Electrification," in *4th International Conference on Properties and Applications of Dielectric Materials*, July 1994, Brisbane, Australia.

[134] Nov. 1992, Personal communication between N. Hosokawa of the Mitsubishi Electric Corp. and Prof. J.K. Nelson of RPI and forwarded to A.P. Washabaugh.

[135] G.J. Shugar and J.T. Ballinger, *Chemical Technicians' Ready Reference Handbook, Third Edition*, McGraw-Hill, Inc., New York, NY, 1990.

[136] P.J. Griffin, "Materials Laboratory Services Report No. C-22600," Technical Report, Doble Engineering Company, 85 Walnut St, Watertown, MA, May 1994.

[137] W.B. Gish and S. Nilsson, "Static Electrification Monitoring on Union Electric Mason Substation Transformer," in *EPRI Workshop Proceedings; Static Electrification in Power Transformers*, Sept. 28–30 1994.

[138] P.M. Morse and H. Feshbach, *Methods of Theoretical Physics*, McGraw-Hill Book Company, Inc., 1953, Part II, Appendix to Chapter 10.

[139] H.L. Walmsley, "The generation of electric currents by the turbulent flow of dielectric liquids: I. Long pipes," *J. Phys. D: Appl. Phys.*, Vol. 15, pp. 1907–1934, 1982.

[140] E.M. Sparrow and S.H. Lin, "Flow Development in the Hydrodynamic Entrance Region of Tubes and Ducts," *The Physics of Fluids*, Vol. 7, No. 3, pp. 338–347, March 1964.

[141] P.M. Gerhart and R.J. Gross, *Fundamentals of Fluid Mechanics*, Addison-Wesley Publishing Company, Reading, Mass., 1985.

[142] M. Abramowitz and I.A. Stegun, *Handbook of Mathematical Functions*, Dover Publications, Inc., New York, NY, 1965, ninth printing.

[143] C.M. Bender and S.A. Orszag, *Advanced Mathematical Methods for Scientists and Engineers*, McGraw-Hill Book Company, New York, NY, 1978.

[144] MINPACK subroutines are available at the electronic mail address: netlib@ornl.gov.